Single-Particle Tracking of the Human Epidermal Growth Factor Receptors (HER) 1-3 in a Breast Cancer Model: the Effect of Tyrosine Kinase Inhibitors

Zanetti Domingues, Laura Carolina

Awarding institution:
King's College London

Single-Particle Tracking of the Human Epidermal Growth Factor Receptors (HER) 1-3 in a Breast Cancer Model: the Effect of Tyrosine Kinase Inhibitors

Laura Carolina Zanetti Domingues

1048628

PhD thesis

Academic Year 2014

Division of Cancer Studies

King's College

University of London

Science & Technology
Facilities Council

This thesis is dedicated to the memory of

Elsa Rossi (01/09/1932-21/06/2013),

Grandmother extraordinaire and breast cancer survivor,

who was always proud of my academic achievements and whose company I missed in her final years because of this project.

Declaration

I hereby declare that the work presented in this thesis is the result of my own investigations and has not been accepted in a previous application for a degree.

Abstract

Over-expression and mutational activation of the Human Epidermal Growth Factor Receptor (HER) 1-4 receptor family are implicated in tumorigenesis and cancer progression. Perturbations of their associated signalling cascades and feed-back loops can amplify aberrant signalling. Inhibition of these signals is a central objective of anti-cancer targeted therapeutics, but to date most drugs have limited success. The reasons are not understood and underscore a lack of understanding of the molecular basis of receptor signalling and drug action. At the heart of these processes are combinatorial interactions leading to receptor homo- and hetero-dimerization To characterise the interactions between HER family homo- and hetero-dimers in basal and activated states, receptors were labelled in their non-active configuration with Affibodies conjugated to fluorophores or activated by fluorescently-tagged ligands. This will enable future application of the method to primary samples.

Cell culture substrates and fluorescent dyes were optimised to reduce the incidence of non-specific probe adhesion and a set of parameters to guide the choice of fluorescent dyes for Single-Molecule applications was determined. Alexa Fluor 488- and CF640R- tagged probes were used for pairwise live-cell tracking of HER1-3 receptors in presence or absence of clinical-grade tyrosine kinase inhibitors. These experiments highlighted the role of tyrosine kinase activity in determining HER1 diffusion at the plasma membrane and likelihood of interaction. Activated HER1 homo-interactions and hetero-interactions with HER2 were the predominant colocalisation pairs identified. Precise determination of the dwell-time distribution of all pairs is pending and will require more precise assessment of photobleaching lifetime contaminations and denoising.

Analysis of the diffusion of HER1 with a novel, globally-optimised Bayesian tracking algorithm developed by Dr Wareham (University of Cambridge) revealed the presence of two populations of receptors characterised by their directional motion components. The most directional population depends on the presence of an intact actin cytoskeleton and on tyrosine kinase activity.

The methods presented in this thesis, will be extended to study the dynamics and kinetics of the whole HER family, laying the foundations for the construction of a quantitative model of the system.

Rationale

The aim of this project is to study the pattern of combinatorial interactions and activation of the HER family of receptors on live cells with a Single-Molecule microscopy system, in order to investigate the dynamic and kinetic parameters of receptor homo- and hetero-interactions in presence or absence of perturbations such as Tyrosine Kinase Inhibitors (TKI).

The focus is on HER1-3, which are particularly relevant to cancer, while the role of HER4 in this setting is more controversial, and on clinically relevant inhibitors such as Lapatinib and Erlotinib, in order to characterise receptor interactions and perturbations of the HER family signalling system which might be relevant for patient care. **Chapter I** will detail background information on the HER family and on the Single-Molecule techniques employed throughout the project.

In order to achieve these programmatic aims, a model breast cancer cell line where all four HER family receptors are expressed at low "physiological" levels was selected, and the receptors were labelled with small ligands tagged with organic dyes, in order to be able to get as much population coverage as possible, without saturating the Single-Molecule detection capabilities of the acquisition and analysis system due to over-crowding.
The improved coverage granted by this method affords a better chance of recording transient events, albeit at the expense of tracking length and localisation precision in comparison with quantum dot-based methods. Furthermore, it was decided to employ this method in order to reduce possible drag effects from bulky GFP moieties or quantum dots on the receptors. This also allows for flexible and specific labelling of the receptors in a 1:1 ratio with different dyes through simple conjugation reactions. The synthesis and basic characterisation (specificity and binding parameters) of the Single-Molecule probes is detailed in **Chapter 3**.

Artefacts arising from substrate adhesion of some of the probe-dye conjugates, which would degrade signal and prevent the drawing of any meaningful conclusion about the data, were observed during the first multicolour Single-Particle Tracking trial runs. An optimisation phase was carried out to find a way of eliminating or at least minimising the artefacts. Growth substrate composition and dye characteristics were the main focus as possible sources of artefacts. Panels of growth substrates (**Chapter 4**) and dyes suitable for multicolour Single-Molecule applications (**Chapter 5**) were systematically investigated, identifying the best conditions for the acquisition of Single-Particle Tracking data.

The attention was finally shifted on the main topic of the project: the study of the HER family of receptors in its native membrane context, in conditions as close as possible to "physiological", focusing on the determination of receptor dynamics and homo- and hetero-interactions parameters in presence or absence of the clinically relevant drugs Lapatinib and Erlotinib by using two-colour quantitative Single-Particle Tracking (**Chapter 6**). The role of the plasma membrane context in the dynamics of HER1 was analysed using quantitative single- and two-colour tracking and further examined with a new globally optimised tracking algorithm, highlighting the importance of actin fibres in basal HER1 motility (**Chapter 7**).

Procedures and reagents used throughout the project are detailed in **Chapter 2**.

Multidisciplinary projects are necessarily a team effort. Throughout the thesis, the author was responsible for sample preparation, confocal and Single-Molecule imaging, data analysis and data interpretation. The algorithms for data analysis were devised, written, implemented and validated by Dr Daniel Rolfe, Dr Michael Hirsch and Dr Richard Wareham, with the author acting as a mere end-user. Fluorescent conjugations with NHS ester and maleimide dyes were performed by Dr David Clarke on behalf of the author. Advice on protein expression was obtained from Mr Anil Verma and Dr Ray Owens, however the expression procedures were carried out by the author. Dr Christopher Tynan helped with the determination of the localisation precision and gave logistic and technical support to the imaging, together with Dr Stephen Webb. Dr Sarah Needham and Dr Selene Roberts advised and helped with unfamiliar sample preparation issues.

Finally, the core material for **Chapters 4** and **5** has been published in [1] and [2], of which the candidate is first author. Part of the material for Chapter VII has been submitted as a publication in Wareham *et al.* [3] of which the author is joint first author. For a fuller account of the contributions of the author to 5 papers published and 2 papers in preparation, see the **Author Publications and Contributions** section.

Objectives and Aims

The programmatic aims of this project are:

- To investigate the diffusion of native HER 1-3 family receptors and its possible regulators, such as the actin cytoskeleton, lipid rafts and the tyrosine kinase activity of the receptors, by Single-Particle Tracking on a breast cancer cell line model expressing similarly low levels of all HER family receptors.
- To investigate the pairwise colocalisation likelihood of HER1-3 and the effects of receptor competition and tyrosine kinase inhibition on reception interaction preferences.
- To derive quantitative parameters for receptor diffusion and interactions in different conditions. These parameters will be input into a mathematical model of the HER family signalling.

In order to achieve these aims, the following experimental objectives were pursued:

- Synthesis and/or testing of monovalent probes for HER1and HER3 in their activated and inactive states, and for HER2.
- Optimisation of labelling conditions to ensure minimal contribution of artefacts to the data.
- Characterisation of the signal-to-noise ratio of the system.
- Acquisition of two-colour, pairwise, single-particle tracking data for HER1-3 in the presence of perturbations such as tyrosine kinase inhibitors.
- Acquisition of single-particle tracking data for HER1 in the presence of cytoskeleton- and lipid-raft disrupting agents.
- Implementation and validation of a new, globally optimised, Bayesian tracking algorithm, to allow the determination of additional parameters defining the diffusion of HER receptors. This algorithm was then applied to selected single-particle tracking data to investigate the regulation of HER1 diffusion at the cell membrane.

Author Publications and Contributions

1. Clarke DT *et al.*, Optics clustered to output unique solutions: a multi-laser facility for combined single molecule and ensemble microscopy. Rev Sci Instrum. 2011 Sep; 82(9):093705. doi: 10.1063/1.3635536.
   Provided Single-Molecule samples used to demonstrate system performance.
2. Webb SE *et al.*, Multicolour single molecule imaging on cells using a supercontinuum source. Biomed Opt Express. 2012 Mar 1; 3(3):400-6. doi: 10.1364/BOE.3.000400.
   Prepared samples to test the system.
3. Zanetti-Domingues LC *et al.*, A systematic investigation of differential effects of cell culture substrates on the extent of artefacts in single-molecule tracking. PLoS One. 2012; 7(9):e45655. doi: 10.1371/journal.pone.0045655.
   Performed tracking and confocal experiments, analysed data, and contributed to writing the manuscript.
4. Needham SR *et al.*, Measuring EGFR separations on cells with ~10 nm resolution via fluorophore localization imaging with photobleaching. PLoS One. 2013 May 1;8(5):e62331. doi: 10.1371/journal.pone.0062331.
   Performed control western blot experiments.
5. Zanetti-Domingues LC *et al.*, Hydrophobic Fluorescent Probes Introduce Artifacts into Single Molecule Tracking Experiments Due to Non-Specific Binding. PLoS ONE 2013; 8(9): e74200. doi: 10.1371/journal.pone.0074200.
   Performed tracking and confocal experiments, analysed tracking data. Contributed to writing the manuscript.
6. Wareham R *et al.*, A globally optimal tracking solution reveals basal cell surface EGFR transport underpinned by F-actin. In review.
   Performed tracking experiments. Contributed to the interpretation of the data. Reviewed draft.
7. Zanetti-Domingues *et al.*, A molecular model of the cell surface HER1-4 network in a breast cancer cell model. In preparation.
   Performed tracking experiments and interpreted data.

Contents

Table of Figures

Table of Tables

Table of Equations

Acknowledgements

This work was funded by the BBSRC under grant no. BB/G006911/1 (LoLa grant).

I would like to thank my supervisors, Prof Tony Ng and Dr Marisa Martin-Fernandez for their helpful advice and guidance.

My most sincere thanks go also to:

The entire FBI team of the LSF, and especially Dr Daniel Rolfe, without which none of this would have been possible;

Dr Michela Perani of King's College, for her expertise in the field of biochemistry;

Dr Ray Owens and Mr Anil Verma of the Oxford Protein Production Facility for their help and supervision in cloning and expressing HER3 and NRG1b-MCP;

Dr Sarah Cartmell of the Manchester X-Ray Imaging Facility and Dr Paul Roach of the Institute for Science and Technology in Medicine, Keele University, for helpful suggestions about PEG-based biomaterials;

Prof Linda Pike of Washington University for the gift of a Cho cell line stably and inducibly expressing HER1;

Prof Donna Arndt-Jovin for the gift of Cho-HER1-eGFP cells;

Dr John Löfblom of KTH Royal Institute of Technology, Sweden, for providing the HER3 Affibody plasmid (under Material Transfer Agreement from Affibody Inc.);

Whoever discovered coffee, and Mr David Strang who invented instant coffee, without which, this thesis might have never been written;

And, last but not least, to my family and my partner Guglielmo, for coping with me even in moments of intense stress.

1. General Introduction

This chapter provides general background information on the system in study, the HER family of receptor tyrosine kinases, and on the advanced fluorescence microscopy techniques employed to study it in native mammalian plasma membranes.

1.1. Signalling from the Plasma Membrane: The Human Epidermal Growth Factor Receptor (HER) Family and its Role in Carcinogenesis and Cancer Therapy

The plasma membrane of mammalian cells fulfils the dual role of isolating the intracellular environment from extracellular bodily fluids and, at the same time, transferring information from the outside in and vice versa. It relays extracellular environmental cues to the intracellular milieu to effect biological outcomes and projects information about the state of the cell to neighbour cells or distant targets, integrating each cell into its "social context". The collection, integration and transmission of all these different signals are effected through protein-protein and protein-lipid interactions happening on different time- and distance-scales. The extent and likelihood of such interactions in the membrane surface is regulated by the nano- and micro- structure of the membrane itself and by the modes of motion of the species involved in each information exchange, as well as by the ways in which internal or external cues modify it [4]. Diffusion is used to transport proteins to the sites of the membrane where interacting partners are located and where specific activity is required.

The plasma membrane was initially envisioned as an unpartitioned bidimensional fluid of amphipathic proteins embedded in a bilayer of phospholipids, which acted as a solvent for the proteins [5]. While thermodynamically sound and consistent with the experimental findings of the time, this model fails to account for the differences in protein and lipid macroscopic diffusion coefficients when measured in intact plasma membranes compared to reconstituted lipid bilayers, and for the oligomerisation-induced reduction in macroscopic diffusion displayed by some proteins [6]. According to the Saffman-Delbruck model, a cylindrical inclusion of radius a, moving in a membrane of thickness h and viscosity η_m, surrounded by fluid of viscosity η_f is described byError! Reference source not found.,

$$D_{sd} = \frac{k_B T}{4\pi\eta_m h}\left[\ln\left(\frac{2L_{sd}}{a}\right) - \gamma\right]$$

Equation 1-1 - The Saffman-Delbruck equation for the diffusion of a particle in a biologic membrane

where $L_{sd} = \left(\frac{h\eta_m}{2\eta_f}\right)$ and *γ* is the Euler-Mascheroni constant (≈0.577).According to this model the diffusion of a particle in the plasma membrane is chiefly determined by the temperature, the thickness of the membrane and its viscosity and depends only weakly on the size (radius) of the diffusant [7]. Such a model would predict that the oligomerisation of a diffusant should not significantly alter its macroscopic diffusion coefficient and that proteins embedded in the membrane would move in a random, stochastic fashion explainable through Brownian motion. For example, if $k_BT \approx 4 \cdot 10^{-21}$ J; η_m= 0.27 Pa · s[8]; η_f = 0.001 Pa · s [9]; h ≈ 4 x 10^{-9} m [10] and the radius of the single transmembrane α-helix domain of HER1 (a) ≈2 x 10^{-9} m, the predicted D_{sd} should be ≈ 1.7 $\mu m^2/s$. Doubling the radius a to 4 x 10^{-9} m will yield a D_{sd} of 1.4 $\mu m^2/s$ and even a tenfold increased radius will only decrease the D_{sd} to 1.01 $\mu m^2/s$.

Assuming that the movement of a particle is random, and approximating the plasma membrane to a 2-D surface, according to Brownian theory, one can derive the molecular mean square displacement (MSD) from the ensemble average diffusion coefficient (*D*) through **Equation 1-2**, where r stands for the (x,y) coordinates of the particle. The two- dimensional MSD equates roughly to the amount of surface "explored" by a particle in the time unit.

$$MSD \equiv \left\langle \left(r(t) - r_0\right)^2 \right\rangle = 4Dt$$

Equation 1-2 – The two-dimensional MSD of a particle diffusing on a biological membrane.

The average distance at which a particle can move in the unit of time is better described by the squared root of the MSD, $RMSD = \sqrt{4Dt}$.

In practice, a single-particle track can be viewed as the sequence of particle locations (x,y) at time points where the particle was detected. For a given time difference Δt=j, j=1…N, where N is less than the number of time points in the track, all squared distances $(\mathbf{r}_j)^2$ between particle locations with time difference Δt=j can be calculated (for simplicity we are assuming that the time gap between two subsequent frames is constant). The MSD curve is generated by calculating the average of the squared distances $(\mathbf{r}_j)^2$ between locations with the same time difference Δt=j, and plotting it as a function of the time difference, as shown in **Figure 1-1**Error! Reference source not found..

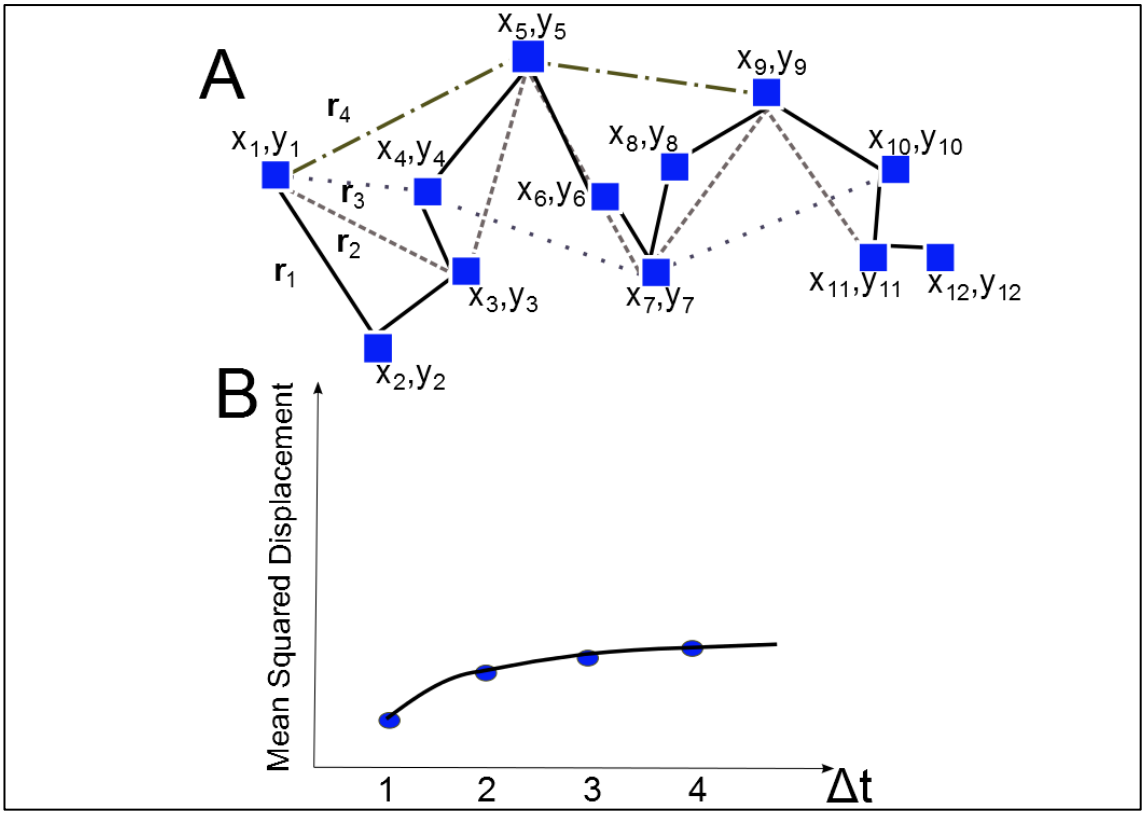

Figure 1-1 - A: Given a single-particle track, the distances r_j between particle positions (x_i,y_i) that have a time difference Δt=j are calculated. Only a subset of the possible distances is shown in the figure for clarity purposes. Black continuous line: Δt=1; Grey dashed line: Δt=2; Grey dotted line: Δt=3; Grey composite line: Δt=4.

B: The MSD curve for a given single-particle track is generated by plotting the average value of the squared distances $(r_j)^2$ of all locations that have a time difference Δt=j over the time differences. E.g. for Δt=2 the average would be calculated of the squared distances between locations (x_1, y_1) and (x_3,y_3), (x_2,y_2) and (x_4,y_4), (x_3,y_3) and (x_5,y_5) and so forth.

A Brownian particle on an unpartitioned membrane should display a motion described by a linear MSD, i.e. MSD $\propto \Delta t$, where t is the time during which molecules are observed. Motions other than normal diffusion will result in non-linear MSD v Δt plots (**Figure 1-2**). At the plasma membrane it is often found that the power law governing MSD motion is sublinear, i.e. MSD $\propto \Delta t^{\alpha}$, where $\alpha < 1$. This diffusive behaviour is referred to as confined motion (*e.g.* traces I-II in **Figure 1-2**). In some cases, it is also found that $\alpha > 1$, which is referred to as anomalous superdiffusion or directional motion (*e.g.* trace IV in **Figure 1-2**).

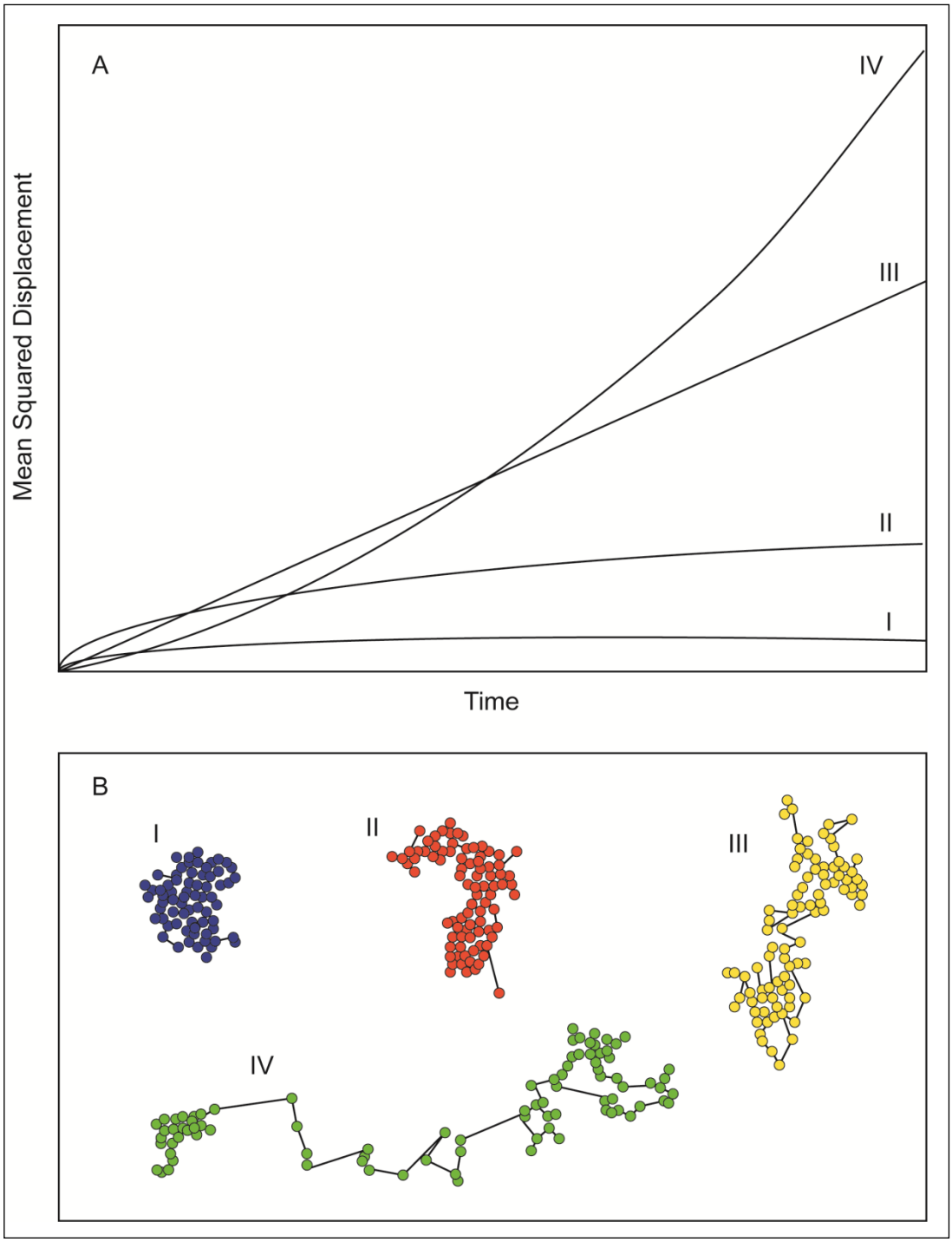

Figure 1-2 - (A) Simulated mean squared displacement plots for particle tracking. Trace I shows diffusion for confined molecules, II shows obstructed diffusion, III normal diffusion, and IV shows MSD for directed motion. **(B)** Example particle tracks for the motion types plotted in **(A)**. From Martin-Fernandez and Clarke [11].

In contrast to the Saffman-Delbruck model, high-speed tracking experiments have determined that the diffusion of both proteins [12] and lipids [13] on live cell membranes is confined by

nanoscale membrane domains of variable size (30-230 nm)[14], which are dependent on the actin membrane cytoskeleton [13]. These findings have brought about a shift in the conception of the plasma membrane towards an alternative "picket-fence" model [6], according to which the membrane is finely partitioned in nanoscale compartments by the meshwork of the actin-based membrane cytoskeleton (the "fence"). Transmembrane proteins interacting with actin ("pickets") further hinder the free diffusion of molecules on the membrane via steric hindrance and hydrodynamic friction-like effects, which can propagate over several nanometers, particularly if the "pickets" are immobile. This model (**Figure 1-3**) allows for free diffusion of membrane -localised molecules on the nanoscale, within the compartments; however, the macroscopic diffusion coefficient is dominated by the rate of escape from each compartment to the next ("hop rate"), which depends critically on the radius of the diffusant. Therefore signal-induced oligomers or multiprotein complexes of a diffusant are expected to display reduced diffusion compared to monomers of the same diffusant. Moreover, any signalling event that induces binding of a diffusant to the actin membrane skeleton or the "pickets" will also induce changes in diffusant mobility.

The effect of the actin cytoskeleton likely works in concert with membrane "crowding", lateral interactions between membrane components, and inhomogeneities in membrane composition and state to effect a reduction in molecular mobility in intact plasma membranes compared with model lipid bilayers [15].

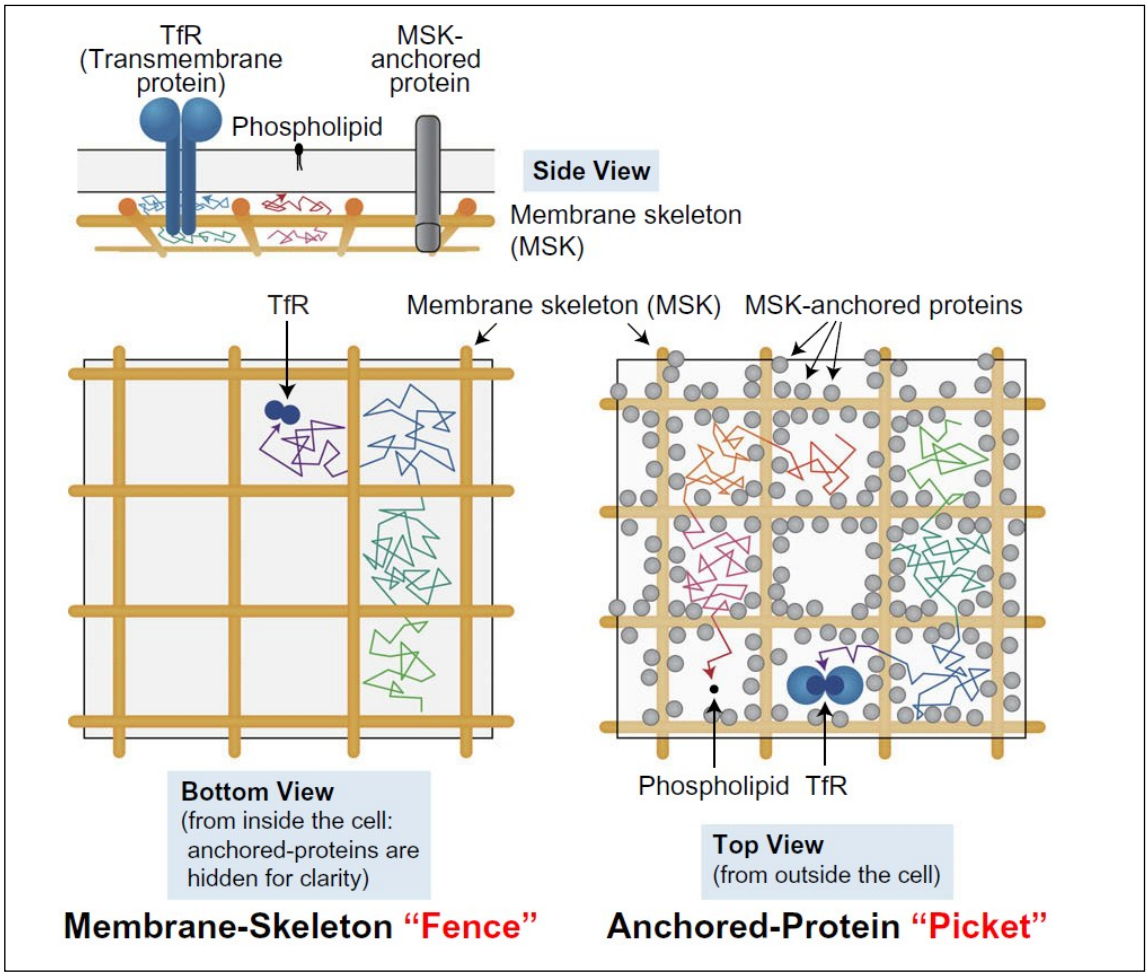

Figure 1-3 – Scheme of the "picket-fence" model, showing the constraint to the diffusion of both proteins and phospholipids. Adapted from Kusumi *et al.* (2010) [16]**.**

Temporal dynamics and spatial distribution of key signalling effectors contribute to crucial cell decisions, and differences in the spatiotemporal organisation of signalling components can bring about dramatic changes in the information output in terms of activation of downstream signalling pathways and cell fate outcomes [17]. In this light, the partitioning of the membrane seems a sound evolutionary strategy for confining the downstream transmission of extracellular signals in both space and time [14]. In addition to that, individual membrane compartments, with their complement of receptors, regulators and effectors, can act as nanoscale reaction chambers and accelerate the reaction rates of signalling events, creating gradients of concentration that are governed by the half-life and the diffusion of the products. Local, temporally and spatially restricted increases in the concentration of a signalling species at the plasma membrane can greatly influence the local efficiency of the downstream transduction of signals, creating localised peaks of signal, which encode spatial as well as intensity information [17]. The repetition rate of signalling peaks is predicted to be important

for the specificity of transmitted information [18]. Further on this point, the partitioning of the membrane is predicted to enhance signal reliability by initiating a more graded downstream response to changes in the input signal and by reducing background noise via decorrelation of signalling molecules in adjacent compartments, so that a larger number of distinct input signals can be encoded by the network response [19].
Lipid rafts, defined in the Keystone Symposium on Lipid Rafts and Cell Function (2006) as "small (10-200 nm) heterogeneous, highly dynamic, sterol- and sphingolipid-enriched domains that compartmentalise cellular process and can sometimes be stabilised to form larger signalling platforms through protein-protein and protein-lipid interactions" [20], might add a further/parallel level of complexity to the plasma membrane environment.

The **Human Epidermal Growth Factor (HER) family of receptors** (reviewed from the point of view of signalling in Olayioye *et al.* (2000) [21], Yarden and Silwkowski (2001) [22], and Avraham and Yarden (2011) [23], among others) is one of the key entry points for extracellular cues resulting in cell-to-cell inductive processes and cell fate decisions.It is one of the 18 sub-families of the Receptor Tyrosine Kinase (RTK) superfamily [24] and consists of 4 highly homologous receptors (HER1, HER2, HER3 and HER4 – see **Figure 1-4**) with a transmembrane single-pass configuration [25] and a modular structure, and at least 13 different Epidermal Growth Factor (EGF)-related peptides [26] which bind to the receptors.

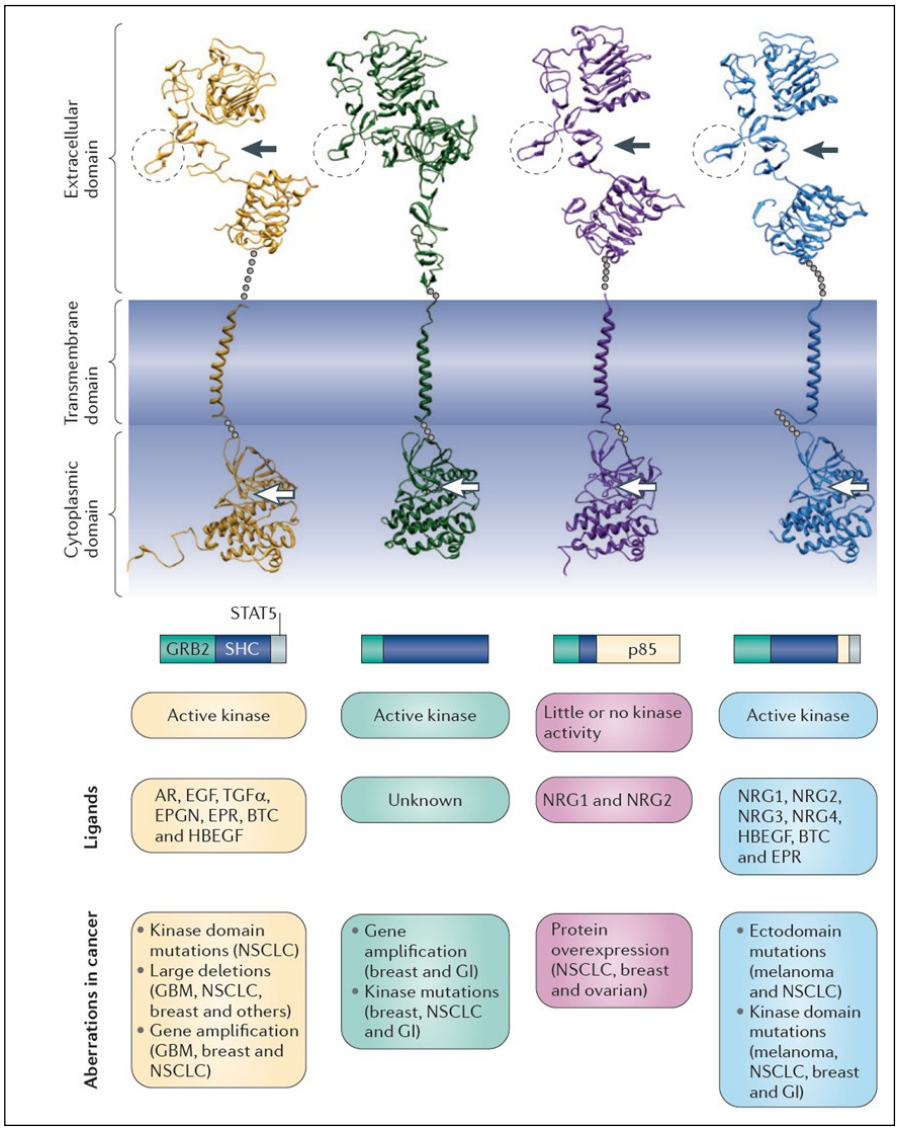

Figure 1-4 – "Family portrait" of the HER family of receptors, highlighting unique and shared features of each, from Yarden and Pines (2012) [27]**.** In the top register, HER1 (yellow), HER2 (green), HER3 (red) and HER4 (blue), from left to right, are represented by a collage of the available crystal structures of their extracellular, transmembrane and intracellular domains. The C-terminal tail is missing due to its lack of crystallisable structure, as are parts of the extracellular and intracellular domain near the membrane (grey dots). The "dimerization arm" is highlighted by a dashed circle and the ATP-binding pocket by a white arrow. The bars below represent the fractions of specific binding sites for downstream mediators present in the C-terminal tail of each receptor, normalised against the total number of phosphotyrosine sites in each receptor. Abbreviations: AR, amphiregulin; BTC, β-cellulin; EGF, epidermal growth factor; EPGN, epigen; EPR, epiregulin; GBM, glioblastoma; GI, gastrointestinal tract; GRB2, growth factor receptor-bound protein 2; HBEGF, heparin- binding EGF-like growth factor; NRG, neuregulin; NSCLC, non-small-cell lung cancer; SHC, SRC-homology domain-containing; STAT5, signal transducer and activator of transcription 5; TGFα, transforming growth factor-α.

The HER family of receptors plays a prominent **role in** many **cancer** histotypes, in accordance with its pleiotropic **physiological roles**. For example, **HER1** has a physiological role in skin, lung, gut and nervous system biogenesis and function [21]and is necessary for duct formation in normal breast [28]. Mutations of the tyrosine kinase domain of HER1 are oncogenic in lung cancer [29], while large deletions in the extracellular domain (EGFR vIII) [30] or in the intracellular domain (EGFR vIV) [31] are frequently reported in glioblastomas, with or without gene amplification. Overexpression of HER1 is frequent in colorectal and head-and-neck carcinomas [32], but also in the Triple-Negative subtype of breast cancer (TNBC)[28], where it is thought to promote brain metastasis [33].

HER2 instead is necessary for heart development, breast morphogenesis and migration of neural crest precursors [21] and is involved in breast maturation and lactation[28]. HER2 is found amplified in approximately 25% of breast cancer cases, where it used to confer a worse prognosis before the advent of targeted therapies such as the monoclonal antibody Trastuzumab and the small-molecule Tyrosine Kinase Inhibitor Lapatinib [34]. Point mutations of the HER2 tyrosine kinase domain were found in lung cancer [35]and breast cancer, where they are mutually exclusive with HER2 amplification [34].

While HER2 and HER4 are necessary for the formation of cardiac trabeculae in mouse embryos, **HER3** is involved in the biogenesis of cardiac valves in mice and also in the migration of neural crest precursors and in the myelination of nerves [21]. Its role in breast morphogenesis is associated with mammary development in pregnancy and lactation[36]. While HER3 is not amplified at the genomic level in breast cancer, protein overexpression is quite common and associated with worse prognosis [37]. HER3 works in concert with HER2 in breast cancer, where their association can be targeted by the anti-HER2 monoclonal antibody Pertuzumab [38], and with HER1 in head and neck carcinomas, melanoma and pancreatic cancer, where it is associated with decreased survival and resistance to HER1-targeted therapies [37]. HER3 mutations have been identified both in the extracellular and in the kinase domains in lung [39], colon and gastric cancer [40], where they display ligand-independent, HER2-dependent oncogenic activity.

While the role of **HER4** in normal physiology seems to overlap that of HER2 [21,28], its role in cancer development is less clear-cut. Recurrent HER4 mutations with independent oncogenic activity have been identified in malignant melanomas [41], however the role of this receptor in breast cancer is contradictory [28], with some studies reporting HER4 association with worse prognosis and some with better prognosis. The likely cause of the contradictory findings in

breast cancer may be explained by the expression of different isoforms of HER4 in different cancer subtypes, some of which might exert a pro-apoptotic effect on cancer cells due to cytoplasmic release of BH3-only Intracellular Domain [42].

EGF-related peptides also play an important role in oncogenesis and are often overexpressed in an autocrine or paracrine way by the cancer cells themselves or by their immediate microenvironment [22]. Overexpression of Transforming Growth Factor α (TGF-α), Amphiregulin and Heparin Binding-EGF, in particular, is associated with poor prognosis and enhanced tumour aggressivity in many cancer histotypes [26], as well as with resistance to HER-targeted therapies [43]. Neuregulins, in particular, are known for modulating the effects of anticancer treatments [44] and for sustaining signalling through the HER family and through Phosphatidyl Inositol 3 Kinase (PI3K) even in presence of HER-targeted drugs [26,45,46].

As with most RTKs, the **signalling mechanism** of the HER family of receptors involves binding of the ligand by an extracellular domain, followed by transmission of the signal through the membrane and into the cytoplasmic environment via a ligand-induced dimerization event that activates the tyrosine kinase activity of the receptor and starts downstream signalling [24], so that the receptors essentially function as ligand-regulated allosteric enzymes [47]. HER family receptors homo- and hetero-dimerize in response to the binding of different ligands, potentially forming 10 different types of complexes, but not all the possible dimers may be functionally relevant [48], possibly depending on the cellular context.

The primary structure of full-length HER receptors, which is shared with all RTKs and highly conserved within the HER family, consists of a single polypeptide chain (1,186 amino acids for HER1) of ≈170 kD, which displays a modular configuration.

The heavily glycosylated 622-amino acid residue amino-terminal Extracellular Domain (**ECD**), which binds the ligand, is made up by 4 sub-domains (I-IV): the two leucine-rich β- helix solenoid domains (I and III) are involved in ligand binding, with both sub-domains contacting the ligand at the same time; cysteine-rich domains II and IV are instead involved in the dimerization interface[49]. Upon ligand binding, HER family receptors are thought to undergo a major conformational change [50], that breaks an auto-inhibitory interaction between domains II and IV [51–53], freeing the dimerization interfaces on both domains and especially on domain II, which contains a so-called “dimerization arm”, so that the receptors can interact in a back-to-back configuration [54–57] (**Figure 1-5**).

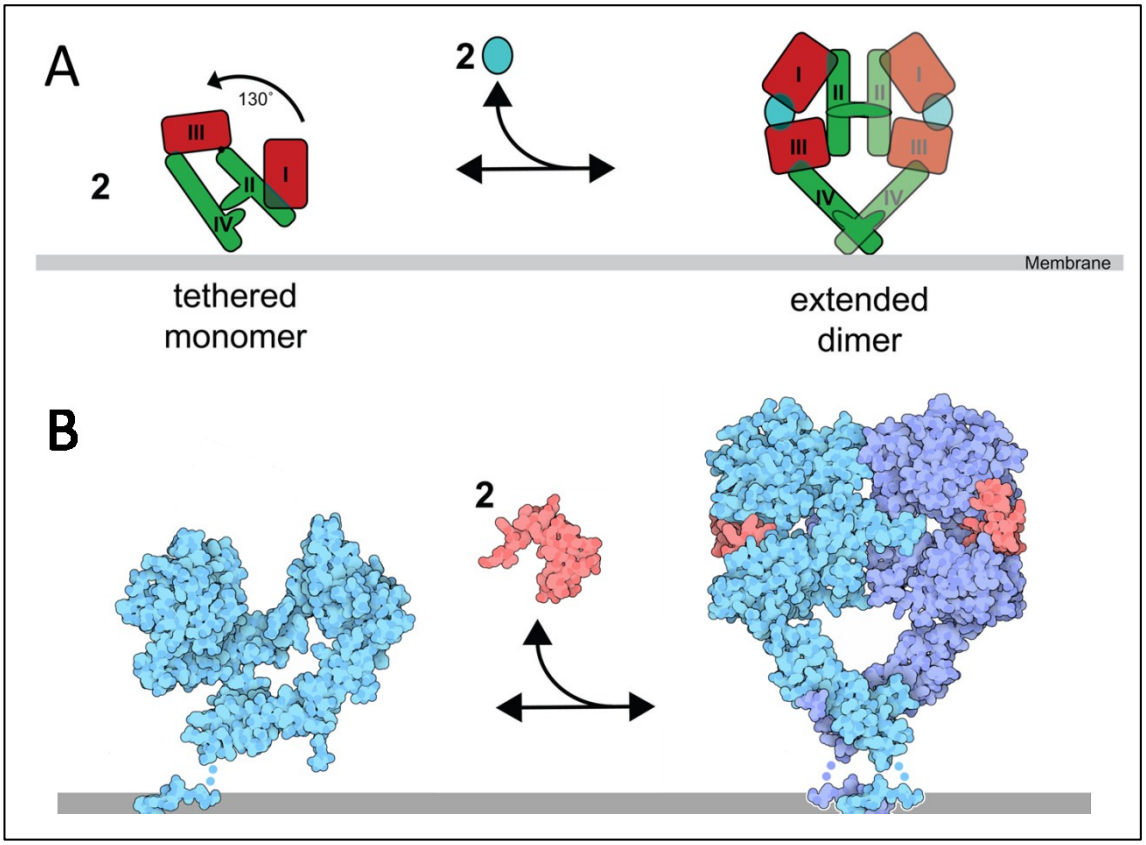

Figure 1-5 – A) Schematic representation of the ligand-induced conformational change and dimerization process of the HER family receptors, adapted from Lemmon (2009) [49]**. B)** The same conformational change from the structural point of view, adapted from Goodsell (2010) [58]

However, the biological significance of this structural rearrangement, whose existence has been postulated from crystallographic results obtained from soluble ECD-only proteins, is still not completely certain. In fact mutations that abrogate domain II-IV interactions do not significantly impact ligand binding or signalling properties of full-length HER1 receptor [59]. Imaging studies of full-length receptors have offered an alternative model for the ligand-induced conformational switch, which involves a change in the orientation of the extracellular domain[60–63] . This mechanism (**Figure 1-6**) might exist as an alternative or in parallel with the "tethered-extended" conformational rearrangement.

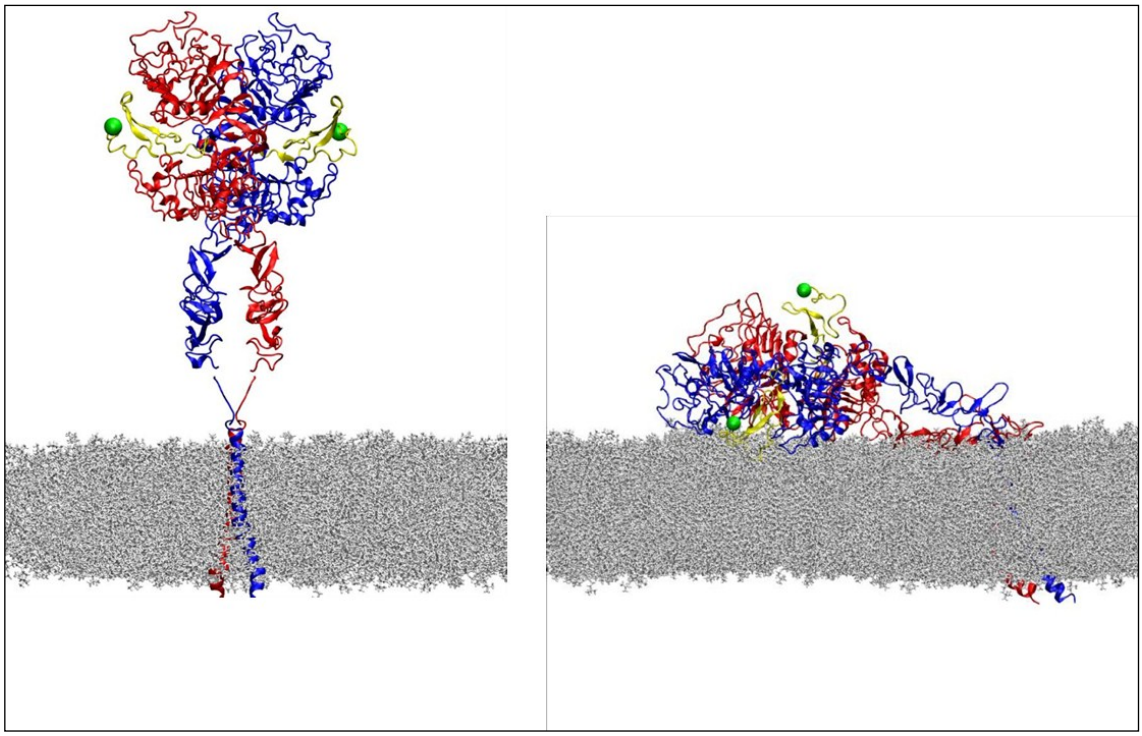

Figure 1-6 – Molecular simulation of the HER1 ECD standing proud from (left) or lying flat on (right) the plasma membrane. From Tynan *et al.* (2011) [61]**.**

Connecting the extracellular domain with the intracellular domain, there is a single transmembrane domain (**TMD**) of 23 residues, with an α-helical structure, which is also involved in the regulation of receptor dimerization via one or more GxxxG motifs [64]. In HER1, whose TMD presents two GxxxG motifs placed at either end of the domain, ligand binding is thought to produce structural rearrangements that propagate to the TMD, causing its interaction to switch from the C-terminal dimerization motif (residues 637-641 - ALGIG) to the N-terminal one (residues 624-629 - TGMVGA), a change in conformation which in turn propagates downstream to the intracellular domain [63,65,66].

The 500+ residue-Intracellular Domain (ICD) is composed of three different modules: Juxtamembrane Domain (JMD), catalytic Tyrosine Kinase Domain (TKD) and C-terminal tail. The **JMD**, is unique in sequence and function to the HER family [67] and can be further sub-divided in two JM-A and JM-B segments. It performs a regulatory function, undergoing a conformational change upon ligand binding. In inactive receptors, the JM-A segment is buried in the plasma membrane via extensive contacts with negatively charged lipids, including phosphatidylinositol 4,5-bisphosphate (PIP_2) [68], while the JM-B segment is prevented from interacting with the kinase domain by the C-terminal tail, which occupies its binding cleft. Upon ligand-dependent activation, the rearrangements in the ECD and TMD cause JM-A

segment extraction from the plasma membrane, favouring the formation of an antiparallel helix-to helix contact between JM-A segments of two receptors forming a dimer. The JM-B segments are now able to displace the C-terminal tail from its binding cleft on each receptor and stabilise the active kinase dimer by running along the C-lobe of each receptor [69,70]. Substitution of this segment with an unstructured sequence abolishes ligand-induced phosphorylation without significant effects on dimerization and ligand-binding, a finding which suggests that the transmission of the conformational change across the membrane is sequential, so that TKD activation is subsequent to ligand-induced conformational changes in the ECD and to TMD-mediated dimerization[71].

The **TKD** is the core component of the downstream signalling function. It is about 250 residues long [72] and conserved within the HER family, with few, functionally very significant differences between the different family members [67]. Its structure comprises two lobes: an N –terminal ATP binding lobe and a C-terminal substrate binding lobe, between which the catalytic cleft is located (indicated by an arrow in **Figure 1-7 B and D**) [73]. In its inactive state, the HER TKD adopts a structure similar to that of cyclin-dependent kinase (CDK) 2 and of Src family kinases, characterised by the outward orientation of the αC helix (red)in the N-lobe, a conformation which disrupts important contacts for the receptor's catalytic activity. This outward orientation of the αC helix is coupled to a "closed" conformation of the activation loop (purple - **Figure 1-7 C**), which prevents the substrate (the receptor's C-terminal tail) from entering the active site and stabilises the inactive conformation through the packing of the DFG motif (brown) against the αC helix (red) [74]. Contrary to most RTKs, the TKD of HER family receptors is not activated via phosphorylation of tyrosine residues in the activation loop, but via an allosteric mechanism. Upon ligand activation, the TKDs of two receptors forming a dimer interact in an asymmetric, "head-to-tail" fashion [75], via hydrophobic patches located on their N-lobe and the C-lobes . Thus, the "top" kinase (the activator, in yellow in **Figure 1-7 E**) interacts via its αH helix (orange) with the αC helix (red) of the "bottom" kinase (the receiver, in light blue in **Figure 1-7 E**), and stabilises an alternative conformation , where the αC helix (red) is swung inwards and the activation loop (purple) is extended to allow substrate binding (**Figure 1-7A**) [74]. The inactive kinase can also dimerize in a symmetric, "head-to-head" configuration (**Figure 1-7 F**) involving the N-lobe and the AP-2 helix in the C-terminal tail (residues 993-1002 of HER1 – dark green in **Figure 1-7 D**) of each receptor, while acidic side chains at positions 979-981 of the C-terminal tail (green) interact with key residues

in the catalytic pocket, and the following segment of the C-terminal tail (residues 982-990 - teal) occupies the cleft to which the JM-B segment binds in the active structure [70].

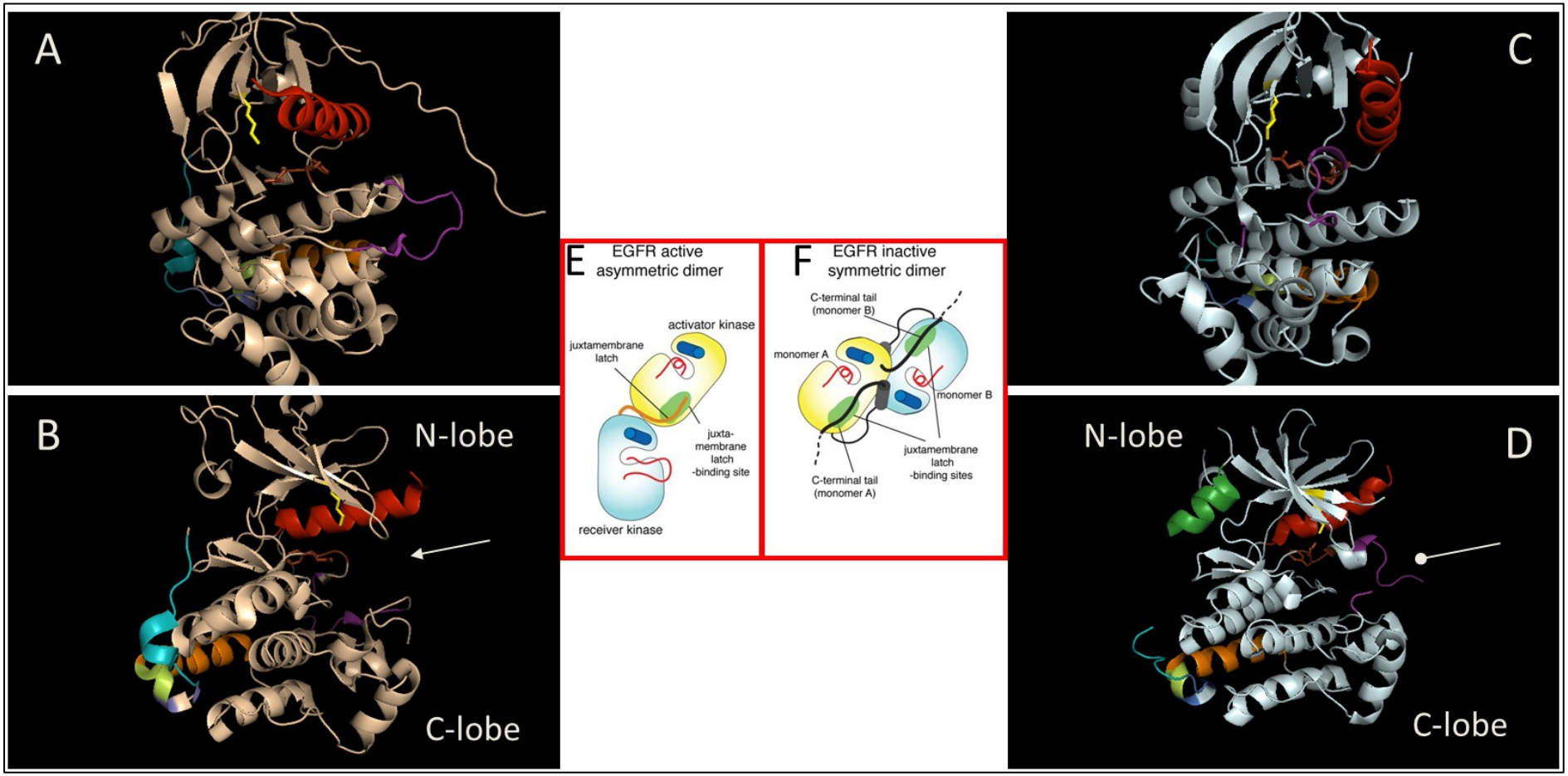
A
B
N-lobe
C-lobe
E
EGFR active
asymmetric dimer
activator kinase
juxtamembrane
latch
juxta-
membrane
latch
-binding site
receiver kinase
F
EGFR inactive
symmetric dimer
C-terminal tail
(monomer B)
monomer A
monomer B
juxtamembrane
latch
-binding sites
C-terminal tail
(monomer A)
C
N-lobe
D
C-lobe

Figure 1-7 (previous page) – A and B: structure of the HER1 TKD in the active conformation, from the PDB structure file 2GS6. **A)** View of the catalytic pocket, showing the catalytic Lys 721 in yellow, the DGF motif in brown, the αC-helix (swung in) in red and the activation loop in purple. **B)** Side view showing the αC-helix in red, the activation loop in purple, the αH-helix in orange, the acidic residues in green, the LVI motif interaction motif in blue and part of the C-lobe latch in teal. The arrow indicates the catalytic pocket (open) **C and D:** structure of the HER1 TKD in the inactive conformation, from the PDB structure file 4HJO. **C)** View of the catalytic pocket, showing the catalytic Lys 721 in yellow, the DGF motif in brown, the αC-helix (swung out) in red and the activation loop (blocking the pocket) in purple. **D)** Side view showing the αC-helix in red, the activation loop in purple, the αH-helix in orange, the acidic residues in green, the LVI motif interaction motif in blue, part of the C-lobe latch in teal and the AP-2 helix in dark green. The ball indicates the catalytic pocket (closed). **E)** Schematic representation of the HER1 active asymmetric dimer. **F)** Schematic representation of the HER1 symmetric inactive dimer. Panels **E** and **F** are adapted from Jura *et al.* (2011) [74]**.**

Finally, the **C-terminal tail** is also unique to the HER family of RTKs and shows regions of high conservation between family members [67]. It functions as an allosteric regulator of the activity of the TKD not only by binding to it in its inactive state, where it is involved in the stabilisation of the inactive conformation and of the "head-to-head", symmetric dimer [70], but also by controlling the pivot point for inter-lobe movement via interactions with a conserved glutamine and by interfering with the substrate binding pocket via its AP-2 helix[67] (**Figure 1-8**). Its regulatory function is crucially controlled in HER1 by a putative "hinge" at residues 960-961, the disruption of which leads to hyperactivation of receptor phosphorylation and downstream signalling [76].

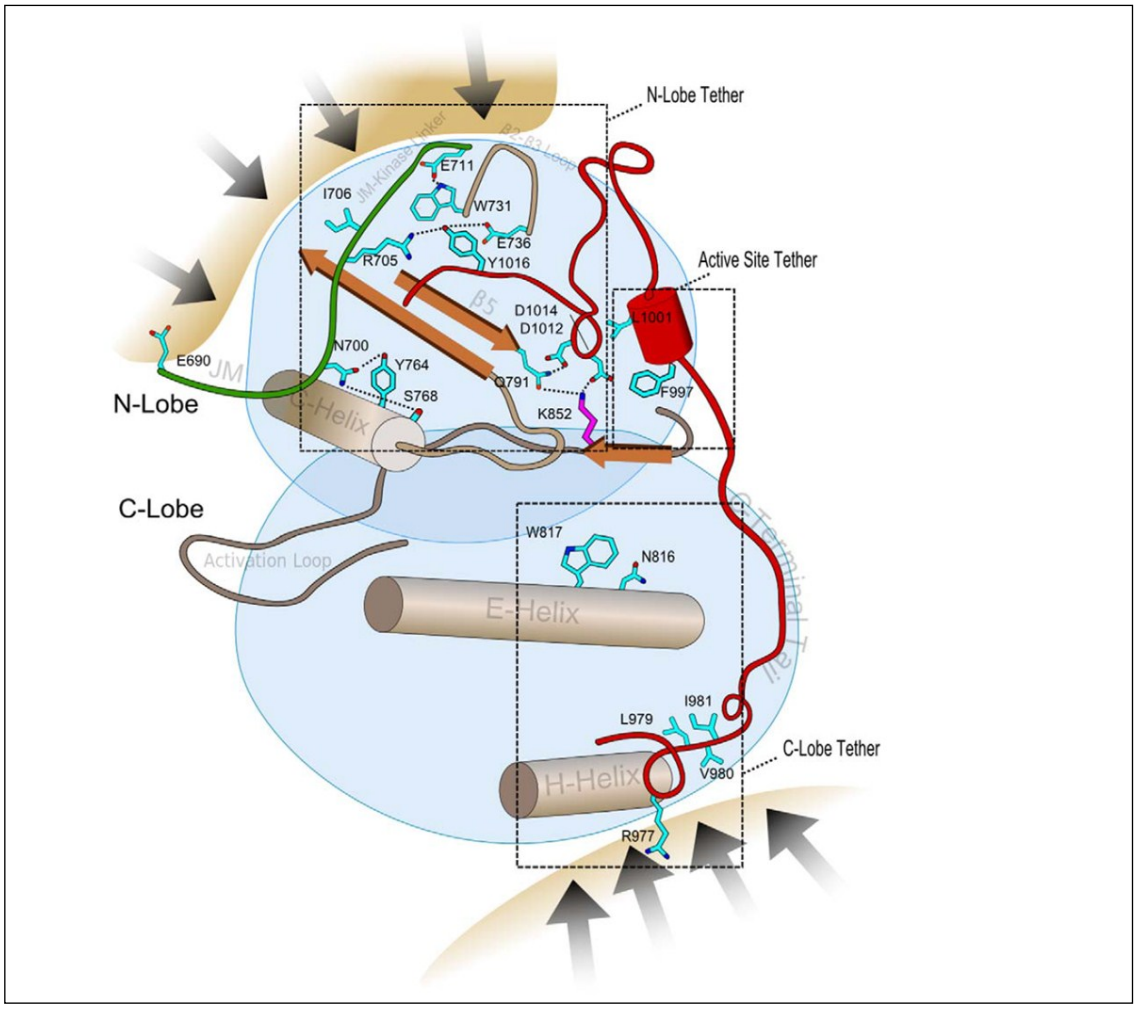

Figure 1-8 – Schematic representation of the HER family TKD showing the conserved interactions that regulate catalytic activity (based on PDB structure 2J5F). Residues in cyan are conserved across kinase domains of the HER family and residues in pink are conserved across all RTKs. The JMD backbone is shown in green and the C-terminal tail in red. The black arrows indicate the N-and C-lobe interfaces involved in the asymmetric kinase dimer. Residues are numbered according to the sequence of full-length HER1. After Mirza *et al.* (2010) [67].

In addition to its structural role, the C-terminal tail contains multiple phosphorylatable tyrosine residues, which act as substrates of the receptor's catalytic activity and as docking points for downstream effectors bearing SH2 or PTB domains, activating them and concentrating them, so that they can then initiate downstream signalling cascades [22]. Each member of the HER family has a different complement of docking sites for different effectors (**Figure 1-9**), and the phosphorylation pattern of the C-terminal tail tyrosines depends on the precise nature of the activating ligand [77] and of the dimerization partner [21,78].

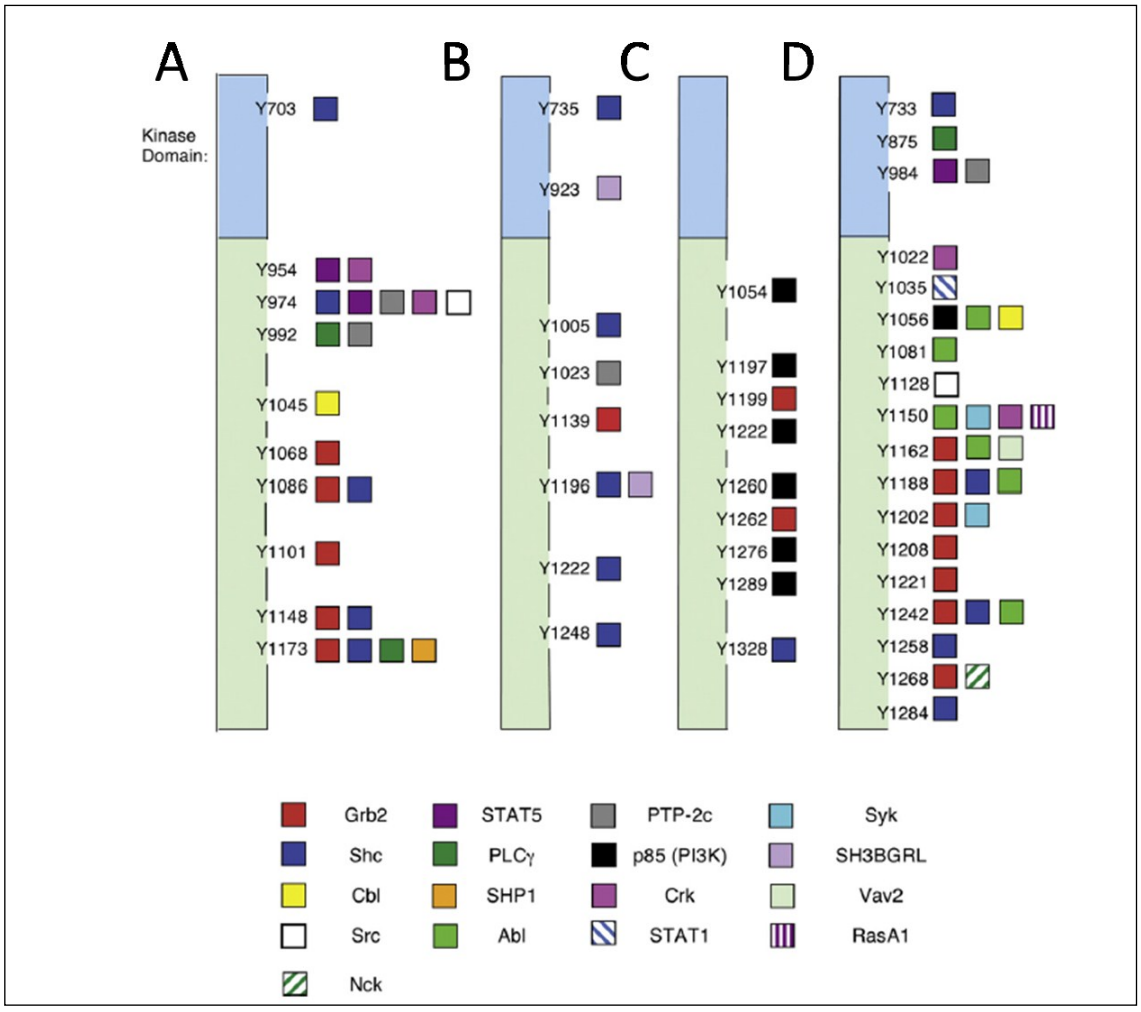

Figure 1-9 – Schematic representation of the docking sites for downstream effectors present on the C-terminal tails of: HER1 (A); HER2 (B); HER3 (C) and HER4 (D). From Wilson *et al.* (2009)[26].

Finally, it is worth noting that the isolated intracellular domain is spontaneously active in solution, while spontaneous, basal activation of a wild-type TKD is only seen in membrane-expressed full-length receptors when HER family members are highly overexpressed [66], a fact that underlines how the whole structure of the HER family of receptors functions as a system of checks and balances to tightly regulate the activity of the TKD. In this context, the ECD seems to perform an inhibitory role, shutting down the transmission of information until external signals are received. However, recent electron microscopy studies have pointed out that the ECD and the ICD of HER1 might have independent dimerization properties, so that ECD dimers might be coupled to asymmetric or symmetric ICD dimers, or to non-dimerized ICD, and vice versa [79,80], a finding which suggests a further level of complexity in the regulation of HER1 signalling.

The 13 **EGF-related peptides** that bind the HER family of receptors (EGF, Transforming Growth factor (TGF)α, Epiregulin (EPR), Amphiregulin (AR), Betacellulin (BTC), Epigen (EPG), Heparin-binding (HB-) EGF and Neuregulins (NRG) 1-6 - reviewed in Wilson *et al.* [26]) also share a conserved, modular structure. Synthesised as large, transmembrane pro-ligands, the EGF-related peptides share a conserved EGF-like domain, which is the minimal unit required for binding specificity [21]. Soluble ligands are produced via proteolytic processing of the transmembrane precursors by a set of proteases of the ADAM family [81], which display some substrate specificity, but are also differentially regulated by extracellular stimuli transmitted through G-protein coupled receptors (GPCRs) via PKC isoforms [82], c-Src [48], or downstream components of the signalling network of RTKs, such as PKB [83,84], resulting in fine-tuning of ligand availability in response to environmental cues. Ligand availability is a critical regulator of the activation of HER family receptors and therefore the expression of most ligands is restricted to specific cell lineages or developmental phases [21].
EGF-related soluble ligands can be divided in three main groups: ligands specific to HER1 (EGF, TGFα, AR), bispecific ligands for both HER1 and HER4 (HB-EGF, EPR and BTC) and Neuregulins, which bind to either HER3 or HER4 or to both [26], and which comprise a wide array of alternatively spliced isoforms with different roles in the development of mammary gland, heart and nervous system [85] . Each ligand is characterised by its affinity for its primary receptor(s), by the pH resistance of its binding and by the ability of attracting secondary co-receptors such as HER2 [21]. Structural and biochemical studies of some ligands, such as NRG1/NDF, even suggest that they might be bivalent, bearing a high-affinity binding site at the N-terminus of their EGF-like domain and a low-affinity, broad specificity binding site at the C-terminus, with which they might bind HER2 or other HER family members that act as co-receptors [86]. How this finding might fit in the back-to-back dimerization model is not clear, however.

HER receptors and EGF-related ligands constitute the **input layer** of the HER family signalling network (**Figure 1-11**), which shows a "bow-tie" architecture, with multiple, combinatorial input points, a few common signal integrators and a series of possible downstream outputs in terms of cell fate decisions and activation of gene expression programmes. This architecture is typical of so-called "robust", evolvable systems and enables them to withstand perturbations through redundancy [48]. As discussed above, both components of the input layer seem to display some redundancy: the HER receptors can activate common downstream effectors, and

the ligands show redundant binding, with multiple ligands binding to the same receptor and the same ligand binding to multiple receptors. This redundancy protects the system from perturbations in the levels of input signal. Deficiencies in the signalling of one receptor might be compensated by the remaining family members to effect the same level of downstream output signal, which might be critical for cell division or survival [48].
The specificity of signal transmission is guaranteed by several mechanisms: first of all the differential affinity of the ligands for their primary receptors [87] ensures fine-tuning of the cellular outcome in response to variations of the availability of the ligands; secondly, different ligands induce different biological effects by binding to the same receptor through selective induction of the phosphorylation of different C-terminal tail tyrosine residues [77,88,89], possibly through subtle differences in the structure of the ECD [54,56] and the ICD [90] of receptors bound to different ligands, as in the case of HER1 bound to EGF or TGFα.

In addition to the differential functions and properties of the ligands, the HER family receptors themselves show functional specialisation alongside redundant features. HER1 and HER4 are the only independent receptors, capable of both ligand binding and downstream signalling, while HER2 is binding-defective and HER3 is kinase-defective [22].

HER1 binds to several EGF-related peptides (see above) and displays negative cooperativity in the binding of EGF, a finding which has been traditionally explained by postulating the existence of two populations of EGF binding sites on the cells at the same time: a high-affinity population, binding EGF at concentrations of 300 pM and a low affinity population, binding EGF at concentrations of ca. 2 nM [49]. According to this model, which has been extensively verified by biochemical and radiological methods by the Pike laboratory [91], the binding of the first ligand in a crystallographic dimer occurs at high affinity and stabilises the dimers, while the second binding event is energetically unfavoured and occurs at lower affinity, leading to dimer dissociation.
Structural explanations of this phenomenon, invoking asymmetry of the dimer structure, have been offered, based on asymmetric contacts in the ECD [92], or on an alternative orientation of the HER1 ECD involving asymmetric contacts with the plasma membrane [61]. Imaging studies, however, have reported findings consistent with positive cooperativity of EGF binding at dimeric binding sites on whole cells, while binding at monomeric binding sites was much slower [93], a finding which seems to suggest that negative cooperativity observed in biochemical studies might arise from the fact that a sub-population of HER1 is dimerized in

absence of ligand (pre-dimerized) on cells, as evidenced by many studies conducted with different imaging methods and on different cell types [94–110]. This population of receptors would show high-affinity binding, while the monomeric sub-population would constitute the pool of low-affinity binding sites. This phenomenon might be concomitant with the tethered-untethered conformational switch [111]. Furthermore, EGF binding kinetics have been proven to depend on the cellular context and on HER1 expression levels [112].
HER1 alone in the HER family is able to bind to actin filaments through one or more actin binding sites in its C-terminal tail [113], in a region that is required for ligand-induced cell motility stimulation [114] and internalisation [115]. This feature is likely to influence HER1 membrane dynamics. Activation of HER1 with EGF induces actin reorganisation [116] and polymerisation localised at sites of HER1 activation [117]. The actin cytoskeleton is likely to be involved in control mechanisms that regulate HER1 function [118].

HER2 has no known soluble ligand [55] and its ECD is constitutively locked in an extended conformation both in crystallographic studies [55,119] and in SAXS measurements [50]. However, structural studies also suggest that homo-dimerization between HER2 ECD monomers might be unlikely, due to steric clashes in domain II [120]. Furthermore, it has been hypothesised that the very close interaction between domains I and III in the HER2 ECD might act as a sort of tether, in analogy to what happens in the *Drosophila Melanogaster* homolog of HER1, dEGFR, preventing the correct alignment of domain II for dimerization [121] (**Figure 1-10**). Homo-association of HER2, however, has been demonstrated to occur in cells [100–102,122–125], especially when the receptor is overexpressed, and seems to be promoted by a short hydrophobic sequence in the C-terminal tail [126] of the receptor. Alvarado *et al.* suggest that the binding of HER2 ECD to a membrane-anchored ligand, such as the EGF-like domain of Mucin4 [127,128], might release the tether and allow HER2 dimerization [121].

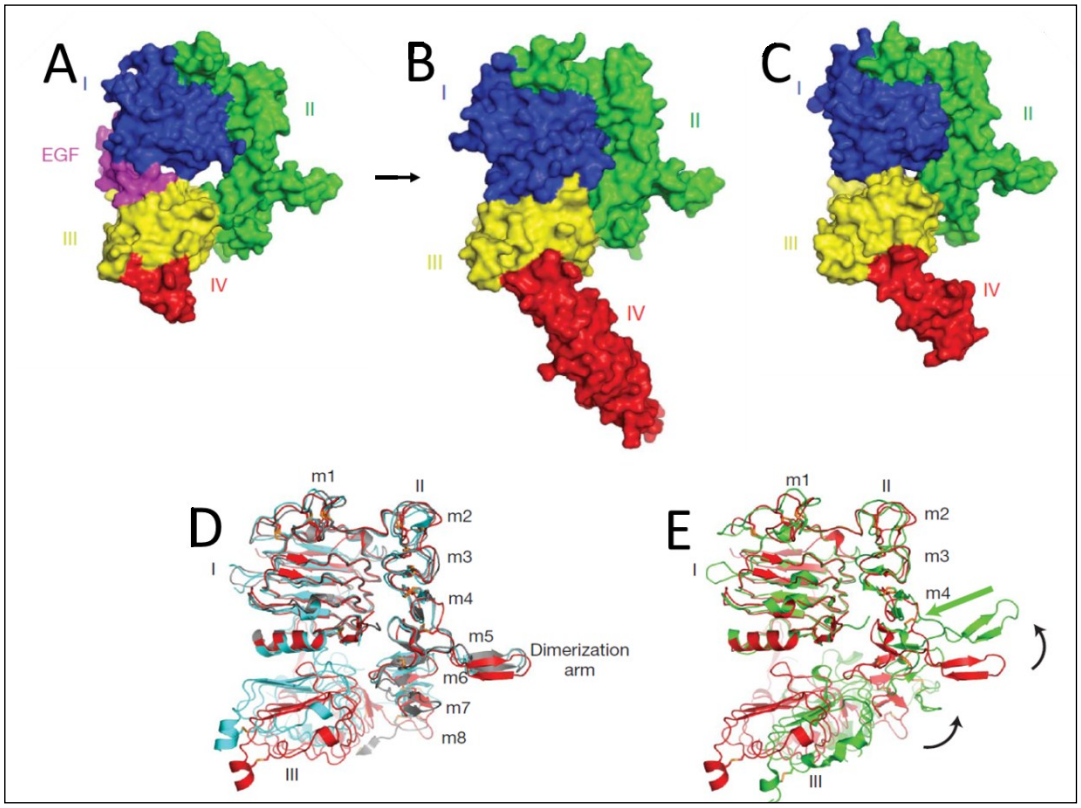

Figure 1-10 – The Domain I-III "tether" in the ECD of HER2, as proposed by Alvarado *et al.* (2009) [121]**. A-C:** HER2 ECD (**B**) shows a tight interaction between domains I-III (arrow), which is conserved in *Drosophila* HER1 (**C**), but is released in EGF-bound human HER1 (**A**). D-E: As a consequence of the domain I-III tether, domain II of HER2 is kept in an "inactive-like" conformation. D) red = dEGFR, grey= inactive human HER1; light blue = HER2. E) red= dEGFR (reference); green = active human HER1, showing a rearrangement in domain II (arrows).

Due to its peculiar ECD conformation, HER2 is the preferred dimerization partner of the other HER family receptors [129,130], and is able to mediate lateral signalling between HER family members [130–132]. In particular, its dimerization with the other defective member of the HER family, HER3, results in increased signalling throughput to downstream effectors and increased proliferation of cancer cells co-expressing the two receptors [133]. Moreover, HER2 works in concert with HER1, acting as a positive regulator of its signalling by altering its autophosphorylation pattern[78]. HER2 prolongs HER1 signalling by sequestering it at the plasma membrane [134], due to the fact that its internalisation rate is much slower than that of ligand-bound HER1[135]. HER2 is also thought to skew the equilibrium between high affinity

and low affinity EGF binding sites towards the high-affinity end when co-expressed with HER1 on cells, effectively enhancing the binding of ligand [111].

HER3, the third member of the family, has an impaired TKD, which is able to bind ATP, but shows a 1000x reduced catalytic activity compared to the TKD of HER1 and adopts a conformation that resembles that of inactive HER1 and HER4 [136]. The HER3 TKD also shows lack of conservation of critical residues in the receiver interface, and might therefore be specialised to serve as an activator of other HER family receptors. However, a recent study revealed that HER3 complexes isolated from cells show up-regulation of kinase activity after NRG1 stimulation, even when HER1, HER2 and c-Src are blocked by inhibitors, but not when a K723M mutation was introduced in the TKD of HER3 [137]. Crystallographic studies have also evidenced the formation of a symmetric N-lobe dimer between HER3 TKDs, stabilised by the exchange of C-terminal tails between the participating monomers [138], which might represent an inhibitory interaction *in vivo*.

While it can switch between tethered [51] and untethered [139] alternative conformations like HER1 [50], the ECD of HER3 also shows additional, unique features which might represent additional levels of regulation. HER3 shows a high degree of self-association even on cells that express low levels of the receptor, and this association is disrupted by ligand binding [140]. Addition of ligand, however, does not induce homodimerization and downstream signalling in chimeric HER3-HER1 receptors. NRG binding, however, does induce responses when HER3 is co-expressed with HER2 through induction of heterodimerization [141].

HER3 appears to have both a ligand-sensitive and a ligand-insensitive homo-interaction interface in its ECD. Its extended conformation, in fact, hosts both a ligand- sensitive interface that promotes ligand-independent high-order oligomerisation, and a ligand-insensitive interface that favours stable dimers with HER2 in presence of NRG [142,143]. It seems reasonable to suggest that the oligomerisation of the ECD might be linked to the “daisy-chain” N-lobe dimerization mode of the HER3 TKD in its inactive conformation [138], and that it might perform a regulatory role in live cells. In fact, it has been shown that HER3 receptors in resting MCF7 cells are segregated from HER2 receptors and that ligand binding induces a spatial reorganization of the receptors [144]. While homo-dimerization of HER3 seems to be unlikely, also due to the fact that the HER3 TMD only contains a single GxxxG association domain[64], and possibly unproductive, imaging studies have evidenced a certain degree of pre-association not only between HER3 receptors, as expected, but also between HER2 and HER3 [101,102]. The co-expression of HER3 and HER2 seems also to be able to influence the localisation of

HER3, shifting it from the nucleus to the plasma membrane [102]. Addition of NRG enhances the hetero-association of HER2 and HER3, but it also appears to be able to enhance the clustering of HER3 receptors on cell membranes [101] in some contexts, in contradiction to the results reported by the Landgraf group.
In addition to this, HER3 also shows quite interesting ligand binding properties. The HER3 ECD is able to bind to its ligand NRG even when constitutively locked in a tethered configuration, albeit with lower affinity compared with the wild-type receptor. However, the affinity of the locked HER3 ECD improves with increasing pH. In fact, it appears that NRG binding to HER3 might be retained at endosome-like pH [145], a finding that is in contrast with the fact that NRG dissociates from HER3 in real-life endosomes [21], a feature that is thought to contribute to the enhanced recycling of HER3 after its slow internalisation [135]. By analogy with findings reported for HER1, HER3 also seems to display negative cooperativity for NRG binding [146], which might be caused by structural effects analogous to those cited for HER1, with the added complication of the preferential heterodimerization of HER3 with HER2, which is known to enhance affinity for NRG ligands [87]. It seems reasonable to suggest that high-affinity NRG binding sites might be formed by HER2-HER3 pre-dimers.

The fourth and last member of the HER family, **HER4**, is an independent receptor capable of both ligand binding and downstream signalling [22]. It can be alternatively spliced in functionally specialised isoforms differing in the JMD and therefore differentially susceptible to proteolytic processing, called JM-a and JM-b [147], or in the C-terminal tail and therefore differentially able to recruit phosphatidyl inositol 3-kinase (PI3K), called CYT-1 and CYT-2 [148]. Its ligand-dependent proteolytic processing results in the shedding of a 80 kDa ICD fragment, which has a role in nuclear signalling [149] and in the regulation of apoptosis [42]. HER4 can bind to various NRG isoforms and its binding is enhanced by heterodimerization with HER2 [87]. As this receptor is not going to be investigated in this thesis, further discussion of its properties goes beyond the scope of this introduction.

From the discussion above, it is clear that **heterodimerization** represents a key advantage for signalling differentiation and enhancement. In fact, heterodimerization contributes to the diversification of the complement of effectors recruited upon ligand binding, with HER2-HER3 heterodimers having the largest pool of potential downstream interactors, followed by HER1-HER3, HER1-HER2 and finally HER1-HER1 [150], a feature that correlates well with the transforming potencies of HER family dimers [151]. The HER2-HER3 dimer is, in fact the most

potent dimer in terms of stability and signalling potency, and is the most effective oncogenic transformator when expressed in normal cells [152]. HER2 and HER3 have been proven to form an oncogenic unit for signalling, and it has been demonstrated that, HER3 requires HER2 for downstream phosphorylation, but also HER2 requires HER3 to deploy its full signalling potential [133]. Dimerization with HER2 is also advantageous for HER1 in terms of acquiring the ability of prolonged signalling from the membrane, due to receptor sequestration from the clathrin-coated pits and impaired ubiquitinylation [134].

While crystal structures of HER family heterodimers are not available yet, clues on the structure and on signalling mechanisms of HER1-HER2 and HER2-HER3 heterodimers have been obtained through sophisticated biochemical and mass spectrometry studies. For the HER1-HER2 heterodimer, luciferase complementation studies have indicated that EGF binding causes HER1 to adopt the receiver position in the asymmetric kinase dimer, so that it is activated first and is able to phosphorylate the C-terminal tail of HER2 [153]. The HER1-HER2 heterodimer binds EGF with a 7x higher affinity than HER1-HER1 homodimers and is not subject to negative cooperativity-associated destabilisation upon binding of a second ligand, a fact which would enhance its stability and allow more prolonged signalling [154].

Recently a similar study has found the presence of pre-formed HER3-HER3, HER1-HER1 and HER1-HER3 dimers in cells transfected with specific receptor pairs [143]. As expected by the findings of the Landgraf group discussed above [140], treatment with NRG1β induced a decrease in HER3-HER3 association with an EC_{50} of 35 pM and an increase in HER2-HER3 association with an EC_{50} of 380 pM. The association of HER2-HER3 was inhibited by the A30 aptamer, which interferes with the secondary interface on the ECD of HER3 [142]. Conversely, high doses of NRG1β could promote HER1-HER3 association, but even small doses of EGF promoted dissociation of this interaction, even in the presence of NRG1β.

On the structural side, mass spectrometry studies, have revealed that dimerization of HER2 and HER3 TKD on artificial membranes in the presence of ATP leads to adoption of the activator position by receiver interface-impaired HER3, and to conformational changes in the HER2 activation loop that are consistent with the activated conformation of the kinase [155].

The role of **high-order association or oligomerisation** of HER family members is less well understood. Homo-oligomerisation of HER1 and HER2 is known to occur on cell membranes, especially when the receptors are overexpressed, however its functional significance is in most cases still unclear. As discussed above, basal oligomerisation of HER1 has been detected by a host of different techniques [94–110] and is known to increase with ligand binding.

Oligomerisation in clathrin-coated pits is a prerequisite for ligand-dependent HER1 internalisation [135], however the role of other forms of higher-order association of HER1 is still unclear. However, higher-order association has been proposed as a key process both for ligand-independent signalling in HER1-overexpressing cells [98], and for ligand-dependent signalling on cells that express low, "physiological" levels of HER1 [96,99]. Moreover, basal HER1 dimers or clusters have been proposed as high-affinity sites for EGF binding [93]. High-order association has also been detected for both HER2 [100–102,122–126] and HER3 [101,102,140] on the membrane of mammalian cells. In both cases these clustering events have been proposed as mechanisms for the negative regulation of HER family signalling through spatial segregation of receptor populations, however, recent studies have evidenced that disruption of HER3 oligomers with an aptamer leads to an increase in NRG1 binding sites but a decrease in their affinity [156], and to selective inhibition of HER2 and MAPK phosphorylation in response to NRG1, while HER3 and Akt phosphorylation is maintained [157], a finding that seems to corroborate the hetero-oligomeric model of HER2-HER3 signalling proposed by Huang *et al.* [132].

Another source of ambiguity resides in the effects of HER family-targeted **Tyrosine Kinase Inhibitors (TKIs)** on the association state of the receptors. This is also due to the existence of two different classes of anti-HER family TKIs, characterised by different binding preferences. Class I inhibitors like Gefitinib and Erlotinib are believed to preferentially bind to the active conformation of the TKD [73], however both have recently been crystallised with an inactive-like HER1 TKD [158,159], while Class II inhibitors, such as Lapatinib, can only bind to the inactive conformation of the TKD, due to the presence of bulkier substituents on their structure [160]. Different studies conducted with different TKIs and different methods have produced results that are not always readily compatible.

Class I TKIs, such as Gefitinib, Erlotinib, AG1478, AG1517 and PD168393, have been found to increase HER1 homo-association or hetero-association between HER1 and HER2, while Class II inhibitors like Lapatinib and HKI-272 do not do so [79,80,161–164], and in fact can disrupt ligand-induced dimerization of HER family members as well as pre-formed receptor dimers [165]. Formation of an asymmetric TKD dimer is required for Class I TKI-induced dimer formation [80], however there are indications that the ECD conformation might differ from the canonical back-to-back dimer in this case [163].

Interestingly, PD153035 and Gefitinib were found to alter the properties of EGF binding to HER1, abolishing high- and low-affinity binding sites and introducing a population of

intermediate-affinity sites associated with a population of inactive dimers [166]. The formation of Gefitinib-induced dimers has also been associated with an increase in EGF binding sites that is not linked with an increase in HER1 protein levels at the cell surface [167,168], a finding that parallels what reported by Chen *et al.* on NRG1 binding to HER3 in cells treated with an oligomerisation-disrupting aptamer [156], and which seems to indicate that Gefitinib might disrupt HER1 oligomers, favouring the formation of inactive dimers. Gefitinib has also been found to favour the formation of inactive HER1-HER2 and HER1-HER3 dimers on BT474 cells, while still preventing signalling from either NRG1 or EGF [169]. Treatment of cells with Erlotinib can lead to the stabilisation of interactions between activated HER1 and HER2, however this is associated with a reduction in receptor phosphorylation [170]

Some reports have shown that AG1478 can cause dispersal of sub-micron HER1 clusters, reducing their receptor content but increasing their density per membrane area [98,103]. Type I inhibitor PD153035, instead, could prevent EGF-induced increase in HER2 clustering on SKBR3 cells in near-field scanning optical microscopy (NSOM) experiments [122] , while AG1478 could only reduce HER2 phosphorylation but not clustering in Immuno-EM experiments [101].

PF00299804 (dacomitinib), a new-generation irreversible pan-HER TKI, which has been shown to bind to the HER1 TKD both in its active and inactive conformations, even if the covalent interaction is formed only with the inactive conformation [159], could block HER1-HER2, HER2-HER3 and HER3-HER4 hetero-association on SNU216 cells [171].

Recently, ensemble luciferase complementation experiments in Cho cells transfected with HER receptor pairs have shown that both Lapatinib and Erlotinib can increase the pre-dimerization of HER1-HER1, HER1-HER2, HER1-HER3, HER2-HER3 and HER3-HER3, with Erlotinib having a larger effect than Lapatinib, even if phosphorylation is blocked [143]. In addition to this, TKIs inhibited the phosphorylation-associated decrease in HER1-HER2 association in response to EGF and stabilised the formation of HER1-HER3 dimers in the presence of NRG1β. These authors postulate that TKI binding to kinase-impaired HER3 might be involved in this behaviour.

In conclusion, the role of TKIs in HER family homo-and hetero-associations is still unclear and ambiguous and likely dependent on minute differences in the changes introduced by TKI binding in the TKD of the receptor and in their binding kinetics. In fact, kinetic data has shown that Lapatinib binding blocks HER family TKDs in an inactive conformation for a long timescale (20+ hours) even in the absence of a covalent alteration of the TKD, while the binding of Gefitinib is transient and the receptor could conceivably cycle between conformations even in the presence of the inhibitor. The result is that Gefitinib inhibition is fast but incomplete, with

chronic low-level activation of a sub-population of receptors, while Lapatinib inhibition has a delayed onset, required for the receptors to adopt the inactive TKD conformation, but is complete [172].

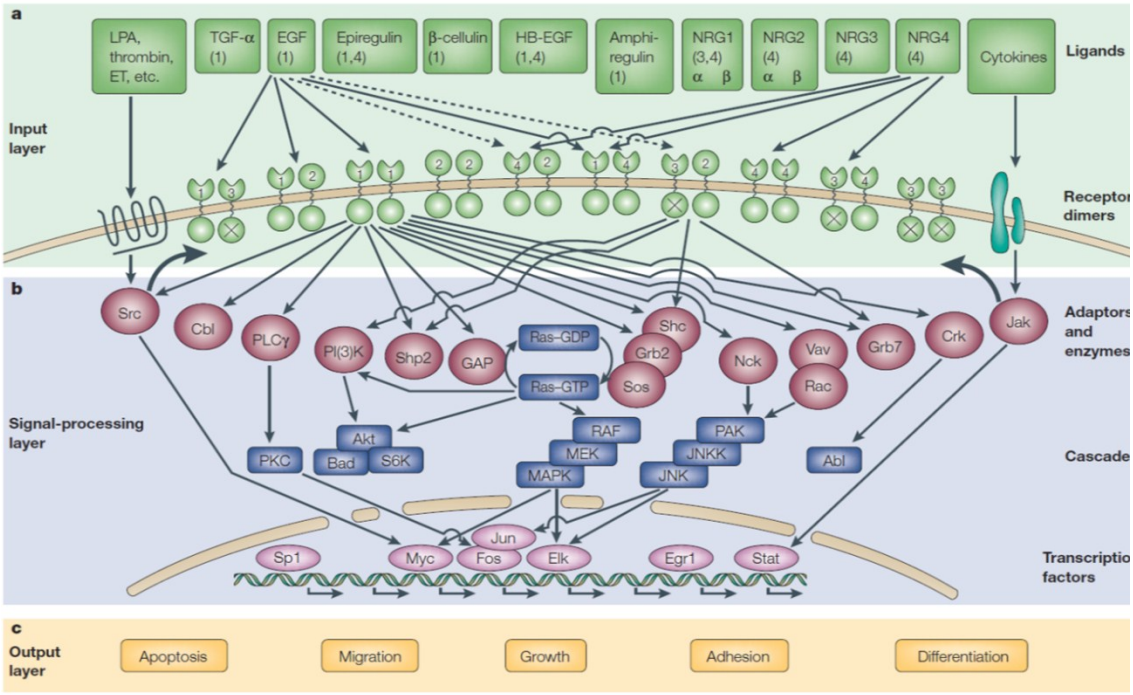

Figure 1-11 - Simplified scheme of the HER family signalling network, adapted from Yarden and Sliwkowski (2001) [22]**.**

The so-called "signal-processing layer**"** of the HER family network is constituted by a set of conserved and versatile downstream effectors, which are recruited either directly or indirectly to phosphotyrosine residues on the C-terminal tail of the receptors. Recruitment specificity and kinetics depend on the phosphorylation pattern of the tyrosine residues on the C-terminal tail of the receptors, which, as discussed above, is ultimately dependent on the specificity and kinetics of ligand binding and receptor association [22,48], resulting in biological outcomes that are context-dependent, dimer-dependent and ligand-dependent. The main outcomes of the HER family network are cell proliferation, regulation of adhesion and motility, protection against apoptosis and promotion of invasion and angiogenesis [22], which underlie the roles of the receptors in both their physiological contexts and in cancer.

Among the key players of HER family downstream signalling there are the Mitogen-Activated Protein (MAP) cascade, initiated by recruitment of Grb2 and Shc on sites present of most family members [173] and PI3K. The latter can be activated indirectly and weakly activated by all receptors via the MAP cascade [22], but is directly and strongly recruited upon ligand binding to 6 tandem phosphotyrosine motifs on HER3 [174]. All six motifs are functional [175],

and PI3K can bind both tyrosine residues in one motif at the same time using its two SH2 domains [176]. Both HER1 and HER4 can interact with STAT5 [173], while the unique interaction of HER1 with c-Cbl is important for the negative regulation of its signalling via ligand-dependent endocytosis and degradation[135].

In general, HER2 is the most promiscuous receptor in the family, and is able to bind a much more diverse array of SH2- and PTB- containing proteins than its fellow family members [150]. According to proteomic array studies, HER1 and HER2 become more promiscuous in their binding as the receptor concentration increases, while HER3 does not [150], a finding which might highlight two important concepts: that HER1 and HER2 overexpression has profound effects on signalling that go beyond an increase in intensity, and that the function of HER3 is specialised and restricted to the activation of a critical subset of downstream effectors.

The core of the signalling processing layer is regulated by an array of positive and negative feedback loops [48] and serves as an integration module [22], which collects and relays information from different signalling pathways working in concert. These feedback loops can critically modify receptor functions via several different mechanisms, such as: phosphorylation of the tail or of the TKD of HER family receptors, induction of receptor expression or degradation, activation or inactivation of phosphatases that down-regulate receptor signalling, and induction of ligand expression and cleavage.

Among the key feedback mechanisms involved in the regulation of the HER family signalling at the input layer are:

1) the ligand-induced internalisation and degradation of HER1 via the E3 Ubiquitin ligase c-Cbl, which is actively recruited and phosphorylated by HER1 [177], a mechanism which is fast and requires HER1 TKD activity and the N-terminal GxxxG TM domain of the receptor [178];

2) the activation of c-Src via GPCRs and other receptors, which results in regulatory phosphorylation of the TKD of HER1 [179], but also in the induction of pro-ligand cleavage via ADAM proteases [21], which can also be regulated by PKC isoforms [82], PKB [83,84]and the MAPK cascade[23];

3) HER1 signalling down-regulation via SHP1 and SHP2 [48] and other phosphatases such as PTPB1 and DEP1[23];

4) interplay with other RTKs, such as c-Met [180–182], FGFRs [182], IGF-1R [183–185] and Axl [186] and withTGF-β receptor [187,188],CD44 [189] and integrins ([188,190–193], reviewed in[194]).

Downstream signalling, instead, is chiefly regulated by the MAP cascade feedback loops and by the PI3K/AKT/FOXO3 loop. Cross-regulation of the two main signalling routes is present [195]

and contributes to the robustness of the system.

The MAPK feedback systems result in different effects according to the origin of the stimulus: HER1 activation via EGF results in transient activation of the MAPK cascade, due to a negative feedback loop resulting in RAF1 [23] and Sos [48] inactivation by ERK1/2, while NRG1 activation of HER3/4 results in sustained MAPK signalling [196], probably through a positive feedback from ERK1/2 to RAF1[23]].

The PI3K/AKT pathway [195] is involved in the control of cell growth and survival in response to external cues. Its feedback system has a homeostatic role in the signalling of the HER family, acting as a rheostat to control the flow of information through the pathway. In normal circumstances, HER3 membrane protein levels are tightly regulated via a series of transcriptional, translational and post-translational mechanisms under the control of this pathway [197,198]. When signalling through the PI3K/AKT axis is disrupted by perturbations that reduce the information flow (among which, targeted therapeutics for breast cancer treatment [199]), the PI3K/Akt pathway tends to conserve the information flow by increasing HER3 protein and mRNA levels [200–203], and inducing NRG production [83,204]. Furthermore, the intrinsic anti-apoptotic signalling of the PI3K/Akt axis has a role in cancer development and drug resistance [205].

The robustness and the feedback mechanisms of the HER family network, which have evolved to maintain homeostasis in physiological conditions, are readily hijacked by carcinogenic processes and, as a result, it is quite challenging to effectively shut down the network with a single targeted agent. As discussed before, the PI3K/Akt module compensates for reductions in signalling through the HER family network by up-regulating key components of the network, thus maintaining its own activation levels and downstream signalling. Furthermore, key components of this module are often mutated or deregulated in cancer, PI3K mutations and PTEN loss being the most common alterations [195].

The MAPK signalling cascade can also be de-regulated, for example by activating mutations in K-Ras or in BRAF which result in enhanced downstream signalling and cause resistance to HER family targeted agents [206]. The activation of secondary or alternative RTKs (see **Figure 1-12**) might also sustain the signalling through critical points of the network [207], as exemplified by the up-regulation of HER2 activity upon HER1 blockade [46] or vice-versa [43,208] , and by the induction of alternative HER family dimers upon blockade of one interactor [84,209,210], in addition to cross-talk with other RTKs or integrins (see above). Furthermore, autocrine or paracrine secretion of EGF-like ligands, activated in response to network perturbation, can also

contribute to the maintenance of the information flow through the network and to drug resistance [45,211].

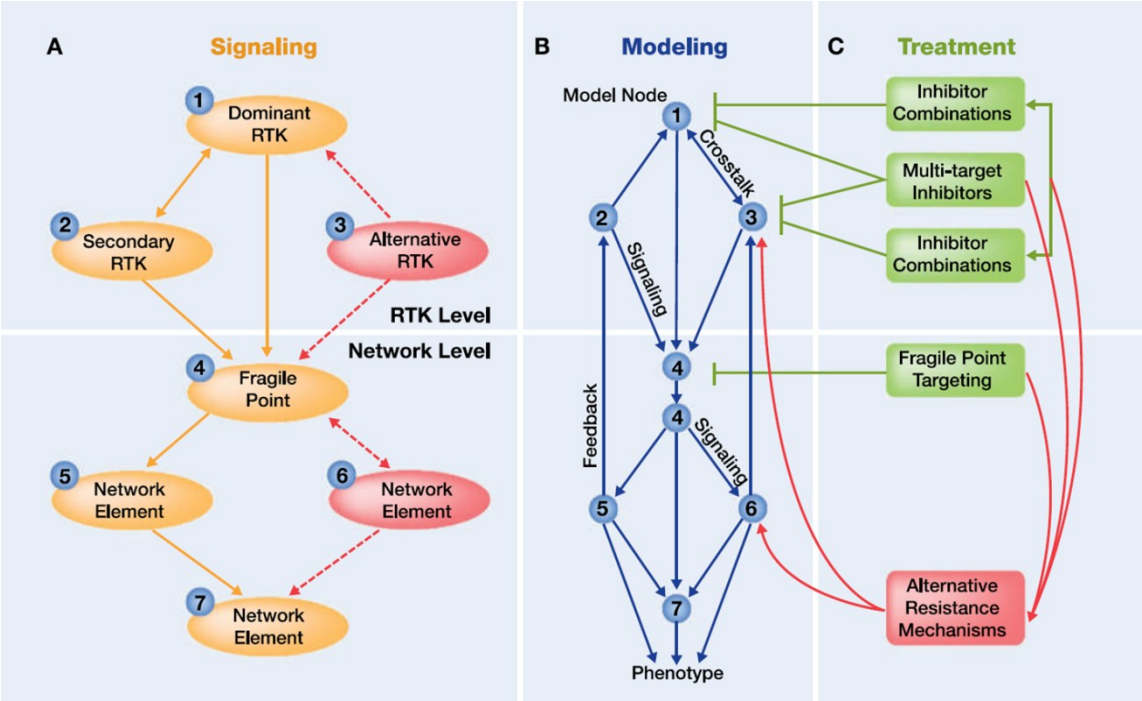

Figure 1-12 – Schematic representation of the process of activation of secondary or alternative RTKs in response to perturbations or blockade of the signalling of the dominant RTK in a robust network, such as the HER family network. From Xu and Huang (2010) [207]**.** The fragile point identified in this scheme, is loosely defined as a druggable signal transducer downstream of the RTK level. It can be one of the common integrators of the system, or the mediator of the activation of a specific network function (e.g. cell survival) further down in the network hierarchy.

In conclusion, the complexity and robustness of the HER family network, which performs a critical role in the physiology and development of mammalians, are turned against the host by epithelial cancers, which exploit and pervert in-built checks and balances to maintain deregulated signalling through key points in the network and sustain unlimited proliferation, invasion and metastasis. The processes which are at the root of these phenomena are still not completely understood and, in particular, the “rules of engagement” and the kinetics of receptor association and dissociation at the plasma membrane in presence of different stimuli and perturbations are not completely understood. The role of membrane structure and cytoskeletal determinants in the regulation of HER receptors association and signalling are not completely clarified, and there is currently no unified theory on the role of high-order molecular association between members of the HER family in signalling. All these points need

to be clarified before it will be possible to construct a reliable and clinically relevant model of the HER family signalling.

In order to contribute to shedding some light on these “dark areas”, quantitative, real-time and multi-parametric data are needed, such as might be obtained by Single-Molecule Fluorescence techniques.

An overview of such techniques and their advantages for the study of complex membrane processes will be provided in the following section of the introduction.

1.2. Single-Molecule Fluorescence Techniques for the Study of Membrane Processes

Fluorescence is the physical phenomenon whereby a quantum of light, a photon, is emitted, typically within nanoseconds from the absorption of an exciting photon, by a substance that has absorbed light or other electromagnetic radiation. In the greatest majority of cases, molecules disperse absorbed energy as heat; however some molecules, called fluorophores, are able to absorb specific amounts of energy from electromagnetic radiations and be promoted to a higher electronic state. These molecules then release some of the energy as fluorescence. Emission of energy from a triplet state, usually within the order of microseconds to milliseconds, is called phosphorescence [212].

When a fluorophore absorbs a quantum of light or photon, the energy from the photon is transferred to the fluorophore. The energy conveyed by a photon is inversely proportional to its wavelength, as described by **Equation 1-3**, where h is Planck's constant and c and λ are the speed and wavelength of light in vacuum. The frequency (ν) of a photon is defined as c/λ.

$$E = h \times c / \lambda$$

Equation 1-3 – The energy of a photon.

When they are not excited by photons, fluorophores exist in a distribution of energy sub-states within the ground state (S_0), characterised by different vibrational and rotational energy, as shown in **Figure 1-13**. Excited energy states (S_1, S_2, etc.) also exist in a number of vibrational and rotational sub-states. The difference in energy content between the ground and the first excited state, however, is large enough that fluorophores cannot jump between the two just by absorbing thermal energy.

When a fluorophore absorbs an incident photon ($h\nu_A$) of sufficient energy, it transitions to one of its excited states in ~ 10^{-15}s. When the absorbed energy is higher than that required to reach the first level of the first excited state, it is dissipated via **thermal and vibrational relaxation** (brown path) to the lowest sub-level of the first excited state. Alternatively, when a molecule reaches a higher excited level, a phenomenon of non-radiative dissipation termed **internal conversion** (light grey path) occurs. Both phenomena have a timescale of approximately 10^{-12} s. The residual energy is emitted as a photon with a decay rate k_{rad}, and the molecule transitions back to one of the sub-levels of the ground state S_0. Thermal and vibrational relaxation will then bring the fluorophore back to the lowest energy level. The range of

energies of the possible emitted photons determines the width of the emission spectrum. The lifetime of fluorescence emission, τ_F, is typically determined by the time the molecule spends in the lowest sub-level of the excited state S_1 and is a characteristic feature of each fluorophore. Typical emission lifetimes for small organic fluorophores are in the order of 10^{-8} s, so relaxation and internal conversion are usually complete before emission (red path). Processes that increase the dispersion of energy via non-radiative (dark grey) paths also reduce τ_F. The parameter k_{nr} in the figure below groups the decay rates of various non-radiative processes that compete with fluorescence emission.

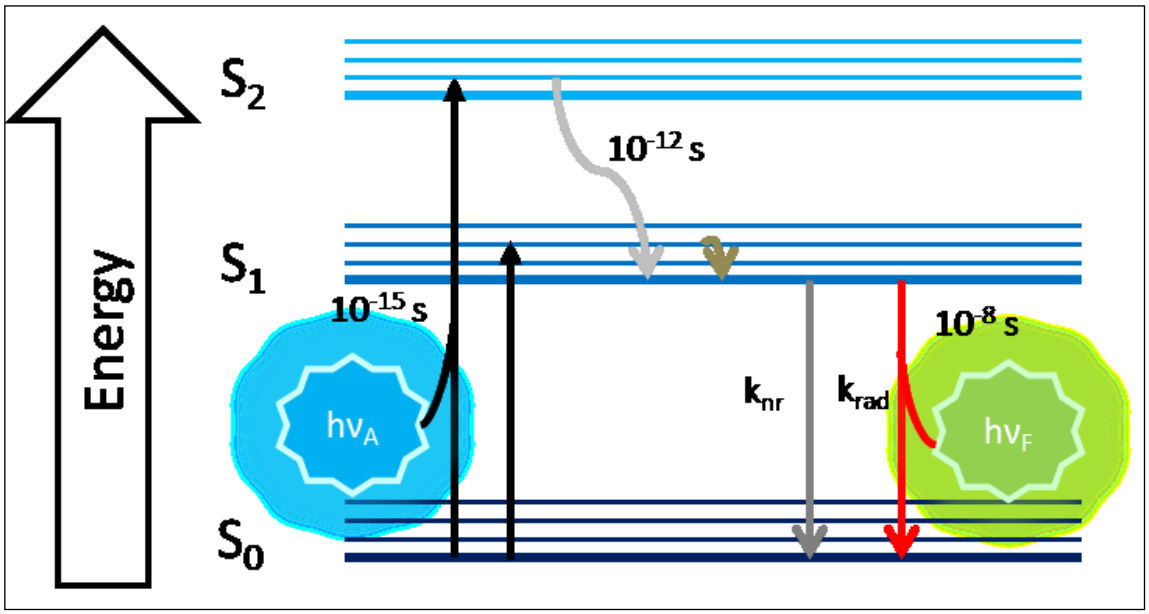

Figure 1-13 – Simplified Jablonski diagram, illustrating the principal phenomena regulating fluorescence emission (after Lackowicz (2006) [212]**).**

Due to the energy losses of the relaxation and conversion processes, the emitted photon will have a lower energy ($h\nu_F$), and therefore a longer wavelength, than the absorbed photon, which means that the emission will be red-shifted. This red-shift is known as **Stokes' shift**. However, molecules can also be excited when they reside in higher sub-levels of the ground state S_0, therefore the energy jump required to come back to the ground state is higher than the energy absorbed; this phenomenon is at the basis of the overlap of excitation and emission spectra seen for some fluorophores.

Usually, fluorophores have a large enough gap in energy between the first excited state and the ground state that the path to eliminate this extra energy ends in the expulsion of a visible photon, however absorbed energy can also be dispersed via several non-radiative paths, which do not result in the emission of a photon, such as quenching [212] and rotational relaxation

[213], all of which are grouped, for simplicity, under the decay rate k_{nr}. Among the most relevant non-radiative paths is **intersystem crossing**, a process that results in a "forbidden" transition to a triplet state of overlapping energy [214]. This phenomenon can occur because in some fluorophores the vibrational levels of the triplet state T_1 may overlap with those of the excited (singlet) state S_1. Molecules converting to triplet state have no easy relaxation path back, as emission entails another "forbidden" transition to the singlet state, therefore, the lifetime of emission is in the order of microseconds. Intersystem crossing is the origin of phosphorescence emission and effectively acts as a "bottleneck" for fluorescence emission, as it sequesters affected molecules in a "dark" state that no longer emits photons. Triplet molecules, however, can still absorb photons, which cause transitions to higher energy triplet states and delay the emission even further. Additionally, due to their longer lifetime, triplet state molecules are particularly reactive with singlet oxygen and other free radical molecules, which can covalently alter the fluorophore structure and inactivate it permanently [214].

The ratio of fluorescent emission to non-radiative energy losses is defined as **Quantum Yield** (**Equation 1-4**).

$$QY = k_{rad} / \left(k_{rad} + k_{nr} \right)$$

Equation 1-4- Quantum Yield of a fluorophore

QY can be close to unity for very good fluorophores, where $k_{nr} << k_{rad}$, however, it will always be <1, due to the energy losses of the relaxation phase [212].
Another very important parameter that determines the emission of a fluorophore, especially under low light excitation, is the **extinction coefficient** (**ε** [$M^{-1}cm^{-1}$]), which describes the probability with which a solution of a given fluorophore absorbs exciting light passing through it [214]. This parameter is conceptually similar to the **absorption cross-section of a dye** (**σ** [cm^2]), which describes the probability that a single dye will absorb an incident photon [213]. Maximising this parameter is very important for low-light or very high-sensitivity applications.

Organic fluorophores usually have a high degree of conjugated double (C=C) bonds or aromatic ring structures with *pi* electronic clouds. Dyes that redistribute their outermost electrons on a large area, delocalising the optical transition, are called resonant dyes. Alternatively, in order to emit, dyes can undergo intramolecular charge transfer transitions, as in the case of coumarins and other charge-transfer (CT) dyes [215]. Both classes of dyes are commonly used in biological applications.

As rotational or vibrational rearrangements can compete with fluorescence emission for the dissipation of absorbed energy, usually the best organic dyes in terms of Quantum Yield have a rigid, planar structure, characterised by multiple aromatic rings [213]. Atto dyes (ATTO-TEC GmbH - Siegen, Germany) are a prime example of this synthetic strategy [216].

Fluorescence microscopy is a well-established technique for the investigation of biological systems. Fluorescent molecules that can be excited and emit in the visible range of the spectrum are not very abundant in most mammalian cells, and intrinsic fluorophores such as tryptophan, flavins and flavonoids are not as bright as synthetic, purpose-designed fluorophores. For this reason, fluorescence-based imaging techniques enjoy considerable specificity and sensitivity in detecting the molecules of interest, allowing researchers to distinguish them from the very complex biological matrix that surrounds them, in contrast to more morphologic techniques such as histochemistry, and electron and X-ray microscopy. Furthermore, careful selection of fluorophores with well separated emission spectra and the use of filters to prevent cross-contamination of the different signals allows multiplexed detection of fluorescence signals with different wavelengths at the same time. In addition to that, fluorescence imaging techniques have the advantage over both biochemistry and electron microscopy of being able to follow biological processes through time in live cells. Reagents for fluorescence microscopy are generally soluble in cell growth medium or other aqueous buffers and cause minimal perturbations to the cell structures being imaged. A great wealth of fluorescent reagents is available, covering the whole visible spectrum and, more recently, also the near infra-red wavelengths. Fluorescent indicators are available as reporters for a variety of cell processes, making fluorescence microscopy techniques very versatile.

The very basic setup requirements for a fluorescence microscopy include a light source of suitable wavelength to provide photons for fluorophore excitation, an objective to focus the excitation light and collect the emitted fluorescence, a detection system, and filters that allow the separation of the excitation light from the emitted fluorescence [214].
The light source can be either an arc lamp or a laser and ideally should be stable in time. Filters are used to select narrow excitation bands, especially if multiple excitation wavelengths are used at the same time. A dichroic beamsplitter, which reflects the excitation light, but lets the emitted fluorescence through, is then used to re-direct the excitation wavelength to the sample through the objective. In the most common microscopy setup, the collection of the emitted fluorescence is also done through the same objective, in a geometry called "**epi-**

fluorescence" [217]. The emitted fluorescence is conveyed via the dichroic beamsplitter to an emission filter, which selects a relatively narrow emission band and conveys it towards the detection system.
Basic epi-fluorescence microscopy is a wide-field technique, which collects fluorescence from the whole illuminated area at the same time.

In all microscopy techniques, the main challenge is to obtain sufficient contrast to discriminate the objects of interest from irrelevant background. For fluorescence techniques, this translates into the need to optimise signals from fluorescent molecules of interest, and maximise the difference in intensity between the signal arising from the molecules of interest and that of the background, *i.e.* the **signal-to-background ratio** (**SBR**).

The QY and ε are the main parameters that determine the brightness of any given fluorophore, but, however high they might be, the total output of photons from a given fluorophore is limited by several processes.
One of the main processes that reduce photon output is the optical **saturation of the transition to the excited state**. As the excitation intensity increases, when the rate of photon absorption equals or exceeds the emission rate, there is a net decrease in photon uptake and, consequently, in extinction coefficient, because the molecule cannot decay to the ground state fast enough to absorb another photon. As described by **Equation 1-5**, the intensity of saturation depends on the energy of the excitation light and on the fluorophore lifetime and absorption cross-section [213].

$$I_S = h\nu / \left(2\sigma\tau_F\right)$$

Equation 1-5 – Saturation intensity for a given fluorophore.

Another process which causes a net reduction in the number of photons emitted by a given fluorophore is **photobleaching,** defined as any process that causes an **irreversible** conversion of a fluorophore into a form that is unable to emit photons [213]. The photochemical processes underlying photobleaching are not yet completely understood, but the likelihood of intersystem crossing into a triplet state is related to this phenomenon. As discussed before, the longer lifetime of the triplet state (in the order of μs-ms), gives molecules higher chances to interact with reactive species present in the micro-environment than the singlet excited state (lifetime in the order of ns). In particular, interactions with singlet oxygen, which itself is

produced by the interaction of molecules in the triplet state with molecular oxygen, and with other radicals, which may even be excited singlet molecules of the same species [218], are known to cause irreversible alterations to the structure of a fluorophore and terminate photon emission [214]. The likelihood of the transition to the triplet state is determined by the QY of a fluorophore: the closer the QY is to 1, the less likely alternative paths to relaxation other than fluorescence emission are. Another mechanism for photobleaching is the re-excitation of a molecule already in the excited state, which can lead to the conversion of the fluorophore into an unstable, more easily inactivated, form [219]. The latter phenomenon is related to the lifetime of the excited state and to the saturation intensity for the fluorophore.

Quenching, which, is a reversible process, can be caused by proximity to other fluorophore molecules of the same species, or to other molecules able to syphon energy from nearby fluorophores and by changes in pH or ionic strength in the local environment [212].

Photoblinking, which is another major cause of reduction in photon output, is reversible, but can be related to the conversion of a fluorophore into the triplet state or to the switching of some fluorophores, such as Cy5, into a photoinactive state [219]. Even if they are defined as transient, dark states induced by photoblinking can be quite long-lived, and this can reduce the quality of the fluorescence signal, particularly in advanced applications such as Single Molecule techniques.

1.2.1. Optical principles underlying TIRF techniques and advantages thereof

In order to maximise the SBR, it is not only necessary to maximise the signal, for example by choosing fluorophores with high QY and ε and long photobleaching half-lives, but also to minimise the background.

One of the main methods of reducing background noise is minimising the excitation volume, which for conventional epi-fluorescence has a depth of ca. 1-3 μm [217]. This will result in reduced excitation of out-of-focus fluorescent molecules and reduced fluorescence scatter by the non-fluorescent bulk of the sample.

Confocal techniques, reduce illumination volume by scanning a tightly focused spot of light in a point-by-point fashion all over the sample and collecting the emitted fluorescence through a small pinhole placed in the light path at the conjugated focal plane [220]. This device reduces the contribution from the light coming from out-of-focus planes, granting higher SNR and the ability to optically section the sample with a depth of ca. 500-600 nm [217]. A related method exploits the reduction of the excitation volume through manipulation of the excitation light

through special high intensity lasers (STED [221]). This technique is also point scanning, but it has the added advantage of not only reducing the emission volume, but also the excited volume.

Another popular strategy for limiting the excited volume is **Total Internal Reflection Fluorescence** (**TIRF**) Microscopy [222]. This technique exploits the generation of an "evanescent field" by an incident beam of light at the interface between a medium with high refractive index (n_1) in which the beam was traveling and a medium with lower refractive index (n_2), when the incidence angle of the light is greater than a critical angle θ_c where:

$$\theta_c = \sin^{-1}(n_1 / n_2)$$

Equation 1-6 – The Critical Angle

The parameters n_2 and n_1 are the refractive indices of the low-refractive index medium and the solid, respectively, and the ratio n_1 / n_2 needs to be <1 for Total Internal Reflection to happen. If the incidence angle $\theta < \theta_c$, the incident light propagates into the sample with a refraction angle given by Snell's law in **Equation 1-7**.

$$\frac{\sin\theta_1}{\sin\theta_2} = \frac{n_2}{n_1}$$

Equation 1-7 –Snell's Law

When $\theta > \theta_c$, however, all the light reflects back into the high-*n* medium, but some of the incident light energy penetrates into the lower *n* medium as an "evanescent field" and propagates parallel to the surface of reflection, thus exciting the fluorescent molecules closest to the interface [223]. The intensity of the evanescent field decays exponentially with increasing distances from the surface of reflection, as described in **Equation 1-8**,

$$I(z) = I(0)e^{-z/d}$$

Equation 1-8 – Intensity decay of the evanescent field

where *z* is the perpendicular distance from the surface of incidence and *d* is the depth of the evanescence field. The depth of the evanescence field, *d*, is described by **Equation 1-9**,

$$d = \frac{\lambda_0}{4\pi n_2}\left(\sin^2\theta - \beta^2\right)^{-1/2}$$

Equation 1-9 – The depth of the evanescent field

where λ_0 is the wavelength of the incident light and β stands for the ratio of n_1/n_2<1. A schematic of the TIR process is shown in **Figure 1-14**.

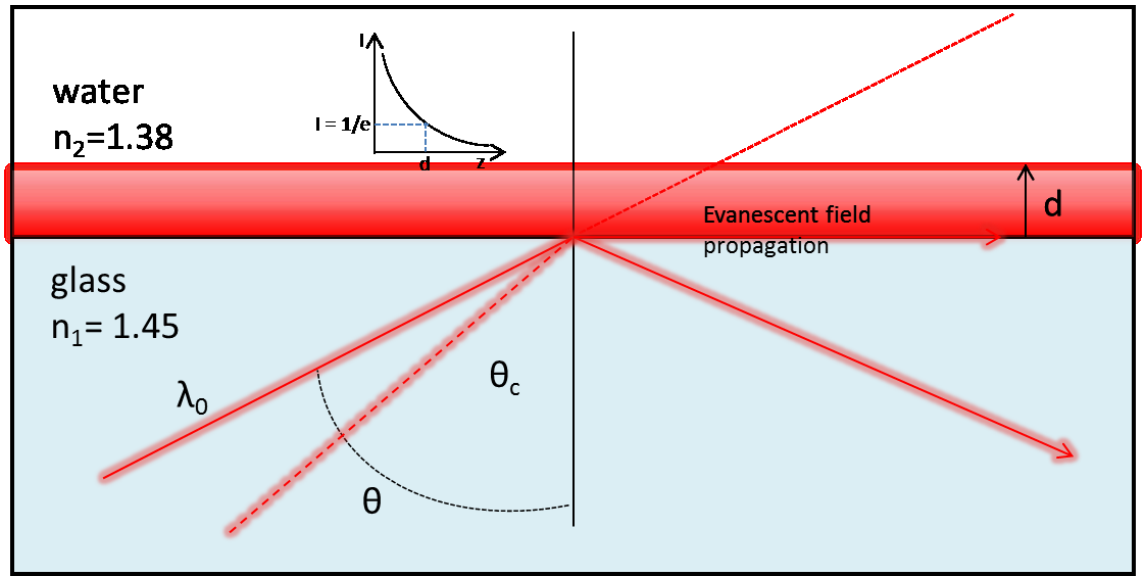

Figure 1-14 – Diagram of TIR process. A light beam of wavelength λ_0, travelling in a medium of refractive index n_1 will undergo total internal reflection at the interface with a second medium of refraction index $n_2<n_1$ if its incidence angle θ is greater than a critical angle θ_c given by the relation $\theta_c = \sin^{-1}(n_1/n_2)$. If this condition is verified, the incident beam will be totally reflected back into the high-refractive index medium and only some of the incident energy will propagate into the low-refractive index medium as a standing wave called "evanescent field". This propagates parallel to the surface of reflection and decays exponentially with the distance from it. The depth, *d*, of an evanescent field is the distance from the reflection surface at which the field decays to 1/e.

The depth, *d,* of the evanescent field, defined as the distance from the interaction surface at which the intensity decays to 1/e (37%), decreases with the incidence angle θ and is usually in the order of λ_0 or smaller. Typical values for *d* are in the range of 100-150 nm [223].

There are two main classes of TIRF setup for biological applications: through-the-prism TIRF and through-the-objective TIRF (or prism-less TIRF).
In the through-the-prism setups, a trapezoidal prism is inserted in the condenser mount and kept in optical contact with the sample coverslip through a layer of immersion oil or other

mounting medium. The beam is then reflected off one of the slopes of the prism via an extra lens upbeam of the prism, so that it reflects at a high incidence angle on the coverslip. The fluorescence signal is then detected from above using a water-immersion objective directly immersed in the buffered solution of the sample [223]. The main advantages of this class of setups are that they are relatively inexpensive and that the TIRF signal is exceptionally "pure" with no excitation light scattering in the optics. While trapezoidal prisms do not allow flexibility in the choice of θ, the prism does not need to be *n*-matched to the glass coverslip in order to obtain TIRF, and the two can be optically coupled with a variety of media. Moreover, a hemispherical prism can be substituted for the trapezoidal prism in order to be able to vary θ over a continuous range. The objective setup, however, poses restrictions to sample accessibility and the possibility of transferring fluorescent reagents present in the aqueous medium between samples via the objective is conceivable.

Through-the objective setups, instead, rely on the use of special objectives, which can collect light from a wider range of incident angles. The critical parameter that determines the ability of an objective to collect light is the **Numerical Aperture** (**NA**), which is given by NA=$n\sin\vartheta/2$, where *n* is the refractive index of the medium between the objective and the sample and $\vartheta/2$ is the half-angle of the cone of light captured by the objective. The higher the NA, the wider the cone from which the objective can collect light. In this setup, the exciting laser beam is focused off-axis on the back focal aperture of a high-NA objective, so that it emerges in a collimated form and is incident on the sample with angle θ. In order for TIRF to be generated at the interface between the glass coverslip and the aqueous buffer, the NA of the objective must exceed n_1, the refractive index of the aqueous buffer. The average refractive index of the cell cytoplasm is 1.38, therefore, to produce acceptable TIRF an expensive objective with NA>1.4 is needed. In addition to this, the glass coverslip and the immersion oil need to be *n*-matched and have n_3> NA. Commercial objectives with NA = 1.45 are well suited for TIRF in cells, as long as they do not have too many granules or organelles that may raise intracellular n_1, and are compatible with standard glass and immersion oil, however, higher NA objectives require the use of very expensive high-NA glass and oil [224]. Another drawback of the prism-less setup is that the TIRF signal is less "pure" as excitation light scatter cannot be eliminated, however, this setup allows total sample accessibility and is to be preferred if complex sample manipulation is required.

With both setups, the small excitation depth achieved by TIRF techniques allows a reduction of the noise from excitation of out-of focus fluorescent molecules, and the thickness of the

optical section is smaller compared to that attained by confocal microscopy (100-200 nm vs. 600 nm). In addition, this technique also protects the bulk of the sample from photodamage, which is especially important when working with live cells, and does not require expensive equipment compared to STED techniques.

Moreover, TIRF is a wide-field technique, and as such is not limited by the speed of the scanning head or by the capabilities of the reconstruction software, which makes it ideally suited to following biological processes in real time in live cells, where time-resolution is essential.

In summary, the features of TIRF microscopy make it ideally suited for the study of the basal membrane in adherent cells cultured on glass coverslips. TIRF setups are also very well suited for advanced fluorescence microscopy techniques, such as Single-Molecule Microscopy.

The diagram in **Figure 1-15**, below provides a diagram of the TIRF microscope used for the project described in this thesis.

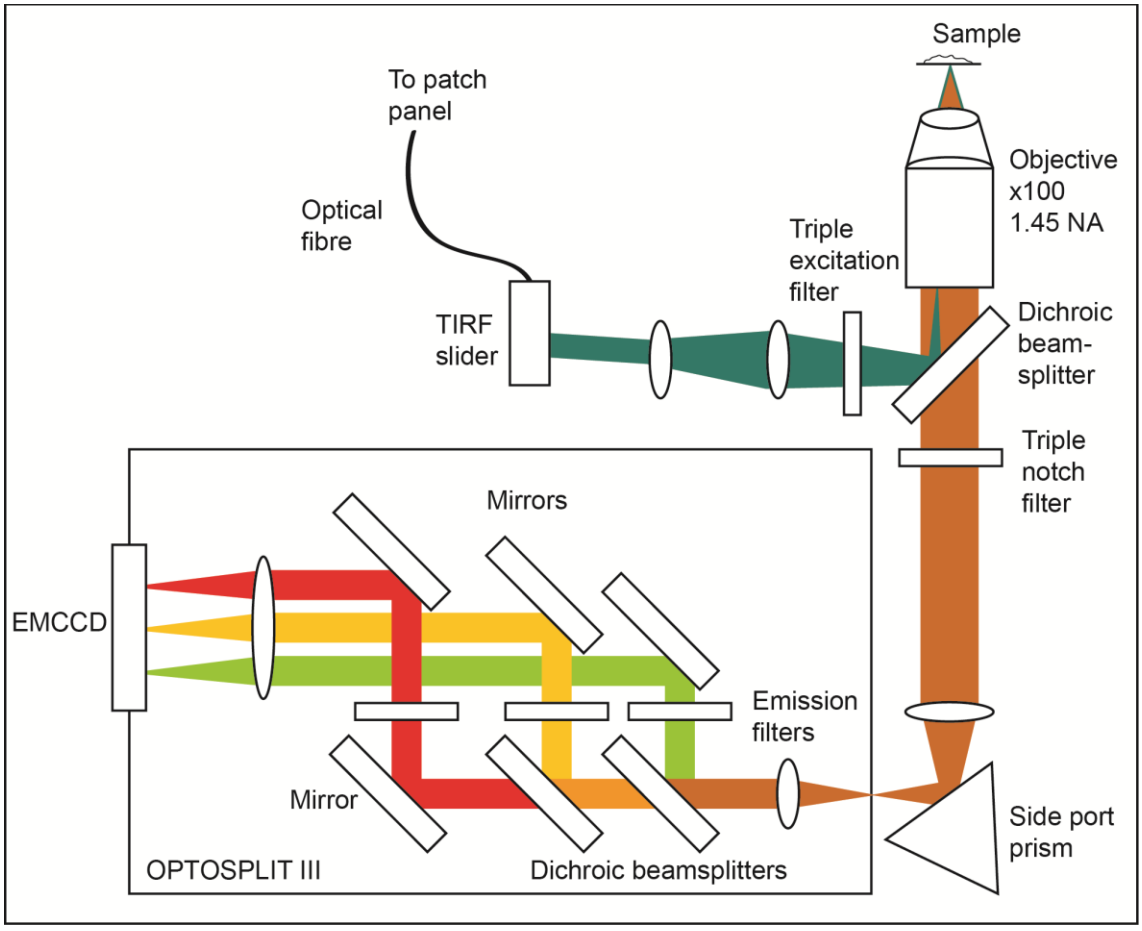

Figure 1-15 – Scheme of the three-colour TIR microscope employed in this project. Adapted from Clarke *et al.* [225].

It is a commercial system (Zeiss, Axiovert 200M) based on the "through-the-objective" TIRF configuration, and it uses a commercial TIRF slider from Zeiss to adjust the angle of incidence θ. The excitation light is provided by fibre-coupled lasers from the Octopus cluster [225]. The objective is a Zeiss, α-plan fluar, 100× magnification, nominal N.A. 1.45, which allows the use of standard glass coverslips and immersion oil for the production of TIR. Images are collected via an Optosplit III beam splitter and imaged on an Andor iXIon EMCCD detector. Further details on the microscope setup are available in **Chapter 2**. This microscope has been developed for fluorescence excitation and detection in three channels. This system could be used, to follow up to three different protein species labelled with spectrally compatible fluorophores, for example to study protein-protein interactions within a signalling network, or to measure spFRET between one FRET donor and two acceptors or vice versa.

1.2.2. Single-Molecule Microscopy Techniques and their advantages for the investigation of transient and dynamic biological phenomena

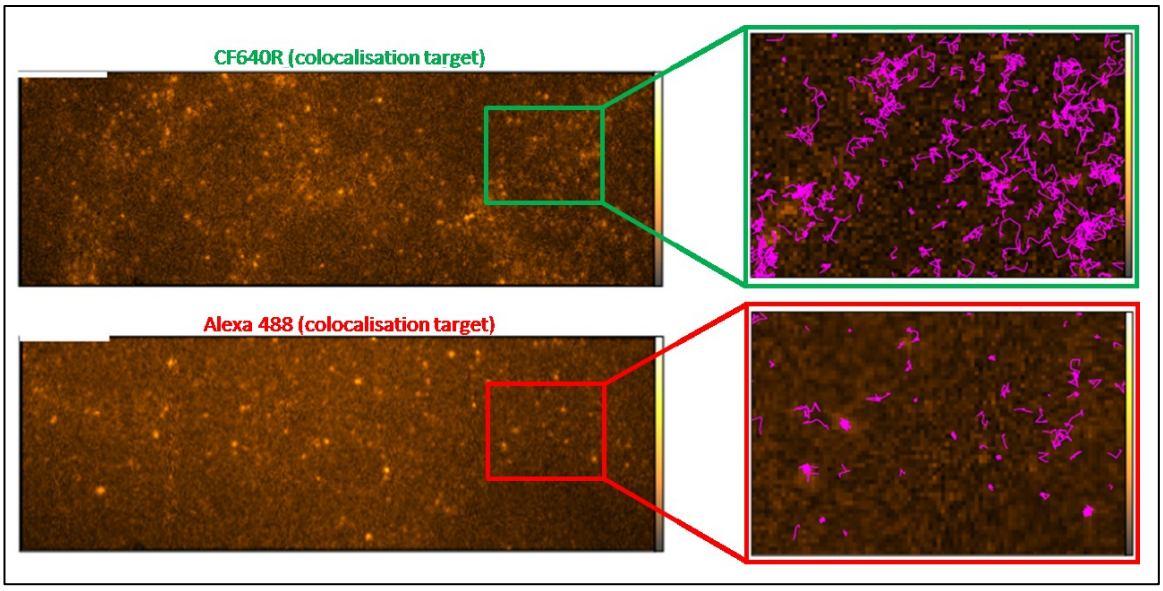

Figure 1-16 – Example of a two-colour Single-Particle Tracking field of view. Insets: in purple, Single-Particle trajectories recorded at 20 Hz. Each field of view is 80x 30 µm. Scale bar (white, top left corner of the panels) = 10 µm. Inset magnification = 3.33x.

Possibly the most important parameter in microscopy is the **resolution**, which is defined as "the minimum distance at which two distinct and neighbouring features in the (*x*-*y*) plane can be still identified as separate entities" [217].

When an emitter of dimensions significantly smaller than the excitation wavelength (defined

as a “point emitter”) emits fluorescence, its profile can be described as an Airy disk with a bright centre and progressively fainter outer rings, whose effective diameter is defined by the characteristics of the excitation light and of the collection optics [217]. In conditions relevant to Single-Molecule techniques, the Airy function can often be well approximated as a **Gaussian Point Spread Function (PSF)** [226,227].

The ***x-y*** (lateral) resolution of a conventional fluorescence microscope is given by the Raleigh criterion (**Equation 1-10**) [218].

$$d_{x,y} = 0.61\lambda / NA$$

Equation 1-10 – Lateral resolution limit according to Raleigh’s criterion.

For wide-field fluorescence microscopy, the typical lateral resolution is ca. 200-400 nm, depending on λ, however deconvolution or fitting techniques can localise the centre of the PSF, which should well approximate the localisation of the emitter, with nanometric precision [213,217,228]. The specific value of the localisation error depends on the **Signal-to-Noise Ratio of the fluorophore** (SNR) of the fluorescent feature.

Single-Molecule techniques rely on sparse, un-crowded labelling and sub-pixel localisation techniques to distinguish and analyse single fluorescence point emitters on a dark background in optimised SNR conditions.

Single-Molecule Microscopy techniques are a powerful, if challenging, tool for the investigation of biological phenomena. As every fluorescent molecule is independently recorded and analysed, Single-Molecule methods can report on the distribution of values for a variable in the population under study and not just on the spatial average taken over the entire population[229]. This allows for a more complete description of the population behaviour and provides information on its heterogeneity, taking into account both static and dynamic disorder [230]. Single-Molecule techniques do not require synchronization of the population under study in order to analyse dynamic processes and can report on rare or transient states, whose signal would be drowned by the dominant species in ensemble measurement [213,229], depending on label density and time-resolution. It is also possible to calculate kinetic parameters for a particular state from the distribution of the dwell times for that state and, as information is time-resolved, it is also possible to introduce variations in the conditions of the system in real time, for example by changing the chemical conditions of the sample medium or by applying force [229,230].

In order to obtain such information, Single-Molecule techniques need to optimise SNR

conditions. Assuming that the major contributions to the detection-limiting noise are Poissonian shot noise fluctuations of the fluorescent signal, background signal and dark counts originating by the detection system, the **SNR** for a Single-Molecule fluorescence experiment can be defined as:

$$SNR = \frac{D\varphi_F \left(\frac{\sigma_p}{A}\right)\left(\frac{P_0}{h\nu}\right)T}{\sqrt{\left(\frac{D\varphi_F \sigma_p P_0 T}{Ah\nu}\right) + C_b P_0 T + N_d T}}$$

Equation 1-11- SNR according to Moerner and Fromm [213]**.**

where φ_F and σ_p are the fluorescence QY and absorption cross-section of the fluorophore, respectively, T is the detector counting interval, A the excitation beam area, P_0/hν the number of incident photons per second, C_b the background signal and N_d the dark count rate. In this equation, D is an instrument-dependent parameter that describes the total collection efficiency and takes into account the detector quantum efficiency, the angular collection factor of the detection system, which in turn depends primarily on the NA of the objective, and the transmission of the optics and the filterset [213].

From **Equation 1-11** it follows that Single-Molecule techniques require fluorophores with a high QY and photon absorption efficiency. Excitation power is also an important factor, but, as defined by **Equation 1-5**, it cannot be increased indefinitely, as excitation saturation would reduce the net photon absorption by the fluorophore and also cause molecules to photobleach faster. In addition to that, background signal and dark counts need to be minimised.

In general, Single-Molecule techniques require very bright and photostable fluorophores, which should be specifically conjugated to the target of interest or a ligand for the target and should not perturb its native behaviour [219,229]. Light sources (lasers) should be stable, and detection systems should be very efficient and high frame-rate to allow for high time resolution measurements [219]. In addition to these quite stringent instrumental requirements, microscopes for Single-Molecule techniques should be kept insulated from vibrations and temperature variations, as they can introduce artefacts that can mimic fluctuations in the observables [229] .

Single-Molecule techniques are divided in two broad classes, based on the method used to reduce the illumination area and improve resolution: confocal-based and TIRF-based[213,230]. The focus of this work is on TIRF-based applications.

TIRF-based Single-Molecule techniques are optimally suited for the analysis of purified molecules immobilised on a functionalised surface [219,229,230], from which important structural and functional information can be derived. These techniques can rely on very pure preparations of labelled protein, immobilised on glass surfaces functionalised so that non-specific binding of fluorescently labelled analytes is minimised. Moreover, photobleaching can be reduced by the use of oxygen scavengers and antioxidants, which reduce the formation of singlet oxygen [214], or by lowering oxygen tension.

TIRF-based Single-Molecule technology can also be used to study molecules in real time on living cells. **Single-Particle Tracking (SPT)** is used to probe the diffusive properties of either native or transfected proteins in their cellular environment [228], more specifically, on the basal membrane in the vicinity of the glass/buffer TIRF interface. Multicolour applications are unique in their ability to dissect interactions between target proteins labelled with different fluorophores and extract their kinetic parameters in a quantitative fashion, exploring the rare fluctuations that might be fundamental for the regulation of biological outcomes [229].
In this technique, fluorescent spots are detected on the surface of cells and localised in a frame-by-frame fashion, then trajectories are reconstructed by joining in the most likely fashion the position of each spot in one frame with that in the next, using different statistical algorithms [228]. Among the parameters that might be calculated from SPT experiments are: the Mean Square Displacement (MSD) of a molecule (see **Figure 1-2** and relative text), which is a measure of the area covered by the molecule in the time unit; the fitted instantaneous diffusion coefficient; parameters that relate to its motion such as directionality, degree of confinement and area of confinement, and colocalisation frequencies of two target molecules in different spectral channels. From the colocalisation data, the lifetimes that characterise the interactions of two target molecules can be extracted, which are very useful in the construction of quantitative mathematical models of cell signalling networks.
While they offer significant advantages for the study of complex biological systems, in addition to the technical challenges posed by immobilised-molecule and fixed-cell Single-Molecule applications, live cell applications have to deal with significant extra problems.
In contrast with immobilised molecule techniques, however, there is no easy solution to the problem of photobleaching, as commonly used oxygen scavengers and antioxidants can perturb cell conditions and the cell environment is naturally rich in oxygen, ATP and radical species. Furthermore, live mammalian cell samples need to be imaged at a constant

temperature of 37°C, a temperature at which fluctuations in the viscosity of the immersion oil might occur due to the temperature gradient formed between the heated stage and the surrounding air at RT. These fluctuations might interfere with the TIRF process, but can be minimised by the use of a wrap-around incubator [218], which would also contribute to the general thermal stability of the system.

As SPT is used to follow dynamic processes, the frame-rate of the acquisition should be kept as high as possible to accurately sample target trajectories and capture transient events, however high frame-rates result in reduced photon collection per frame, which in turns reduces the SNR [228]. The obvious solution of increasing the excitation power is even less practicable than in immobilised-molecule applications, not only as fluorophores are not protected by photoprotective buffers, but also because high light intensities can cause photodamage to the cells [219].

Due to their sensitivity, Single-Molecule techniques require a high specificity of labelling of the targets. This requirement is especially challenging to meet when labelling cells, as target proteins are immersed into a very diverse and crowded biological matrix and non-specific binding to cognate proteins present in the matrix can hardly be prevented by passivation techniques. Optimal labelling is crucial for the success of SPT experiments: over-labelling can result in degradation of feature detection and therefore of trajectory reconstruction, while under-labelling will reduce the chances of capturing protein-protein interactions. Colocalisation studies, in particular, can be critically affected by under-labelling.

A typical detection system for SPT applications is an Electron-Multiplying Charge-Coupled Device (EMCCD) camera, which can record the entire field of view from a TIRF microscope on its chip. EMCCD output is significantly affected by dark noise (thermally generated electrons within the CCD chip) at room temperature, so these devices are usually cooled at -80/ -100°C, a temperature at which noise is dominated by the read-out noise generated during the amplification phase, especially when the electron gain register is operating at high gain to amplify the signal [218]. Detectors usually have a wavelength-dependent sensitivity and this should be taken into account when calculating SNR, as explained by **Equation 1-11**.

In summary, SPT applications operate on a trade-off between frame-rate, which needs to be maximised to capture fast biological processes such as hop diffusion [12], but leads to lower SNR with shorter integration times; laser power, which needs to be increased to maintain SNR levels at suitable levels during high frame-rate acquisition, but not so much as to bleach the fluorophores too early or damage the sample; and labelling density, which needs to be maximised to capture rare events, but also to be kept within acceptable levels of crowding to

prevent degradation of spot localisation and track reconnection.
All these parameters need to be carefully optimised for each experimental system (instrument and target) in order to obtain high-quality results with minimal artefacts.

1.2.3. Protein labelling strategies and their advantages and disadvantages for Single-Molecule imaging techniques

As discussed in the previous sections, SPT techniques require high-performance fluorescent probes. For a SPT experiment to study membrane proteins there are effectively two possible strategies for target labelling: the fluorophore is either attached directly to the target, or indirectly to a physiologic or synthetic high-affinity and high-specificity ligand for the target. In both cases, the probe should consist of a bright, photostable, and non-blinking fluorophore, conjugated 1:1 with high specificity to the protein, so that it does not perturb its structure or function [219,230,231], and does not induce crosslinking, which can alter the diffusional properties of the target [219,228,230,231]. Flexibility in the choice of fluorophore and easy labelling procedures would also be desirable [231].
Various techniques are available to obtain these results:

Direct labelling of target proteins with fused Fluorescent Proteins (FPs)

Genetic fusion of FPs to a target protein has been widely used for specific labelling of proteins in live cells, both for ensemble and SM applications. A panel of different FPs with a range of spectral characteristics is available (for a review, see for example Shaner *et al.* 2005 [232]), so that labelling can be tailored to specific experimental requirements.
Cloning the FP to the N-term or the C-term of the target protein, so that the two proteins are physically linked in the product, guarantees specificity, however, this does not imply that 100% of the target proteins will be fluorescently labelled, as FPs can fail to fold properly and maturate into fluorescence-emitting species depending on cell culture conditions [232]. As some of the most popular FPs display weak dimeric behaviour [232], great care needs to be exercised in accounting for possible artefacts introduced by label dimerization and controlled low-level expression is usually required [228,233]. In addition to that, due to their relatively big size (ca. 27 kDa [231] and ca. 2.4 nm and 4.2 nm diameter and height respectively for a GFP monomer [234]) FPs can alter target behaviour, disrupting interactions and trafficking, or

altering target structure due to steric hindrance, therefore the behaviour of the fusion protein should always be compared with that of the wild-type target protein [228,231,233]. Incorrect folding of the target protein or of the FP in the fusion product can eventually lead to enhanced degradation, which would compromise data collection [233]. In addition to these disadvantages, FPs also display low brightness and photostability [228,231,233] and therefore are not ideally suited for SPT applications.

Direct labelling of target proteins with other fusion tags

Many different fusion tags have been developed along the years in order to overcome some of the technical limitations of FPs.

Among the most popular non-FP tags are: ACP/MCP tags, Halo tag, SNAP tag, biotin ligase (BirA) tag, tetracysteine tag and 6-His-tag [231,233,235]. Most of these tags are smaller than FPs and claim to have greater flexibility of labelling with better performing organic dyes. They also require cloning at the N-or C-term of the target protein and expression of an exogenous fusion protein, and like FPs they guarantee specificity of labelling, but are subject to the same caveats about overexpression and steric hindrance artefacts. However, their tendency to dimerize is generally lower than for FPs.

ACP tag [236] and its derivative **MCP tag** are a commercially available (New England Biolabs) orthogonal labelling system, based on the covalent enzymatic labelling of the tag by modified bacterial phosphopanteinyl transferases, ACP synthase and SFP synthase, using fluorescent CoA derivatives. ACP and MCP proteins are smaller than FPs (ca. 8 kDa vs ca. 27 kDa) and there is a decent range of CoA derivatives suitable for different applications. In addition, custom-labelled CoA derivatives are relatively easy to synthesize via maleimide chemistry.

Biotin Ligase tags have been developed starting from the large biotin carboxyl carrier protein (BCCP), and ending into a 14 residue long peptide which is the minimal functional unit for the acceptance of biotin transfer from *E. Coli* biotin ligase (BirA) [237]. This system is commercially available from Avidity LLC and exploits the enzymatic activity of BirA to transfer a biotin molecule on the peptide which can then be bound to functionalised streptavidin molecules with high specificity. Potentially, due to its very small size, this tag could give better results when steric hindrance could be an issue, by using non-natural biotin analogues as a substrate for peptide modification: a ketone isostere of biotin can be used for subsequent reactions with

hydrazide or hydroxylamine functionalised fluorophores [233], which are commonly available from industrial providers. On the other hand, using streptavidin (Mw = 52.8 kDa) to tag the biotin moiety would result in a more cumbersome system.

The **Snap tag** system is based on the covalent auto-labelling of the tag, derived from the human protein O^6-alkylguanine-DNA alkyltransferase (hAGT), with a functionalised O^6-benzylguanine (BG) molecule [238]. The covalent nature of the interaction makes labelling with this system suitable for long-term studies. The two major drawbacks of this system are that the tag, in order to be functional, must be quite big (19.7 kDa) and that non-specific labelling of the endogenous hAGT can occur in certain reaction conditions [233]. The system is commercially available from New England Biolabs, as are various fluorescent derivatives of the O^6-BG substrate.

The **Halo tag** system is also based on a self-labelling tag with intrinsic enzymatic activity, modified from a bacterial haloalkane dehalogenase. The tag catalyses the reaction and forms a stable bond with the modified chloroalkane substrate [239]. This system offers great specificity as it does not cross-talk with endogenous cellular enzymes, however the auto-catalytic tag is quite bulky (33 kDa) and can still pose the same problems of steric hindrance as FP tags [233].

Tetracysteine tags containing a CCPGCC motif can be used to non-covalently label proteins with fluorescent **biarsenical compounds** [240]. The binding of biarsenical compounds to the tag is reversible but very stable (k_d=2-4 pM), so that long-term studies are feasible [235]. Initial applications were prone to non-specific labelling of endogenous C-rich motifs, but the optimisation of hairpin structure tetracysteine motifs such as HRWCCPGCCKTF and FLNCCPGCCMEP has provided improved binding and higher fluorescence [241]. Biarsenide labelling is sensitive to the redox environment and arsenide toxicity is a potential issue both for samples and for personnel, however, a variety of functionalised biarsenical compounds has been synthesized [242], and improved versions of the motif are in continuous development [235]. The small size of the tag (less than 2 kDa for the improved hairpin sequences [231]) reduces the relevance of steric hindrance artefacts. Biarsenide labelling is also suitable for structural studies. By inserting a tetracystein domain in a region of interest so that the biarsenical compound can only bind when the region is in a certain conformation, conformational rearrangements can easily be measured by measuring the fluorescent signal. This system has been used to probe the conformational rearrangements of the HER1 intracellular domain during EGF- and TGFα- induced signalling [243].

Oligohistidine tags consisting of ≥6 His residues (normally 6-10) are known to react with transition metals such as Ni^{2+}. This reactivity has been extensively exploited for the purification

of recombinant proteins; however, labelling proteins using the same reactivity is also possible. The first labelling reagents for this system were developed using monovalent or divalent **nitrilotriacetic acid complexes of Ni^{2+}**, which bound non-covalently to oligo-His tags and displayed a low affinity (K_d =1-20 μM) [242,244,245]. In spite of this, Ni-NTA-based fluorophores have been used for Single-Molecules studies of membrane, exploiting the low affinity to replace photobleached probes with fresh fluorescent ones by means of simply washing the sample [246,247]. Ni-NTA probes such as those used by Guignet *et al.*, conjugated to Atto dyes, are commercially available from Sigma. Ni-NTA probes with higher valence, such as tris-NTA, display higher binding stability and affinity in the sub-nanomolar range, while retaining the ability to be washed off by mild imidazole or EDTA concentrations [242] and look like the best option for Single-Molecule imaging within this class of probes.

While the likelihood of steric hindrance effects from the oligo-his tag is quite low and its effects on protein function are likely to be minimal, Ni-based probes can display cellular toxicity and the paramagnetic Ni^{2+} ion is known for quenching of nearby fluorophores, which can degrade the SNR [231,242].

An alternative approach to the labelling of oligo-His tags, which circumvents the cytotoxicity and quenching problems, is the use of Zn^{2+} -based probes such as HisZiFit [248]. As Zn^{2+} is an ubiquitous, essential micronutrient for cells, the probe is non-toxic, and since the ion is diamagnetic and redox-inert, the probe does not display fluorophore quenching and is less sensitive to environmental conditions [242]. With a K_d of 40 nM, HisZiFit can stand on par with multivalent Ni-NTA probes [242], however the variety of available ligands is essentially restricted to one and even this is not commercially available.

Recently, a method for covalently attaching PEG moieties to an oligo-His tag has been developed by Cong *et al.* [249]. This method can be applied, with minor modifications, also to the **covalent labelling of His-tagged proteins** with small-molecule organic dyes and should be compatible with cellular conditions (D Korovesis, personal communication).

Indirect labelling of target proteins with labelled physiologic or synthetic ligands

Indirect methods of receptor labelling rely on the use of highly specific and highly purified binders for the protein(s) under study. The binders are labelled in vitro using a variety of techniques, and then a further purification step is necessary to separate the labelled binder from the unlabelled fraction and free dye. Indirect labelling poses the additional challenges of

having to optimise the binding of the labelled binder to the target protein; however, label density on cells can be controlled more easily by fine-tuning the concentration of the binder in each experiment. Also, many binders naturally perform the function of, or can be engineered to act as, activators or inhibitors (direct or allosteric) of the protein of interest, a fact that can be exploited to measure activation kinetics and downstream events, such as changes in the oligomerisation state or the diffusional behaviour of the target, just to name a few.
Possible sources of artefacts, when employing this labelling strategy, are cross-reactivity of the binder with other cognate receptors, non-specific binding to different cellular structures or the extracellular matrix, crosslinking of adjacent receptors by divalent and multivalent probes and spurious activation. All these factors need to be accounted for during probe selection and optimisation. Also, when using multiple probes for the same target protein, it is useful to assess competition between them.
Among the classes of proteins suitable for indirect labelling of target membrane proteins are: natural soluble ligands, monoclonal antibodies and their fragments, and small non-antibody-scaffold binders. In addition to these classes of binders, some membrane proteins, such as neurotransmitter receptors, might be amenable to labelling with fluorescently labelled small chemicals [246,250], while fluorescently labelled enzyme inhibitors might be synthesized from their non-fluorescent parent compounds [251], however, the detailed discussion of these labelling methods goes beyond the scope of this introduction.
Natural soluble poly-peptide ligands are the easiest choice when labelling membrane proteins, as affinity optimisation has already been performed by evolution. Binding of the same ligand to multiple cognate receptors, however, is possible and should be accounted for. Moreover, most endogenous ligands trigger downstream signalling events in their target proteins and modify even drastically their behaviour, which might or might not be a desired effect, depending on the application used and the problem of interest. In addition to this, activation of membrane receptors can cause removal of the receptor from the plasma membrane through ligand-mediated internalisation, resulting in an undesirable, progressive loss of signal. The size and complexity of natural soluble poly-peptide ligands is quite widely variable, going from the handful of amino acids of Substance P and related peptidic neurotransmitters [252] to the 728 amino acids and two chains of HGF [253], therefore there is no optimal labelling strategy for all of them. Direct 1:1 chemical labelling might be possible for relatively small polypeptides bearing a single Lys or Cys residue or using the N-terminal free NH group, however, the position of the labelled residue in the structure and its proximity to the binding site need to be considered, and the potency and affinity of the fluorescent conjugate

need to be carefully assessed. Larger and more complex natural ligands might benefit from tagging techniques.

When activation of the target protein is not desired or the use of natural ligands is prevented by poor affinity and specificity, or by their complexity, one of the possible options is to use labelled **monoclonal antibodies** or engineered **antibody fragments**. Antibodies are high-affinity, specific, multi-domain protein recognition reagents. The most commonly used antibodies in biotechnological applications belong to the IgG class, and consist of two heavy and two light chains, each containing a variable domain, involved in antigen binding, and constant domains involved in structural and effector recruitment functions, one for each light chain and three for each heavy chain. Each Ig domain is kept together by redox-sensitive disulphide bonds.

IgG molecules have two binding sites constituted by the variable domains of their light and heavy chains, the specificity of which is determined by six hypervariable loops, three from each chain [254], which are formed through combinatorial recombination of V and J segments in the light chain Ig genes or V, D and J segments in the heavy Ig chains genes, combined with localised insertions and deletions at the junctions [255].

An intact IgG protein has a molecular weight of about 150 kDa (length ca. 13 nm[228]) and is further modified by glycosylation on different sites, a modification which is essential for its functions [256]. Full-length **monoclonal antibodies** produced from mammalian hybridomas have an affinity that can reach the picomolar range [257] and are one of the staple reagents of imaging applications such as immunohistochemistry, immunofluorescence and fluorescence-activated cell sorting, however, their size and valence make them ill-suited for Single-Molecule imaging applications [228] as they can introduce significant crosslinking and steric hindrance artefacts.

Recombinant antibody fragments that retain the specificity and affinity of the parental IgG while displaying monovalent binding, have been engineered to overcome these drawbacks. **Fabs**, which comprise one light chain, the variable domain of the heavy chain and one heavy chain constant domain, and single-chain variable fragments (**scFvs**), which comprise only the light and heavy chain variable domains, kept together by a peptidic linker, are much smaller than intact IgGs (55 kDa and 28 kDa respectively for Fabs and scFvs) and are amenable to expression in prokaryotic systems, however, their stability still depends on the integrity of the disulphide bonds in their IgG folds and some of them have an increased tendency towards aggregation in vitro, especially when fused to tags[258]. Moreover, while monoclonal

antibodies are available for a variety of targets, the availability of scFv reagents is still restricted and in order to obtain Fabs via enzymatic methods a large quantity of starting IgG is required.

Ig-like molecules from camelids (**nanobodies**) and sharks (**IgNARs**) have recently come to the forefront as antibody alternatives due to the fact that their binding sites are formed by a single IgG domain and are amenable for the production of very small (ca. 15 kDa) and stable VhH and V-NAR soluble Ig domains with potential clinical applications [254,258]. Their use in Single-Molecule applications is however limited by their limited availability. As an added benefit of reduced structural complexity, both antibody fragments and Ig-like fragments can be generated in a faster and more efficient way, compared to IgG production, by using display and selection techniques [258].

Due to the presence of critical disulphide bonds in the IgG fold, antibody and Ig-like fragments are not suitable for direct maleimide labelling on cysteine residues. Direct labelling of amino groups could prove tricky as well, due to the complexity of their sequence and can result, depending on the specific sequence, in reduced affinity and binding, due to interference with critical residues in the hypervariable regions, or in multiple labelling. Engineered antibody fragments might require tagging with recombinant fusion tags. The choice of oligo-His tags seem particularly appropriate, due to their small size and to the fact that they are also used for purification of recombinant proteins.

In order to overcome the limitations of antibodies for clinical and advanced imaging applications, a variety of **small non-antibody-scaffold (SNAS) binders** has been developed, starting from a host of different structures, ranging from the variable lymphocyte receptors of jawless vertebrates (repebodies [259]) to bacterial protein A (Affibodies [260]). The core concept of SNAS development is the fact that antibody and Ig-like proteins recognise their targets through a combination of a structurally conserved framework (the Ig fold) with a spatially defined combinatorial site, composed by segments that are hypervariable in sequence, length and conformation [254]. SNAS should have a robust architecture consisting of a compact and structurally rigid core that presents surfaces or loops of varying sequence and structure, which constitute the ligand binding site, tolerating replacements and exposition of hydrophobic regions without significant changes in the core structure[254,255]. While antibodies are combined, selected and optimised by the immune system in a complex process that requires a fairly long time, SNAS are synthesised by screening of libraries obtained by random recombination or mutation and successive rounds of artificial antigen maturation.

Many SNAS display antibody-like affinities for their targets; however, as this is a relatively new technology, the palette of available targets is still somewhat limited. SNAS should be relatively small, single-chain proteins, that do not require extensive glycosylation or other post-translational modifications and are amenable to expression in a variety of hosts and in particular in the cytoplasm of *E.Coli* strains. High resistance to thermal and chemical denaturation and reversible unfolding are also desirable characteristics for certain applications, as well as ease of conjugation to effectors or imaging tags and compounds [255,256]. The multitude of SNAS currently available have been developed from structurally different scaffolds, some based on Ig-like folds like fibronectin domains, some on other core-loop structures like lipocalin-derived anticalins, and some on binding surfaces, like protein A-derived Affibodies and designer ankyrin repeat proteins (DARPins) . A complete review of the available alternative scaffolds goes beyond the scope of this introduction and is available, among others in Skerra (2003 and 2007) [254,255] and Bintz *et al.* [256].
SNAS present many favourable characteristics for Single-Molecule applications: their small size and monovalence reduces the likelihood of artefacts due to steric hindrance and crosslinking and, as some of them do not have structural disulphide bonds (*e.g.* Affibodies and DARPins [254]), they can be modified by addition of a single cysteine residue at the end of the sequence, enabling site-specific, 1:1 conjugation with fluorophores via maleimide chemistry. Other SNAS might need to be tagged in order to be specifically labelled.

The conjugation of the binder to the fluorescent reporter is a crucial step for indirect labelling techniques. The conjugation reaction needs to be efficient, quantitative and irreversible, in order to prevent loss of signal via dissociation of the fluorophore from the binder. Many **conjugation techniques** are available **for binder labelling.** In contrast with targets, the **direct chemical labelling** of binders might be possible, depending on the structure and sequence of the binder. The robust reaction of solvent-accessible thiols like cysteine residues with **maleimide groups** occurs in protein-friendly conditions and with high specificity [233], however it can only be applied to proteins that have only a single cysteine residue, like Affibodies and DARPins, otherwise the preparation will not be homogeneously 1:1 and the activity of the protein might be compromised. This is especially important for proteins in which disulphide bonds are essential for the maintenance of a correct fold, like Ig derivatives. Alternatively, the **ε-amino group of lysine** residues or the **N-terminal α-amino group** can be modified with **succinimidyl esters or NHS esters**. The reaction is more specific with Lys residues than with the N-term and will happen preferentially with ε-amino groups, if they are

available [233], *i.e.* if Lysine residues are present in the protein. Moreover, the preparation will only be 1:1 if the protein has only one available Lys or none, in which case the reaction will target the N-terminal α-amino group.

Another, more complex strategy is the insertion of **non-natural amino acids** in the sequence of the binder, so that **bio-orthogonal reactions** with fluorescent hydrazides and other functional groups can occur under mild, aqueous conditions [261]. This approach, however, requires the use of specialised bacterial strains, where unnatural amino acid carrier tRNAs have been introduced and associated with either amber stop codons or degenerate codons (strategies reviewed in de Graaf *et al.* [261] and Young and Schultz [262]), so while it can guarantee high specificity, it is not very common yet.

While not as bright or photostable as Quantum Dots (see below) **chemical dyes** are very small (ca. 0.5 nm) and easy to conjugate to proteins. A wide variety of well-characterised fluorescent reagents, functionalised with different reactive groups, is commercially available and label preparation is easy and reproducible. The choice of fluorophore, as outlined in the previous section of this introduction, is critical for the quality of Single-Molecule data, so it should be oriented towards photostable reagents with high QY and ε.

Quantum dots (QD) are an alternative class of fluorescent reagents that overcome some of the pitfalls of conventional fluorescent dyes, while introducing some other problems of their own. QD are nanocrystals of a semi-conductor such as CdSe or CdTe, with a core diameter of 1-6 nm. Usually, the CdSe core is coated with a ZnS shell, which electronically passifies the QD [263] and prevents non-radiative deactivation [215]. The fluorescent emission of QDs relies on the formation of an electron-hole pair upon absorption of a photon. The electron-hole pair recombines in about 10-20 ns, leading to the emission of a photon. The energy of the emitted photon, and therefore its wavelength, depend on the size of the QD core, with smaller cores emitting more energetic photons (shorter λ)[264]. The emission spectrum of QDs is very narrow (FWHM ca. 20-40 nm [265]), and determined by the QD size distribution [215]. The size of QD cores can be finely controlled during their synthesis in order to achieve monodispersed preparations of emitters for the full visible spectrum and also for Near-InfraRed (NIR) wavelengths [263]. The excitation spectrum of QDs, instead, is core-size invariant and broad, with absorbance increasing as wavelength decreases into the near-UV and blue ranges [215], a characteristic which allows excitation of multiple spectrally separable emitters with a single excitation wavelength [264,265]. In addition to this, QDs are brighter than conventional chemical dyes, have much higher QY and ε and are very resistant to photobleaching [215], with fluorescence bleaching half-lives in the order of hours [265]. All these characteristics would

make QDs ideally suited to Single-Molecule imaging techniques; however, their structure also poses a series of barriers to their use. Even “naked” core-shell QDs are much larger than conventional chemical dyes and in the range of FP size (**Figure 1-17 A**); in addition to this, ZnS coated QDs are hydrophobic, therefore they need to be functionalised with a bio-compatible coating of silica or siloxane (thickness 1-5 nm), encapsulated with phospholipid micelles or derivatized with dihydroxylipoic acid or polyacrylic acid [265]. The resulting coated QD has a hydrodynamic diameter of 6-60 nm [215]. Moreover, the conjugation of QDs to ligands is usually performed by adsorbing multiple copies of either avidin (67 kDa) or protein A and/or G (30 kDa and 42 kDa, respectively) to the biocompatible shell and then exploiting the binding of this adaptor protein to biotinylated proteins or antibodies (150 kDa each) [258]. The resulting binder-conjugated QD can behave in the worst-case-scenario as a protein of nearly 500-750 kDa (**Figure 1-17 B**), and is nearly always multivalent [265], both characteristics which constitute significant drawbacks for Single-Molecule imaging techniques due to the introduction of crosslinking and steric hindrance artefacts.

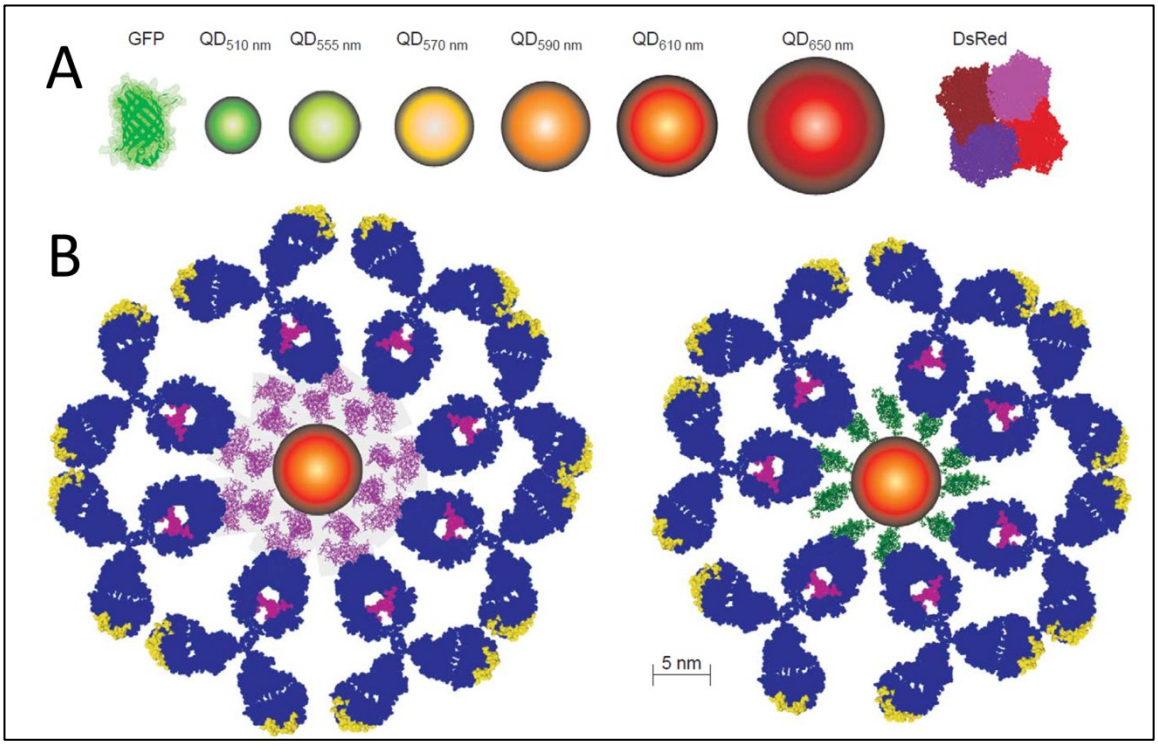

Figure 1-17 – A: The size of “naked” core-shell QD compared to commonly used FPs. **B**: Examples of fully-functionalised QDs bound to full-length IgG molecules using the avidin-biotin conjugation system **(left)** and the protein A/G conjugation system **(right**). Adapted from Jaiswal and Simon (2004)[265] .

Alternative strategies which employ the insertion of oligo-His tagged proteins in the biocompatible shell can reduce the size of the final conjugate, however reducing the valence is more complex [215,265] and commercial QDs usually rely on the avidin-biotin system [266]. Furthermore, conjugation procedures are more difficult to control and fine-tune than those involved in conventional dye conjugation, and the availability of standard protocols is still very limited [215]. The colloidal structure of the QDs also introduces another potential drawback: irreversible aggregation of QDs may occur in buffers of high ionic strength and in biological matrices [215], or even upon freezing or storage [265], a phenomenon which might reduce shelf-life and binding specificity.
Finally, Single-Molecule data quality might be impacted by the slow blinking of QDs, which has an average lifetime of ca. 500 ms but can be up to 100 s for some commercial products [265]. This phenomenon can hamper trajectory reconstruction in Single-Particle Tracking.

The use of **fusion tags** to label purified binders can be necessary if the sequence of the binder does not offer any specific attachment point for conventional dyes. Fusion tags are generally not as big as QDs and provide specific and stoichiometric labelling; however they can alter the specificity and affinity of the binder by sterically interfering with the binding site. Fusion-tagged binders need to be thoroughly tested to assess not only the functionality of the binder side, but also that of the tag, as steric clashes can also affect the labelling. In addition to the points discussed previously, it is worth noting that ACP tags are not suitable for expression in E.Coli, as they can be substrates of endogenous bacterial acyl synthases carrying unlabelled CoA.
An ideal tag system for purified proteins could be the **oligo-His tag**, which is routinely fused to recombinant proteins for purification purposes; however Ni-NTA and HisZiFit dyes are not covalently bound to the tag and can wash off relatively easily, leading to a degradation of the fluorescent signal. Covalent methods of conjugating reactants to oligo-His tags, when adapted to the conjugation of fluorescent dyes, could prove invaluable to label complex or Lys/Cys-rich binders [249].
In conclusion, there is no optimal way of labelling targets for Single-Molecule imaging techniques. The labelling strategy needs to be planned and optimised in a case-by-case fashion, taking into account the structural and sequence features of the target and/or its binders and the properties of the labelling systems available. Apart from brightness and stability, affinity, specificity and artefact incidence are key parameters that need to be optimised in order to acquire high-quality data.

2. General Materials and Methods

This chapter provides information on all general-purpose methods and reagents used in more than one chapter of this thesis. For each general method, information on chapter relevance will also be provided. Information regarding methods specific for single chapters will be provided in the relevant chapters.

2.1. Cell culture

Cell Line (Origin)	Complete Medium Composition	Seeding Density in 35mm Dishes	Main Use
A431 (ECACC)	DMEM, -Phe Red, + 10% FBS, 2 mM glutamine and 1% penicillin/streptomycin	10^5 cells /dish	Anti-HER1 Affibody characterisation
SkBr3 (ECACC)	RPMI 1640, -Phe Red, + 10% FBS, 2 mM glutamine and 1% penicillin/streptomycin	3 x 10^5 cells /dish	Anti-HER2 Affibody characterisation
MCF7 (ECACC)	RPMI 1640 -Phe Red + 10% FBS, 2 mM glutamine and 1% penicillin/streptomycin	3 x 10^5 cells /dish	HER1 confinement
HeLa (ECACC)	MEM -Phe Red + 10% FBS, 2 mM glutamine and 1% penicillin/streptomycin	10^5 cells /dish	HER1 confinement
Cho+HER1-eGFP (Gift of Dr Arndt-Jovin)	DMEM -Phe Red + 10% FBS, 2 mM glutamine, 1% penicillin/streptomycin and 2 ml/L geneticin	10^5 cells /dish	Dye conjugate optimisation
Wt Cho (ECACC)	DMEM -Phe Red + 10% FBS, 2 mM glutamine and 1% penicillin/streptomycin	0.5 x 10^5cells/dish	MCP-GPI plasmid transfection
T47D (ECACC)	RPMI 1640 +Phe Red + 10% FBS, 2 mM glutamine, 1% penicillin/streptomycin and 10 mM Sodium Pyruvate	3 x 10^5 cells /dish	**Main cell line model**
HCC1954 (Gift of Dr Michela Perani)	RPMI 1640 +Phe Red + 10% FBS, 2 mM glutamine, 1% penicillin/streptomycin and 10 mM Sodium Pyruvate	10^5 cells /dish	Confirmation experiments for HER1*-HER1* interactions ± TKI
Cho + TetOn HER1 (LP-Cho) (Gift of Prof Linda Pike) [91]	DMEM, -Phe Red + 10% FBS, 2 mM glutamine, 1% penicillin/streptomycin, 2 ml/L geneticin and 2 ml/L hygromycin B. HER1 expression was induced by treating 50 ng/ml doxycycline hyclate for 24 h for Single Molecule experiments and with 250 ng/ml for WB experiments	0.5-1 x 10^5cells/dish	HER1 confinement, control WBs for HER1 Affibody characterisation

Table 2-1 - Summary of the characteristics of the cell lines used throughout the project.

All cell culture reagents were from Invitrogen.

All cells were cultured at 37°C in presence of 5% CO_2 in 75 cm^2 flasks (Nunc).

All cells were passaged every two days. Exhausted medium was removed, cell monolayers were rinsed with 10 ml HBSS (Life Technologies), then treated with 0.25% Trypsin without phenol red (Life Technologies)at 37°C until complete cell detachment was achieved. T47D, MCF7 and SkBr3 cell suspensions were diluted 1/2 in fresh complete medium at each passage, whereas A431 and HCC1954 were diluted 1/6, HeLa, and wt Cho, Cho+EGFR-eGFP and LP-Cho were diluted 1/12.

Cells were seeded at the densities detailed in **Table 2-1** onto 35 mm glass bottomed-dishes bearing a glass insert of either 20 mm or 10 mm of diameter and 0.16 - 0.19 mm thickness (MatTek Corporation). Uncoated or Poly-L-Lysine (Sigma) coated dishes were used for confocal data acquisition and fixed-cell Single-Molecule experiments. Details of dish coating with different cell growth substrates will be provided, as required, in specific chapters.

All cell samples were rinsed twice with Serum-Free Medium (SFM) and starved for 2 h upon reaching approx. 80% confluence, in order to remove serum-derived growth factors which can interfere with probe binding prior to labelling with fluorescently labelled probes. Starvation also synchronises all cells in the G_0 phase of the cell cycle, avoiding the emergence of cell-cycle specific differences in cell behaviour.

2.2. *Fluorescent labelling of proteins and other ligands*

Protein or Reagent (Manufacturer)	**Dyes Used (Manufacturer)**
EGF (Peprotech)	Alexa 488 and Alexa 546 (Molecular Probes - Invitrogen); Atto647N (AttoTec); CF640R (Biotium)
Anti-HER1 Affibody (Abcam)	Alexa 488, Alexa 546, Rhodamine Red C2, Bodipy FL and Tetramethylrhodamine6 (Molecular Probes - Invitrogen); CF488A, CF568, CF633 and CF640R (Biotium); Atto 565 and Atto647N (AttoTec); Fluorescein (Sigma Aldrich)
Anti-HER2 Affibody ZHER2:477 (d) (Affibody Inc.)	Alexa 488 and Alexa 546 (Molecular Probes - Invitrogen); Atto647N (AttoTec)
Anti-HER2 Affibody ZHER2:477 (m) (Affibody Inc.)	Alexa 488 (Molecular Probes - Invitrogen); CF640R (Biotium)
Anti-HER3 Affibody	Alexa 488, Tetramethylrhodamine6 and Alexa 546 (Molecular Probes - Invitrogen); Atto647N (AttoTec); CF640R (Biotium)
Hen Egg White Lysozyme (HEWL –Sigma Aldrich)	Alexa 488 and Alexa 546 (Molecular Probes - Invitrogen); Atto647N (AttoTec);
CoA (New England Biochemicals)	Atto 488, Dyomics 547 and Dyomics 647 (commercial conjugates from New England Biochemicals); Alexa 488 (Molecular Probes – Invitrogen); CF640R (Biotium)
Neuregulin1β (NRG1β – Peprotech)	Alexa 488, Alexa 546 and Alexa 647 (Molecular Probes – Invitrogen)

Table 2-2 – Summary of fluorescent dye conjugates of ligands used in this project.

EGF conjugates were custom-conjugated with NHS-ester or SE-ester dyes by Cambridge Research Biochemicals. Only 1:1 labelled fractions were used in Single-Molecule experiments.

All Affibodies were conjugated in-house with maleimide dyes following manufacturers' instructions.

HEWL and NRG1β were conjugated in-house with NHS-ester dyes following manufacturers' instructions.

CoA was custom-conjugated with maleimide Alexa 488 and CF640R by Cambridge Research Biochemicals. CoA-At488, CoA-Dy547 and CoA-Dy647 conjugates were purchased from New England Biochemicals.

2.3. Cell preparation and labelling

After serum starvation, samples for **Single-Molecule and confocal receptor binding saturation curves and competition assays** (**Chapter 3**) were washed twice with ice-cold PBS supplemented with 0.1% BSA and incubated for 10 minutes on ice. Cells were incubated at 4°C for 4 hours with the appropriate fluorescence derivatives (0.05-1 nM for single-molecule experiments, 1-100 nM for confocal experiments) in phosphate-buffered saline (PBS) supplemented with 0.1% BSA, and in presence or absence of unlabelled competitors when necessary. Cells were washed and then fixed by incubation with 3% paraformaldehyde (Electron Microscopy Sciences), 0.5% Glutaraldehyde (Sigma) for 15 minutes at 4°C and then for 15 minutes at room temperature, then washed 5 times with PBS.

For the **determination of live-cell Single-Molecule ligand binding time-courses** (**Chapter 3**), after starvation, live cells were washed twice with SFM pre-heated at 37°C. Solutions of the required fluorescently tagged protein (EGF, anti-HER1 Affibody, anti-HER2 Affibody, anti-HER3 Affibody or NRG1β) were added to the samples and they were then promptly imaged at 37°C on a TIRF microscope, acquiring datasets at different time points (0-1500 sec) to follow the binding time-course of the various probes.

For **single-colour or multicolour Single-Particle Tracking experiments** (**Chapters 3-7**), starved cells were rinsed twice with SFM + 25 mM HEPES pH 7.2 pre-heated at 37°C. Labelling with fluorescently labelled Affibodies or NRG1β was carried out for 10 minutes at 37°C. Cells were rinsed twice with SFM + HEPES 25 mM pre-heated at 37°C and promptly imaged as described below. For EGF conjugates, starved cells were rinsed twice with Serum-Free Medium + 25 mM HEPES pre-heated at 37°C, conjugates were added and cells were promptly imaged as described below, without rinsing steps, in order to minimise internalisation during labelling and imaging. For mixed experiments, labelling was performed in series, first for 10 minutes at 37°C with NRG1β and/or Affibody conjugates, which display slow internalisation kinetics and then directly with EGF conjugates, which internalise quickly at 37°C. This was done to maximise the amount of signal at the membrane for the various probes.

2.4. Single-Molecule data acquisition (Chapters 3-7)

Single- molecule images were acquired on an Axiovert 200M microscope with TIRF illuminator (Zeiss, UK) and incorporating a 100x oil-immersion objective (α-Plan-Fluar, NA=1.45; Zeiss, UK) and an EMCCD (iXIon X3; Andor, UK). Samples were illuminated with lasers λ= 491nm (100

mW, Cobolt Calypso), 561 nm (100 mW, Oxxius SLIM), 639 nm (30 mW, PTI IQIC30) or a 638 nm (100 mW, Vortran), combined via a polarisation maintaining triple laser combiner (Oz Optics) in the Octopus hub [225].

Alternatively, a Vortran Stradus Versalase Combiner (Vortran Laser Technology Inc., USA) equipped with a 50 mW 491nm line, a 100 mW 561 nm line and a 100 mW 640 nm line, or an Andor Revolution Laser Combiner (Andor, Belfast, UK) including a 50+50 mW 491+532 nm dual wavelength diode-pumped solid state (DPSS) laser (Dual Calypso, Cobolt, Solna, Sweden), a 50 mW 561 nm DPSS laser (Jive, Cobolt) and a 100 mW 640 nm diode laser (CUBE, Coherent, Santa Clara, USA), all of which are continuous wave (CW), were used.

A wrap-around incubator (Pecon XL S1) was used to maintain a constant temperature and protect the samples from air currents.

The field of view of each channel for single-molecule imaging was 80 x 30 µm.

Unless otherwise stated, **fixed cell** data of singly, doubly and triply labelled cells or proteins adsorbed on substrates was acquired at 10 Hz for 60 seconds.

Unless otherwise stated, **live-cell tracking** data of singly, doubly and triply labelled cells was acquired at 20 Hz for 30 seconds.

Images were saved in HDF5 format for subsequent processing using custom-designed software [226].

2.5. Calculation of MSD curves and Average D Values from Multicolour Single-Particle Tracking data (Chapters 3-7)

All Single-Molecule time series data were analysed using the multidimensional analysis software described in [226]. Briefly, this software uses Bayesian statistics to identify the most probable locations of fluorescent features (particles) in an image, given a model for the shape of the features which includes background fluorescence and stochastic noise.

For each pixel, the algorithm computes the probability of the presence of a feature (H_1) against the presence of only background (H_0). The map of the pixel-by-pixel H_1 v H_0 probabilities is then thresholded, and the pixels where the probability of the presence of a fluorescent feature is highest are identified. This process is called Bayesian Segmentation.

Single-particle tracks are seeded from all fluorescent features in the frame when they are first identified. For each subsequent frame at time *t*, the algorithm computes the probability for each identified feature F_i to be reconnected with each existing track tr_j. Features are connected to tracks using the probabilities calculated, so that each feature is connected only

to one track and each track only to one feature. Unconnected features are used to seed new tracks.

Registration transformations are determined for all channels but feature detection and tracking are performed independently in each channel. Single-Molecule tracks are pooled together for cells imaged under the same conditions and their Mean Square Displacement (MSD) curve is calculated as explained below.

The workflow of Quincy is briefly illustrated in **Figure 2-2**.

For substrate optimisation experiments in **Chapter 4**, in order to compare data coming only from cells which expressed significant levels of HER1-eGFP, for each time series, cell areas were outlined manually using new functionality in the software in [226] and only single-molecule tracks whose mean positions were in the outlined cell areas were pooled together. In all cases, MSD was calculated as $MSD(\Delta T) = \langle |\boldsymbol{r}_i(T+\Delta T)-\boldsymbol{r}_i(T)|^2 \rangle$, where $|\boldsymbol{r}_i(T+\Delta T)-\boldsymbol{r}_i(T)|$ is the module of the vectorial displacement between the positions of track *i* at time *T* and time $T+\Delta T$, and the average value was calculated over all pairs of points separated by ΔT in each track, as shown also in **Figure 1-1**Error! Reference source not found. and relative text. Histograms of instantaneous diffusion coefficients (*D*) were calculated by calculating an MSD curve separately for each track, fitting a straight line to the first 3 points of that MSD curve then calculating *D* directly from the gradient m of the fit, $D=m/4$. Histograms were then produced using the *D* values for the pooled tracks from the selected cell areas.

When the frame-to-frame displacement of a particle is in the range of the localisation error (i.e. particles are scarcely mobile, or immobile) the determination of the MSD curve, and therefore of the *D* coefficient, will be significantly influenced by the localisation error. In order to illustrate this problem, a mixed population of particles undergoing pure Brownian motion with an instantaneous diffusion coefficient $D = 0.05\ \mu m^2/s$ (90%), and of immobile particles with $D = 0\ \mu m^2/s$ (10%) was simulated with a particle localisation error of 0.064 µm. Tracks were simulated for 200 frames at a repetition rate of 0.05 s/frame (for a total of 10 s). Simulated tracks are shown in **Figure 2-1 A**.

For each simulated track, an MSD curve was calculated. Error! Reference source not found. **B** shows two distinct populations of curves, one for the particles undergoing Brownian motion (upper) and another for the immobile particles (lower). Within each population, the gradient and offset of each curve are scattered around the average values, due to the stochastic effect of the localisation error. This can lead to the appearance of MSD curves with negative gradients.For each track in the simulation, the instantaneous diffusion coefficient *D* was estimated from the gradient between the first 3 points of the MSD curves shown in **Figure 2-1**

B.

Figure 2-1 C shows the frequency histogram of the calculated *D* coefficients, with two clearly separated populations of estimated *D*, scattered around the ground-truth average values of *D* = 0.05 $\mu m^2/s$ and *D* = 0 $\mu m^2/s$ (the so called "zero-peak"). The *D* <0 values present in the latter arise from MSD curves whose gradients came out negative due to the effect of the localisation error. Clearly D is not really negative, just very low, but the error in the measurement can result in a negative value if *D* is comparable or lower than the estimated localisation error.

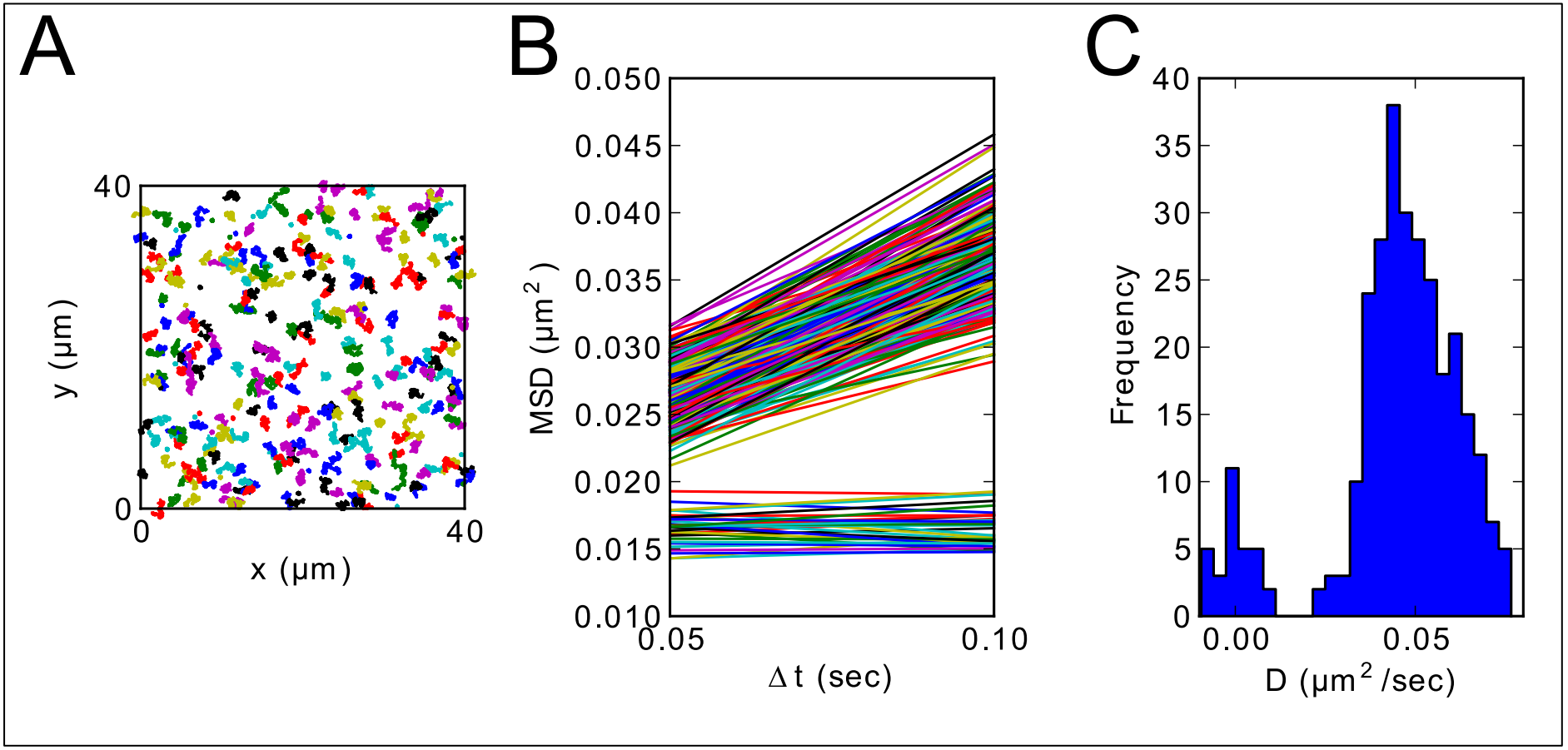
A
40
0
0
40
y (μm)
x (μm)
B
0.050
0.045
0.040
0.035
0.030
0.025
0.020
0.015
0.010
MSD (μm²)
0.05
0.10
Δt (sec)
C
40
35
30
25
20
15
10
5
0
Frequency
0.00
0.05
D (μm²/sec)

Figure 2-1 - (previous page) – Artefactual negative values of *D* arise from the localisation error when tracking low-mobility particles. A) Simulated tracks of particles undergoing Brownian motion with an instantaneous diffusion coefficient $D = 0.05\ \mu m^2/s$ (90%) and immobile particles with an instantaneous diffusion coefficient $D = 0$ (10%). Tracks were simulated for 200 frames at 0.05 s/frame. **B)** Individual MSD curves for each particle shown in panel A. **C)** Histogram of instantaneous diffusion coefficients *D* for the particles in panel A, estimated from the gradient of the first 2 points of the individual MSD curves shown in panel B.

For the artefact minimisation experiments shown in **Chapters 4** and **5**, average *D* values calculated from the pooled MSD curves were used as a metric to compare the mobility of probes on the cell membrane. Instantaneous *D* fit values were compared via Student's t Test using as a reference the mean value of the endogenously expressed HER1-eGFP in **Chapter 4**, and that of the Alexa 488 conjugate across all experiments in **Chapter 5**.

The dimension of the "zero peak" can be used as an estimate of the typical error in *D*.
In **Chapter 5** this property was used to estimate the amount of particles with a diffusive behaviour clearly different from immobile, non-specific molecules. The *D* histograms of populations of HER1 receptors tracked with anti-HER1 Affibodies labelled with different dyes were analysed in order to estimate the size of the spread of the "zero-peak". A conservative threshold of $D > 0.1\ \mu m^2/s$ was set for further analysis. This threshold does not discriminate between truly immobile particles and particles with limited mobility, rejecting both, but allows the identification a subset of particles which are clearly not immobile.

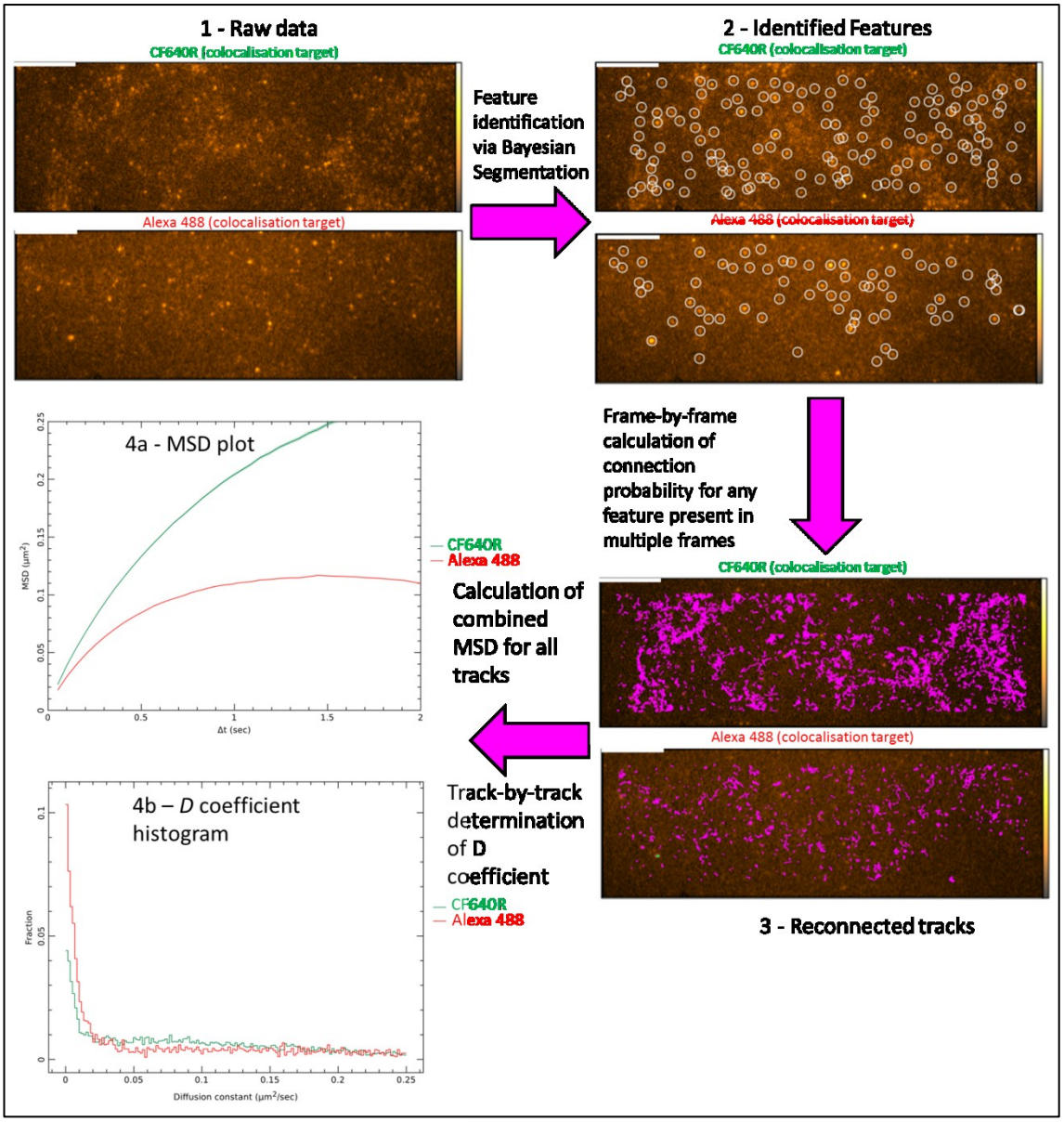

Figure 2-2 – Bayesian feature detection and tracking with the Quincy algorithm [226]**.** The raw data **(1)** is thresholded using a Bayesian Evidence Map of the pixel-by-pixel probability of the presence of a feature point emitter. Features **(2)** are identified as the regions where the presence of an emitting particle is the best explanation for the data. Tracks are seeded for each feature in the first detected frame, then for each frame, a connection probability map for all features and existing tracks is calculated. Features are reconnected to tracks so that each feature is connected only to one track and each track only to one feature **(3)**. From the tracks identified for a condition, MSD curves are calculated as $MSD(\Delta T)=\langle |ri(T+\Delta T)-ri(T)|^2$ **(4a)**. Instantaneous diffusion coefficients are calculated for each track by calculating the corresponding MSD curve and fitting the first three points in the curve with a straight line. The *D* coefficient is calculated from the gradient, *m*, of the fitted line. Individual *D* coefficients are used to build up a histogram **(4b)**. Scale bars (white) = 10 µm.

2.6. Single-Molecule spot density analysis (Chapter 3)

Spot density analysis was performed on single-molecule images processed with the Quincy algorithm for feature detection and localisation [226]. Spot density was calculated by dividing the number of detected spots by the total cell area imaged (≈80x30 µm). Data was plotted in Excel.

2.7. Model fitting of time-dependent single-particle spot density curves (Chapter 3)

Spot density vs time curves for EGF Alexa 488, anti-HER1 Affibody Alexa 488, anti-HER2 Affibody Alexa 488, anti-HER3 Alexa 488 and NRG1β-MCP-Dy547, were analysed using the Origin 8 software package, assuming the binding scheme

$$R + L \rightleftharpoons RL : k_f, k_r$$

where a receptor *R* binds to a single ligand *L* with forward and reverse reaction rates k_f and k_r respectively. If ligand binding proceeds with negligible depletion (*i.e.* ligand concentration is assumed to remain constant at the initial value throughout the experiment), the rate of change of ligand/complex density, *C*, with respect to time, *t*, is given by

$$\frac{dC}{dt} = k_f[R_T - C]L_0 - k_r C$$

where R_T is the total density of receptors and L_0 is the ligand concentration.

If $C(t{=}0) = 0$, a solution for this ordinary differential equation is

$$C(t) = A(1 - e^{-Bt})$$

where $A = \left(\frac{k_f L_0 R_T}{k_f L_0 + k_r}\right)$, and $B = k_f L_0 + k_r$ [267].

Image spot density, $S(t)$, is proportional to $C(t)$ (*i.e.* $C(t) = PS(t)$, where P is a proportionality constant), so the following equation was fit to the data:

$$S(t) = A_S(1 - e^{-Bt}) + Offset$$

where $A_S = PA$. The *Offset* term reflects the presence of baseline signal coming from either the cells or the cell culture substrate in absence of signal.

2.8. Expression and purification of an anti-HER3 Affibody (Chapter 3)

This experimental step was performed in the Oxford Protein Production Facility (Harwell Oxford) with technical counselling from Mr Anil Verma.

Anti-HER3 Affibody [268] plasmid was kindly provided by Dr John Löfblom (Affibody Inc.). HER3 Affibody plasmid (375 ng) was transformed into Omnimax II cells (Invitrogen) by heat shock for 30 seconds at 42°C followed by 2 minutes on ice. Bacteria were recovered with 300 µl LB broth for 1 hour at 37°C and plated onto LB-Kanamycin (25 µg/ml) plates overnight. Colonies were picked and grown overnight at 37°C in 5 ml LB-Kanamycin (25 µg/ml) medium, then spun down at 5000g for 10 minutes and subjected to plasmid DNA extraction with QIAquick Mini-Prep Spin Plasmid Extraction kit (Qiagen) on a QiaCube (Qiagen) workstation according to manufacturer's instructions and quantitated on a Nanodrop 8000 spectrophotometer (Thermo Fisher Scientific). Purified plasmid DNA (50 ng) was transformed by heat-shock into *E.Coli* expression strain B834. Bacteria were plated onto LB-Kanamycin (25 µg/ml) overnight, and then colonies were picked and grown in 5 ml medium plus appropriate antibiotics overnight at 37°C 250 rpm. Cultures were transferred into a 24-well deep-well plate and cultured overnight with either Overnight Express Instant TB autoinduction medium (Novagen), or with LB-broth, both supplemented with 25 µg/ml Kanamycin, and induced with IPTG 0.5 mM or 0.1 mM at OD= 0.59, then aliquoted into two separate 96-well deep-well plates, spun down at 6000 g for 30 min at 4°C in a Beckman Avanti J series centrifuge fitted with a JS-5.3 rotor. Small-scale protein purification was performed with Ni-NTA Magnetic Agarose Beads kit (Qiagen) on an AVISO THeonyx automated workstation according to manufacturer's instructions. Protein purification was assessed by SDS-PAGE electrophoresis on 4-12% Bis-Tris gels at 200V. Gels were stained with Instant Blue solution (Gentaur) for 20 min and imaged on an ImageQuant Las 4000 imaging station (GE Healthcare). Large-scale cultures (2 x 500 ml) were set up overnight and spun down at 6000 g for 30' at 4°C in a Beckman Avanti J series centrifuge fitted with a JLA 8.2 rotor. Pellets were lysed into 40 ml Lysis Buffer (50 mM Tris pH 7.5, 500 mM NaCl, 20 mM Imidazole, 0.2% Tween 20) supplemented with 200 U DNAseI (Sigma) and 1 tablet Complete EDTA-Free Protease Inhibitors Cocktail (Roche), vortexed and passed through a Constant Systems TS Benchtop model cell disruptor at 30 kpsi. The lysate was cleared by centrifugation at 30000 g for 30 min at 4°C in a Beckman Avanti J series centrifuge fitted with a JA-17 rotor. IMAC columns were stripped with 50 mM EDTA in 1x PBS pH8, washed twice with water, re-charged with 100 mM NiSO4, rinsed with water and equilibrated with Wash Buffer

(50 mM Tris pH 7.5, 500 mM NaCl, 20 mM Imidazole). Samples were loaded into an Akta Xpress unit, fitted with a pre-equilibrated IMAC column and a 16/60 Hiload Superdex 75 gel filtration column. Purification was performed overnight at 4°C and protein quality and concentration were assessed by spectrophotometry at 280 nm and SDS-PAGE electrophoresis.

2.9. Production of a Neuregulin β1-MCP fusion protein (Chapter 3)

2.9.1. Cloning of NRG1β EGF-like domain into pACP-tag(m) vector

Neuregulin (NRG) 1β cDNA (accession number NM_013956.2) was purchased from OriGene as a template DNA. The EGF-like domain (residues 177-241) was amplified using the following primers: FW 1046 SacI =CGCCGAGCTCATGAGCCATCTTGTAAAATGTG (containing a SacI restriction enzyme site and an ATG codon); Rev 14 HindII = CCAAGCTTCTCCGCCTCCATAAATTCAATCCC (containing a HindIII site). The PCR Reaction was performed on 10 ng of template with 3 U Pfu polymerase (Promega) using the following parameters on a GeneE thermal cycler: 5min initial denaturation at 95 °C, followed by 32 cycles of 1 min at 95°C, 1min at 54°C and 30 sec at 74 °C, followed by a final extension of 10 min at 74 °C. PCR products were purified with QIAquick PCR Purification kit (Qiagen), according to manufacturer's instructions, and subsequently subjected to digestion with 40 U SacI and 20 U HindIII restriction enzymes (NEB), according to manufacturer's instructions, at 37°C for 2 hours on a GeneE PCR machine. pACP-tag(m) vector (NEB) (1.5 µg) was similarly digested and all digestion products were purified with QIAquick PCR Purification kit (Qiagen) according to manufacturer's instructions. Digested pACP-tag(m) vector and insert were ligated with T4 ligase (NEB) in 1:7, 1:5 and 1:3 v/v proportions, incubating the reaction at 16°C overnight on a GEneE PCR machine. The ligation products were transformed by heat shock (45 sec at 42°C followed by 2 min on ice) into DH5α competent cells (Invitrogen) and plated onto LB-agar plates supplemented with 25 µg/ml Kanamycin sulphate. Colonies were picked and grown overnight in 5 ml LB supplemented with 25 µg/ml Kanamycin sulphate and the plasmid DNA was extracted using QIAQuick Mini-Prep Spin Plasmid Extraction kit (Qiagen) according to manufacturer's instructions. The presence of a correctly ligated plasmid was assessed through a diagnostic digestion with the restriction enzyme XmnI for 2 hours at 37°C, followed by a run on 1% agarose gel. Clone #8 was selected for large-scale culture (2x 500 ml) by diluting 1/1000 the original culture. Cells were spun down at 7000 rpm for 5 minutes at 10°C and plasmid DNA was extracted using Qiagen Plasmid Plus Maxi kit (Qiagen) as per manufacturer's instructions.

2.9.2. Sub-cloning of NRG1β-ACP into a 6-His tag expression vector

This experimental step was performed in the Oxford Protein Production Facility (Harwell Oxford) with technical counselling from Mr Anil Verma.

In order to obtain a purifiable protein, the NRG1β-ACP ORF was sub-cloned from pACP-tag(m) vector by PCR amplification using primers OPPF 8653 Fwd = aggagatataccatgAGCCATCTTGTAAAATGTGCG; OPPF 8653 Rev = gtgatggtgatgtttGGATCCT GGCGCGCCTAT for insertion in pOPINE vector and OPPF 8654 Fwd = gcgtagctgaaaccggcAGCCATCTTGTAAAATGTGCG with the same forward primer for insertion in pOPING vector [269] (lower case = vector InFusion cloning tag, upper case = gene-specific sequence) with KOD Xtreme Hot Start DNA polymerase (Novagen). Amplification was performed on a Veriti thermocycler (ABI) with the following parameters: initial denaturation at 94°C for 2 minutes, 29 cycles of 10 seconds at 98°C, 30 seconds at 60°C and 2'30" at 68°C, followed by a final extension of 2 minutes at 68°C. 8653 Rev primer was used together with 8654 FW primer for insertion in pOPING vector. PCR products were assessed by agarose gel electrophoresis and purified with Ampure XP Magnetic Bead Purification kit (Agencourt) according to manufacturer's instructions. Purified PCR inserts were cloned into 6-his tag containing vectors pOPINE and pOPING (modified from pTrieX vector - [269]) by In-Fusion PCR Cloning System (Clontech) as per manufacturer's instructions (8653 insert was cloned into pOPINE vector and 8654 into pOPING vector). Subcloned vectors were transformed into Omnimax II competent cells (Invitrogen) by heat-shock (30 sec at 42°C followed by 2 min on ice) and subjected to blue/white screening on LB-carbenicillin plates containing a 1/1000 dilution of 20% X-Gal in DMF and 1/500 IPTG (0.5 mM). White colonies, in which LacZ was disrupted by insert ligation, from both sub-cloning reactions were picked and grown overnight in 5 ml LB-Carbenicillin medium, then spun down at 5000g for 10 minutes into a Beckman Avanti J series centrifuge fitted with a JLA 16.250 rotor and subject to plasmid DNA extraction using QIAquick Mini-Prep Spin Plasmid Extraction kit (Qiagen) on a QiaCube (Qiagen) workstation according to manufacturer's instructions, and quantitated on a Nanodrop 8000 spectrophotometer (Thermo Fisher Scientific).

2.9.3. Transient expression of NRG1β-ACP in mammalian cells

This experimental step was performed in the Oxford Protein Production Facility (Harwell Oxford) with technical counselling from Dr Ray Owens.

NRG1β-ACP constructs were transfected into HEK 293T (kindly provided by the OPPF facility) cells using GeneJuice (Novagen). Briefly, 4 µl of GeneJuice were incubated with 120 µl serum-free MEM (Invitrogen) and 2 µg plasmid DNA for 15 minutes, then the transfection mixture was added to cells plated into a 6-well plate drop-wise and the plates were incubated for 48 h at 37°C. One ml of the conditioned medium from the transfected cells was harvested into 1.5 ml microcentrifuge tubes and centrifuged at 15600 rpm for 5' in a tabletop centrifuge (Eppendorf). Cells were lysed into 400 µl Lysis Buffer (50 mM Tris pH 7.5, 500 mM NaCl, 20 mM Imidazole, 0.2% Tween 20) for 30 minutes on ice; lysates were harvested into 1.5 ml microcentrifuge tubes and cleared by centrifugation at 15600 rpm for 10 minutes in a tabletop centrifuge (Eppendorf). Both supernatants and lysates were assessed for protein presence by western blot with an antibody against 6-His tag. Briefly, lysates and supernatants were subject to SDS-PAGE on 4-12% Bis-Tris NuPAGE polyacrylamide gels (Invitrogen), and then proteins were blotted onto nitrocellulose membrane using iBlot apparatus (Invitrogen) according to manufacturer's instructions. Membranes were blocked with 5% non-fat dry milk in PBS + 1% Tween 20 overnight at room temperature. The membrane was blotted with primary mouse anti-His6 BMG-His1 (Roche) in 0.5% non-fat dry milk in PBS + 1% Tween 20 for 2 hours at room temperature, washed twice with 0.5% non-fat dry milk in PBS + 1% Tween 20 and blotted with secondary goat anti-mouse -HRP (Pierce) for 1 h at room temperature. The membrane was washed twice with 0.5% non-fat dry milk in PBS + 1% Tween 20 and developed with ECL Plus (GE Healthcare) for 5 minutes at room temperature, then imaged on ImageQuant Las 4000 (GE Healthcare), using precision mode, for 2 minutes.

2.9.4. Site-directed mutagenesis of ACP to MCP

In order to obtain a plasmid suitable for expression in *E.Coli*, NRG1β-ACP pOPINE plasmid was mutagenised using QuikChange II XL Site-Directed Mutagenesis kit (Agilent) to mutate D36 and D39 of ACP into T36 and G39 of MCP. Oligonucleotide design was performed using QuikChange Primer Design software (available on the Agilent website). D36T_D39G= aagacctgggcgcgacttctcttggcaccgttgagctgg; D36T_D39G_antisense= ccagctcaacggtgccaagagaagtcgcgcccaggtctt. Mutant strand synthesis reaction was performed on 10 ng plasmid DNA template with 125 ng of each oligonucleotide primer on a G-Storm PCR machine with the following cycling parameters: initial denaturation 1 minute at 95°C; 18 cycles of 50 seconds at 95°C, 50 seconds at 60°C, 6 minutes at 68°C and a final extension of 7 minutes at 68°C. Parental wt DNA was digested by incubating the SDM reaction with DpnI restriction enzyme 1 hour at 37°C. Five µl of reaction were transformed into Omnimax II cells (Invitrogen)

by heat-shock (30 seconds at 42°C followed by 2 minutes on ice). Cells were recovered in 450 µl SOC medium. Cells were incubated for 1 hour at 37°C and plated onto LB-Ampicillin plates and left to grow overnight at 37°C. Colonies were picked and grown overnight into 5 ml of LB-Ampicillin medium, then spun down at 10000 rpm and subjected to plasmid extraction with QIAquick Mini-Prep Spin Plasmid Extraction kit (Qiagen) on a QiaCube (Qiagen) workstation according to manufacturer's instructions and quantitated on a Nanodrop 2000 spectrophotometer (Thermo Fisher Scientific), then sent to sequencing at Source Bioscience.

2.9.5. Expression of NRG1β-MCP in *E.Coli* strains

This experimental step was performed in the Oxford Protein Production Facility (Harwell Oxford) with technical counselling from Mr Anil Verma.

Purified plasmid DNA (100 ng) was transformed by heat-shock into *E.Coli* expression strains B834, Rosetta, C41 and BL21DE3, in order to perform a small-scale expression screening. Bacteria were plated onto LB-AMP plates overnight, and then colonies were picked and grown in 5 ml medium plus appropriate antibiotics overnight at 37°C 250 rpm. Cultures were transferred into a 24-well deep well-plate and cultured overnight either with Overnight Express Instant TB auto-induction medium (Novagen), or with LB-broth and induced with IPTG 0.5 mM or 0.1 mM at OD= 0.59, then aliquoted into two separate 96-well deep-well plates and spun down at 6000 g for 30 min at 4°C in a Beckman Avanti J series centrifuge fitted with a JS-5.3 rotor. Small-scale protein purification was performed with Ni-NTA Magnetic Agarose Beads kit (Qiagen) on an AVISO THeonyx automated workstation or a Qiagen Biorobot 8000 (Qiagen) according to manufacturer's instructions. Protein purification was assessed by SDS-PAGE electrophoresis. Gels were stained with Instant Blue solution (Gentaur) for 20 min and imaged on ImageQuant Las 4000 (GE Healthcare).

2.9.6. Labelling of NRG1β-MCP with fluorescent CoA derivatives

NRG1β-MCP was labelled with CoA-Atto 488, CoA-Dyomics 547, CoA Dyomics 647 (all NEB), or with CoA-Alexa 488 and CoA-CF640R (custom synthesis by Cambridge Research Biochemicals) by enzymatic labelling with SFP Synthase (NEB), according to manufacturer's instructions. Briefly, 5 µM of NRG1β-MCP protein were incubated with 10mM $MgCl_2$, 50 mM HEPES, 1 mM DTT, 10 µM of CoA substrate and 1 µM of SFP Synthase (total reaction volume 50 µl) for 1h at 37°C in a GeneE thermal cycler. This yields a strict 1:1 labelling ratio, as only one site on each MCP protein can be conjugated to a CoA moiety. Labelled proteins were aliquoted and stored at -20°C.

2.10. Confocal imaging of HER family probes for the determination of binding curves (Chapter 3)

Confocal images were acquired using a commercial microscope setup (Nikon, Eclipse Ti), with confocal imaging provided through a scanning unit (Nikon, D-Eclipse C1) equipped with photomultipliers (PMC100-1, Becker & Hickl GmbH). The output from the AOTF of supercontinuum laser sources (Fianium, SC450-4, 40 MHz repetition rate) was used as an illumination source (power ~ 15 μW for 640 nm line, and ~ 25 μW for 488 nm line).

2.11. Confocal data analysis (Chapter 3)

Average intensity from confocal images was calculated with ImageJ software (NIH)[270] by applying an intensity threshold to the image and converting it into a binary mask, then subtracting it from the original image (using the Subtract operation from the Image Calculator function of Image J) and obtaining the list of pixel intensity frequencies through the Pixelhoover v1 plugin (for 16-bit images) or through the built-in histogram analysis tool. Pixel intensity frequencies for different areas of the same sample were imported in Excel spread sheets. Pixel frequencies of the same intensity bin from different areas taken from the same sample were added up and then multiplied by the intensity values of their respective bins (1-255). An average of the pooled, multiplied pixel frequencies was then calculated to obtain the average pixel intensity.

2.12. Transient transfection with MCP-GPI plasmid and labelling with fluorescent CoA conjugates (Chapter 3)

Due to the difficulties in labelling the NRG1β-MCP protein construct with fluorescent CoA conjugates wild-type Cho cells were used for MCP-GPI plasmid transfection, in order to test whether CoA conjugates are able to label a control protein.

Cells were seeded on uncoated glass-bottomed dishes, at a density of 0.5x 10^5/dish, and grown for 48h, then transfected using Fugene HD (Promega) transfection reagent at a 3:2 μl/μg ratio with the MCP-GPI plasmid (NEB), according to manufacturer's instructions. Transfection was performed in Pen/Strep free DMEM High-glucose and expression was carried on for 24 h at 37°C in complete medium without antibiotics.

Cells were then starved for 2h, then rinsed twice with SFM + 0.5% w/v BSA (Sigma) and enzymatically labelled for 1h at 37°C with 5 μM total labelled CoA, 10 mM $MgCl_2$ (NEB) and 1 μM SFP Synthase (NEB) in SFM + 0.5% w/v BSA. Cells were then washed 3x with SFM+0.5% BSA

and imaged promptly at 37°C on a Single-Molecule microscope, as described in **Chapter II**. At least 10 independent areas were acquired for each experimental condition.

2.13. Assessment of receptor activation by fluorescently tagged anti-HER1 Affibody (Chapter 3)

A431 cells were seeded on 10 cm dishes and 6-well plates, grown to 80% confluence and serum-starved overnight. Cells were treated with 100 nM murine EGF (positive control), 2 nM anti-HER1 Affibody Alexa 488, 1 nM anti-HER2 Affibody z:HER2 477 dimer Alexa 488 or PBS-BSA for 4 h. After washing off excess label, samples were treated with 1mg/ml Bis[sulfosuccinimidyl] suberate (BS3, a membrane-impermeable crosslinker -Sigma) in PBS for 30 min at 4°C to cross-link proteins. The reaction was quenched with 20 mM Tris pH 7.5 for 15 min on ice, and then samples were washed twice with ice-cold PBS. Ten cm dishes were lysed for 5 min on ice with 1 ml lysis buffer (50 mM Tris pH 7.5, 5 mM EGTA, 150 mM NaCl, 1% Triton, supplemented with 25 mM benzamidine, 1/100 Protease Inhibitor cocktail (Sigma) and 100 mM NaF, 1 mM Na_3VO_4) followed by scraping with a cell scraper. Six-well plates were lysed with 200 µl 2x NuPAGE LDS Sample Buffer (Invitrogen), reducing agent 1x supplemented with 25 mM benzamidine, 1/100 Protease Inhibitor cocktail (Sigma), 100 mM NaF and 1 mM Na3VO4 . Lysates were cleared by centrifuging at 14000 g for 5 min at 4°C. Protein S resin (Sigma) was washed twice with PBS and incubated with anti-HER1 antibody (#2256 Cell Signaling Technology) for 1 h at room temperature, then washed twice with PBS to remove unbound antibody. Lysate was incubated with resin overnight at 4°C and resins were washed four times with TBS-0.1% Triton X-100. Immunoprecipitated proteins were eluted by incubation with 2x NuPAGE LDS Sample Buffer and 10x Sample Reducing Agent (Invitrogen) by boiling for 5 minutes. Samples were run on 1.5 mm thick 3-8% Tris –Acetate NuPAGE gels (Invitrogen) with HiMark Prestained HMW protein standard (Invitrogen) on an XCell apparatus (Invitrogen). Proteins were blotted using iBlot system (Invitrogen) on nitrocellulose membranes, blocked for 1h at room temperature with 3% Non-fat dry milk in TBS and probed overnight with 1/1000 mouse anti-phosphotyrosine 4G10 antibody(Upstate - Millipore). Blots were then probed with secondary anti-mouse-HRP antibody (Jackson ImmunoResearch) for 1 h at room temperature, and incubated with Supersignal West Pico Chemiluminescent Substrate solution (Pierce) for 5 min, then imaged with a Kodak Imagestation 4000MM Pro. Blots were stripped and re-probed sequentially with 1/1000 rabbit anti-HER1 pY1045 antibody (Cell Signaling Technology) and 1/1000 rabbit-anti total HER1antibody (Cell Signaling Technology). Anti-rabbit- HRP antibody diluted 1/1000 (Jackson ImmunoResearch) was used for both blots

and images were acquired as above. Densitometry analysis was performed with ImageJ software (NIH). Bands were normalized against the amount of total HER1 and relative quantity was expressed as fold change compared to the negative control.

2.14. Surface passivation (Chapters 4-7)

Glass-bottom cell culture dishes (MatTek Corporation) were used for all surface treatments. Details of surface passivation treatments were as follows:

2.14.1. "Piranha" cleaned dishes

A 3:1 solution of concentrated sulphuric acid and 30% w/v hydrogen peroxide was applied on glass coverslips. The solution was left for 15 minutes at room temperature and the dishes were then rinsed well with deionised water. Dishes were allowed to dry and stored at room temperature.

2.14.2. Polyethylene glycol (PEG)

Dishes were first cleaned with piranha solution as described above. Dishes were then treated with 4-aminopropyl triethoxysilane (APTES; Sigma Aldrich), as follows. A 2% v/v solution of APTES in 95% ethanol was made up immediately prior to treatment. The APTES solution was added to the dishes, completely covering the glass, and dishes were incubated for 10 minutes at room temperature. Dishes were then rinsed extensively, first with 95% ethanol and then with deionised water and allowed to dry. Dishes were left overnight at room temperature before the next stage. PEG solutions were prepared immediately before use. Either 8-arm PEG-vinyl sulfone, MW 10K "Star-PEG" (Creative PEGWorks), or PEG-succinimidyl valerate, MW 5K "linear PEG" (Laysan Bio), were dissolved at a concentration of 200 mg/ml in filtered sodium bicarbonate buffer, pH 8.5. The solution was added to the dishes, and incubated for 3 hours at room temperature. Dishes were then rinsed thoroughly with deionised water, allowed to dry, and stored at 4 °C for use within 2-4 weeks. In dishes to be used for cell culture, GRGDS peptide (Anaspec) was added to the PEG solution at concentrations of 0.2 μM or 0.4 mM. Laminin A Chain Peptide (cat. No L1225-39 USBiological) was used at a concentration of 30 nM. Concentrations were chosen in order to closely match concentrations used in published reports in the field of biomaterial synthesis [271–273]

2.14.3. PEG-BSA nanogels

PEG-BSA nanogels were prepared using 8-arm PEG-vinyl sulfone and BSA, as described by Tessler *et al.* [274]. Dishes were first cleaned with piranha solution and treated with APTES as

described above, then 10% w/v nanogel in PBS was added to the dishes, and they were incubated for 1 hour at 37°C. Dishes were then washed in PBS and incubated for 1 hour at 37°C with 50 mg/ml BSA in PBS and exposed to 1 M Tris, pH 8.0 for 15 minutes at room temperature to quench unreacted vinyl sulfone groups. Finally, dishes were washed with PBS. Dishes were filled with PBS to prevent layer desiccation and stored at 4 °C for use within 2-4 weeks.

2.14.4. Poly-L-lysine (PLL)

0.01% w/v poly-L-lysine (Sigma) in deionised water was added to dishes, covering the surface of the glass. Dishes were incubated for 3 hours at room temperature, and the poly-L-lysine solution was then aspirated off, and the dishes stored at room temperature for use within 2-4 weeks.

2.14.5. Bovine serum albumin (BSA)

A solution of 1% w/v of Bovine Serum Albumin (Sigma) in PBS was prepared and sterile filtered. Enough solution to cover the glass was added to the dishes and incubated at room temperature for 1 hour. BSA solution was then aspirated off and dishes were stored at 4°C for use within 2-4 weeks.

2.14.6. Foetal calf serum (FCS)

Pure Foetal Calf Serum (Gibco) was added to the glass coverslips and incubated at room temperature for 1 hour. FCS was then aspirated off and dishes were stored at 4°C for use within 2-4 weeks.

2.14.7. Laminin

25 µg/ml laminin (Sigma) in PBS was added to dishes, covering the surface of the glass. Dishes were incubated for 2 hours at room temperature, and the laminin solution was then aspirated off, and the dishes stored at 4 °C for use within 2-4 weeks. For cell culture experiments, dishes were rinsed with culture medium before plating cells.

2.14.8. Fibronectin

25 µg/ml fibronectin (Sigma) in PBS was added to dishes, covering the surface of the glass. Dishes were incubated for 45 minutes at room temperature, the fibronectin solution was then

aspirated off, and the dishes stored at 4 °C for use within 2-4 weeks. For cell culture experiments, dishes were rinsed with culture medium before plating cells.

2.14.9. Collagen

Commercially available collagen-coated glass-bottomed dishes were used (MatTek Corporation).

2.15. Colorimetric MTT vitality assay for the assessment of cell growth on doped PEG adhesion substrates (Chapter 4)

The wells of a 96-well glass-bottomed plate (MatTek) were coated as described above with PLL (positive control), Fibronectin, Laminin (adhesion controls for derived peptides) or Linear PEG doped with different peptides: GRGDS (Anaspec) 1 μM, 100 μM or 0.4 mM; Laminin A Chain Peptide (IKVAV – USBiological) 30 nM, 100 nM or 300 nM or Laminin B1 peptide aa 925-933 (YIGSR – USBiological) 62 nM or 103 nM. Wells were coated in triplicate.

Cells were seeded at a density of 5000 cells/well and grown to 70% confluence, then viability was assessed via MTT assay (Sigma cat no CGD-1KT) as per manufacturer's instructions. Absorbance at 570 nm was read after 3h incubation at 37°C in a SpectraMax Plate Reader (Molecular Devices), correcting for baseline absorbance at 690 nM. Data were exported in Excel and Multiple Anova test was performed. Pairwise post-tests between positive control and test samples were also performed.

2.16. Cell-free assessment of nonspecific protein binding to passivated surfaces (Chapter 4)

Glass- bottomed dishes were imaged filled with PBS solution, in order to ascertain the presence and amount of impurities, taking single-frame images of 5 non-overlapping areas. PBS was then aspirated off and glass dishes were treated with a solution of triply labelled protein (10 nM of each labelled species for EGF and Hen Egg White Lysozyme (HEWL), 11 nM of each labelled species for anti-HER2 Affibody). Single-frame images of 5 non-overlapping areas were taken at 150 s, 300 s, 600s, and 1200 s.

Experiments were performed in triplicate and spot density/μm^2 was calculated for each imaged area using custom software described in [226] and logged in a spreadsheet. Mean ± SEM of 15 areas was plotted for each datapoint.

2.17. TIRF imaging of peptide persistence on PEG surfaces and cell-substrate contacts (Chapter 4)

Glass-bottomed dishes were coated with Linear PEG as described above, adding 200 µM-0.2 µM of FITC-labelled GRGDSP peptide (AnaSpec) in the polymerization step.

T47D cells were seeded on FITC-labelled dishes as described above and cultured for 48h at 37°C. Cells were serum-starved as described above and labelled with 1 µM DiD membrane probe (Invitrogen) for 10 min at 37°C, then promptly imaged on a TIRF microscope (as described in **Paragraph 2.4** on page 84), exciting with 491 nm and 638 nm (Vortran) lasers under controlled temperature conditions at 37°C.

2.18. Determination of bleaching half-lives and molecular brightness of anti-HER1 Affibody conjugates (Chapter 5)

For bleaching assessment, starved cells were rinsed twice with chilled PBS pH 7.4 and labelled with the appropriate amount of HER1 Affibody for 1 h on ice. Cells were rinsed twice with chilled PBS pH 7.4 and fixed in 3% paraformaldehyde (Electron Microscopy Sciences), 0.5% glutaraldehyde (Sigma) for 30 minutes prior to imaging.

Data were acquired as described in **Paragraph 2.4**, except at 10 fps for 50 seconds. These parameters were chosen to enable recording of a timescale suitable for the analysis of the bleaching half-lives of the different fluorophores. At least 5 areas were acquired for each dye. Images were saved in HDF5 format for subsequent processing using custom-designed software [226].

To determine Single-Molecule bleaching parameters, feature intensity v. time traces were extracted for every dataset. Traces recorded under the same experimental conditions were combined and a single exponential decay was fitted to the data in Origin 8 to determine the photobleaching time constant. The feature intensities of single molecules tracked within each series of images were combined to produce feature intensity histograms for each dye, and a Gaussian or sum of Gaussians model was fitted to the data as appropriate. The position of the first peak was taken to be the mean intensity of a single molecule. The number of detected photons, N_P, was calculated from the measured fluorescence intensities, *I*, using $N_P = IS/G\eta_{\mathrm{det}}$, where the sensitivity of the detector, *S*, in electrons per digital level, and the efficiency of the detector, η_{det}, were taken from performance test data supplied by the

manufacturer and specific to the EMCCD used. *G* was the EM gain setting used during image acquisition.

2.19. Direct measurement of dye-substrate binding by spot density (Chapter 5)

0.5 nM of dye-conjugated anti-HER1 Affibody species in SFM + 25 mM HEPES pH 7.2 were incubated on PEG-BSA nanogel-coated dishes for 10' at 37°C, under the same experimental conditions used for cell tracking experiments, then rinsed twice with SFM+HEPES and imaged at 37°C as described in **Paragraph 2.4**. At least 10 independent areas were acquired for each experimental condition. Raw data was saved in HDF5 format and analysed with custom software as described above. The number of Single-Molecule spots for each dye channel was calculated by the analysis software and divided by the surface area of the imaged region (≈ 80 x 30 µm). Resulting Single-Molecule spot density values were logged in a spreadsheet and correlated with relevant electrostatic dye parameters (net charge and logD pH 7.4).

2.20. Assessment of Single-Particle localisation precision (Chapter 6)

Starved cells at 70-80% confluence were rinsed twice with Serum-Free Medium at 37°C, then pre-chilled at 4°C and labelled with the appropriate combination of fluorescently labelled proteins for 1 hour at 4°C. Samples were washed twice with ice-cold PBS and fixed with 0.5% Glutaraldehyde, 3% Paraformaldehyde for 15 minutes on ice and 15 minutes at room temperature, then imaged, as described in **Paragraph 2.4**, for 30 seconds at 10, 20 and 33Hz frame-rate, while varying the excitation laser power between 1.2-4 mW on 491 nm (Cobolt Calypso) and 640 nm (Vortran) CW lasers. Time series of single molecule images were analysed with custom Bayesian feature detection and tracking software [226]. The measured intensity of detected features was used to produce a probability density distribution of feature intensity. These distributions were used to determine the probability that detected features have intensity greater than an arbitrary threshold I_t (e.g. 1000 photon counts). The threshold was then set at a higher arbitrary value (e.g. 2000 photon counts), iterating the process until all features were accounted for. The probability of $I>I_t$ was then plotted as a function of I_t for each combination of laser power and frame-rate.

MSD plots were generated for each dataset as described in **Paragraph 2.5**. Feature localisation precision was calculated from the *y*-axis intercept of the MSD plots.

2.21. Drug Treatments (Chapter 6-7)

2.21.1. Erlotinib

Cells were treated with 1 µM Erlotinib (Erl – Tocris Bioscience) for 2h during starvation in Serum-Free Medium, a concentration reported in the literature as sufficient to abolish HER1 phosphorylation, but not to induce cell death [275]. Cells were then rinsed twice with SFM and, due to the fast wash-off kinetics of the drug [172], 1 µM Erlotinib was also added to buffers during labelling and imaging.

2.21.2. Excess Unlabelled EGF

After starvation in SFM, 100 nM unlabelled EGF (Peprotech) was added to labelling solutions and incubated for 10 min at 37°C. Cells were then rinsed twice and imaged as described above

2.21.3. Excess Unlabelled NRG1β

After starvation in SFM, 200 nM unlabelled NRG1β-MCP (in-house expression) was added to labelling solutions and incubated for 10 min at 37°C. Cells were then rinsed twice and imaged as described above

2.21.4. Gefitinib

Cells were treated with 1 µM Gefitinib (Gef - Tocris Bioscience) in SFM for 2h during serum starvation. This treatment acted as a control for kinase inhibition.

2.21.5. Lapatinib

Cells were treated with 1 µM Lapatinib (Lap – Tocris Bioscience) for 2h during starvation in SFM, a concentration sufficient to abolish HER1 and HER2 phosphorylation, but not to induce cell death [275–277]. Cells were then rinsed twice with SFM and 1 µM Lapatinib was also added to buffers during labelling and imaging.

2.21.6. Latrunculin A (Chapter 7)

After starvation, cells were treated with 1 µM Latrunculin A (LatA – Sigma) in serum-free media for 10 minutes at 37°C. Cells were then rinsed twice with SFM +25 mM HEPES pH 7.2 and labelled as appropriate.

2.21.7. Methyl-β-cyclodextrin (Chapter 7)

After starvation, Serum-Free Medium was removed and replaced with SFM + 10 mM Methyl-β-cyclodextrin (MβCD - Sigma). Cells were incubated at 37°C for 30 min before being rinsed twice with SFM + 25 mM HEPES pH 7.2 and labelled as appropriate.

2.21.8. α-Lactose (Chapter 7)

Cells were treated with 10 mM α-Lactose (Sigma) in complete medium for at least 24h in order to interfere with the galectin lattice. α-Lactose 100 mM was also added to SFM during starvation, and to SFM+ 25 mM HEPES pH 7.2 during labelling and imaging.

2.21.9. Blebbistatin (Chapter 7)

Cells were starved for at least 2 h in SFM, washed twice and labelled with anti-HER1 Affibody for 10' at 37°C, prior to being washed twice again and then incubated with 50 µM InSolution racemic Blebbistatin (Bleb - EMD Chemicals) in SFM for 4' at 37°C. After incubation, cells were washed twice yet again and, if necessary, labelled with EGF.

2.21.10. Cytochalasin D (Chapter 7)

After starvation, cells were treated with 10 µM Cytochalasin D (CYTCD – Sigma) in serum-free media for 30 minutes at 37°C. Cells were then rinsed twice with SFM +25 mM HEPES pH 7.2, and CYTCD was also added to buffers during labelling and imaging.

2.21.11. Jasplakinolide (Chapter 7)

After starvation in SFM, cells were treated with 500 nM InSolution Jasplakinolide (Jasp- EMD Chemicals) in SFM for 5 min at 37°C. Cells were then washed twice with SFM and labelled as described above.

2.21.12. Nocodazol (Chapter 7)

Cells were incubated with 10 µM Nocodazol (Noc - AppliChem) in SFM for 10 min at 37°C. Cells were then rinsed twice with SFM and nocodazol was added to buffers for labelling and imaging, following the protocol used by M. Boggara *et al.* [278].

2.22. Determination of the toxicity of cell treatments and the growth-inducing activity of ligands with a colorimetric MTT assay (Chapters 6-7)

In order to determine the toxicity or the proliferative effect of the different treatments used in this phase of the project, a colorimetric vitality assay was employed.

T47D cells were seeded at a density of 2 x 10^4 cells/well in a 96-well tissue culture plate and grown for 24h until they reached 70% confluence. For the MTT experiment described in **Chapter 7**, cells were then starved for 2h and treated with Latrunculin and MβCD as described above. Tyrosine kinase inhibitors (1 μM of Lapatinib, Erlotinib or Gefitinib or a combination of 1 μM Erlotinib + 1 μM Lapatinib) were added during starvation and kept on the cells throughout the experiment. Ligands were incubated on cells for 1h at 4°C and rinsed out. Cell viability was assessed via MTT assay (Sigma) according to manufacturer's instructions. Absorbance at 570 nm was read out after 3h incubation at 37°C on a Paradigm Multi-Mode Microplate Detection Platform (Molecular Devices), correcting for baseline absorbance at 690 nm. All samples were read in triplicate. Data were exported in Excel and corrected, blank-subtracted average absorbances were compared with untreated values via two-tailed Student T-Test.

2.23. Assessment and measurement of colocalisation (Chapters 6-7)

Single molecule features were detected and tracked independently in both channels using the analysis pipeline described in Rolfe *et al.* (2011) [226].

The output of this is a series of single molecule intensity and position vs time traces, each one corresponding to a feature in only one of the channels.

Colocalisation between these tracks was assessed by comparing every track in one channel with every track in the other, and counting the total number of frames, N_{coloc}, during which a feature was detected in both tracks and where these features were at furthest R_{coloc} (nm) apart. Any track which has a value of $N_{coloc} >= N_{coloc\_min}$ (chosen to be 3 here) with at least one other track was considered to be colocalised. The total number of tracks identified as colocalised in this way were counted, and the proportion of such tracks to the total number of tracks in all channels was recorded as the colocalisation fraction, F_{coloc}. For example a dataset with just two tracks, one in each channel, where the tracks did spend a total of at least N_{coloc_min} frames within R_{coloc} of one another would have F_{coloc}=100%.

2.23.1. Assessment of coincidental colocalisation frequencies

Coincidental colocalisation statistics were calculated for each dataset as follows. In each channel, a randomised set of tracks of the same size as the measured set was produced, where each track in the random sample was chosen (with replacement) from the measured tracks for that channel, re-centred at random with uniform probability density across the field of view, rotated through a random angle with uniform probability density between 0° and 360°, and randomly flipped on the *x* axis with probability P=0.5. The random tracks therefore have key properties, such as duration and path structure, representative of the true tracks, but are now randomised in distribution and orientation. The colocalisation statistics were then calculated for the randomised tracks. This was performed for a total of 50 times for each dataset, and then the colocalisation statistics were pooled to give a final estimated coincidental colocalisation fraction for that dataset.

For each experimental conditional, the proportion of datasets for which the measured colocalisation fraction was greater than the coincidental fraction was taken as a measure of the confidence that there was true colocalisation.

2.24. Globally optimised spatiotemporal tracking with the Biggles algorithm (Chapter 7)

For a complete description of the Biggles algorithm, its implementation and its validation, the readers are referred to Wareham *et al.* [3].

Biggles uses some data, D, which are the spatial and temporal (x, y, t) coordinates of the particle image spots detected in the images (referred to as features), a hypothesis for the set of tracks, the track configuration T, and some global parameterized model, Θ, for the properties of the system. Information for any feature detector [279] can be folded in the algorithm and a set of spurious measurements can be allowed for in each frame. A flexible yet simple model for particle motion [280] is used: a random-walk.

Biggles finds the probability of any given set of particle reconnections and motion parameters given the data. In a Bayesian framework [281], this is equivalent to optimising the joint track and parameters empirical (or *posterior*) probability function: $P(T, \Theta \mid D)$. To avoid having to sample from the *posterior* directly, Biggles uses a Gibbs sampler [282], which allows to alternatively draw trains of samples T_i and Θ_i from two conditional distributions: $T_i \sim P(T \mid \Theta_{i-1}, D)$ and then $\Theta_i \sim P(\Theta \mid T_i, D)$, where T_0 and Θ_0 are initialised to some values. In principle only loose 'plausible' bounds of T_0 and Θ_0 need to be specified; e.g. track lengths will never be shorter than 1 frame or have more frames than the maximum number of acquired frames. The

current implementation initialises Θ_0 to uncontroversial typical values and initialises T_0 to a state where all features are assumed to be spurious detections. This choice of initial state is to ensure that the tracks produced are not unduly influenced by any other tracking algorithm which may have been used to initialise Biggles.

It must be noted that, while the parameters can be sampled directly because their *posterior* distribution is known and separable, sampling from the track configuration is non-trivial, as only a small number of analytical Probability Density Functions (PDFs) have known direct sampling algorithms. For this the Metropolis-Hastings algorithm is used, which can draw samples from almost any PDF [283] and which, at convergence, yields candidate-sets of tracks whose distribution matches the *track assignments posterior* (P (T | D, Θ)) independently of any choice of parameter values.

At the point of convergence, the Gibbs sampler returns candidate-sets of tracks and parameters whose distribution matches that of the joint *posterior* distribution. Results such as the sample mode and sample variance can be interpreted as maximum empirical estimates and experimental errors respectively. The ability of Biggles to directly return a representative sample of tracking results and parameters, and to place confidence limits on these, is powerful and, as far as it can be ascertained, it is novel in this field.

2.24.1. Automatic estimation of directionality in each frame of each track

In Biggles the internal (hidden) state X of a particle at time T is parameterized by four variables, as shown in **Equation 2-1**Error! Reference source not found.,

$$X = \left(x, x', y, y'\right)^T$$

Equation 2-1 – Biggles parameterization of the hidden state of a particle

where $x' = \frac{dx}{dt}$ and $y' = \frac{dy}{dt}$, i.e. $(x', y')^T$ is the instantaneous velocity vector v. The "T" indicates the transposition of the vector, i.e. X is a column vector. A linear state-space model is assumed for both the time evolution of the moving particle, $X_{t+1} = AX_t + \boldsymbol{w}$, where $\boldsymbol{w}$~N(0,P) is noise that follows a 4-variate normal distribution with mean=0 and covariance matrix P. The matrix A reflects the usual kinematics: $x_{t+1} = \Delta t x'_t + x_t$ and $x'_{t+1} = x'_t$ (analogous for y). The motion of the particle is therefore modelled by two elements: the velocity $v = (x', y')^T$ and diffusion due to the positional components of the noise $\boldsymbol{w}$. If $v = 0$, then then the particle has pure Brownian motion where the diffusion rate depends on the covariance matrix P. The

states of the particles are estimated by the Kalman filter with a Rauch-Tung-Striebel backwards smoothing filter [284]. The Kalman filter also estimates the state of the particle if it was not observed in a frame, e.g. due to blinking. This filter also outputs the covariance (or error) of the states and the covariance matrix (or error) of the state estimates across the length of its associated track. By pooling the instantaneous velocity and its covariance matrix for a particular particle in a particular frame for every possible posterior sample tracking solution in which it is included in a track, for each particle a mean instantaneous velocity $v = (\bar{x}', \bar{y}')^T$ and covariance matrix, Σ_v, can be obtained , can be obtained, fully exploiting Biggles' assessment of uncertainties. This is the breakthrough that allows the derivation of a robust frame-by-frame estimation of motion directionality.

If the null hypothesis is assumed to be that the true instantaneous velocity is zero (this is intended as the fact that a particle undergoing instantaneous diffusion has an equal probability at each time-step of moving in every direction)), it is reasonable to represent it as a multivariate Gaussian with zero mean and covariance equal to the estimated velocity covariance. The number of standard deviations *d* from the null hypothesis at which the estimated velocity measurement is positioned can therefore be calculated as:

$$d = \sqrt{v^T \Sigma_v^{-1} v}$$

Equation 2-2 – The directionality metric *d*

This metric is termed *directionality*. In the 1-dimensional case d would be equivalent to the velocity estimate divided by the error of that estimate. A *state* with a high directionality is considered to be inconsistent with the null hypothesis. It must be noted, however, that, conversely, non-directional motion cannot be identified with confidence.

3. Labelling HER1-3 in Basal and Active State: Synthesis and Characterisation of Fluorescent Probes for Single-Molecule Microscopy

3.1. Introduction

The aim of this chapter is to describe the synthesis and/or characterisation of small-molecule ligands for HER1 and HER3 in their basal and activated states, and for HER2, to be labelled with organic fluorescent dyes for Single-Molecule imaging techniques.

While it would have allowed unparalleled specificity of labelling, direct labelling of the HER family receptors with FPs or other fusion tags was discarded not only due to practical considerations on label size and the likelihood of crosslinking and steric hindrance artefacts, but also because the aim of the project is to study the system in conditions as physiological as possible, in a cell line that naturally expresses all four HER family receptors at low protein levels. Similarly, labelling of small peptidic binders with QDs was also discarded due to the possibility of crosslinking and the size of the label, notwithstanding its advantages in terms of brightness and photostability.

The principal aim of this phase of the project was to obtain 1:1 conjugated probes able to specifically label cells at nanomolar concentrations. The active-state probes should display robust activation of target receptors, and the basal-state, or neutral, probes should not stimulate receptor activity significantly above background.

To label **HER1 in its active state**, the most obvious choice is one of its native ligands, EGF, which is by far the best-characterised of the EGF-related peptides and has been used for most of the structural studies on HER1. As discussed before in **Chapter 1**, this ligand robustly activates EGFR within seconds of its administration and displays very high affinity, with two affinity constants of ~ 300 pM and ~2 nM [49]. The murine isoform of the EGF domain contains no lysine residues [285], which enables 1:1 labelling of its N- terminal α-amino group with N-reactive dyes such as NHS-ester or Succinimidyl Ester dyes.

To label **HER3 in its active state**, instead, NRG1β appears the most logical choice, due to its ability to induce phosphorylation of HER3 and elicit its downstream biological responses [88] and due to the fact that it is commercially available. NRG1β is the highest-affinity ligand for HER3, however it binds with comparative affinity also to HER4 [87]. A blocking anti-HER4 antibody is available [286] to block NRG1β binding to HER4 and downstream signalling, but it

could cross-link HER4, causing artefacts that could impact the function or dynamics of the other receptors in study.

As discussed before, **HER2** has no known soluble ligand, therefore, in order to track it without affecting its activation status, an artificial binder is needed, as is the case for **HER1** and **HER3** in their **basal states**.

Affibody molecules are small non-antibody high-affinity binders derived by random mutation from the scaffold of Protein A from *S. Aureus* [260]. Their small size and the possibility of specifically labelling them in a 1:1 ratio, thanks to their terminal single cysteine, which enables easy and specific maleimide labelling, make them ideal probes for Single-Molecule applications in which endogenous proteins are to be studied in their native environment.

High-affinity Affibodies directed against HER1 [287], HER2 [288–290], and HER3[268] have been already selected and those directed against HER1 and HER2 are commercially available. Anti-HER1 Affibody $(ZEGFR:955)_2$ competes with both EGF and Cetuximab, which indicates that its binding site might be on domain III. Cellular uptake is as slow as that of Cetuximab, occurring maximally between 4 and 8h from administration [291]. Anti-HER1 Affibody $(ZEGFR:955)_2$ does not induce HER1 phosphorylation [292]. The commercially available anti-HER1 Affibody is a close relative of ZEGFR:955, from which it differs by two non-conserved residues and three partially conservative substitutions (**Figure 3-1**) and is therefore expected to share many of its structural and signalling features. It must be noted that the commercial Anti-HER1 Affibody is a tandem dimer, with the same binder sequence repeated twice in order to improve binding avidity.

```
Abcam          GSSLQVDNKFNKEMWAAWEEIRNLPNLNGWQMTAFIASLVDDPSQSANLLAEAKKLNDAQ 60
Friedman       ------------------------------------------------------------


Abcam          APKVDNKFNKEMWAAWEEIRNLPNLNGWQMTAFIASLVDDPSQSANLLAEAKKLNDAQAP 120
Friedman       ---VDNKFNKELEKAYNEIRNLPNLNGWQMTAFIASLVDDPSQSANLLAEAKKLNDAQAP 57
                  ********:  *::****************************************

Abcam          KVDC 124
Friedman       K--- 58
               *
```

Figure 3-1 – ClustalW 2.1 [293] **alignment output for the protein sequences of the commercially available dimeric anti-HER1 Affibody (Abcam) and monomeric ZEGF:955 (Friedman).** Residues are colour-coded according to charge and hydrophobicity: pink = basic, blue= acidic, green= polar, red= hydrophobic. *= conserved residue, := partial conservation.

Like the Anti-HER1 Affibody, anti-HER3 Affibodies Z05416 and Z05417 compete with NRG1 for HER3 binding, and are able to block HER3 phosphorylation, downstream signalling and cell proliferation [294], a feature which makes them particularly attractive as basal probes. Finally, the anti-HER2 Affibody ZHER2:342 has been co-crystallized with the ECD of its target, showing binding to the bottom face of domain IV, well away from the binding sites of both Trastuzumab and Pertuzumab [295], an advantageous feature if analysis of the effects of therapeutic antibodies is required. ZHER2:342 Affibody is not commercially available, however its close structural relative ZHER2:477 [289] is supposed to share most of its structural features and is available in both bivalent and monovalent formulations.

Due to their high sensitivity, Single-Molecule techniques are particularly vulnerable to artefacts such as non-specific binding and background impurities, overcrowding or under-labelling, and to low signal-to-noise conditions. In order to characterise multiple parameters of a heterogeneous population of receptors on the cell membrane, the probes used need to be assessed for affinity, specificity of binding, and binding kinetics. Moreover, to investigate the system in both inactive and activated states, it is fundamental to verify that “neutral”, basal-state probes do not cause spurious activation of receptors, and to account for competition between different probes for the same receptor.

This chapter describes:

1) the characterisation of commercial probes such as the anti-HER1 Affibody from Abcam and anti-HER2 ZHER2:477 dimeric and monomeric Affibodies from Affibody Inc.;

2) the synthesis and characterisation of an anti-HER3 Affibody from a plasmid provided by Dr John Löfblom of Affibody Inc.;

3) the de novo cloning, expression, labelling and characterisation of an NRG1β-MCP fusion protein, compared to a conventionally labelled commercially available NRG1β protein.

3.2. Results

3.2.1. Part I: Labelling HER1 in its Basal State

Characterisation of an anti-HER1 Affibody to label HER1 in its Basal State

In order to label HER1 in its resting state, a commercial anti-HER1 Affibody from Abcam was selected. This is a small (14 kDa) probe displaying high affinity and is a close relative of the well-characterised ZEGF:955 Affibody probe. Among the commercially available options to label HER1, it seemed the most reasonable option. Alternative strategies, such as preparing antibody fragments from an anti-HER1 antibody targeting the HER1 ECD, were discarded due to their low yield and laboriousness and also because Ig-like proteins are more difficult to label specifically due to the presence of multiple cysteins in the Ig-fold.

Determination of probe specificity and fractional saturation by Single-Molecule microscopy and confocal microscopy

Results in this section have been published in Zanetti-Domingues *et al.* (2012) [1].

The specificity of anti-HER1 Affibody and therefore the extent of non-specific binding to the cells was assessed both by confocal and Single-Molecule microscopy. A431 cells, which overexpress HER1, were used for confocal experiments for higher intensity, and T47D cells, which express low levels of HER1, were used in Single-Molecule experiments to enable detection of individual spots. As shown in **Figure 3-2**, competing the labelled species with 100x unlabelled Affibody reduced the labelling to background levels, which should rule out non-specific interactions with the membrane. Single-Molecule microscopy data seem to indicate that the spot density rapidly plateaus at nanomolar concentrations, indicating high affinity-binding. A comparatively high level of spots in blank samples can be reasonably attributed to the presence of impurities in the glass or background spots which are more easily picked up as features by the localisation algorithm in absence of strong fluorescence signal.

Anti-HER1 antibody competes with EGF for binding to the receptor

Results in this section have been published in Zanetti-Domingues *et al.* (2012) [1].

The specificity of HER1 Affibody for the HER1 receptor was assessed by competing a labelled species (EGF or Affibody) with a 100x higher concentration of the other species. Cross-

competition, already demonstrated for ZEGFR:955 [291], a close sequence relative of the commercial Affibody used in our experiments, reduced the signal to background levels for both species (**Figure 3-2 C**). A431 cells were used for this experiment due to their high level of HER1 expression.

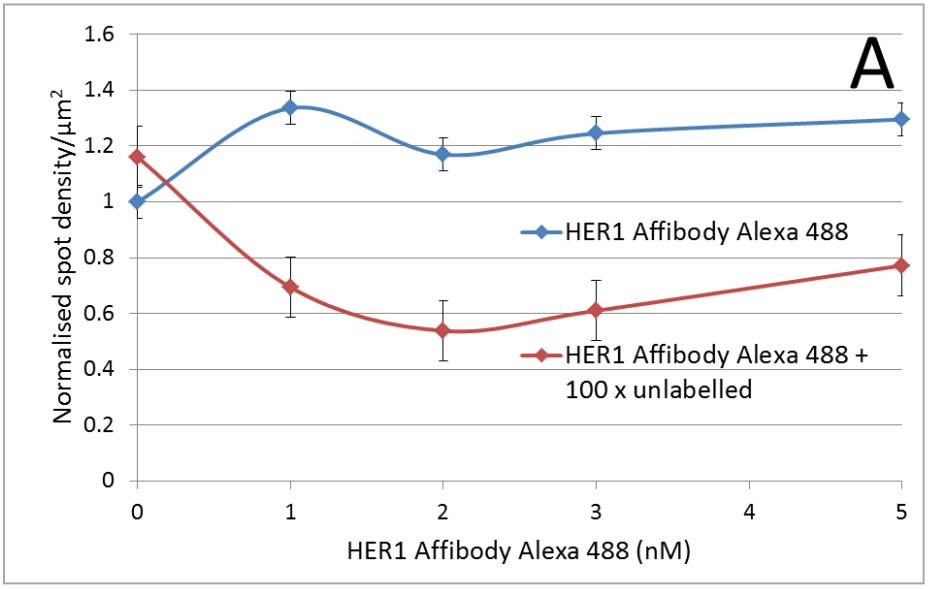
A
Normalised spot density/µm²
1.6
1.4
1.2
1
0.8
0.6
0.4
0.2
0
0
1
2
3
4
5
HER1 Affibody Alexa 488 (nM)
HER1 Affibody Alexa 488
HER1 Affibody Alexa 488 + 100 x unlabelled

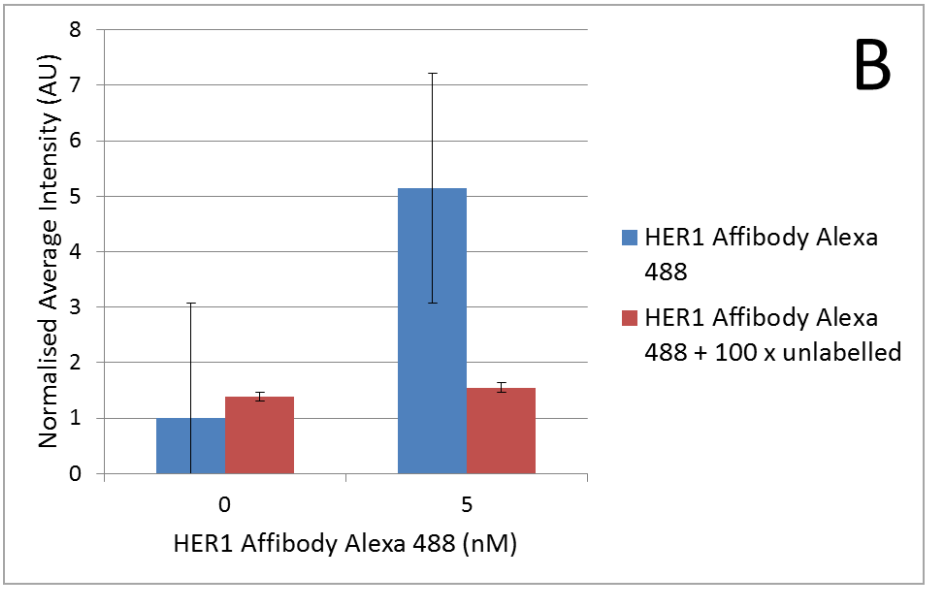
B
Normalised Average Intensity (AU)
8
7
6
5
4
3
2
1
0
0
5
HER1 Affibody Alexa 488 (nM)
HER1 Affibody Alexa 488
HER1 Affibody Alexa 488 + 100 x unlabelled

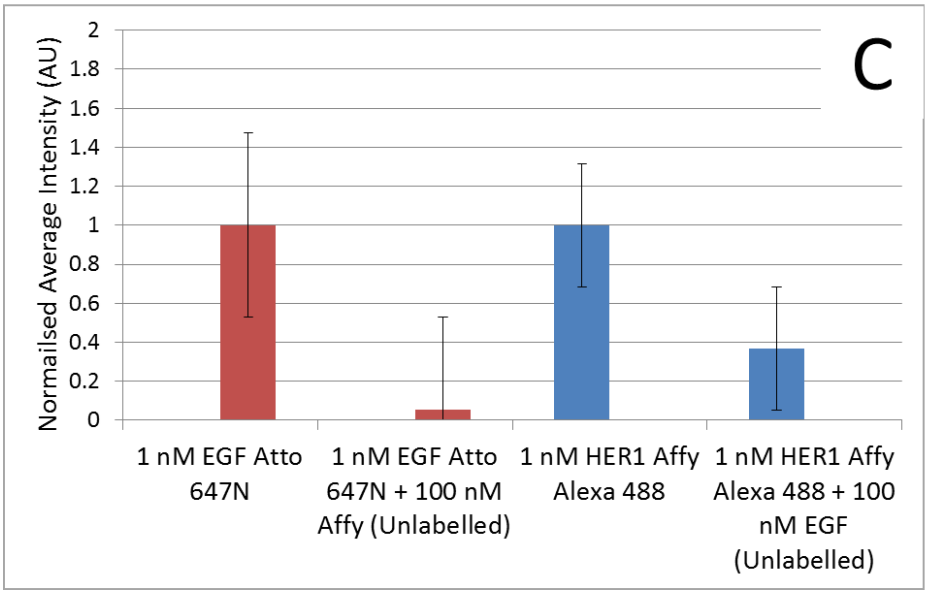
C
Normailsed Average Intensity (AU)
2
1.8
1.6
1.4
1.2
1
0.8
0.6
0.4
0.2
0
1 nM EGF Atto 647N
1 nM EGF Atto 647N + 100 nM Affy (Unlabelled)
1 nM HER1 Affy Alexa 488
1 nM HER1 Affy Alexa 488 + 100 nM EGF (Unlabelled)

Figure 3-2 (previous page) - Determination of level of non-specific binding of anti-HER1 Affibody to cells. **A)** Spot density/μm^2 plot for HER1 Affibody Alexa488 on T47D cells in presence (red) or absence (blue) of 100x excess unlabelled HER1 Affibody as determined by fluorescent Single-Molecule detection. Values were normalised against the unlabelled (0 nM) spot density value for the no-competition (blue) series. **B)** Average intensity histogram of HER1 Affibody Alexa488 on A431 cells in presence (red) or absence (blue) of 100x excess unlabelled HER1 Affibody as determined by confocal imaging. Values were normalised against the unlabelled (0 nM) intensity value of the no-competition (blue) series **C)** Average intensity histogram of HER1 Affibody Alexa488 (blue) and EGF Atto 647N (red) on A431 cells in presence or absence of 100x excess unlabelled competitor. Values were normalised against the no-competition (1 nM) value for each series.

The effect of anti-HER1 Affibody on the activation of HER1 in cells

Part of the results in this section have been published in Needham *et al.* (2013) [95].

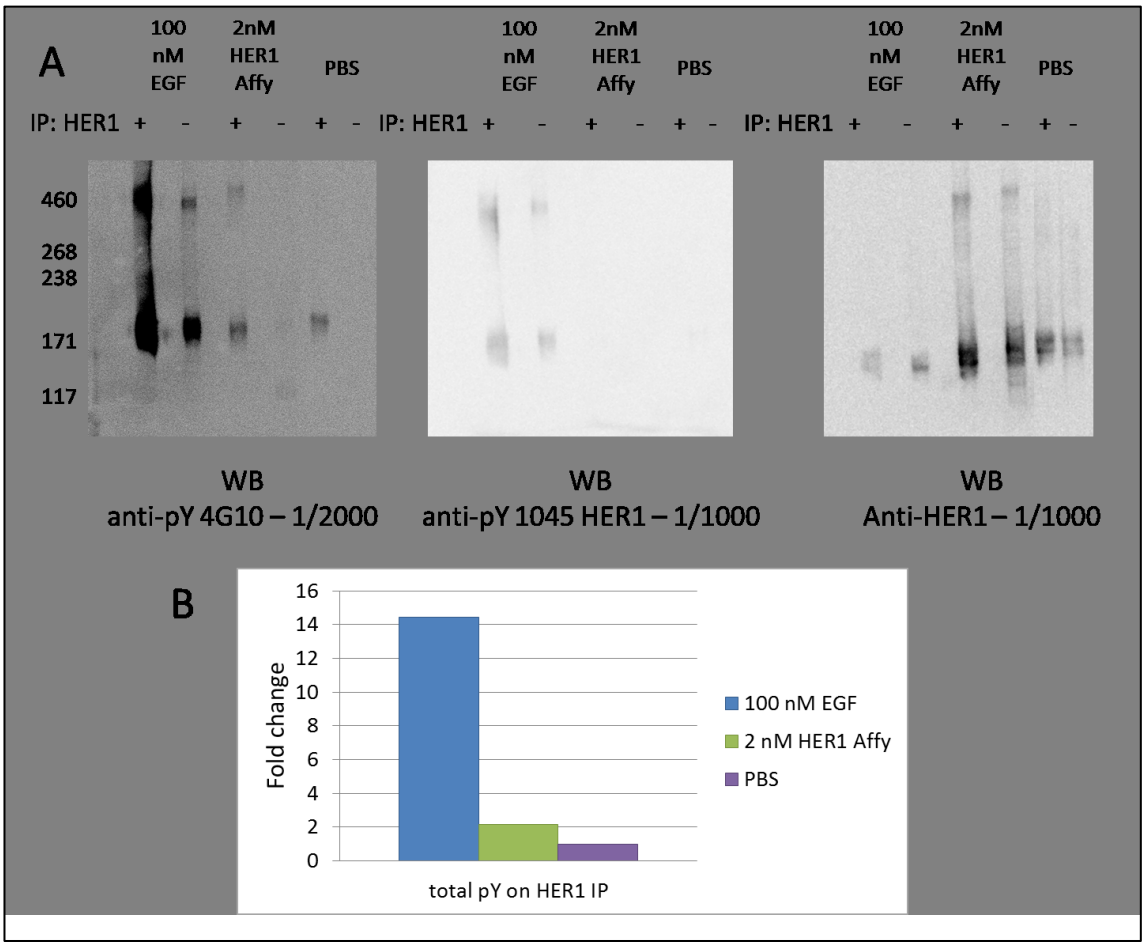

Figure 3-3 – The effects of anti-HER1 Affibody molecule on the overexpressed endogenous wt receptor on A431 cells. A) Western blots of A431 cell anti-HER1immunoprecipitates (+) and whole cell lysates (-) from unstimulated cells (PBS) and cells stimulated with either 100 nM EGF A488 or 2 nM anti-HER1 Affibody A488. Lysates were prepared after treatment with BS3 to crosslink membrane proteins. Blots were probed (left to right) for non-specific tyrosine phosphorylation of proteins (Anti-pY4G10), tyrosine phosphorylation of HER1 (Anti-pY1045 HER1), and presence of HER1 (Anti-HER1). **B)** Results of anti-HER1 IP anti-pY 4G10 densitometry. Data was normalized against the total HER1 and relative quantity was expressed as a fold change compared to the unstimulated control. Densitometry was performed on the lower protein band (~ 171 kDa), due to lack of control high-Mw bands in the PBS lane.

HER1 activation by anti-HER1 Affibody binding was assessed by Western Blot on A431 cells and compared to EGF. Dimerization was assessed by treating cells with BS3 crosslinking agent. Bands which might correspond to dimers are present in the immunoprecipitated positive control sample probed for anti-pY 4G10 and probed for HER1 pY1045, but not in the lanes

corresponding to anti-HER1 Affibody. Anti-HER1 Affibody was not found to activate the receptor compared with PBS control at the concentrations used in our experiments, as demonstrated by densitometry analysis (**Figure 3-3 B**). As an Alexa 488 EGF conjugate was used as a positive control, the data also shows that labelled EGF is able to induced HER1 phosphorylation in cells.

As A431 cells express a great excess of HER1 receptor and display baseline receptor phosphorylation due to autocrine secretion of TGF-α, Western Blot experiments were also performed on Cho cells stably transfected with wt HER1 under a Tet-On promoter. Results are shown in **Figure 3-4**.

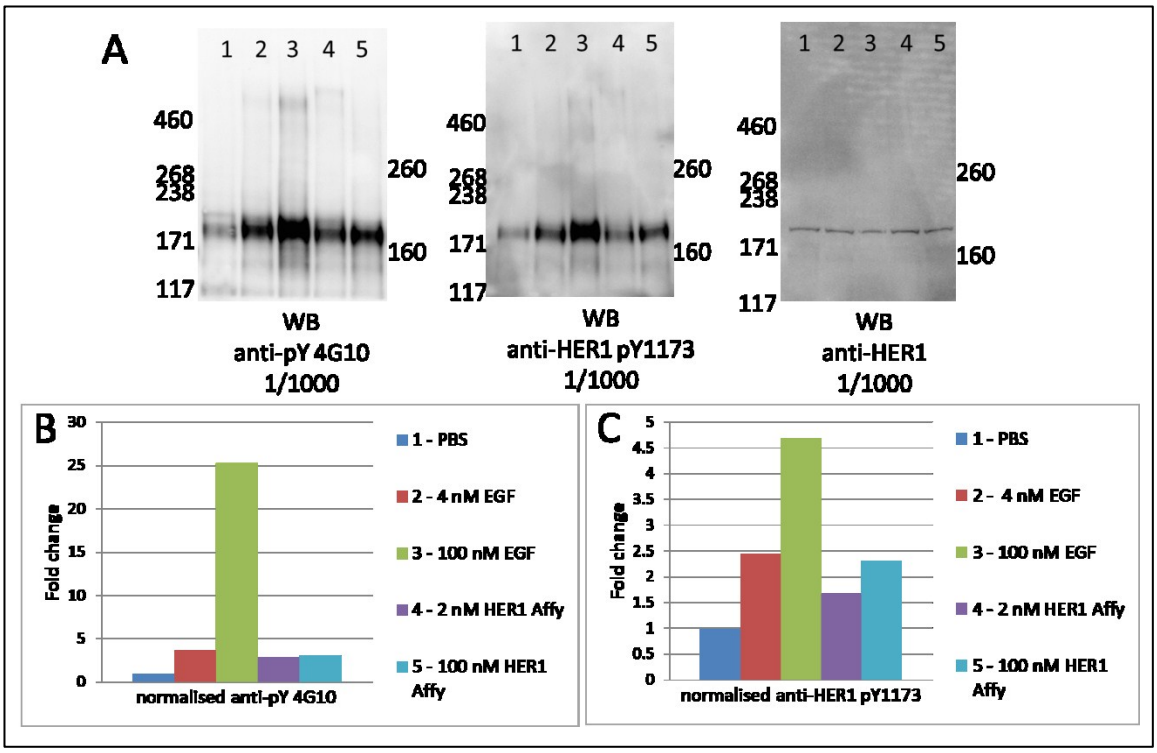

Figure 3-4 - The effects of anti-HER1 Affibody molecule on the wt receptor expressed on Cho cells under an inducible Tet-On promoter. A) Western blots of Cho+wtEGFR cells unstimulated (mock-treatment with PBS - 1) and cells stimulated with: 4 nM EGF A488 (2); 100 nm EGF A488 (3); 2 nM anti-HER1 Affibody A488 (4) or 100 nM anti-HER1 Affibody A488 (5). Lysates were prepared after treatment with BS3 to crosslink membrane proteins. Blots were probed (left to right) for non-specific tyrosine phosphorylation of proteins (anti-pY4G10), tyrosine phosphorylation of HER1 (anti-pY1173 HER1), and presence of HER1 (anti-HER1).

B) Results of anti-pY 4G10 densitometry. Data was normalized against the total HER1 and relative quantity was expressed as a fold change compared to the unstimulated control. Densitometry was performed on the lower protein band (~ 171 kDa), due to lack of control high-Mw bands in the PBS lane.

C) Results of anti-pY1173 HER1 densitometry. Data were normalized against the total HER1 and relative quantity was expressed as a fold change compared to the unstimulated control. Densitometry was performed on the lower protein band (~ 171 kDa), due to lack of control high-Mw bands in the PBS lane.

This second set of experiments show again that labelled EGF is able to elicit phosphorylation of HER1 receptors. Treatment with 4 nM EGF at 4°C yields submaximal activation, both when assessing the phosphorylation of a single tyrosine residue and when assessing the global phosphorylation status of HER1.

Treatment with 2 nM anti-HER1 Affibody results in a signal that is about 2x that of the control in both cases, a result that is comparable to those obtained in A431 cells. The submaximal signal elicited by 4

nM EGF is slightly higher, at 3.5x times the signal of the negative control. Interestingly, treatment with high doses (100 nM) of Affibody does not increase the global phosphorylation of HER1 above the levels obtained with 2 nM of the same reagent, even if it increases the specific phosphorylation of Y1173. This result, however, was not considered to be alarming, as this saturating dose was not intended for use in Single-Particle Tracking experiments.

3.2.2. Part II: Labelling of HER1 in its Activated State

As stated in the introduction to this chapter, in order to label HER1 in its activated state, commercially available murine EGF (Peprotech), was labelled on its N-terminus with NHs ester functionalised commercially available dyes. Custom 1:1 conjugations were performed by Cambridge Research Biochemicals.

3.2.3. Part III: Labelling HER2

Characterisation of anti-HER2 zHER2:477 monomeric and dimeric Affibodies

As HER2 does not have a natural, soluble ligand, in order to label HER2 without artificially activating it, anti-HER2 Affibody ZHER2:477 [289] was tested as a probe due to its picomolar affinity for the receptor and small size (~7 kDa for the monomeric form).
An in-house labelled dimeric ZHER2:477 Affibody-Atto647N conjugate was assessed for binding specificity and affinity by incubation on SkBr3 cells, which express on average 2×10^6 receptors/cell, in presence or absence of 100x excess unlabelled Affibody compared to the concentration of labelled species, followed by confocal imaging (**Figure 3-5**). Binding appeared to be specific and plateaued well after 10 nM, which might be a result of the high level of receptor overexpression, as probe affinity has been reported as ~ 22 pM in previous publications [289]. Nonspecific binding in presence of 100x excess probe was found to be in the same range as background autofluorescence (data not shown), further confirming the specificity of the probe. The 100 nM + 100x excess unlabelled HER2 Affibody datapoint was omitted to conserve material.

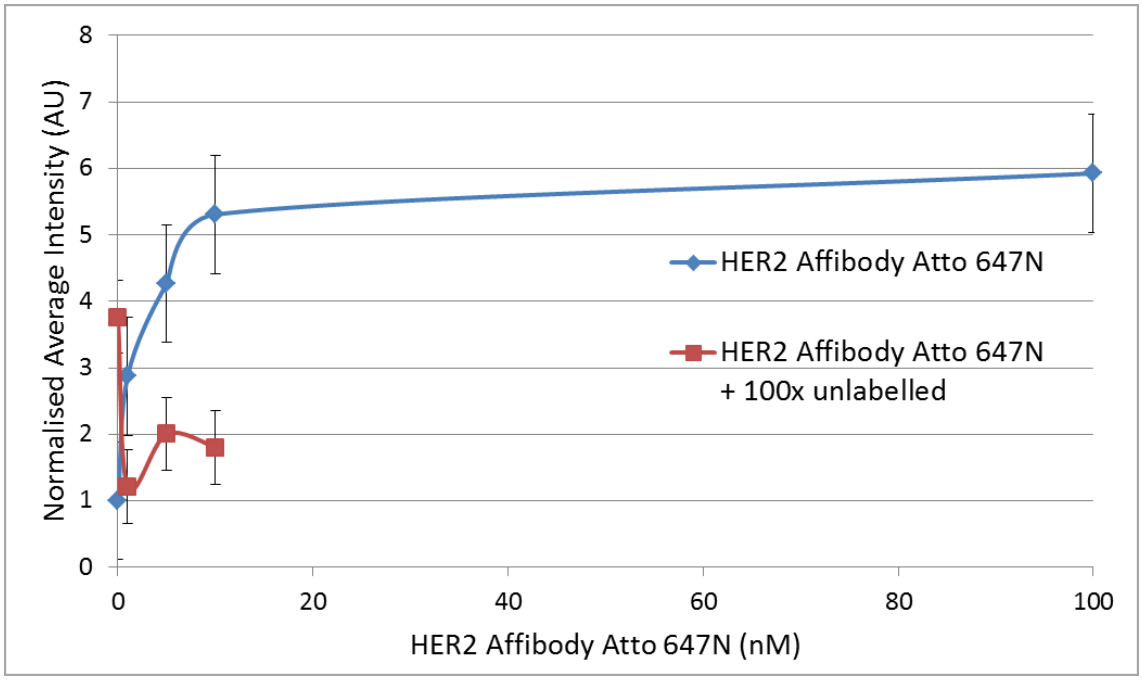

Figure 3-5 - Determination of level of non-specific binding of dimeric anti-HER2 Affibody to cells. Average intensity plot of HER2 Affibody Atto 647N on SkBr3 cells in presence (red) or absence (blue) of 100x excess unlabelled HER2 Affibody as determined by confocal imaging. Intensity values were normalised against the unlabelled (0 nM) datapoint of the blue series. Data are plotted as average +SEM.

HER2 Affibody binding was also tested on T47D cells (data not shown) and was shown to be specific, as the labelled probe could be displaced by an excess of unlabelled competitor. The acquisition of analogous data in a Single-Molecule setting was prevented by the propensity of the probe to stick non-specifically to cell-culture surfaces, which made spot density measurements unreliable. This problem, however, was not relevant to confocal imaging as a plane passing through the middle of the cell, and therefore well away from the glass, was acquired.

The literature is ambiguous on receptor activation by anti-HER2 Affibody ZHER2:477. Tests to evaluate the effect of commercially available ZHER2:477 dimeric and monomeric formulations were performed by a partner lab in the context of a large collaborative project and of the sharing of probes and standard operating procedures between the partner labs. The results (shown in **Supplementary Figure S1**) show that dimeric anti-HER2 Affibody ZHER2:477 was able to robustly activate HER2 and to trans-activate both HER3 and HER4 receptors, a property which would render the probe useless to report on the receptor in a neutral way (Dr Michela Perani, personal communication). The dimeric form of the Affibody is obtained by expressing the binding sequence twice in tandem, separated by a short linker sequence, to improve the

avidity of the complex and its binding kinetics [288], however the monomeric isoform is also commercially available. Contrary to its dimeric isoform, monomeric ZHER2:477, was not able to activate HER2 above background levels (Dr Michela Perani, personal communication). Considering that high-affinity anti-HER2 Affibodies (lilac) bind to the underside of Domain III of the extracellular domain of HER2 (yellow) at a site that is not part of either the ligand-binding interface or the back-to back dimerization interface in HER family receptors (arrows - see **Figure 3-6**), it was hypothesised that the robust activation of HER2 seen with the dimeric isoform would come from dimerization of adjacent receptors, caused by cross-linking through the two binding sites on the probe.

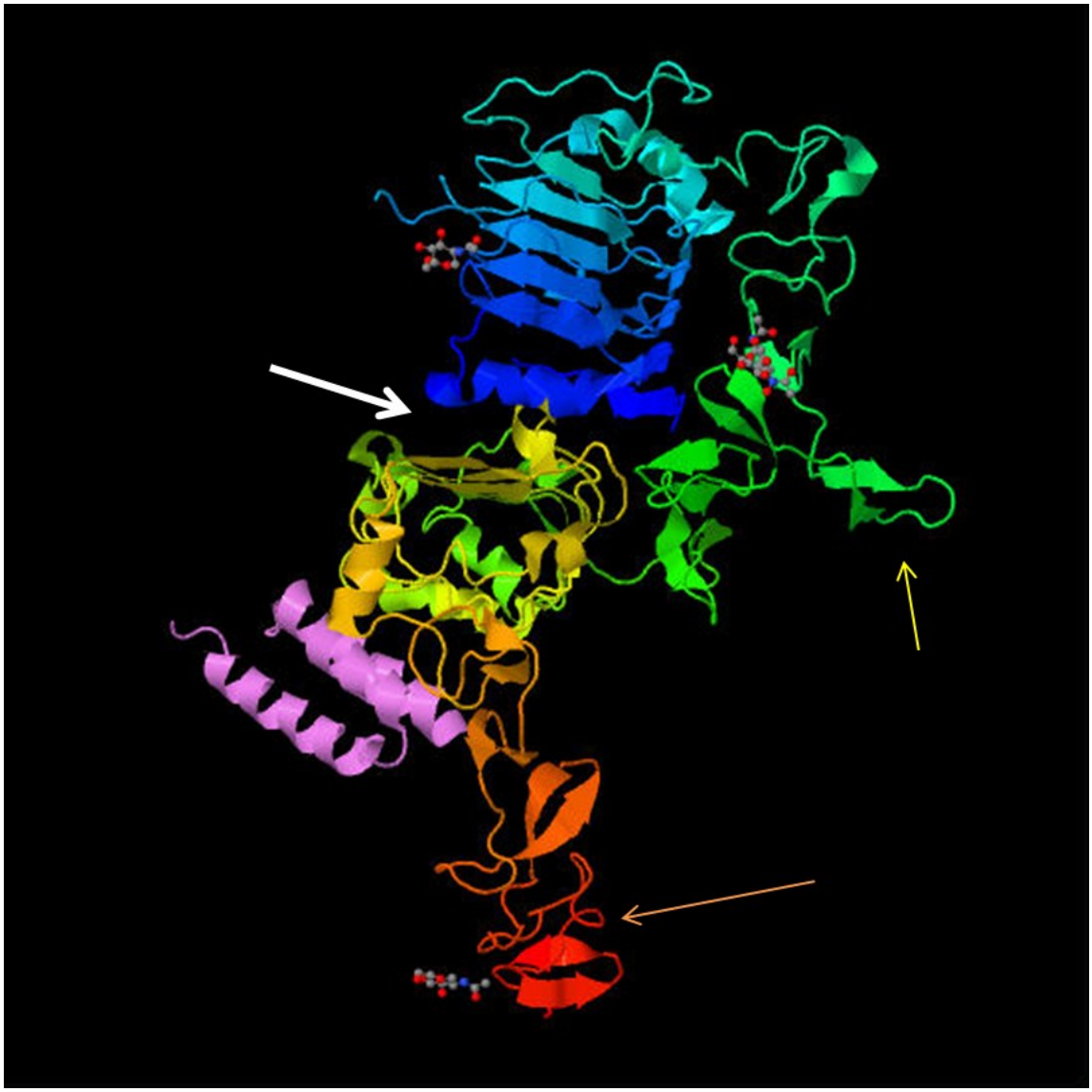

Figure 3-6 – Side view of anti-HER2 Affibody ZHER2:342 in complex with HER2 extracellular domain. Lilac: anti-HER2 Affibody; green-yellow = HER2 domain III; orange-red = HER2 domain IV. The putative ligand-binding site is indicated by the bold white arrow. Sites involved in back-to-back dimerization are

highlighted by a yellow arrow (dimerization arm on domain II) and an orange arrow (additional dimerization contacts on domain IV).

Cross-linking experiments with BS3, a cross-linking reagent which is unable to cross the plasma membrane, however, seemed to disprove the hypothesis, as dimer populations were quite similar in all test samples (Dr Michela Perani – personal communication, see **Supplementary Figure S1**).

3.2.4. Part IV: Labelling HER3 in its basal state

Synthesis and characterisation of an anti-HER3 Affibody

In order to label HER3 in its basal state, we selected a recently published [268] Affibody probe. Anti- HER3 Affibody plasmid was obtained from Affibody Inc. under a Material Transfer Agreement and was initially transformed into Omnimax II cells in order to amplify it for further experiments. A scheme of the protein production strategy employed is detailed in **Figure 3-7**.

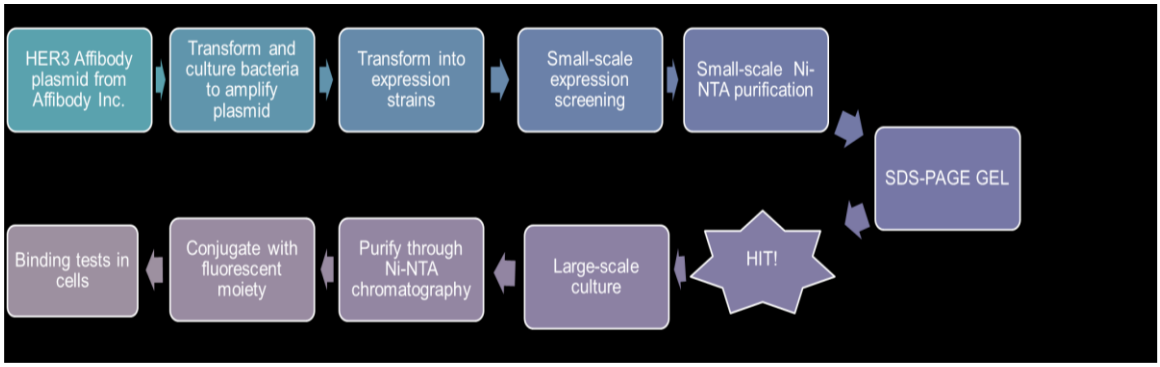

Figure 3-7 - Experimental design for anti-HER3 Affibody production.

Expression of anti-HER3 Affibody in *E.Coli* strains

A small-scale expression screening (SSES) was performed by transforming an equal amount of the plasmid in *E.Coli* expression strains Rosetta (two different stocks, identified as batch #2 and #3), C41 (DE3), C43, B834 (two different stocks identified as batch #1 and #2) and BL21DE, comparing expression levels across strains and between auto-induction media and traditional IPTG induction. Autoinduction media (see for example [296]) are formulations that include a mix of carbon sources that allows first a rapid growth to high densities and then induction of protein expression from *lac* operons thanks to the presence of lactose in the carbon source mix. This allows a seamless transition from the growth phase to the induction phase just by

lowering the growth temperature. This feature is very convenient for expression screens such as the one described in this section.

Positive hits, meaning good levels of HER3 Affibody expression without formation of high-MW aggregates were found in B834 and BL21DE (**Figure 3-8 A and B**) strains and "traditional" IPTG induction was found to be more effective than auto-induction.

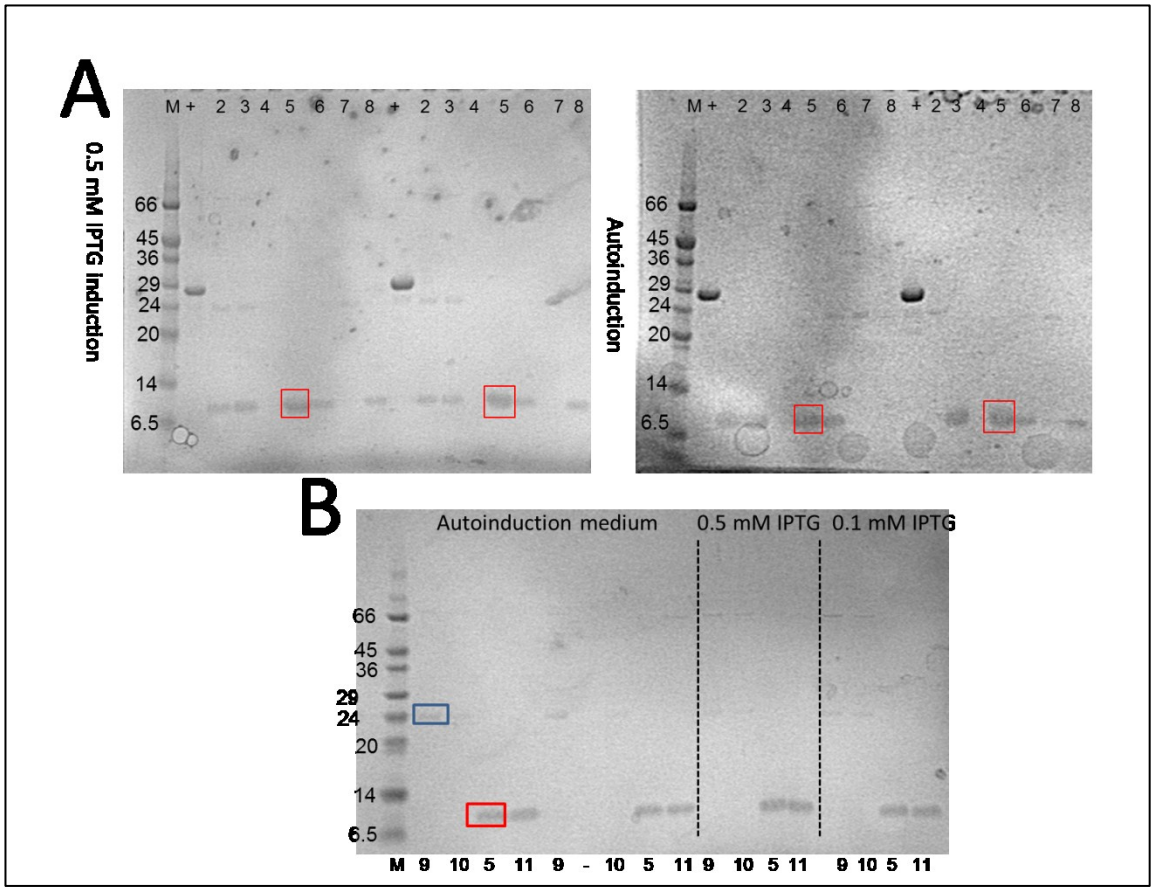

Figure 3-8 - Small-Scale Expression Screening of anti-HER3 Affibody. A) + = GFP expression control; 2 = Rosetta batch #2; 3 = Rosetta batch #3; 4 = B834 batch #1; 5 = B834 batch #2; 6 = C41 (DE3) batch #1; 7 = C41 (DE3) batch #2; 8 = C43. Experiments were performed in duplicate and run on the same gel. **B)** 9 and 10 = NRG1β-MCP expression in B834 and BL21DE; 5= 5 = B834 batch #2; 11= BL21DE. Both gels were stained with Coomassie staining. M = Sigma Low Mw Marker. Boxed (red): protein bands corresponding to HER3 Affibody in best hits (~ 7 kDa). Boxed (blue): protein band corresponding to NRG1β-MCP in the best hit (expected Mw ~ 18 kDa)

B834 strain was selected to perform large-scale expression and purification on Ni-NTA resins followed by gel chromatography fractionation. The procedure was successful, with protein recovery from several chromatography fractions without significant degradation or aggregation (**Figure 3-9**). Final protein yields after fraction pooling and concentration down to

2ml ranged from 1.5 mg/ml to 9.35 mg/ml in three separate protein production runs, with a maximum yield of 18 mg of protein from 2 L of *E.Coli* culture.

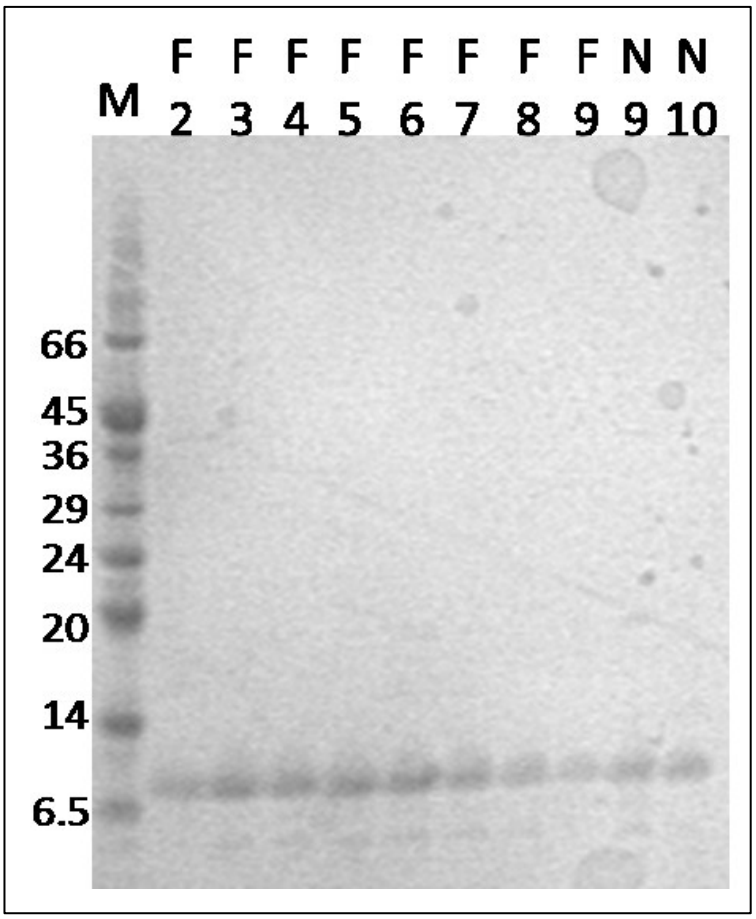

Figure 3-9 – Large Scale Expression of anti-HER3 Affibody and NRG1β-MCP. M= Sigma Low Mw marker. F2-F9 = large-scale Ni-NTA purification fractions for anti-HER3 Affibody, displaying the correct Mw (~ 7 kDa – boxed in red). N9-N10 = large-scale Ni-NTA purification fractions for NRG1β-MCP. Lower than expected Mw bands (ca. 7 kDa v. ca. 18 kDa) in fractions N9 and N10 are indicative of the presence of partial degradation products.

Determination of probe specificity and fractional saturation by Single-Molecule microscopy

An in-house labelled anti-HER3 Affibody Alexa 488 conjugate was assessed for binding specificity and affinity by incubation on T47D cells, which should express ~ 30 x 10^3 receptors/cell, in the presence or absence of 100x unlabelled anti-HER3 Affibody, followed by confocal imaging (**Figure 3-10**).

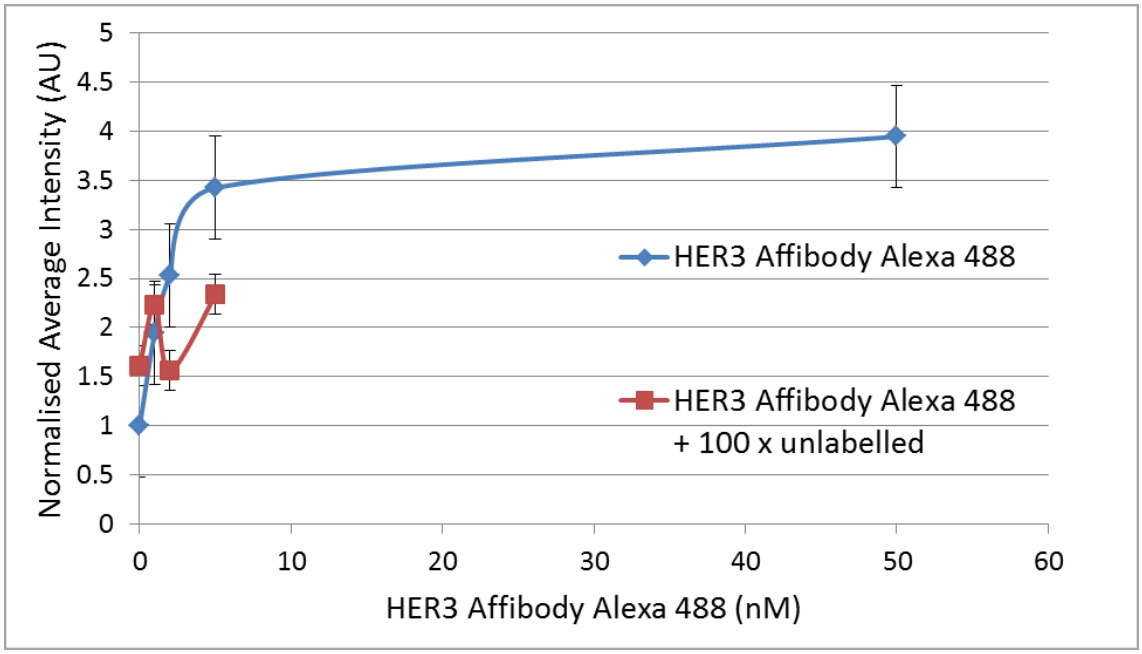

Figure 3-10 - Determination of level of non-specific binding of anti-HER3 Affibody to cells. Average intensity plot of anti-HER3 Affibody Alexa 488 on T47D cells in presence (red) or absence (blue) of 100x excess unlabelled HER3 Affibody as determined by confocal imaging.

Binding appeared specific and plateaued after 5 nM, a value which seems to be in good accordance with the published affinity of 3.0 nM [268].

In the context of the same probe and SOP-exchange program discussed in the HER2 section, the characterisation of the effects of the binding of anti-HER3 Affibody on receptor activation were performed by a partner lab. Anti-HER3 Affibody was demonstrated not to activate HER3 above background levels and does not cross-activate HER4 or trans-activate HER2 (Dr Michela Perani, personal communication). These results are in good accordance with data recently published by the manufacturer, which show that anti-HER3 Affibody is a non-activating probe for HER3 [294].

3.2.5. Part V: Labelling HER3 in its Activated State

Neuregulin (NRG) 1β is an EGF-like ligand that activates both HER3 and HER4 receptors. Among the possible HER3 ligands, NRG1β displays the highest affinity (K_d ca. 5 nM)[87] and is the best characterised, so it seemed the most logical choice in picking an active-state ligand for HER3, especially since there are no well characterised exclusive natural ligands for HER3.
The 9 kDa active chain is produced via proteolytic processing of a 71 kDa transmembrane precursor by metalloproteases such as ADAM17 and ADAM19 [44,81]. Its structure is roughly similar to that of EGF and its sequence (Uniprot Q02297 [aa 20-241]) contains multiple cysteine and lysine residues. Due to this, 1:1 labelling of NRG1β is unfeasible with maleimide dyes, out of concerns for the correct folding of the protein, and quite difficult to obtain with NHS ester or succynimidyl ester dyes, due to the presence of multiple reactive residues.
Two alternative strategies for labelling NRG1β were investigated: the main objective was to synthesise a tandem protein containing the EGF-like domain of NRG1β and a labelling tag, the ACP protein, in order to be able to enzymatically label the construct with fluorescently tagged CoA derivatives in a strict 1:1 ratio. This option would have allowed great flexibility and specificity of labelling, but required multiple steps of cloning and optimisation and raised concerns about the final activity of the construct, as steric clashes between the two proteins cloned in tandem could have prevented labelling, or binding, or proper receptor activation. As a backup, a second, quicker and less challenging labelling strategy was considered, that of employing a commercially available protein (produced by Peprotech) and traditional N-labelling techniques. While the labelling obtained could have been less precise and specific, this technique was more likely to produce active proteins.

Synthesis and characterisation of NRG1β-derivatives

A scheme of the strategy employed for the cloning of NRG1β-ACP is detailed in **Figure 3-11**.

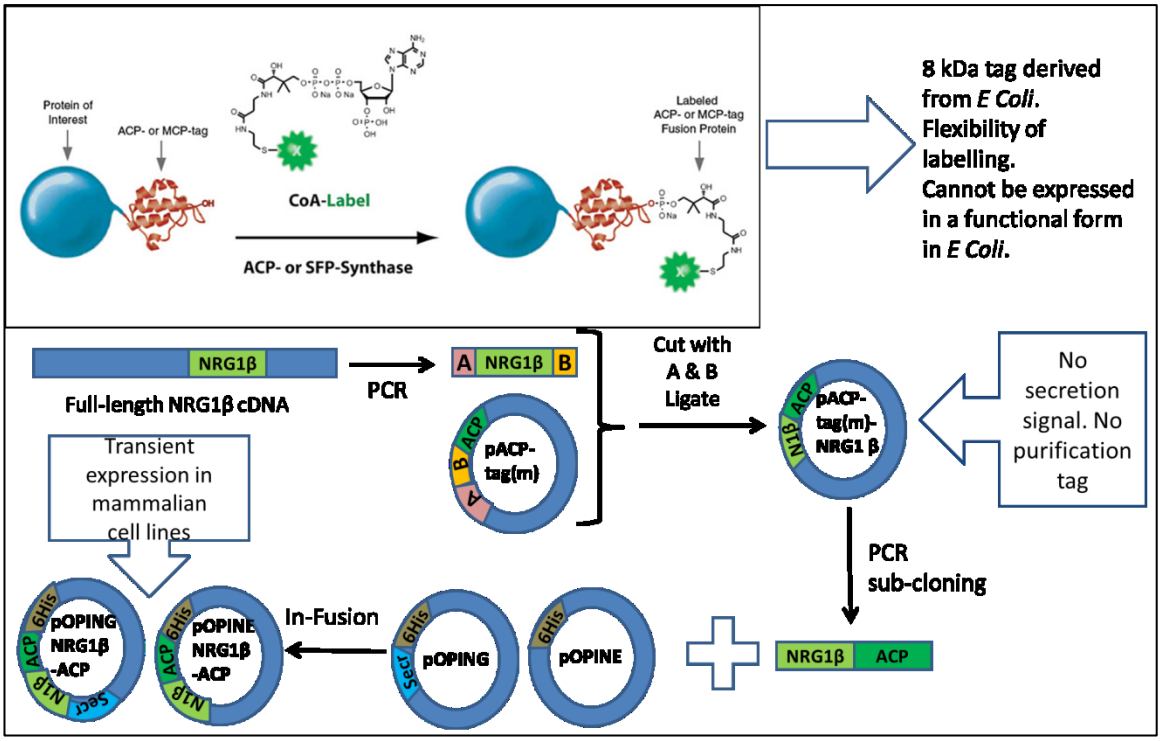

Figure 3-11 – Experimental plan for NRG1β-ACP cloning and expression. The ACP protein schematic in the insert was adapted from the NEB website.

Cloning NRG1β EGF-like domain into pACP-tag(m) vector and then into shuttle expression vectors pOPINE and pOPING

NRG1β EGF-like domain was amplified from full-length cDNA using restriction site- (Sac I and Hind III) tagged primers. (**Figure 3-12 A**) A hot-start protocol was tested alongside a standard PCR protocol, in order to maximise specificity, however the standard protocol appeared to grant a higher amplicon yield.

The purified amplicon was ligated at 3:1, 5:1 or 7:1 ratio into a pACP-tag(m) vector cut with the same (SacI and Hind III) restriction enzymes. Ligation products were amplified in *E.Coli* and 12 colonies from different plates were subject to a diagnostic digest with XmnI to ascertain the presence of the insert. Unligated vector product was expected to be a single fragment of 5088 bp (single cut) , while ligated vector products was expected to yield two fragments of 1243bp (lower, fainter bands) +4019 bp (higher, brighter bands), respectively. Of the 7 colonies containing a correctly ligated plasmid (**Figure 3-12 B**), clone #8 was chosen for sub-cloning in shuttle expression vectors pOPINE and pOPING [269] using In-Fusion technology, which employs a proprietary enzyme derived from the Vaccinia Virus DNA polymerase to fuse a fragment of interest into a linearized vector, provided that the two fragments share 15bp

homology at the ends. pOPINE contains a C-terminal 6-his tag, while pOPING contains an N-terminal eukaryotic secretion leader sequence, to allow release on the protein of interest in the conditioned medium of mammalian cell transfectants, and a C-terminal 6His tag. Both vectors contain a double set of prokaryotic and eukaryotic regulatory sequences and can be used to express target proteins either in *E.Coli* strains or in mammalian cells.

Sub-cloning of the NRG1β-ACP region from the parental vector was performed with the same forward oligo and different reverse oligos for insertion in the two different vectors. Both amplicons were obtained with good yield (**Figure 3-12 C**). In-Fusion reaction was performed on linearized vectors and purification of recombinant vectors after bacterial amplification was successful with yields up to 200ng/µl.

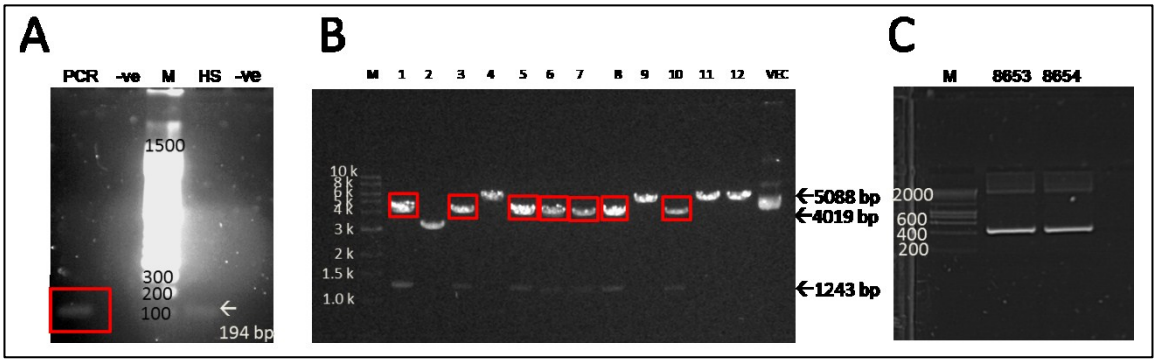

Figure 3-12 – NRG1β-ACP two-step cloning into pOPINE and pOPING vectors. A) Amplification of NRG1β EGF-like domain from full-length cDNA. M = Promega 100 bp Step Ladder (1 µl); PCR = standard protocol; HS = hot-start protocol. Boxed: target amplicon (expected Mw 194 bp). **B)** Diagnostic digestion of NRG1β EGF-like domain ligation into pACP-tag(m) vector. 1-12= colonies; VEC = uncut vector; M = NEB TriDye 1 kb Ladder (10 µl). Boxed: digestion products from correctly ligated vectors. **C)** PCR Amplification of NRG1β-ACP from pACP-tag(m) vector for insertion in pOPINE (8653) and pOPING (8654) vectors. M = Bioline Hyperladder 1kb (8 µl).

Expression of NRG1β-ACP in an eukaryotic cell line

The ACP protein employed in this experiment is derived from *E.Coli*, therefore attempting the expression of NRG1β-ACP constructs in this system would result in production of a protein that cannot be labelled in vitro, due to site occupancy by endogenous, unlabelled CoA from the bacterial host. It has been therefore decided to attempt transient expression of the constructs in eukaryotic cells. Both pOPINE and pOPING constructs were transiently transfected into HEK293T cells and expression was assayed by anti-6His Western Blot in lysates and supernatants 48h after transfection. The product of the pOPINE vector, which does not contain any secretion signal, was expected to be found in the lysate, while the product of the pOPING

vector, which contains a canonical mammalian secretion signal, was expected to be found primarily in the supernatant.

Expression, however, was poor and limited to the pOPING construct (**Figure 3-13**). The product however, was found in the lysate and not in the supernatant, which could indicate aggregation of non-functional protein. Repeat experiments have shown this expression to be poorly reproducible and expression levels were deemed too low for scale-up and mass-purification (data not shown).

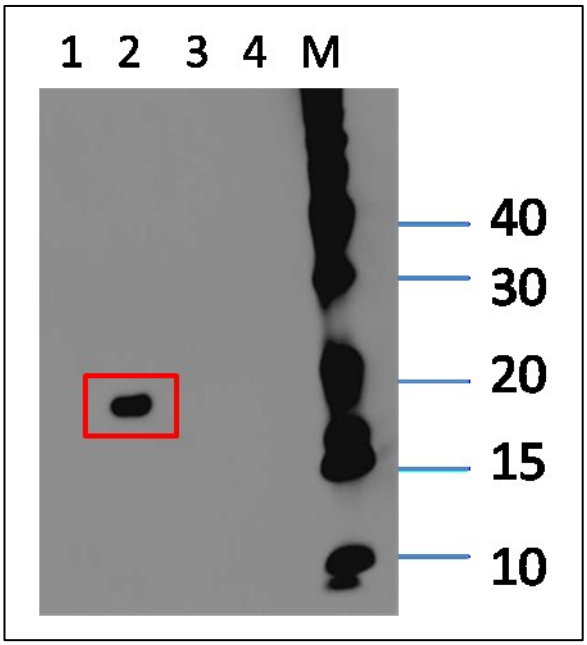

Figure 3-13 – Western Blot of transient expression of NRG1β-ACP constructs in HEK293T. 1 = pOPING construct, supernatant; 2 = pOPING construct, lysate; pOPINE construct, supernatant

Site-directed mutagenesis of NRG1β-ACP in NRG1b-MCP

Due to the failure of the mammalian expression experiments, an alternative strategy for the expression of tagged NRG1β constructs was developed (detailed in **Figure 3-14**). Modified Carrier Protein (MCP) is a derivate of ACP protein, which differs from the parental sequence by just two amino acids (D36T and D39G). This prevents the protein from being conjugated with CoA by *E. Coli*'s endogenous ACP synthase, and allows only conjugation by cognate enzyme SPF synthase from *B. Subtilis*. This would render large-scale expression feasible and simplify experimental procedures.

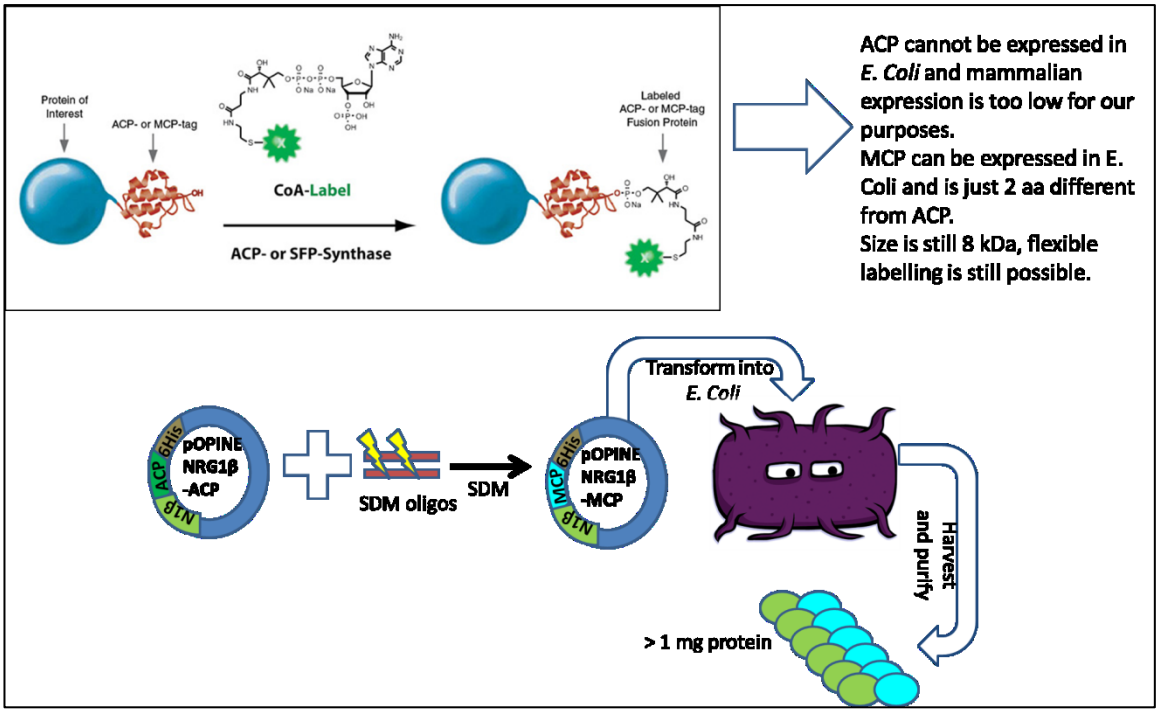

Figure 3-14 – Experimental plan for the production of NRG1β-MCP in *E. Coli*.

Mutagenesis was performed with the commercial Quicxchange II kit from Agilent, using a single oligonucleotide for both nucleotide changes. Ten bacterial colonies were amplified and extracted, of which three yielded DNA of sufficient quality and concentration for sequencing. Two out of three colonies contained the desired mutations and colony #7 was selected for further work.

NRG1β-MCP expression in *E.Coli* strains

A Small Scale Expression Screening was initially set up for NRG1β-MCP testing strains B834 and BL21DE with auto-induction medium and IPTG induction. B834 expression with auto-induction medium was deemed the best hit (**Figure 3-8**, blue box), notwithstanding the position of the protein band at a higher than the expected Mw. Large-scale expression was attempted, but no intact protein was recovered in the fractions at the expected Mw (**Figure 3-9**), while aggregates of >100 kDa were found (data not shown). Expression was attempted again in second-best hit BL21DE3 under IPTG induction, to better control the timing and duration of expression. Small-scale purification of an aliquot of culture was successful at least in one of several identical batches of culture (**Figure 3-15 A –** only one of the failed batches is shown), yielding protein of the correct molecular weight, however large-scale purification, both by Ni-affinity chromatography, and in bulk resin followed by chromatographic separation by gel filtration, failed (**Figure 3-15 B and C**), probably due to aggregation of the protein.

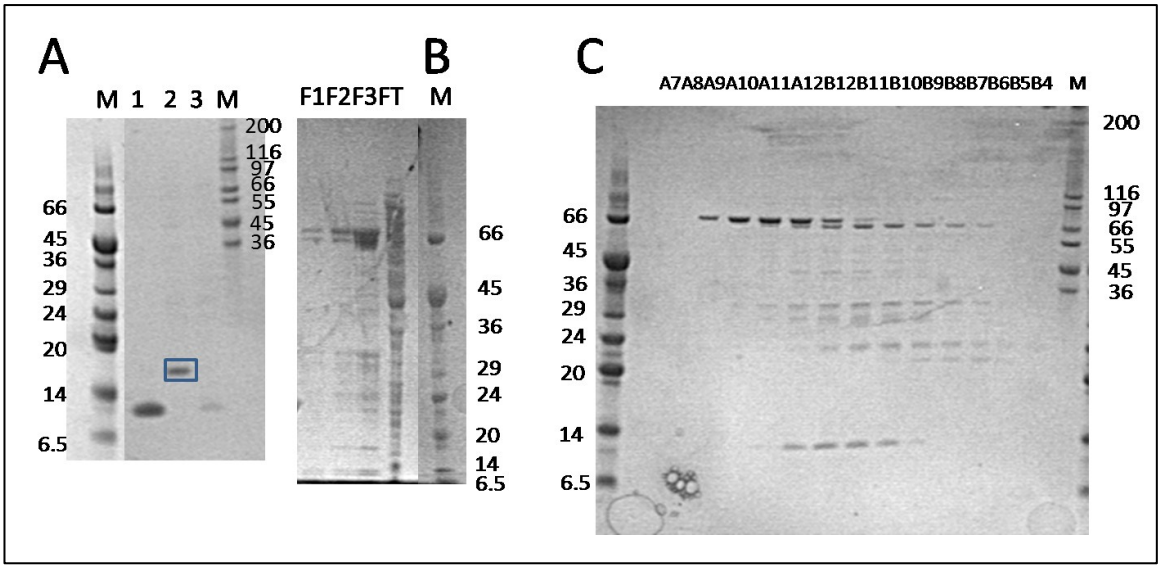

Figure 3-15 – NRG1β-MCP large-scale expression in *E.Coli* strain BL21DE3. A) Small-scale purification of aliquots from large-scale culture. 1= HER3 Affibody; 2= NRG1β-MCP batch #1; 3= NRG1β-MCP batch #2. Boxed: protein band with the correct Mw. **B)** Batch purification of NRG1β-MCP with Ni Sepharose6 fast flow resin, aliquots from fractions 1-3 (F1-F3) and flow-through. Faint protein bands of the correct molecular weight are visible, but overwhelmed by aggregation/degradation. **C)** Column fractionation of batch-purified protein, fractions A7-B4. Faint protein bands of the correct Mw are present, but aggregates are the majority.

Another Small-Scale Expression Screening was attempted, using strains C41, Rosetta and B834, with auto-induction medium or IPTG induction. Protein was successfully extracted with the small-scale extraction protocol (**Figure 3-16**). While small amounts of degraded and aggregated protein are visible, they are much reduced and IPTG induction (0.5 mM for 24 h) granted the best results. Protein yields of up to 0.3 mg/ml from 3 ml of culture were obtained, enough for small-scale enzymatic labelling with SFP synthase. At the same time, the introduction in the sequence ofNRG1β of mutations aimed at increasing its affinity for HER3 and decreasing its affinity for HER4, such as those described by Jones *et al.* (1998)[297] and simulated in Luo *et al.*[139] was considered, however the mutants were not developed to fullness. The expression of the EGF-like domain of NRG2β (as reported in Jones *et al.* (1999)[87])fused in tandem with MCP was also attempted and subsequently abandoned. Fusing a protein tag to an effector protein does not always preserve the function of the effector. Steric clashes and disruption of active conformations can abolish biological functions of tandem proteins [228,231,233]. The NRG1β-MCP protein, however, was demonstrated to robustly activate HER3 and HER4 and to be able to significantly trans-activate HER2 in T47D cells at concentrations of 100 nM (Dr Michela Perani, personal communication). These results

demonstrate that NRG1β-MCP is suitable as a probe for the activated states of HER3 and HER4, and at the same time that dimerization of these two receptors with HER2 occurs in the main cell model of used in this project.

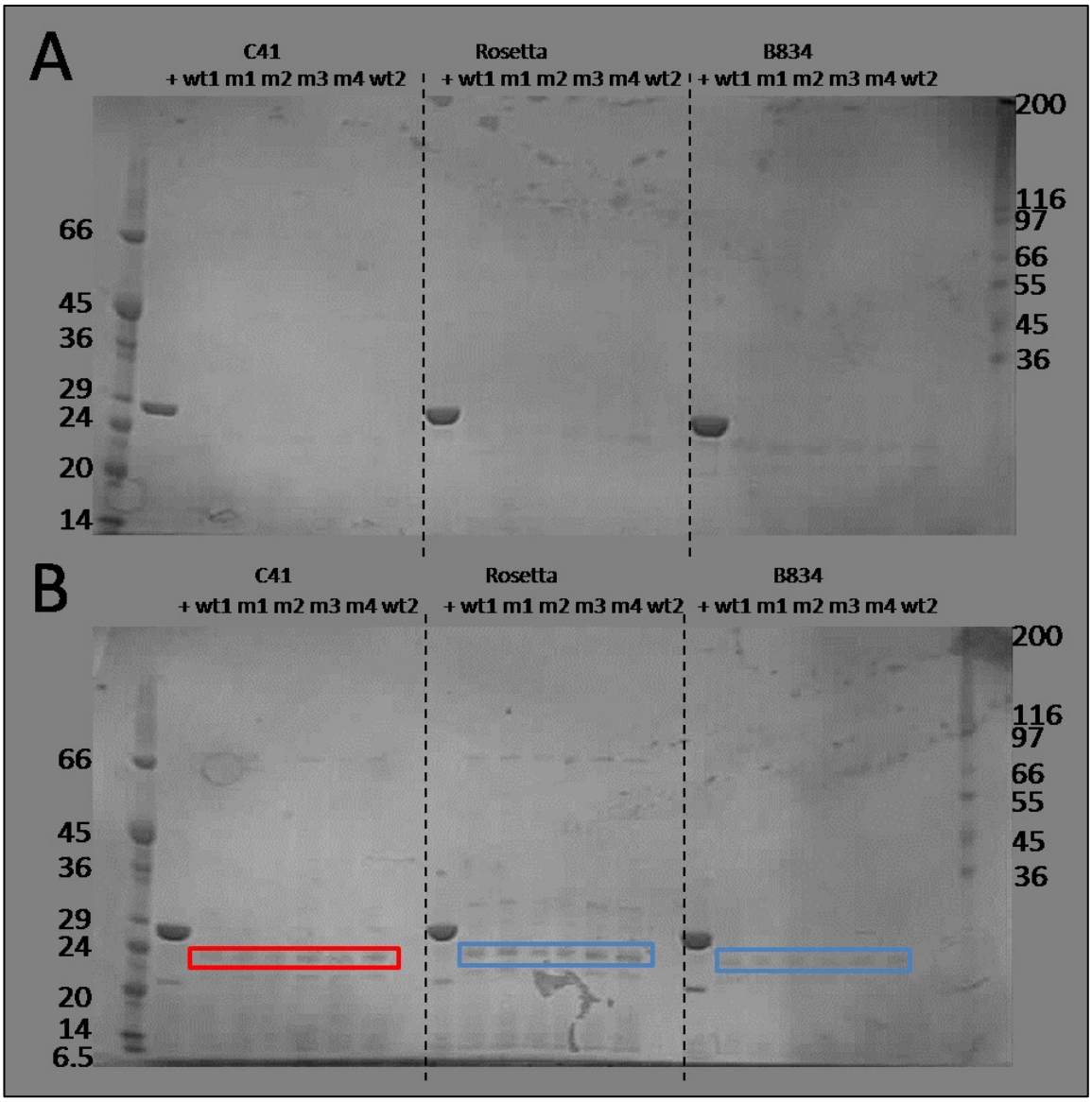

Figure 3-16 – Small Scale Expression Screening of Neuregulin Variants. A) Auto-induction medium. **B)** IPTG induction 0.5 mM 24h. += GFP positive control; wt1 = NRG1β-MCP; m1= NRG1β-MCP_S27A; m2 = NRG1β-MCP_3KE (K3E_K7E_K11E); m3 = NRG1β-MCP_K5A; m4 = NRG1β-MCP_F53A; wt2 = NRG2β-MCP. Boxed = protein bands corresponding to target proteins (expected Mw 18-16.5 kDa). Red= best hits.

Enzymatic labelling of NRG1β-MCP with fluorescent CoA derivatives

NRG1β-MCP was enzymatically labelled with CoA-Atto488, CoA-Dyomics 547 (Dy547) and CoA-Dyomics 647 (Dy647) in first instance, and then with CoA-Alexa 488 and CoA-CF640R. NRG1β-MCP-Dy547 was used for subsequent Single-Molecule ligand binding experiments and all NRG1β-MCP conjugates were used to test probe reliability in Single-Molecule experiments (see below).

3.2.6. Determination of binding equilibrium curves at 37°C for all probes

In order to be able to label the highest possible proportion of receptors without "over-labelling", which would prevent the detection of Single-Molecule spots, binding curves were determined for all probes at 4 different concentrations for each probe. Time-lapse series of images were acquired over the course of 25 minutes using samples in which the fluorescent label was left in solution for the whole duration of the experiment. Alexa 488-conjugated probes were used for this experiment due to their low propensity for non-specific binding to cell growth substrates, except for NRG1β-MCP, for which the Dyomics547 conjugate was used due to better conjugation efficiency, brightness and photostability than either the Atto 488 or the Dyomics 647 conjugate. **Figure 3-17** shows the time courses for spot density increase as a factor of bulk concentration of ligand for all 5 probes tested.

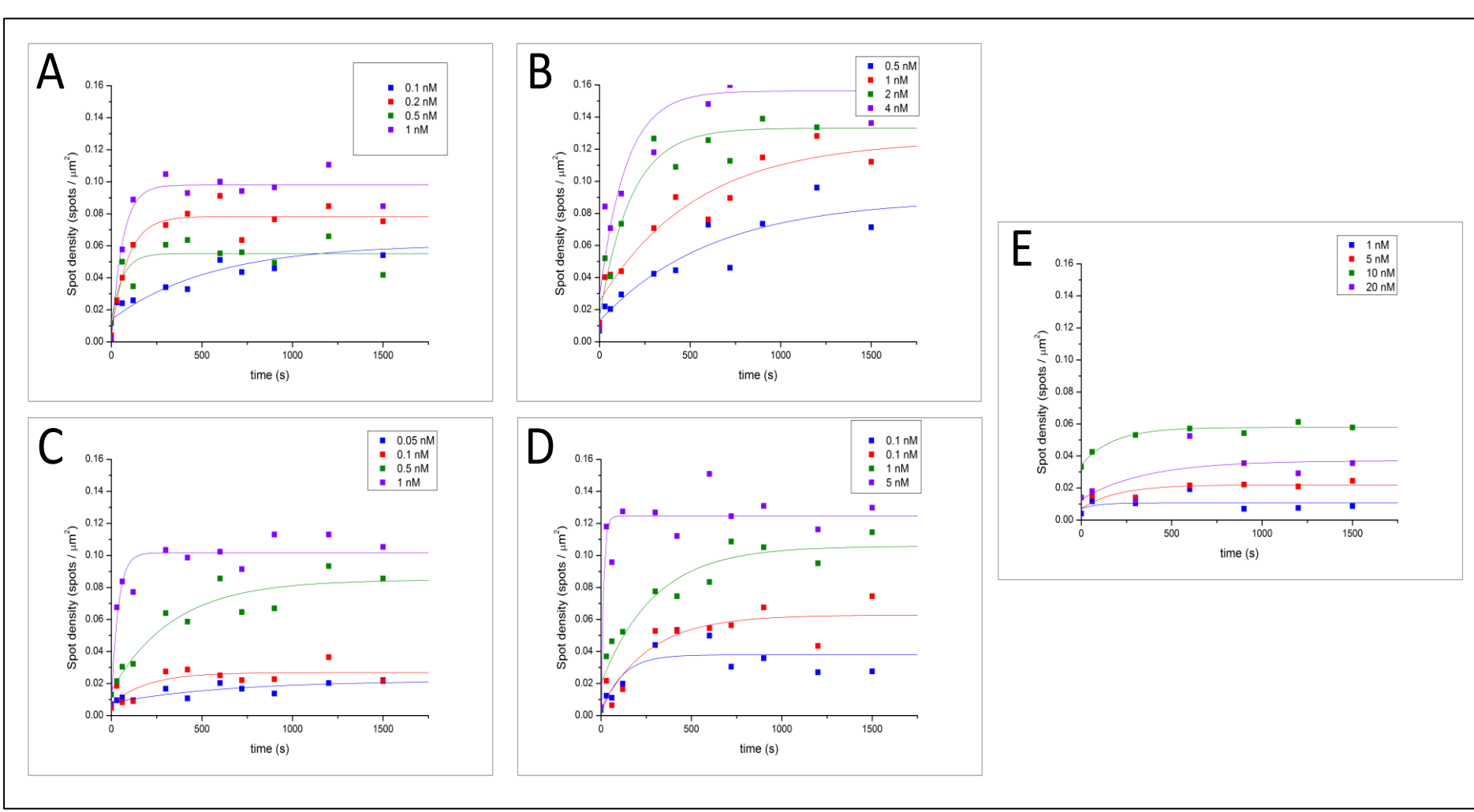
A
0.1 nM
0.2 nM
0.5 nM
1 nM
Spot density (spots / μm²)
time (s)
B
0.5 nM
1 nM
2 nM
4 nM
Spot density (spots / μm²)
time (s)
C
0.05 nM
0.1 nM
0.5 nM
1 nM
Spot density (spots / μm²)
time (s)
D
0.1 nM
0.1 nM
1 nM
5 nM
Spot density (spots / μm²)
time (s)
E
1 nM
5 nM
10 nM
20 nM
Spot density (spots / μm²)
time (s)

Figure 3-17(previous page) - Determination of time-dependent spot density curves at 37°C for fluorescent probes. A) EGF Alexa 488 (0.1 nM = blue; 0.2 nM = red; 0.5 nM = green; 1 nM = purple). **B)** Anti-HER1 Affibody Alexa 488 (0.5 nM = purple; 1 nM = blue; 2 nM = red; 4 nM = green). **C)** Anti-HER2 Affibody Alexa 488 (0.05 nM = blue; 0.1 nM= red; 0.5 nM = purple; 1 nM = green). **D)** Anti-HER3 Affibody Alexa 488 (0.1 nM= blue; 0.5 nM= red; 1 nM = green; 5 nM = purple). **E)** NRG1β-MCP-Dy547 (1 nM= blue; 5 nM= red; 10 nM = green; 20 nM = purple). Data were fit with an exponential growth model in Origin 8.

The spot density curves were fit with the exponential growth model

$$S(t) = A_S(1 - e^{-Bt}) + Offset$$

using the Origin 8 software package, as described in **Paragraph 2.7.**
Fitting parameters for all curves are displayed in **Table 3-1** for EGF Alexa 488, **Table 3-2** for anti-HER1 Affibody Alexa 488, **Table 3-3** for anti-HER2 Affibody Alexa 488, **Table 3-4** for anti-HER3 Affibody Alexa 488, and **Table 3-5** for NRG1β-MCP-Dy547.

Conc (nM)	*As*	SEM	*Offset*	SEM	*B*	SEM	Adj R^2
0.1	0.04708	0.01032	0.01399	0.005	0.0018	0.00105	0.79793
0.2	0.07419	0.00727	0.0041	0.00689	0.01142	0.00278	0.92246
0.5	0.04162	0.01099	0.01359	0.01034	0.01651	0.01038	0.5878
1	0.09646	0.00869	0.00152	0.00818	0.0163	0.00349	0.93314

Table 3-1 – Fitting parameters for EGF Alexa 488 spot density curves. All data are presented ± SEM.

Conc (nM)	*As*	SEM	*Offset*	SEM	*B*	SEM	Adj R^2
0.5	0.07579	0.01813	0.01424	0.00701	0.00154	9.01999E-4	0.82161
1	0.09941	0.01936	0.03553	0.00609	0.00135	6.01496E-4	0.90523
2	0.09261	0.01412	0.05004	0.01031	0.00271	0.00125	0.82819
4	0.10874	0.01366	0.04972	0.01264	0.00506	0.00196	0.86182

Table 3-2 – Fitting parameters for anti-HER1 Affibody Alexa 488 spot density curves. All data are presented ± SEM.

Conc (nM)	*As*	SEM	*Offset*	SEM	*B*	SEM	Adj R^2
0.05	0.01394	0.00497	0.00788	0.002	0.00158	0.0014	0.64932
0.1	0.0199	0.00543	0.00697	0.00503	0.00512	0.00429	0.53859
0.5	0.06922	0.00825	0.06922	0.00825	0.00293	0.00107	0.88341
1	0.09207	0.0109	0.00956	0.01033	0.02691	0.00728	0.8808

Table 3-3 - Fitting parameters for anti-HER2 Affibody Alexa 488 spot density curves. All data are presented ± SEM.

Conc (nM)	*As*	SEM	*Offset*	SEM	*B*	SEM	Adj R^2
0.1	0.03662	0.00948	0.00133	0.009	0.00895	0.00621	0.60111
0.5	0.05816	0.0089	0.00459	0.00766	0.00373	0.00178	0.80438
1	0.0858	0.00935	0.01998	0.00777	0.00342	0.00116	0.89450
5	0.11899	0.0158	0.00557	0.01497	0.07599	0.04323	0.84559

Table 3-4 - Fitting parameters for anti-HER3 Affibody Alexa 488 spot density curves. All data are presented ± SEM.

Conc (nM)	As		Offset		B		Adj R^2
1	0.00363	0.00433	0.00714	0.00342	0.01076	0.01887	-0.0152
5	0.01482	0.00337	0.00722	0.00241	0.00496	0.0025	0.81848
10	0.02338	0.00198	0.03443	0.00136	0.00572	0.00113	0.96791
20	0.02433	0.01152	0.01279	0.00641	0.00283	0.00356	0.41016

Table 3-5 - Fitting parameters for NRG1β-MCP-Dy547 spot density curves. All data are presented ± SEM

The tabulated R^2 parameters show that the model fits the data reasonably well (R^2>0.8), except for some conditions. For example the curve for 1nM NRG1β-MCP-Dy547 does not really fit the model at all, however, the signal level is so low that it is likely attributable entirely to background.

Taken together, the data seem to indicate that high levels of binding can be achieved by labelling with 1 nM EGF, 4 nM anti-HER1 Affibody, as low as 2 nM anti-HER2 Affibody (concentration at which, depending on cell-by-cell protein expression, saturation of the

feature detection algorithm is already achieved), or 5 nM anti-HER3 Affibody. Depending on the Single-Molecule imaging technique to be applied to samples, variable levels of spot density might be desirable. For example, intensity-based applications such as spFRET and localisation-based techniques require well-separated spots, to prevent interference from neighbouring particles on the calculations, while tracking applications can tolerate variable levels of crowding, depending on the tracking algorithm. The calculation of colocalisation percentages will be heavily influenced by variations in the number of spots of the two species to be colocalised and interactions would be difficult to observe with very sparse particles.

3.2.7. Single-Molecule assessment of NRG1β-MCP enzymatic conjugates and traditional NRG1β conjugates binding and behaviour on cells

As seen above in **Figure 3-17 E**, when determining ligand spot density time-courses for NRG1β-MCP-Dy547, which is supposed to have an affinity of ~ 5 nM for HER3 and HER4 [87], a concentration of 10 nM of the probe was deemed submaximal, due to the low density achieved compared with HER3 Affibody, which reports on the same receptor. Higher concentrations (up to 50 nM) were tested (data not shown) but fluorescent labelling of cells did not improve dramatically, while non-specific signals on the glass increased worryingly. Since NRG1β-MCP tandem protein conjugates seemed to be the hardest to optimise, all fluorescent conjugates were further tested on live T47D cells to assess their binding, brightness and stability.

Atto488 and Dyomics647 conjugates showed low brightness and stability, yielding signals barely above background noise, and all conjugates showed very low spot density compared to HER3 Affibody (**Figure 3-18 D**), with values comparable to that of unlabelled cell, or even lower for the Dy647 conjugate (two-tailed T test - P= 0.24; 0.98 and 0.00078 for NRG1β-CoA-At488; NRG1β-CoA-Dy547 and NRG1β-CoA-Dy647 respectively). Moreover, as shown in **Figure 3-18 B and C**, their MSD curve at 37°C was comparable to that of background autofluorescence Single-Molecule spots on untreated cells. Two more conjugates, labelled with brighter and more stable dyes, were then tested, but even NRG1β-MCP-Alexa488 and NRG1β-MCP-CF640R performed particularly poorly. NRG1β-CoA-CF640R displayed low, background-level spot density (P= 0.22 – two-tailed T test), but while signal levels for NRG1β-CoA-Alexa488 were definitely above background noise ($P=6 \times 10^{-9}$) (**Figure 3-18 D**), however, the MSD curve of both fluorescent particles was still comparable to that of background noise spots, as shown in **Figure 3-18 A**. It is likely that the main signal contribution arose from free dye even when using very high concentrations of protein (100 – 200 nM)

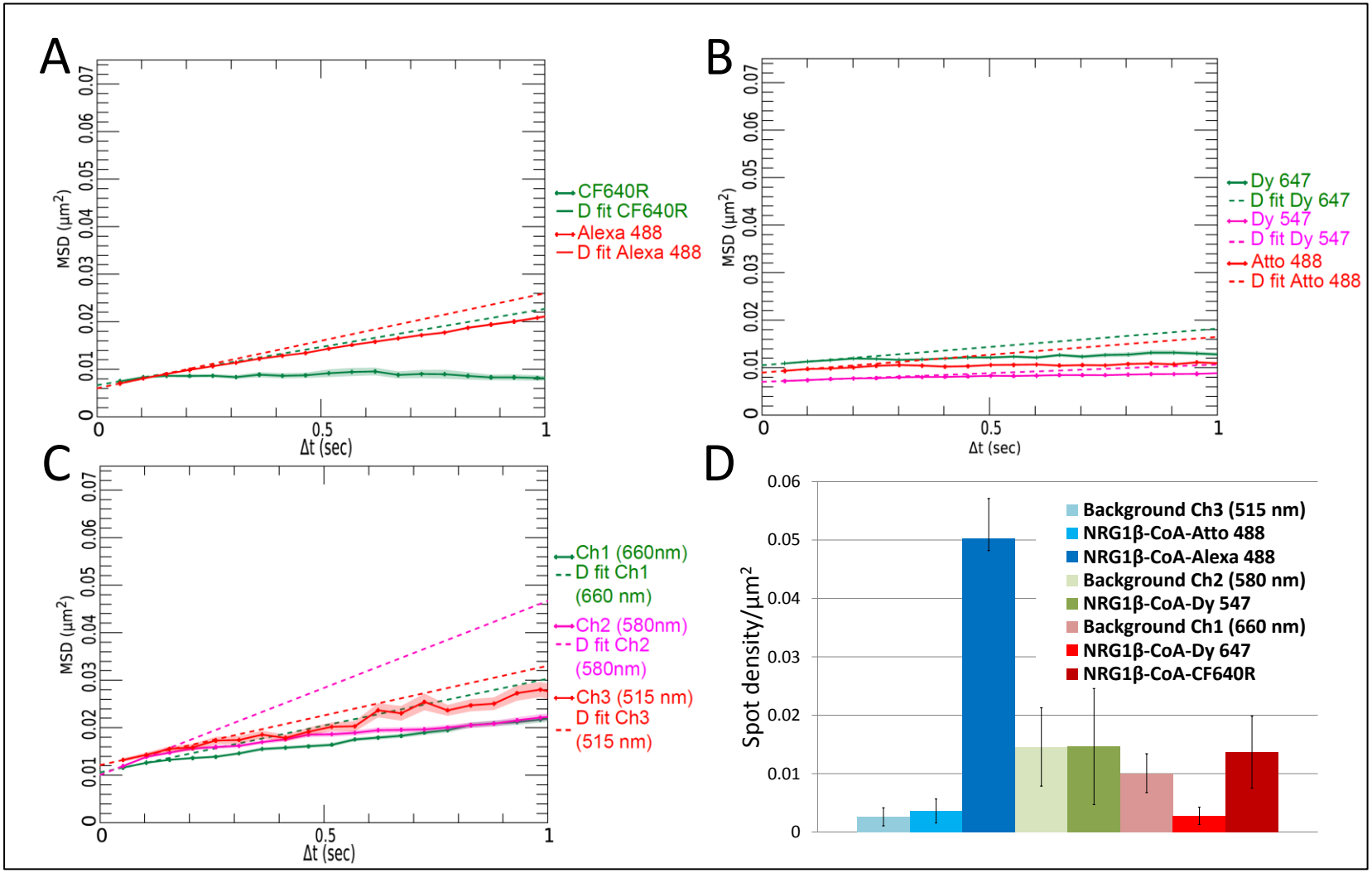
A
MSD (µm²)
Δt (sec)
CF640R
D fit CF640R
Alexa 488
D fit Alexa 488
B
MSD (µm²)
Δt (sec)
Dy 647
D fit Dy 647
Dy 547
D fit Dy 547
Atto 488
D fit Atto 488
C
MSD (µm²)
Δt (sec)
Ch1 (660nm)
D fit Ch1 (660 nm)
Ch2 (580nm)
D fit Ch2 (580nm)
Ch3 (515 nm)
D fit Ch3 (515 nm)
D
Spot density/µm²
Background Ch3 (515 nm)
NRG1β-CoA-Atto 488
NRG1β-CoA-Alexa 488
Background Ch2 (580 nm)
NRG1β-CoA-Dy 547
Background Ch1 (660 nm)
NRG1β-CoA-Dy 647
NRG1β-CoA-CF640R

Figure 3-18 – NRG1β-MCP conjugates labelled with fluorescent CoA derivatives perform poorly in Single-Molecule experiments. A-C: MSD curves of **A)** 100 nM each of NRG1β-CoA-Alexa488 (red) and –CF640R (green) on T47D cells, **B)** 40 nM each of NRG1β-CoA-Atto488 (red), -Dyomics 547 (pink) and –Dyomics 647 (green) on T47D cells, and **C)** background signal (impurities from substrate and cells) from unlabelled wt Cho cells. Curves were calculated over at least 7 independent areas. **D)** Histogram of spot density/μm^2 of NRG1β-CoA conjugates and background signals. Data referring to channel 3 are plotted in blue, data referring to channel 2 in green and data referred to channel 3 in red. Data were averaged over at least 7 independent areas and are plotted ± SD. T Test calculations were performed using the background values for the appropriate channel as a reference.

In order to exclude that this observation might be caused by defects in the commercially available or custom-synthesised fluorescent CoA conjugates used to enzymatically label the protein, a MCP-GPI control plasmid, which encodes a GPI-anchored MCP protein, was transfected into wild-type Cho cells and enzymatic labelling of the transfected cells was performed with all CoA conjugates. All conjugates seemed able to label MCP-expressing cells, resulting in comparable levels of labelling for all dyes, except for the Alexa488 conjugate, which showed a superior performance (**Figure 3-19** and **Figure 3-20 D**). Cells labelled with CF640R and Alexa 488 also display lower levels of background and sharper spots (compare **Figure 3-19 B** and **E** with **A** and **C-D**).

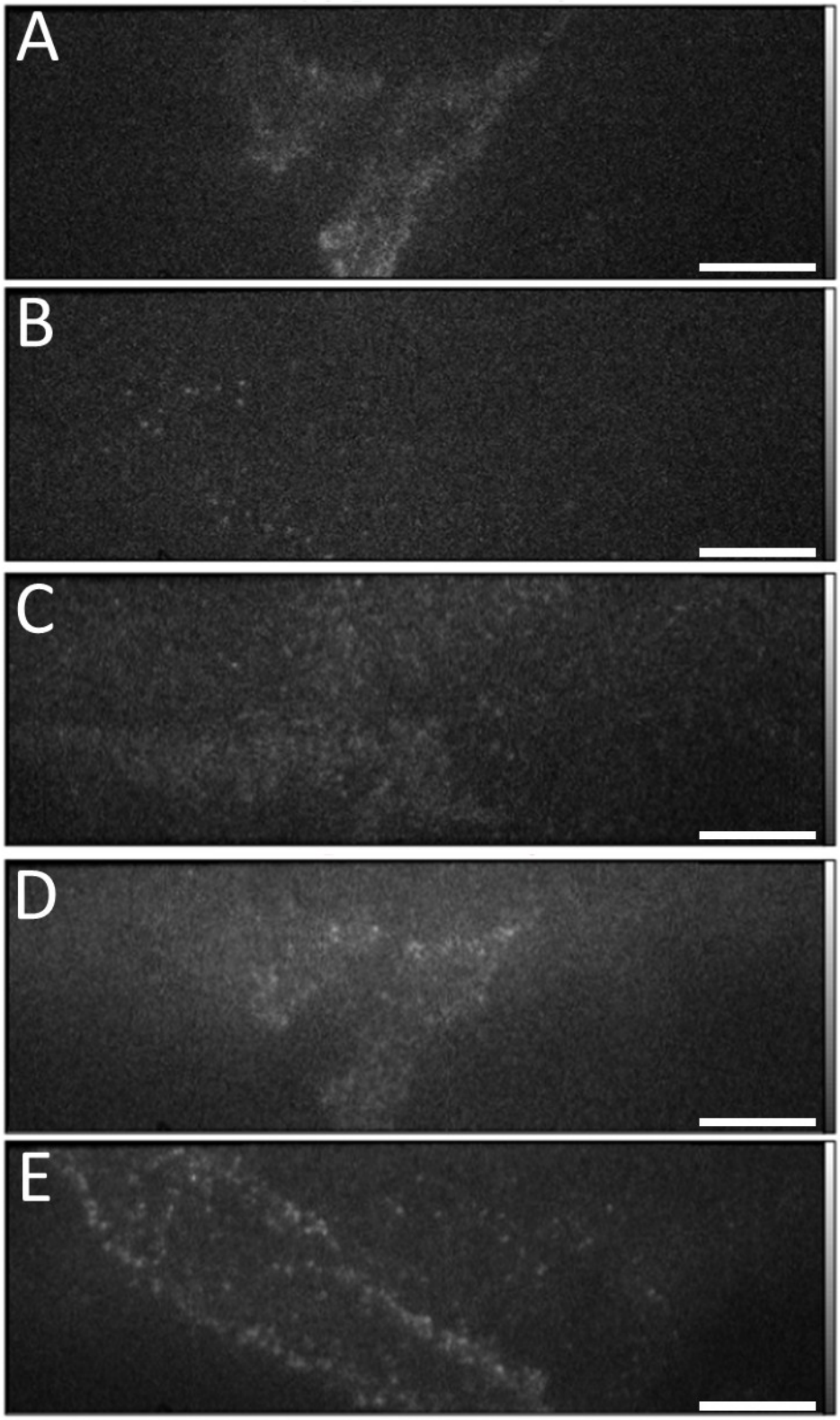

Figure 3-19 – Labelling of wt Cho cells transiently transfected with GPI-MCP with fluorescent CoA derivatives. A) Dyomics 647; **B)** CF640R; **C)** Dyomics 547; **D)** Atto 488; **E)** Alexa 488. Bars (white)= 10 µm.

The MSD of the GPI-anchored MCP proteins, however, was not the same for all dyes tested, with CoA -Atto488, -Alexa488 and -CF640R showing faster diffusion compared to CoA-Dy547 and –Dy647. In particular, the *D* coefficient values of CoA-Dy547 on MCP-GPI transfected cells were close to those of non-specific fluorescent spots on mock-transfected cells and were an order of magnitude smaller than those of CoA-Alexa 488 on transfected cells. (Compare **Figure 3-20 A-C** – $D_{CoA\text{-}Dy547}$= 0.0163 $\mu m^2/s$, $D_{CoA\text{-}A488}$ = 0.146 $\mu m^2/s$). As GPI-anchored proteins usually display a high macroscopic diffusion coefficient (see for example observations in [298,299]), the Alexa 488 value was taken to reflect more closely the actual diffusive behaviour of the target protein.

CoA-Dy547 also showed an increased propensity to non-specifically adhere to the substrate and /or to non-transfected cells in mock transfection experiments, demonstrating a much higher spot density than CoA-Alexa488 and CoA-CF640R (P= $1.62x10^{-5}$ and $9.88x10^{-6}$ for CoA-Dy547 spot density v CoA –A488 and CoA-CF640R spot densities respectively, Student's T Test - **Figure 3-20 E**).

The results above seem to demonstrate that, while all the fluorescent CoA derivatives tested are able to label MCP proteins in standard conditions, CoA derivatives labelled with Dyomics dyes perform remarkably worse.

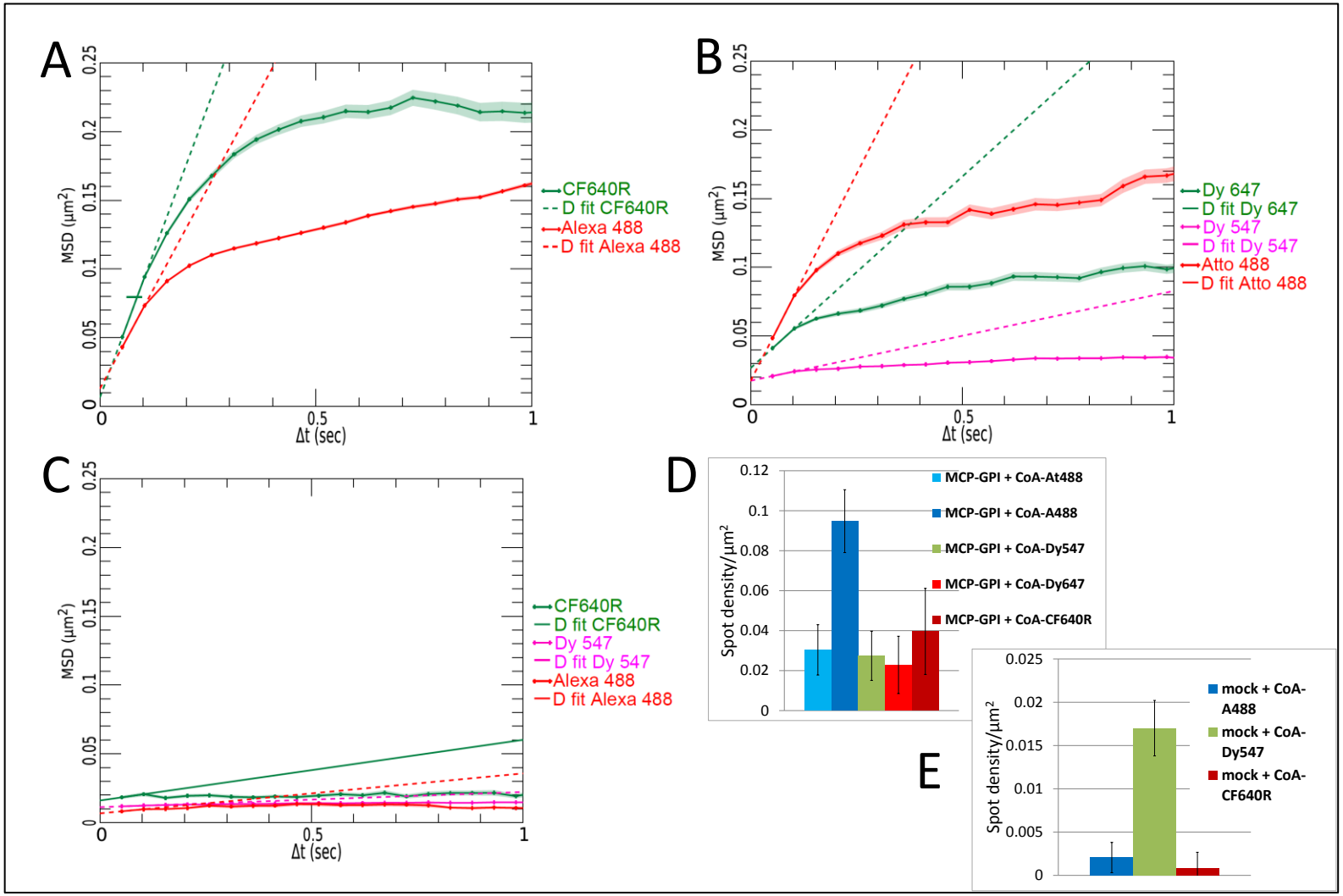
A
MSD (µm²)
Δt (sec)
CF640R
D fit CF640R
Alexa 488
D fit Alexa 488
B
MSD (µm²)
Δt (sec)
Dy 647
D fit Dy 647
Dy 547
D fit Dy 547
Atto 488
D fit Atto 488
C
MSD (µm²)
Δt (sec)
CF640R
D fit CF640R
Dy 547
D fit Dy 547
Alexa 488
D fit Alexa 488
D
Spot density/µm²
MCP-GPI + CoA-At488
MCP-GPI + CoA-A488
MCP-GPI + CoA-Dy547
MCP-GPI + CoA-Dy647
MCP-GPI + CoA-CF640R
E
Spot density/µm²
mock + CoA-A488
mock + CoA-Dy547
mock + CoA-CF640R

Figure 3-20 (previous page) – CoA derivatives are able to label transiently expressed MCP-GPI on Cho cells. A-C: MSD curves of **A)** 2.5 µM each of CoA-Alexa488 (red) and –CF640R (green) on Cho cells + MCP-GPI plasmid **B)** 1.67 µM each of CoA-Atto488 (red), -Dyomics 547 (pink) and –Dyomics 647 (green) on Cho cells + MCP-GPI plasmid, and **C)** 1.67 µM each of CoA-Alexa488 (red), -Dyomics 547(pink) and –CF640R (green) on mock transfected Cho cells. Curves were calculated over at least 7 independent areas. **D)** Histogram of spot density/μm^2 of CoA conjugates on MCP-GPI transfected Cho cells. **E)** Histogram of spot density/μm^2 of CoA conjugates on mock-transfected Cho cells. Data were averaged over at least 7 independent areas and are plotted ± SD. T Test calculations were performed using the CoA-Alexa 488 and CoA-CF640R values as references.

Taken together, the HER3/HER4 phosphorylation data and the NRG1β-MCP labelling data suggest that that, while the NRG1β-MCP protein is still active, the labelling of the MCP tag might be incomplete or impossible for structural reasons, possibly due to steric clashes between the NRG1β EGF-like domain and the MCP tag, and that only a small, variable fraction of the protein, if any, might be labelled and attaching to the cells, with the main contribution to the fluorescent signal coming from cell background and free dye adhesion to the substrate. Finally, T47D cells were labelled with conventionally conjugated NRG1β-Alexa 488, Alexa 546 and Alexa 647 and demonstrated binding at concentrations as low as 20 nM (**Figure 3-21 B**). While the A546 conjugate does not appear highly specific, due to its higher spot density and lower diffusion coefficient values (D= 0.014 μm^2/s compared to 0.035 μm^2/s and 0.057 μm^2/s for NRG1b-Alexa 488 and –Alexa 647 respectively), the Alexa 488 and Alexa 647 conjugates yielded a sufficiently low non-specific signal and seemed suitable for Single-Molecule imaging (**Figure 3-21 A**).

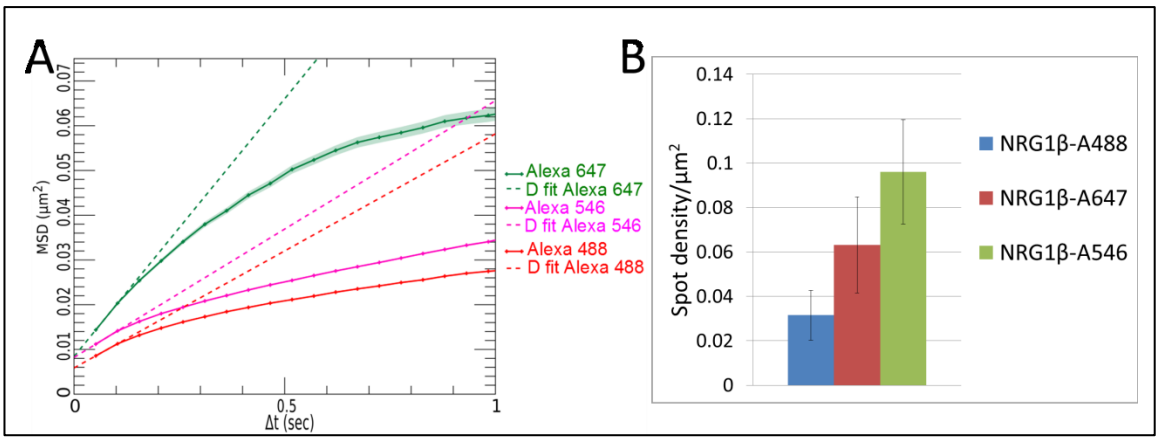

Figure 3-21 – Conventional NRG1β NHS-ester dye conjugates are able to bind to T47D cells. A) MSD curves of 20 nM each NRG1β-Alexa488 (red), - Alexa 546 (pink) and -Alexa-647 (green) on T47D cells. All calculations were made on at least 10 independent areas. **B)** Histogram of spot density/µm^2 of 20 nM each NRG1β-Alexa488, - Alexa 546, and -Alexa-647 (green) on T47D cells. Data were averaged over at least 10 independent areas and are presented as average ± SD.

Taken together, these results warranted the discontinuation of the development of NRG1β-MCP proteins except for the purpose of activating the receptors, and the decision to fall back on conventional chemical labelling of commercially available NRG1β with succinimidyl ester or NHS ester organic dyes.

3.3. Discussion

This chapter demonstrates the synthesis and characterisation of an array of small, peptidic probes conjugated to small-molecule chemical dyes, suitable for the Single-Molecule imaging of the HER1, HER2 and HER3 receptors in their basal and activated states, where applicable. All definitive probes (EGF, anti- HER1, HER2 and HER3 Affibodies and untagged NRG1β) showed good SNR and affinity and in Single-Molecule acquisition conditions. A collection of Single-Molecule images of the probes bound on T47D cells is shown in **Figure 3-22**, below.

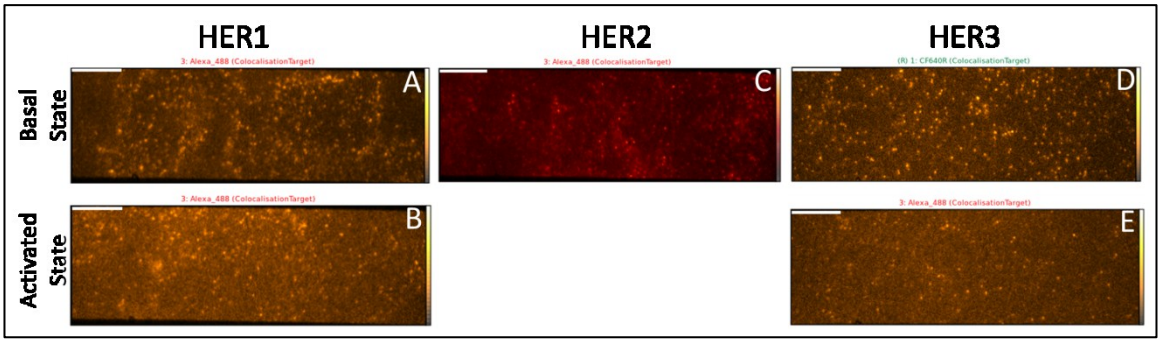

Figure 3-22 – Single-Molecule images of **A)** anti-HER1 Affibody Alexa 488; **B)** EGF Alexa 488; **C**) anti-HER2 Affibody Alexa 488; **D)** anti-HER3 Affibody CF640R and **E)** NRG1β Alexa 488 on T47D cells. Bars (white)= 10 µm

As the different probes were being tested, issues of specificity arose in the form of the tracking artefacts, already evidenced in **Figure 3-21 A**, where the same probe conjugated to different dyes appeared to report on different modes of diffusion. In order to solve this issue, systematic investigations on probe and substrate parameters potentially affecting probe binding and specificity were performed. Detailed discussions of the methods employed to eliminate or at least minimise such artefacts can be found in **Chapter 4**, which focuses on the role of the growth substrate, and in **Chapter 5**, in which the analysis of the role of the dye chemistry in favouring electrostatic interactions with surfaces is reported.

4. Investigating the Effect of Substrates on Single-Particle Tracking Artefacts

The core material of this chapter has been published in Zanetti-Domingues *et al.* (2012) [1].

4.1. Introduction

In this chapter, ten cell-growth substrates and fourteen fluorescent dyes for the 491 nm, 561 nm and 638 nm wavelengths were systematically investigated, in order to determine the best combination of dye and substrate to minimise the introduction of artefacts in Single-Molecule data and still allow reproducible cell growth.

This investigation was prompted by the fact that, during the course of the label optimisation phase of the project, it was evidenced that some combinations of label and fluorophore have an increased tendency to bind non-specifically to the glass and produce artefacts. In particular, it was noted that Alexa546 and Atto647N conjugates tend to adhere quite readily to uncoated glass surfaces. This phenomenon was not apparent during the Confocal Microscopy experiments used to assess the specificity of the probes because the plane of acquisition was sufficiently distant from the growth substrate.

Uncoated glass substrates are typically used for Single-Molecule fluorescence measurements, because of their optical transparency, the ability to immobilize molecules on their surface, and their ability to support consistent cell growth by forming electrostatic interactions with the cell membrane [300]. Unfortunately, this also means that they readily bind fluorescent molecules, such as labelled proteins, non-specifically. Non-specific binding contributes spurious fluorescence signals that cannot be readily distinguished from fluorescent labels in cells. The presence of large numbers of non-specifically bound fluorescent molecules also makes it more difficult for detection algorithms to successfully locate molecules of interest, contributing to overcrowding of spots.

In order to address the non-specific binding of fluorescent probes to the glass, it is common to passivate glass substrates by coating them with a material that does not interfere with optical transmission or cell growth, but minimizes non-specific binding. Many approaches are available to passivate glass surfaces, which include: saturation of non-specific binding sites with inert proteins, such as BSA or serum, or with matrix proteins like laminin, fibronectin or collagen isoforms, which have the added benefit of promoting cell growth and attachment, or

creating a monolayer that is resistant to non-specific binding. The most commonly used molecule for the latter purpose is polyethylene glycol (PEG), in either its linear or its branched form [301]. Cells cannot adhere to pure PEG layers, so, for Single-Molecule experiments in cells layers, it must be supplemented with molecules that allow the cells to bind. RGD peptides, that mimic cell adhesion proteins [302], have been used for this purpose. Finally, a recent publication describes a hybrid approach, using PEG-BSA nanogels [274] for surface passivation.

4.2. Results

4.2.1. Preliminary Observations on the Single-Particle Tracking of Different Labelled Fluorescent Probes

Despite having proven the specificity of the probes for their targets in confocal experiments, which are not sensitive to artefacts arising from the glass coverslip, during preliminary Single-Particle Tracking experiments most of the fluorescent probes described in **Chapter 3** showed different diffusive behaviour depending the dye used for conjugation. In particular, all the HER-antagonist Affibody probes, and especially anti-HER1 (**Figure 4-1 A-B**) and anti-HER3 (**Figure 4-1 C-D**), seemed to diffuse more slowly when conjugated to Alexa 546 and to Atto 647N than when conjugated to Alexa 488.

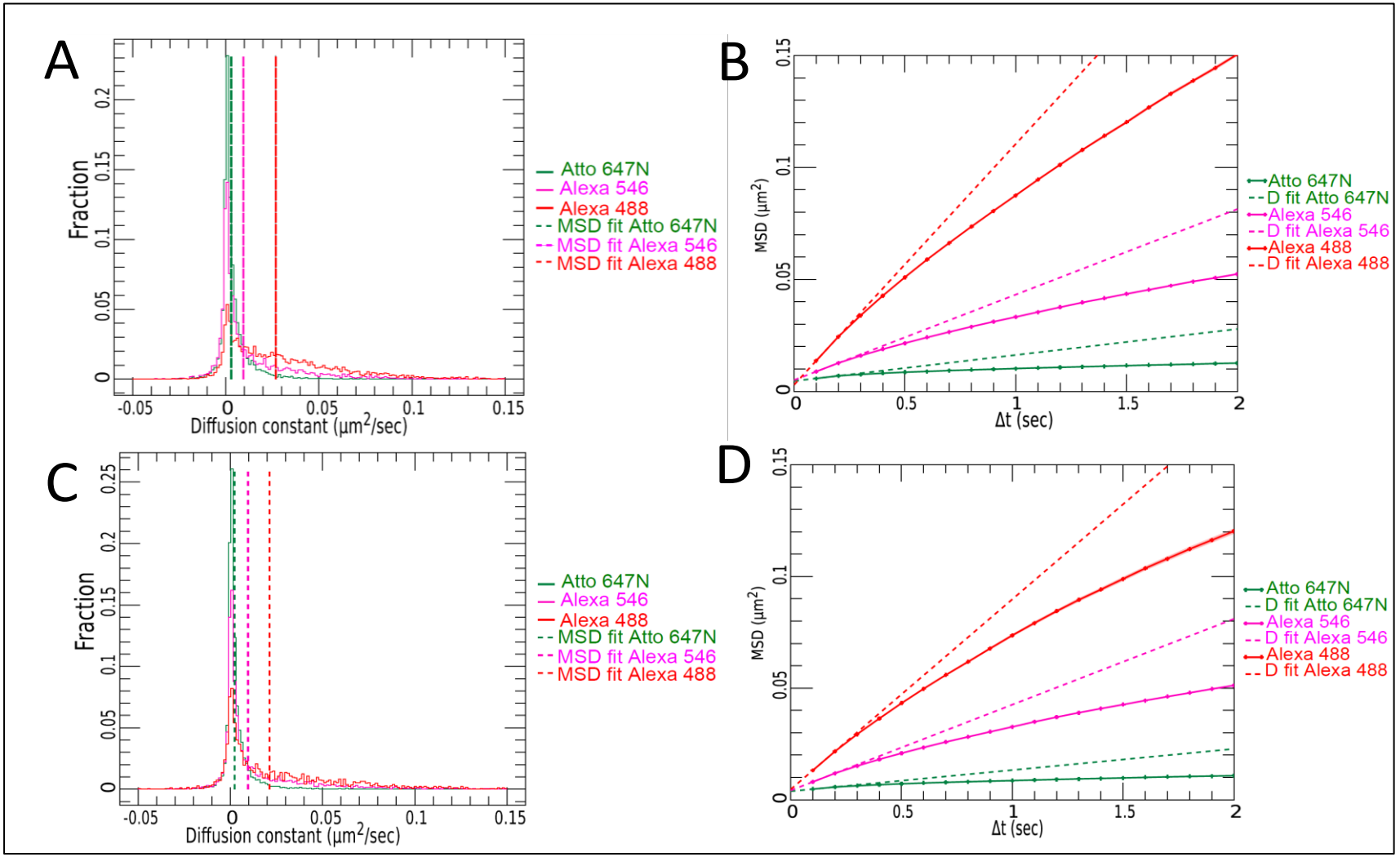
A
Fraction
Diffusion constant (μm²/sec)
Atto 647N
Alexa 546
Alexa 488
MSD fit Atto 647N
MSD fit Alexa 546
MSD fit Alexa 488
B
MSD (μm²)
Δt (sec)
Atto 647N
D fit Atto 647N
Alexa 546
D fit Alexa 546
Alexa 488
D fit Alexa 488
C
Fraction
Diffusion constant (μm²/sec)
Atto 647N
Alexa 546
Alexa 488
MSD fit Atto 647N
MSD fit Alexa 546
MSD fit Alexa 488
D
MSD (μm²)
Δt (sec)
Atto 647N
D fit Atto 647N
Alexa 546
D fit Alexa 546
Alexa 488
D fit Alexa 488

Figure 4-1 (previous page) – Tracking artefacts impact different probes in comparable ways. A and B: Diffusion coefficient distribution **(A)** and MSD curves **(B)** of HER1 Affibody Alexa 488 (red), HER1 Affibody Alexa 546 (pink) and HER1 Affibody Atto 647N (green). **C and D:** Diffusion coefficient distribution **(C)** and MSD curves **(D)** of HER3 Affibody Alexa 488 (red), HER3 Affibody Alexa 546 (pink) and HER3 Affibody Atto 647N (green). Parameters were calculated from at least 10 independent areas for each condition.

The figure above shows that the profile of the diffusion coefficients distribution and the MSD curves for the same protein labelled with A488, A546 and At647N are noticeably different for both anti-HER1 and anti-HER3 Affibody. Proteins labelled with A564 and At647N showed a reduction in MSD and a reduction in the population of tracks showing diffusion coefficients > 0.03 $\mu m^2/s$ compared to proteins labelled with A488. This phenomenon was correlated with an increase in amounts of fluorescent probe adhering to the glass, to the point that spot density on glass was much higher than on cells in some cases (see for example **Figure 4-2 A**).

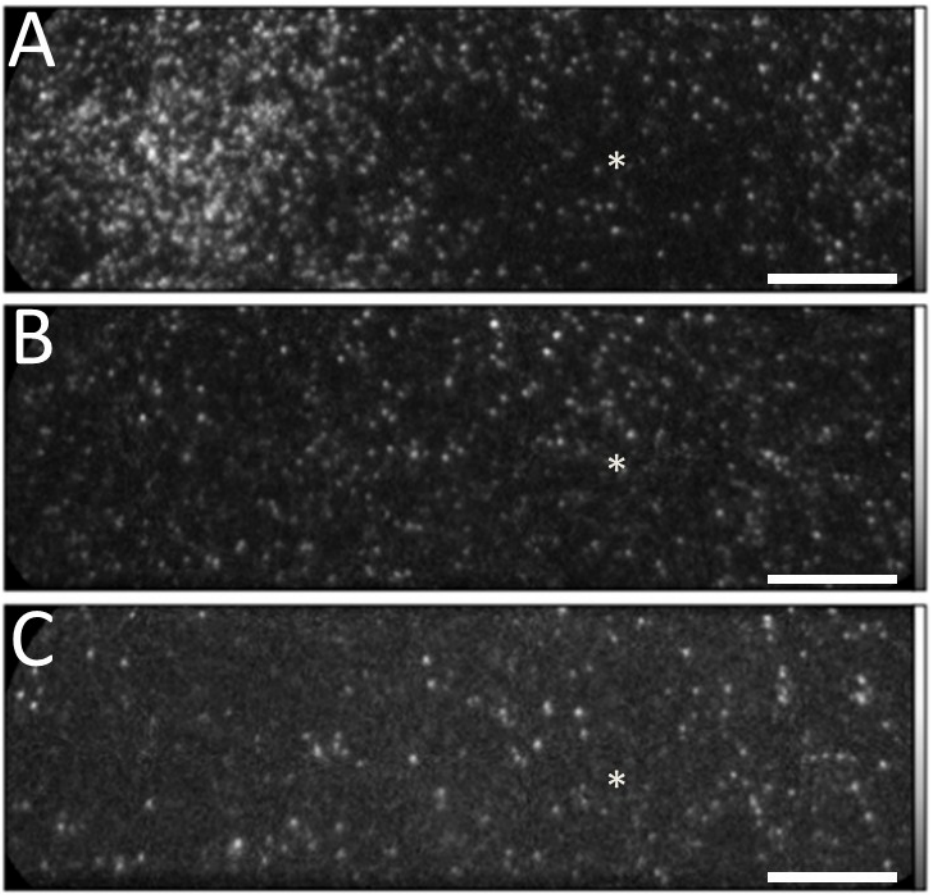

Figure 4-2 – Conjugate-dependent artefacts on T47D cells labelled with anti-HER3 Affibody Atto 647N (A); Alexa 546 (B) and Alexa 488 (C). The asterisk indicates the position of the cell. Bars (white) = 10 μm.

Binding to the glass introduced a significant artefact in the determination of the *D* coefficients ($P << 0.0001$ for HER1 Affibody conjugated to either Alexa 546 or Atto 647N compared to A488, and $P << 0.0001$ for HER3 Affibody conjugated to either Alexa 546 or Atto 647N compared to A488, respectively – Kolmogorov-Smirnov (K-S) test). The effect of fluorescent probe binding to the glass on the diffusion coefficient of EGF, however, was milder (see below). This could result from particular electrochemical or structural properties of the EGF protein, which can override the effect of the dye. Alternatively, it can be argued that the effect of a population of static molecules, or of a drag on the average *D* coefficient of a protein, would be more significant if the "true" value of the *D* coefficient was higher.

4.2.2. The impact of tracking artefacts becomes more significant as diffusion coefficient increases

Since the diffusion of EGF molecules on cell membranes appears to be quite slow, the effect of glass-binding artefacts could be less readily noticeable than with Affibody probes.
In order to test the origin of these artefacts and the impact that they can have on the Single-Particle Tracking of receptors moving at different speeds, and to elucidate the causes of the apparent resistance of EGF probes to dye effects, T47D cells were treated with 2 nM EGF Alexa 488, Alexa 546 and Atto 647N in presence or absence of 1 µM Lapatinib and tracked at 20Hz for 30 minutes at 37°C. This was done as preliminary experiments had shown an increase in the instantaneous *D* of EGF molecules in the presence of the TKI. Using the same probe to follow slow diffusion and faster diffusion resulted in comparable levels of non-specific binding to the glass in both conditions, as shown in **Figure 4-3**

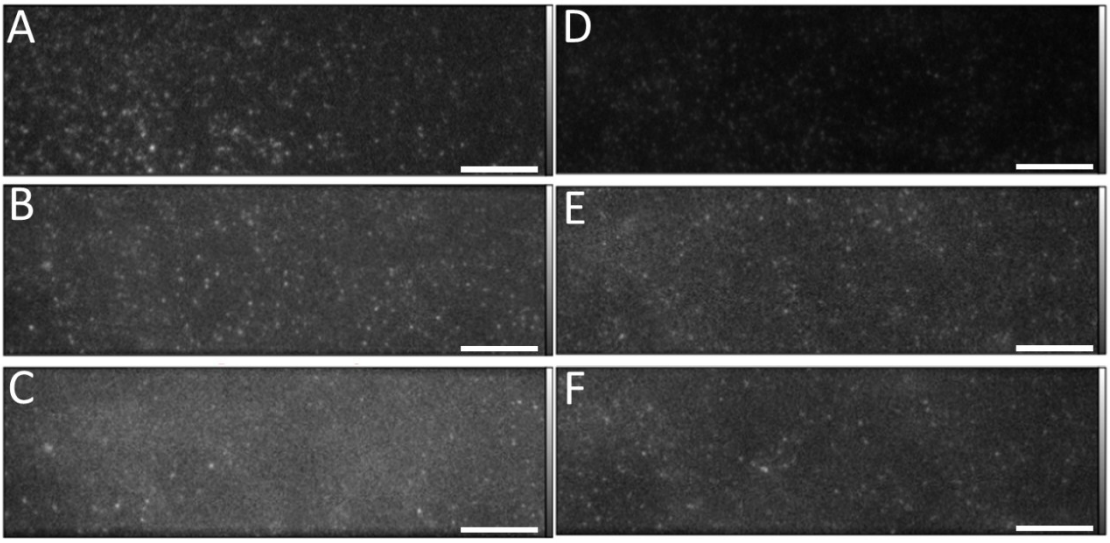

Figure 4-3 – Labelling of T47D cells with EGF conjugates in absence (A-C) or presence (D-F) of Lapatinib. A and **D:** Atto 647N; **B** and **E:** Alexa 546; **C** and **F:** Alexa 488.

It was observed that EGF Alexa 488 displayed a quite confined mobility on untreated cells, with a mean *D* coefficient of 0.028 ± 0.008 μm^2/sec, while after treatment with Lapatinib for 2h at 37°C, the diffusion coefficient increased to 0.11 ± 0.015 μm^2/sec, a value 4x higher.
When simultaneously tracking EGF bound to three different fluorophores, *D* values for EGF Alexa 488, EGF Alexa 546 and Atto 647N were 0.008 ± 0.004 μm^2/s; 0.005 ± 0.002 μm^2/s and 0.004 ± 0.002 μm^2/s, respectively. EGF Alexa 488 has a slightly higher mobility than the other two probes (P= 0.033 and 0.012 compared against A546 and At647N, respectively – K-S test) but lower than that recorded during single-channel tracking of EGF Alexa 488 (P< 0.0001). The

latter observation can be explained by the fact that by labelling with multiple colours and therefore increasing the total EGF concentration, we are increasing the chances of tracking dimers or oligomers, which are expected to diffuse more slowly than putative monomers labelled at low density [6].

When tracking the same three probes in cells treated with 1 μM Lapatinib, the *D* coefficient of EGF Alexa 488 increased to 0.084 ± 0.027 $\mu m^2/s$ (P<<0.0001). The *D* coefficient of EGF Alexa 546 and EGF Atto 647N, increased significantly after Lapatinib treatment (P = 0.009 and $6.141x\ 10^{-15}$ respectively compared to the untreated *D* coefficient), however the extent of the increase was much smaller than for EGF A488, only to 0.007 ± 0.002 $\mu m^2/s$ and 0.008 ± 0.003 $\mu m^2/s$ respectively (P= 1.82×10^{-21} and 3.65×10^{-21} respectively, for the *D* coefficients of EGF A546 + Lapatinib and EGF At647N +Lapatinib compared to the *D* coefficient of EGF Alexa 488 + Lapatinib).

Figure 4-4 (A and C) shows that the *D* coefficient distribution for EGF both in presence and in absence of Lapatinib is characterised by a peak around *D*=0, whose width is determined by molecular drift and localisation error. As explained in **Chapter 2** (see **Figure 2-1** and related text), the presence of un-physical *D*<0 values is due to the effect of the localisation errors on the determination of the MSD curve, whose slope can become negative if the frame-to-frame displacement of a tracked spot is in the range of the localisation error. Since the determination of the *D* coefficients is performed track-by-track by fitting the individual MSD curves, negative MSD slopes will result in artefactual negative *D* values.

When EGF is tracked on untreated cells, most of the diffusion coefficients fall in this area and the distribution has only a small "tail" of highly mobile molecules, while, in presence of Lapatinib, the "tail" of EGF Alexa 488 is increased, and mobile molecules make a much bigger contribution to the global diffusion coefficient. This might be due to the disruption of EGF-induced oligomerisation or to the inhibition of specific interactions between HER1 and cytoskeletal proteins. This "tail" is practically absent from the diffusion histograms of the Alexa 546 and Atto 647N probes, where the population of molecules non-specifically bound to the glass masks the increase in motility of the labelled HER1 population, and the two distribution profiles (+/- Lapatinib) are remarkably similar.

These results suggest that the apparent resistance of EGF to dye effects is due to its slow diffusion on cell membranes. While artefacts might be less readily apparent when the underlying motion of the molecule of interest is slow, they appear to be very significant when the tracked molecules move fast, as in the case of HER1 treated with Lapatinib.

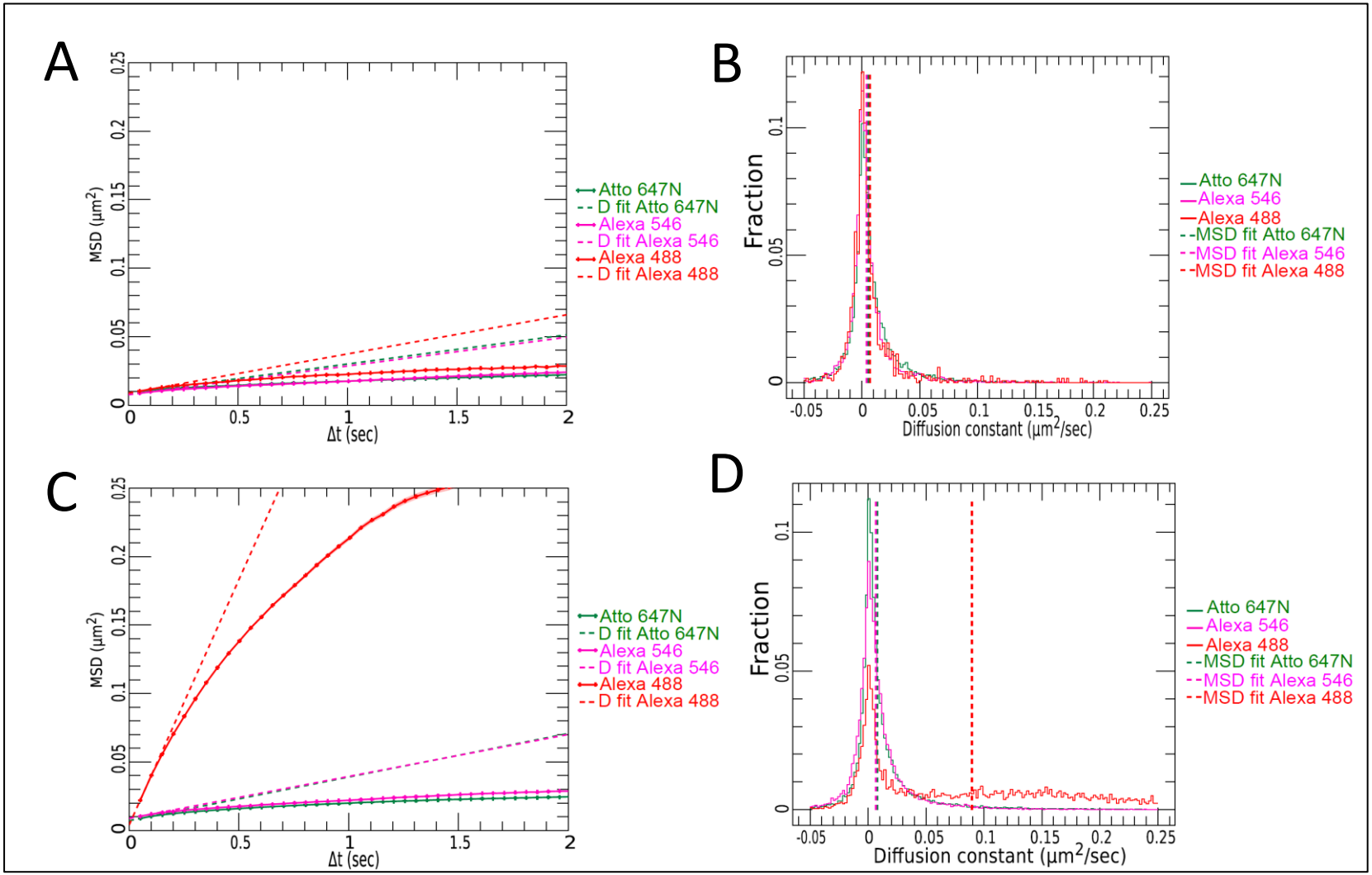
A
MSD (μm²)
Δt (sec)
Atto 647N
D fit Atto 647N
Alexa 546
D fit Alexa 546
Alexa 488
D fit Alexa 488
B
Fraction
Diffusion constant (μm²/sec)
Atto 647N
Alexa 546
Alexa 488
MSD fit Atto 647N
MSD fit Alexa 546
MSD fit Alexa 488
C
MSD (μm²)
Δt (sec)
Atto 647N
D fit Atto 647N
Alexa 546
D fit Alexa 546
Alexa 488
D fit Alexa 488
D
Fraction
Diffusion constant (μm²/sec)
Atto 647N
Alexa 546
Alexa 488
MSD fit Atto 647N
MSD fit Alexa 546
MSD fit Alexa 488

Figure 4-4 (previous page) – The diffusion of untreated EGF on cells is within error levels of D=0, masking artefacts in diffusion introduced by non-specific binding of probes to the glass. A and B: Diffusion coefficient distribution **(A)** and MSD curves **(B)** of EGF Alexa 488 (red), EGF Alexa 546 (pink) and EGF Atto 647N (green) in absence of Lapatinib. **C and D:** Diffusion coefficient distribution **(C)** and MSD curves **(D)** of EGF Alexa 488 (red), EGF Alexa 546 (pink) and EGF Atto 647N (green) on cells treated with 1 µM Lapatinib for 2h at 37°C .

4.2.3. Non-specific binding of probes to the glass depends predominantly on the dye

To address the issue of non-specific binding of fluorescent probes to the glass, first, the ability of different glass-coating substrates to prevent non-specific binding of proteins was tested in a cell-free assay using three different proteins, conjugated with three widely-used dyes, Alexa 488, Alexa 546 and Atto647N, taking into account the background contribution of the substrate itself.

In order to find a strategy to minimise artefacts in Single-Molecule tracking experiments, the systematic investigation of cell growth substrates started from the analysis of the background properties of a panel of the most popular ones.

Figure 4-5 A compares both individual and the mean spot density for all the channels observed for untreated glass with that of treated glass, before the addition of fluorescently labelled protein. The figure shows comparable mean spot densities for all the treatments, although the density with FCS appears to be marginally higher, which is expected given that serum contains a cocktail of molecules, some of which are expected to be fluorescent. Also, for all coatings tested, spot density levels appear higher for 515 nm and 580 nm channels compared with the far-red channel. In addition to the higher density of spots, higher levels of background fluorescence haze were seen with both FCS and BSA (data not shown). Background fluorescence was also observed for star PEG: five out of the 9 dishes tested showed bright streaks and patches of autofluorescence in all detection channels (example shown in **Figure 4-5 B**), which might be due to product impurities.

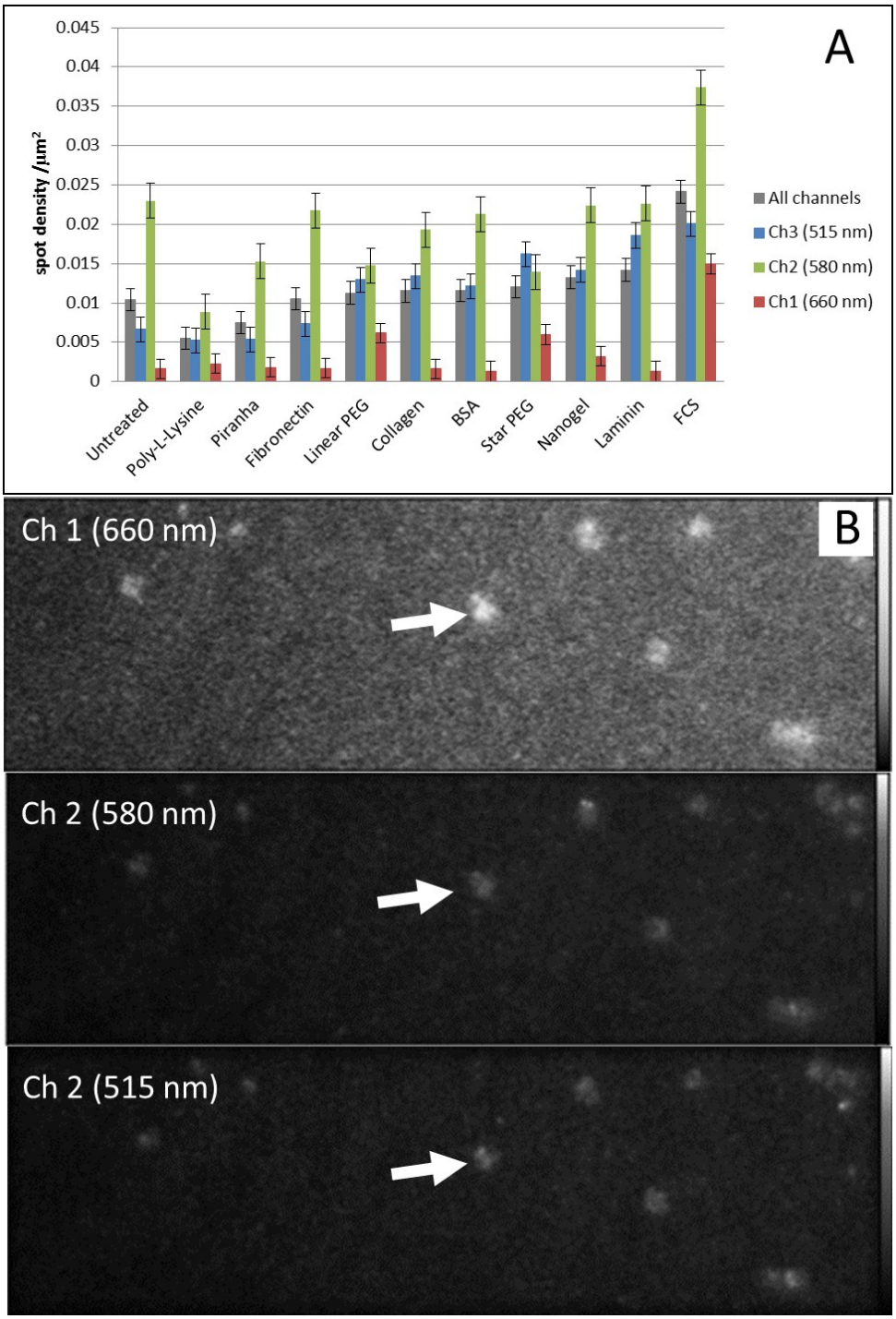

Figure 4-5 - Background fluorescence of treated surfaces. A) Mean spot density/µm^2 histograms for each surface treatment before exposure to fluorescently-labelled protein (grey columns represent the average calculated on all three channels - each data point corresponds to mean ± SEM from 135 areas, coloured columns represent the averages for each single channel – each data point corresponds to mean ± SEM from 45 areas)**. B)** TIRF fluorescence image of star PEG-treated dish, showing patches of background fluorescence in all detection channels (example arrowed) (bar 8 µm). All channels were imaged with the same gain (250) and exposure settings.

The relative efficacy of the coatings in preventing non-specific binding of proteins was determined by counting the number of Single-Molecule fluorescent spots, detected using Bayesian segmentation (see **Chapter 2**, **Paragraph 2.6**), adhering to different coated surfaces exposed to different fluorescently labelled proteins. The characteristics of the proteins and coatings employed are detailed in **Table 4-1**.

Figure 4-6 shows the average density of Single-Molecule fluorescent spots recorded for each treatment. The totals displayed in **Figure 4-6 A** illustrate the general trends observed. As expected, untreated glass has the highest level of non-specific binding. Vigorous cleaning with Piranha solution, a 1:3 mixture of H_2O_2 and H_2SO_4, only marginally reduces the level of binding. Moderate blocking of non-specific binding is observed for protein-based treatments, collagen being the least effective and FCS and BSA the most effective. Best blocking of non-specific binding is achieved by the PEG-based treatments, with nanogel and star-PEG [303] being slightly more effective than linear PEG.

The effectiveness of blocking of non-specific binding is also dependent on the protein in use, and on the fluorescent dye with which it is labelled. **Figure 4-6 B** and **C** show the average densities of fluorescent spots, grouped by dye molecule and by protein, respectively. These data show that the effect of the dye is, in most cases, significantly greater than the effect of the protein. Proteins labelled with Alexa 488 show lower levels of non-specific binding than proteins labelled with the other dyes, with most of the surface treatments showing similar levels of effectiveness. Alexa 546- and Atto 647N-labelled proteins show similar degrees of non-specific binding, although there are some differences in the effectiveness of surface treatments for the different dyes. For example, linear PEG works well with Alexa 546 and less well with Atto 647N, while the reverse is true for Nanogel. Differences in non-specific binding between different proteins are less pronounced. The better surface treatments, particularly linear PEG, appear to be marginally less effective against Affibody binding. Some specific effects can also be observed. For example, poly-L-lysine prevents binding of HEWL very effectively, but performs poorly with EGF, but the opposite is observed with BSA treatment. This would be expected given the expected net charge of the proteins and coats (see **Table 4-1**).

	Mw (Da)	pI	GRAVY[1]	Aliphatic index[2]	Net charge at pH 7
Ligand					
EGF	6,045	4.69	-0.506	55.09	-2.2
HEWL	14,313	9.32	-0.472	65.12	7.7
HER2 Affibody	6,736	8.9	-0.625	84.58	2
HER1 Affibody	13,860	4.65	-0.507	79.68	-5
Coating					
Poly-L-Lysine	variable (150,000-300,000)	9.6	-3.9	0	poly-cation
Fibronectin	269,110	5.28	-0.513	69.06	-66
Laminin[3]	~ 700,000	~ 5.3	~ -0.5	~ 70	-227
Collagen[4]	~ 300,000	~ 7.8	-0.261 to 0.919	~ 40 to 80	35
BSA	66,433	5.6	-0.475	76.14	-17
FCS	mixture of proteins	variable	variable	variable	variable
Linear PEG	5,000	-	-	-	0
Star PEG	10,000	-	-	-	0
Nanogel	mixture of Star PEG and BSA	-	-	-	-
Fluorophore					
Alexa Fluor 488	643	-	-	-	-2
Alexa Fluor 546	1,079	-	-	-	-2
Atto 647N	868	-	-	-	1

Table 4-1 - Characteristics of ligands, coatings, and fluorophores. [1]GRAVY is the grand average of hydropathicity; more negative values indicate greater hydrophilicity [304]; [2]Aliphatic index: the relative volume occupied by aliphatic side chains [305]; [3]Laminin values were taken as average of α1, β1, and γ1 chains; [4]Collagen values are representative of the range of collagen types as commercially prepared dishes do not specify type; – = not applicable or not known.

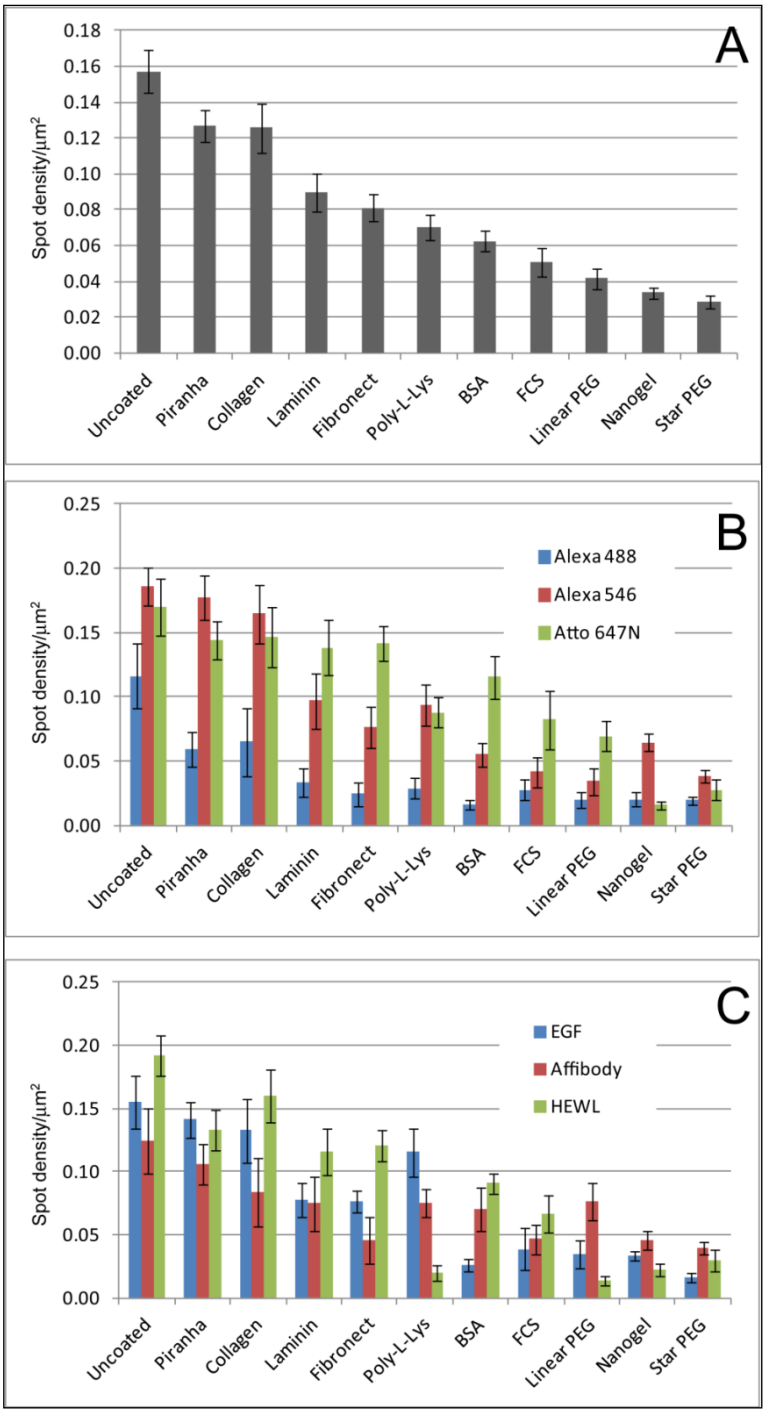

Figure 4-6 - Fluorescent spot densities of treated surfaces after exposure to labelled proteins. A) Histogram showing average spot densities/µm^2 for each surface treatment, after incubation with fluorescently-labelled proteins for 1200 seconds. Each data point corresponds to mean ± SEM from 135 areas, data from all protein-fluorophore combinations being averaged for each treatment. This reflects a general trend for the capability of preventing non-specific protein adhesion of each coat. **B)** Average spot densities/µm^2 for each fluorophore (each data point corresponds to mean ± SEM from 45 areas, 3 different proteins). **C)** Average spot densities/µm^2 for each protein, each data point corresponds to mean ± SEM from 45 areas, 3 different fluorophores).

Time-course data for non-specific binding for all the protein conjugates are shown in **Figure 4-7**. As expected, levels of non-specific binding increase with longer incubation times. In general, the individual proteins follow the trends observed in the average data shown in **Figure 4-6**. Some anomalous behaviours are observed, for example Affibody-Atto 647N shows relatively high levels of non-specific binding to linear PEG-treated glass, which is in general one of the more effective treatments. However, it is still reasonably effective with this protein if incubation times are kept short.

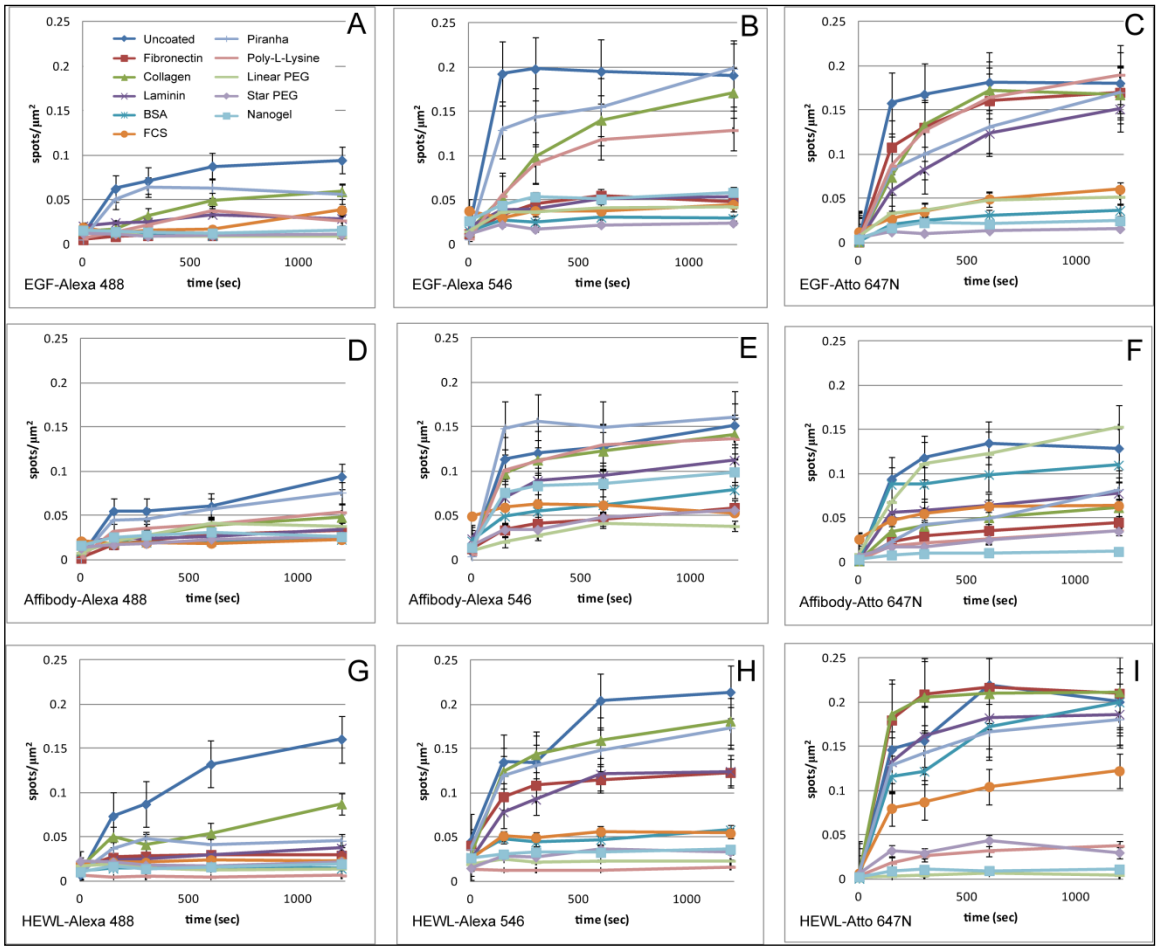

Figure 4-7 - Fluorescent spot density/µm^2 plots for treated surfaces exposed to labelled proteins for 150, 300, 600 and 1200 seconds at room temperature. A) EGF-Alexa 488; **B)** EGF-Alexa 546; **C)** EGF-Atto 647N; **D)** anti-HER2 Affibody-Alexa 488; **E**) anti-HER2 Affibody -Alexa 546; **F)** anti-HER2 Affibody -Atto 647N; **G)** HEWL C-Alexa 488; **H)** HEWL C -Alexa 546; **I)** HEWL C -Atto 647N. Each data point corresponds to mean ± SEM of 15 areas acquired from 3 independent samples.

4.2.4. Non-specific binding of proteins to glass can cause artefacts when tracking molecules on cell membranes

Non-specific binding of fluorescent labels to the glass substrate is also very problematic for Single-Molecule measurements on cultured cells. Adherent cells are not completely flat on the substrate and Affibodies are able to access a significant area between adherent cells and the glass, particularly when non-confluent cells are used. This permits labelling of receptors in the basal membrane, but also allows non-specific binding to the glass, resulting in fluorescent spots that are undistinguishable from membrane-bound labels .The effectiveness of surface treatments against non-specific binding of fluorescent proteins was investigated in the presence of cultured cells.

These experiments were performed using Chinese hamster ovary (CHO) cells expressing an HER1-eGFP fusion protein, incubated with anti-HER1 Affibody conjugated with Alexa 546 and Atto 647N. Cells were imaged in a 3 colour TIRF imaging system and single fluorescent molecules were tracked separately in each channel. The eGFP channel acts as a control, as the only fluorescent Single Molecules detected by the system are those expressed by the cells and localised in the plasma membrane, without the introduction of an additional label. Cell fluorescence contributed by HER1-eGFP molecules localised in trafficking vesicles or internal membranes is not detected as Single-Molecule spots, but rather as a diffuse haze.

Autofluorescence of the parental cell line was assessed by imaging unlabelled cells, seeded on the same substrates used in the main experiment, using all three lasers. **Figure 4-8** shows that the background signal of the cells is in the same range as that of the unlabelled dishes (**Figure 4-5 A**), indicating that the main contribution stems from impurities of the substrate rather than from significant cell autofluorescence.

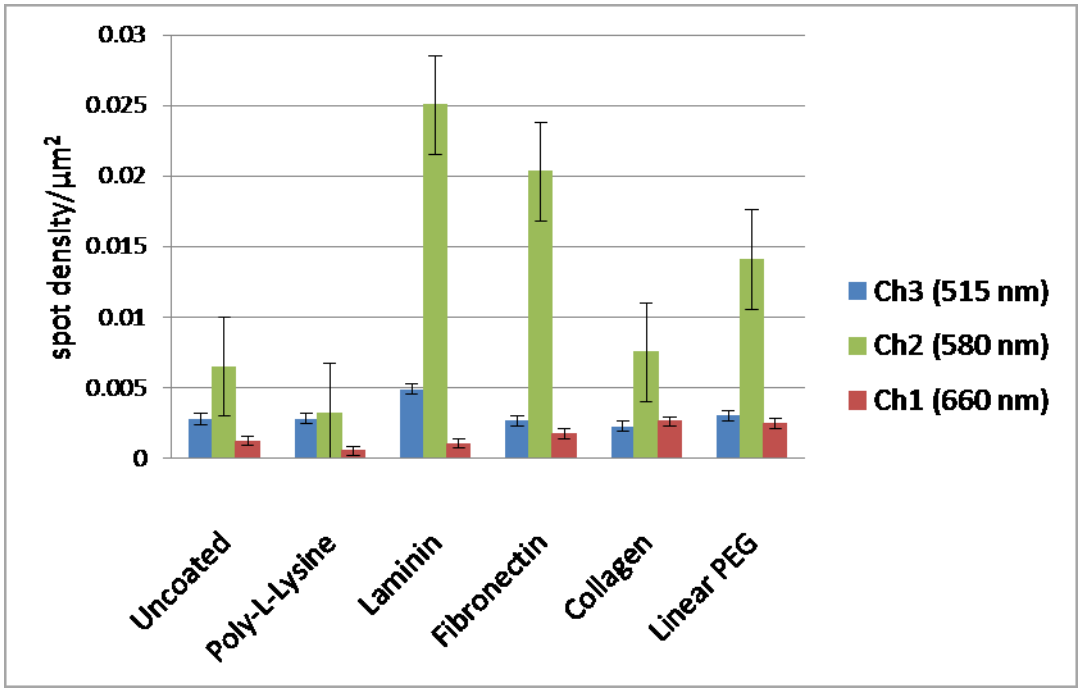

Figure 4-8 - Mean spot density/µm^2 histograms of background fluorescence of wt Cho cells seeded on different substrates. Each data point corresponds to mean ± SEM from at least 15 areas.

After proving that anti-HER1 Affibody is a specific probe for the HER1 receptor (see **Figure 3-2** in **Chapter 3**), assessment of non-specific binding to the substrate vs. specific binding of the Affibodies to HER1 was performed by monitoring the diffusion coefficients of the fluorescent spots observed in the eGFP, Alexa 546, and Atto 647N channels. In the absence of non-specific binding, all channels would be expected to show similar rates of diffusion, with similar numbers of non-mobile molecules. As non-specifically bound molecules were seen to be immobile in previous experiments, higher levels of non-mobile molecules in the Alexa 546 and Atto 647N channels with respect to the eGFP channel would indicate the presence of non-specific binding.

A number of surface treatments typically used in Single-Molecule experiments on cells were investigated: 0.01 % poly-L-lysine, 25 µg/ml fibronectin, 25 µg/ml laminin, collagen, 1 % BSA, and linear PEG. Star PEG and nanogel were not used for cell experiments, at this stage, because of higher levels of background autofluorescence.
As cells do not adhere to linear PEG surfaces, the coating was doped with GRGDS peptide [302]. In order to confirm that GRGDS peptide was correctly incorporated into the PEG layer and retained even after cell culture and labelling procedures including multiple washing steps, PEG layers containing FITC-labelled GRGDS were prepared and imaged in TIRF mode (**Figure**

4-9). The figure shows that FITC-GRGDS is still present on the glass after routine sample handling.

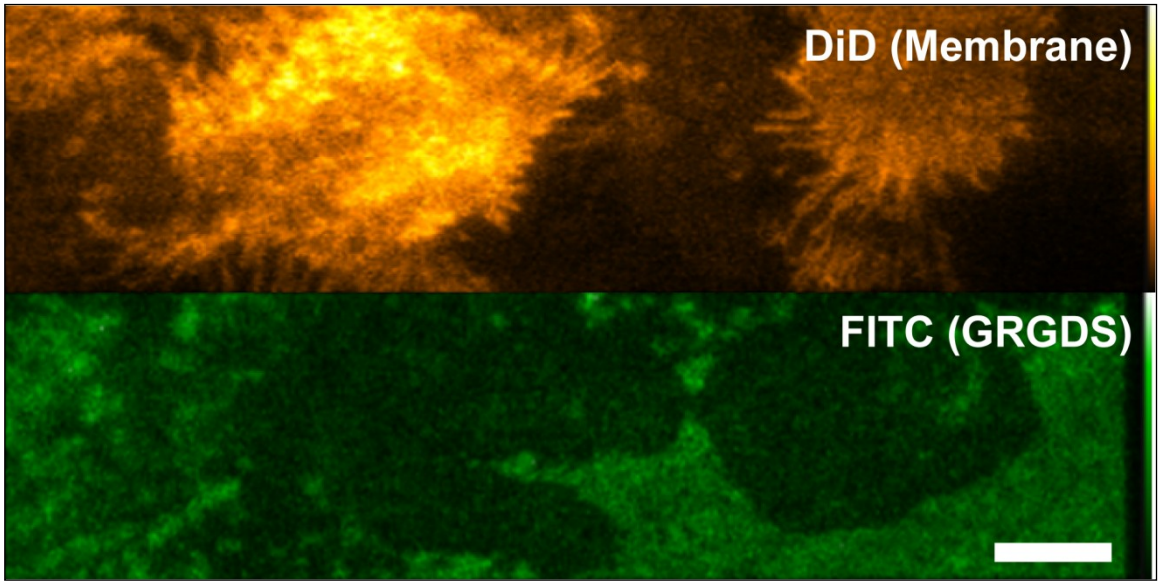

Figure 4-9 - TIRF image of PEG-treated glass doped with fluorescent GRGDS peptide and T47D cells treated with DiD membrane probe to highlight membrane protrusions and membrane-glass contact areas (bar 8 μm).

In **Figure 4-9**, it looks like cells are present preferentially in areas of lower FITC-GRGDS staining. This could be due to a preference of Cho cells towards areas of lower GRGDS density, but the low signal from the peptide could be also due to active uptake from the cells or to FRET between FITC and the membrane probe.

Cells grew well on both uncoated and linear PEG/GRGDS substrates, and typical images are shown in **Figure 4-10**. The motion of fluorescent spots was tracked and percentages of immobile fluorescent spots are plotted in **Figure 4-11**.

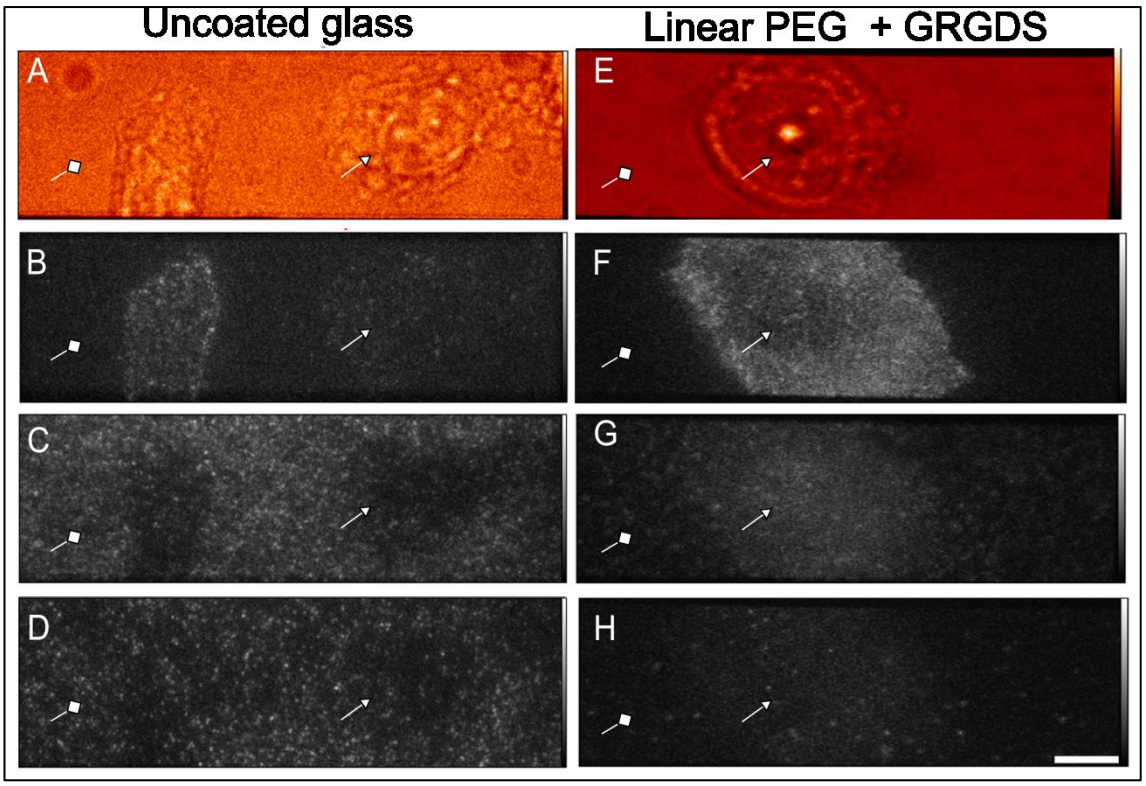

Figure 4-10 - Representative images of cells exposed to labelled proteins. Panels A-D: representative images of CHO-HER1-eGFP cells grown on uncoated glass. **A)** White light; **B)** HER1-eGFP; **C)** anti-HER1 Affibody Alexa 546 ; **D)** anti-HER1 Affibody Atto 647N. **Panels E-H:** representative images of CHO-HER1-eGFP cells grown on linear-PEG + 0.4 mM GRGDS peptide-coated glass. **E)** White light**; F)** HER1-eGFP**; G)** anti-HER1 Affibody Alexa 546**; H)** anti-HER1 Affibody Atto 647N. White arrow = area occupied by a cell. White diamond = coating only (bar 10 µm).

This figure shows that on uncoated glass there is a high density of fluorescent spots in areas unoccupied by cells (white diamonds - compare panels **C-D** with panel **B**), with few if any spots on the surface of the cells. When cells are seeded on Linear PEG-coated substrates, the amount of spots on areas unoccupied by cells is greatly reduced (white diamonds - compare panels **G-H** with panel **F**). The treatment is not supposed to have any effect on the amount of spots present on the surface of the cells (white arrows).

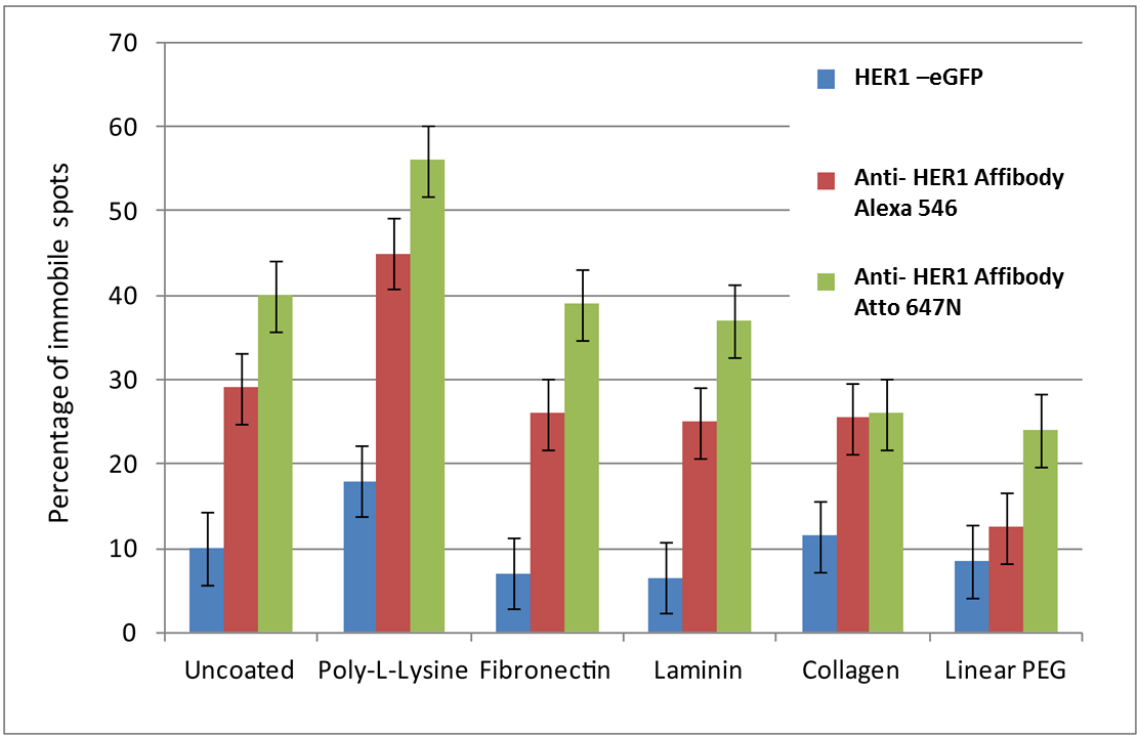

Figure 4-11 - Histogram showing percentage of tracks with diffusion coefficient falling in the *D*=0 bin of the *D* distribution histogram in the three acquisition channels on CHO-HER1-eGFP cells grown on differently coated glass surfaces and labelled with anti-HER1 Affibody Alexa 546 and Atto 647N for 15 minutes at 37°C. Each datapoint corresponds to mean ± SEM of 15 areas acquired from 3 independent samples.

In general, there was a higher level of non-specific binding for Affibody labelled with Atto 647N than with Alexa 546. Both collagen and linear PEG treatment significantly reduced binding for Atto 647N Affibody, but only linear PEG treatment resulted in significantly lowered binding for Alexa 546 Affibody. None of the other treatments significantly reduced non-specific binding, and poly-L-lysine treatment increased binding for Affibodies labelled with either dye. The effect of non-specific binding on tracking experiments can be seen in **Figure 4-12**, which compares the motion of anti-HER1 Affibody labelled with Alexa 546 and Atto 647N on CHO cells cultured on untreated glass, and glass treated with linear PEG doped with GRGDS peptide. Comparison of the diffusion coefficient distribution histograms in **Figure 4-12 A** (untreated) and **B** (linear PEG) reveals that the motion of anti-HER1 Affibody in the latter experiment is closer to the motion of the reference eGFP; for uncoated glass, the distribution of Affibody mobility is skewed towards slower moving and stationary molecules. Similarly, in the mean squared displacement plots shown in **Figure 4-12 C** (untreated) and **D** (linear PEG), displacements in the linear PEG experiment are much closer to the displacements in the

reference channel than for untreated glass. Varying offsets at t=0 are observed in the MSD plots. These are likely to be the result of different levels of spot localization errors, a function of the signal-to-noise of individual data sets.

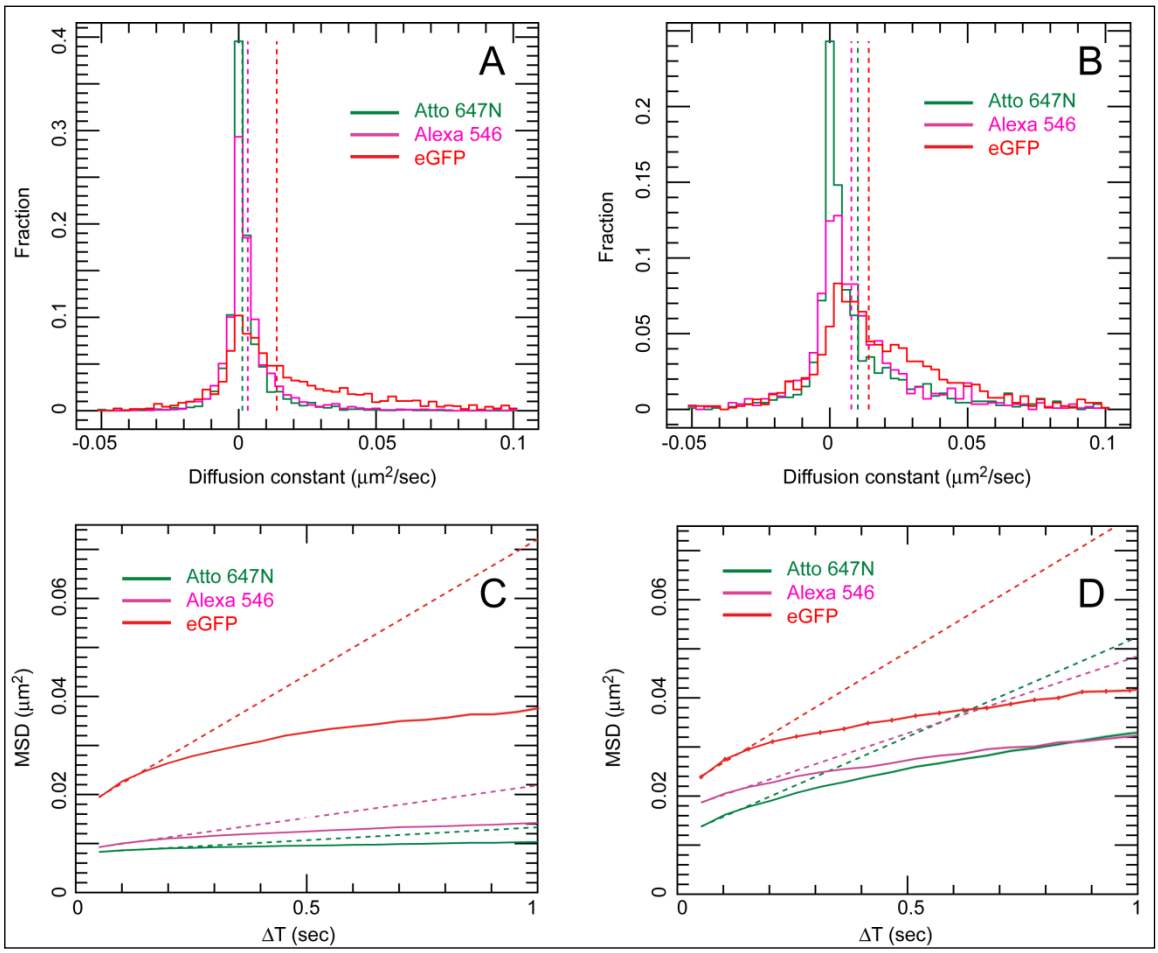

Figure 4-12 - Side-by-side comparison of mean squared displacement (MSD) curves and diffusion coefficient (*D*) histograms from CHO-HER1-eGFP cells grown on uncoated glass vs. linear-PEG+0.4 mM GRGDS-coated glass. Data were plotted from at least 15 areas acquired from 3 independent samples. Each MSD value comes from at least 6500 (ranging up to 300,000) individual ΔT, resulting in very small standard error in the MSD. Error bars are plotted but too small to be visible.

Panels A (uncoated) and B (linear PEG + GRGDS): diffusion coefficient histogram of tracked spots. HER1-eGFP (red), anti-HER1 Affibody Alexa 546 (magenta), anti-HER1 Affibody Atto 647N (green). Dotted lines show the mean *D* coefficient extrapolation.

Panels C (uncoated) and D (linear PEG + GRGDS): Mean Square displacement plot. HER1-eGFP (red), anti-HER1 Affibody Alexa 546 (magenta), anti-HER1 Affibody Atto 647N (green). Dotted lines show the mean *D* coefficient extrapolation.

4.2.5. Optimisation of substrate composition for experiments in T47D cell model

In the stated conditions, CHO-HER1-eGFP were able to grow on Linear PEG functionalized with as little as 0.2 μM GRGDS peptide (data not shown), albeit at the expense of faster apoptosis under serum deprivation conditions during experimental time. Using GRGDS peptide at a concentration of 0.4 mM resulted in a surface that was able to sustain the growth of CHO-HER1-eGFP, yielding confluent monolayers of cells with a normal morphology (flat, polygonal, and elongated, compared with a rounded appearance and ruffled membrane for unhealthy cells) and HER1-eGFP expression level. GRGDS peptide is known to bind to αvβ3, α5β1 and αvβ5 integrins [302,306]. Different peptides, such as laminin-derived YIGRS and IKVAV [271,306,307] could be better suited to cell lines expressing a different complement of adhesion receptors.

In order to determine which peptide or mix is better suited to the needs of the main breast cancer cell model used in this project, the T47D cell line, an MTT growth assay was performed on cells grown on different cell substrates for 48 h and then starved for 2 h, mimicking as closely as possible the cell culture steps usually performed prior to cell labelling. Poly-L-Lysine was used as a positive control. Three different concentrations of GRGDS peptide (1 μM, 100 μM and 0.4 mM), three concentrations of IKVAV peptide (30 nM, 100 nM and 300 nM) and two concentrations of YIGSR peptide (62 nM and 103 nM) were tested, alongside 25 μg/ml fibronectin and 25 μg/ml laminin, proteins which contain the test peptides and which would serve as controls for peptide activity. Samples were assayed in triplicate and the background absorbance of cells at 690 nm was subtracted from the absorbance of MTT at 570 nm. The absorbance of blank wells was used as a baseline reading and subtracted from the data.

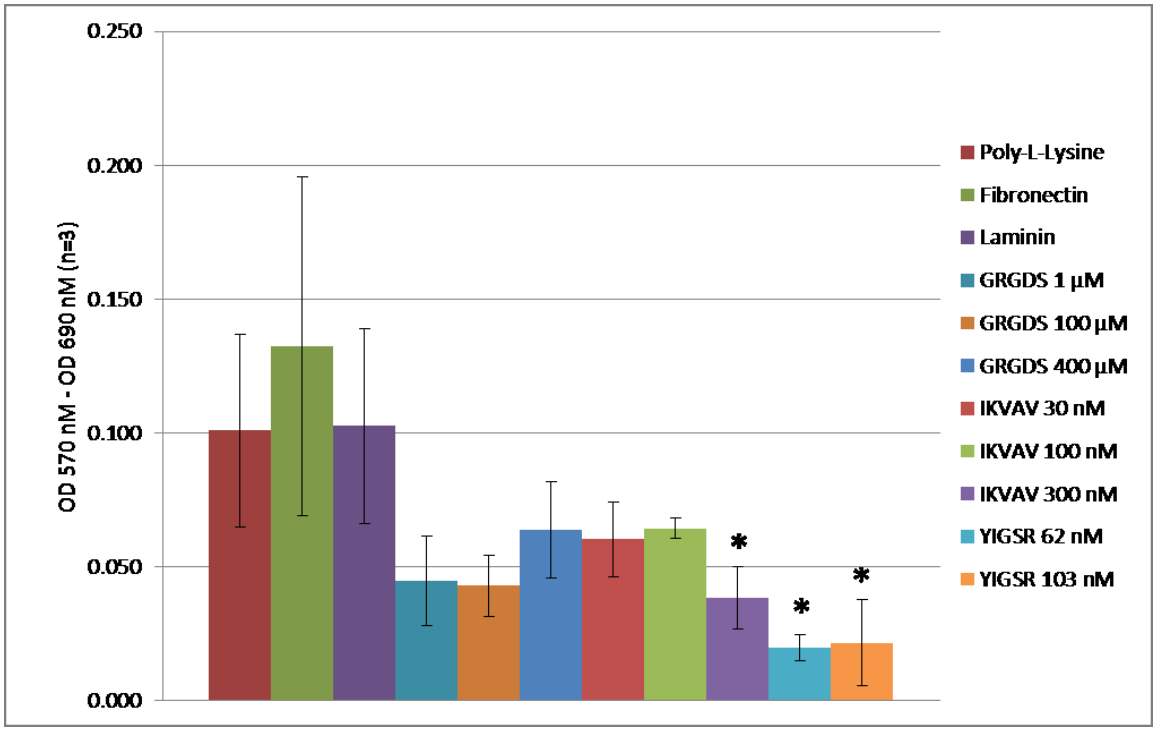

Figure 4-13 – MTT growth assay of T47D cells on different glass coating substrates. T47D cells were cultured for 48h in complete medium and then starved for 2 h before MTT assay was performed. Absorbance at 570 nm was normalised against background cell absorbance at 690 nm. All measures were performed in triplicate. Two-tailed t-Test was calculated for each condition using Poly-L-Lysine (positive control) as a reference dataset. * = P<0.05

Figure 4-13 shows that, while there is a trend towards decreased viability, cell growth on Linear PEG supplemented with all concentrations of GRGDS peptide and 30 nM or 100 nM IKVAV (substrate for α6β4 integrins) is not significantly different from growth on Poly-L-Lysine or on the parental proteins fibronectin and laminin. Cell growth on 300 nM IKVAV, instead, was significantly hindered (P= 0.046), a finding which can be explained with a requirement for a certain range of peptide densities to foster optimal cell growth. Despite being derived from laminin as well, both concentrations of the YIGSR sequence (also a binding site for α6β4 integrins) yielded inferior results, promoting significantly less (P = 0.018 and 0.025 respectively) growth of T47D on PEG surfaces.

GRGDS 0.4 mM and IKVAV 30 nM were both tested in full-scale tracking experiments with T47D cells, however cells were poorly attached and tended to detach under serum deprivation conditions (data not shown), which lowered data quality and increased the difficulty of carrying experiments to completion.

4.3. Discussion

The results reported in this chapter show that typical levels of non-specific binding can significantly affect measured diffusion coefficients and MSD curves in SPT experiments. This problem cannot be eliminated by discounting data from immobile molecules, as it has been reported that transmembrane receptors, and in particular HER1, can be immobilized or slowed down for variable periods of time when they are actively engaged in signalling [12,110,194,308], or even in the resting state [308,309]. Immobilisation of HER1 molecules has been observed in different cell lines and with different techniques such as Fluorescence Recovery After Photobleaching (FRAP) [309] and Single-Particle Tracking [12,109,110,308]. Possible mechanisms underlying the immobilisation of HER1 molecules are likely to be manifold. HER1 is known to bind to actin filaments [113] and indeed the depolymerisation of actin can alter the diffusional behaviour of the receptor [110,309,310]. HER1 is also associated with lipid rafts (reviewed in [311] and [312]), which regulate its activation and diffusion. Disruption of caveolae [308] and cholesterol depletion [110,310] are also able to alter the immobile fraction of HER1 in the membrane, at least in some cell systems. Another candidate for receptor immobilisation is the galectin lattice that cross-links glycoproteins on the extracellular side of the membrane. The disruption of this lattice leads to increased mobility of HER1 [313]. Finally, the immobilisation of active receptors is linked to the activity of the tyrosine kinase domain [109]. The presence of an immobile fraction of basal state HER1 [12,308,309] is confirmed in by the observed percentage (5-15%) of immobile molecules in the eGFP reference channel. This variability may be due to differential activation of adhesion receptors by the substrates: fibronectin, laminin, collagen and GRGDS peptide activate different complements of integrin subunits (reviewed in [306,314]), while Poly-L-Lysine is supposed to act by favouring electrostatic interactions with the cell membrane. The differential effect of different substrates on cell behaviour (migration, survival, proliferation) has been reported in the biomaterials field [315–320]. In the case under examination, the effect of the choice of biomaterial can be more striking due to the fact that integrin signalling is known to cross-talk with HER1 signalling, leading to ligand-independent activation of the receptor (reviewed in [194]). Differential activation of integrins by growth substrates could then modify the basal levels of HER1 activation, which in turn can have an effect on its diffusive behaviour and its interactions.

Activation-dependent HER1 immobilization [12,109,110,308] was postulated as a feature of its

signalling which might have a significant impact on the regulation and localisation of signal transmission. Since it is impossible to separate truly immobilised specific spots from non-specific signal arising from artefacts on the glass, it is essential to keep the levels of non-specific binding to a minimum for all Single-Molecule experiments in order to quantitatively assess phenomena such as this.

When Single-Molecule experiments involve measurements in cells, the choice of surface treatment is made more complex by the fact that coatings which prevent non-specific binding of proteins tend to hinder the interactions that allow cells to adhere to surfaces. On the other hand, adsorption of proteins from the cell culture medium, extracellular proteases and extracellular matrix (ECM) deposition by cells can modify the culture substrate [306]. Modification of substrates by cells, such as matrix degradation by extracellular matrix metalloproteases, may make the substrates more susceptible to adsorption of spurious proteins, which might explain why coatings such as poly-L-lysine, fibronectin, collagen and laminin, which were moderately effective in preventing non-specific binding in the absence of cells, were ineffective when cells were present (see above). The most effective treatments for non-cell measurements were those based on PEG, and the results with linear PEG confirm this to be the case for cell experiments as well.

Growing cells on synthetic biomaterial substrates, such as PEG, is a staple technique of tissue engineering and regenerative medicine, where PEG is employed due to its ability to repel non-specific protein adhesion ([321] and reviewed in [322–324]). PEG is an uncharged, hydrophilic polymer which displays low toxicity to cells. It is able to undergo extensive hydration in aqueous mediums, by virtue of displaying two hydrogen-bond acceptor groups for each repeat. This, along with its conformational flexibility, causes a volume restriction effect that hinders protein deposition on PEG layers [325]. The compression of the polymer layer by incoming proteins is unfavourable from a thermodynamic standpoint [326].While these properties, and the fact that the polymer is not biodegradable [322], make PEG an ideal and stable reagent for passivation, they also make cell adhesion problematic and anchorage-dependent cell viability low, therefore PEG surfaces and other biomaterials are routinely doped with adhesion peptides and biomolecules derived from ECM proteins and proteoglycans to encourage cells to grow, divide and differentiate [314]. Various adhesion peptides are available, GRGDS being one of the most widely used [306].

Following disappointing results in growing T47D cells on doped PEG substrates, the use of PEG-BSA nanogel as the main cell culture substrate for tracking experiments appeared to be the best option. This composite biomaterial is more efficient than Linear PEG and than its components Star PEG and BSA in lowering non-specific adhesion of proteins [1,274], possibly because PEG polymers can display weak attractive interactions with nonpolar or hydrophobic side chains on protein surfaces, while BSA lacks such attractive interactions, and interacts with other proteins in solution only in terms of excluded volume [327]. PEG-BSA nanogels, contrary to pure PEG layers, are also able to sustain cell growth without the need for adhesive peptide doping, possibly through interactions between BSA and the cells. This could be beneficial because adhesive peptides are difficult to consistently incorporate in PEG layers at the correct density, and integrin binding and activation can alter the properties of the system under study [320]. This hypothesis seems to be supported by the finding that T47D cells display an increased percentage of immobile anti-HER1 Affibody-Alexa488 spots when cultured on laminin (**Figure 4-14**). T47D cells express a relatively high level of integrin α6β4 [191,328] , which is the laminin receptor [306], and is also involved in crosstalk with HER1 to promote cell motility and invasion [194]. An analogous increase in immobile spot fraction also happens for Cho-HER1-eGFP cells cultured on collagen but not on laminin, possibly due to differences in integrin repertoire and levels between the two cell lines.

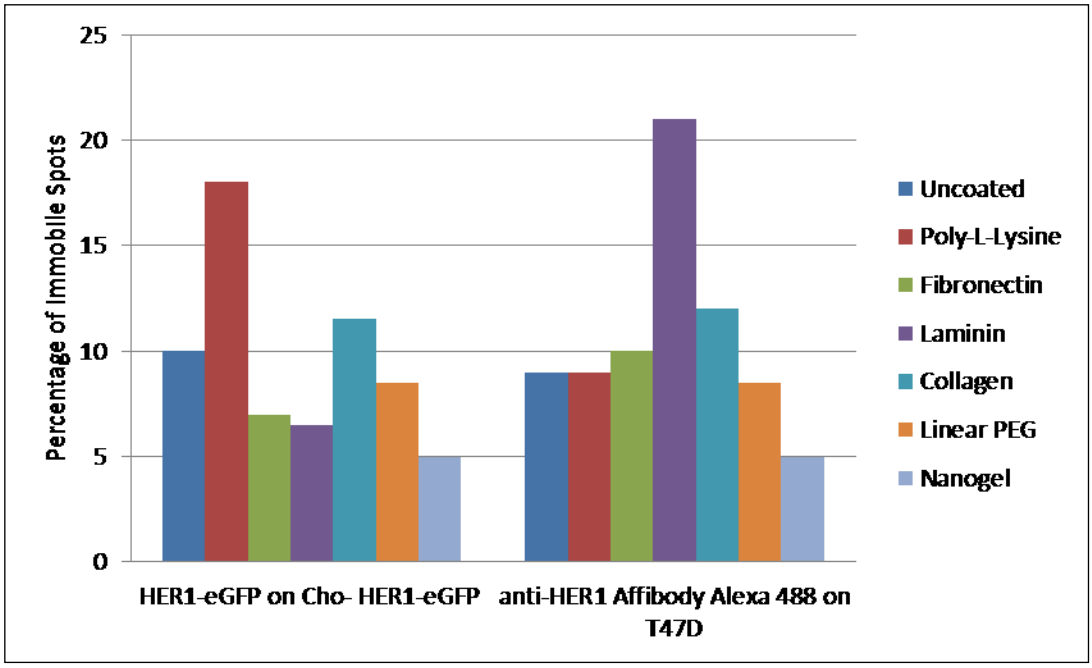

Figure 4-14 – Mean immobile spots percentages for HER1-eGFP on a stably transfected Cho cell line and anti-HER1 Affibody Alexa 488 on T47D. Cho-EGFR-eGFP or T47D cells were cultured on different substrates for 48 h, and then starved for 2 h. Cho-EGFR-eGFP were imaged at 20 fps at 37°C without any label, while T47D cells were labelled with 4 nM anti-HER1 Affibody for 10' at 37°C prior to imaging. Percentages of immobile spots were calculated from the zero-bin of the respective diffusion coefficient histograms, calculated on at least 15 areas acquired from at least three independent biological replicates.

5. Investigating the Effect of the Electrostatic Characteristics of Dyes on Single-Particle Tracking Artefacts

The core material of this chapter has been published in Zanetti-Domingues *et al.* (2013) [2].

5.1. Introduction

The systematic study of the effects of various surface treatments (**Chapter 4**) shows that levels of non-specific binding are the result of the interaction of three factors: the glass-coating treatment employed, the carrier protein, and the fluorescent dye with which the protein is labelled. Lower levels of non-specific binding were consistently observed for proteins labelled with Alexa 488, while Atto 647N-labelled proteins showed the highest levels of non-specific binding. This may be caused by the different electrostatic characteristics of the dyes; Alexa 488 is negatively charged and hydrophilic, whereas Atto 647N has a positive charge and is hydrophobic [329–331]. Careful selection of the dye may therefore be an important starting point when planning Single-Molecule experiments. If a choice of dyes is available, it would be advisable to perform test experiments and select the dye that results in the lowest levels of non-specific binding. However, other considerations such as appropriate spectral characteristics and photostability will affect dye choice.

In order to choose a dye best suited to the project requirements, several different fluorescent dyes suitable for the 491 nm, 561 nm and 638 nm laser lines were tested. Specifically, their Single-Molecule photophysical properties, as well as their propensity to promote non-specific binding of labelled probes to coated glass surfaces, were systematically analysed. Alexa 488 was used as a reference dye due to its behaviour in the set of experiments described in **Chapter 4**. Due to the relative ease of cell propagation and growth on PEG-BSA Nanogel films compared with doped Linear PEG surfaces, experiments were conducted on cells grown on this substrate.

5.2. Results

5.2.1. Overview of fluorescent dyes

Many different alternative dyes are available for every spectral class, each characterized by extinction coefficient, photostability, quantum yield, pH sensitivity and water solubility. Alexa Fluor and Atto dyes are commonly used for Single-Molecule applications, alongside cyanine dyes such as Cy3. Atto 647N is a popular dye in Single-Molecule experiments due to its outstanding brightness and photostability [332]. However, this dye is positively charged and hydrophobic [330] and high levels of non-specific binding of Atto 647N conjugates have been reported previously [329]. CF-series dyes are a new class of dyes derived from the structures of coumarin, pyrene, rhodamine or cyanine [333], for which improved water solubility, brightness and stability, as well as specificity when conjugated proteins and oligonucleotides are claimed [334], all characteristics which, if verified, would be appealing for Single-Molecule work.

Publicly available information about the dyes used in this paper is summarised in **Table 5-1**. Net molecular charge ranges from strongly negative (Alexa Fluor 488) to moderately positive (Atto 647N). There is also a significant variation in the hydrophobicity of the dyes, as expressed by the log of the distribution coefficient, logD, which is a measure of the expected ratio of dye concentrations in water and a non-polar solvent (octanol). LogD is defined in **Equation 5-1**:

$$\log D_{\mathrm{oct/wat}} = \log\left(\frac{[\mathrm{solute}]_{\mathrm{octanol}}}{[\mathrm{solute}]_{\mathrm{ionized\,water}} + [\mathrm{solute}]_{\mathrm{neutral\,water}}}\right)$$

Equation 5-1 – Calculation of the logD pH7.4 of a small molecule

So, a molecule with a negative value of logD (e.g. Alexa Fluor 488) is hydrophilic, and a molecule with a positive logD (Atto 647N) is hydrophobic.

All dyes used in this optimisation phase were in their maleimide form and were conjugated to an anti-HER1 Affibody molecule following manufacturer's instructions. Each spectral class is represented by at least three different dyes and a wide range of net charge and hydrophobicity values is covered.

Dye	excitation max (nm)	emission max (nm)	ε ($cm^{-1}M^{-1}$)	QY	net charge pH 7.4[1]	logD at pH 7.4[1]
Alexa Fluor 488 [23]	493	519	71,000	0.92	-3.94	-10.48
CF 488A [12]	490	515	70,000	N/A	-3	-8.83
Fluorescein	494	518	70,000	0.76	-1.9	-1.30
Bodipy FL	505	513	80,000	0.71	0	-1.99
TMR6	544	572	84,000	~ 0.2	0	-5.6
Alexa Fluor 546 [23]	561	572	104,000	0.79	-3.41	-2.53
Alexa Fluor 555 [23]	553	568	150,000	0.1	Unavailable	Unavailable
Cy3 [24]	550	570	150,000	0.15	0	+3.03
Rhodamine Red C2	560	580	N/A	N/A	-0.99	+1.53
CF 568 [12]	562	583	100,000	N/A	-3	-3.74
Atto 565	563	592	120,000	0.9	0	-0.83
Atto 647N [9]	644	669	150,000	0.65	+0.61	+1.96
CF 633 [12]	630	650	100,000	N/A	-2	-5.44
CF 640R [12]	642	662	105,000	N/A	-3	-10.29

Table 5-1 - Summary of dye characteristics.

ε = molar extinction coefficient; QY = quantum yield.

[1]Calculated from structures using "Marvin Sketch" software (Chemaxon). Structures of CF dyes are unavailable but charge and logD were calculated by the manufacturer, using the same method.

Structure-derived characteristics, such as net charge and logD could not be obtained for Alexa 555, due to patent issues. Extinction coefficient and quantum yield were not publicly available for Rhodamine Red C2.

Raw data of T47D cells labelled at 37°C for 10’ with 4 nM of all conjugates is shown in **Figure 5-1**.

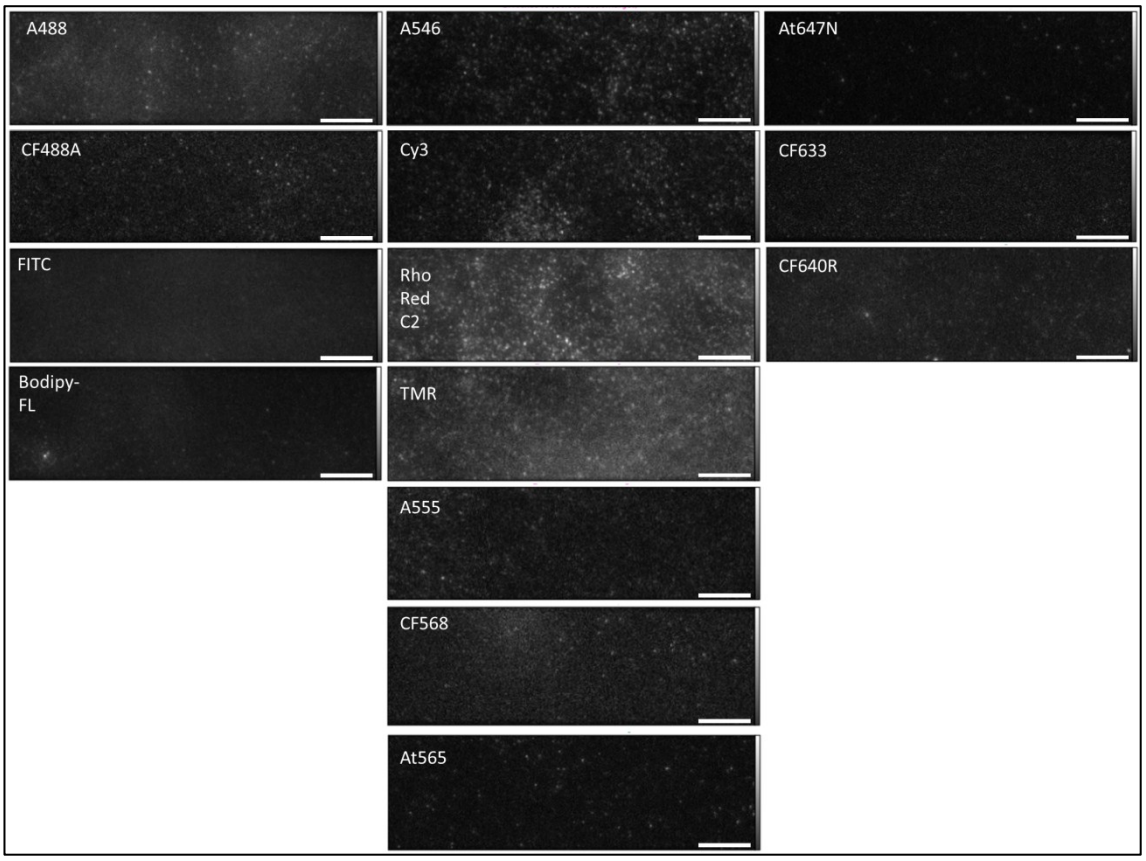

Figure 5-1 – Labelling of T47D cells with all anti-HER1 Affibody conjugates. Bars (white) = 10 µm.

5.2.2. Assessment of dye brightness and photostability for Single-Molecule methods

Photostability and high brightness are essential characteristics for dyes used in Single-Molecule methods, in order to achieve the highest possible signal-to-noise-ratios. Single-Molecule brightness and photostability of the dye conjugates were tested under conditions suitable for multi-colour Single-Molecule imaging. T47D cells were labelled with anti-HER1 Affibody probes and imaged on a TIRF microscope. The mean number of photons emitted per single molecule and photobleaching time constants measured for each dye are shown in **Table 5-2**.
These measurements give a guide to how the dyes perform in our system for Single-Molecule experiments, but will vary depending on the wavelength of illumination, laser power, choice of emission filter, and buffer conditions such as pH. Quantum yield and extinction coefficients also give a useful guide to a dye’s photophysical characteristics and expected performance; these can be obtained from the manufacturers.

Dye	Excitation wavelength (nm)	Laser flux exiting microscope objective ($\mu W/\mu m^2$)	Mean photon detection rate from a single molecule (s^{-1})	Apparent photobleaching time constant (s)
Alexa 488	491	3.2	1164 ± 181	15.1 ± 0.2
Bodipy FL	491	3.2	2586 ± 393	21.3 ± 0.6
CF488	491	3.2	1200 ± 213	17.8 ± 0.4
Fluorescein	491	3.2	2436 ± 350	1.4 ± 0.1
Alexa546	561	3.2	2697 ± 230	24.0 ± 0.1
Alexa555	561	3.2	1112 ± 223	33.6 ± 0.3
Atto 565	561	3.2	2850 ± 535	14.5 ± 0.2
CF568	561	3.2	1042 ± 194	40.7 ± 0.5
Cy3	561	3.2	986 ± 198	25.3 ± 0.2
RhoRed C2	561	3.2	3268 ± 453	8.3 ± 0.1
TMR6	561	3.2	832 ± 223	7.5 ± 0.1
Atto 647N	638	3.4	3290 ± 231	36.0 ± 0.2
CF633	638	3.4	851 ± 170	16.4 ± 0.1
CF640R	638	3.4	1084 ± 202	37.7 ± 0.2

Table 5-2 - Single-Molecule brightness and apparent bleaching lifetimes of dyes

For the dyes excited at 491 nm, Alexa 488 and CF488 produce similar numbers of photons per image frame, and photobleaching time constants show similar photostability. More photons are produced by Bodipy FL and Fluorescein, with Bodipy FL showing good photostability, unlike fluorescein, which under the conditions used has the shortest photobleaching time constant of all the dyes. Based on photophysical characteristics alone, Bodipy FL would appear to be the dye of choice for this wavelength range.

Of the 561 nm-excited dyes, Rhodamine Red C2, Atto 565, and Alexa 546 emit the highest numbers of photons per image frame. Of these dyes, Alexa 546 is the most photostable, with poor photostability being observed for Rhodamine Red C2. CF568, whilst emitting fewer photons, has the highest photostability of all the dyes in this wavelength range.

For 638 nm excitation, Atto 647N has a high number of emitted photons, and good photostability, and based only on photophysical characteristics would be the best dye excited at this wavelength. CF640R also has good photostability, but produces fewer photons. CF633 is not optimally excited at 638 nm, and also displays poor photostability.

5.2.3. Hydrophobicity is the major determinant for non-specific binding

Good photophysical characteristics are necessary, but not sufficient for a dye to be suitable for Single-Molecule imaging. A dye conjugate needs to be not only bright and stable, but also to be specific to its target so as to minimise artifacts in the data. The specificity of all dye conjugates was therefore investigated by analyzing their motility when bound to EGF receptors on the surface of T47D cells, cultured on PEG-BSA nanogel coated substrates [274].

Mean instantaneous diffusion coefficient (*D*) values were previously used (**Chapter 4**) as a measure of the mobility of dye conjugates bound to receptors in the plasma membrane and it has been shown that anti-HER1 Affibody conjugated to Alexa Fluor 488 shows similar levels of mobility, in terms of immobile populations, when bound to HER1 in cells compared to endogenously labeled HER1-GFP [1]. It was therefore decided to use the mean value of *D* calculated for Alexa Fluor 488-labelled Affibody as a reference for the mobility of Affibody conjugated to other dyes. Mean *D* values calculated for all the dye conjugates are shown in **Figure 5-2**.

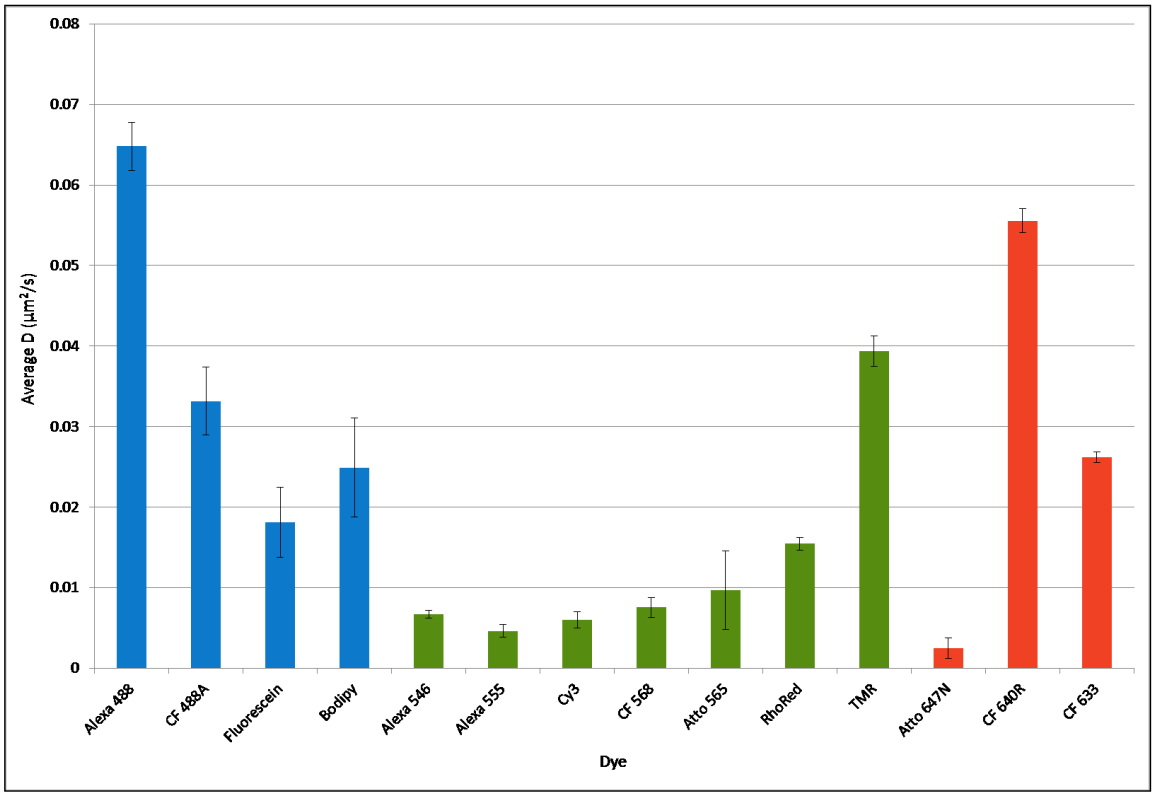

Figure 5-2 - Bar chart showing mean instantaneous *D* fit values for different anti-HER1 Affibody conjugates. Each datapoint corresponds to mean ± SEM of at least 10 areas acquired from 3 independent samples. Blue bars indicate dyes excited at 491 nm, green at 561 nm, and red at 638 nm.

The figure indicates that all the other dye conjugates have lower mobility than Alexa Fluor 488. This was confirmed by a comparison with Alexa Fluor 488 using a two sample independent t-test. All conjugates displayed significantly lower mobility ($P \leq 0.001$) than the reference, except CF640R ($P = 0.047$). This statistical test assumes a Gaussian distribution of the data to be compared, however, this is not the case for the average *D* coefficient of HER1 Affibody molecules on cell membrane, and therefore the assessment was repeated using the Kolmogorov-Smirnov (K-S) test [335,336]. This test is non-parametric and therefore does not assume a particular underlying distribution for the data and requires only that the distribution for each sample is continuous. All conjugates displayed significantly lower mobility ($P \leq 0.001$) than the reference, except CF640R ($P = 0.097$).

Full K-S test results are displayed in **Figure 5-3**.

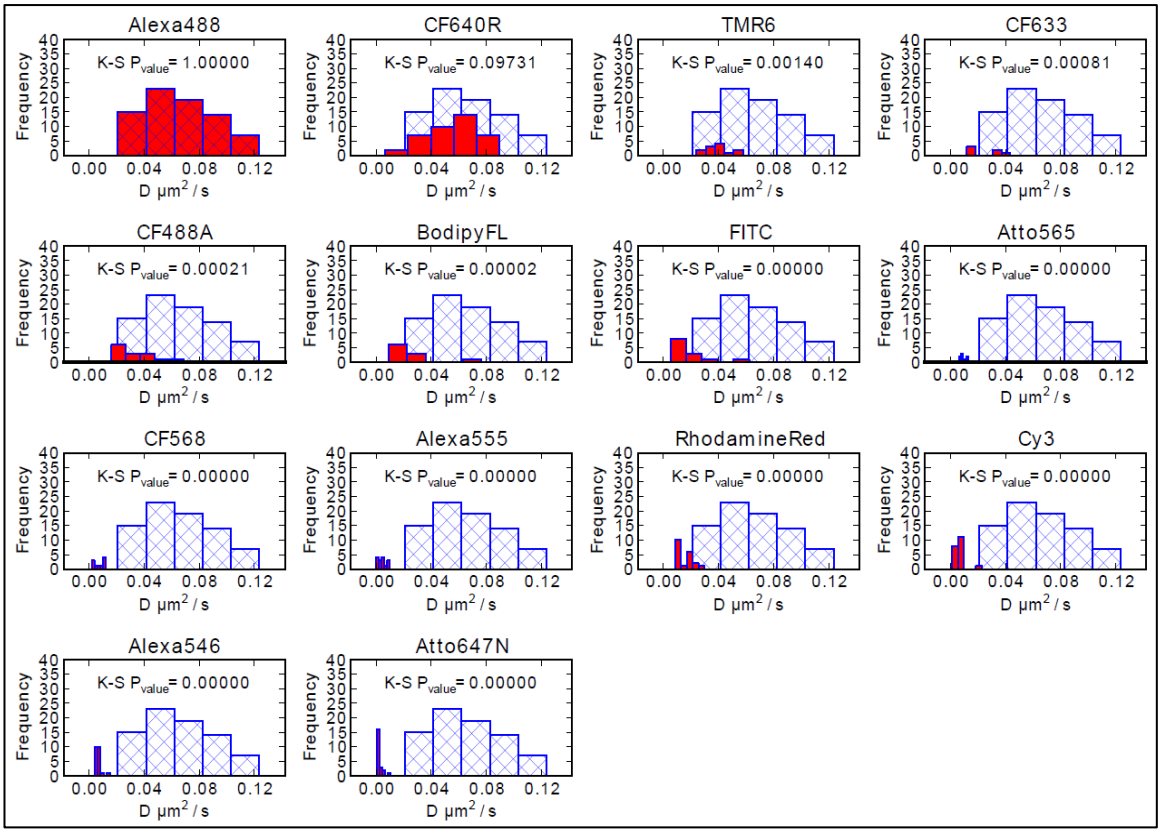

Figure 5-3 – Kolmogorov-Smirnov test results for all conjugates. Distributions of *D* values (red histograms) were compared to the Alexa 488 distribution (patterned histograms).

Both statistical tests (t-Test and K-S test) show that the dyes excited at 561 nm performed particularly poorly, the best being TMR, which still shows only two thirds the mobility of the reference dye. Of the red dyes, CF 640R performs well, with a mobility close to that of the reference.

The hypothesis that physicochemical properties of the dyes could be used to predict the degree of non-specific binding, and therefore be used to guide the selection of dyes for Single-Molecule experiments, was then investigated. Two possible properties were investigated, net charge and hydrophobicity (logD). **Figure 5-4** shows plots of diffusion coefficient vs logD (A) and vs net charge (B). The data show a strong correlation between logD and dye conjugate mobility (R^2 0.75), but only a weak correlation between net charge and mobility (R^2 0.2). This demonstrates that dye hydrophobicity is a major factor in determining its propensity for non-specific binding. To confirm that low *D* values were an indication of a high number of dye molecules bound to the substrate, the effect of hydrophobicity on the number of fluorescent spots observed on PEG-BSA nanogel treated glass substrates after exposure to selected dyes,

in the absence of cells, was also examined. These data are plotted in **Figure 5-4 C**, which shows a strong correlation between logD and spot density, confirming the association between hydrophobicity and non-specific dye binding to the substrate. The non-specific binding of probes to the cell surface in presence of excess unlabeled EGF, which should out-compete the Affibody molecules, also seems to be influenced by hydrophobicity parameters, as shown in **Figure 5-4 D**.

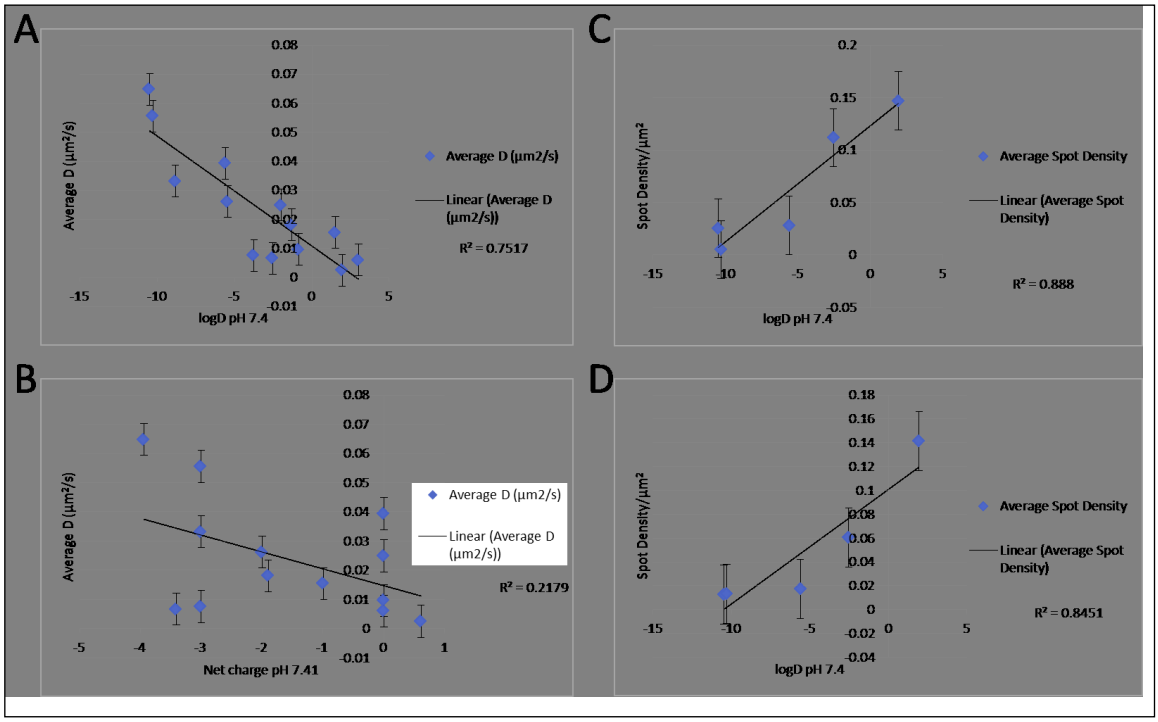

Figure 5-4 - Dependence of tracking artefacts on dye parameters. Plots of mean instantaneous *D* fit for different anti-HER1 Affibody conjugates vs logD **(A),** and charge at pH 7.4 **(B). C)** Plot of spot density for selected anti-HER1 Affibody conjugates on PEG-BSA nanogel coated glass-bottomed dishes vs. logD at pH 7.4. **D)** Plot of spot density for selected anti-HER1 Affibody conjugates (non-specific spots) on T47D cells treated with excess unlabelled EGF vs. logD at pH 7.4. Each datapoint corresponds to mean ± SEM of at least 10 independent areas.

Figure 5-5 shows the distribution of *D* values for Affibody-dye conjugates selected for high, medium, low, and very low levels of mobility (Alexa Fluor 488, CF 633, Alexa Fluor 546, and Atto 647N, respectively). All *D* distributions show a peak at zero and a tail of varying magnitude extending out to > 0.3 $\mu m^2/s$. The zero-peak will consist of a mixture of immobile molecules bound to the glass substrate and immobile and slow-moving molecules in the cells, and the tail will correspond to mobile molecules in the cells. The less mobile dyes have a higher fraction of spots in the zero-peak, consistent with higher levels of binding to the substrate. However, the

possibility that the difference in mean diffusion coefficients measured for different dye conjugates was not only due to differences in levels of binding to the substrate, but also due to variations in the mobility of the conjugates when bound to HER1 in the plasma membrane was also considered. This was investigated by recalculating diffusion coefficients only including data from spots that were clearly mobile. The size of the "zero-peak" can be used as an estimate of the error in the measurement of *D.* The *D* histograms for all probes were analysed in order to assess the extent of the error and determine a conservative threshold for the identification of unambiguously mobile spots and for comparisons across samples. **Figure 5-5** shows a selection of *D* histograms from the dye optimisation experiments. A high-mobility probe (Alexa 488), an intermediate-mobility probe (CF633) and two low-mobility probes (Alexa 546 and Atto 647N) are shown. In all histograms negative *D* values can be observed, extending to approximately -0.1 $\mu m^2/s$. As a spot cannot have a value of $D < 0$, these negative *D* values reflect errors in the estimation of *D* resulting mainly from the impact of the localization error. For the entire set of dye optimisation data the maximum *D* error was estimated to be ±0.1 $\mu m^2/s$. It was then assumed that spots with values of $D > 0.1\ \mu m^2/s$ would be definitely mobile, therefore this value has been taken as the cut-off point in order to analyse only unambiguously mobile spots.

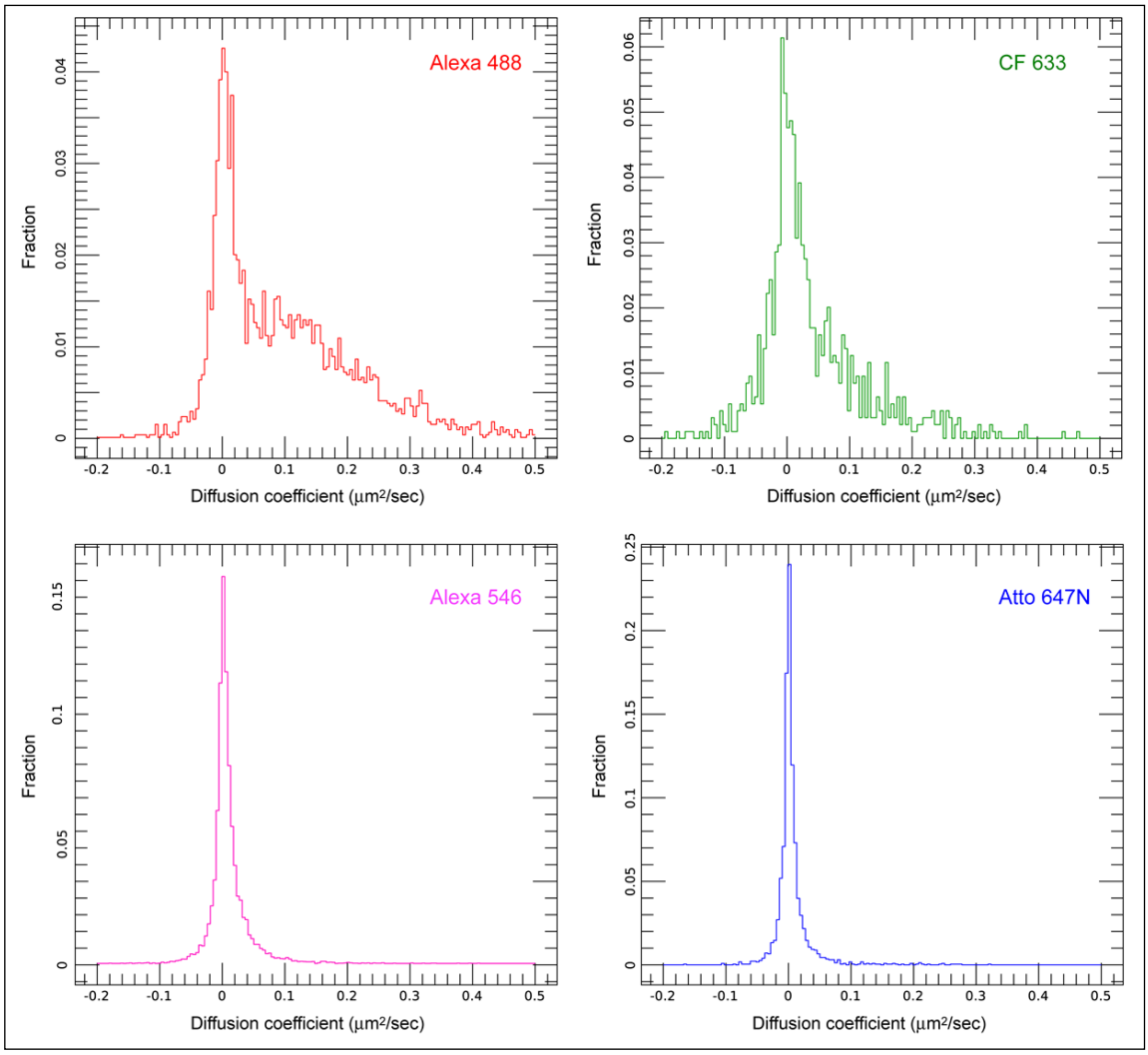

Figure 5-5 - Plots of distributions of mean instantaneous *D* fits for Affibody-dye conjugates representing high (Alexa 488), moderate (CF 633), low (Alexa 546), and very low (Atto 647N) spot mobility.

The results of the analysis of these "definitely mobile" spots are plotted in **Figure 5-6**, and show that it was not possible to detect any significant differences in *D* values between the different conjugates. The number of spots included in this analysis, however, varied quite widely from dye to dye. As a comparison, for each dye, the percentage of spots with diffusion coefficients below the 0.1 $\mu m^2/s$ cut-off was also plotted (**Figure 5-6 B**). Although all dyes show relatively high numbers of spots with measured diffusion coefficients below 0.1 $\mu m^2/s$, the dyes having the lowest mean diffusion coefficients have the lowest percentages of spots identified as definitely mobile. For example, Atto 647N, which is among the worst performing dyes in the set has a percentage of "non-mobile" spots >90%. This relation is confirmed by plotting the *Deff* values for all tracked spots against the percentages of spots falling below the

0.1 $\mu m^2/s$ cut-off for each dye (**Figure 5-6 C**). A linear fit shows a strong correlation ($R^2 = 0.83$), with high levels of overall mobility being correlated with higher levels of unambiguously mobile spots. This adds weight to the argument that low diffusion coefficients largely result from higher levels of non-specific binding to the substrate.

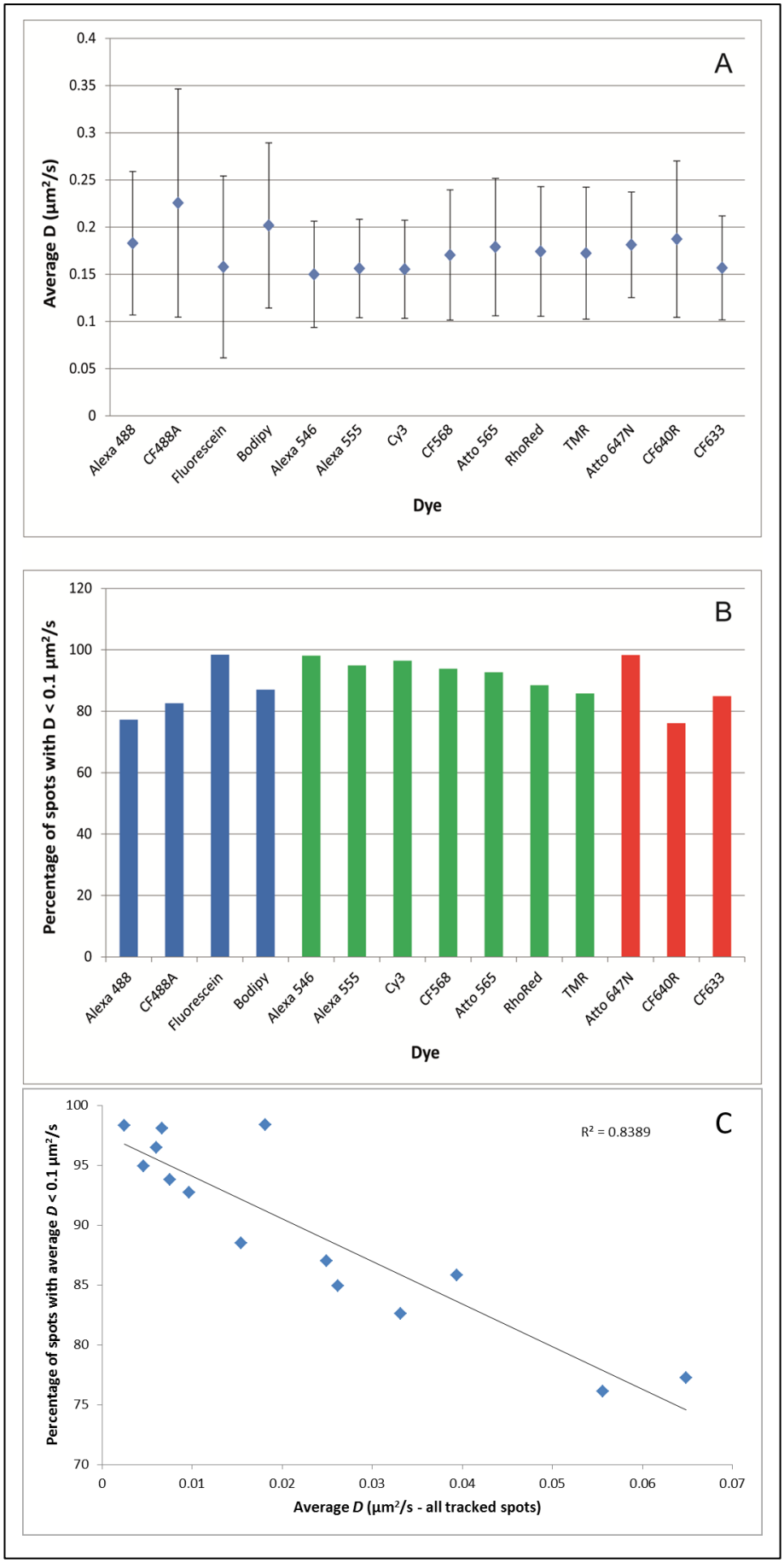
A
Average D (µm²/s)
0.4
0.35
0.3
0.25
0.2
0.15
0.1
0.05
0
Alexa 488
CF488A
Fluorescein
Bodipy
Alexa 546
Alexa 555
Cy3
CF568
Atto 565
RhoRed
TMR
Atto 647N
CF640R
CF633
Dye
B
Percentage of spots with D < 0.1 µm²/s
120
100
80
60
40
20
0
Alexa 488
CF488A
Fluorescein
Bodipy
Alexa 546
Alexa 555
Cy3
CF568
Atto 565
RhoRed
TMR
Atto 647N
CF640R
CF633
Dye
C
R² = 0.8389
Percentage of spots with average D < 0.1 µm²/s
100
95
90
85
80
75
70
0
0.01
0.02
0.03
0.04
0.05
0.06
0.07
Average D (µm²/s - all tracked spots)

Figure 5-6 (previous page) - Tracking artefacts are mostly due to immobile spots on the substrate. A) Mean instantaneous *D* fit for different anti-HER1 Affibody conjugates, after removing data for spots with *D* values below 0.1 $\mu m^2/s$. Each datapoint corresponds to mean ± SD of the tracks contained in at least 10 different areas containing a minimum of 50 different cells. Blue bars indicate dyes excited at 491 nm, green at 561 nm, and red at 638 nm. **B)** Percentages of spots for each dye with *D* values below 0.1 $\mu m^2/s$. **C)** Plot of mean instantaneous *D* fit for different anti-HER1 Affibody conjugates (calculated from all spots) vs. percentage of spots with *D* values < 0.1 $\mu m^2/s$. Line shows linear regression fit to the data, R^2 value indicating goodness of fit.

Finally, the possibility that conjugation of dyes disrupts Affibody function through unfolding, and that this effect may explain the observed variations in mobility, was considered. To investigate this, the affinity of labelled Affibody for its receptor was assessed by measuring its degree of binding in competition with unlabelled Affibody. These measurements were made for three Affibody conjugates selected to cover the mobility range: Alexa 488 (high mobility), CF 633 (moderate mobility), and Atto 565 (low mobility). **Figure 5-7** shows the fluorescence intensity measured from confocal microscopy images of T47D cells labelled with 50 nM dye-conjugated HER1 Affibody, and a mixture of 25 nM dye-conjugated Affibody and 25 nM unlabelled Affibody. If the affinities of conjugated and unlabelled Affibody are similar, it would be expected for cells treated with the conjugated/unlabelled mixture to show approximately 50% of the fluorescence intensity of cells treated with only conjugated Affibody. The data shown in **Figure 5-7** are consistent with this. No significant differences in the reduction of fluorescence intensity on addition of unlabelled Affibody were observed between the three Affibody conjugates tested. In previously published work it has also been shown that Affibody-dye conjugates retain their specificity for HER1, using competition assays with unlabelled Affibody [1] (**Chapter 3**). These data confirm that dye conjugation does not significantly reduce the affinity of the Affibody for its target, and that the variations in conjugate mobility cannot be caused by varying levels of Affibody unfolding on dye conjugation.

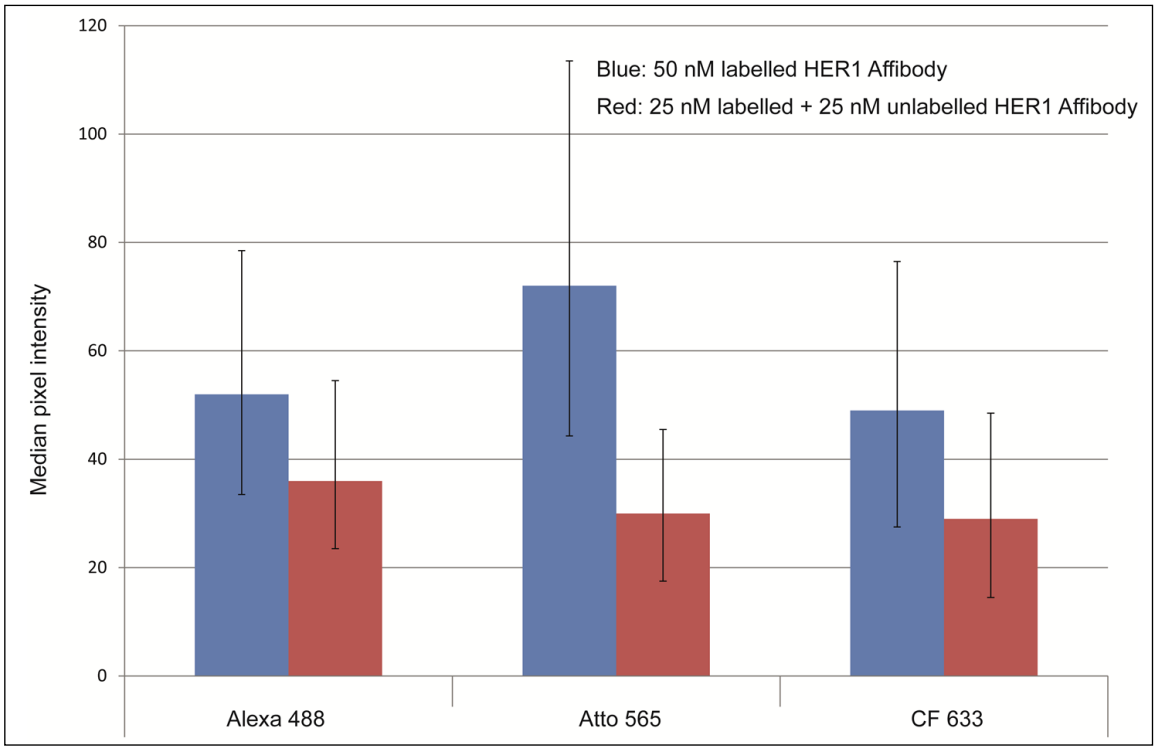

Figure 5-7 - Fluorescence intensity measured from confocal microscopy images of T47D cells labelled with 50 nM dye-conjugated HER1 Affibody, and a mixture of 25 nM dye-conjugated Affibody and 25 nM unlabelled Affibody. Three dyes were selected to cover the range of mobilities (Alexa 488 = high mobility; CF 633 = moderate mobility; Atto 565 = low mobility). Columns represent the median of the distribution of membrane region pixel intensities derived from at least 100 cells. Error bars represent the positions of the 1st and 3rd quartile of the distributions.

5.3. Discussion

In this chapter, the properties of 14 chemically different dyes, excitable by one of three commonly used laser lines (491 nm, 561 nm and 638 nm), were investigated in order to ascertain their suitability for Single-Molecule work with live cell samples. Specifically, focusing on a single, high-performance passivating substrate, PEG-BSA nanogel, and a single protein of proven specificity, anti-HER1 Affibody, brightness, photostability and non-specific adhesion of fluorescent conjugates of this protein were explored as key characteristics that influence data quality in Single-Molecule experiments.

To assess probe mobility, the diffusion of fluorescently-conjugated anti-HER1 Affibodies [287] on the surface of T47D breast carcinoma cells was compared and instantaneous *D* coefficient were calculated for each treatment group, using the Alexa 488 conjugate as a reference. Anti-

HER1 Affibody-Alexa 488 has been demonstrated to be a specific probe for HER1 and displays a very low non-specific binding on PEG-BSA nanogel surfaces (**Figure 4-7 D**). The measured *D* coefficients reported in the literature for HER1 under basal conditions vary widely, ranging from 0.0025 to 0.28 $\mu m^2/s$ (see **Table 6-1** in **Chapter 6**, for a more detailed discussion). These were measured using a wide range of techniques including fluorescence photobleaching recovery (FPR) [337,338], single particle tracking with colloidal gold [12], single molecule tracking (mainly using quantum dots) [109,110,308,310,339], fluorescence correlation spectroscopy (FCS) and image correlation spectroscopy (ICS) [340–342], and fluorescence intensity distribution analysis (FIDA) [104]. Because of the wide range of values of *D* reported, the wide range of techniques used, and the varying expression levels of the receptor, it is difficult to draw any conclusions, except to say that the mean *D* coefficient for HER1 labelled with anti-HER1 Affibody-Alexa488 measured under the stated experimental conditions (0.060 ± 0.026 $\mu m^2/s$) falls within the range previously measured. When D is measured only from molecules that are definitely mobile (**Figure 5-6**), an average value around 0.17 $\mu m^2/s$ is obtained, which is also within the previously measured range.
From the tracking data it can be concluded that the CF640R conjugate, whose diffusion is not statistically significantly different from that of the Alexa 488 conjugate, is likely to accurately and specifically report on the diffusion of HER1.

The *D* coefficients measured for the other dye conjugates are lower, and in some cases very significantly lower, than the "true" value measured using Alexa 488. This is a very significant effect, with some dyes showing over an order of magnitude lower *D* coefficients than that of Alexa 488. Where Single-Molecule measurements are used to determine the diffusion rates of molecules, this variation in *D* raises the possibility of serious errors in diffusion rate calculations, if the wrong dyes are used. Non-specific binding of dye molecules to the substrate would be expected to be a result of either charge-based interactions or hydrophobic interactions. It has been stated that low dye net charge is important to minimize non-specific binding to the substrate [331], but under the conditions stated there is only a very weak correlation between non-specific binding and charge. Some quite highly charged dyes show low levels of non-specific binding and therefore high measured *D* coefficient (e.g. CF640R), while others with similar charge bind strongly to the substrate (e.g. CF568). On the other hand, a correlation between hydrophobicity and low measured values of *D,* and therefore high levels of non-specific binding to the substrate, has been demonstrated. The best dyes (Alexa 488, CF640R) have highly negative logD values, i.e. very low hydrophobicity.

The widely varying level of non-specific substrate attachment between the dyes tested in this project demonstrates that photophysical characteristics alone are insufficient to determine whether a particular dye is suitable for Single-Particle tracking in live cells. For example, Atto 647N is often identified as a good dye for single molecule experiments, because of its relatively high resistance to photobleaching and its potential to yield a high number of photons. However, under our experimental conditions it shows a very high level of attachment to the substrate.

One other factor that should be considered when choosing a dye for Single-Molecule experiments is the potential for the dye to influence the properties of the labelled molecule. Alterations of probe specificity and affinity for different fluorophore conjugates are well known in the field of antibody conjugation, where it is established that excess negative charges in the dye can cause loss of specificity by altering the electrostatic parameters of the antibody [343]. The effect of spectrally equivalent but chemically different dyes on probe specificity for in vivo use has been analysed for Cy5.5- and Alexa 680-conjugated antibodies [344] and for four different Near Infra-Red fluorophore conjugates of an anti-HER1 Affibody Molecule [345]. Both papers report differential binding affinity and in-vivo Tumor-to-Background ratios, but Ogawa *et al.* [344] also investigate the possible causes of this difference, concluding that the presence of multiple aromatic rings and negative charges in the structure of Cy5.5 enhances the lipophilicity of the fluorophore, possibly altering the pharmacokinetic characteristics of the antibody. Conversely, Qi *et al.* [345] determine that Cy5.5 and Alexa 680 anti-HER1 Affibody conjugates display equally specific binding in vivo, while SR680 and IRDye 800CW perform remarkably poorer, however Ogawa *et al.* label a humanized full-length antibody (148 kDa) at multiple sites, while Qi *et al.* label the Affibody (Mw ca. 14 kDa) at a single cysteine residue. The effect of single versus multiple labelling on the net charge of the protein and the differences in protein charge and size might explain the differential behaviour of the conjugates.

Interestingly, Bennett and Simmons [252] conducted an optimization similar to that reported here for the oligopeptide Substance P labelled with Alexa 488, Bodipy FL, Fluorescein, Orgeon Green 488 and TMR. This oligopeptide consists of 11 amino acid residues (RPKPQQFFGLM-NH_2) and has a MW of 1348.6 Da and a pI of 11.00 (Calculated using the Expasy ProtParam tool on TKN1_HUMAN (P20366) – residues 58-68). The peptide was labelled on the positively charged K residue on position 3, which is involved in an interaction with the receptor. The authors reported nearly no binding for the Alexa 488 conjugate, probably due to the addition of the

dye's three negative charges, while the TMR conjugate was able to bind but displayed reduced efficacy in eliciting downstream signalling, and the Fluorescein conjugate displayed reduced affinity. In general, smaller and neutral dyes, such as Bodipy FL and Oregon Green 488, performed better than bigger and charged dyes. It must also be noted that the Alexa 488 dye (MW = 643 Da) is half as big as the peptide to be labelled and, as such, could pose serious problems of steric hindrance to binding.
The labelling of very small oligopeptides poses different problems from the labelling of bigger polypeptides such as EGF, small non-antibody binders and antibodies: the position of the label and the charge of the label and peptide need to be carefully considered and conclusions drawn from the optimization of one system should not be extended to the other without careful consideration.

As a final example, it might be interesting to consider the case of the NHS-ester labelled NRG1β conjugates examined in **Chapter 3**. The results reported in **Figure 3-21** show that the Alexa 546 conjugate displays higher non-specific binding than the Alexa 488 conjugate. The Alexa 647 conjugate, however, displays relatively low non-specific binding and fast tracking (0.057 $\mu m^2/s$), even significantly higher than that of Alexa 488 conjugate (0.035 $\mu m^2/s$ – P> 0.001). Alexa 647 is a rather hydrophobic cyanine-based dye with logD pH7.4 = 0.86 and a net charge of +1 at pH 7.4 (Calculated using Marvin Sketch – Chemaxon), so it would not seem the ideal candidate for Single-Particle Tracking, however the characteristics of the protein also need to be taken into account. NRG1β is rather more hydrophobic than either EGF or anti-HER1 Affibody (GRAVY = -0.342 vs. -0.506 and -0.507 for EGF and anti-HER1 Affibody respectively – calculated with Expasy ProtParam). The theoretical pI of NRG1β is also quite higher than that of either EGF or anti-HER1 Affibody (6.05 vs. 4.89 and 4.65 respectively) and its sequence contains a more or less balanced amount of negatively and positively charged residues, while both EGF and anti-HER1 Affibody have a surplus of negative charges. Taken together, these factors could influence the way in which protein and dye interact in the conjugate and therefore the effect of the dye on non-specific binding. Also, Alexa 647 has a rather more "spread" and flexible structure compared with the other Alexa dyes investigated and compared with Atto 647N in particular (see **Figure 5-8**). Atto dyes have a very rigid molecular structure, which does not allow isomerization and renders of their optical properties independent from solvent and temperature [216]. This rigidity, however, would not allow redistribution of the positive charge and would limit the possible interactions of the dye with the protein. Alternatively, the sulphonated residues of Alexa 647 could become

deprotonated near the cell surface due to slight variations in pH caused by the cellular metabolism.

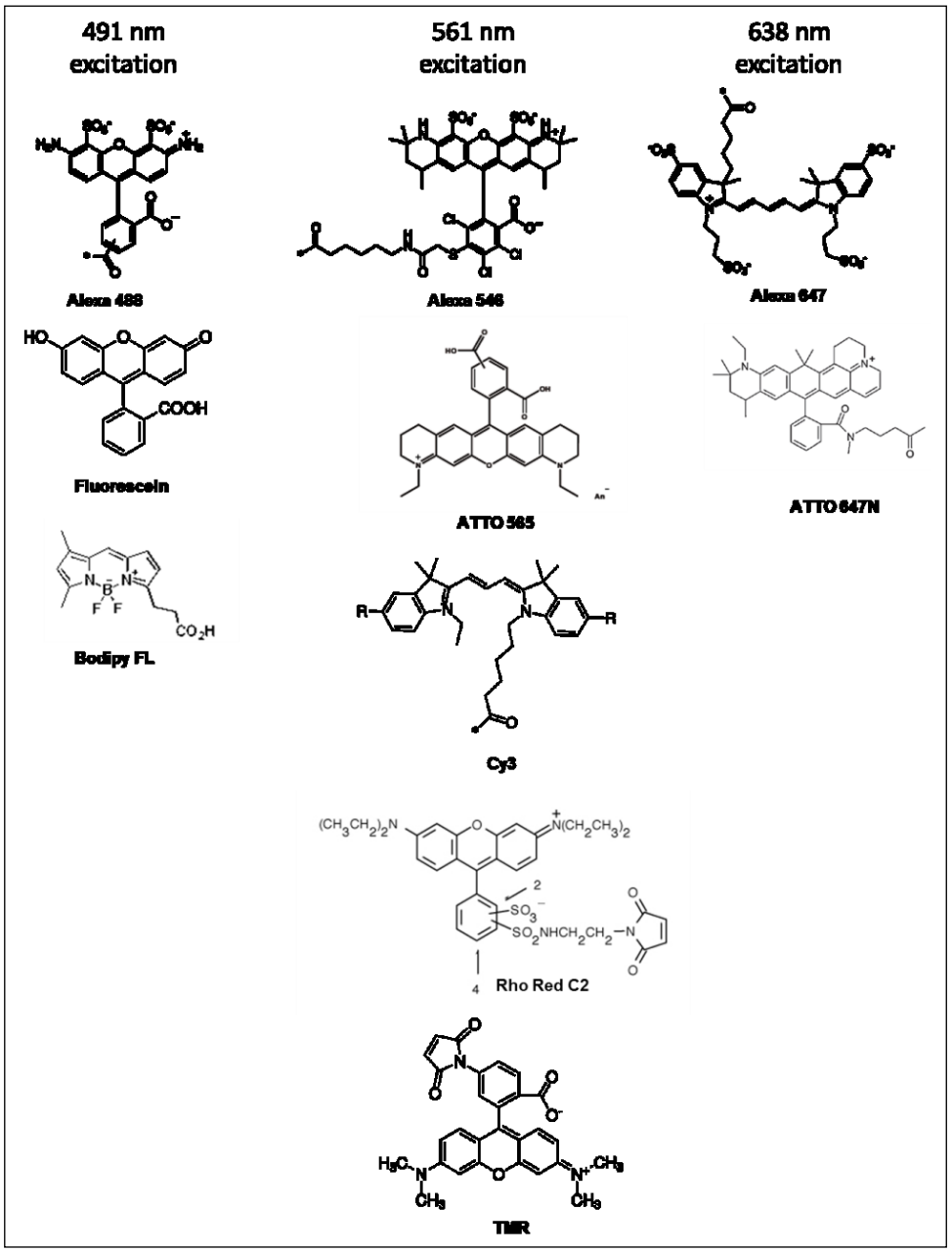

Figure 5-8 – Available structures of the dyes used in this project. Alexa 488, Alexa 546, Alexa 647 and Cyanine 3 structures were adapted from http://www.atdbio.com; Fluorescein and Bodipy FL structures were adapted from http://commons.wikimedia.org; TMR structure was adapted from the Sigma-Aldrich website; Rhodamine Red C2 structure was adapted from the Invitrogen website; Atto 565 structure was adapted from the AttoTec website; Atto 647N structure was adapted from Cordes T *et al.* [346]. Structures of Alexa 555 and of the CF-series dyes are not yet publicly available.

5.4. Conclusions

The choice of organic fluorescent dyes is large and ever-increasing, however not all of them are suited to the demanding SNR and specificity requirements of Single-Molecule techniques. While the effect of fluorophore labelling on antibodies is well known and single instances of fluorophore optimization for in vivo work have been published, this systematic analysis of dyes suited for the laser lines 491 nm, 561 nm and 638 nm is, as far as it could be ascertained, the first to deal with visible dyes and to investigate the suitability of conjugates by analysing brightness, photostability and specificity at the Single-Molecule level. The results show that non-specific binding of dye conjugates to the substrate is a significant effect, highly variable between dyes. It is therefore important to consider this in addition to photophysical characteristics when selecting a dye. They demonstrate that hydrophobicity is the major determinant of the propensity of a dye for binding to the substrate. It would be therefore advisable to select hydrophilic dyes (strongly negative logD) with good photophysical characteristics in the first instance. Of the dyes examined, Alexa 488 appears to be the dye of choice for excitation with blue light, TMR for green, and CF640R for red. However, before undertaking experiments, dye conjugates should be tested under the specific conditions to be used, and their effect (or lack of it) on the labelled molecule should be investigated.

From the optimization experiments carried out in **Chapters 3-5** a series of parameters guiding the choice of suitable probe-dye conjugates for Single-Molecule experiments.

1. Conjugates should display low levels of non-specific binding to the cell culture surfaces employed in a given Single-Molecule experiment. Optimisation of cell culture substrates towards low protein adhesion is also required.
2. Conjugates should show some mobility when used to track membrane receptors on live cells. A completely immobile probe should be treated as highly suspicious.
3. When choosing conjugates for two-colour labelling of a target, the two conjugates should display comparable mobility.
4. A labelled probe should be subject to displacement by an excess of unlabelled probe. This test eliminates the possibility that binding might be driven by interactions of the fluorescent dye with the cell membrane. On this point, the data on dye-bilayer interaction reported by Hughes *et al.* [347] might be helpful in label selection.
5. Activating probes (such as EGF or NRG1β in this project) need to retain their ability to activate the receptor even after dye conjugation.

6. The photochemical characteristics of the dyes need to be considered, as they have a significant impact on the SNR of the data. If two or more conjugates with comparable specificity are available, the one labelled with the dye with higher QY, ε and photobleaching lifetime should be preferred, as these parameters determine the total photon output of the dye.
7. Dyes need to be chosen also according to the commercially available labelling moieties (e.g. maleimide vs NHS ester), in order to match the best labelling strategy for each probe.

6. Single-Particle Imaging of the HER Receptor Family in Live Breast Cancer Cells

6.1. Introduction

Receptor dimerization, and possibly high-order oligomerisation, are key processes that regulate downstream signalling.

The characterisation of receptor dynamics and pairwise interactions of HER family members in the native cell membrane is a further step in the quest for understanding receptor interactions and activation modes and the response to perturbations such as TKIs.

Biochemical methods and bulk imaging methods have been extensively used to characterise the interactions of HER family members, however neither are suitable to capture transient events that may be fundamental for signalling or the heterogeneity of the system. Moreover, the fixation techniques used in fluorescence imaging and electron microscopy might introduce artificial crosslinking and bias receptor distributions towards the oligomeric state.

The diffusion of HER1 molecules on the surface of live cells has been quite extensively studied before, using various different cell models and both bulk and Single-Molecule methods. As a result, the findings reported vary quite significantly. **Table 6-1**, below, summarises the principal findings related to HER1 diffusion in a basal state, except where noted.

Paper	Technique	Cell system	*D* coefficient ($\mu m^2/s$)
Livneh *et al.* 1986 [337]	FPR	COS-HER1	0.015
Benveniste *et al.* 1988 [338]	FPR	NIH3T3-HER1	0.28 - 0.066 [1]
Kusumi *et al*. 1993 [12]	SP tracking with colloidal gold particles, 30 Hz	mouse keratinocytes	0.0112 ± 0.015
Orr *et al*. 2005 [310]	SP tracking, 7.5 Hz	HME184A1	0.023 ± 0.002
Adkins *et al*. 2007 [340]	FCS	HEK239T-HER1-eGFP	0.162 ± 0.022
Kannan *et al*. 2007 [342]	TIRF-FCS, 28 Hz	Cho-HER1-mRFP	0.0548 ± 0.051
Saffarian *et al.* 2007 [104]	FIDA	Cho-HER1-eGFP	0.25 ± 0.06
Keating *et al.* 2008 [341]	ICS	COS7-HER1-eGFP	0.0025
Xiao *et al.* 2008 [308]	SP tracking, 10 Hz	HeLa-HER1-eGFP	0.049
Chung *et al.* 2010 [109]	SP tracking with Quantum Dots	Cho-HER1-eGFP	0.17 ± 0.06
Danglot *et al*. 2010 [339]	SP tracking with Quantum Dots, 26 Hz	HeLa	0.029 ± 0.0066
Low-Nam *et al.* 2011 [110]	SP tracking with Quantum Dots, 20 Hz	A431	0.05

Table 6-1 - Summary of published D coefficients for the EGFR protein on live cell membranes. FCS = Fluorescence Correlation Spectroscopy, FIDA = Fluorescence Intensity Distribution Analysis, FPR = Fluorescence Photobleaching Recovery, ICS = Image Correlation Spectroscopy, SP = single-particle, TIRF-FCS= Fluorescence Correlation Spectroscopy in Total Internal Reflection mode.

[1] Values correspond to cells expressing 20×10^3 – 1.5×10^6 receptors/cell, respectively.

This table shows that the diffusion coefficients obtained vary substantially depending on the experimental technique employed, with FCS-based techniques yielding higher values due to

their inability to account for the immobile fraction. Even among the results obtained with the same technique, *e.g.* Single-Particle Tracking, differences might be seen depending on the acquisition speed and the cell system analysed. There is also evidence [338] that suggests that the level of expression of the receptor on the cell surface may influence diffusion.

HER2 has been studied less extensively and HER3 even less so. Using Single-Particle Tracking techniques , Orr *et al.* [310] reported a diffusion coefficient of 0.035 ± 0.004 $\mu m^2/s$ for HER2 on HME184A1 cells transfected with HER2, while Xiao *et al.* [348] reported a coefficient of 0.055 ± 0.0030 $\mu m^2/s$ in MCF7 cells transfected with HER2-GFP, a value that increased to 0.085 ± 0.0032 $\mu m^2/s$ in presence of NRG1. The NRG1-induced increase in HER2 *D* coefficient was prevented both by an antibody that prevents HER2-HER3 interactions and by kinase inhibition of both HER1 and HER2.
As for HER3, multispot FRAP experiments by Hagen *et al.* [349] have reported an apparent diffusion coefficient of 0.036 ± 0.016 $\mu m^2/s$ in A431 cells transfected with HER3-citrine, a value that increased to 0.072 ± 0.021 $\mu m^2/s$ when cells were treated with EGF, while SPT measurements have reported *D* coefficients of 0.038 $\mu m^2/s$ for inactive HER3 tagged with Hemagglutinin A (HA) and labelled with an anti-HA Fab-QD, and of 0.01 μm2/s for HER3 activated with NRG1-QD [137].

There are, so far, only two Single-Molecule studies of the interactions of HER family receptors the author is aware of : that of Low-Nam *et al.* [110], who investigated the homo-association between ligand-activated and inactive HER1 molecules by tracking them with QDs on the surface of A431 cells, and that of Steinkamp *et al.* [137], who tracked HER2 and HER3 in SkBr3 and Cho cells. The method of tracking used in both papers, however, relies on very low fractional saturation of HER receptors on cells which substantially overexpress the receptor, and on the use of multiply-liganded QDs as long-lived, bright emitters. This approach allows the determination of the distance between interacting particles on a scale of few nanometres. However, as shown by Murase *et al.* using gold nanoparticles [14], while multivalent nano-probes are usually better than conventional fluorescent dyes in terms of signal and therefore spatial and temporal resolution, crosslinking effects and non-specific interactions with cellular structures can introduce systematic variations in the observables.

This work addresses the challenge of measuring receptor-receptor interaction at a molecular levels from a different perspective: it aims towards high fractional saturation of receptors in T47D cells, which express low-to-medium levels of all the HER family receptors [350]. This was

achieved with chemical dyes bound in a 1:1 stoichiometry to small poly-peptide agonists and antagonists. This method should in principle be applicable to a variety of cell types, which might express very different, and not necessarily matched, levels of multiple receptors by optimising the fractional saturation of the receptors of interest. The optimised labelling and data acquisition protocols allowed probe binding to a substantial fraction of the receptor pool in T47D cells (~33-50% for HER1, assuming that each fluorescent feature contains a single receptor – calculated from the average number of single-particle traces recorded for each image series) and grants a much better chance of capturing interaction events and a smaller chance of introducing artefacts from cross-linking of receptors by using monovalent probes. In fact, in an ideal scenario where all particles of a certain species interact (100%), a labelling fraction of 50% particles in each channel would result in a 25% colocalisation frequency. In the same scenario, labelling only 10% of the particles in each channel would result in a 0.25% colocalisation frequency, making the detection of colocalisation events unlikely. Thus, using a cell line that expresses low-to-mid levels of receptor, the high density of labelling constitutes a key advantage of the method presented in this thesis.

Due to the difficulty of finding a 561 nm dye with optimal specificity (**Chapter 5**), it was decided to limit current experiments to pairwise interactions in two channels. In the future, ongoing optimisation of 561 nm and Near Infrared dyes and refinement of data analysis algorithms will enable multicolour detection of HER family receptors, possibly of the entire family in the same experiment.

Throughout this chapter, activated HER1 and HER3 receptors (denoted as HER1* and HER3*) were treated as separate species from their inactive counterparts, effectively transforming the problem into a 5-component system (HER1, HER1*, HER2, HER3, HER3*), as depicted in **Figure 6-1**.

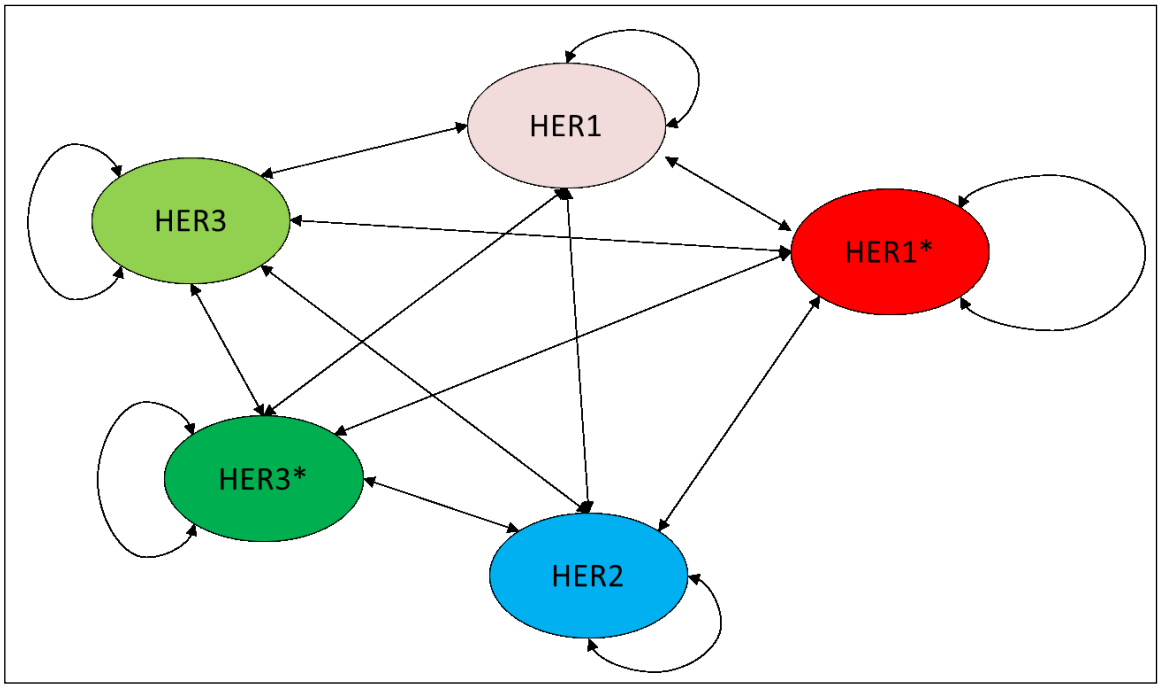

Figure 6-1 – The HER family system, as investigated in this project.

The interactions in this 5-component system were investigated in untreated cells, to analyse normal physiological behaviour in terms of receptor dynamics at the cell surface and pairwise interaction likelihood. The following system perturbations were also investigated:

1) The presence of 100 nM unlabelled EGF for HER3/HER3* containing combinations and 100 nM unlabelled NRG1β for HER1/HER1* containing combinations. This was done to investigate the competition for interactors, mainly HER2, between HER family members and determine the hierarchy of interactions within the HER family of receptors;
2) Treatment with clinically achievable concentrations of class I (Erlotinib) and class II (Lapatinib) Tyrosine Kinase Inhibitors (TKI), which are believed to bind preferentially to the active conformation of the kinase and to the inactive conformation, respectively. This was done to investigate the response of the HER family receptors to tyrosine kinase inhibition, both in terms of receptor dynamics on the membrane and of likelihood of interactions with other family members. Ideally, this should give some information about changes in the modes of HER family signalling after TKI treatment.

This experimental plan yielded a total of 48 different interaction/treatment conditions, for each of which at least 3 independent biological replicates have been acquired, each consisting of at least 10 independent datasets (*i.e.* ca. 30 technical replicates per condition). Basal state HER1 was labelled with 7.5 – 8 nM anti-HER1 Affibody; activated HER1* with 4 nM EGF; HER2 with 1 nM anti-HER2 Affibody; basal state HER3 with 30 nM anti-HER3 Affibody and activated

HER3* with 40 nM NRG1β. All probes were labelled either with Alexa 488 or CF640R, except for NRG1β, which was labelled with either Alexa 488 or Alexa 647. This was due to the fact that NRG1β conjugations were performed prior to the main phase of dye optimisation with what was at the time one of the few viable alternatives to At647N, however as the A647 conjugate was shown to be only marginally affected by non-specific adhesion artefacts (see **Figure 3-21** in **Chapter 3**), it was decided to keep using it. It is worth noting that, at the concentrations employed in this project, NRG1β binds to and activates both HER3 and HER4, therefore, the species noted as HER3* is likely to be a mixture of activated HER3 and HER4, as it would be naturally occurring in cells exposed to NRG1β in the native extracellular microenvironment.
As far as it can be ascertained, this is the first systematic analysis of the membrane dynamics, and interactions of HER1 and HER2 and, in particular, of HER3, whose organisation on the membrane has mainly been analysed on fixed cells (see for example [140,144]). The ultimate aim of this project will be to use the experimental data collected using the method described here to build a quantitative model of the input layer of the HER family signalling network.
In this chapter, all statistical tests were performed with the non-parametric Kolmogorov-Smirnov test [335,336].

6.2. Results

6.2.1. Optimisation of incident laser power and acquisition rate is important in maximising SNR and localisation precision

The localisation precision of a single molecule feature depends on the number of photons collected from it in any given image. The number of photons collected and hence the localisation precision can be increased by increasing the excitation laser power, which increases the rate of absorption and consequently fluorescence emission, and/or increasing the exposure time so that more photons are collected per image. Acquiring images at low frame rates, however, has the serious drawback of limiting the ability to record very transient events, such as the interactions between inactive HER1 receptors [110]. Also, higher laser powers leads to enhanced photobleaching, which reduces the observation time of molecules and can bias the observed colocalisation frequencies in multichannel data and, in particular, of any kinetic rates derived from the durations of colocalisation events.

A compromise can be found by determining the lowest power and exposure time required to give an acceptable number of photons from features in a frame, or an acceptable average localisation precision over all the data.

In order to characterise the SNR parameters of the chosen dyes, Alexa 488 and CF640R, Single-Particle time-course experiments were performed on fixed T47D cells labelled with anti-HER1 Affibody Alexa 488 and CF640R, using optimised gain and EMCCD parameters to minimise noise [351], and varying excitation power and frame rate over a scale of 1.2 -4 mW and 10-33 Hz respectively, acquiring data for a total time of 15 seconds.

For each combination of excitation power and exposure time, probability density functions of single molecule feature intensity (which is proportional to the number of collected photons) were generated from all detected features. From these probability distributions the probability that detected features have an intensity greater than a given threshold intensity was plotted as a function of that threshold (**Figure 6-2 A-C** and **Figure 6-3 A-C**).
These plots allow visual inspection of the fraction of detected features that have an acceptable intensity (depending on the experimental needs) for the measured combinations of power and exposure. Consistent with the lower photon output of CF640R compared to Alexa 488, CF640R shows a larger localisation error in comparable conditions.

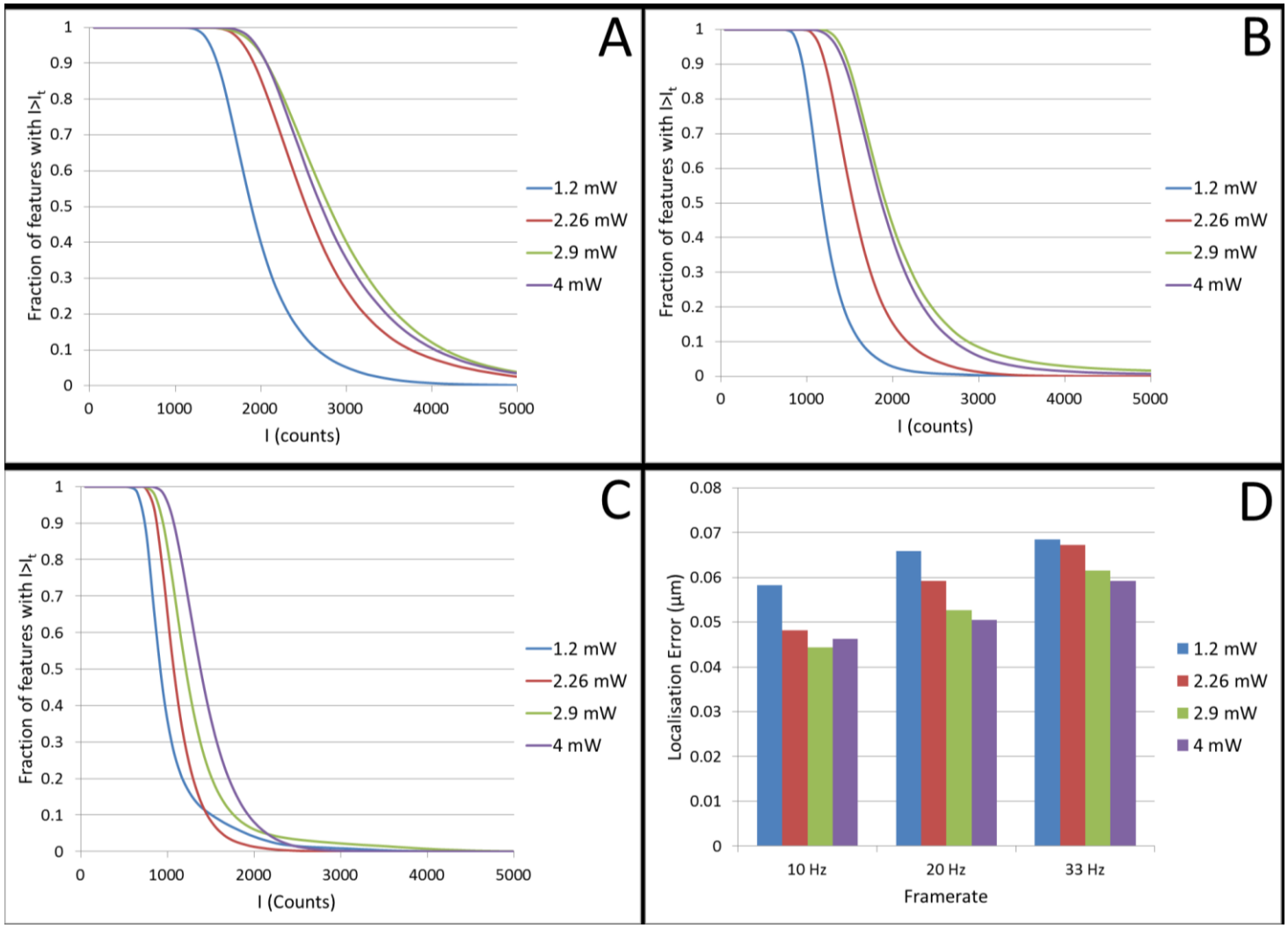
A
Fraction of features with I>I$_t$
I (counts)
1.2 mW
2.26 mW
2.9 mW
4 mW
B
Fraction of features with I>I$_t$
I (counts)
1.2 mW
2.26 mW
2.9 mW
4 mW
C
Fraction of features with I>I$_t$
I (Counts)
1.2 mW
2.26 mW
2.9 mW
4 mW
D
Localisation Error (µm)
10 Hz
20 Hz
33 Hz
Framerate
1.2 mW
2.26 mW
2.9 mW
4 mW

Figure 6-2 (previous page) – Assessment of fluorescent signal and particle localisation error for CF640R conjugates. A-C: Fraction of frames with intensity greater than a threshold (I_t) for CF640R molecules conjugated to anti-HER1 Affibody, excited with a 640 nm CW laser at different powers and recorded at 33 Hz **(A**), 20 Hz **(B)** and 10 Hz **(C)** on an Andor iXIon EMCCD camera. Each measurement was performed over at least 5 independent areas. **D:** Localisation error for CF640R molecules conjugated to anti-HER1 Affibody excited with a 640 nm CW laser at different powers and recorded at 33 Hz, 20 Hz and 10 Hz**,** on an Andor iXIon EMCCD camera.

The plots also show that CF640R has an overall lower photon output than Alexa 488 when excited with comparable laser intensities, as predicted by the brightness data in **Table 5-2** (**Chapter 5**). This data will be useful for the assessment of localisation precision from photon statistics once a complete noise model for the detector is implemented in the data analysis pipeline.

Alternatively, the average localisation error for the entire set of detected features can be calculated from the positive offset introduced to the MSD curve calculated from all the tracks. These are shown for all acquisition conditions in **Figure 6-2 D** for CF640R and in **Figure 6-3 D** for Alexa 488, respectively.

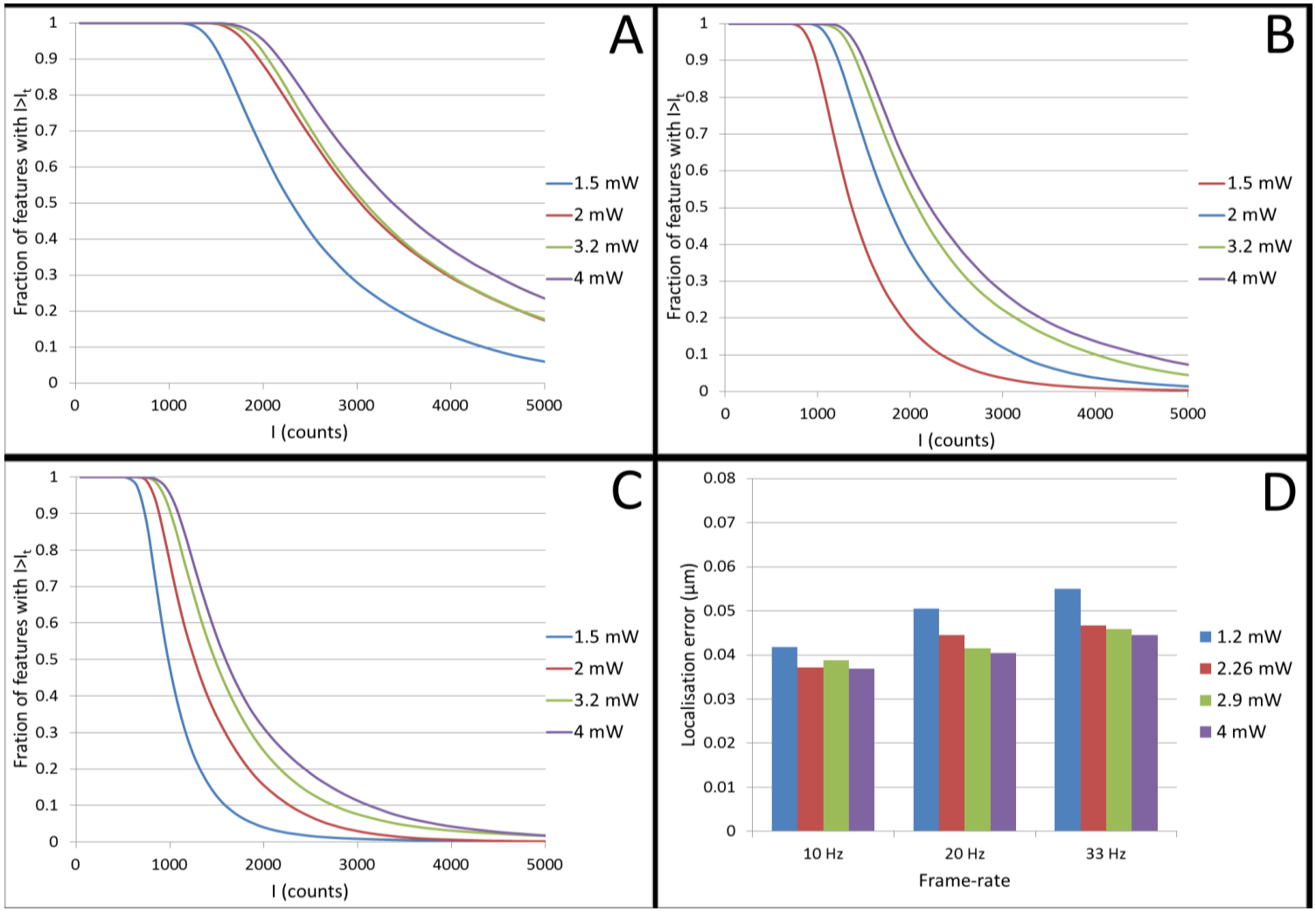
A
Fraction of features with I>I$_t$
I (counts)
1.5 mW
2 mW
3.2 mW
4 mW
B
Fraction of features with I>I$_t$
I (counts)
1.5 mW
2 mW
3.2 mW
4 mW
C
Fration of features with I>I$_t$
I (counts)
1.5 mW
2 mW
3.2 mW
4 mW
D
Localisation error (µm)
10 Hz
20 Hz
33 Hz
Frame-rate
1.2 mW
2.26 mW
2.9 mW
4 mW

Figure 6-3 (previous page) - Assessment of fluorescent signal and particle localisation error for Alexa 488 conjugates. A-C: Fraction of frames with intensity greater than a threshold (I_t) for A488 molecules conjugated to anti-HER1 Affibody, excited with a 491 nm CW laser at different powers and recorded at 33 Hz **(A**), 20 Hz **(B)** and 10 Hz **(C)** on an Andor iXIon EMCCD camera. Each measurement was performed over at least 5 independent areas. **D:** Localisation error for A488 molecules conjugated to anti-HER1 Affibody, excited with a 491 nm CW laser at different powers and recorded at 33 Hz, 20 Hz and 10 Hz**,** on an Andor iXIon EMCCD camera.

Localisation errors range between 44-70 nm for CF640R and 35-55 nm for Alexa 488. As expected, the largest errors are present in the datasets with the highest frame rate and lowest excitation laser power and the best results are achieved when acquiring data at 10 Hz and with high laser power.This data, together with the photobleaching data shown in **Table 5-2** (**Chapter 5**), and literature data on the interaction kinetics of HER family receptors [110], was used to decide on a compromise setup for the acquisition of Single-Particle Tracking data, allowing the system to achieve a reasonably high localisation precision, and still retain the ability to capture short-lived interactions. By tracking at 20 Hz with an average laser power of ~ 4 mW of 640 nm laser to excite CF640R, and 3.5-4.0 mW of 491 nm, localisation errors of ~ 50 nm for the CF640R conjugates and ~ 40 nm for the Alexa 488 conjugates can be obtained. These errors do not allow the system to discriminate whether two interacting molecules are close enough to form a dimer or are just co-confined, but only to determine colocalisation within a fixed threshold, which was chosen to be at least twice the largest localisation error (*i.e.* at least 90-100 nm at 20 Hz with 4 mW of exciting laser). These calculations are likely to be an underestimation of the true localisation error of fluorescent particles moving on the surface of live cells, as it would result from the combination of the localisation error (dependent on SNR) and of blurring effects caused by the motion of the particles. In order to be considered as colocalised, two particles will then have to reside within of 160 nm of each other for at least 3, not necessarily consecutive, frames.

An example dataset from the two-colour colocalisation data pool is shown in **Figure 6-4**.

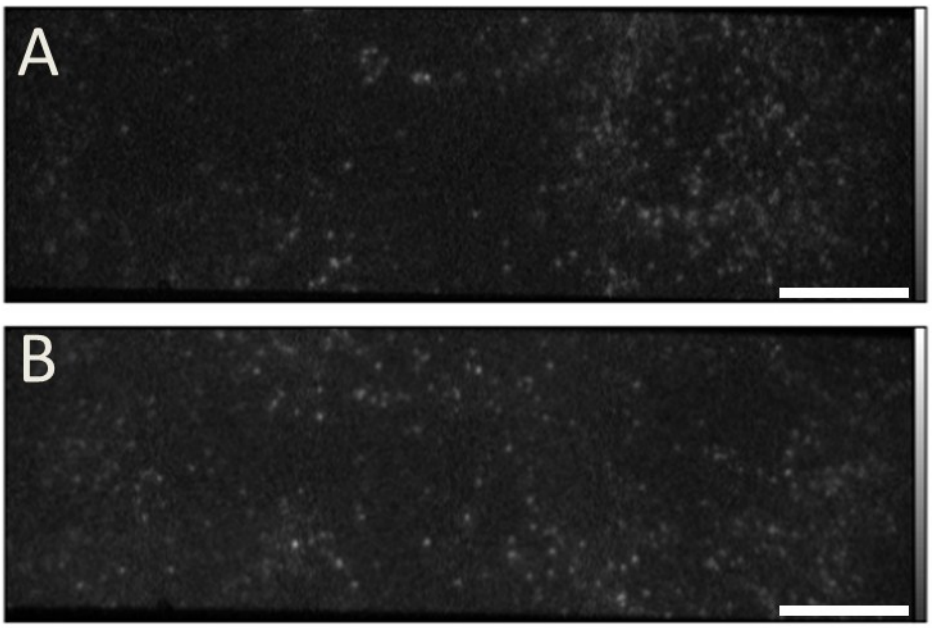

Figure 6-4 – Example two-colour tracking dataset. A) 4 nM EGF CF640R; **B)** 1 nM anti-HER2 Affibody Alexa 488. Both probes were tracked at 37°C on T47D cells with an integration interval of 50 ms and a laser power of 4 mW for each channel (out of the objective in epi-fluorescence mode).

6.2.2. Determination of the toxicity of cell treatments and the proliferative effect of ligands with a colorimetric MTT assay

When performing Single-Molecule experiments on live cells, especially on functionalised substrates, ideally one would want to keep the cells in conditions as close to physiological as possible, in order to avoid retraction of cells from the surface and detachment, which will deteriorate the quality of the data or render acquisition nearly impossible.

To certify that the treatments employed did not significantly impair cell vitality in the short-to medium term, while still being effective at a molecular level, a simple colorimetric MTT assay was performed on T47D cells (**Figure 6-5 A**). In addition, the ability of ligands for HER1, HER3 and HER4 to induce cell proliferation in presence or absence of different tyrosine kinase inhibitors or combinations thereof was also assessed with the same method (**Figure 6-5 B** and **C**). A decrease in OD_{570} indicates decreased cell vitality.

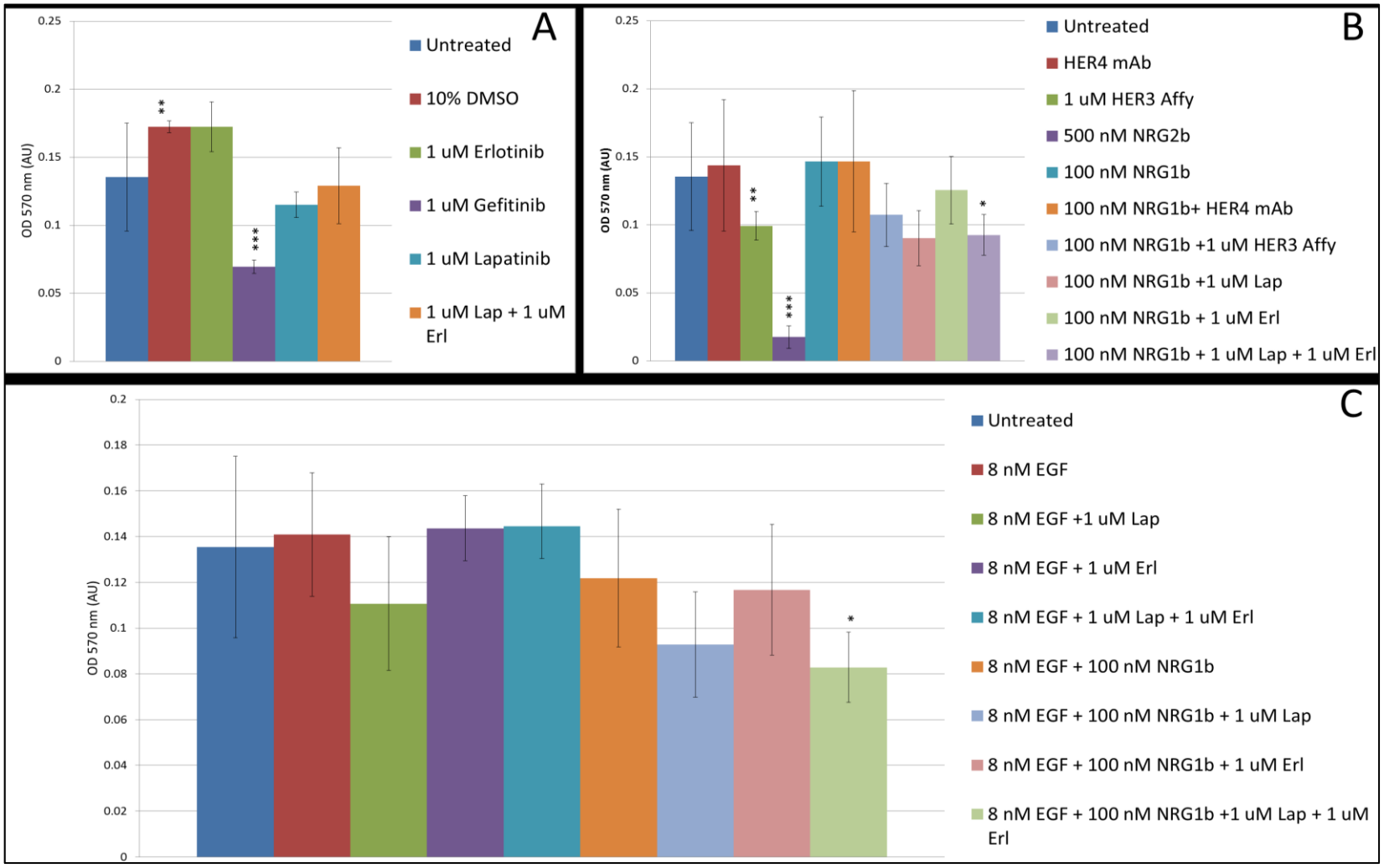
A
OD 570 nm (AU)
0.25
0.2
0.15
0.1
0.05
0
**
***
Untreated
10% DMSO
1 uM Erlotinib
1 uM Gefitinib
1 uM Lapatinib
1 uM Lap + 1 uM Erl
B
OD 570 nm (AU)
0.25
0.2
0.15
0.1
0.05
0
**
***
*
Untreated
HER4 mAb
1 uM HER3 Affy
500 nM NRG2b
100 nM NRG1b
100 nM NRG1b+ HER4 mAb
100 nM NRG1b +1 uM HER3 Affy
100 nM NRG1b +1 uM Lap
100 nM NRG1b + 1 uM Erl
100 nM NRG1b + 1 uM Lap + 1 uM Erl
C
OD 570 nm (AU)
0.2
0.18
0.16
0.14
0.12
0.1
0.08
0.06
0.04
0.02
0
*
Untreated
8 nM EGF
8 nM EGF +1 uM Lap
8 nM EGF + 1 uM Erl
8 nM EGF + 1 uM Lap + 1 uM Erl
8 nM EGF + 100 nM NRG1b
8 nM EGF + 100 nM NRG1b + 1 uM Lap
8 nM EGF + 100 nM NRG1b + 1 uM Erl
8 nM EGF + 100 nM NRG1b +1 uM Lap + 1 uM Erl

Figure 6-5 – Toxicity (A) and proliferative effect (B-C) or treatments used during Single-Particle Tracking, as assessed by a colorimetric MTT assay. T47D cells were cultured for 24 h in complete medium before starvation for 2 h. All TKIs were added to cell culture medium during starvation and kept in solution throughout the treatment with growth factors (1h). All samples were treated and acquired in triplicates, normalised against empty wells and averaged values were compared against untreated controls via two-tailed Student's t-Test. Statistical analysis was performed in Excel. *= P<0.01; **=P<0.001; ***=P<0.0001.

As expected from published IC_{50} data for the inhibition of proliferation[275,276], treatment with 1 µM of either Erlotinib or Lapatinib did not significantly decrease the vitality of T47D cells. Treatment with 1 µM of Gefitinib, on the other hand, had a significant toxic effect, which is unexpected as T47D cells are not thought to depend on HER1 signalling for survival. Treatment with a combination of Erlotinib and Lapatinib, instead, did not show any further toxicity over that of the single drugs, and 10% DMSO, used as control for the effects of concentrated drugs, significantly promoted cell growth.

None of the ligands for HER1 and HER3, or combinations thereof, seems able to robustly promote proliferation on the timescale analysed, but, in accordance with the results published by Naresh *et al.* [42], treatment of T47D cells with a saturating concentration of NRG2β, a specific HER4 activating ligand [87], potently inhibited cell survival, via activation of HER4-mediated pro-apoptotic pathways. Treating cells with NRG1β, which can activate both HER3 and HER4, in conjunction with an anti-HER3 blocking Affibody showed a trend towards reduced vitality, but it did not reach the threshold for significance. Treating cells with high doses of anti-HER3 Affibody, however, resulted in a significant loss of vitality. This could be due to the interference of the Affibody with basal HER3 signalling, but it should not represent a problem for SPT experiments as the incubation time is greatly reduced (10' vs 1h) and the concentrations employed are at least 20x smaller.
The sensitivity of the cell model to HER4-mediated apoptosis could represent a problem in future, when attempting to specifically activate HER4 for tracking experiments. Careful optimisation of ligand concentrations, considering both particle density and cell vitality, will be required.

6.2.3. Determination of average instantaneous diffusion coefficient (*D*) values for all pairs of receptors in presence or absence of saturating concentrations of non-competing HER family ligands and TKIs

Single-Particle Tracking produces very high-content data. Because of this, many different parameters can be calculated from the same datasets. From the MSD curves calculated for each track, one can calculate the instantaneous *D* coefficient, the degree of deviation from pure diffusion of the particles' diffusion and their degree of confinement. From the Single-Particle tracks themselves one can calculate the frequency of interactions between two particles in different channels, and the lifetimes of the interactions.

First of all, the diffusional behaviour of labelled receptors on cell membranes was analysed in a somewhat coarse fashion by calculating the average instantaneous diffusion coefficient *D.* Cells were labelled and tracked as described in **Paragraphs 2.3 and 2.4**, and the *D* coefficient was calculated by fitting a straight line to the first 3 points of that MSD curve then calculating *D* directly from the gradient m of the fit, so that *D*=m/4, as described in **Paragraph 2.5**. As for the analysis of the effects of perturbations, the effects of the following treatments on *D* were analysed:

- 100 nM EGF, when tracking HER3 or HER2;
- 100 nM NRG1β, when tracking HER1 or HER2;
- 1 μM Erlotinib;
- 1 μM Lapatinib.

Double treatments with inhibitors were not performed, but might be considered in the future to paint a more complete picture of the behaviour of the HER family and of the dynamics of resistance development.

The average *D* coefficients for all pairs of receptors and conditions are presented in **Table 6-2** and **Figure 6-6** below.

Data acquisition was performed in a pairwise fashion, however in **Table 6-2** each diffusing species is tabulated separately in rows. The tracking partners are indicated by the column labels. Pairs of identical receptors tracked together are on the diagonal of the table. In this case, the *D* value is the average of the values across both channels.

The *D* values for each member of a pair of non-identical receptors tracked together can be found across the diagonal. For each condition (within a box), *D* values from treatment

datasets (coloured) were compared to the reference untreated *D* value (black) using the Kolmogorov-Smirnov non-parametric test. The P Values for each treatment refer to the null hypothesis that both the treated and the reference sample come from the same distribution. Due to the large format of **Table 6-2** and **Figure 6-6**, both captions will be found after the material.

Partner →	HER1 +NRGβ1 +lapatinib +erlotinib	HER1* +NRGβ1 +lapatinib +erlotinib	HER2 +EGF +NRGβ1 +lapatinib +erlotinib	HER3 +EGF +lapatinib +erlotinib	HER3* +EGF +lapatinib +erlotinib
HER1 Diffusion ($\mu m^2/s$)	0.0227 ± 0.0134 0.0322 ± 0.0134 (**) 0.0347 ± 0.0179 (*) 0.0490 ± 0.0229 (***)	0.0272 ± 0.0128 0.0511 ± 0.0287 (*) 0.0509 ± 0.0239 (**) 0.0615 ± 0.0291 (**)	0.0490 ± 0.0245 NR 0.0304 ± 0.0112 (*) 0.0272 ± 0.0143 (*) 0.0580 ± 0.0200	0.0485 ± 0.0149 NR 0.0520 ± 0.0194 0.0391 ± 0.0129 (#)	0.0468 ± 0.0145 NR 0.0487 ± 0.0228 0.0454 ±0.0249
HER1* Diffusion ($\mu m^2/s$)	0.0185 ± 0.0082 0.0239 ± 0.0091 (*) 0.0423 ± 0.0231 (***) 0.0599 ± 0.0244 (***)	0.0232 ± 0.0096 0.0256 ± 0.0121 0.0995 ± 0.0283 (***) 0.0876 ± 0.0232 (***)	0.0248 ± 0.0102 NR 0.0276 ± 0.0099 0.0862 ± 0.0381 (***) 0.0625 ± 0.0294 (***)	0.0309 ± 0.0091 NR 0.1007 ± 0.0198 (***) 0.1012 ± 0.0251 (***)	0.0342 ± 0.0168 NR 0.0483 ± 0.0276 0.1317 ± 0.0251 (***)
HER2 Diffusion ($\mu m^2/s$)	0.1127 ± 0.0203 0.1096 ± 0.0165 0.0897 ± 0.0305 (*) 0.1088 ± 0.0169	0.0810 ± 0.0192 0.0743 ± 0.0258 0.0879 ± 0.0217 0.0925 ± 0.0274 (*)	0.0956 ± 0.0292 0.0943 ± 0.0369 0.0846 ± 0.0292 0.091922 ± 0.0215 NR	0.1173 ± 0.0161 0.1316 ± 0.0184 (*) 0.1071 ± 0.0207 NR	0.1539 ± 0.0157 0.1399 ± 0.0276 0.1146 ± 0.0237 (***) NR
HER3 Diffusion ($\mu m^2/s$)	0.0372 ± 0.0159 NR 0.0350 ± 0.0147 0.0547 ± 0.0158 (**)	0.0259 ± 0.0161 NR 0.0528 ± 0.0238 (**) 0.0448 ± 0.0169 (**)	0.0465 ± 0.0173 0.0385 ± 0.0285 (*) NR 0.0553 ± 0.0176 NR	0.0217 ± 0.0159 0.0174 ± 0.0145 NR NR	0.0566 ± 0.0238 0.0589 ± 0.0189 NR NR
HER3* Diffusion ($\mu m^2/s$)	0.0562 ± 0.0139 NR 0.1036 ± 0.0300 (***) 0.0564 ± 0.0196	0.0605 ± 0.0156 NR 0.0792 ± 0.0244 (*) 0.0805 ± 0.0178 (***)	0.0614 ± 0.0133 0.0743 ± 0.0140 (*) NR 0.0922 ± 0.0171 (***) NR	0.0586 ± 0.0182 0.0707 ± 0.0157 NR NR	0.0547 ± 0.0155 0.0489 ± 0.0211 NR NR

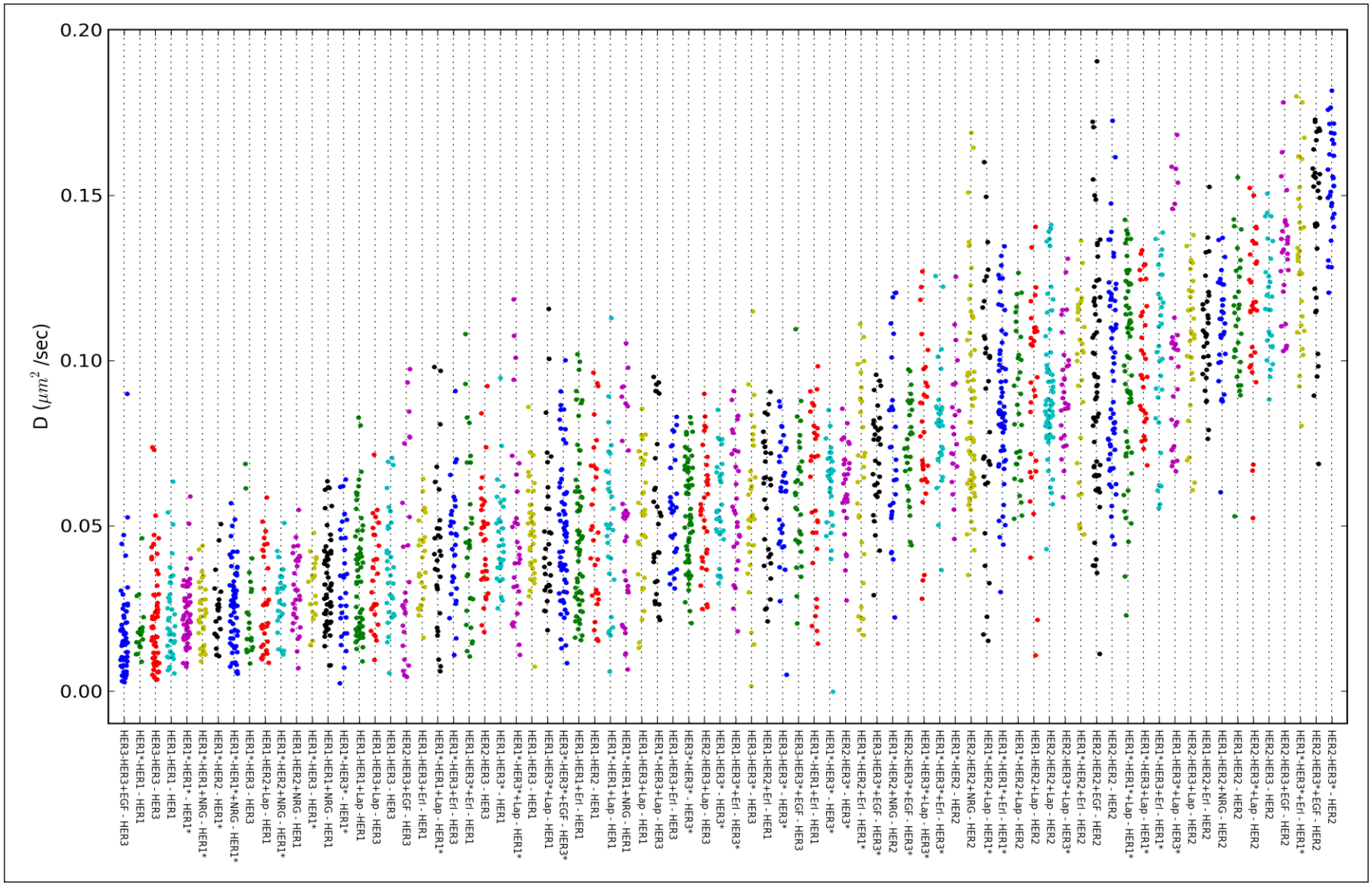
D (μm^2 /sec)
0.20
0.15
0.10
0.05
0.00
HER3-HER3+EGF - HER3
HER1*-HER1 - HER1
HER3-HER3 - HER3
HER1-HER1 - HER1
HER1*-HER1* - HER1*
HER1*-HER1+NRG - HER1*
HER1*-HER2 - HER1*
HER1*-HER1*+NRG - HER1*
HER1*-HER3 - HER3
HER1-HER2+Lap - HER1
HER1*-HER2+NRG - HER1*
HER1-HER2+NRG - HER1
HER1*-HER3 - HER1*
HER1-HER1+NRG - HER1
HER1*-HER3* - HER1*
HER1-HER1+Lap - HER1
HER1-HER3+Lap - HER3
HER1-HER3 - HER3
HER2-HER3+EGF - HER3
HER1-HER3+Efi - HER1
HER1*-HER1+Lap - HER1*
HER1*-HER3+Efi - HER3
HER1-HER3+Efi - HER1
HER2-HER3 - HER3
HER1*-HER3* - HER1
HER1*-HER3*+Lap - HER1*
HER1-HER3 - HER1
HER1-HER3*+Lap - HER1
HER3*-HER3*+EGF - HER3*
HER1-HER1+Efi - HER1
HER1-HER2 - HER1
HER1*-HER1+NRG - HER1
HER1*-HER1+Lap - HER1
HER1*-HER3+Lap - HER3
HER1-HER3+Lap - HER3
HER1*-HER3+Lap - HER3*
HER1-HER3+Efi - HER3
HER3*-HER3* - HER3*
HER2-HER3+Lap - HER3
HER1-HER3* - HER3*
HER1*-HER3*+Efi - HER3*
HER3-HER3* - HER3
HER1-HER2+Efi - HER1
HER3-HER3* - HER3*
HER3-HER3*+EGF - HER3
HER1*-HER1+Efi - HER1
HER1*-HER3* - HER3*
HER2-HER3* - HER3*
HER1*-HER2+Efi - HER1*
HER3-HER3*+EGF - HER3*
HER1*-HER2+NRG - HER2
HER2-HER3*+EGF - HER3*
HER1*-HER3*+Efi - HER3*
HER1*-HER3*+Lap - HER3*
HER1*-HER2 - HER2
HER2-HER2+NRG - HER2
HER1*-HER1*+Efi - HER1*
HER1*-HER2+Lap - HER2
HER1-HER2+Lap - HER2
HER2-HER3*+Lap - HER3*
HER1*-HER2+Efi - HER2
HER2-HER2+EGF - HER2
HER2-HER2 - HER2
HER1*-HER1*+Lap - HER1*
HER1*-HER3+Efi - HER1*
HER1-HER3+Lap - HER3*
HER2-HER3+Lap - HER2
HER1-HER2+Efi - HER2
HER1-HER2+NRG - HER2
HER1-HER2 - HER2
HER2-HER3*+Lap - HER2
HER2-HER3 - HER2
HER2-HER3+EGF - HER2
HER1*-HER3*+Efi - HER1*
HER2-HER3*+EGF - HER2
HER2-HER3* - HER2

Table 6-2 (two pages prior) – Average *D* coefficients for homo and hetero-interactions between HER1-3 in the presence of perturbation (ligand binding to other receptors or TKIs). For homo-interactions, diffusion rates of the two channels were combined. NR = not relevant. Significance levels are calculated using as a reference the value recorded from untreated (black) samples in each group: *P< 0.01; **P<0.001; ***P<0.0001; #= borderline (P = 0.05 -0.01) significance (Kolmogorov-Smirnov test). Data are presented as average ± SD and all averages were calculated on at least 30 independent areas from at least 3 independent biological replicates.

Figure 6-6 (previous page) – Distributions of *D* coefficients for the data in Table 6-2. The average *D* derived from every technical replicate (n ~30) from every individual receptor is plotted as an independent dot for each of the 48 possible interaction/treatment combinations. Data deriving from the two channels of homo-pair combinations were combined for plotting.

The data in **Figure 6-6** display a quite large spread in the average *D* coefficients calculated for each technical replicate, however the width of the spread seems to be reasonably conserved throughout the entire set of data. Among the slowest diffusing receptors, on the left-hand side of the plot, are basal state HER3 and activated HER1* with *D* ~ 0.015- 0.020 ($\mu m^2/s$), while, at the right-hand side of the plot, the fastest receptors appear to be HER2 in most interaction/treatment combinations, and HER1* upon TKI treatment, with *D* ~ 0.1- 0.15 ($\mu m^2/s$).

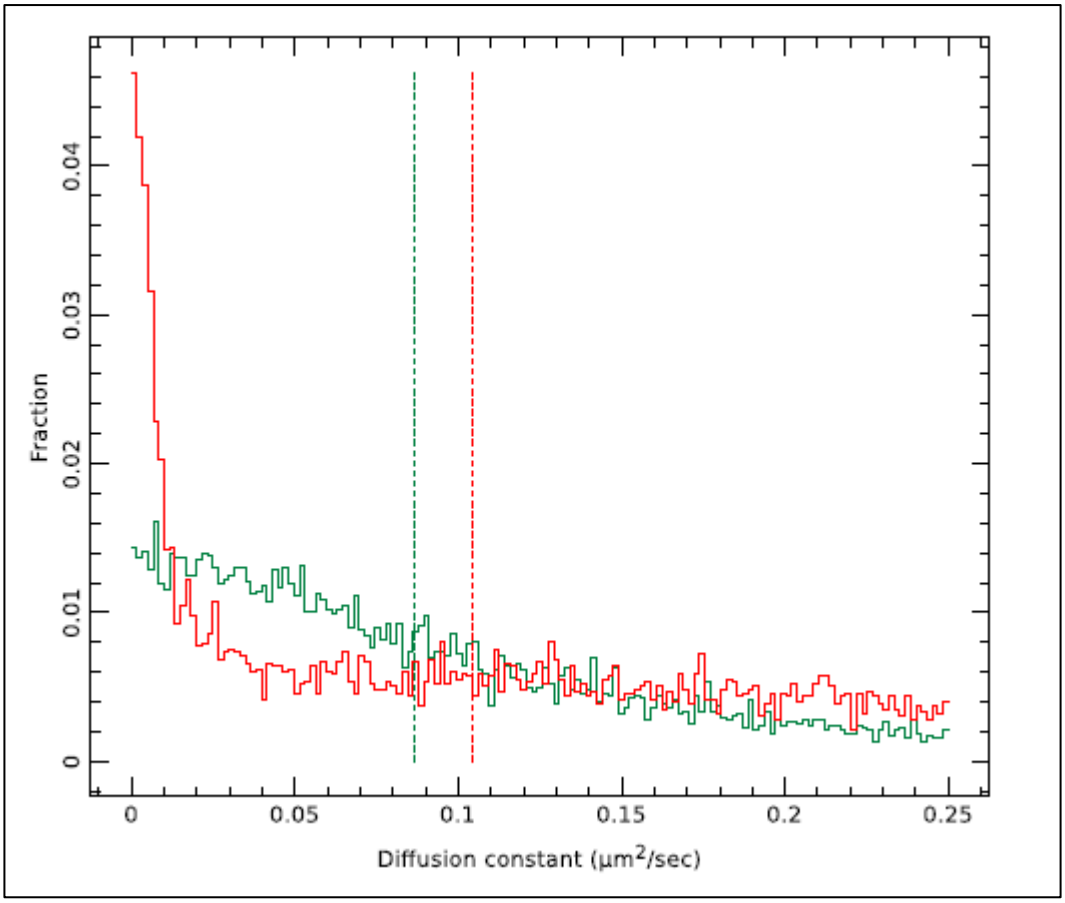

Figure 6-7 – Example two-colour diffusion plot from the systematic tracking set of data: HER2 Alexa 488 (red line) vs. HER1* CF640R (green line) + 1 µM Lapatinib. For each analyte, the solid lines are the distributions of per-track instantaneous *D* derived from the fitting of per-track MSD for all the tracks acquired for a set of experimental conditions. The dotted vertical lines represent the instantaneous *D* calculated from the combined MSD fit derived from all the tracks combined for that experimental condition.

Despite the spread in their measurements, the average *D* coefficients reflect only an aspect of the variability in diffusion of the HER family receptors, especially of the faster-diffusing ones. As an example, **Figure 6-7** depicts the instantaneous *D* coefficient distributions for the HER1*-HER2 combination in presence of 1 µM Lapatinib, plotted from the *D* coefficients calculated from the individual MSD plots for each track in the 30 technical replicates. It is clear for HER2 (red line) that there are at least two separate populations of receptors, one of scarcely mobile receptors clustered around zero (peak) and at least one of highly mobile receptors, whose *D* exceeds 0.05 $\mu m^2/s$ and which goes on well beyond the scale of the plot (smeared tail). The profile of the second distribution (or sum of distributions) is convoluted with the profile of the immobile population. The expected distributions of the two populations are gamma distributions [352] with different shape and scale parameters. The distribution of the immobile

fraction will be limited on the left by the fact that *D* values below zero are physically meaningless. This finding suggests the presence of heterogeneous populations of HER2 receptors on the cell surface. The distribution of *D* of HER1* (green line), instead, does not appear to show two distinct populations, but seems to be decreasing monotonically.

Even with these limitations, the *D* results in **Table 6-2** and **Figure 6-6** clearly show interesting changes in the diffusive behaviour of the probes.

Figure 6-8 A shows the behaviour of HER1 probes under the different perturbations employed. The reference *D* value has been taken to be that of basal HER1 on untreated cells and is highlighted in pink in the figure. Data-points are colour-coded according to the P Value of the difference between their *D* distribution and that of the reference sample. Data-points in green are not significantly different from the reference, data-points in yellow show a borderline significant difference (0.01 < P Value <0.05), and data-points in red show a significant difference with the reference sample (P Value <0.01)

When cells are treated with either Erlotinib or Lapatinib, HER1* diffusion increases significantly (to 0.087 $\mu m^2/s$ to and 0.099 $\mu m^2/s$, respectively), compared both to the activated, un-inhibited activated state (P= <<0.0001 and <<0.0001, respectively), and to the basal state (P <<0.001and <<0.0001, respectively). This seems to indicate that *D* is dependent on kinase activity, as shown also by Low-Nam *et al.* [110].

The diffusion of HER2, instead, seems to be relatively unaffected by perturbations remaining at around 0.1 $\mu m^2/s$; however it is interesting to note that addition of EGF to cells labelled with both anti-HER2 and anti-HER3 Affibodies provokes an increase in HER2 diffusion coefficient to 0.13 $\mu m^2/s$ and at the same time a decrease in HER3 diffusion coefficient from 0.046 $\mu m^2/s$ to 0.0385 $\mu m^2/s$.

The diffusional behaviour of HER3 probes is discussed here considering the set of samples labelled with HER1 and HER3. As shown in **Figure 6-8 B**, HER3 diffusion appears to be regulated in a complex fashion, depending not only on its activation status, but also by the activation status of cognate receptors. NRG1β –bound HER3* diffusion is significantly increased compared to the basal state. This is in contrast with what was reported by Steinkamp *et al* [137]. The diffusion of basal HER3 is increased when HER1 is inhibited with 1 μM Erlotinib, and is decreased when HER1 is activated by EGF. Moreover, the diffusion of activated HER3*seems to be consistently increased by treatment with 1 μM Lapatinib (see also **Table 6-2**), while basal HER3 behaviour is less unequivocal. Changes in HER3* diffusion upon Lapatinib treatment, however, are not related to differences in its interactions with its partners (see **Table 6-3**,

below). It appears that HER3 species are able to sense HER1/HER2 activation status, probably through interactions with downstream effectors or possibly via direct contact, and regulate their own behaviour accordingly.

It is also interesting to note that NRG1β treatment increases the diffusion of Affibody-bound HER3 receptors in cells labelled with both NRG1β and anti-HER3 Affibody compared to cells labelled only with anti-HER3 Affibody ($P << 0.0001$). The diffusion of HER3 in presence of NRG1β is not significantly different from that of the receptors bound to NRG1β tracked on the same cells ($P = 0.76$). The diffusion of HER2 is also very significantly increased when tracked with NRG1β ($P << 0.0001$) or with HER1* ($P << 0.0001$) as interaction partners, compared to HER2 tracked alongside HER1 Affibody, but there is no significant difference in the diffusion of HER1 or HER1* on cells labelled with anti-HER3 Affibody compared to NRG1β ($P = 0.8$ and 0.16, respectively).

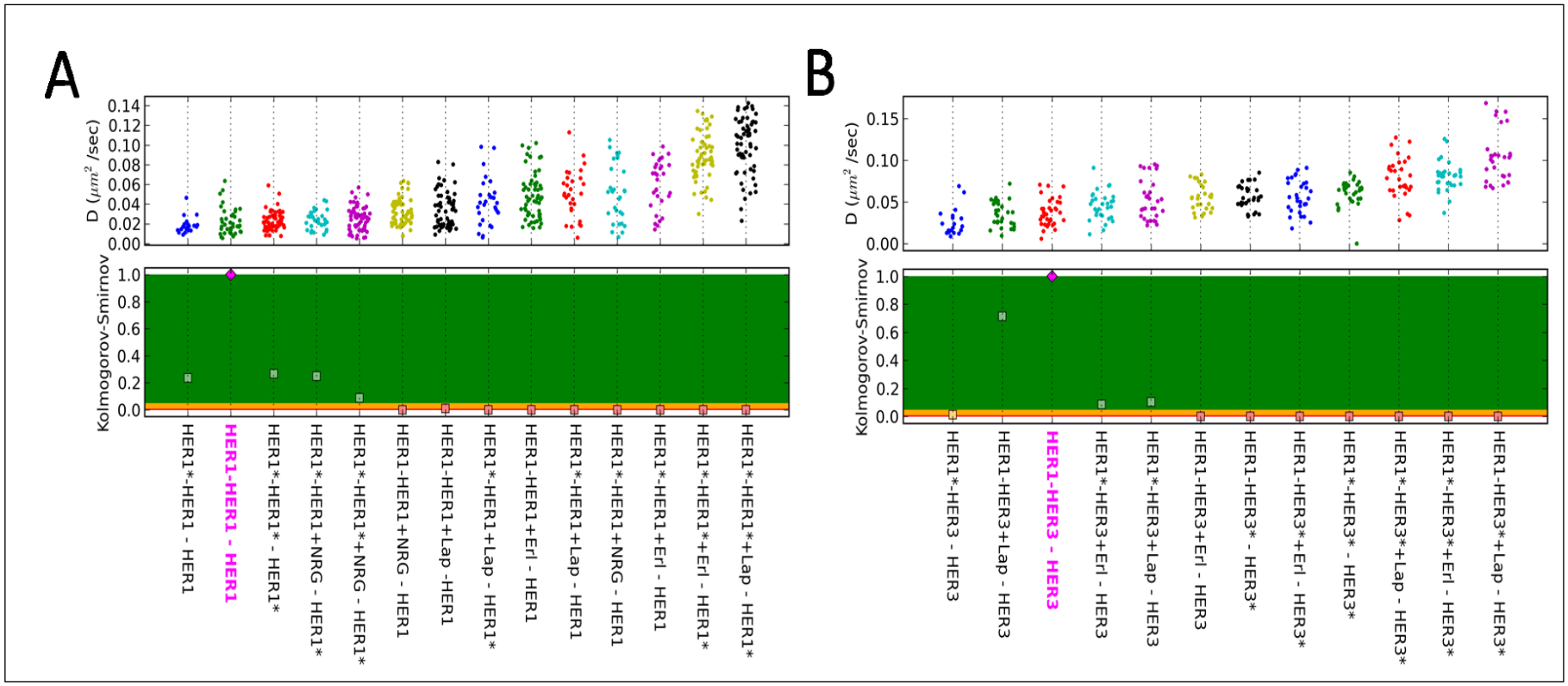

Figure 6-8 – Distributions and significance levels for A) HER1 *D* and B) HER3 *D* under different treatment conditions. Data labels are structured as follows: tracked pair – receptor considered. The average *D* coefficient, calculated from each of the at least 30 technical replicates, collected over at least 3 independent biological replicates is plotted as a single dot in the top section of the figure. Data are compared with the condition highlighted in pink in the bottom section of the figure. Points falling in the green area: P Value >0.05; points in the yellow area: P Value <0.05, >0.01; points falling in the red area = P Value < 0.01. Data were sorted according to *D* value.

6.2.4. Determination of colocalisation frequencies for all pairs of receptors in presence or absence of saturating concentrations of non-competing HER family ligands or TKIs

The Single-Particle Tracking method described in this thesis has the unique advantage of providing high coverage for the features in study, allowing easy detection of transient colocalisation events. Despite its advantages in terms of coverage and stoichiometry of labelling, it does not allow to localise the particles with sufficient precision to accurately measure nanometric distances between two interacting particles as done by Low-Nam *et al*. [110]. Its localisation precision, however, is in the range of the size of HER1 high-order structures as measured by CI-FLIP [95], so that the dynamics of the clusters might be investigated. In keeping with the localisation error measured for the laser power and acquisition frame rate settings used in this part of the project, two particles in different channels were defined as colocalised when they were together within a radius of 160 nm for at least 3 frames, not necessarily consecutive, during their lifetime.

An overview of the distributions of pairwise colocalisation frequencies for all receptor pairs, in presence or absence of saturating concentrations of non-competing HER family ligands (EGF when tracking HER3 or HER2, NRG1β, when tracking HER1 or HER2) and Lapatinib or Erlotinib is provided in **Figure 6-9**. The frequency of colocalisation was calculated as the fraction of particles interacting with a particle in another channel according to the criteria stated above, compared to the total number of particles in all channels. All average values, error ranges and K-S test significance values are presented in **Table 6-3**, below.

Partner →	HER1 +NRGβ1 +lapatinib +erlotinib	HER1* +NRGβ1 +lapatinib +erlotinib	HER2 +EGF +NRGβ1 +lapatinib +erlotinib	HER3 +EGF +lapatinib +erlotinib	HER3* +EGF +lapatinib +erlotinib
HER1 (%)	0.43 ± 0.21 0.21 ± 0.22 (**) 0.78 ± 1.48 0.21 ± 0.19 (*)				
HER1* (%)	0.42 ± 0.33 0.19 ± 0.22 (#) 0.14 ± 0.29 (**) 0.20 ± 0.16 (#)	2.11 ± 1.61 2.63 ± 2.32 0.31 ± 0.25 (***) 0.38 ± 0.26 (***)			
HER2 (%)	0.15 ± 0.13 0.11 ± 0.12 0.29 ± 0.27 0.40 ± 0.37 (#)	0.77 ± 0.64 1.04 ± 0.86 0.14 ± 0.12 (**) 1.25 ± 0.88	0.43 ± 0.39 0.45 ± 0.49 0.63 ± 0.49 0.83 ± 0.77 (#) NR		
HER3 (%)	0.30 ± 0.22 NR 0.20 ± 0.20 0.57 ± 0.30 (*)	0.22 ± 0.22 NR 0.13 ± 0.15 (*) 0.21 ± 0.17	0.25 ± 0.15 0.12 ± 0.11 (*) NR 0.35 ± 0.31 (#) NR	0.25 ± 0.25 0.12 ± 0.21(#) NR NR	
HER3* (%)	0.17 ± 0.16 NR 0.13 ± 0.12 0.11 ± 0.12	0.15 ± 0.20 NR 0.26 ± 0.48 (*) 0.09 ± 0.08	0.35 ± 0.18 0.35 ± 0.21 NR 0.39 ± 0.29 NR	0.33 ± 0.21 0.19 ± 0.18(*) NR NR	0.22 ± 0.20 0.14 ± 0.19 (#) NR NR

Table 6-3 - Two-colour colocalisation frequencies (threshold = 160 nm, 3 frames) for homo and hetero-interactions between HER1-3 in the presence of perturbation (ligand binding to other receptors or TKIs). NR = not relevant. Significance levels are calculated using as a reference the value recorded from untreated (black) samples in each group: *P< 0.01; **P<0.001; ***P<0.0001; #= borderline (P = 0.05 -0.01) significance (Kolmogorov-Smirnov test). Data are presented as average ± SD and all averages were calculated on at least 30 independent areas from at least 3 independent biological replicates.

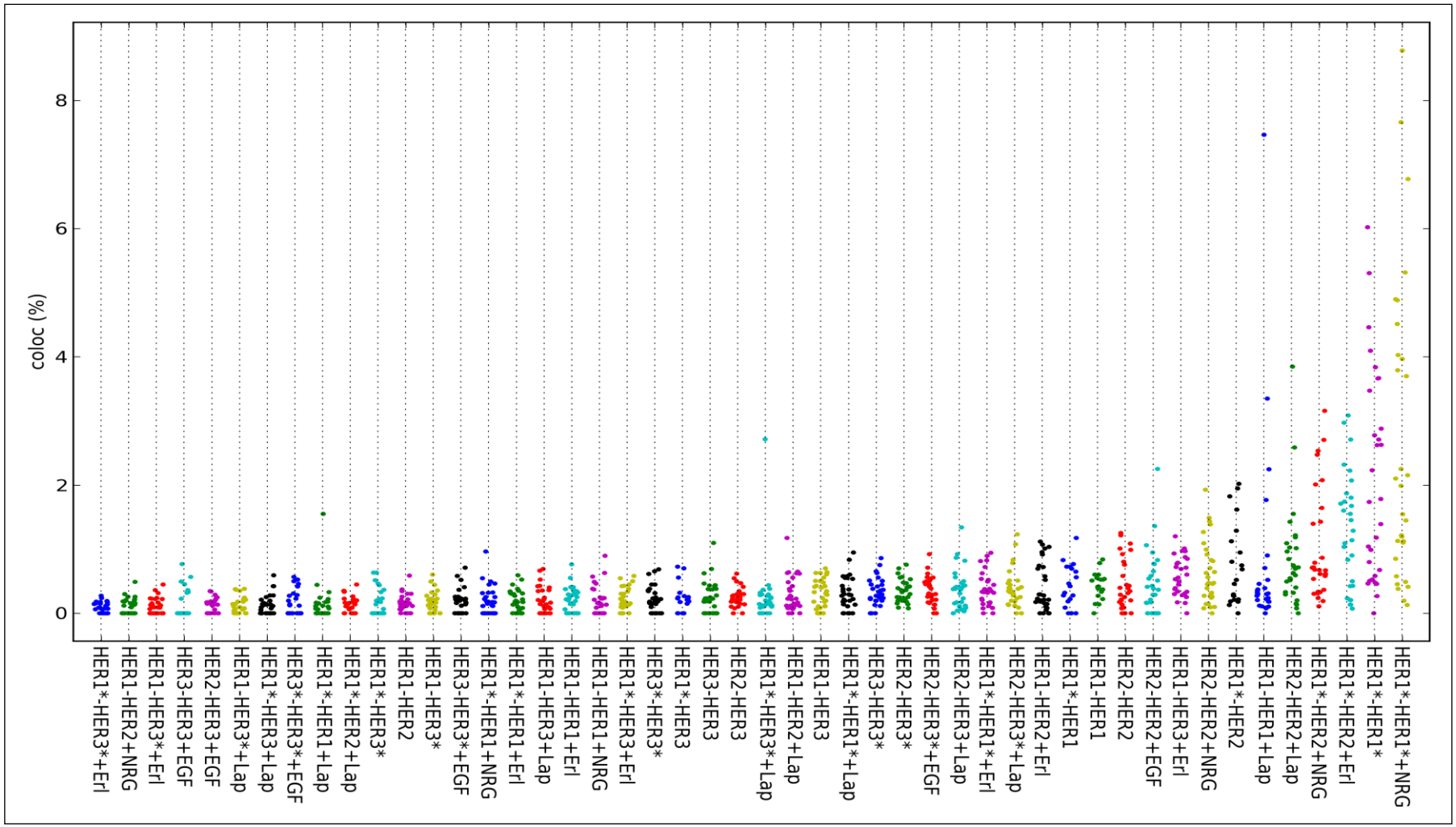

Figure 6-9 - Distributions of colocalisation frequencies for the data in Table 6-3. The average colocalisation frequency derived from every technical replicate (n ~30) from each of the 48 possible interaction/treatment combinations is plotted as a single dot.

Taken together, these results seem to indicate that in T47D cells there is a hierarchy of interactions between HER family receptors as previously reported by other studies (see the **Chapter 1** for a more detailed discussion).

As shown in the cartoon in **Figure 6-10**, the main receptor pairs, in terms of frequency, are HER1*-HER1* and HER1*-HER2.

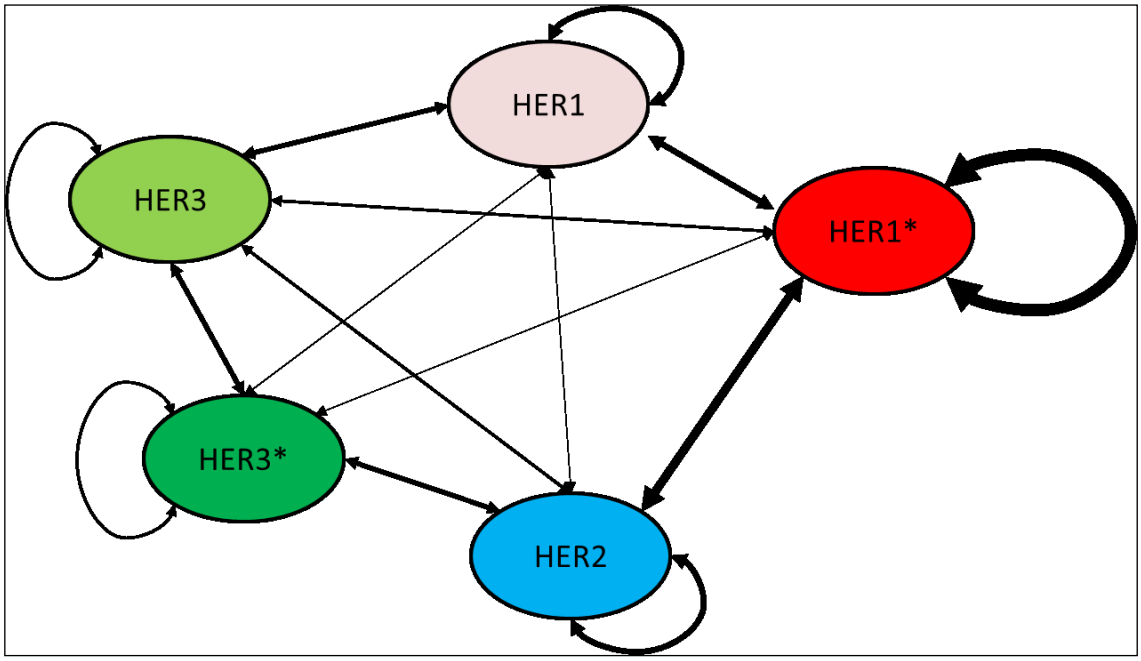

Figure 6-10 - Schematic representation of the interactions between HER family receptors in the untreated state. The thickness of the arrows connecting the nodes is proportional to the likelihood of interaction between the receptors.

The error in the determination of the frame-by-frame position of two particles can result in the spurious detection of transient colocalisation events between two particles moving in the vicinity of one another. In order to remove artefactual colocalisation events from the detected pool, the data can be denoised or smoothed with a filter. The Chung-Kennedy (C-K) filter [353], first used to extract small biological signals from noisy single-channel voltage-clamp experiments, allows to smooth the data getting rid of noise-derived fluctuations but preserving sharp changes in the signal such as changes of state as depicted in **Figure 6-11**. This allows reasonably accurate measurements of kinetics and exponential decays even from noisy data, a feature that will be indispensable in future work for the determination of association and dissociation kinetics.

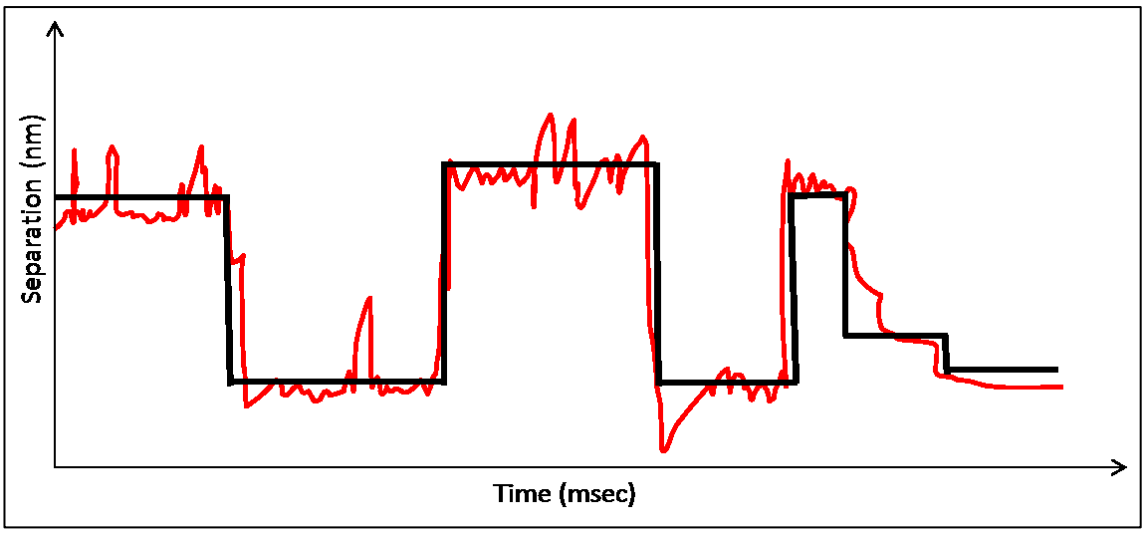

Figure 6-11 – Schematic representation of the output of a Chung-Kennedy filter. In red: real, noisy data. In black: C-K filter output.

The whole set of two-channel single-molecule colocalisation data was subject to smoothing with a Chung-Kennedy (C-K) filter, using different parameters to vary the width of the filter. The filter was applied on the spatial separation (nm). This was done because the error in the localisation of the particles putatively undergoing colocalisation can cause the particle separation parameter to float around the colocalisation threshold, resulting in a degradation of the assessment of colocalisation frequencies.

Let's consider two particles colocalising with a "true" distance of 40 nm for a number of frames n. Each particle has a noise-dependent localisation error estimated within 10-35 nm per frame and the threshold for colocalisation is 90 nm. The stochastic nature of the localisation error can make the particle distance cross the colocalisation threshold repeatedly from frame to frame even if the underlying separation remains the same. The C-K filter can smooth out the frame-to-frame fast fluctuations in particle separation which are due to localisation error, but wouldn't be able to smooth out a sustained change in separation due to the complex coming apart. This denoising step, as expected, lead to the loss of part of the colocalisation events and to the loss of significance of some differences between conditions, however most of the main findings were conserved (see **Table 6-4**).

Partner →	HER1 +NRGβ1 +lapatinib +erlotinib	HER1* +NRGβ1 +lapatinib +erlotinib	HER2 +EGF +NRGβ1 +lapatinib +erlotinib	HER3 +EGF +lapatinib +erlotinib	HER3* +EGF +lapatinib +erlotinib
HER1 (%)	0.43 ± 0.21 ** NS NS * NS				
HER1* (%)	0.42 ± 0.33 # NS **NS # NS	2.11 ± 1.61 NS *** ***			
HER2 (%)	0.15 ± 0.13 NS NS # NS	0.77 ± 0.64 NS ** NS #	0.43 ± 0.39 NS NS # § NR		
HER3 (%)	0.30 ± 0.22 NR NS *	0.22 ± 0.22 NR * NS NS	0.25 ± 0.15 * NS NR # NS NR	0.25 ± 0.25 # NS NR NR	
HER3* (%)	0.17 ± 0.16 NR NS NS	0.15 ± 0.20 NR * NS NS	0.35 ± 0.18 NS NR NS NR	0.33 ± 0.21 * NS NR NR	0.22 ± 0.20 # NS NR NR

Table 6-4 – Robustness of the differences between conditions after application of C-K filters.

Significance levels for all conditions were taken from **Table 6-3** and compared with those obtained after filtering with different iterations of C-K filter. Values were greyed out if they were not conserved in filtered datasets. Green values were taken from the consensus of filtered datasets.

§ There was no consensus between filtered datasets for this value. Borderline significance was maintained under some circumstances but not all.

Additionally, “false positives” in the colocalisation can arise from particles randomly passing by each other. In this analysis, the spatial colocalisation threshold has been set at 160 nm and the temporal colocalisation threshold has been set at 150 ms (3 frames). If a particle diffuses with D = 0.02 μm^2, the distance at which it can travel in 150 ms can be calculated as $< x > = \sqrt{4Dt}$ = 109 nm. This means that two particles diffusing in these conditions might appear to be colocalised entirely by random chance. The likelihood of this phenomenon decreases as D increases. For example, if D = 0.06 μm^2, the average distance to which a particle can travel in 150 ms will increase to 190 nm and to 268 nm if D increases to 0.12 μm^2.

In order to account for these artefactual colocalisation events, an additional analysis has been performed on the data. For each condition, colocalisation analysis was repeated after randomising the particles positions in one of the two channels as described in **Paragraph 2.23.1**. The colocalisation events counted in these conditions are “false-positives” caused by the coincidental diffusion of two particles in the same area. The estimated percentage of events for each condition is given in **Table 6-5**. The data show that the percentage of coincidental colocalisation events is consistently low, with average values in the range of 0.04-0.21%.

Partner →	HER1 +NRGβ1 +lapatinib +erlotinib	HER1* +NRGβ1 +lapatinib +erlotinib	HER2 +EGF +NRGβ1 +lapatinib +erlotinib	HER3 +EGF +lapatinib +erlotinib	HER3* +EGF +lapatinib +erlotinib
HER1 (%)	0.19 ± 0.08 0.13 ± 0.06 0.15 ± 0.09 0.11 ± 0.05				
HER1* (%)	0.12 ± 0.07 0.10 ± 0.08 0.06 ± 0.04 0.11 ± 0.06	0.16 ± 0.10 0.21 ± 0.14 0.05 ± 0.02 0.11 ± 0.06			
HER2 (%)	0.07 ± 0.04 0.06 ± 0.03 0.12 ± 0.09 0.13 ± 0.14	0.10 ± 0.09 0.10 ± 0.05 0.04 ± 0.03 0.15 ± 0.06	0.06 ± 0.04 0.05 ± 0.03 0.07 ± 0.04 0.08 ± 0.04 NR		
HER3 (%)	0.14 ± 0.08 NR 0.10 ± 0.08 0.17 ± 0.05	0.20 ± 0.09 NR 0.06 ± 0.03 0.09 ± 0.06	0.09 ± 0.04 0.05 ± 0.04 NR 0.14 ± 0.10 NR	0.13 ± 0.08 0.04 ± 0.05 NR NR	
HER3* (%)	0.09 ± 0.04 NR 0.05 ± 0.04 0.04 ± 0.03	0.06 ± 0.04 NR 0.06 ± 0.04 0.04 ± 0.02	0.04 ± 0.02 0.04 ± 0.02 NR 0.03 ± 0.02 NR	0.20 ± 0.09 0.09 ± 0.05 NR NR	0.05 ± 0.03 0.04 ± 0.02 NR NR

Table 6-5 - Two-colour coincidental colocalisation frequencies (threshold = 160 nm, 3 frames) for homo and hetero-interactions between HER1-3 in the presence of perturbation (ligand binding to other receptors or TKIs). NR = not relevant. Data are presented as average ± SD and all averages were calculated on at least 30 independent areas from at least 3 independent biological replicates.

In order to better evaluate the impact of coincidental localisation on the total colocalisation frequency, for each dataset of each condition the difference between the total colocalisation fraction and the coincidental colocalisation fraction was calculated, and then the fraction of datasets where the difference is >0 was computed for each condition and plotted in **Figure 6-12**.

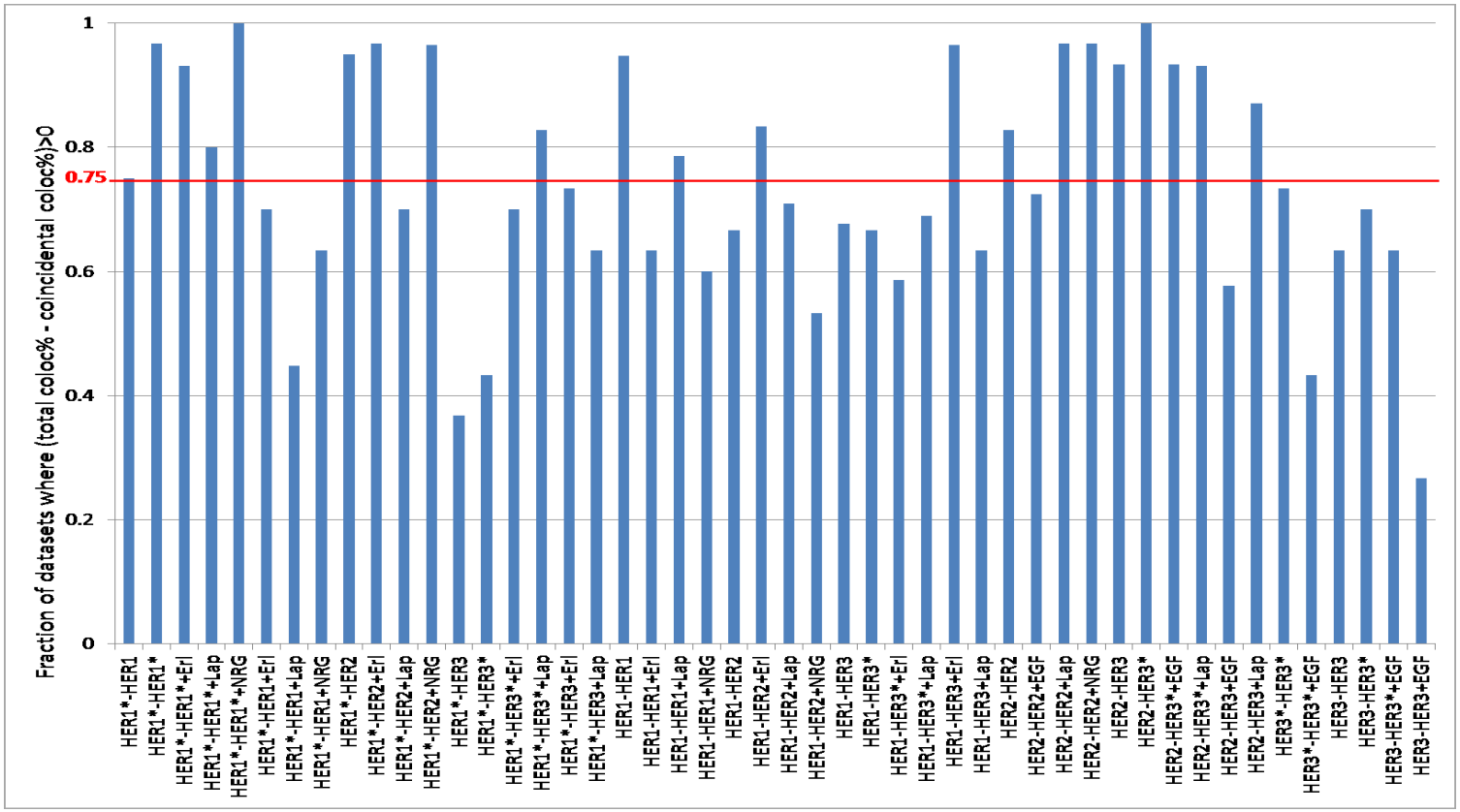

Figure 6-12 – Assessment of the impact of coincidental colocalisation on the determination of colocalisation frequencies. For each dataset of each condition, the coincidental colocalisation fraction was calculated and subtracted from the total colocalisation fraction. For each condition, the fraction of datasets where the difference is positive was plotted. A threshold of 0.75 was set to identify the conditions for which the confidence of having measured colocalisation levels significantly above the coincidental colocalisation background.

A threshold of 0.75 was chosen to discriminate conditions for which there is a high confidence of having measured colocalisation events above the basal coincidental colocalisation. The results indicate that there is a reasonable confidence in the measurement of colocalisation frequencies for:

- HER1*-HER1
- HER1*-HER1*
- HER1*-HER1*+ Erlotinib
- HER1*-HER1* + Lapatinib
- HER1*-HER1* + NRG1β
- HER1*-HER2
- HER1*-HER2 +Erlotinib
- HER1*-HER2 + NRG1β
- HER1*-HER3*+Lapatinib
- HER1-HER1
- HER1-HER1 + Lapatinib
- HER1-HER2 + Erlotinib
- HER1-HER3 + Erlotinib
- HER2-HER2
- HER2-HER2 + Lapatinib
- HER2-HER2 + NRG1β
- HER2-HER3
- HER2-HER3 + Lapatinib
- HER2-HER3*
- HER2-HER3* + EGF
- HER2-HER3* + Lapatinib

As it could have been reasonably expected, the conditions with highest colocalisation frequencies, such as HER1*-HER1* and HER1*-HER2, had a high fraction of datasets where the total colocalisation was higher than the coincidental colocalisation, but, somewhat surprisingly, even low-frequency interactions such as HER2-HER3 and HER2-HER3* were significantly above the estimated levels of coincidental colocalisation. For all other datasets, it cannot be determined with high enough confidence whether the colocalisation fractions obtained are due to more than random chance. Results will be further discussed using the normalised colocalisation frequency for each condition,

$$normalised\ Coloc = total\ Coloc - coincidental\ Coloc\ .$$

Despite the fact that HER2 has been defined as the preferred dimerization partner for the whole HER family by biochemical studies [129,130], in the normalised data, HER1*-HER1*interactions are more frequent than HER1*-HER2 interactions despite the fact that HER2 expression levels are higher than HER1 expression levels in T47D cells (P= 0.007 – K-S test).Consistent with what was reported by Szabo *et al.* [123], activation of HER1 leads to a significant and robust increase in its interactions with HER2 (P= 0.0002). HER2-HER2 interactions are not significantly less frequent than HER1*-HER2 interactions (P= 0.41) in the normalised data. The frequency of HER2-HER2 interactions does not appear to be significantly different from that of HER2-HER3* interactions (P=0.32).The likelihood of interaction between HER2 and HER3, instead shows a significant (P = 0.008) increase upon HER3 activation with 40 nM NRG1β. The HER2-HER3* dimer was reported as the major supramolecular interaction in which HER2 is involved by Tzahar *et al.* [354], however these findings highlight a substantial parity between HER2 homo-interactions and interactions with activated HER3*. It should however be noted that, as the HER2-HER3*receptor pair is the most efficient signalling unit of the HER family [133], a relatively small number of interacting pairs might be sufficient for maximal downstream signalling to the PI3K axis.

Inactive HER1-HER1 and HER2-HER2 interactions are present in this cell model despite the low levels of expression of the receptors, which is not surprising, as homo-interactions of both receptors have been previously reported in literature using a variety of methods.

As discussed in **Chapter 1**, structural evidence points out to an inherent inability of HER2 to homo-dimerize, due to steric clashes between the C-term of domain II in the ECD [120], and apparently HER2 ECD does not readily homo-dimerize in solution [355]. However, homo-dimerization of full-length HER2 receptor in cells has been demonstrated before, especially in cells that either endogenously or exogenously overexpress HER2 [100–102,122–126]. The role of these clusters is poorly characterised and they have mostly been viewed as reservoirs of receptors that are not involved in signalling. The effect of ligand binding on the extent of macroscopic HER2 interactions has also been disputed. Some groups report a decrease in HER2 homo-cluster size with EGF stimulation [100,124], while it has been reported that HER2 instantaneous diffusion coefficient increases with NRG treatment [348], which hints to a decrease in clustering. However, increased clustering with EGF or NRG treatment has also been reported [122].

Despite the fact that T47D cells express low, physiological levels of HER2 (ca. 3×10^4 receptors/cell)[350], HER2-HER2 interactions were nonetheless found, and their levels did not significantly change with either EGF or NRG1β treatment.

Basal dimerization and oligomerisation of the HER1 receptor have been detected with many different biochemical and imaging methods [94–107], and form the basis for some models of signalling [96,98,99]. The extent of the detected basal homo-interactions varies with the HER1 expression levels of the cell model employed and with the technique, however, HER1-HER1 interactions, albeit transient, have been detected using Single-Particle Tracking methods by both Chung *et al.* [109], and Low-Nam *et al.* [110].

There is good agreement on the EGF-mediated increase in HER1*-HER1* interactions, and indeed, in this model system the extent of HER1*-HER1* interactions is significantly higher than that of HER1-HER1 interactions (~5x increase in mean colocalisation frequency – $P= 10^{-6}$). Interestingly, interactions between activated HER1* and inactive HER1 are few in all conditions studied. They are significantly reduced in comparison to HER1*-HER1* and are not significantly different from HER1-HER1 interactions ($P= 3x 10^{-4}$ and 0.29, respectively) in both C-K filtered and unfiltered conditions, a finding which seems somewhat counter-intuitive. This however suggests the hypothesis that the liganded/active receptor population might be spatially segregated from the basal population, possibly through differential interactions with either the cortical actin cytoskeleton [115–118,356] or lipid microdomains [357,358]. A more thorough investigation of the determinants of the putative segregation of the two receptor populations is described in **Chapter 7**.

Furthermore, the colocalisation likelihood of partially activated HER1*-HER1 and inactive HER1-HER1 interactions is not significantly different from that of completely activated HER1*-HER1* in presence of Lapatinib or Erlotinib (P=0.48 and 0.74 for HER1-HER1* compared to HER1*-HER1* treated with Lapatinib and Erlotinib; P=0.61 and 0.56 for HER1-HER1 compared to HER1*-HER1* treated with Lapatinib and Erlotinib).

Interactions between HER1 and HER3 have generally been considered minor and possibly secondary to either HER1*-HER2 or HER3*-HER2 interactions [129,132]. Weak and uni-directional transactivation of HER3 by EGF-activated HER1* has been reported [130], however recent reports seem to point to the possibility that EGF activation might preferentially drive HER1*-HER1* interactions in cells transfected with HER1 and HER3, resulting in a net decrease in hetero-interactions, while treatment with NRG1 β would promote HER1-HER3* interactions. In the T47D model system, low frequencies (<0.5%) of interactions between HER1 and HER3 were recorded for all possible activation combinations (see **Table 6-3**, above). Most of these interactions are very rare in the cell model employed, and do not attain significance level after subtraction of the coincidental colocalisation levels. Basal HER3-HER3 interactions and HER3*-

HER3* interactions are not very frequent and are not significantly higher than the coincidental colocalisation levels calculated from the same datasets; however we have no way of telling, at the moment, how many receptors might be involved in these rare interactions. Based on literature reports about basal HER3 clustering, and on the low diffusion coefficient of basal HER3, it is conceivable that large clusters of receptors might be involved at one time [137].

According to simulations made by Shankaran *et al.* (2006) [359], the concomitant expression of HER1, HER2 and HER3 on the cell surface should drive the formation of high levels of HER2-HER3* dimers, however, such results have been contradicted by simulations by Hsieh *et al*. [360], in which the possibility of spatial confinement of different receptors is also taken into account. According to the latter simulation, confinement of receptors would drive the interactions towards the predominance of homo-interactions. The findings from the colocalisation experiments seem to agree with the findings from Hsieh *et al.*, which might mean that the receptors are at least partially subject to spatial partitioning on the cell membrane.

In order to better assess the role of **competitive interactions** between HER family members, all experiments were repeated, where relevant, adding saturating concentrations of the ligand for the competing HER family member (EGF for interactions involving HER3, and NRG1β for interactions involving HER1).

As shown in **Table 6-3**, above, addition of saturating concentrations of unlabelled EGF, resulting in maximal activation of the HER1 receptor, significantly reduces HER2-HER3 interactions to coincidental colocalisation levels (P = 0.007), suggesting some level of competition between HER3 and HER1* for binding partners. Interestingly, even maximal activation of HER1* does not seem to have any effect on the likelihood of HER2-HER3*interactions (P = 0.82 - see also **Figure 6-14 A**).

Conversely, maximal activation of HER3* with 100 nM NRG1β leads to a significant reduction in inactive HER1-HER1 interactions (P=0.006), and in HER1-HER1* interactions (P= 0.01) in the normalised datasets, with both values falling to coincidental colocalisation levels upon treatment.NRG1β treatment instead has very little effect on HER1*-HER1* interactions (P= 0.76), as expected by previous reports [129–131,354], or on interactions of activated HER1* with HER2 (P = 0.28 - see also **Figure 6-14 B**).

HER2-HER2 interactions are not significantly perturbed by saturating concentrations of EGF or NRG1β (P = 0.93 and P =0.25, respectively – see also **Figure 6-14 A and B**).

Taken together, these results seem to suggest that reciprocal competition is present between HER1 and HER3 receptors.

In order to gain some insight in the **mechanics of tyrosine kinase inhibition** and the paths used by the HER family to rewire itself and resist the shutdown of some of its nodes, all experiments were repeated, where relevant, by treating the cells either with 1 μM Lapatinib (Lap) or 1 μM Erlotinib (Erl).

Lapatinib is a class II TKI, with a high potency for both HER1 and HER2 kinase domains (IC_{50} = 10.8 ±0.53 nM and 9.2 ± 0.75 nM respectively) [275]. It can only bind to the inactive conformation of the HER kinase domain due to its bulkier head-group [160]. Lapatinib has also a very weak inhibitory activity on the HER4 kinase, but the IC_{50} is thirty times higher, due to the lack of essential water-based contacts in the HER4 structure [361].

Erlotinib, instead, is a class I TKI, which preferentially binds to the active conformation of the tyrosine kinase domain [73], though it can also bind to the inactive conformation, at least in the conditions necessary to form crystals [158].

The concentrations used have been chosen to be well within the range of clinically achievable serum concentrations for Lapatinib [362] and Erlotinib [363], but below the IC_{50} for T47D cell growth inhibition (3.0 ± 0.2 μM and 14.5 ±0.6 μM for Lapatinib and Erlotinib, respectively) reported by Rusnak *et al.* [275]. Lack of T47D growth inhibition was also confirmed independently (see **Figure 6-5 A**). According to a recent report, Lapatinib and class I anti-HER1 TKIs not only differ in their preference for the kinase conformation, but also in their binding kinetics. Lapatinib displays a much slower binding, owing to the slow transition between the active and inactive conformation of the tyrosine kinase, but also a very slow dissociation ($\tau \sim$ 20 h), which practically locks the kinase in the inactive conformation. Conversely, class I inhibitors, which bind to the activated conformation of the kinase, have much faster binding and dissociation kinetics (τ = 11 s and 12 s respectively), and therefore might display incomplete kinase inhibition as they cannot efficiently bind to the population of inactive TKDs [172]. In order to minimize the effect of the different binding characteristics of the two classes of TKI, inhibition was performed for at least 2 h in order to allow for Lapatinib binding, and the inhibitors were kept in solution throughout the experiment to prevent Erlotinib dissociation.

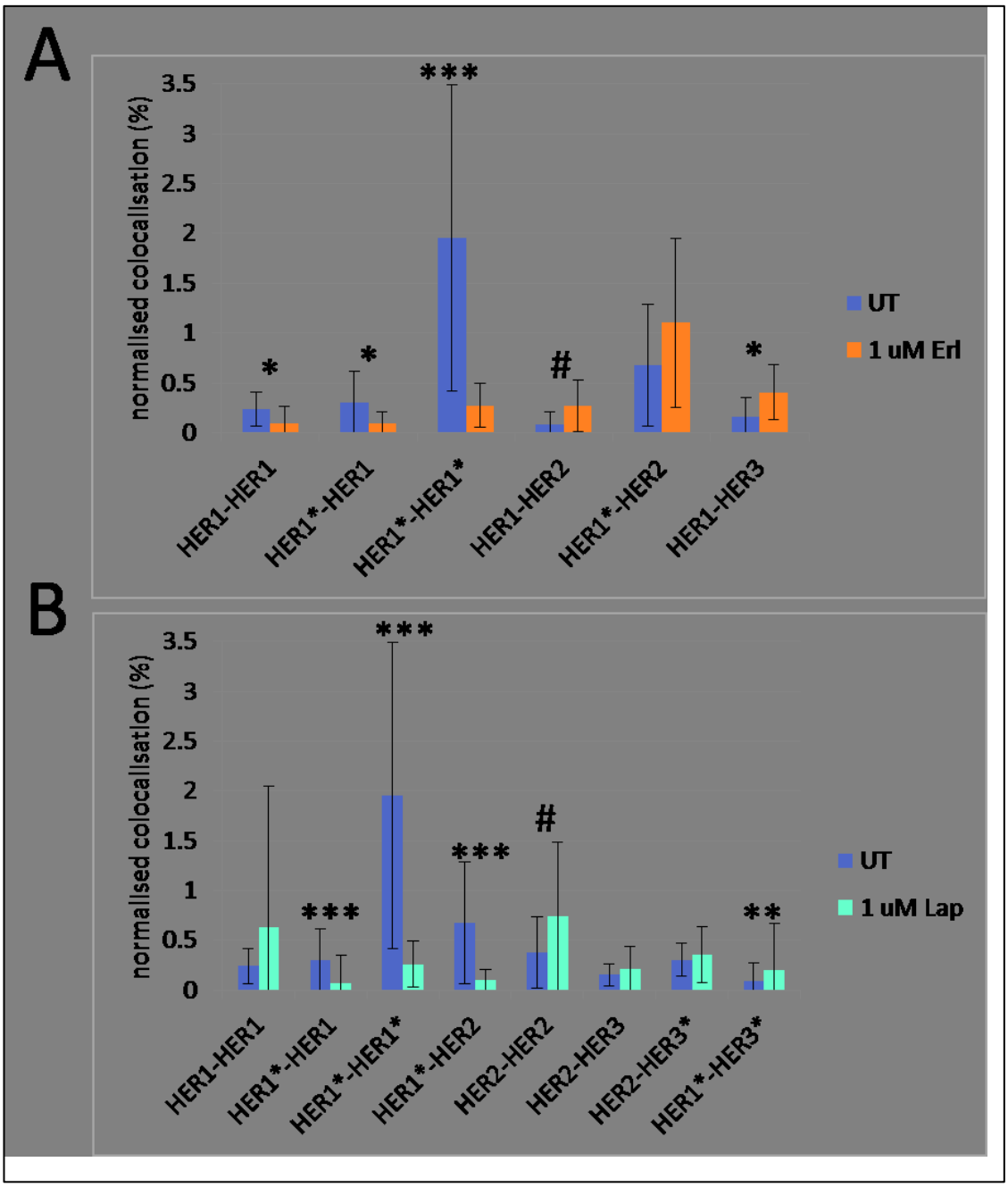

Figure 6-13 – Average normalised colocalisation frequencies for selected HER family pairs in presence A) of 1 µM Erlotinib or B) 1 µM Lapatinib. Colocalisation events were added to the frequency count when the two particles remained within 160 nm of each other for at least three frames (150 ms). ***= P Value <0.0001; **=P Value < 0.001; *=P Value <0.01; #= 0.01<P Value<0.05. All data were averaged over at least 30 independent areas, acquired over at least 3 independent biological replicates and are presented as average ± SD

In the normalised datasets, Erlotinib (**Figure 6-13 A**) appears to significantly disrupt all HER1 homo-interactions, regardless of the activation status of the receptors but, at the same time it favours hetero-interactions of inactive HER1 with both HER2 and HER3. In the unfiltered dataset Erlotinib is ineffective in disrupting HER1*-HER2 interactions.
These results are in contrast with the findings of Bublil *et al.* [162] and Lu *et al.* [80], who reported that class I TKIs such as Gefitinib and Erlotinib promoted the formation of "quasi-dimers" or "kinase dimers" between HER1 receptors. Since the proposed dimers are only kept together by the kinase domains, it might be argued that the ectodomains, which are the tagged component of the receptor in the reported experiments, might be too far away to be considered colocalised. The colocalisation parameters used in the present analysis, however, only require for the particles to be within 160 nm of each other for at least 3 frames in total, so even "kinase-dimers" should be picked up by the filtering algorithm. Similarly, the findings reported here contradict the results from Macdonald-Obermann *et al.* [143], who reported that both Erlotinib and Lapatinib favoured basal HER1-HER1 interactions.
The Erlotinib-dependent induction of HER1-HER3 interactions reported here is conserved even in the filtered datasets and is in line with the findings reported by Anido *et al.* [169] with Gefitinib in BT-474 breast cancer cells, and by Defazio-Eli *et al.* [170] and Macdonald-Obermann *et al.* [143] with Erlotinib.

Lapatinib, instead (**Figure 6-13 B**), efficiently disrupts unfiltered HER1*-HER1*, HER1*-HER1 and HER1*-HER2 interactions, but, contrary to Erlotinib, does not seem to have a significant effect on HER1-HER1 interactions. Lapatinib appears, to slightly favour HER2 homo-interactions, which might represent a pool of signalling-incompetent receptors. The Lapatinib-induced increase in HER3*-HER1* interactions, which, instead, might be involved in residual signalling, is significant.
Interestingly, Lapatinib has no significant effect on the frequency of interactions between HER2 and inactive HER3 or activated HER3*(see **Table 6-3**). This is in contrast with the findings from Mukherjee *et al.*, who reported a decrease in HER2-HER3* interactions in T47D cells, with a consequent decrease in the interactions between HER3* and PI3K [364].
No significant effects were reported on the extent of Akt phosphorylation, which might suggest that alternative paths to signalling through Akt might be open in presence of Lapatinib. Taken together, these findings seem to point to the presence of possible compensatory interactions between HER family receptors when the signalling of some of them is blocked by

TKIs, especially by Erlotinib, a finding that seems consistent with the variations in HER3 diffusional behaviour highlighted in the previous section.

A **summary of the treatment-induced variations in the colocalisation likelihood** of all receptor pairs is provided in **Figure 6-14 A-D**.

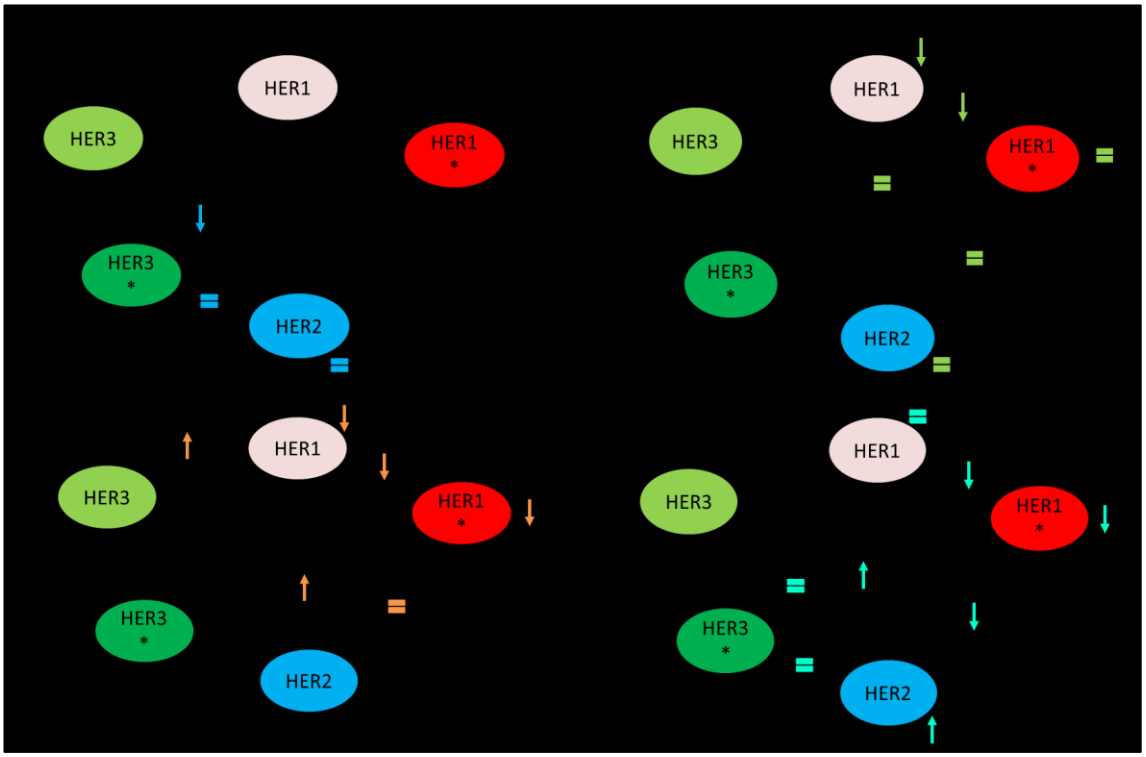

Figure 6-14 – Summary of treatment-induced changes in colocalisation frequency – normalised data. **A)** 100 nM EGF; **B)** 100 nM NRG1β-MCP; **C)** 1 µM Erlotinib; **D)** 1 µM Lapatinib. The thickness of the arrows connecting the nodes is proportional to the likelihood of interaction between the receptors. ↑ increased colocalisation; ↓ decreased colocalisation; = no significant changes (all K-S test).

6.2.5. The incidence of temperature- and dye-dependent artefacts on the measurement of interaction parameters

As a final control for the incidence of artefacts in the determination of colocalisation frequencies and interaction lifetimes, a series of Single-Particle Tracking experiments was performed on a different cell model, the HCC1954 cell line, a HER2+, ER-/PR- breast cancer cell line [365] that expresses high levels of both HER1 and HER2 [208,366,367] and is resistant to trastuzumab [208,366] and pertuzumab [366]. This cell line was chosen both for its potential clinical relevance and for its ability to grow on Nanogel-functionalised surfaces.

HCC1954 cells were independently imaged in presence or absence of 1 μM Gefitinib in three different sets of conditions:

1) at 37°C with Alexa 488- and CF640R-conjugated EGF (optimised conditions –OPT)
2) at 22.5 °C with Alexa 488- and CF640R-conjugated EGF (temperature –TEMP)
3) at 22.5 °C with Alexa 546 and Atto647N-conjugated EGF (sticky dyes –STK)

As shown in **Figure 6-15**, below, on cells imaged at 37°C with optimised dyes expected, the *D* of HER1* particles diffusing on HCC1954 cells is significantly increased in presence of 1 μM Gefitinib ($P << 0.01$), as expected.

The diffusion coefficient of HER1* tracked with optimised dyes on untreated cells at room temperature, instead, was decreased to ~ 0.033 ± 0.009 $\mu m^2/s$ from 0.089 ± 0.014 $\mu m^2/s$ recorded at 37 °C ($P << 0.01$).

While for both sets of dyes the significant increase in *D* upon Gefitinib treatment is maintained ($P << 0.01$ for both), the value recorded on untreated cells using suboptimal dyes (STK) is significantly lower than that recorded using optimised dyes (TEMP– $P << 0.01$). The same significant difference ($P << 0.01$) is recorded also between STK+GEF and TEMP+GEF.

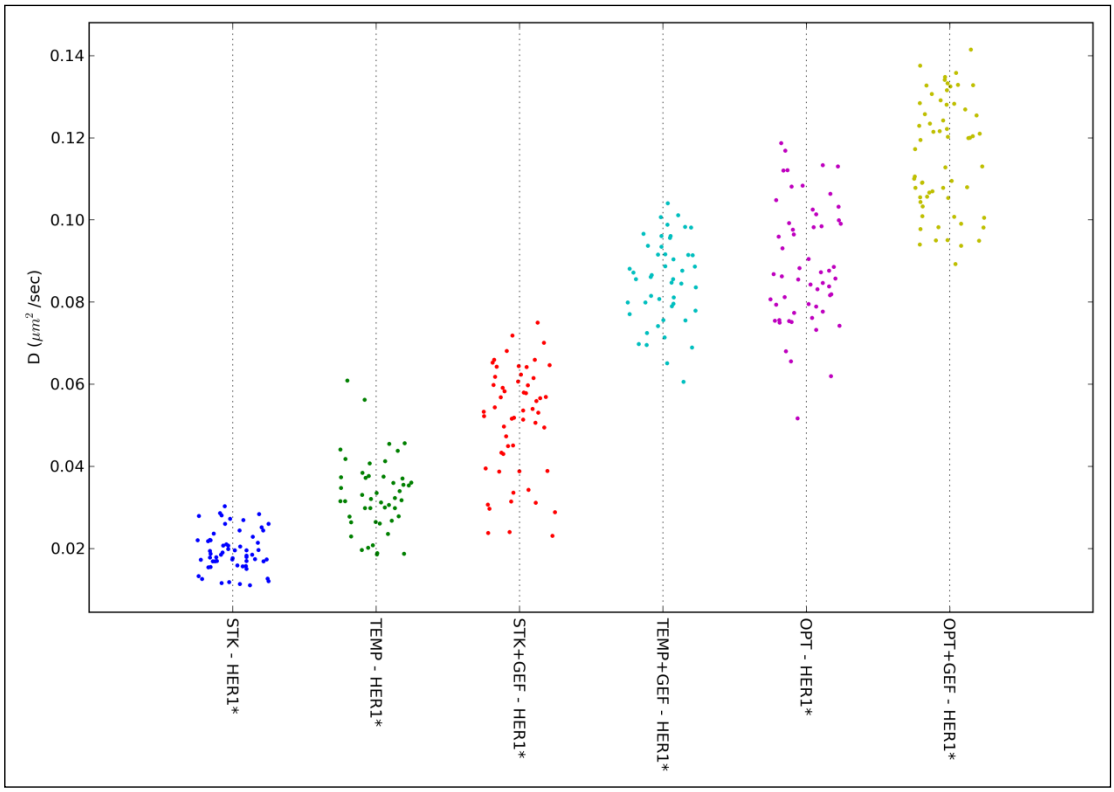

Figure 6-15 – Distributions of *D* values for HCC1954 cells imaged with different dye pairs and temperature conditions. OPT= 37°C – Alexa 488 and CF640R; TEMP= 22.5 °C – Alexa 488 and CF640R; STK= 22.5 °C – Alexa 546 and Atto647N. Data was combined over at least 30 independent areas acquired over at least 3 independent biological replicates. Datasets are sorted according to *D* value.

Figure 6-16, below, shows that on cells imaged at 37°C with optimised dyes, the frequency of HER1*-HER1* colocalisation was not significantly affected by treatment with 1 µM Gefitinib in the unfiltered dataset (P= 0.082), while the difference was statistically significant after application of a C-K filter. This is due to a lower level of colocalisation of HER1*-on cells treated with Gefitinib in the filtered datasets. A high level of artefacts in the unfiltered dataset is attributable to the fact that the faster-moving HER1*+Gef particles have a higher localisation noise and are more likely to be crossing each other compared to the same particles in the untreated sample.

The likelihood of colocalisation between HER1* particles was increased from 1.62 ± 0.59% to 5.17 ± 2.35% in untreated cells imaged at RT with Alexa 488 and CF640R compared to those imaged at 37°C (P <<0.01 in both filtered and unfiltered datasets). The difference in colocalisation between HER1* particles tracked at RT with optimised vs sub-optimal dyes, however was not significant in both filtered and unfiltered datasets. This finding seems to

indicate that temperature is the major source of artefacts in this context.

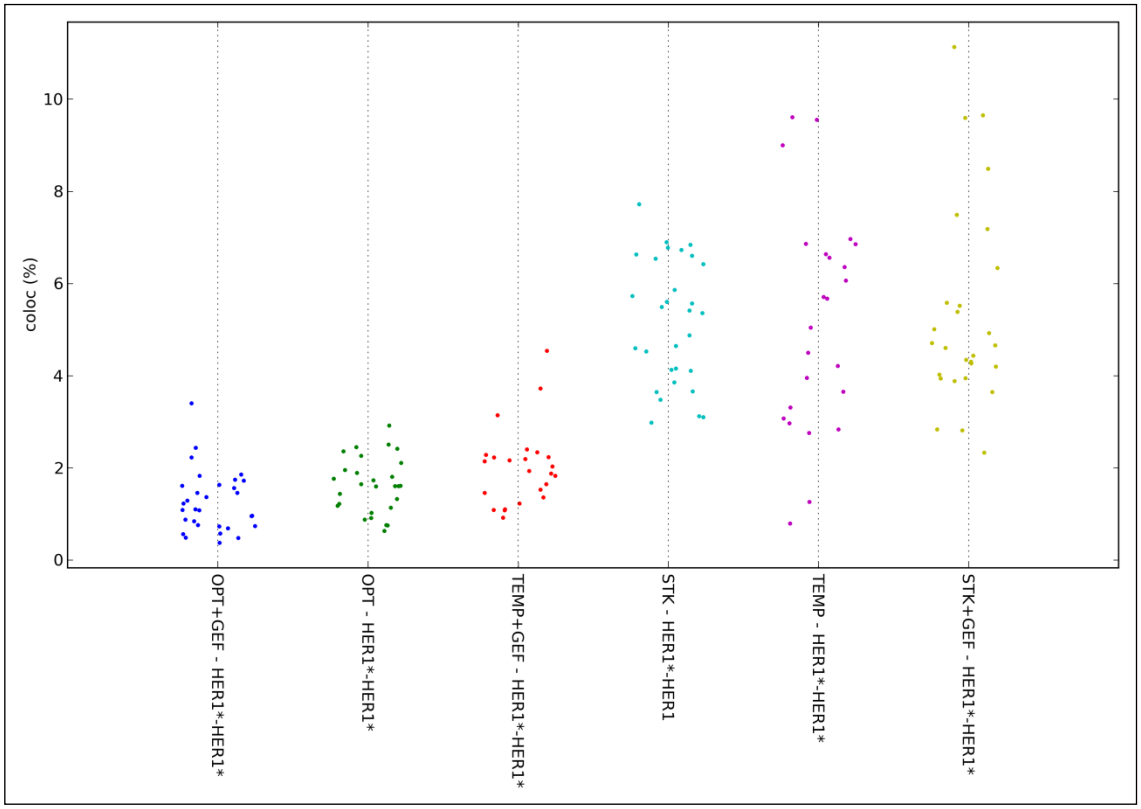

Figure 6-16 - Distributions of colocalisation frequencies at 160 nm for HCC1954 cells imaged with different dye pairs and temperature conditions (unfiltered). OPT= 37°C – Alexa 488 and CF640R; TEMP= 22.5 °C – Alexa 488 and CF640R; STK= 22.5 °C – Alexa 546 and Atto647N. Data was combined over at least 30 independent areas acquired over at least 3 independent biological replicates. Datasets are sorted according to colocalisation %.

In summary, it can be concluded that both temperature and dye characteristics impact the measurements of interaction frequencies, as well as diffusion, on live cells. Dyes are likely to be a bigger source of artefacts for the calculation of diffusion coefficients than for the determination of colocalisation frequencies, where temperature seems to be the main contributor to the generation of artefacts.

Keating *et al.* [341] have previously reported that differences in temperature can affect the aggregation and the diffusion of HER1 on cells, with lower temperatures resulting in increased aggregation and lower diffusion, as evidenced also by the results presented in this section. Furthermore, phase transitions between a liquid-ordered phase and a gel phase has been recorded in mammalian cells at temperatures close to RT [368]. This transition impacts lipid

diffusion, and is also likely to impact the diffusion of proteins immersed in the lipid bilayer. Tracking at low temperatures not only yields data of questionable translational value, as clinically relevant processes happen at 37°C in the human body, but also introduces significant artefacts in the measurement of interaction parameters.

Much time has been devoted in this project to carefully optimise the acquisition conditions for the most accurate results. The optimisation of dyes for Single-Particle Tracking, reported in **Chapters 4** and **5** demonstrated that suboptimal dyes can strongly affect the diffusion of probes on the cell membrane. The data presented above also demonstrate that suboptimal dyes can introduce artefacts in the measurement of interaction parameters.

Once again, it is important to stress the absolute need for the optimisation of the acquisition conditions to obtain high-quality Single-Particle Tracking data.

6.3. Discussion

The Single-Particle Tracking method presented in this thesis affords higher coverage of the receptors expressed on the membrane of living cells thanks to the use of 1:1 conjugates of small peptidic ligands with optimised organic dyes and of a cell model expressing low-mid "physiological" levels of all four HER family receptors. Careful optimisation of cell growth substrates, label concentrations and dyes, as reported in **Chapters 3-5**, allowed the acquisition of high-quality and high-content data. Thanks to the high population coverage, colocalisation events involving sub-populations of receptors can be recorded and analysed.

In contrast, QD-based tracking methods rely on very sparse labelling of cells which overexpress one (or more) HER receptor in order to be able to capture and quantify colocalisation events. While these methods afford a higher spatial resolution due to the inherently better SNR characteristics of QDs, the picture they can paint of the HER family signalling is necessarily skewed by the need to analyse an unrepresentative system. High levels of receptor expression, in fact, have been found to influence the diffusion of HER receptors on cell membranes [338], the extent of pre-oligomerisation [98,164], and the response to EGF [112,164]. So, while T47D cells, which are ER+ and do not overexpress any HER receptor, might not be directly relevant to a clinical or translational setting, because their survival and growth are not directly dependent on HER family signalling, they constitute a good model to paint a baseline picture of the system, which can be used to draw hypotheses which, in the future, could be tested on more clinically relevant cell models and even on primary cultures from breast cancer patients.

This method would be well suited, in particular to the study of receptor behaviour in cells that express mismatched levels of different HER family receptors, while its strategic advantages would be lost when used for the exclusive study of overexpressed receptors.

Compared to QD-based methods, the Single-Particle Tracking method used in this project does not allow the determination of nanometric distances on the scale required to identify *bona fide* dimerization, but only interaction in a more loose sense of the term. However, the SNR-limited localisation precision calculated for the system (80-90 nm) is in keeping with the observed size of HER1 oligomers on T47D cells [95].

Moreover, as noted above, tracking with QDs in overexpressing cells is performed under very low coverage conditions, which might mean that the oligomerisation of the receptor is under-estimated. In those conditions, for every visible receptor there might be many more unlabelled ones travelling with it.

In fact, the assumption that the interacting species are monomers forming dimers must be taken with a certain caution as it is possible that unlabelled receptors of various species are also taking part in the interaction, as can be hypothesised from the findings of Needham *et al.* [95]. It is possible that groups of receptors, possibly of different species, diffusing as a unit take part in interactions and that the oligomers are rearranged during each cycle of interaction, as schematised in **Figure 6-17**.

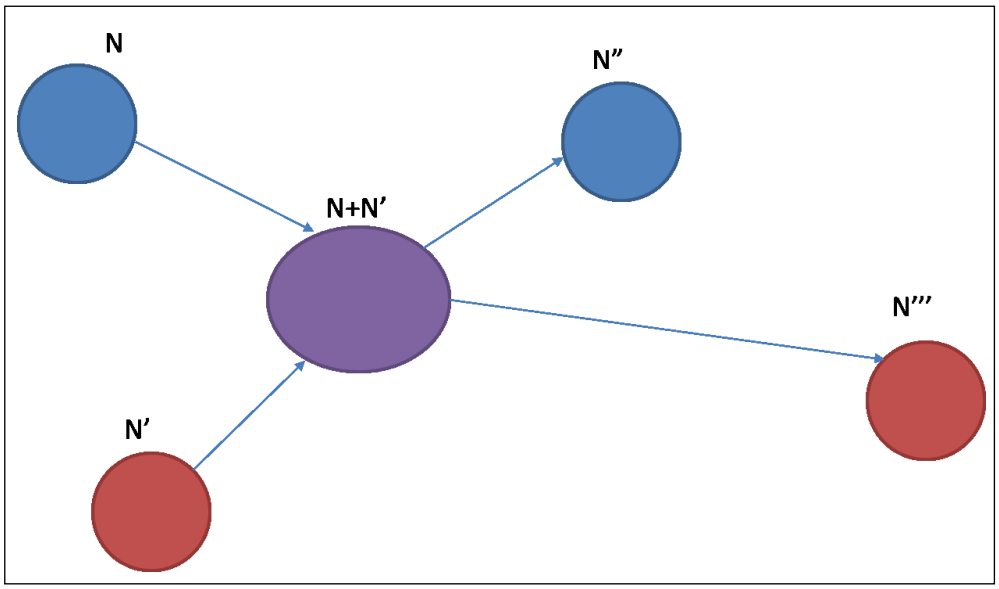

Figure 6-17 – Scheme of the hypothetical rearrangement of receptors between interacting oligomeric receptor units. The indexed Ns indicate the total number of receptors of any species (both labelled and unlabelled) in a diffraction-limited fluorescent feature.

The tracking method employed for this project, with its high coverage of the receptor population, might in future provide information on the minimal stoichiometry of interacting species thanks to intensity-based calculations. A precise determination of such parameters, however, requires the determination of the full noise model of the acquisition system, *i.e.* of all the contributions to the spurious signal arising from the detector. Once this is implemented in the data analysis algorithms, it will be possible to assign confidence levels to intensity estimates and improve feature detection, which will also lead to an improvement in the determination of tracking parameters. Any intensity-based parameters are however likely to be under-estimated due to photobleaching.
The interaction frequencies presented in this thesis are likely to be under-estimated as well, due to photobleaching, which will allow preferential detection of short-lived events, and due to the intrinsic time resolution of the data, which will not allow the detection of any change in state faster than the integration time. In addition to this, even if the greatest care has been exercised in choosing non-saturating concentrations of labels, local fluctuations in the density of receptors in certain areas of the cell surface might deteriorate the SNR and introduce tracking artefacts due to crowding.

In this section, two main parameters were analysed for 48 different interaction/treatment conditions: the instantaneous diffusion coefficient *D* which is a measure of the area sampled by each particle; and the colocalisation frequency of two particles in two different channels. Both parameters were measured:

1) on untreated cells;

2) on cells treated with saturating amounts of the activating ligand for the third receptor not included in the pair (NRG1β for HER1-HER1 and HER1-HER2 pairs and EGF for HER2-HER3 and HER3-HER3 interactions – HER2-HER2 interactions were analysed in both cases);

3) on cells treated with clinically relevant concentrations of either Lapatinib or Erlotinib.

The diffusion of inactive HER1 seems to be linked to the extent of its interactions with other receptors, while the diffusion of activated HER1* depends mostly on the activity of its kinase (**Figure 6-8 A**). When HER1* is tracked in untreated cells, its diffusion rate is significantly lower compared to that of inactive HER1, while it is significantly faster in TKI-treated cells. The diffusion rate of HER1*-TKI is even larger than that of HER1, which seems to point to the

differential regulation of the motility of the liganded and unliganded receptor, either by structural constraints or by interactions with the cytoskeleton/rafts.

This is likely to be dependent on ligand-induced dimerization, which enhances the effect of the cytoskeletal picket-fence on receptor diffusion [6]. The increase in diffusion rate of the ligand-bound and kinase-inhibited receptor compared with the basal state may be due to the presence of a small but sizable fraction of pre-formed dimers, or possibly oligomers, in the basal receptor population. As predicted by the picket-fence membrane model, these dimers will show a reduced mobility compared to the majority of monomers [6]. Upon EGF treatment, the pre-formed dimers, likely characterised by a symmetric kinase conformation, are broken due to conformational changes in the extracellular, transmembrane and juxtamembrane domains that do not allow the kinases to keep their original conformation, however, the inhibition of the kinase activity by TKIs prevents the receptors from adopting an asymmetric kinase dimer conformation. The net result will be that the fraction of monomers in the receptor population will increase and therefore the general average *D* will increase.

On the other hand, the diffusion of HER3 seems to be regulated in a more complex fashion. HER3 activation with NRG1β leads to increased mobility not only of NRG1β-bound HER3*, but also of Affibody-bound HER3 receptors tracked on the same cells. The inhibition of HER1 and HER2 signalling through Lapatinib treatment is also able to induce a significant increase in basal HER3 diffusion, suggesting that lateral/feedback signalling paths from HER1/HER2 towards HER3 might be involved.

The analysis of the colocalisation frequencies, instead, has revealed that HER1*-HER1* is the dominant interaction in the T47D cell model, closely followed by HER1*-HER2. They are the most frequent and their frequency is decreased by both Class I and Class II TKIs. Independent experiments have also been performed in HCC1954 cells, a cell model representative of a different clinical subtype of breast cancer, and yielded comparable results, with a decrease in HER1*-HER1* colocalisation upon Gefitinib treatment when the data is appropriately filtered to avoid noise-driven artefacts (**Figure 6-16**).
Returning to T47D cells, in this cell line HER1-HER1 interactions and HER1*-HER1 interactions are not different in terms of frequency, and are about as frequent as interactions between HER1*-HER1* + TKIs. These findings are in keeping with the signalling model recently proposed by McCabe Pryor *et al.* [369], which stipulates that relatively short and repeated interactions between receptors might be necessary for full HER1* signalling. For each

interaction event, in fact, each receptor has 50% chances of positioning itself in the receiver position and being activated, so that repeated events would be necessary to ensure that both are activated. Compared to Low-Nam *et al.*, however, the likelihood of HER1*-HER1 interactions reported in this thesis is lower. This difference could be an effect of the difference in HER1 expression between the A431 cell line used by Low-Nam *et al.*, which expresses at least 10^6 HER1 receptors, and T47D cells, which express ~ 10^4 receptors/cell. Physical separation of the HER1 and HER1* species is likely to be an important factor in signalling regulation in cells that do not overexpress HER1.

Further on the colocalisation, apart from HER1*-HER2 interactions, heterodimers are quite infrequent, even if the T47D cell model expresses comparable levels of all receptors. This finding might be due to spatial segregation of the different HER family members, as predicted by the simulations of Hsieh *et al.* (2008) [360].
Shankaran *et al.* (2013) [370], however, predict that, at the HER1, HER2 and HER3 expression levels of T47D cells, phosphorylation of HER2 should be dependent principally on HER2-HER3* interactions, with a <40% contribution of HER1*-HER2 interactions, which however are predicted to contribute ~ 40% of the total HER1 phosphorylation. The contribution of HER2-HER2 interactions to HER2 phosphorylation is predicted to be minor. HER3 phosphorylation, instead, is predicted to arise almost exclusively from HER2-HER3* interactions, with minimal contributions from interactions with HER1 species. These predictions are roughly in keeping with the interaction hierarchy reported in this thesis (**Figure 6-10**).

The analysis of the effects of TKIs treatments of the interactions of the HER family members has revealed that Class I and Class II inhibitors display differential abilities to inhibit receptor interactions, as evidenced before in the literature (see **Chapter 1** for a complete discussion). Both Classes of TKIs are equally able to inhibit HER1 homo-interactions, but their behaviour with heterodimers is quite specific.
Erlotinib, on one hand, favours HER1-HER3 interactions (**Figure 6-13 A**).
Lapatinib, on the other hand, slightly favours HER2-HER2 interactions and has no effect on interactions involving HER3. However, this TKI is able to effectively disrupt HER1*-HER2 interactions (**Figure 6-13 B**). This finding, combined with the reported Lapatinib-dependent increase in basal HER3 motility, might point to the existence of some sort of lateral/feedback signalling mechanism through HER3 that is activated in case of disruptions of the flow of information through HER1 and/or HER2.

There is evidence of reciprocal competition between HER1 and HER3 for interaction partners (**Figure 6-14 A-B**) in normalised datasets. These results might not be incompatible with a mixed hetero-oligomer signalling model as that proposed by Huang *et al*. [132], in which both HER1 and HER2 interact with HER3 at the same time and are both necessary for the activation of signalling downstream of HER3.

Further data on the minimal stoichiometry of the interacting complexes will likely shed more light on the real-time transmission of signals through the HER family.

At this stage, the determination of colocalisation k_{ON} and k_{OFF} values for the different conditions was not attempted. This is due to the fact that the determination of these parameters is much more sensitive to noise and localisation errors than the mere determination of colocalisation frequencies. An accurate determination of colocalisation lifetimes requires a more complex handling of the noise, which is current in implementation.

Additionally, the data presented here does not discriminate between activated HER3 and HER4 due to the fact that NRG1β binds to both receptors with comparable affinities. In order to disentangle the interactions of these two species, tracking experiments involving HER3* will be repeated blocking HER3 with excess unlabelled anti-HER3 Affibody, or HER4 with a Fab fragment from the blocking anti-HER4 monoclonal antibody H4.72.8 (Millipore), as described, among the others, by Jay *et al.* [286].

7. Characterisation of the Cytoskeletal Determinants of HER1 Membrane Dynamics

7.1. Introduction

The signalling of RTKs is tightly regulated both spatially and temporally, in order to maintain regulation of downstream signalling cascades and mediators [14,17–19]. The partitioning of the plasma membrane into nanoscale domains, or corrals, as proposed by Simons [371] and Kusumi [6], respectively, would serve to confine signalling events, stamping them with precise spatial information. This spatial stamping is especially fundamental in cases where extracellular cues can influence cytoskeleton polarity and cell adhesion via actin filament remodelling, or via crosstalk with integrins and other adhesion molecules.

Various mechanisms have been proposed to influence signalling and motility of HER1 receptors. The main ones are discussed below.

7.1.1. Protein corralling by the meshwork of the cortical actin cytoskeleton

The structure of the cortical actin cytoskeleton is modular and regulated by intracellular and extracellular cues and covers the whole membrane surface on the intracellular side [372]. It is believed that its interactions with membrane receptors hinder receptor diffusion via steric clashes with the intracellular domains of the receptors. In this model, transmembrane proteins can only escape from the cortical actin “corrals” once their energy is high enough due to random chance, or thanks to fluctuations in corral structure [6]. In addition to this, the cortical actin cytoskeleton can also bind certain transmembrane proteins, transiently immobilising them. Such proteins work as “pickets” on a fence and slow diffusion down by hydrodynamic interactions which act over a scale of tens of nanometers [6]. HER1 itself is able to associate with the actin cytoskeleton via an actin-binding motif in its C-terminal tail [113]. Along with the reduction in diffusion caused by oligomerisation [6], this could be one of the causes of receptor stalling under activating conditions.

The role of the actin cytoskeleton in HER1 diffusion has been previously analysed with Single-Molecule techniques. Orr *et al.*, for example, report that Cytochalasin D and Latrunculin A, two actin-depolymerising drugs, are able to increase the diffusion coefficient of HER1 tracked on HME184A1 cells, while only Latrunculin A produces an effect on HER2 [310]. Similar findings have been reported by Low-Nam *et al.* for HER1 using Latrunculin B [110] , for HER2 by Xiao *et al.* [348], also using Latrunculin B, and by Hagen *et al.* [349] for HER3, using KabC, a macrolide

that binds to the same site on G-actin as gelsolin, resulting in the severing and capping of the (+) end. Since HER2 and HER3 do not have known specific actin-binding sites, this might reflect a general mechanism of motility increase due to the disruption of the cortical actin fence.

7.1.2. Inclusion/exclusion from lipid rafts

Lipid rafts are believed to be "small (10-200 nm), heterogeneous, highly dynamic, sterol- and sphingolipid-enriched domains that compartmentalize cellular processes" [20]. The coalescence of small rafts through interaction between lipids and proteins can stabilise larger signalling rafts, as seen, for example, in T cell signalling [371]. The association of HER1 with rafts has been extensively studied, mainly by assessing receptor interactions and localisation with respect to GM1 ganglioside and cholesterol, or to "markers" of raft-like domains such as Placental Alkaline Phosphatase (PLAP) and flotillin or caveolin [311,312]. HER1 is found in raft-like fractions together with outer leaflet and inner leaflet phospholipids [373], Ras [374], GM1 gangliosides [357,375,376] phosphoinositides [377] and phosphatidic acid [378], the latter of which can regulate HER1 clustering following ligand stimulation in a Phospholipase D2-dependent fashion.

While several lines of evidence suggest interaction between HER1 and lipid rafts, the functional significance of this interaction remains somewhat controversial, as different authors report either activating or inhibitory roles for HER1 inclusion in rafts and interactions with raft components, such as cholesterol and sphingolipids. Upon cholesterol depletion, several groups have reported an increase in EGF binding sites and EGF-induced HER1 phosphorylation as well as in the ligand-independent phosphorylation of the receptor, a fact which seems to point to an inhibitory effect for HER1 interactions with cholesterol [375,379–384]. However, EGF-dependent activation of HER1 has been reported to lead to coalescence of HER1-GM1 lipid domains with GPI-rich lipid domains and to their enlargement, possibly resulting in the formation of signalling platforms [357,376]. Cholesterol depletion can reduce the turnover of Phosphoinositides in presence of EGF [377], which hints to a role of lipid rafts in at least some signalling events downstream of HER1. Finally, HER1 is localised in the lipid raft fractions of TKI-resistant breast cancer cell lines and in this context cholesterol depletion with lovastatin has a synergic effect with Gefitinib treatment [358], which suggests that, at least in some cases, lipid rafts might provide positive regulation for HER1 signalling, or, alternatively, that cholesterol depletion by lovastatin favours the transition of HER1 towards a conformation that is more efficiently blocked by Gefitinib.

For a more thorough and systematic discussion of the role of rafts in HER1 signalling, readers

are also referred to the reviews by Pike (2005) [312] and Balbis and Posner (2010) [311].
Lipid rafts have been proposed as possible sources of transient confinement following Single-Particle Tracking experiments of lipids and GPI-anchored proteins on the surface of live cells, however, the mechanisms underlying this type of confinement are not very well characterised [385]. In analogy with other imaging studies that have detected increased clustering and decreased diffusion of HER1 upon cholesterol depletion [104,382], some Single-Molecule studies have reported significant reductions in the diffusion of monomeric HER1 and HER2 [310] upon cholesterol depletion, while others have reported no effect on the motility of doubly-liganded HER1 dimers [110].
Quite surprisingly, cholesterol depletion increased the diffusion of HER3 [349], as measured by FRAP, a finding that suggests that HER3 might have a different basal localisation from the other two receptors.

7.1.3. Interactions with the extracellular Galectin lattice

Galectins are a family of non-classically secreted proteins which bind to sugar chains present on N-glycoproteins [313]. Galectin 3 is a chimeric member of the galectin family, which is composed of a C-terminal carbohydrate binding domain and an N-terminal non-lectin domain, which, in presence of multivalent ligands, promotes Galectin 3 oligomerisation into pentamers, generating a sort of molecular lattice [386] . Galectin 3 displays high affinity towards multimeric Gal-GlcNAc chains (poly-N-acetyllactosamine), which are inserted as a post-translational modification on N-glycosylated proteins during their Golgi processing [387]. By crosslinking the extracellular domain of N-glycoproteins, the galectin lattice regulates protein motility and ligand affinity, favouring homotypic and heterotypic interactions between N-glycosylated proteins on the cell surface [313].
HER1 bears 10-12 N-glycan moieties, a subset of which is modified with high affinity sites for Gal-3 binding [388]. Interaction of HER1 and Galectin 3 has been confirmed by chemical cross-linking on the cell surface and disruptions of this interaction, either by suppression of Mgat5, the Golgi enzyme responsible for introducing high-affinity Gal-3 sites on the oligosaccharide chains, or by competition with excess lactose, results in strongly reduced EGF binding and ERK1 activation, while receptor affinity for its ligand was preserved. This phenomenon was explained with a fourfold enhanced endocytosis [387]. Addition of lactose or suppression of the Mgat5 gene resulted in greater HER1 mobility as assessed by FRAP, and in reduced association with inhibitory Cav-1 domains at the membrane. The Gal-3 lattice seems to cooperate with the actin cytoskeleton to reduce the mobility of HER1 molecules on the cell

surface, possibly by stabilising HER1 interactions with other actin-associated membrane proteins [309].

Late in the project, a new, globally optimised algorithm for the analysis of Single-Particle Tracking data was made available by Dr Richard Wareham of the University of Cambridge. This algorithm, called Biggles (Bayesian Inference-based, Gibbs-sampler, GLobal ESTimator), is, as far as it can be ascertained, the first algorithm that converges towards the most accurate globally optimal spatiotemporal solution to SPT in a computational time compatible with 'real-world' biological experiments. Biggles is able to produce an empirical probability density of all possible sets of tracks and track parameters, which relates directly to how well the observed data justifies each solution. This allows objective derivation of the most suitable tracking solutions, allowing for challenges such as low SNR and high crowdedness [3].

Biggles was used on a subset of the single-colour and two-colour tracking data of basal and activated HER1, HER2 and HER3 acquired during the course of the project, in order to quantitatively analyse the membrane dynamics of the receptors, revealing activation-dependent changes in the directionality of HER1 and HER3 diffusion.

The diffusional properties of HER1 have been more thoroughly investigated in order to ascertain the structural causes of its activation-status-dependent mode of motion, by using a panel of chemical compounds to block the activation of the receptor (Lapatinib), or disrupt cytoskeletal components (Latrunculin A, Cytochalasin D, Jasplakinolide, Blebbistatin, Nocodazol), the galectin lattice (α-Lactose), or lipid rafts (Methyl-β-Cyclodextrin). The effect of some of these compounds (Cytochalasin D, Methyl-β-Cyclodextrin and α-Lactose) was also tested on a limited panel of extra cell lines (MCF7, HeLa, Cho+EGFR-eGFP), in addition to T47D, in order to account for cell-specific effects. In this context, the effect of receptor levels on HER1 diffusion was also tested. Finally, the effect of a subset of the aforementioned compounds (LatrunculinA, Jasplakinolide, Blebbistatin and Methyl-β-Cyclodextrin) on receptor colocalisation frequency and kinetics was also tested in two-colour SPT experiments.

7.2. Results

Part of the results in this section have already been presented in Wareham *et al.* [3], of which the author of this thesis in joint 1st author and to which she contributed the live cell tracking data.

7.2.1. Determination of the toxicity of cytoskeletal disruptors with a colorimetric MTT assay

In order to assess the effects of cytoskeletal disruptors used in Single-Particle Tracking experiments on T47D cells, a colorimetric MTT assay was performed, as described also in **Chapter 6**. The results for Latrunculin A (LatA) and Methyl-β-cyclodextrin are shown in **Figure 7-1**.

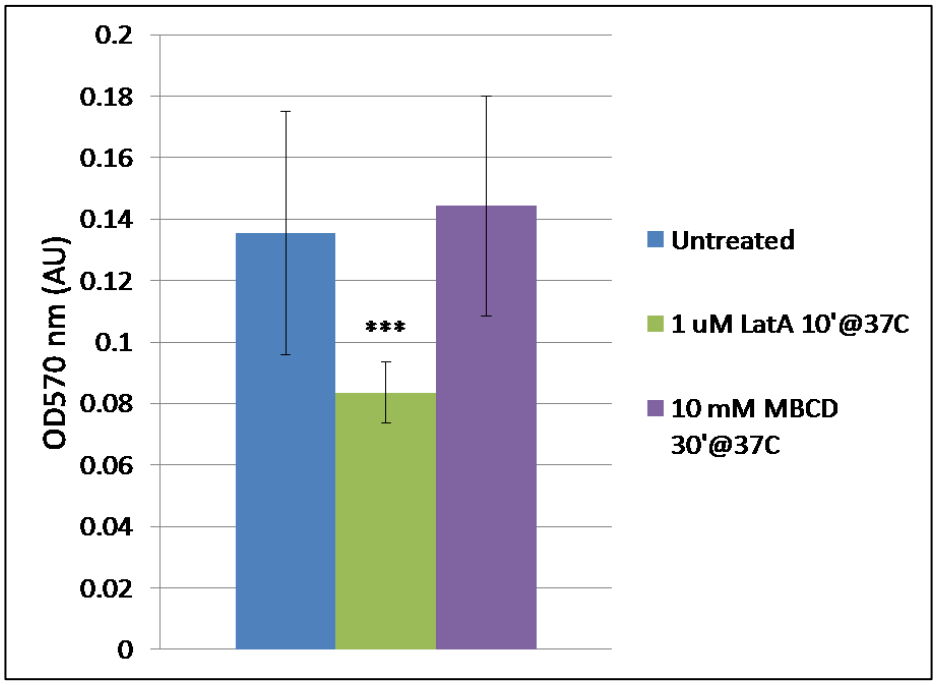

Figure 7-1 - Toxicity of cytoskeletal disruption treatments used during Single-Particle Tracking, as assessed by a colorimetric MTT assay. T47D cells were cultured for 24 h in complete medium before starvation for 2 h. All samples were treated and acquired in triplicates, normalised against empty wells and averaged values were compared against untreated controls via two-tailed Student's t-Test. Statistical analysis was performed in Excel. *= P<0.01; **=P<0.001; ***=P<0.0001.

Among the cytoskeleton disruptors, 10 µM of Latrunculin A were enough to cause a significant decrease in vitality in this assay. This toxic effect could be overstated due to the characteristics of the assay, which requires a further incubation at 37°C for 2-4h after drug treatment.

Samples for SPT, instead, are subject to a much shorter turnover, with an average time-to-microscope after Latrunculin A treatment of 5-10 minutes and a total acquisition time of 35-45 minutes, which could possibly allow avoiding the worst of the compound's toxic effects.

7.2.2. Determination of the directionality of HER1, HER2 and HER3 diffusion with a globally optimised tracking algorithm

The analysis of particle motion is currently based on fitting trajectories with competing mathematical models, most commonly based on particle mean square displacements (MSD), whose deviations from the linearity characteristic of pure diffusion are interpreted in terms of standard types of particle motion like confined or directed (for example in [12,385,389–391]), but also on hidden Markov calculations [392]. However, the heterogeneity often showed by the trajectories is not easily resolved by such fitting. For model fitting approaches to be effective, the particles must either maintain the same type motion for multiple consecutive frames (typically >50 frames [389]) and/or display sufficiently long tracks [390,392].

Achieving the globally optimal solution has been the goal of SPT for decades, but in the past it has proven computationally prohibitive because of the colossal size of the configuration space of particle reconnection possibilities at the high particle density, low signal-to-noise ratio (SNR) and fast particle movement typical of single molecule images in cells [393], which roughly scales as the factorial of the number of particles (thousands), motion parameters (dozens), and frames (hundreds). To make the problem tractable, all previous algorithms therefore reduced the size of the configuration space both by imposing *a priori* narrow bounds on the motion parameters, derived from modelling or previous knowledge, and by approaching the globally optimal solution by taking many locally optimal solutions (see for example [394–398]). The latter approach typically produces 'tracklets' separated by gaps, after which longer tracks may be recovered, for example, via minimal path techniques (*e.g.* [399,400]), or maximum likelihood methods (*e.g.* [110,279,401,402]). Although these algorithms addressed many of the tracking challenges deriving from high particle density and low signal-to-noise, manual intervention is required to derive tracks, it is difficult to ascertain how sensitive the results are to their choice of parameters [393], and the loss of temporal globality hinders access to the very statistical information one requires to evaluate dynamic motion.

To evaluate particle motion in general, one must measure the instantaneous values of motion parameters as they fluctuate along the particle trajectory. This ultimately requires single track-frame sensitivity. The most accurate way to achieve this is from the globally optimal

spatiotemporal track probability distribution from Biggles. This approach tries each possible choice of particle reconnections and associated motion parameter values and compares their consequences along the entire length of the tracks, therefore automatically exploiting all the information content in the data to output the empirical probability distribution of both, from which one can derive their values and confidence limits and modelled parameters and particle states. In contrast, model fitting can only use the much reduced information content remaining in the derived tracks.

Among the parameters estimated in a frame-by-frame fashion by the Biggles tracking algorithm are the instantaneous velocity of any give particle and the covariance of this parameter. Particles moving by pure diffusion should have an instantaneous velocity =0, that is, should have an equal probability, at each time-step, of moving in all possible directions. For each particle, the null hypothesis of pure diffusion is treated as a multivariate Gaussian with zero mean and covariance equal to the estimated velocity covariance. The number of standard deviations *d* from the null hypothesis at which the estimated velocity measurement is positioned is calculated frame-by-frame using **Equation 2-2**, as described in **Paragraph 2.24.1**Error! Reference source not found..

Tracks whose dynamics are due only to pure diffusion, or where the uncertainties are too large to distinguish between directional and non-directional modes of motion, are expected to have a low overall directionality, while if a track has states with a consistently high directionality, it will be inconsistent with the null hypothesis of pure diffusion.

The algorithm was validated by Dr Wareham with simulated data with a known "ground truth". Simulations were created with 0% directional tracks, 50% and 100%. By directional we mean that tracks were given a large initial velocity: v= [0.5,1] px/frame (equivalent in the experimental data to [1.6 – 3.2] μm/s). **Figure 7-2 A-C** shows stereotypical sets of tracks for these simulations, coloured according to the directionality metric. The empirical distributions of Log *d* were used for display purposes, because they amplify small differences compared to the pure *d* distributions. On this scale, a directional velocity larger than one standard deviation is equivalent to Log $d > 0$. The metric correctly returns increasing directionality as the fraction of directional tracks increases in the simulations.

Using the empirical distributions of Log *d* the number of frames that display directional motion can be quantified. For the 0% directionality simulation, the metric returns a single peak where the confidence of directionality is low (i.e. Log $d < 0$) (**Figure 7-2 D**). For the simulation with 50% directional tracks the method correctly returns two peaks, one similar to the 0%

directionality simulation and a second with larger Log *d* and therefore more significantly directional (**Figure 7-2 E**). For the 100% directionality simulation the metric correctly returns a single peak with the larger Log *d* values (**Figure 7-2 F**).

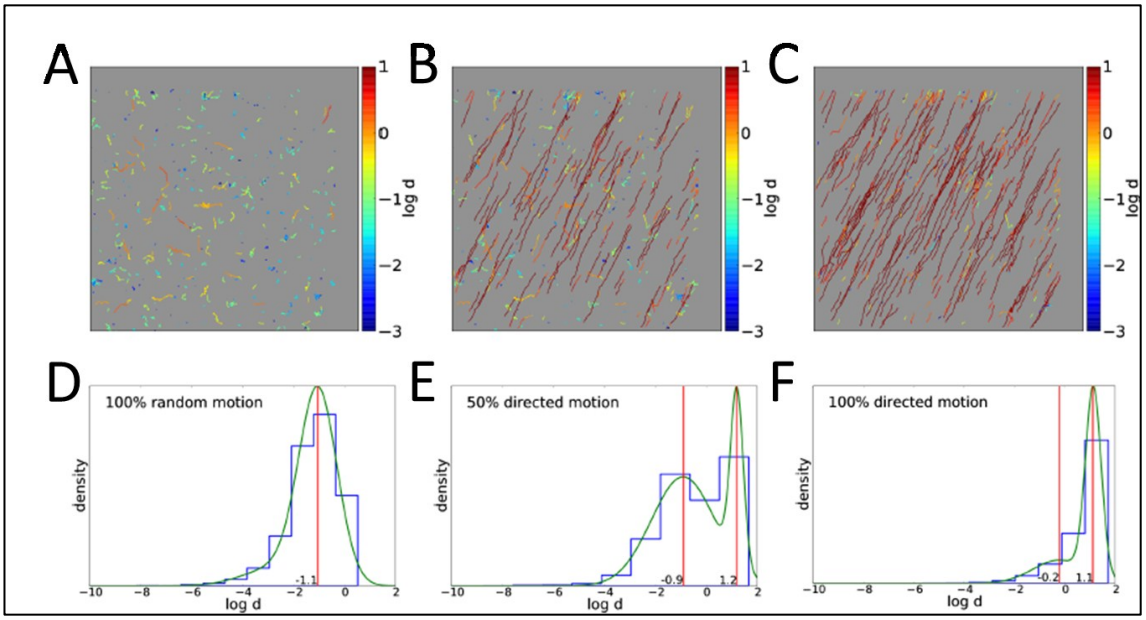

Figure 7-2 - Plots of pair-wise directionality. Simulated data sets with of 0% (**A**), 50% (**B**) and 100% (**C**) tracks that show directional motion. The tracks (*x, y, t*) are projected into the *x*-*y* plane and colour-coded according to their directionality, where Log *d* > 0 indicates more directional parts of tracks (red) and Log *d* < 0 indicates less directional parts of tracks (blue). **D-F)** Directionality histograms for the data shown in **A-C**. The blue line is the empirical directionality histogram containing one value for every particle *state* in every frame of every track in every posterior sample track partition *T*. Time points at which the particle in a track is not observed (dark) are also included. A track with 10 time points in a particular posterior track partition *T* will contribute 10 values to the histogram. The data are fitted with Gaussian mixture models (green) and the maxima of the models are shown in red.

Biggles was then used to analyse the directionality of the motion of HER1 molecules diffusing on the cell surface after activation with fluorescently labelled EGF, or in their basal state, bound to a fluorescent anti-HER1 Affibody. **Figure 7-3**, below, shows examples of tracks for the two conditions, colour-coded in units of Log *d*, directionality histograms and MSD plots for all particles tracked in each condition. The leftmost panels shows that receptors change their directionality status several times along their trajectory, most evidently for basal HER1 (**Figure 7-3 A**).

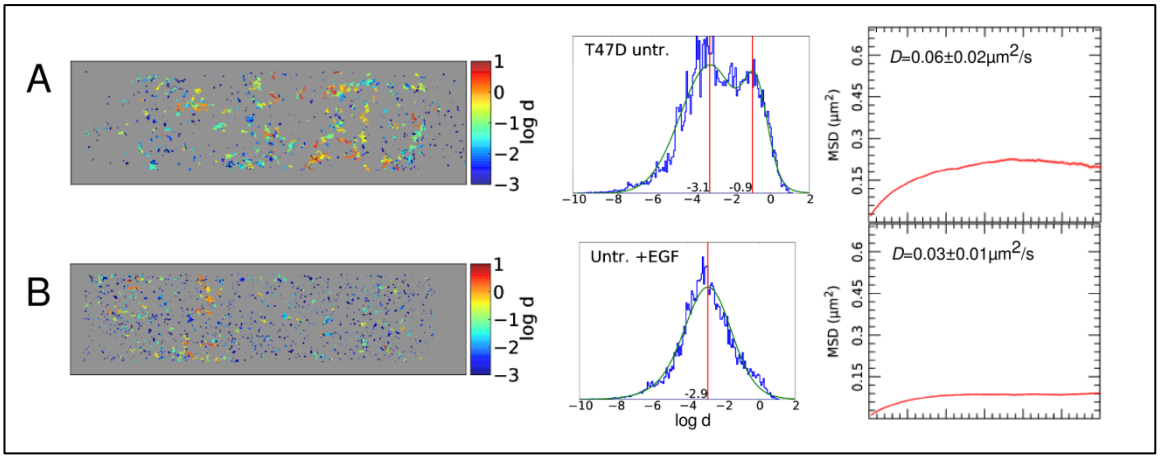

Figure 7-3 – Inactive HER1 tracked on T47D cells displays less confinement and more frequent changes in directionality compared to active HER1. Left: x-y coordinates of Biggles-reconstructed tracks, colour-coded by directionality, Middle: directionality histograms, and Right: combined MSD curves for all the features tracked on **A)** inactive HER1 and **B)** activated HER1* on the surface of T47D cells. Data was acquired at 20 Hz and combined over at least 10 independent areas.

To quantify the difference in directionality between HER1 in its active and basal state, the probability distribution of Log *d* per frame was plotted for both. **Figure 7-3 B (middle)** shows a higher abundance of track segments where Log *d* < 0 for EGF-bound HER1*. In contrast, for basal HER1, **Figure 7-3 A (middle)** shows a higher number of frames with larger values of Log *d*. More specifically, the particle *states* contributing to the peak with the larger Log *d* values have instantaneous velocity values in the range of ~0.2-0.8 μm/s and directional velocity significance *d* between ~0.2 and 2.7 standard deviations. This suggests that under basal conditions HER1 molecules can undergo directional motion. Complementary information on motion dynamics was extracted from the associated MSD plot (**Figure 7-3, right**), the plateau of which suggests that the motion of basal HER1 is confined to restricted areas of the plasma membrane [12]. This confinement effect is even more marked for activated HER1* (**Figure 7-3 B, right**)

To place EGFR's motion in context, the basal motion of HER1, HER2 and HER3 was tracked simultaneously using three different colour fluorescent antagonists. **Figure 7-4 A**, below, shows that basal HER2 is as directional as basal HER1, and that both are more directional than basal HER3 (left panel). Interestingly, from the associated MSD plots (right panel), the diffusion coefficients follow the same trend, with HER1 and HER2 being more similar to each other and faster than HER3.

Results from cells exposed to fluorescent EGF and either anti-HER2 or anti-HER3 Affibody molecules are shown in **Figure 7-4 B**. Upon binding EGF, the previously observed decrease in EGFR directionality (**Figure 7-3 B**) was not accompanied by a change in the directionality HER2 or HER3 from their basal values. The directionality of EGF-activated HER1 now resembles more the low value of HER3. This change is also reflected in the diffusion coefficients derived from the MSD plots (right panel), the values of which become now more similar for HER1 and HER3 and different from HER2.

In cells pre-treated with Lapatinib (**Figure 7-4 C**), which binds to both HER1 and HER2, and labelled with EGF and either anti-HER2 or anti-HER3 Affibody the directionality results for the three receptors resemble those observed under basal conditions: both the directionality (left panel) and diffusion coefficient (right panel) of HER1 are similar to those of HER2 and different to HER3. It should be noted that one difference from the basal state is the decrease in HER1 confinement, as evidenced by the higher MSD curve.

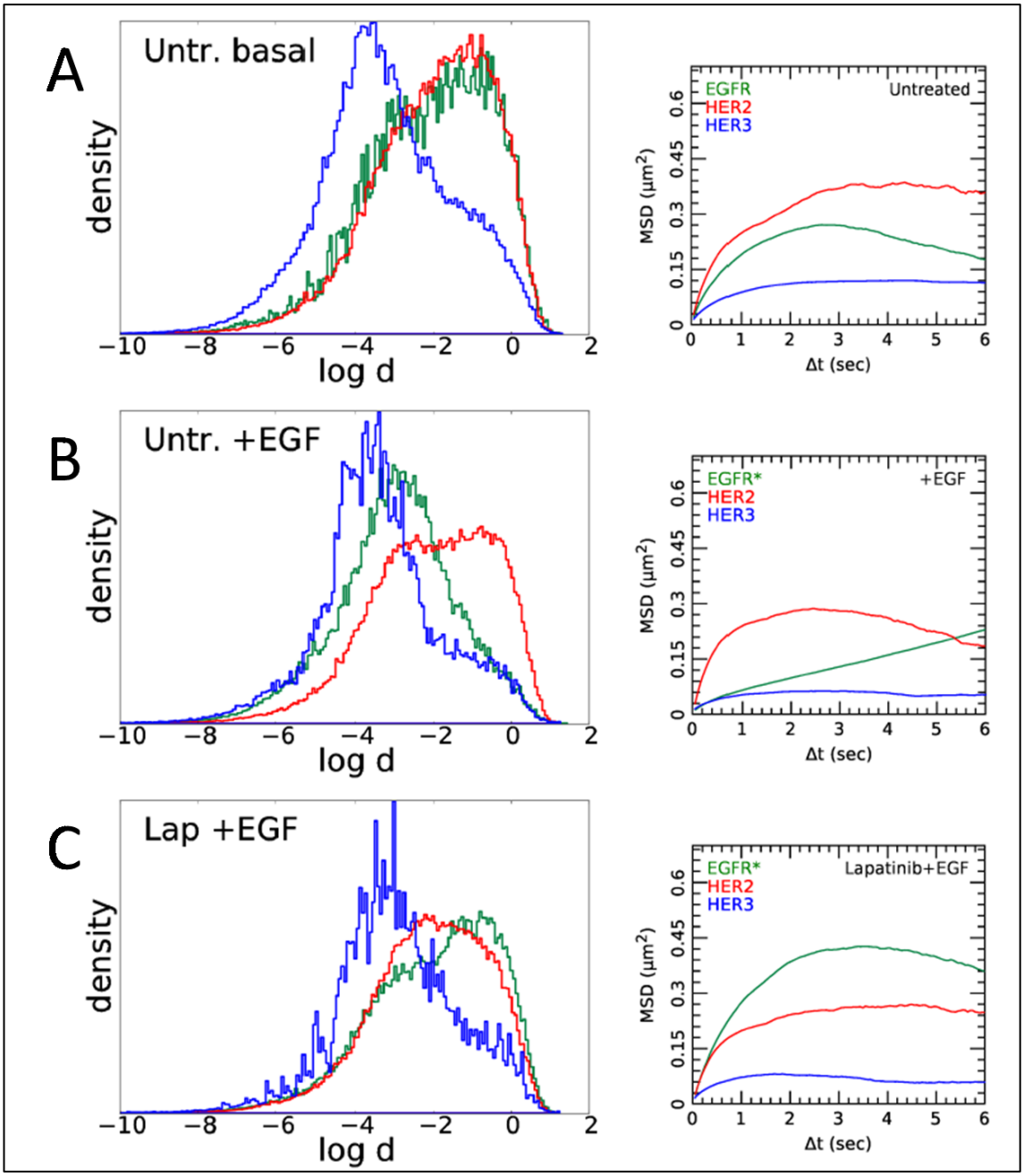

Figure 7-4 – Biggles directionality plots and MSD plots for HER1 (green lines), HER2 (red lines) and HER3 (blue lines) diffusing on the membrane of T47D cells at 37°, A) in absence of signalling (all receptors tracked with Affibodies), B) in presence of HER1 signalling (HER1* was tracked with EGF, HER2 and HER3 with Affibodies) and C) in presence of both EGF and 1 µM Lapatinib. Data were acquired at 20 Hz. HER1(*)-HER2 and HER1(*)-HER3 data were acquired separately and at least 10 independent areas were acquired for each set of experiments.

These results reinforce the hypothesis that HER3 might be spatially segregated from the other two receptors in basal conditions, and lend support to the possible role of HER1 in the regulation of HER3 dynamics at the cell membrane, as discussed in **Chapter 6**.

For the rest of the chapter, it was decided to focus on HER1, whose putative mechanisms of confinement and interaction with membrane structures are better defined.

7.2.3. Determination of the effect of receptor expression on HER1 membrane dynamics

In order to assess the effect of different variables on the behaviour of HER1 molecules on the surface of cells, HER1 was tracked on five different cell lines, which express the receptor at various levels. Luminal breast cancer cell lines T47D and MCF7 express low levels of HER1 (1.0-1.5 x 10^4 receptors/cell [370]and ~10^4 receptors/cell [403] respectively). Cervical carcinoma cell line HeLa, and Cho cells stably transfected with inducible wt HER1 express ~5 x 10^4 receptors/cell [164]. Stably transfected Cho+HER1-eGFP cells [404] express ~6 x 10^5 receptors/cell [124] . HER1 expression was induced with 50 ng/ml doxycycline hyclate for 48h in Cho+wt HER1 cells, which should result in an expression of approximately 10^5 receptors/cell [91]. HER1 was tracked in its resting state by labelling with anti-HER1 Affibody Alexa 488 in T47D, MCF7, HeLa and Cho + wt HER1 cells and by tracking the endogenously tagged receptor in Cho+HER1-eGFP.

The Quincy algorithm, described in Rolfe *et al.* [226] was used to derive the MSD and calculate the instantaneous diffusion coefficient *D* for this panel of cell lines.

As evidenced in **Figure 7-5** and **Table 7-1**, even when tracked in identical conditions, with the same probe and the same instrument, different cell lines show widely and significantly different HER1 diffusion coefficients. The *D* value of the T47D cell line was used as a reference due to the fact that this is the main cell model used throughout the project.

Cell Line	Average *D* ± SD ($\mu m^2/s$)	Average surface HER1 expression (receptors/cell)	P Value (K-S test)
T47D	0.0645 ± 0.0252	1.0-1.5 x 10^4	Ref.
MCF7	0.0233 ± 0.0170	10^4	<<0.0001 (***)
HeLa	0.0529 ± 0.0109	5 x 10^4	0.012 (#)
Cho + HER1-eGFP	0.0291 ± 0.0107	6 x 10^5	<<0.0001 (***)
Cho+ wt HER1	0.0667 ± 0.0243	10^5	0.14

Table 7-1 – Basal HER1 *D* and HER1 expression for a panel of cell lines used in single-colour Single-Particle Tracking experiments. ***= P Value < 0.0001; ** = P Value <0.001; * = P Value < 0.01; # = 0.5 > P Value >0.01 (borderline significance). Data was pooled over at least 10 independent areas for each cell line.

Contrary to expectations based on the baseline propensity of receptors to aggregate in cells expressing high levels of HER1 [124,164] and on the findings of Benveniste *et al.* [338], the diffusion coefficient *D* did not obviously correlate with the amount of HER1 expression (R^2= 0.1059), as shown in **Figure 7-5 B**. Causes of the different behaviour of the HER1 receptor on different cell lines are likely to be found in the different lipid composition of cell membranes across cell lines or in the differential expression of other membrane proteins that could act as interaction partners or pickets for HER1, affecting its mobility.

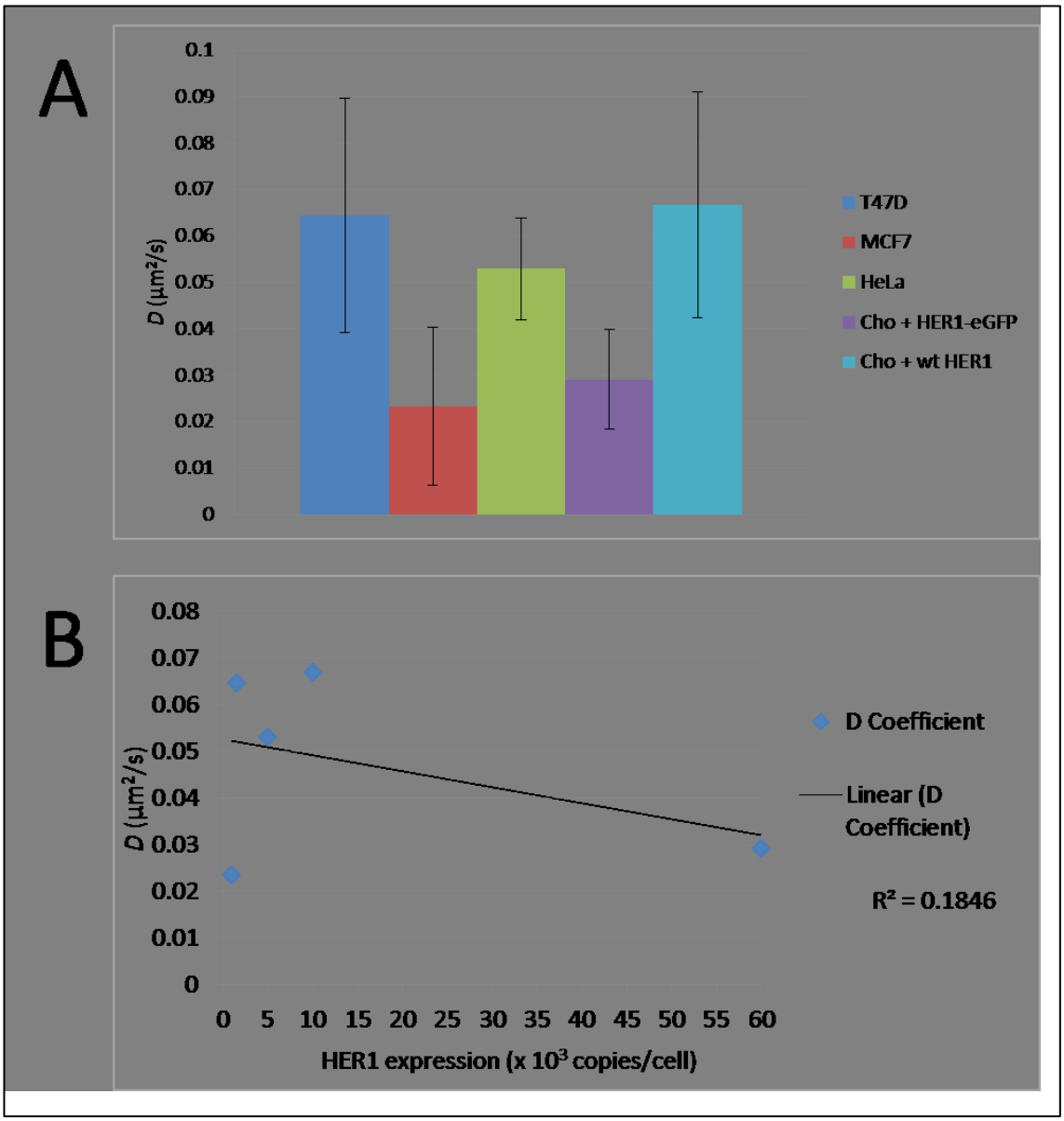

Figure 7-5 – HER1 mobility varies between cell lines expressing different levels of surface HER1 but is not directly correlated with expression levels. A) Histogram of average *D* coefficients for untreated cell lines expressing variable levels of surface HER1. Receptors were tracked with non-activating probe anti-HER1 Affibody Alexa 488 for T47D, MCF7, HeLa and Cho + wt HER1 cell lines and with the endogenously fused eGFP protein for Cho+HER1-eGFP. Data was averaged over at least 10 areas. **B)** Scatter plot of average *D* values v average HER1 expression levels for each cell line, showing no significant linear correlation between the two parameters.

The directionality of the diffusion of HER1 on HeLa and MCF7 cells was also analysed using the Biggles algorithm (**Figure 7-6**).

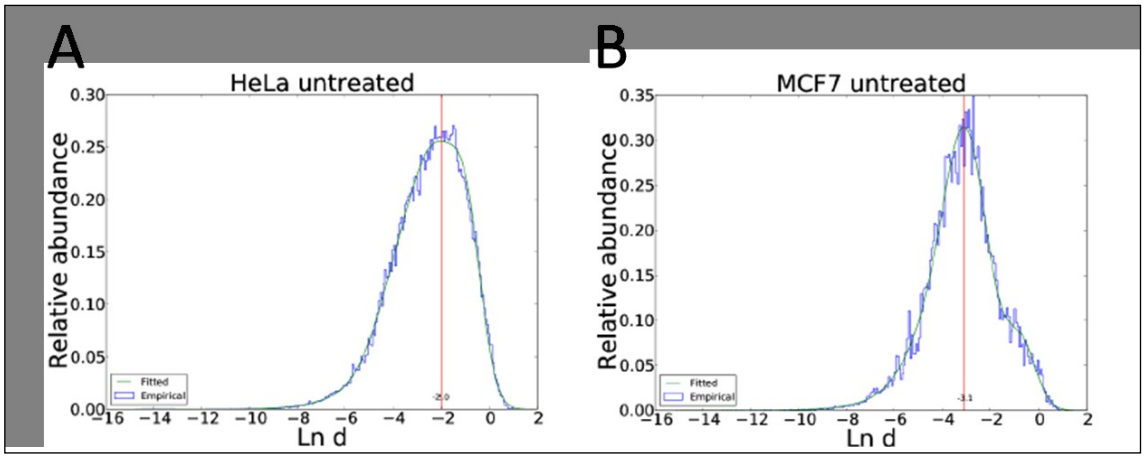

Figure 7-6 - Biggles directionality plots for HER1 diffusing on the membrane of A) HeLa and B) MCF7 cells at 37°C. Data were collected at 20 Hz and over at least 10 independent areas for each condition.

Biggles evidenced differences in the diffusion of HER1 in these two cell lines between themselves and compared with T47D cells (see **Figure 7-3 A, middle**). In HeLa cells, it has not been possible to resolve two Log *d* peaks, and the single resolvable peak has a Log *d* =- 2.0. MCF7 cells also display a single HER1 directionality peak with Log d =-3.1.

7.2.4. HER1 membrane dynamics are regulated by the actin cytoskeleton in T47D cells

To investigate the mechanisms underlying HER1 directionality, the effects of a panel of drugs on the mobility of both basal and activated HER1 were tested on T47D cells.
The cytoskeleton was disrupted with Cytochalasin D, Jasplakinolide and Latrunculin A, lipid rafts with Methyl-β-Cyclodextrin, the galectin lattice with excess α-Lactose, and the tyrosine kinase activity of the receptor was inhibited with Lapatinib. As a control for general cell toxicity, cells were inhibited with Nocodazol, which inhibits the polymerization of α-tubulin and, while it can alter the diffusion of HER1*-containing clusters [278], should not have any specific effect on the diffusional behaviour of single HER1 receptors on cell membranes. HER1 behaviour was investigated in resting state (**Figure 7-7 A**) by labelling with anti-HER1 Affibody Alexa 488 and in the active state (**Figure 7-7 B**) by labelling with EGF Alexa 488. The analysis of the effects of this panel of drugs on *D* was performed using the Quincy tracking algorithm [226]. Data are presented as average ±SD and were averaged over at least 15 independent areas.

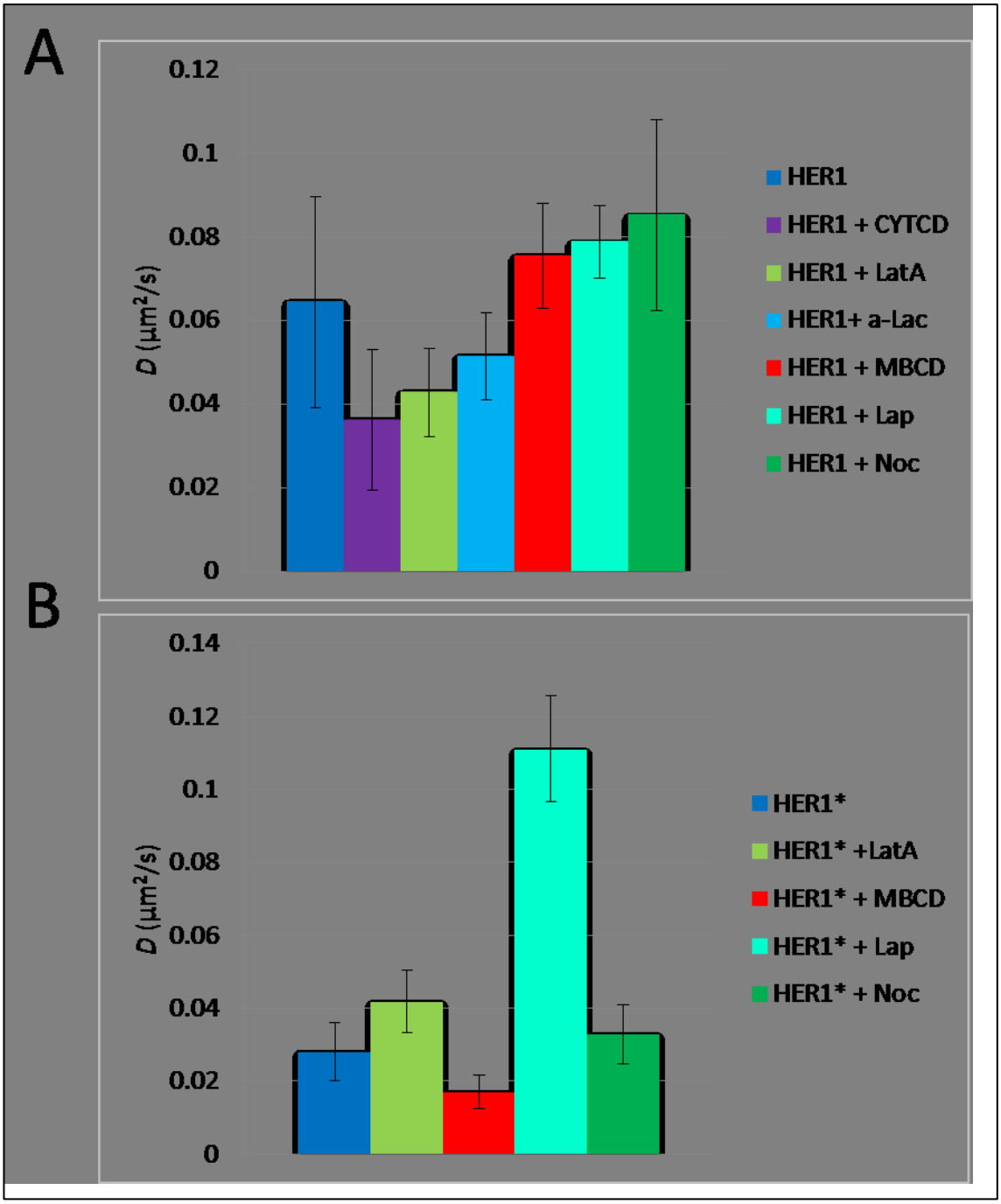

Figure 7-7 – Average *D* of HER1 receptors tracked on T47D cells in their A) basal and B) activated state in presence of different perturbing agents. CYTCD= Cytochalasin D 10 µM; LatA = Latrunculin A 10 µM, MBCD = Methyl-β-cyclodextrin 7.5 µM; Lap= Lapatinib 1 µM, Noc = 10 µM Nocodazol; a-Lac = 100 mM α-Lactose. All data are presented as average ± SD and were averaged over at least 10 independent areas.

Table 7-2, below, details the average *D* values ± SD for HER1 receptors tracked in their resting state (HER1) or in their active state (HER1*).

Treatment of cells with CYTCD, which binds to the barbed end of actin filaments, preventing elongation [405,406], results in decreased diffusion of resting-state HER1. Moreover, treatment of cells with Latrunculin A, another actin-disrupting drug that binds to G-actin preventing its incorporation in nascent actin filaments [407,408], is also able to reduce basal HER1 diffusion (**Figure 7-7 A**). On the other hand, treatment with LatA has a significant pro-diffusive effect on activated HER1* (**Figure 7-7 B**).

Taken together, these results seem to point towards a role for the actin cytoskeleton in the regulation of the diffusion of HER1 in both states.

Treatment with MBCD seems to have a slight but significant anti-diffusive effect on activated HER1*, possibly owing to the restriction of the available diffusion area for the receptor (**Figure 7-7 B**), but at the same time a borderline significant pro-diffusive effect on basal HER1 (**Figure 7-7 A**), possibly due to the effects of cholesterol disruption on the polymerisation of the cortical actin cytoskeleton [409].

Treatment with 1 μM Lapatinib, as already discussed in **Chapter 6**, has a slight pro-diffusive effect on resting HER1 and, even more strikingly, on EGF-activated HER1*, whose average *D* increases four- to five-fold (**Figure 7-7 B**). Interestingly, the diffusion of EGF-activated HER1* in presence of Lapatinib is significantly greater than both the diffusion of untreated resting-state HER1 ($P << 0.0001$) and the diffusion of lapatinib-treated resting-state HER1 ($P << 0.0001$).

These results support the hypothesis that, in the basal state, the population of HER1 receptors on the cell surface is made up of a mixed population of free monomers, but also of dimers and oligomers, possibly held together by symmetric interactions between their kinase domains, or by interactions with scaffold proteins, such as the actin cytoskeleton. Treatment with Lapatinib partially disrupts the pre-formed dimers/oligomers, and slightly but significantly increases the diffusion of inactive HER1. Ligand-induced activation, instead, induces a shift in the receptor population, favouring dimerization and higher-order interactions, as well as the build-up of a signalling complex on the C-terminal tails of the receptors. As predicted by the "picket-fence" membrane model, the bulkier aggregates have a lower probability of crossing the barrier between compartments and the macroscopic average diffusion is consequently reduced, keeping the signalling burst confined in time and space [4,17–19]. Treatment with Lapatinib prevents the activation of the receptor and locks its kinase domain in the inactive conformation, which cannot form the asymmetric dimer, however, the diffusion of liganded-inhibited HER1 is higher than that of unliganded-inhibited HER1, which allows the hypothesis that conformational changes induced by the ligand might be involved in the extra increase in diffusion.

Finally, treatment of cells with Nocodazol didn't have a significant effect on EGF-activated HER1* macroscopic diffusion, while the effect of Nocodazol on the diffusion of inactive HER1 is only borderline significant.

Experimental Group	**Average *D* ($\mu m^2/s$)**	**SD ($\mu m^2/s$)**	**P Value (K-S test)**
HER1	0.0645	0.0252	
HER1 + MBCD	0.0755	0.0126	0.018 (#)
HER1 + CytcD	0.0363	0.0168	0.002 (*)
HER1 + LatA	0.0429	0.0105	<<0.0001 (***)
HER1 + a-Lac	0.0515	0.0104	0.008(*)
HER1 + Lap	0.0788	0.0087	0.013 (#)
HER1 + Noc	0.0852	0.0228	0.04 (#)
Experimental Group	**Average *D* ($\mu m^2/s$)**	**SD ($\mu m^2/s$)**	**P Value (K-S test)**
HER1*	0.0282	0.0080	
HER1* + MBCD	0.0171	0.0046	<<0.0001 (***)
HER1* +LatA	0.0418	0.0085	<<0.0001 (***)
HER1* + Lap	0.1110	0.0145	<<0.0001 (***)
HER1* + Noc	0.0329	0.0081	0.13

Table 7-2 - Average diffusion coefficient and P Values (K-S test) for resting-state and activated HER1 tracked on T47D cells after drug treatment. ***= P Value < 0.0001; ** = P Value <0.001; * = P Value < 0.01; # = 0.5> P Value >0.01 (borderline significance). All data are presented as average ± SEM and were averaged over at least 10 independent areas. Untreated Affibody and untreated EGF were used as reference values for K-S test calculations.

In order to extract directionality information, a subset of this data was re-analysed with the Biggles tracking algorithm as described above.

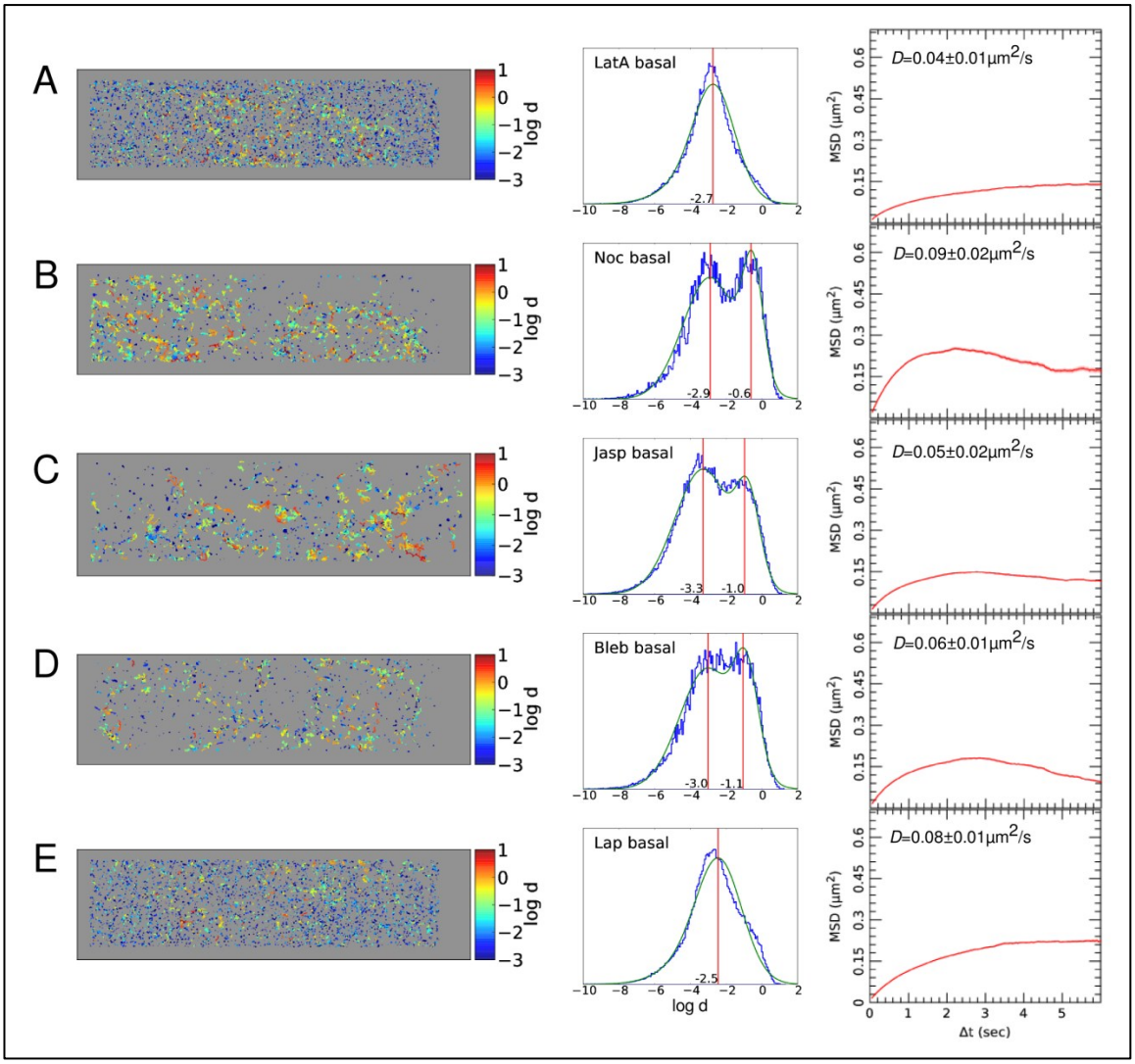

Figure 7-8 – From left to right: X-Y coordinates of Biggles-reconstructed tracks, colour-coded by directionality, directionality histograms and combined MSD plots for A) HER1 + LatA, B) HER1 + Noc, C) HER1 + Jasp D) HER1 + Bleb and E) HER1 + Lap. Data were collected at 20 Hz and over at least 10 independent areas for each condition.

Figure 7-8 shows the effect of various treatments on the diffusion of basal HER1. Compared with the data in **Figure 7-3**, the x-y plots and the Log d plots clearly highlight a drop in the directionality of HER1 tracked on LatA treated cells (**A**) and on Lap treated cells (**E**).

The higher directionality component of HER1 diffusion, seen in **Figure 7-3 A**, is lost upon LatA treatment (**Figure 7-8 A**) and, somewhat counter-intuitively, upon Lap treatment (**E**). The HER1 directionality profile, under these conditions, resembles that of activated HER1* (see **Figure 7-3 B**) and shows a less directional single population. LatA, but not Lap, also increased the degree of confinement of basal HER1, as shown by the MSD plots.

The dependence of the higher-directionality motion on the integrity of cortical filamentous

actin (F-actin) suggests that basal HER1 undergoes some form of actin-guided transport. In contrast, disruption of microtubule dynamics with Nocodazol [410] did not reduce basal HER1 directionality (**Figure 7-8 B**), suggesting that microtubules are not involved in this mode of motion.

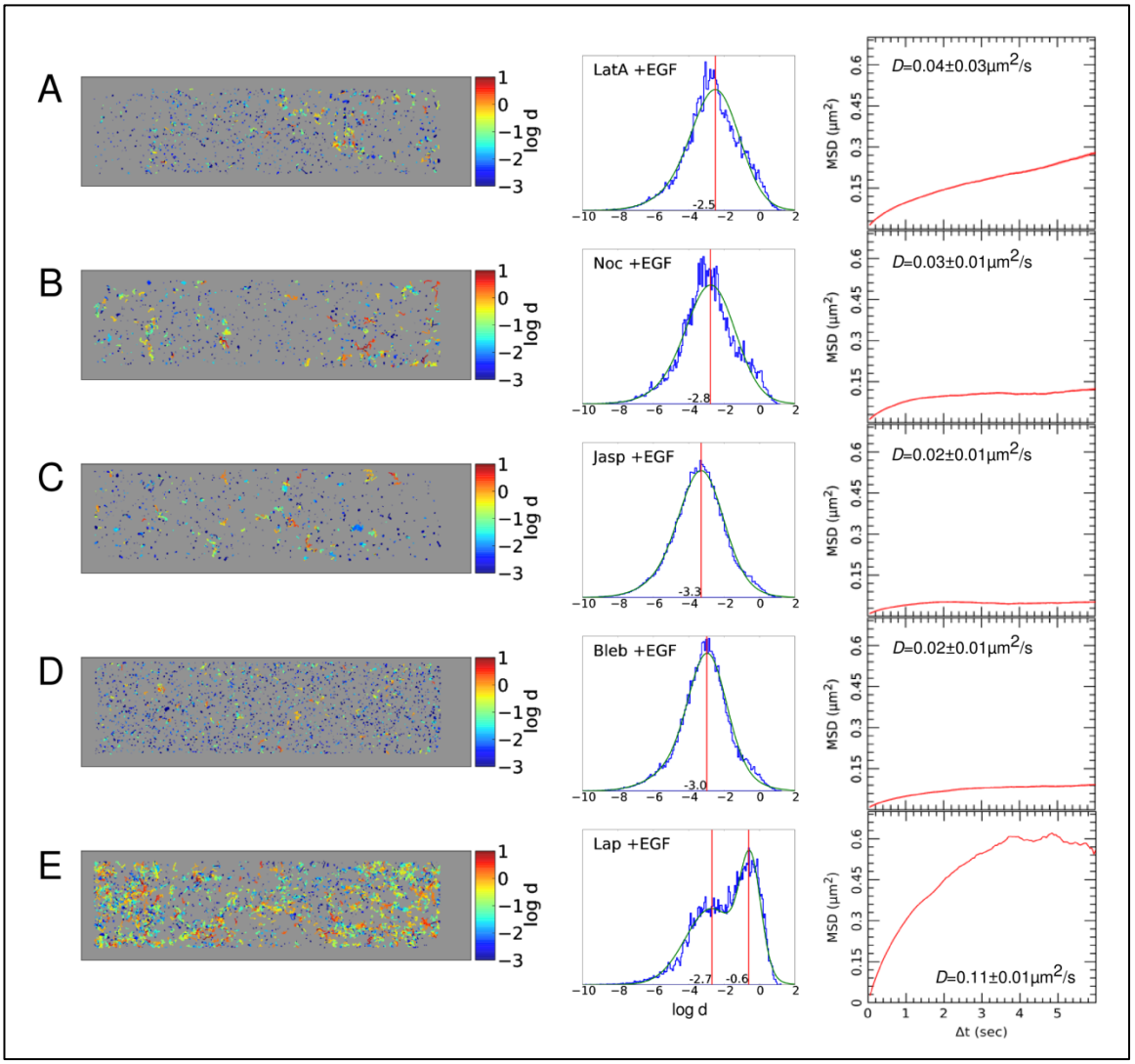

Figure 7-9 - From left to right: X-Y coordinates of Biggles-reconstructed tracks, colour-coded by directionality, directionality histograms and combined MSD plots for A) HER1* + LatA, B) HER1* + Noc, C) HER1* + Jasp, D) HER1* + Bleb and E) HER1* + Lap. Data were collected at 20 Hz and over at least 10 independent areas for each condition.

Figure 7-9 shows that on cells pre-treated with Class II TKI Lapatinib the diffusion of EGF-bound HER1* undergoes a significant increase in directionality, with the re-appearance of a higher-

directionality population (**Figure 7-9 E**). This increase was paralleled by a significant decrease in the degree of confinement of HER1* particles in presence of Lap, as seen from the MSD plot. This suggests that, when the kinase domain is maintained in an inactive configuration by the binding of Lapatinib, the higher-directionality motion of HER1 is no longer abolished by EGF binding. This effect, as well as the reduction in basal HER1 directionality, are not specific to Lap, but are seen also upon treatment with 1 µM Erlotinib (**Figure 7-10**). This suggests that basal directionality requires a signalling-competent kinase, which is consistent with the observation that basal HER3, which has an intrinsically incompetent kinase, displays the lowest directionality (**Figure 7-4**).

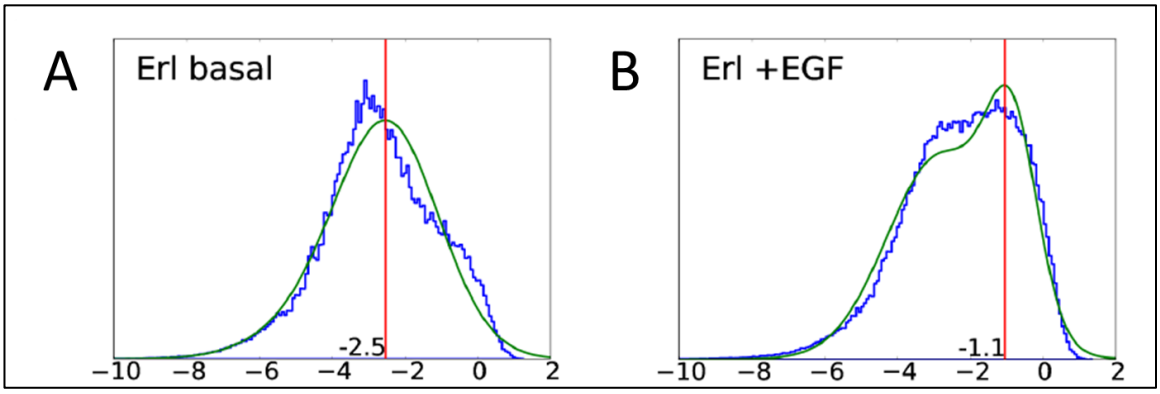

Figure 7-10 – Directionality histograms for A) HER1 + Erl and B) HER1*+Erl. Data were collected at 20 Hz and over at least 30 independent areas for each condition.

Treatment with LatA and Noc, on the other hand, did not have any effect on the directionality of EGF-activated HER1*(**Figure 7-9 A-B**). LatA treatment, however, reduced the degree of confinement of activated HER1*, as expected from the “picket-fence” membrane model.

Clues on actin-related processes that may be involved in basal HER1 dynamics can be sought from the initial velocity displayed by basal HER1 molecules, calculated to be in the range of ~0.2-0.8 µm/s. This is ~10x faster than the retrograde transport of activated HER1 along filopodia [390] and than the retrograde flow of F-actin *in vivo* [411], and ~10x slower than the rate of delivery of monomeric G-actin to the leading edge of the cell [412]. Dynamic F-actin treadmilling, where one end of a filament grows in length while the other end shrinks, resulting in a section of filament seemingly "moving" has, however, a compatible speed ~200 - 1000 nm [413].

To test this possibility, cells were treated with Jasplakinolide (Jasp), a drug that stabilises F-actin by halting actin dynamics [414,415], but that failed to have any significant effect on the directionality of basal state HER1 (**Figure 7-8 C**).

In order to assess the role of acto-myosin contractile fibres in basal HER1 diffusion, the effect of Blebbistatin (Bleb), an inhibitor that blocks myosin in an actin-detached state [416] was also investigated. While myosin is involved in the regulation of actin treadmilling [413,417], this drug did not inhibit the higher-directionality motion of basal HER1 (**Figure 7-8 D**), suggesting that myosin-based contractility is not involved in HER1 directional diffusion.
It is interesting to note, however, that Blebbistatin treatment seems to induce the localisation of HER1 to the edges of treated cells; while Jasplakinolide treated cells do not show this effect. Both treatments, however, increased the degree of confinement of HER1, as seen from the MSD plot.

Jasplakinolide and Blebbistatin had no effect on the directionality of activated HER1* (**Figure 7-9 C-D).** Jasplakinolide, however, increased the degree of confinement of HER1* particles, as seen from the MSD plot (**Figure 7-9 C, right panel**).

Taken together, these results highlight the requirements of an intact actin cytoskeleton, but not necessarily of a dynamic one, and of an uninhibited TKD for the directional motion of basal HER1. Ligand binding abolishes the higher component of HER1 diffusion in a way that is not restored by the disruption of the cytoskeleton. Treatment with LatA increases HER1* diffusion and decreases its confinement, as predicted by the membrane structure model [6]. Treatment with Lapatinib also reduces confinement and increases diffusion of HER1* particles, however HER1* particles appear to be in a state that is different from that of basal HER1 particles tracked on untreated cells. HER1*+Lap particles, in fact, show higher diffusion and lower confinement than basal HER1 particles, which might suggest that HER1 exists in a state of at least partial oligomerisation on resting cells, as evidenced also by the colocalisation data presented in **Chapter 6**. However, starting from this assumption, treatment of basal HER1 particles with Lapatinib should further decrease HER1 confinement and increase diffusion by breaking up the oligomers; however this is not the case. In contrast with the results recorded for basal HER1, Lapatinib treatment also re-introduces a directional component in HER1* diffusion, a finding whose cause is not immediately clear, but which might be linked to a rearrangement of receptor interactions.

7.2.5. Investigating the cell membrane and cytoskeletal determinants of HER1 dynamics in a panel of cell lines that express different levels of HER1

In order to investigate in more depth the possible determinants of the differences in resting-state HER1 diffusion between cell lines, HeLa, MCF7 and Cho+HER1-eGFP cell lines were subjected to treatment with 100 mM α-Lactose, to disrupt the extracellular galectin lattice; 7.5 µM MBCD to deplete cellular cholesterol through sequestration; and with 10 µM CytcD, an actin disruptor. HER1 diffusion was tracked in its basal state with anti-HER1 Affibody Alexa 488, using the Quincy tracking algorithm. Diffusion coefficient values and statistical significance values (computed using the *D* from untreated basal state HER1 tracked on T47D cells as a reference - see **Table 7-1**) are provided in **Table 7-3**, below.

Cell Line	**MBCD (P Value)**	**CytcD (P Value)**	**a-Lac (P Value)**
MCF7	N/A	0.0066 ± 0.0048 (0.004 - *)	0.0215 ± 0.0178 (0.59)
HeLa	0.0594 ± 0.0196 (0.51)	0.0391 ± 0.0122 (0.021 - #)	N/A
Cho+HER1-eGFP	0.0236 ± 0.0061 (0.19)	0.0172 ± 0.0036 (0.002 - *)	0.0201 ± 0.0074 (0.07)

Table 7-3 – Average diffusion coefficient and P Values (K-S test) for resting-state HER1 after treatment with MBCD, CytcD and a-Lac in a panel of cell lines. ***= P Value < 0.0001; ** = P Value <0.001; * = P Value < 0.01; # = 0.5 > P Value >0.01 (borderline significance). All data are presented ± SD and were averaged over at least 10 independent areas.

As shown in **Figure 7-11** below, in all cell lines examined, treatment with CYTCD significantly lowered basal HER1 mobility compared with untreated samples. While cytoskeletal disruption increases HER1* mobility in T47D cells, the results obtained with HER1 on the cell line panel and in T47D seem to contradict previous findings [110,310,418], according to which the actin cortical cytoskeleton would constitute a barrier to diffusion by forming a sort of "molecular fence" that excludes cholesterol and impedes protein diffusion. Treatment with 10 µM CYTCD lowers the turnover of cortical actin to about 10% of the untreated, as shown recently via quantitative FRAP [419] . Rearrangements in the cortical actin structure resulting in increased filament rigidity and thickness were reported in algae cells [420] and the drug is known to

make the actin collapse into bundles. These actin rearrangements could cause entrapment of HER1 among the tighter, thicker and less dynamic bundles and therefore reduce the lateral mobility of the receptor. Alternatively, a decrease in *D* could be due to a decrease in the directionality of HER1 motion, as evidenced in T47D treated with LatA.

The pro-confinement effect, however, could be also due to general cell toxicity slowing down cellular processes, or to off-target effects of the drug.

Cholesterol disruption with MBCD, which might also produce general toxicity effects, and disruption of the galectin lattice with α-Lactose, instead, didn't produce any significant effect on the cell lines examined, which seem to hint to the fact that resting-state receptors might be excluded from cholesterol-rich domains and from the galectin lattice.

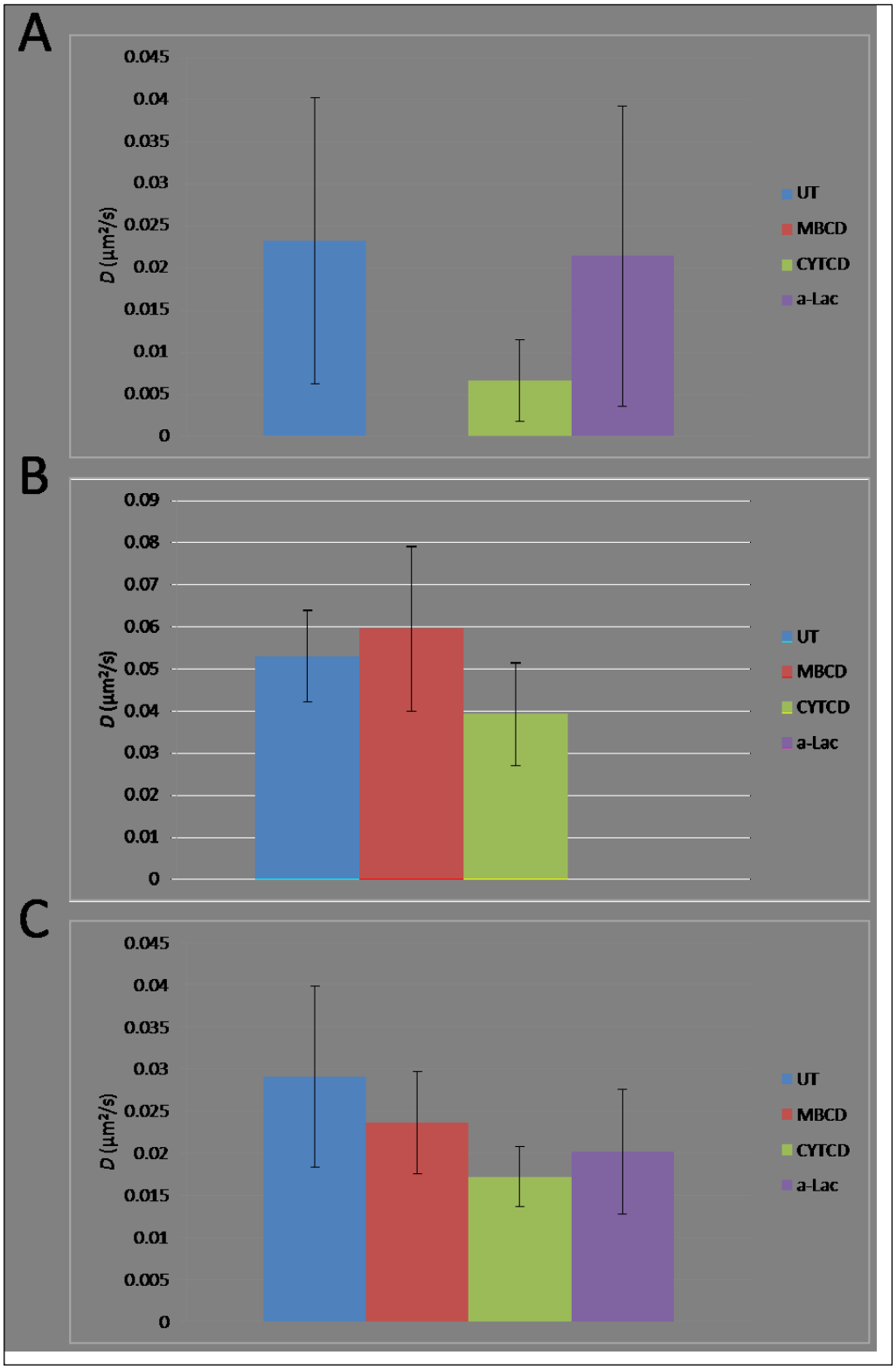

Figure 7-11 - Average diffusion of basal HER1 receptors in presence of different perturbing agents in A) MCF7, B) HeLa and C) Cho+HER1-eGFP cell lines. CYTCD= Cytochalasin D 10 µM; MBCD = Methyl-β-cyclodextrin 7.5 µM; a-Lac = α-Lactose 100 mM. All data are presented ± SD and were averaged over at least 10 independent areas

Further analysis with the Biggles tracking algorithm of basal HER1 on HeLa and MCF7 cells treated with 10 µM CYTCD revealed that, while the directionality profile of HER1 on HeLa cells is altered to reflect a decrease in directionality (**Figure 7-12 A** vs **Figure 7-6 A** – -3.0 vs -2.0 Ln d) paralleled by a decrease in *D* (**Figure 7-11 B**), CYTCD treatment has only a small effect on the directionality of HER1 on MCF7 cells (**Figure 7-12 B** vs **Figure 7-6 B** – -3.3 vs -3.1 Ln d) even if CYTCD treatment induces a decrease in *D* (**Figure 7-11 A**).

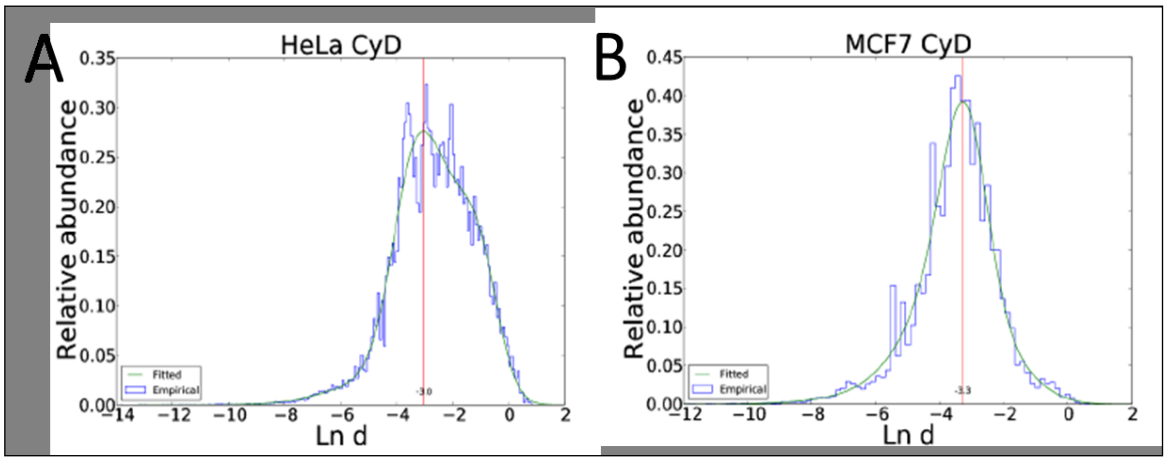

Figure 7-12 - Biggles directionality plots for HER1 + CYTCD diffusing on the membrane of A) HeLa and B) MCF7 cells at 37°C. Data were collected at 20 Hz and over at least 10 independent areas for each condition.

7.2.6. Two-colour tracking of HER1 and HER1* reveals the role of dynamic actin in regulating HER1 but not HER1* motility

As shown in the previous sections of this chapter, cytoskeletal determinants seem to play a major role in the control of HER1 dynamics at the cell membrane. In order to ascertain the role of the cytoskeleton in the regulation of HER1 motion, the effect of LatA, MBCD, Jasp and Bleb on HER1 interaction likelihood and kinetics was analysed via two-colour tracking with the Quincy tracking algorithm [226]. In particular, the focus was on the interactions between HER1* and HER1, whose low frequency in untreated cells might reflect spatial segregation of active and inactive receptors. Diffusion coefficients, interaction likelihoods and lifetimes were calculated for each condition. Data was pooled over at least 30 independent areas, acquired over at least 3 independent biological replicates.

Membrane structure-disrupting reagents significantly impact the diffusion coefficient of HER1 and HER1*

As shown in **Table 7-4** and **Figure 7-13**, cytoskeleton disruption with various reagents has a quite significant effect of the diffusion of HER1 both in its basal and in its ligand-activated state.

D ($\mu m^2/s$)	UT (ref.)	LatA (P Value)	MBCD (P Value)	Jasp (P Value)	Bleb (P Value)
HER1	0.0227 ± 0.0134			0.0526 ± 0.0222 (***)	0.0578 ± 0.0125 (***)
HER1 **HER1***	0.0272 ± 0.0128 0.0185 ± 0.0081	0.0436 ± 0.0314 (#) 0.0114 ± 0.0080 (**)	0.0594 ± 0.0175 (***) 0.0210 ± 0.0081	0.0761 ± 0.0148 (***) 0.0187 ± 0.0062	0.0723 ± 0.0108 (***) 0.0223 ± 0.0060 (#)
HER1*	0.0232 ± 0.0096			0.0164 ± 0.0088 (***)	0.0167 ± 0.0101 (**)

Table 7-4 - Average two-colour diffusion rates for HER1 and HER1* in the presence of cytoskeleton disrupting reagents. For homo-interactions, the diffusion rates of the two channels were combined. Significance levels are calculated using as a reference the value recorded from untreated samples in the first column: *P< 0.01; **P<0.001; ***P<0.0001; #= borderline (P = 0.05 -0.01) significance (Kolmogorov-Smirnov test). Data are presented as average ± SD and all averages were calculated on at least 30 independent areas from at least 3 independent biological replicates.

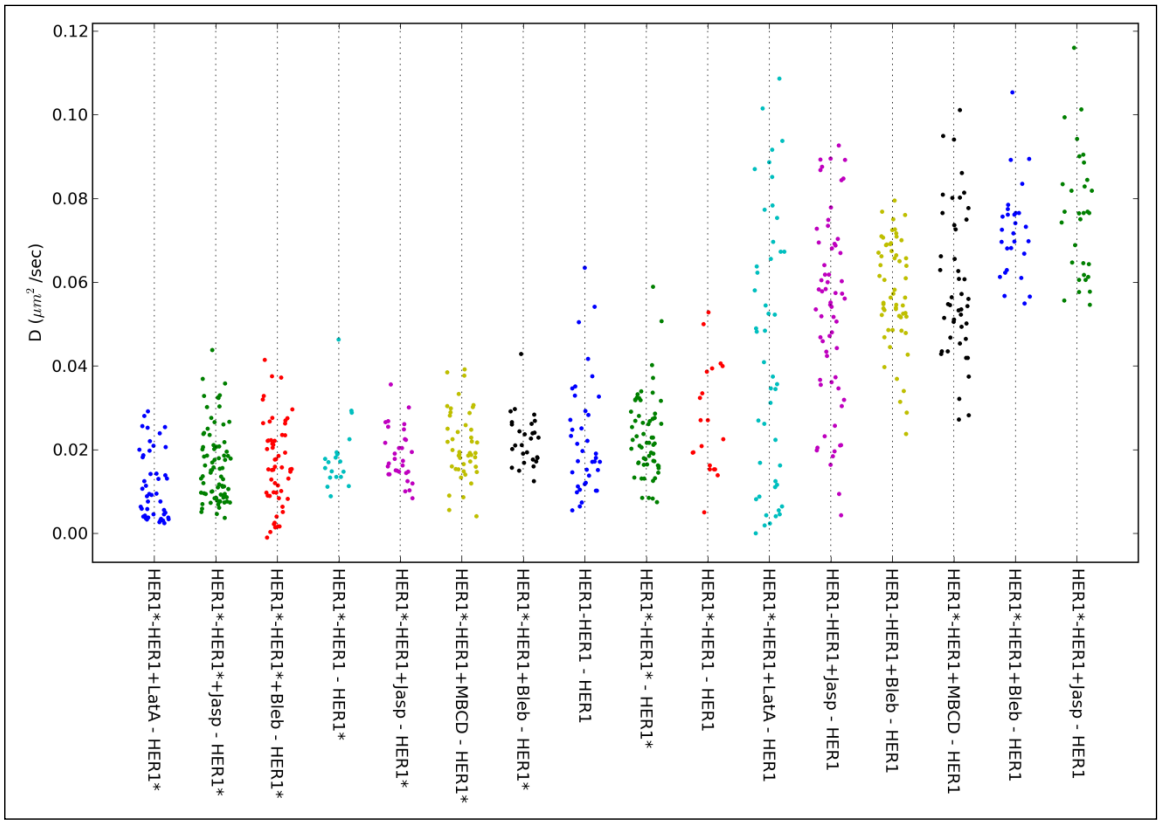

Figure 7-13 - Distributions of *D* for HER1 and HER1* tracked on T47D treated with Latrunculin A (LatA), Methyl-β-cyclodextrin (MBCD), Jasplakinolide (Jasp) and Blebbistatin (Bleb). The average *D* derived from every technical replicate (n ~30) is plotted as an independent dot for each receptor-pair/treatment combination. Data deriving from the two channels of homo-pair combinations has been combined for plotting. Datasets were sorted according to their *D* values.

Jasplakinolide favours the increase in F-actin and actin bundles, concomitant with a decrease in G-actin, which results in a coarser but more stable cortical actin meshwork [414,415]. This drug significantly increased the diffusion of inactive HER1, while it decreased the diffusion of active HER1* in "doubly-activated" cells and showed no effect on HER1* diffusion in cells labelled with both Affibody and EGF at the same time.

In general, all treatments investigated in this phase seem to increase the diffusion of the inactive HER1, but, at the same time, to decrease the diffusion of the active HER1*, with the exception of MBCD, which has no effect on HER1* diffusion. Blebbistatin seems to have an ambiguous effect, as it significantly slows down HER1* when the receptor is tracked with its ligand in both channels, while its effect on "half-activated" cells is slightly pro-diffusive.

In all cases considered, the difference between the diffusion of inactive HER1 and active HER1* for the same treatment group is highly significant ($P < 0.0001$).

Membrane structure disruption does not have a significant impact on the extent of HER1-HER1* colocalisation

Next, colocalisation frequencies were analysed for all the treatment combinations, constraining the distance threshold to 90 nm, which corresponds more or less to the size of the postulated HER1 nanodomains. In order to be computed as colocalised, two particles would have to move within 90 nm of each other for at least 3 frames (**Table 7-5**).

Coloc (%)	UT (ref.)	LatA (P Value)	MBCD (P Value)	Jasp (P Value)	Bleb (P Value)
HER1-HER1	0.19 ± 0.12			0.14 ± 0.14	0.12 ± 0.12
HER1-HER1*	0.13 ± 0.17	0.16 ± 0.26	0.24 ± 0.32	0.17 ± 0.18	0.17 ± 0.12
HER1*-HER1*	1.52 ± 1.23			1.58 ± 1.67	1.42 ± 1.67

Table 7-5 – Unfiltered two-colour colocalisation percentages (threshold: 90 nm, 3 frames) for homo and hetero-interactions between HER1 and HER1* in the presence of cytoskeleton disrupting reagents Significance levels are calculated using as a reference the value recorded from untreated samples in each group: *P< 0.01; **P<0.001; ***P<0.0001; #= borderline (P = 0.05 -0.01) significance (Kolmogorov-Smirnov test). Data are presented as average ± SD and all averages were calculated on at least 30 independent areas from at least 3 independent biological replicates.

Denoising the data with a Chung-Kennedy filter can tease out biological signals from otherwise noisy data and reduce the contribution from spurious colocalisation events derived from fluctuations in the localisation of the two particles. The consensus significance levels of the differences between untreated and treated samples are shown in **Table 7-6**, below.

Coloc (%)	UT (ref.)	LatA (P Value)	MBCD (P Value)	Jasp (P Value)	Bleb (P Value)
HER1-HER1	0.19 ± 0.12			NS	NS
HER1-HER1*	0.13 ± 0.17	NS	*	*	NS
HER1*-HER1*	1.52 ± 1.23			NS	NS

Table 7-6 – Consensus significance levels after C-K filtering for the data in Table 7-5.

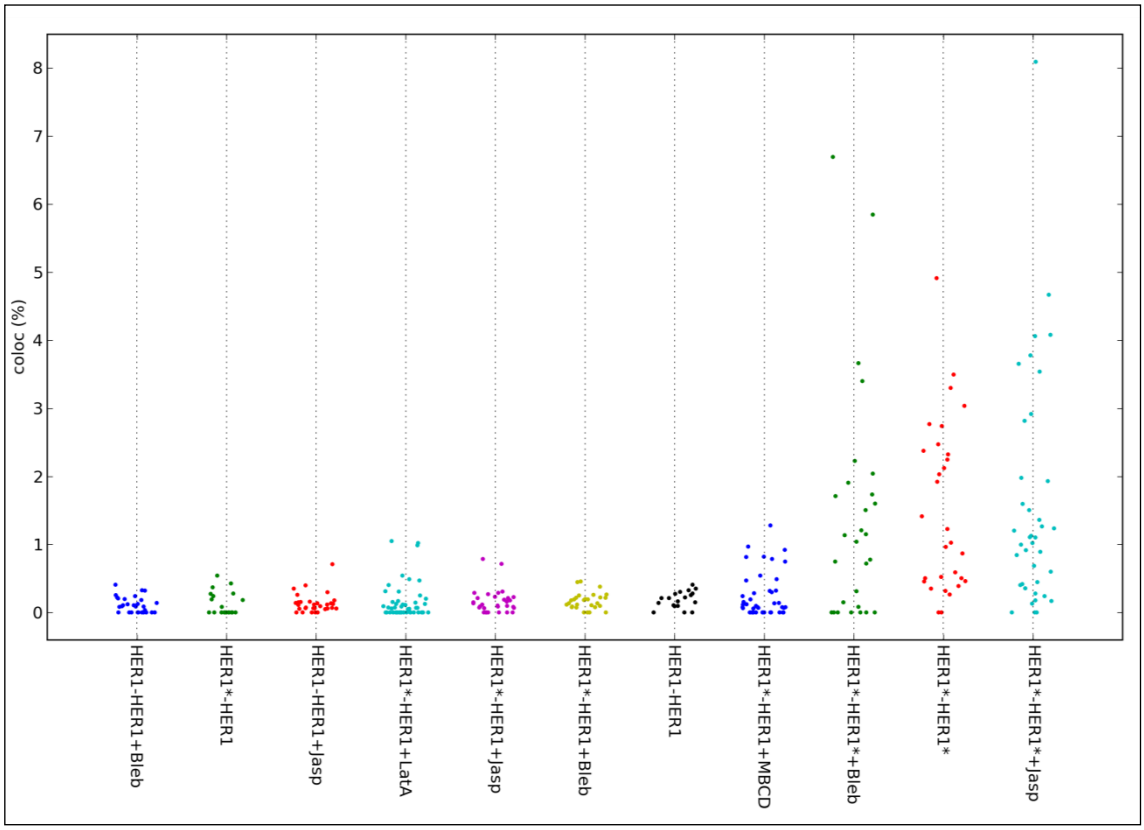

Figure 7-14 - Distributions of colocalisation frequencies for HER1 and HER1* tracked on T47D treated with Latrunculin A (LatA), Methyl-β-cyclodextrin (MBCD), Jasplakinolide (Jasp) and Blebbistatin (Bleb). The average colocalisation frequency derived from every technical replicate (n ~30) is plotted as an independent dot for each receptor-pair/treatment combination. Datasets were sorted according to their colocalisation % values.

While in the previous section it has been demonstrated that cytoskeleton disruption has a very significant effect on the diffusion of HER1 and HER1*, the effect of the same drugs on the interactions between the two species of the HER1 receptor is minimal (see **Figure 7-14** and **Table 7-5**).

Blebbistatin, a drug that prevents Myosin II from interacting with actin [416] does not seem to have any effect on the colocalisation of activated or inactive HER1 receptors. Jasplakinolide, which prevents actin remodelling [415], and Methyl-beta-cyclodextrin, instead, induce a significant increase in the colocalisation of HER1-HER1*, probably by altering the motility and the distribution of the receptors. It is worth noting that cholesterol depletion with MBCD has been linked by various authors to an increase in HER1 activation [375,379–384].
All treatments investigated conserve the highly significant difference in colocalisation likelihood between HER1-HER1 and HER1*-HER1* (all $P < 0.0001$).

7.3. Discussion and conclusions

In this chapter, the mode of movement of HER1 on the cell surface was additionally analysed using a novel globally optimised tracking algorithm: BIGGLES. This algorithm has the unique capability of producing an empirical probability density of each set of particle reconnections and associated model parameters.

The distributions of all possible tracks and parameters provided by BIGGLES also crucially provides probability distributions for any parameter of interest which can be calculated from a set of tracks this includes the frame-by-frame instantaneous particle velocity for each track, from which is derived an objective metric of the likelihood of the particle displaying directed motion in any given frame. This is required to measure the fluctuations of motion parameters along a track and therefore for evaluation of dynamic motion. Given its single frame sensitivity, the method in principle allows the use of any fluorescent probe, including those with poor photostability leading to short tracks, which are challenging for MSD-based methods.

Analysis with the Biggles tracking algorithm highlighted an unreported form of fast, higher-directionality motion in cell surface basal HER1. This motion requires an inactive tyrosine kinase domain and the integrity of the cortical F-actin cytoskeleton.

The MSD-based analysis of the effect of cytoskeleton-disrupting drugs on the diffusion of HER1 has revealed that both CYTCD and LatA have an anti-diffusive effect on inactive HER1, however LatA increases the diffusion of activated HER1*.
Jasplakinolide, instead, increases the diffusion of HER1, while decreasing the diffusion of HER1*.

Both LatA and CYTCD cause disruption of the actin network, possibly breaking down the "actin" into fragments which are still held in position by the transmembrane "pickets". Thus,

the activated and dimerized or oligomerized HER1*could conceivably encounter fewer barriers to its diffusion in the bulk membrane, due to the gaps in the fence. Conversely, by strengthening the “fence” and making it more rigid and less prone to fluctuate, Jasplakinolide would further restrict the diffusion of oligomers and bulky signalling platforms.

The opposite effect of these two classes of drugs on inactive HER1 is harder to explain. However, a structurally intact actin cytoskeleton is necessary for the directional motion of HER1, as evidenced by the presence of a higher-directionality peak in Jasp-treated HER1 but not in LatA-treated HER1. It is possible then, that the loss of directional velocity might be the cause of the reduction in diffusion caused by actin-disrupting drugs such as CYTCD and LatA.

Inactive HER1 might be directly or indirectly (via FERM proteins like Ezrin or Merlin [421] or via adaptors linking to ERM proteins, such as EBP50 [422–424]) associated with an intact actin cytoskeleton and its diffusion might follow the template of actin filaments. According to this model, the breakdown of actin filaments into short, disjointed bundles would restrict the movement of HER1 to smaller areas and the preservation of the meshwork structure by Jasplakinolide would either have no effect on its diffusion or even enhance it. van Bergen en Henegouwen *et al.* [425] proved that HER1 colocalises with filamentous actin in A431 cells and can be pulled down with actin filaments. Further experiments from den Hartigh *et al.* [113], proved that the HER1 receptor contains a C-terminal sequence that is homologous to that of the *Acanthamoeba* profilin, a protein that binds actin filaments, and that this sequence is necessary for actin filament binding. Binding of EGF to HER1 induces actin polymerisation at sites of HER1 activation [117], a mechanism which is involved in the regulation of HER1 signalling [118].
Recently Needham *et al.* [95] found an interesting 36 nm repetition pattern in the distribution of inactive HER1 receptors inside clusters and hypothesised that the repetition pattern could be associated with the F-actin helix period of 35.9 nm [426].

On the other hand, FERM proteins such as Ezrin and Merlin, instead, are known to bridge transmembrane proteins, the membrane and the actin cytoskeleton via their different domains or indirectly through binding to adaptor proteins such as EBP50/NHERF1 and E3KARP [427,428]. These proteins have been found to regulate the activation and function of receptors such as HER1 [421–424], integrins [429] and HGF [430,431]. Ezrin is also able to act as a scaffold of Ras and Sos, and is required for full pathway activation [432,433] .

The linkage between HER1 motility and organisation and the actin cytoskeleton has been strengthened by multiple avenues of investigation. Further work will be required to determine the role of single linkers and adaptors and to extend the analysis to other members of the HER family.

General Conclusions and Future Perspectives

This thesis describes the establishment of a new Single-Particle Tracking method to investigate the dynamics and kinetics of the HER family of RTKs, and the results thereof.

The preparation and characterisation of the labels used to track HER1-3 in their basal and active states, the optimisation of the conjugates to minimise the introduction of artefacts in Single-Molecule measurements, and the optimisation of the acquisition conditions to balance SNR requirements and temporal resolution, described in **Chapters 3-5**, all contributed to maximising the quality of the Single-Particle Tracking data.

HER1-3 were tracked at 37°C on a model breast cancer cell line expressing all four HER family receptors at low-medium "physiological" levels, investigating receptor diffusion at the cell membrane and interaction likelihood in a pairwise fashion. The substantial coverage afforded by this method enabled the detection of colocalisation events taking place between subpopulations of receptors. The data was denoised with Chung-Kennedy (C-K) filters, allowing a more precise determination of the percentage of colocalisation events, by smoothing out fluctuations in the separation of two putatively colocalised particles which were due to noise in the localisation estimate of the particles. The extent of coincidental colocalisation between fluorescent particles was calculated for each dataset and normalised colocalisation fractions were used as a measure of changes in interaction likelihood between receptors.

The effect of the activation of a third HER family receptor and of signalling inhibition with clinically relevant concentrations of TKIs was investigated for each pair of receptor, in order to extract information on system responses to perturbations.

This analysis revealed:

1) the role of HER1* tyrosine kinase activity in the regulation of receptor diffusion at the cell membrane;
2) a putative role for HER1 activity in the regulation of HER3 dynamics at the cell membrane;
3) a hierarchy of pairwise interactions between HER1-3 at the surface of T47D cells, which is modified by competition and by the effect of TKIs.
4) evidence for reciprocal regulation of HER1 and HER3 interactions with HER2, which might be compatible with the hetero-tetrameric model of signalling proposed by Huang *et al.* [132]

In addition to this, the analysis of the modes of HER1 motion with a novel, globally optimised tracking algorithm, BIGGLES, has revealed the existence at the cell membrane of T47D cells of

two populations of receptors, the diffusion of one of which is characterised by higher directionality. This higher directionality component is reduced or lost in presence of drugs that disrupt the actin cytoskeleton such as Cytochalasin D and Latrunculin A, but not in the presence of Jasplakinolide, which blocks actin turnover. The higher directionality component is also lost when the receptor is activated with its endogenous ligand EGF, while treatment with Lapatinib restores the more directional component in EGF-activated HER1*.
These findings highlight a role for both kinase activity and the actin cytoskeleton in the regulation of HER1 dynamics.

From first principles, the T47D cell line is not the ideal model to study the HER family signalling from a strictly clinical point of view, as it is an Estrogen Receptor positive cell line which does not depend on the HER family of receptors for tumorigenesis. However, its relatively low but detectable levels of expression of the HER family receptors make it an ideal model to paint a "ground-state" picture of the system. Hypothesis drawn from this model might in future be tested in other, more clinically relevant models of breast cancer and even on primary samples collected from patients under informed consent, in order to estimate immediate-early drug response parameters in real time. The unique characteristics of the tracking method presented in this thesis would make it suitable also for the analysis of cells expressing mismatched levels of different receptors, as is the case of cancer cells expressing high levels of a driver receptor and comparatively lower levels of accessory receptors.

As discussed previously, denoising of the data is necessary to avoid noise-derived artefacts leading to fluctuations in the localisation estimate. This method leads to the rejection of part of the data; therefore a higher amount of data will need to be collected to accurately measure the kinetics of the system. A full kinetic model of the HER family signalling and inhibition would be highly beneficial to understand from first principles how the system responds to perturbations and how it can be fully inhibited for the therapy of many cancer histotypes.

Before the model can be fully implemented, however, the analysis needs to be extended to the fourth member of the HER family, HER4, which has been left aside in the course of this thesis due to technical reasons linked to the lack of specific probes for this receptor. As a consequence of this, short-term future developments include the synthesis and characterisation of the missing probes and the collection of additional data to characterise HER4 dynamics and interactions.

Anti-HER4 scFv fragments, expressed and selected by the group of Dr Pierre Martineau at the University of Montpellier, as well as other non-antibody binders provided by other partners and collaborators, will be tested for specific binding to HER4 on T47D cells, for activation of HER4 and for competition with NRG1β. If suitable, the fragments will be used to track basal HER4. The labelling of these probes will be performed either with traditional N-reactive dyes, or by exploiting the 6-His tag included in the sequence for the purification process, by adapting the method described in Cong Y *et al.* [249]. In alternative, as a backup plan, an anti-HER4 blocking Fab derived from a monoclonal antibody [286] and labelled using N-reactive dyes will be used to track basal HER4.

Due to the lack of commercially available peptides with a specific binding to HER4, recombinant human NRG2β EGF-like domain will be expressed in collaboration with the Oxford Protein Production Facility and used to track activated HER4. Due to its ability to trigger the pro-apoptotic activity of HER4 ICD, careful optimisation of probe density will be required to minimise cell death during the acquisition phase. The recombinant NRG2β protein will be labelled either with classical N-reactive dyes or with the method described in Cong Y *et al*. [249].

As there is no high-affinity HER3-specific activating ligand, all pairwise tracking experiments performed in this thesis with NRG1β will be repeated blocking HER4 with the aforementioned Fab and the results will be compared and contrasted with the experiments performed in absence of Fab and those in presence of HER4-specific NRG2β, in order to distinguish the effects of HER3 activation from those of HER4 activation.

Ideally, in order to paint a complete picture of the HER family signalling, the recruitment of membrane-proximal adaptors and effectors should be investigated. The tracking of FP-tagged proteins such as Grb2, PLCγ and PI3K p85 expressed in T47D cells will enable the study of adaptors and effectors involved in the HER family signalling pathway to shed light on downstream events. This will aid in the characterisation of the various HER family receptor pairs as signalling species or inactive receptor depots, and will provide interaction lifetimes for different downstream proteins in response to different activating stimuli or TKIs.

All the information collected from the two-colour tracking experiments will be used for the construction of a mathematical model of the HER family system.

On the computational side, improvements to the data analysis algorithms currently in the pipeline, namely the implementation of a noise model for the detection system used to acquire the Single-Particle Tracking data, will enable the calculation of the minimal

stoichiometry of interacting particles from particle intensity. It will also be possible to analyse the relationship between particle intensity, which is an indicator of the minimal size of the group of receptors, and the diffusion coefficient itself. The assessment of the variations in particle diffusion upon interaction between two or more particles will also provide new information on the nature of the species of receptors taking part in the signalling processes and will hopefully help to shed light on the controversies over the role of oligomers in HER family signalling.

In addition to this, all the two-colour HER1-3 data from this thesis will be re-analysed with the globally optimised tracking algorithm BIGGLES, in order to assess various, previously inaccessible parameters, such as the directionality of particle motion, the instantaneous velocity of the diffusing particles, and the extent of merges and splits between traces in the same channel. This analysis toolkit will be used to assess the role of the actin cytoskeleton and lipid rafts in HER2-HER4 dynamics, as described for HER1 in **Chapter VII** of this thesis.

Plans for the mid-long term include the investigations of the structural determinants of HER1 dynamics, to be carried out using a panel of Cho cell lines which express HER1 ICD deletion mutants under a Tet-ON promoter (in collaboration with Prof Linda Pike).

The development of high-performance Near InfraRed dyes and the optimisation of 561 nm visible dyes will allow the extension of high-density tracking to three, four and possibly five colours, enabling the simultaneous visualisation of the whole HER family, a desirable outcome for the analysis of clinical samples, where sample availability is a limiting factor.

Finally, while optimised for the HER family of receptors, the tracking method described in this thesis is potentially applicable to the study of any membrane receptor system, provided that suitable probes are produced. The investigation of the interplay between the HER family and receptors such as Met [180–182], AXL [186] or IGF-1R [183–185], could shed light on clinically relevant interactions underpinning drug resistance mechanisms.

References

1. Zanetti-Domingues LC, Martin-Fernandez ML, Needham SR, Rolfe DJ, Clarke DT (2012) A systematic investigation of differential effects of cell culture substrates on the extent of artifacts in single-molecule tracking. PLoS One 7: e45655. Available: http://www.pubmedcentral.nih.gov/articlerender.fcgi?artid=3458086&tool=pmcentrez&rendertype=abstract. Accessed 10 August 2013.

2. Zanetti-Domingues LC, Tynan CJ, Rolfe DJ, Clarke DT, Martin-Fernandez M (2013) Hydrophobic Fluorescent Probes Introduce Artifacts into Single Molecule Tracking Experiments Due to Non-Specific Binding. PLoS One 8: e74200. Available: http://dx.plos.org/10.1371/journal.pone.0074200. Accessed 17 September 2013.

3. Wareham RJ, Zanetti-Domingues LC, Tynan CJ, Needham SR, Hirsch M, et al. (2013) A globally optimal tracking solution reveals basal cell surface EGFR transport underpinned by F-actin. Prep.

4. Grecco HE, Schmick M, Bastiaens PIH (2011) Signaling from the living plasma membrane. Cell 144: 897–909. Available: http://www.ncbi.nlm.nih.gov/pubmed/21414482. Accessed 5 March 2013.

5. Singer SJ, Nicolson GL (1972) The fluid mosaic model of the structure of cell membranes. Science 175: 720–731. Available: http://www.ncbi.nlm.nih.gov/pubmed/4333397. Accessed 15 August 2013.

6. Kusumi A, Nakada C, Ritchie K, Murase K, Suzuki K, et al. (2005) Paradigm shift of the plasma membrane concept from the two-dimensional continuum fluid to the partitioned fluid: high-speed single-molecule tracking of membrane molecules. Annu Rev Biophys Biomol Struct 34: 351–378. Available: http://www.ncbi.nlm.nih.gov/pubmed/15869394. Accessed 14 July 2012.

7. Saffman PG, Delbrück M (1975) Brownian motion in biological membranes. Proc Natl Acad Sci U S A 72: 3111–3113. Available: http://www.pubmedcentral.nih.gov/articlerender.fcgi?artid=432930&tool=pmcentrez&rendertype=abstract. Accessed 15 August 2013.

8. López-Duarte I, Vu TT, Izquierdo MA, Bull JA, Kuimova MK (2013) A molecular rotor for measuring viscosity in plasma membranes of live cells. Chem Commun (Camb). Available: http://pubs.rsc.org/en/content/articlehtml/2014/cc/c3cc47530a. Accessed 14 April 2014.

9. Bicknese S, Periasamy N, Shohet SB, Verkman AS (1993) Cytoplasmic viscosity near the cell plasma membrane: measurement by evanescent field frequency-domain microfluorimetry. Biophys J 65: 1272–1282. Available: http://www.pubmedcentral.nih.gov/articlerender.fcgi?artid=1225847&tool=pmcentrez&rendertype=abstract. Accessed 14 April 2014.

10. Mitra K, Ubarretxena-Belandia I, Taguchi T, Warren G, Engelman DM (2004) Modulation of the bilayer thickness of exocytic pathway membranes by membrane proteins rather

than cholesterol. Proc Natl Acad Sci U S A 101: 4083–4088. Available: http://www.pubmedcentral.nih.gov/articlerender.fcgi?artid=384699&tool=pmcentrez&rendertype=abstract. Accessed 14 April 2014.

11. Martin-Fernandez ML, Clarke DT (2012) Single Molecule Fluorescence Detection and Tracking in Mammalian Cells: The State-of-the-Art and Future Perspectives. Int J Mol Sci 13: 14742–14765. Available: http://www.pubmedcentral.nih.gov/articlerender.fcgi?artid=3509608&tool=pmcentrez&rendertype=abstract. Accessed 27 September 2013.

12. Kusumi a, Sako Y, Yamamoto M (1993) Confined lateral diffusion of membrane receptors as studied by single particle tracking (nanovid microscopy). Effects of calcium-induced differentiation in cultured epithelial cells. Biophys J 65: 2021–2040. Available: http://www.pubmedcentral.nih.gov/articlerender.fcgi?artid=1225938&tool=pmcentrez&rendertype=abstract. Accessed 16 July 2012.

13. Fujiwara T, Ritchie K, Murakoshi H, Jacobson K, Kusumi A (2002) Phospholipids undergo hop diffusion in compartmentalized cell membrane. J Cell Biol 157: 1071–1081. Available: http://www.pubmedcentral.nih.gov/articlerender.fcgi?artid=2174039&tool=pmcentrez&rendertype=abstract. Accessed 10 August 2013.

14. Murase K, Fujiwara T, Umemura Y, Suzuki K, Iino R, et al. (2004) Ultrafine membrane compartments for molecular diffusion as revealed by single molecule techniques. Biophys J 86: 4075–4093. Available: http://www.pubmedcentral.nih.gov/articlerender.fcgi?artid=1304307&tool=pmcentrez&rendertype=abstract. Accessed 12 March 2013.

15. Jaqaman K, Grinstein S (2012) Regulation from within: the cytoskeleton in transmembrane signaling. Trends Cell Biol 22: 515–526. Available: http://www.pubmedcentral.nih.gov/articlerender.fcgi?artid=3754899&tool=pmcentrez&rendertype=abstract. Accessed 26 March 2014.

16. Kusumi A, Shirai YM, Koyama-Honda I, Suzuki KGN, Fujiwara TK (2010) Hierarchical organization of the plasma membrane: investigations by single-molecule tracking vs. fluorescence correlation spectroscopy. FEBS Lett 584: 1814–1823. Available: http://www.ncbi.nlm.nih.gov/pubmed/20178787. Accessed 8 November 2012.

17. Kholodenko B, Hancock J, Kolch W (2010) Signalling ballet in space and time. Nat Rev Mol Cell … 11: 414–426. Available: http://www.nature.com/nrm/journal/v11/n6/abs/nrm2901.html. Accessed 23 April 2013.

18. Kalay Z, Fujiwara TK, Kusumi A (2012) Confining domains lead to reaction bursts: reaction kinetics in the plasma membrane. PLoS One 7: e32948. Available: http://www.pubmedcentral.nih.gov/articlerender.fcgi?artid=3314009&tool=pmcentrez&rendertype=abstract. Accessed 15 March 2013.

19. Mugler A, Tostevin F, Ten Wolde PR (2013) Spatial partitioning improves the reliability of biochemical signaling. Proc Natl Acad Sci U S A 110. Available: http://www.ncbi.nlm.nih.gov/pubmed/23530194. Accessed 2 April 2013.

20. Pike LJ (2006) Rafts defined: a report on the Keystone Symposium on Lipid Rafts and Cell Function. J Lipid Res 47: 1597–1598. Available: http://www.ncbi.nlm.nih.gov/pubmed/16645198. Accessed 1 November 2012.

21. Olayioye MA, Neve RM, Lane HA, Hynes NE (2000) The ErbB signaling network : receptor heterodimerization in development and cancer. EMBO J 19: 3159–3167.

22. Yarden Y, Sliwkowski MX (2001) Untangling the ErbB signalling network. Nat Rev Mol Cell Biol 2: 127–137. Available: http://www.ncbi.nlm.nih.gov/pubmed/11252954.

23. Avraham R, Yarden Y (2011) Feedback regulation of EGFR signalling: decision making by early and delayed loops. Nat Rev Mol Cell Biol 12: 104–117. Available: http://www.ncbi.nlm.nih.gov/pubmed/21252999. Accessed 14 June 2011.

24. Schlessinger J (2010) Cell signaling by receptor tyrosine kinases. Cell 141: 1117–1134. Available: http://scholar.google.com/scholar?hl=en&btnG=Search&q=intitle:Cell+Signaling+by+Receptor+Tyrosine+Kinases#0. Accessed 13 August 2013.

25. Ullrich A, Schlessinger J (1990) Signal transduction by receptors with tyrosine kinase activity. Cell 61: 203–212. Available: http://www.ncbi.nlm.nih.gov/pubmed/2158859. Accessed 9 August 2013.

26. Wilson KJ, Gilmore JL, Foley J, Lemmon M a, Riese DJ (2009) Functional selectivity of EGF family peptide growth factors: implications for cancer. Pharmacol Ther 122: 1–8. Available: http://www.pubmedcentral.nih.gov/articlerender.fcgi?artid=2665203&tool=pmcentrez&rendertype=abstract. Accessed 19 June 2011.

27. Yarden Y, Pines G (2012) The ERBB network: at last, cancer therapy meets systems biology. Nat Rev Cancer 12: 553–563. Available: http://www.ncbi.nlm.nih.gov/pubmed/22785351. Accessed 1 November 2012.

28. Eccles S (2011) The epidermal growth factor receptor/Erb-B/HER family in normal and malignant breast biology. Int J Dev Biol 44: 685–696. Available: http://www.ijdb.ehu.es/web/descarga/paper/113396se. Accessed 14 August 2013.

29. Sharma S V, Bell DW, Settleman J, Haber D a (2007) Epidermal growth factor receptor mutations in lung cancer. Nat Rev Cancer 7: 169–181. Available: http://www.ncbi.nlm.nih.gov/pubmed/17318210. Accessed 7 July 2011.

30. Furnari FB, Fenton T, Bachoo RM, Mukasa A, Stommel JM, et al. (2007) Malignant astrocytic glioma: genetics, biology, and paths to treatment. Genes Dev 21: 2683–2710. Available: http://genesdev.cshlp.org/content/21/21/2683.long. Accessed 13 August 2013.

31. Pines G, Huang PH, Zwang Y, White FM, Yarden Y (2010) EGFRvIV: a previously uncharacterized oncogenic mutant reveals a kinase autoinhibitory mechanism. Oncogene 29: 5850–5860. Available: http://www.ncbi.nlm.nih.gov/pubmed/20676128. Accessed 13 November 2012.

32. Leemans CR, Braakhuis BJM, Brakenhoff RH (2011) The molecular biology of head and neck cancer. Nat Rev Cancer 11: 9–22. Available: http://dx.doi.org/10.1038/nrc2982. Accessed 13 August 2013.

33. Nie F, Yang J, Wen S, An Y-L, Ding J, et al. (2012) Involvement of epidermal growth factor receptor overexpression in the promotion of breast cancer brain metastasis. Cancer: 1–12. Available: http://www.ncbi.nlm.nih.gov/pubmed/22510844. Accessed 24 April 2012.

34. Rexer B, Arteaga C (2012) Intrinsic and acquired resistance to HER2-targeted therapies in HER2 gene-amplified breast cancer: mechanisms and clinical implications. Crit Rev Oncog 17: 1–16. Available: http://www.dl.begellhouse.com/journals/439f422d0783386a,07ff3a573b26d6e9,237a039b425a836d.html. Accessed 23 April 2013.

35. Greulich H, Kaplan B, Mertins P, Chen T-H, Tanaka KE, et al. (2012) Functional analysis of receptor tyrosine kinase mutations in lung cancer identifies oncogenic extracellular domain mutations of ERBB2. Proc Natl Acad Sci U S A. Available: http://www.ncbi.nlm.nih.gov/pubmed/22908275. Accessed 30 August 2012.

36. Sithanandam G, Anderson LM (2008) The ERBB3 receptor in cancer and cancer gene therapy. Cancer Gene Ther 15: 413–448. Available: http://www.pubmedcentral.nih.gov/articlerender.fcgi?artid=2761714&tool=pmcentrez&rendertype=abstract. Accessed 17 June 2011.

37. Jiang N, Saba NF, Chen ZG (2012) Advances in Targeting HER3 as an Anticancer Therapy. Chemother Res Pract 2012: 817304. Available: http://www.pubmedcentral.nih.gov/articlerender.fcgi?artid=3502787&tool=pmcentrez&rendertype=abstract. Accessed 16 April 2013.

38. Campbell MR, Amin D, Moasser MM (2010) HER3 comes of age: new insights into its functions and role in signaling, tumor biology, and cancer therapy. Clin Cancer Res 16: 1373–1383. Available: http://www.pubmedcentral.nih.gov/articlerender.fcgi?artid=2831167&tool=pmcentrez&rendertype=abstract. Accessed 9 August 2011.

39. Umelo I, Noeparast A, Chen G (2013) A NOVEL HER3/ERBB3 DRIVER MUTATION IN NON-SMALL CELL LUNG CANCER. Ann Oncol 24: 2013. doi:10.1093/annonc/mdt042.34.

40. Jaiswal BS, Kljavin NM, Stawiski EW, Chan E, Parikh C, et al. (2013) Oncogenic ERBB3 Mutations in Human Cancers. Cancer Cell 23: 603–617. Available: http://www.ncbi.nlm.nih.gov/pubmed/23680147. Accessed 22 May 2013.

41. Prickett TD, Agrawal NS, Wei X, Yates KE, Lin JC, et al. (2009) Analysis of the tyrosine kinome in melanoma reveals recurrent mutations in ERBB4. Nat Genet 41: 1127–1132.

Available: http://www.pubmedcentral.nih.gov/articlerender.fcgi?artid=2897709&tool=pmcentrez&rendertype=abstract. Accessed 16 July 2011.

42. Naresh A, Long W, Vidal G a, Wimley WC, Marrero L, et al. (2006) The ERBB4/HER4 intracellular domain 4ICD is a BH3-only protein promoting apoptosis of breast cancer cells. Cancer Res 66: 6412–6420. Available: http://www.ncbi.nlm.nih.gov/pubmed/16778220. Accessed 11 June 2013.

43. Ritter C a, Perez-Torres M, Rinehart C, Guix M, Dugger T, et al. (2007) Human breast cancer cells selected for resistance to trastuzumab in vivo overexpress epidermal growth factor receptor and ErbB ligands and remain dependent on the ErbB receptor network. Clin Cancer Res 13: 4909–4919. Available: http://www.ncbi.nlm.nih.gov/pubmed/17699871. Accessed 15 June 2011.

44. Montero JC, Rodríguez-Barrueco R, Ocaña A, Díaz-Rodríguez E, Esparís-Ogando A, et al. (2008) Neuregulins and cancer. Clin Cancer Res 14: 3237–3241. Available: http://www.ncbi.nlm.nih.gov/pubmed/18519747. Accessed 22 July 2011.

45. Hutcheson IR, Knowlden JM, Hiscox SE, Barrow D, Gee JMW, et al. (2007) Heregulin beta1 drives gefitinib-resistant growth and invasion in tamoxifen-resistant MCF-7 breast cancer cells. Breast Cancer Res 9: R50. Available: http://www.pubmedcentral.nih.gov/articlerender.fcgi?artid=2206726&tool=pmcentrez&rendertype=abstract. Accessed 22 November 2011.

46. Yonesaka K, Zejnullahu K, Okamoto I, Satoh T, Cappuzzo F, et al. (2011) Activation of ERBB2 Signaling Causes Resistance to the EGFR-Directed Therapeutic Antibody Cetuximab. Sci Transl Med 3: 99ra86–99ra86. Available: http://stm.sciencemag.org/cgi/doi/10.1126/scitranslmed.3002442. Accessed 8 September 2011.

47. Schlessinger J (1988) Signal transduction by allosteric receptor oligomerization. Trends Biochem Sci 13: 443–447. Available: http://www.ncbi.nlm.nih.gov/pubmed/3075366. Accessed 2 September 2013.

48. Oda K, Matsuoka Y, Funahashi A, Kitano H (2005) A comprehensive pathway map of epidermal growth factor receptor signaling. Mol Syst Biol 1: 2005.0010. Available: http://www.pubmedcentral.nih.gov/articlerender.fcgi?artid=1681468&tool=pmcentrez&rendertype=abstract. Accessed 7 August 2013.

49. Lemmon MA (2010) Ligand-induced ErbB receptor dimerization. Cell 315: 638–648. doi:10.1016/j.yexcr.2008.10.024.Ligand-induced.

50. Dawson JP, Bu Z, Lemmon M a (2007) Ligand-induced structural transitions in ErbB receptor extracellular domains. Structure 15: 942–954. Available: http://www.ncbi.nlm.nih.gov/pubmed/17697999. Accessed 27 October 2011.

51. Cho H-S, Leahy DJ (2002) Structure of the extracellular region of HER3 reveals an interdomain tether. Science 297: 1330–1333. Available: http://www.ncbi.nlm.nih.gov/pubmed/12154198. Accessed 3 August 2011.

52. Bouyain S, Longo PA, Li S, Ferguson KM, Leahy DJ (2005) The extracellular region of ErbB4 adopts a tethered conformation in the absence of ligand. Proc Natl Acad Sci U S A 102: 15024–15029. Available: http://www.pubmedcentral.nih.gov/articlerender.fcgi?artid=1257738&tool=pmcentrez&rendertype=abstract. Accessed 9 August 2013.

53. Ferguson KM, Berger MB, Mendrola JM, Cho HS, Leahy DJ, et al. (2003) EGF activates its receptor by removing interactions that autoinhibit ectodomain dimerization. Mol Cell 11: 507–517. Available: http://www.ncbi.nlm.nih.gov/pubmed/12620237. Accessed 2 September 2013.

54. Garrett TPJ, McKern NM, Lou M, Elleman TC, Adams TE, et al. (2002) Crystal structure of a truncated epidermal growth factor receptor extracellular domain bound to transforming growth factor alpha. Cell 110: 763–773. Available: http://www.ncbi.nlm.nih.gov/pubmed/12297049. Accessed 2 September 2013.

55. Garrett TPJ, McKern NM, Lou M, Elleman TC, Adams TE, et al. (2003) The crystal structure of a truncated ErbB2 ectodomain reveals an active conformation, poised to interact with other ErbB receptors. Mol Cell 11: 495–505. Available: http://www.ncbi.nlm.nih.gov/pubmed/12620236. Accessed 2 September 2013.

56. Ogiso H, Ishitani R, Nureki O, Fukai S, Yamanaka M, et al. (2002) Crystal structure of the complex of human epidermal growth factor and receptor extracellular domains. Cell 110: 775–787. Available: http://www.ncbi.nlm.nih.gov/pubmed/12297050. Accessed 2 September 2013.

57. Burgess AW, Cho H-S, Eigenbrot C, Ferguson KM, Garrett TPJ, et al. (2003) An open-and-shut case? Recent insights into the activation of EGF/ErbB receptors. Mol Cell 12: 541–552. Available: http://www.ncbi.nlm.nih.gov/pubmed/14527402. Accessed 22 August 2013.

58. Goodsell DS (2010) Epidermal Growth Factor Receptor. RCSB Protein Data Bank: 2–3. Available: http://www.rcsb.org/pdb/static.do?p=education_discussion/molecule_of_the_month/pdb126_1.html. Accessed 8 May 2014.

59. Adak S, DeAndrade D, Pike LJ (2011) The tethering arm of the EGF receptor is required for negative cooperativity and signal transduction. J Biol Chem 286: 1545–1555. Available: http://www.pubmedcentral.nih.gov/articlerender.fcgi?artid=3020763&tool=pmcentrez&rendertype=abstract. Accessed 22 November 2011.

60. Webb SED, Roberts SK, Needham SR, Tynan CJ, Rolfe DJ, et al. (2008) Single-molecule imaging and fluorescence lifetime imaging microscopy show different structures for high- and low-affinity epidermal growth factor receptors in A431 cells. Biophys J 94: 803–819. Available: http://www.pubmedcentral.nih.gov/articlerender.fcgi?artid=2186246&tool=pmcentrez&rendertype=abstract. Accessed 26 July 2011.

61. Tynan CJ, Roberts SK, Rolfe DJ, Clarke DT, Loeffler HH, et al. (2011) Human epidermal growth factor receptor (EGFR) aligned on the plasma membrane adopts key features of Drosophila EGFR asymmetry. Mol Cell Biol 31: 2241–2252. Available: http://www.pubmedcentral.nih.gov/articlerender.fcgi?artid=3133235&tool=pmcentrez&rendertype=abstract. Accessed 31 August 2011.

62. Kästner J, Loeffler HH, Roberts SK, Martin-Fernandez ML, Winn MD (2009) Ectodomain orientation, conformational plasticity and oligomerization of ErbB1 receptors investigated by molecular dynamics. J Struct Biol 167: 117–128. Available: http://www.ncbi.nlm.nih.gov/pubmed/19406245. Accessed 18 September 2011.

63. Arkhipov A, Shan Y, Das R, Endres NF, Eastwood MP, et al. (2013) Architecture and membrane interactions of the EGF receptor. Cell 152: 557–569. Available: http://www.pubmedcentral.nih.gov/articlerender.fcgi?artid=3680629&tool=pmcentrez&rendertype=abstract. Accessed 6 August 2013.

64. Cymer F, Schneider D (2010) Transmembrane helix-helix interactions involved in ErbB receptor signaling. Cell Adh Migr 4: 299–312. Available: http://www.pubmedcentral.nih.gov/articlerender.fcgi?artid=2900627&tool=pmcentrez&rendertype=abstract.

65. Fleishman SJ, Schlessinger J, Ben-Tal N (2002) A putative molecular-activation switch in the transmembrane domain of erbB2. Proc Natl Acad Sci U S A 99: 15937–15940. Available: http://www.pubmedcentral.nih.gov/articlerender.fcgi?artid=138543&tool=pmcentrez&rendertype=abstract.

66. Endres NF, Das R, Smith AW, Arkhipov A, Kovacs E, et al. (2013) Conformational coupling across the plasma membrane in activation of the EGF receptor. Cell 152: 543–556. Available: http://www.pubmedcentral.nih.gov/articlerender.fcgi?artid=3718647&tool=pmcentrez&rendertype=abstract. Accessed 6 August 2013.

67. Mirza A, Mustafa M, Talevich E, Kannan N (2010) Co-conserved features associated with cis regulation of ErbB tyrosine kinases. PLoS One 5: e14310. Available: http://www.pubmedcentral.nih.gov/articlerender.fcgi?artid=3001462&tool=pmcentrez&rendertype=abstract. Accessed 8 July 2011.

68. Matsushita C (2013) Transmembrane helix orientation influences membrane binding of the intracellular juxtamembrane domain in Neu receptor peptides. Proc … 110: 1646–1651. Available: http://www.pnas.org/content/110/5/1646.short. Accessed 6 November 2013.

69. Red Brewer M, Choi SH, Alvarado D, Moravcevic K, Pozzi A, et al. (2009) The juxtamembrane region of the EGF receptor functions as an activation domain. Mol Cell 34: 641–651. Available: http://www.pubmedcentral.nih.gov/articlerender.fcgi?artid=2719887&tool=pmcentrez&rendertype=abstract. Accessed 27 July 2011.

70. Jura N, Endres NF, Engel K, Deindl S, Das R, et al. (2009) Mechanism for activation of the EGF receptor catalytic domain by the juxtamembrane segment. Cell 137: 1293–1307. Available: http://www.pubmedcentral.nih.gov/articlerender.fcgi?artid=2814540&tool=pmcentrez&rendertype=abstract. Accessed 9 August 2013.

71. He L, Hristova K (2012) Consequences of replacing EGFR juxtamembrane domain with an unstructured sequence. Sci Rep 2: 854. Available: http://www.pubmedcentral.nih.gov/articlerender.fcgi?artid=3497011&tool=pmcentrez&rendertype=abstract. Accessed 19 November 2012.

72. Ullrich A, Coussens L, Hayflick JS, Dull TJ, Gray A, et al. (n.d.) Human epidermal growth factor receptor cDNA sequence and aberrant expression of the amplified gene in A431 epidermoid carcinoma cells. Nature 309: 418–425. Available: http://www.ncbi.nlm.nih.gov/pubmed/6328312. Accessed 2 September 2013.

73. Stamos J, Sliwkowski MX, Eigenbrot C (2002) Structure of the epidermal growth factor receptor kinase domain alone and in complex with a 4-anilinoquinazoline inhibitor. J Biol Chem 277: 46265–46272. Available: http://www.ncbi.nlm.nih.gov/pubmed/12196540. Accessed 13 June 2013.

74. Jura N, Zhang X, Endres N, Seeliger M (2011) Catalytic control in the EGF receptor and its connection to general kinase regulatory mechanisms. Mol Cell 42: 9–22. Available: http://www.sciencedirect.com/science/article/pii/S1097276511001808. Accessed 11 January 2013.

75. Zhang X, Gureasko J, Shen K, Cole PA, Kuriyan J (2006) An allosteric mechanism for activation of the kinase domain of epidermal growth factor receptor. Cell 125: 1137–1149. Available: http://www.ncbi.nlm.nih.gov/pubmed/16777603. Accessed 7 August 2013.

76. Yang KS, Macdonald-Obermann JL, Piwnica-Worms D, Pike LJ (2010) Asp-960/Glu-961 controls the movement of the C-terminal tail of the epidermal growth factor receptor to regulate asymmetric dimer formation. J Biol Chem 285: 24014–24022. Available: http://www.pubmedcentral.nih.gov/articlerender.fcgi?artid=2911325&tool=pmcentrez&rendertype=abstract. Accessed 3 January 2012.

77. Roepstorff K, Grandal MV, Henriksen L, Knudsen SLJ, Lerdrup M, et al. (2009) Differential effects of EGFR ligands on endocytic sorting of the receptor. Traffic 10: 1115–1127. Available: http://www.pubmedcentral.nih.gov/articlerender.fcgi?artid=2723868&tool=pmcentrez&rendertype=abstract. Accessed 23 June 2011.

78. Hartman Z, Zhao H, Agazie YM (2012) HER2 stabilizes EGFR and itself by altering autophosphorylation patterns in a manner that overcomes regulatory mechanisms and promotes proliferative and transformation signaling. Oncogene: 1–12. Available: http://www.ncbi.nlm.nih.gov/pubmed/23027125. Accessed 13 November 2012.

79. Mi L-Z, Lu C, Li Z, Nishida N, Walz T, et al. (2011) Simultaneous visualization of the extracellular and cytoplasmic domains of the epidermal growth factor receptor. Nat

Struct Mol Biol 18: 984–989. Available: http://www.ncbi.nlm.nih.gov/pubmed/21822280. Accessed 13 November 2012.

80. Lu C, Mi L-Z, Schürpf T, Walz T, Springer T a (2012) Mechanisms for Kinase-mediated Dimerization of the Epidermal Growth Factor Receptor. J Biol Chem 287: 38244–38253. Available: http://www.ncbi.nlm.nih.gov/pubmed/22988250. Accessed 13 November 2012.

81. Blobel CP, Carpenter G, Freeman M (2009) The role of protease activity in ErbB biology. Exp Cell Res 315: 671–682. Available: http://www.pubmedcentral.nih.gov/articlerender.fcgi?artid=2646910&tool=pmcentrez&rendertype=abstract. Accessed 14 October 2011.

82. Dang M, Dubbin K, D'Aiello A, Hartmann M, Lodish H, et al. (2011) Epidermal growth factor (EGF) ligand release by substrate-specific a disintegrin and metalloproteases (ADAMs) involves different protein kinase C (PKC) isoenzymes depending on the stimulus. J Biol Chem 286: 17704–17713. Available: http://www.pubmedcentral.nih.gov/articlerender.fcgi?artid=3093846&tool=pmcentrez&rendertype=abstract. Accessed 10 August 2011.

83. Gijsen M, King P, Perera T, Parker PJ, Harris AL, et al. (2010) HER2 phosphorylation is maintained by a PKB negative feedback loop in response to anti-HER2 herceptin in breast cancer. PLoS Biol 8: e1000563. Available: http://www.pubmedcentral.nih.gov/articlerender.fcgi?artid=3006345&tool=pmcentrez&rendertype=abstract. Accessed 6 July 2011.

84. Kong A, Calleja V, Leboucher P, Harris A, Parker PJ, et al. (2008) HER2 oncogenic function escapes EGFR tyrosine kinase inhibitors via activation of alternative HER receptors in breast cancer cells. PLoS One 3: e2881. Available: http://www.pubmedcentral.nih.gov/articlerender.fcgi?artid=2483931&tool=pmcentrez&rendertype=abstract. Accessed 11 March 2013.

85. Hayes NVL, Gullick WJ (2008) The neuregulin family of genes and their multiple splice variants in breast cancer. J Mammary Gland Biol Neoplasia 13: 205–214. Available: http://www.ncbi.nlm.nih.gov/pubmed/18415007. Accessed 3 January 2012.

86. Tzahar E, Pinkas-Kramarski R, Moyer JD, Klapper LN, Alroy I, et al. (1997) Bivalence of EGF-like ligands drives the ErbB signaling network. EMBO J 16: 4938–4950. Available: http://www.pubmedcentral.nih.gov/articlerender.fcgi?artid=1170129&tool=pmcentrez&rendertype=abstract.

87. Jones J, Akita R, Sliwkowski M (1999) Binding specificities and affinities of egf domains for ErbB receptors. FEBS Lett 447: 227–231. Available: http://www.sciencedirect.com/science/article/pii/S0014579399002835. Accessed 2 September 2013.

88. Hobbs SS, Coffing SL, Le ATD, Cameron EM, Williams EE, et al. (2002) Neuregulin isoforms exhibit distinct patterns of ErbB family receptor activation. Oncogene 21: 8442–8452. Available: http://www.ncbi.nlm.nih.gov/pubmed/12466964. Accessed 3 January 2012.

89. Wilson KJ, Mill C, Lambert S, Buchman J, Wilson TR, et al. (2012) EGFR ligands exhibit functional differences in models of paracrine and autocrine signaling. Growth Factors 30: 107–116. Available: http://www.ncbi.nlm.nih.gov/pubmed/22260327. Accessed 21 August 2013.

90. Scheck RA, Lowder MA, Appelbaum JS, Schepartz A (2012) Bipartite tetracysteine display reveals allosteric control of ligand-specific EGFR activation. ACS Chem Biol 7: 1367–1376. Available: http://dx.doi.org/10.1021/cb300216f. Accessed 21 September 2013.

91. Macdonald JL, Pike LJ (2008) Heterogeneity in EGF-binding affinities arises from negative cooperativity in an aggregating system. Proc Natl Acad Sci U S A 105: 112–117. Available: http://www.pubmedcentral.nih.gov/articlerender.fcgi?artid=2224169&tool=pmcentrez&rendertype=abstract. Accessed 9 August 2013.

92. Liu P, Cleveland TE, Bouyain S, Byrne PO, Longo P a, et al. (2012) A single ligand is sufficient to activate EGFR dimers. Proc Natl Acad Sci U S A 109: 10861–10866. Available: http://www.ncbi.nlm.nih.gov/pubmed/22699492. Accessed 18 June 2012.

93. Teramura Y, Ichinose J, Takagi H, Nishida K, Yanagida T, et al. (2006) Single-molecule analysis of epidermal growth factor binding on the surface of living cells. EMBO J 25: 4215–4222. Available: http://www.pubmedcentral.nih.gov/articlerender.fcgi?artid=1570442&tool=pmcentrez&rendertype=abstract. Accessed 13 August 2011.

94. Martin-Fernandez M, Clarke DT, Tobin MJ, Jones S V, Jones GR (2002) Preformed oligomeric epidermal growth factor receptors undergo an ectodomain structure change during signaling. Biophys J 82: 2415–2427. Available: http://www.pubmedcentral.nih.gov/articlerender.fcgi?artid=1302032&tool=pmcentrez&rendertype=abstract. Accessed 16 August 2013.

95. Needham SR, Hirsch M, Rolfe DJ, Clarke DT, Zanetti-Domingues LC, et al. (2013) Measuring EGFR Separations on Cells with ∼10 nm Resolution via Fluorophore Localization Imaging with Photobleaching. PLoS One 8: e62331. Available: http://www.pubmedcentral.nih.gov/articlerender.fcgi?artid=3641073&tool=pmcentrez&rendertype=abstract. Accessed 11 June 2013.

96. Clayton AH a, Walker F, Orchard SG, Henderson C, Fuchs D, et al. (2005) Ligand-induced dimer-tetramer transition during the activation of the cell surface epidermal growth factor receptor-A multidimensional microscopy analysis. J Biol Chem 280: 30392–30399. Available: http://www.ncbi.nlm.nih.gov/pubmed/15994331. Accessed 4 August 2011.

97. Kozer N, Henderson C, Jackson JT, Nice EC, Burgess AW, et al. (2011) Evidence for extended YFP-EGFR dimers in the absence of ligand on the surface of living cells. Phys Biol 8: 066002. Available: http://www.ncbi.nlm.nih.gov/pubmed/21946082. Accessed 21 October 2011.

98. Clayton AH a, Tavarnesi ML, Johns TG (2007) Unligated epidermal growth factor receptor forms higher order oligomers within microclusters on A431 cells that are sensitive to tyrosine kinase inhibitor binding. Biochemistry 46: 4589–4597. Available: http://www.ncbi.nlm.nih.gov/pubmed/17381163.

99. Clayton AH a, Orchard SG, Nice EC, Posner RG, Burgess AW (2008) Predominance of activated EGFR higher-order oligomers on the cell surface. Growth Factors 26: 316–324. Available: http://www.ncbi.nlm.nih.gov/pubmed/18937111. Accessed 8 February 2012.

100. Szabó A, Horváth G, Szöllosi J, Nagy P (2008) Quantitative characterization of the large-scale association of ErbB1 and ErbB2 by flow cytometric homo-FRET measurements. Biophys J 95: 2086–2096. Available: http://www.pubmedcentral.nih.gov/articlerender.fcgi?artid=2483738&tool=pmcentrez&rendertype=abstract. Accessed 11 November 2011.

101. Yang S, Raymond-Stintz MA, Ying W, Zhang J, Lidke DS, et al. (2007) Mapping ErbB receptors on breast cancer cell membranes during signal transduction. J Cell Sci 120: 2763–2773. Available: http://www.ncbi.nlm.nih.gov/pubmed/17652160. Accessed 22 September 2011.

102. Tao R-H, Maruyama IN (2008) All EGF(ErbB) receptors have preformed homo- and heterodimeric structures in living cells. J Cell Sci 121: 3207–3217. Available: http://www.ncbi.nlm.nih.gov/pubmed/18782861. Accessed 7 July 2011.

103. Abulrob A, Lu Z, Baumann E, Vobornik D, Taylor R, et al. (2010) Nanoscale imaging of epidermal growth factor receptor clustering: effects of inhibitors. J Biol Chem 285: 3145–3156. Available: http://www.pubmedcentral.nih.gov/articlerender.fcgi?artid=2823441&tool=pmcentrez&rendertype=abstract. Accessed 5 September 2011.

104. Saffarian S, Li Y, Elson EL, Pike LJ (2007) Oligomerization of the EGF receptor investigated by live cell fluorescence intensity distribution analysis. Biophys J 93: 1021–1031. Available: http://www.pubmedcentral.nih.gov/articlerender.fcgi?artid=1913168&tool=pmcentrez&rendertype=abstract. Accessed 17 June 2011.

105. Kawashima N, Nakayama K, Itoh K, Itoh T, Ishikawa M, et al. (2010) Reversible dimerization of EGFR revealed by single-molecule fluorescence imaging using quantum dots. Chemistry 16: 1186–1192. Available: http://www.ncbi.nlm.nih.gov/pubmed/20024999. Accessed 15 August 2011.

106. Bader AN, Hofman EG, Voortman J, en Henegouwen PMPVB, Gerritsen HC (2009) Homo-FRET imaging enables quantification of protein cluster sizes with subcellular resolution. Biophys J 97: 2613–2622. Available: http://www.pubmedcentral.nih.gov/articlerender.fcgi?artid=2770629&tool=pmcentrez&rendertype=abstract. Accessed 31 August 2011.

107. Hofman EG, Bader AN, Voortman J, van den Heuvel DJ, Sigismund S, et al. (2010) Ligand-induced EGF receptor oligomerization is kinase-dependent and enhances internalization. J Biol Chem 285: 39481–39489. Available:

http://www.pubmedcentral.nih.gov/articlerender.fcgi?artid=2998144&tool=pmcentrez&rendertype=abstract. Accessed 5 September 2011.

108. Liu P, Sudhaharan T, Koh RML, Hwang LC, Ahmed S, et al. (2007) Investigation of the dimerization of proteins from the epidermal growth factor receptor family by single wavelength fluorescence cross-correlation spectroscopy. Biophys J 93: 684–698. Available: http://www.pubmedcentral.nih.gov/articlerender.fcgi?artid=1896234&tool=pmcentrez&rendertype=abstract. Accessed 12 July 2011.

109. Chung I, Akita R, Vandlen R, Toomre D, Schlessinger J, et al. (2010) Spatial control of EGF receptor activation by reversible dimerization on living cells. Nature 464: 783–787. Available: http://www.ncbi.nlm.nih.gov/pubmed/20208517. Accessed 15 June 2011.

110. Low-Nam ST, Lidke K a, Cutler PJ, Roovers RC, van Bergen en Henegouwen PMP, et al. (2011) ErbB1 dimerization is promoted by domain co-confinement and stabilized by ligand binding. Nat Struct Mol Biol 18: 1244–1249. Available: http://www.ncbi.nlm.nih.gov/pubmed/22020299. Accessed 25 October 2011.

111. Walker F, Rothacker J, Henderson C, Nice EC, Catimel B, et al. (2012) Ligand binding induces a conformational change in epidermal growth factor receptor dimers. Growth Factors: 1–16. Available: http://www.ncbi.nlm.nih.gov/pubmed/23163584. Accessed 26 November 2012.

112. Björkelund H, Gedda L, Andersson K (2011) Comparing the epidermal growth factor interaction with four different cell lines: intriguing effects imply strong dependency of cellular context. PLoS One 6: e16536. Available: http://www.pubmedcentral.nih.gov/articlerender.fcgi?artid=3031572&tool=pmcentrez&rendertype=abstract. Accessed 14 January 2012.

113. Den Hartigh JC, van Bergen en Henegouwen PM, Verkleij AJ, Boonstra J (1992) The EGF receptor is an actin-binding protein. J Cell Biol 119: 349–355. Available: http://www.pubmedcentral.nih.gov/articlerender.fcgi?artid=2289650&tool=pmcentrez&rendertype=abstract. Accessed 3 September 2013.

114. Chen P, Gupta K, Wells A (1994) Cell movement elicited by epidermal growth factor receptor requires kinase and autophosphorylation but is separable from mitogenesis. J Cell Biol 124: 547–555. Available: http://jcb.rupress.org/content/124/4/547.abstract. Accessed 29 July 2013.

115. Stoorvogel W, Kerstens S (2004) Sorting of ligand-activated epidermal growth factor receptor to lysosomes requires its actin-binding domain. J Biol … 279: 11562–11569. Available: http://www.jbc.org/content/279/12/11562.short. Accessed 23 August 2013.

116. Rijken PJ, Hage WJ, van Bergen en Henegouwen PM, Verkleij AJ, Boonstra J (1991) Epidermal growth factor induces rapid reorganization of the actin microfilament system in human A431 cells. J Cell Sci 100 (Pt 3: 491–499. Available: http://www.ncbi.nlm.nih.gov/pubmed/1808202. Accessed 3 September 2013.

117. Rijken PJ, Post SM, Hage WJ, van Bergen en Henegouwen PM, Verkleij AJ, et al. (1995) Actin polymerization localizes to the activated epidermal growth factor receptor in the plasma membrane, independent of the cytosolic free calcium transient. Exp Cell Res 218: 223–232. Available: http://www.ncbi.nlm.nih.gov/pubmed/7737361. Accessed 3 September 2013.

118. Rijken PJ, van Hal GJ, van der Heyden MA, Verkleij AJ, Boonstra J (1998) Actin polymerization is required for negative feedback regulation of epidermal growth factor-induced signal transduction. Exp Cell Res 243: 254–262. Available: http://www.ncbi.nlm.nih.gov/pubmed/9743585. Accessed 3 September 2013.

119. Cho H, Mason K, Ramyar KX, Stanley AM (2003) Structure of the extracellular region of HER2 alone and in complex with the Herceptin Fab. Nature 421. doi:10.1038/nature01423.Published.

120. Franklin MC, Carey KD, Vajdos FF, Leahy DJ, de Vos AM, et al. (2004) Insights into ErbB signaling from the structure of the ErbB2-pertuzumab complex. Cancer Cell 5: 317–328. Available: http://www.ncbi.nlm.nih.gov/pubmed/15093539.

121. Alvarado D, Klein DE, Lemmon M a (2009) ErbB2 resembles an autoinhibited invertebrate epidermal growth factor receptor. Nature 461: 287–291. Available: http://www.pubmedcentral.nih.gov/articlerender.fcgi?artid=2762480&tool=pmcentrez&rendertype=abstract. Accessed 7 July 2011.

122. Nagy P, Jenei a, Kirsch a K, Szöllosi J, Damjanovich S, et al. (1999) Activation-dependent clustering of the erbB2 receptor tyrosine kinase detected by scanning near-field optical microscopy. J Cell Sci 112 (Pt 1: 1733–1741. Available: http://www.ncbi.nlm.nih.gov/pubmed/10318765.

123. Szabó A, Szöllosi J, Nagy P (2010) Coclustering of ErbB1 and ErbB2 revealed by FRET-sensitized acceptor bleaching. Biophys J 99: 105–114. Available: http://www.pubmedcentral.nih.gov/articlerender.fcgi?artid=2895398&tool=pmcentrez&rendertype=abstract. Accessed 21 October 2011.

124. Nagy P, Claus J, Jovin TMT, Arndt-Jovin DJ (2010) Distribution of resting and ligand-bound ErbB1 and ErbB2 receptor tyrosine kinases in living cells using number and brightness analysis. Proc 107: 16524–16529. Available: http://www.pubmedcentral.nih.gov/articlerender.fcgi?artid=2944731&tool=pmcentrez&rendertype=abstract. Accessed 17 June 2011.

125. Kaufmann R, Müller P, Hildenbrand G, Hausmann M, Cremer C (2011) Analysis of Her2/neu membrane protein clusters in different types of breast cancer cells using localization microscopy. J Microsc 242: 46–54. Available: http://www.ncbi.nlm.nih.gov/pubmed/21118230. Accessed 2 September 2011.

126. Penuel E, Akita RW, Sliwkowski MX (2002) Identification of a region within the ErbB2/HER2 intracellular domain that is necessary for ligand-independent association. J Biol Chem 277: 28468–28473. Available: http://www.ncbi.nlm.nih.gov/pubmed/12000754. Accessed 3 January 2012.

127. Ramsauer VP, Carraway C a C, Salas PJI, Carraway KL (2003) Muc4/sialomucin complex, the intramembrane ErbB2 ligand, translocates ErbB2 to the apical surface in polarized epithelial cells. J Biol Chem 278: 30142–30147. Available: http://www.ncbi.nlm.nih.gov/pubmed/12748185. Accessed 15 December 2011.

128. Bafna S, Kaur S, Batra SK (2010) Membrane-bound mucins: the mechanistic basis for alterations in the growth and survival of cancer cells. Oncogene 29: 2893–2904. Available: http://www.pubmedcentral.nih.gov/articlerender.fcgi?artid=2879972&tool=pmcentrez&rendertype=abstract. Accessed 17 June 2011.

129. Graus-Porta D, Beerli RR, Daly JM, Hynes NE (1997) ErbB-2, the preferred heterodimerization partner of all ErbB receptors, is a mediator of lateral signaling. EMBO J 16: 1647–1655. Available: http://www.pubmedcentral.nih.gov/articlerender.fcgi?artid=1169769&tool=pmcentrez&rendertype=abstract.

130. Zhang Y, Opresko L, Shankaran H, Chrisler WB, Wiley HS, et al. (2009) HER/ErbB receptor interactions and signaling patterns in human mammary epithelial cells. BMC Cell Biol 10: 78. Available: http://www.pubmedcentral.nih.gov/articlerender.fcgi?artid=2776588&tool=pmcentrez&rendertype=abstract. Accessed 16 March 2013.

131. Gamett DC, Pearson G, Cerione R a, Friedberg I (1997) Secondary dimerization between members of the epidermal growth factor receptor family. J Biol Chem 272: 12052–12056. Available: http://www.ncbi.nlm.nih.gov/pubmed/9115272.

132. Huang G, Ouyang X, Epstein RJ (1998) Proxy activation of protein ErbB2 by heterologous ligands implies a heterotetrameric mode of receptor tyrosine kinase interaction. Biochem J 331: 113–119. Available: http://www.ncbi.nlm.nih.gov/pmc/articles/PMC1219327/. Accessed 7 February 2012.

133. Holbro T, Beerli RR, Maurer F, Koziczak M, Barbas CF, et al. (2003) The ErbB2/ErbB3 heterodimer functions as an oncogenic unit: ErbB2 requires ErbB3 to drive breast tumor cell proliferation. Proc Natl Acad Sci U S A 100: 8933–8938. Available: http://www.pubmedcentral.nih.gov/articlerender.fcgi?artid=166416&tool=pmcentrez&rendertype=abstract.

134. Offterdinger M, Bastiaens PI (2008) Prolonged EGFR signaling by ERBB2-mediated sequestration at the plasma membrane. Traffic 9: 147–155. Available: http://www.ncbi.nlm.nih.gov/pubmed/17956594. Accessed 1 September 2011.

135. Sorkin A, Goh L (2009) Endocytosis and intracellular trafficking of ErbBs. Exp Cell Res 314: 3093–3106. Available: http://www.sciencedirect.com/science/article/pii/S0014482708003030. Accessed 13 August 2013.

136. Shi F, Telesco SE, Liu Y, Radhakrishnan R, Lemmon M a (2010) ErbB3/HER3 intracellular domain is competent to bind ATP and catalyze autophosphorylation. Proc Natl Acad Sci U S A 107: 7692–7697. Available:

http://www.pubmedcentral.nih.gov/articlerender.fcgi?artid=2867849&tool=pmcentrez&rendertype=abstract. Accessed 7 July 2011.

137. Steinkamp MP, Low-Nam ST, Yang S, Lidke K a, Lidke DS, et al. (2013) ErbB3 is an active tyrosine kinase capable of homo- and hetero-interactions. Mol Cell Biol. Available: http://www.ncbi.nlm.nih.gov/pubmed/24379439. Accessed 4 January 2014.

138. Jura N, Shan Y, Cao X, Shaw DE, Kuriyan J (2009) Structural analysis of the catalytically inactive kinase domain of the human EGF receptor 3. Proc Natl Acad Sci U S A 106: 21608–21613. Available: http://www.pubmedcentral.nih.gov/articlerender.fcgi?artid=2791034&tool=pmcentrez&rendertype=abstract.

139. Luo C, Xu L, Zheng S, Luo X, Shen J, et al. (2005) Computational analysis of molecular basis of 1:1 interactions of NRG-1beta wild-type and variants with ErbB3 and ErbB4. Proteins 59: 742–756. Available: http://www.ncbi.nlm.nih.gov/pubmed/15822127. Accessed 3 January 2012.

140. Landgraf R, Eisenberg D (2000) Heregulin reverses the oligomerization of HER3. Biochemistry 39: 8503–8511. Available: http://www.ncbi.nlm.nih.gov/pubmed/10913256.

141. Berger MB, Mendrola JM, Lemmon M a (2004) ErbB3/HER3 does not homodimerize upon neuregulin binding at the cell surface. FEBS Lett 569: 332–336. Available: http://www.ncbi.nlm.nih.gov/pubmed/15225657. Accessed 17 June 2011.

142. Kani K, Warren CM, Kaddis CS, Loo J a, Landgraf R (2005) Oligomers of ERBB3 have two distinct interfaces that differ in their sensitivity to disruption by heregulin. J Biol Chem 280: 8238–8247. Available: http://www.ncbi.nlm.nih.gov/pubmed/15611073. Accessed 7 July 2011.

143. Macdonald-Obermann JL, Adak S, Landgraf R, Piwnica-Worms D, Pike LJ (2013) Dynamic Analysis of the EGF Receptor-ErbB2-ErbB3 Network by Luciferase Fragment Complementation Imaging. J Biol Chem. Available: http://www.ncbi.nlm.nih.gov/pubmed/24014028. Accessed 16 September 2013.

144. Park E, Baron R, Landgraf R (2008) Higher-order association states of cellular ERBB3 probed with photo-cross-linkable aptamers. Biochemistry 47: 11992–12005. Available: http://www.pubmedcentral.nih.gov/articlerender.fcgi?artid=2747663&tool=pmcentrez&rendertype=abstract.

145. Kani K, Park E, Landgraf R (2005) The extracellular domains of ErbB3 retain high ligand binding affinity at endosome pH and in the locked conformation. Biochemistry 44: 15842–15857. Available: http://www.ncbi.nlm.nih.gov/pubmed/16313187.

146. Hiroshima M, Saeki Y, Okada-Hatakeyama M, Sako Y (2012) Dynamically varying interactions between heregulin and ErbB proteins detected by single-molecule analysis in living cells. Proc Natl Acad Sci U S A 109. Available: http://www.ncbi.nlm.nih.gov/pubmed/22891299. Accessed 15 August 2012.

147. Muraoka-Cook RS, Feng S-M, Strunk KE, Earp HS (2008) ErbB4/HER4: role in mammary gland development, differentiation and growth inhibition. J Mammary Gland Biol Neoplasia 13: 235–246. Available: http://www.pubmedcentral.nih.gov/articlerender.fcgi?artid=3325098&tool=pmcentrez&rendertype=abstract. Accessed 23 August 2013.

148. Elenius K, Choi CJ, Paul S, Santiestevan E, Nishi E, et al. (1999) Characterization of a naturally occurring ErbB4 isoform that does not bind or activate phosphatidyl inositol 3-kinase. Oncogene 18: 2607–2615. Available: http://www.nature.com/onc/journal/v18/n16/full/1202612a.html. Accessed 16 August 2013.

149. Williams CC, Allison JG, Vidal GA, Burow ME, Beckman BS, et al. (2004) The ERBB4/HER4 receptor tyrosine kinase regulates gene expression by functioning as a STAT5A nuclear chaperone. J Cell Biol 167: 469–478. Available: http://www.pubmedcentral.nih.gov/articlerender.fcgi?artid=2172499&tool=pmcentrez&rendertype=abstract. Accessed 20 August 2013.

150. Jones RB, Gordus A, Krall J a, MacBeath G (2006) A quantitative protein interaction network for the ErbB receptors using protein microarrays. Nature 439: 168–174. Available: http://www.ncbi.nlm.nih.gov/pubmed/16273093. Accessed 16 July 2011.

151. Kolch W, Pitt A (2010) Functional proteomics to dissect tyrosine kinase signalling pathways in cancer. Nat Rev Cancer 10: 618–629. Available: http://www.ncbi.nlm.nih.gov/pubmed/20720570. Accessed 19 July 2011.

152. Baselga J, Swain SM (2009) Novel anticancer targets: revisiting ERBB2 and discovering ERBB3. Nat Rev Cancer 9: 463–475. Available: http://www.ncbi.nlm.nih.gov/pubmed/19536107. Accessed 7 August 2013.

153. Macdonald-Obermann JL, Piwnica-Worms D, Pike LJ (2011) Mechanics of EGF Receptor/ErbB2 kinase activation revealed by luciferase fragment complementation imaging. Proc Natl Acad Sci U S A. Available: http://www.ncbi.nlm.nih.gov/pubmed/22190492. Accessed 4 January 2012.

154. Li Y, Macdonald-Obermann J, Westfall C, Piwnica-Worms D, Pike LJ (2012) Quantitation of the effect of ErbB2 on EGF receptor binding and dimerization. J Biol Chem 4. Available: http://www.ncbi.nlm.nih.gov/pubmed/22822073. Accessed 31 July 2012.

155. Collier TS, Diraviyam K, Monsey J, Shen W, Sept D, et al. (2013) Carboxyl Group Footprinting Mass Spectrometry and Molecular Dynamics Identify Key Interactions in the HER2-HER3 Receptor Tyrosine Kinase Interface. J Biol Chem. Available: http://www.ncbi.nlm.nih.gov/pubmed/23843458. Accessed 23 July 2013.

156. Chen C-HB, Chernis G a, Hoang VQ, Landgraf R (2003) Inhibition of heregulin signaling by an aptamer that preferentially binds to the oligomeric form of human epidermal growth factor receptor-3. Proc Natl Acad Sci U S A 100: 9226–9231. Available: http://www.pubmedcentral.nih.gov/articlerender.fcgi?artid=170900&tool=pmcentrez&rendertype=abstract.

157. Zhang Q, Park E, Kani K, Landgraf R (2012) Functional isolation of activated and unilaterally phosphorylated heterodimers of ERBB2 and ERBB3 as scaffolds in ligand-dependent signaling. Proc Natl Acad Sci U S A: 2–7. Available: http://www.ncbi.nlm.nih.gov/pubmed/22733765. Accessed 14 July 2012.

158. Park JH, Liu Y, Lemmon MA, Radhakrishnan R (2012) Erlotinib binds both inactive and active conformations of the EGFR tyrosine kinase domain. Biochem J 448: 417–423. Available: http://www.pubmedcentral.nih.gov/articlerender.fcgi?artid=3507260&tool=pmcentrez&rendertype=abstract. Accessed 29 May 2013.

159. Gajiwala KS, Feng J, Ferre R, Ryan K, Brodsky O, et al. (2013) Insights into the aberrant activity of mutant EGFR kinase domain and drug recognition. Structure 21: 209–219. Available: http://www.ncbi.nlm.nih.gov/pubmed/23273428. Accessed 1 June 2013.

160. Wood ER, Truesdale AT, Mcdonald OB, Yuan D, Hassell A, et al. (2004) A unique structure for epidermal growth factor receptor bound to GW572016 (Lapatinib) relationships among protein conformation, inhibitor off-rate, and receptor activity. Cancer Res 64: 6652–6659. Available: http://cancerres.aacrjournals.org/content/64/18/6652.short. Accessed 3 July 2013.

161. Arteaga CL (1997) Unliganded Epidermal Growth Factor Receptor Dimerization Induced by Direct Interaction of Quinazolines with the ATP Binding Site. J Biol Chem 272: 23247–23254. Available: http://www.jbc.org/content/272/37/23247.full. Accessed 27 August 2013.

162. Bublil EM, Pines G, Patel G, Fruhwirth G, Ng T, et al. (2010) Kinase-mediated quasi-dimers of EGFR. FASEB J 24: 4744–4755. Available: http://www.pubmedcentral.nih.gov/articlerender.fcgi?artid=2992368&tool=pmcentrez&rendertype=abstract. Accessed 16 March 2012.

163. Gan HK, Walker F, Burgess AW, Rigopoulos A, Scott AM, et al. (2007) The epidermal growth factor receptor (EGFR) tyrosine kinase inhibitor AG1478 increases the formation of inactive untethered EGFR dimers. Implications for combination therapy with monoclonal antibody 806. J Biol Chem 282: 2840–2850. Available: http://www.ncbi.nlm.nih.gov/pubmed/17092939. Accessed 26 July 2011.

164. Yu C, Hale J, Ritchie K, Prasad NK, Irudayaraj J (2009) Receptor overexpression or inhibition alters cell surface dynamics of EGF-EGFR interaction: new insights from real-time single molecule analysis. Biochem Biophys Res Commun 378: 376–382. Available: http://www.ncbi.nlm.nih.gov/pubmed/19014905. Accessed 17 June 2011.

165. Sánchez-Martín M, Pandiella a (2011) Differential action of small molecule HER kinase inhibitors on receptor heterodimerization: Therapeutic implications. Int J Cancer: 1–26. Available: http://www.ncbi.nlm.nih.gov/pubmed/21826647.

166. Lichtner RB, Menrad A, Sommer A, Klar U, Schneider MR (2001) Signaling-inactive epidermal growth factor receptor/ligand complexes in intact carcinoma cells by quinazoline tyrosine kinase inhibitors. Cancer Res 61: 5790–5795. Available: http://www.ncbi.nlm.nih.gov/pubmed/11479217. Accessed 27 August 2013.

167. He P, Li G (2013) Significant increase in hEGF uptake is correlated with formation of EGFR dimers induced by the EGFR tyrosine kinase inhibitor gefitinib. Cancer Chemother Pharmacol 72: 341–348. Available: http://www.pubmedcentral.nih.gov/articlerender.fcgi?artid=3718999&tool=pmcentrez&rendertype=abstract. Accessed 27 August 2013.

168. Sundberg AL, Almqvist Y, Tolmachev V, Carlsson J (2003) Treatment of cultured glioma cells with the EGFR-TKI gefitinib ("Iressa", ZD1839) increases the uptake of astatinated EGF despite the absence of gefitinib-mediated growth inhibition. Eur J Nucl Med Mol Imaging 30: 727–729. Available: http://www.ncbi.nlm.nih.gov/pubmed/12740721. Accessed 3 September 2013.

169. Anido J, Matar P, Albanell J, Guzmán M, Rojo F, et al. (2003) ZD1839, a specific epidermal growth factor receptor (EGFR) tyrosine kinase inhibitor, induces the formation of inactive EGFR/HER2 and EGFR/HER3 heterodimers and prevents heregulin signaling in HER2-overexpressing breast cancer cells. Clin Cancer Res 9: 1274–1283. Available: http://www.ncbi.nlm.nih.gov/pubmed/12684395. Accessed 3 September 2013.

170. DeFazio-Eli L, Strommen K, Dao-Pick T, Parry G, Goodman L, et al. (2011) Quantitative assays for the measurement of HER1-HER2 heterodimerization and phosphorylation in cell lines and breast tumors: applications for diagnostics and targeted drug mechanism of action. Breast Cancer Res 13: R44. Available: http://www.pubmedcentral.nih.gov/articlerender.fcgi?artid=3219207&tool=pmcentrez&rendertype=abstract. Accessed 24 September 2013.

171. Nam H-J, Ching KA, Kan J, Kim H-P, Han S-W, et al. (2012) Evaluation of the antitumor effects and mechanisms of PF00299804, a pan-HER inhibitor, alone or in combination with chemotherapy or targeted agents in gastric cancer. Mol Cancer Ther 11: 439–451. Available: http://www.ncbi.nlm.nih.gov/pubmed/22135232. Accessed 22 March 2012.

172. Kleiman LB, Maiwald T, Conzelmann H, Lauffenburger DA, Sorger PK (2011) Rapid phospho-turnover by receptor tyrosine kinases impacts downstream signaling and drug binding. Mol Cell 43: 723–737. Available: http://www.ncbi.nlm.nih.gov/pubmed/21884975. Accessed 5 September 2011.

173. Schulze WX, Deng L, Mann M (2005) Phosphotyrosine interactome of the ErbB-receptor kinase family. Mol Syst Biol 1: 2005.0008. Available: http://www.pubmedcentral.nih.gov/articlerender.fcgi?artid=1681463&tool=pmcentrez&rendertype=abstract. Accessed 20 July 2011.

174. Prigent SA, Gullick WJ (1994) Identification of c-erbB-3 binding sites for phosphatidylinositol 3'-kinase and SHC using an EGF receptor/c-erbB-3 chimera. EMBO J 13: 2831–2841. Available: http://www.pubmedcentral.nih.gov/articlerender.fcgi?artid=395164&tool=pmcentrez&rendertype=abstract. Accessed 23 August 2013.

175. Hellyer NJ, Kim MS, Koland JG (2001) Heregulin-dependent activation of phosphoinositide 3-kinase and Akt via the ErbB2/ErbB3 co-receptor. J Biol Chem 276:

42153–42161. Available: http://www.ncbi.nlm.nih.gov/pubmed/11546794. Accessed 7 July 2011.

176. Suenaga A, Takada N, Hatakeyama M, Ichikawa M, Yu X, et al. (2005) Novel mechanism of interaction of p85 subunit of phosphatidylinositol 3-kinase and ErbB3 receptor-derived phosphotyrosyl peptides. J Biol Chem 280: 1321–1326. Available: http://www.ncbi.nlm.nih.gov/pubmed/15520002. Accessed 5 September 2011.

177. Fukazawa T, Miyake S, Band V, Band H (1996) Tyrosine phosphorylation of Cbl upon epidermal growth factor (EGF) stimulation and its association with EGF receptor and downstream signaling proteins. J Biol Chem 271: 14554–14559. Available: http://www.ncbi.nlm.nih.gov/pubmed/8662998. Accessed 26 August 2013.

178. Heukers R, Vermeulen JF, Fereidouni F, Bader AN, Voortman J, et al. (2013) EGFR endocytosis requires its kinase activity and N-terminal transmembrane dimerization motif. J Cell Sci: jcs.128611–. Available: http://jcs.biologists.org/content/early/2013/08/12/jcs.128611.abstract?maxtoshow=&hits=4&RESULTFORMAT=&title=EGFR&andorexacttitle=and&titleabstract=EGFR&andorexacttitleabs=and&fulltext=EGFR&andorexactfulltext=and&searchid=1&usestrictdates=yes&resourcetype=HWCIT&ct. Accessed 26 August 2013.

179. Biscardi JS, Maa MC, Tice DA, Cox ME, Leu TH, et al. (1999) c-Src-mediated phosphorylation of the epidermal growth factor receptor on Tyr845 and Tyr1101 is associated with modulation of receptor function. J Biol Chem 274: 8335–8343. Available: http://www.ncbi.nlm.nih.gov/pubmed/10075741. Accessed 26 August 2013.

180. Engelman J a, Zejnullahu K, Mitsudomi T, Song Y, Hyland C, et al. (2007) MET amplification leads to gefitinib resistance in lung cancer by activating ERBB3 signaling. Science 316: 1039–1043. Available: http://www.ncbi.nlm.nih.gov/pubmed/17463250. Accessed 6 July 2011.

181. Stabile LP, He G, Lui VWY, Henry C, Gubish CT, et al. (2013) c-Src Activation Mediates Erlotinib Resistance in Head and Neck Cancer by Stimulating c-Met. Clin Cancer Res 19: 380–392. Available: http://www.ncbi.nlm.nih.gov/pubmed/23213056. Accessed 14 February 2013.

182. Singleton K, Kim J, Hinz T (2013) A Receptor Tyrosine Kinase Network Comprised of FGFRs, EGFR, ERBB2 and MET Drives Growth and Survival of Head and Neck Squamous Carcinoma Cell Lines. Mol …. Available: http://molpharm.aspetjournals.org/content/early/2013/01/31/mol.112.084111.short. Accessed 23 April 2013.

183. Huang X, Gao L, Wang S, McManaman JL, Thor AD, et al. (2010) Heterotrimerization of the growth factor receptors erbB2, erbB3, and insulin-like growth factor-i receptor in breast cancer cells resistant to herceptin. Cancer Res 70: 1204–1214. Available: http://www.ncbi.nlm.nih.gov/pubmed/20103628. Accessed 24 August 2011.

184. Desbois-Mouthon C, Cacheux W, Blivet-Van Eggelpoël M-J, Barbu V, Fartoux L, et al. (2006) Impact of IGF-1R/EGFR cross-talks on hepatoma cell sensitivity to gefitinib. Int J

Cancer 119: 2557–2566. Available: http://www.ncbi.nlm.nih.gov/pubmed/16988945. Accessed 19 October 2011.

185. Desbois-Mouthon C, Baron A, Blivet-Van Eggelpoël M-J, Fartoux L, Venot C, et al. (2009) Insulin-like growth factor-1 receptor inhibition induces a resistance mechanism via the epidermal growth factor receptor/HER3/AKT signaling pathway: rational basis for cotargeting insulin-like growth factor-1 receptor and epidermal growth factor receptor. Clin Cancer Res 15: 5445–5456. Available: http://www.ncbi.nlm.nih.gov/pubmed/19706799. Accessed 25 October 2011.

186. Meyer AS, Miller MA, Gertler FB, Lauffenburger DA (2013) The Receptor AXL Diversifies EGFR Signaling and Limits the Response to EGFR-Targeted Inhibitors in Triple-Negative Breast Cancer Cells. Sci Signal 6: ra66–ra66. Available: http://stke.sciencemag.org/cgi/content/abstract/sigtrans;6/287/ra66. Accessed 7 August 2013.

187. Wang SE, Xiang B, Guix M, Olivares MG, Parker J, et al. (2008) Transforming growth factor beta engages TACE and ErbB3 to activate phosphatidylinositol-3 kinase/Akt in ErbB2-overexpressing breast cancer and desensitizes cells to trastuzumab. Mol Cell Biol 28: 5605–5620. Available: http://www.pubmedcentral.nih.gov/articlerender.fcgi?artid=2546920&tool=pmcentrez&rendertype=abstract. Accessed 8 August 2011.

188. Wang SE, Xiang B, Zent R, Quaranta V, Pozzi A, et al. (2009) Transforming growth factor beta induces clustering of HER2 and integrins by activating Src-focal adhesion kinase and receptor association to the cytoskeleton. Cancer Res 69: 475–482. Available: http://www.pubmedcentral.nih.gov/articlerender.fcgi?artid=2629389&tool=pmcentrez&rendertype=abstract. Accessed 10 August 2011.

189. Pályi-Krekk Z, Barok M, Kovács T, Saya H, Nagano O, et al. (2008) EGFR and ErbB2 are functionally coupled to CD44 and regulate shedding, internalization and motogenic effect of CD44. Cancer Lett 263: 231–242. Available: http://www.ncbi.nlm.nih.gov/pubmed/18276068. Accessed 23 June 2011.

190. Wang H, Leavitt L, Ramaswamy R, Rapraeger AC (2010) Interaction of syndecan and alpha6beta4 integrin cytoplasmic domains: regulation of ErbB2-mediated integrin activation. J Biol Chem 285: 13569–13579. Available: http://www.pubmedcentral.nih.gov/articlerender.fcgi?artid=2859518&tool=pmcentrez&rendertype=abstract. Accessed 22 July 2011.

191. Ieguchi K, Fujita M, Ma Z, Davari P, Taniguchi Y, et al. (2010) Direct binding of the EGF-like domain of neuregulin-1 to integrins ({alpha}v{beta}3 and {alpha}6{beta}4) is involved in neuregulin-1/ErbB signaling. J Biol Chem 285: 31388–31398. Available: http://www.ncbi.nlm.nih.gov/pubmed/20682778. Accessed 20 July 2011.

192. Huang C, Park CC, Hilsenbeck SG, Ward R, Rimawi M, et al. (2011) beta1 Integrin mediates an alternative survival pathway in breast cancer cells resistant to lapatinib. Breast Cancer Res 13: R84. Available: http://www.ncbi.nlm.nih.gov/pubmed/21884573. Accessed 3 October 2011.

193. Yu X, Miyamoto S, Mekada E (2000) Integrin alpha 2 beta 1-dependent EGF receptor activation at cell-cell contact sites. J Cell Sci 113 (Pt 1: 2139–2147. Available: http://www.ncbi.nlm.nih.gov/pubmed/10825287. Accessed 3 September 2013.

194. Soung YH, Clifford JL, Chung J (2010) Crosstalk between integrin and receptor tyrosine kinase signaling in breast carcinoma progression. BMB Rep 43: 311–318. Available: http://www.ncbi.nlm.nih.gov/pubmed/20510013.

195. De Luca A, Maiello MR, D'Alessio A, Pergameno M, Normanno N (2012) The RAS/RAF/MEK/ERK and the PI3K/AKT signalling pathways: role in cancer pathogenesis and implications for therapeutic approaches. Expert Opin Ther Targets 16 Suppl 2: S17–27. Available: http://www.ncbi.nlm.nih.gov/pubmed/22443084.

196. Nagashima T, Shimodaira H, Ide K, Nakakuki T, Tani Y, et al. (2007) Quantitative transcriptional control of ErbB receptor signaling undergoes graded to biphasic response for cell differentiation. J Biol Chem 282: 4045–4056. Available: http://www.jbc.org/content/282/6/4045.long. Accessed 26 August 2013.

197. Fry WHD, Simion C, Sweeney C, Carraway KL (2011) Quantity Control of the ErbB3 Receptor Tyrosine Kinase at the Endoplasmic Reticulum. Mol Cell Biol 31: 3009–3018. Available: http://www.ncbi.nlm.nih.gov/pubmed/21576364. Accessed 7 July 2011.

198. Amin DN, Sergina N, Lim L, Goga A, Moasser MM (2012) HER3 signalling is regulated through a multitude of redundant mechanisms in HER2-driven tumour cells. Biochem J 447: 417–425. Available: http://www.pubmedcentral.nih.gov/articlerender.fcgi?artid=3722874&tool=pmcentrez&rendertype=abstract. Accessed 11 August 2013.

199. Baselga J (2011) Targeting the phosphoinositide-3 (PI3) kinase pathway in breast cancer. Oncologist 16 Suppl 1: 12–19. Available: http://theoncologist.alphamedpress.org/content/16/suppl_1/12.full. Accessed 26 August 2013.

200. Sergina N V, Rausch M, Wang D, Blair J, Hann B, et al. (2007) Escape from HER-family tyrosine kinase inhibitor therapy by the kinase-inactive HER3. Nature 445: 437–441. Available: http://www.pubmedcentral.nih.gov/articlerender.fcgi?artid=3025857&tool=pmcentrez&rendertype=abstract. Accessed 6 August 2011.

201. Chakrabarty A, Sánchez V, Kuba MG, Rinehart C, Arteaga CL (2011) Feedback upregulation of HER3 (ErbB3) expression and activity attenuates antitumor effect of PI3K inhibitors. Proc Natl Acad Sci U S A 2011: 3–8. Available: http://www.ncbi.nlm.nih.gov/pubmed/21368164. Accessed 5 October 2011.

202. Garrett JT, Olivares MG, Rinehart C, Granja-Ingram ND, Sánchez V, et al. (2011) Transcriptional and posttranslational up-regulation of HER3 (ErbB3) compensates for inhibition of the HER2 tyrosine kinase. Proc Natl Acad Sci U S A 108: 5021–5026. Available: http://www.pubmedcentral.nih.gov/articlerender.fcgi?artid=3064360&tool=pmcentrez&rendertype=abstract. Accessed 14 June 2011.

203. Grøvdal LM, Kim J, Holst MR, Knudsen SLJ, Grandal MV, et al. (2011) EGF receptor inhibitors increase ErbB3 mRNA and protein levels in breast cancer cells. Cell Signal 24: 296–301. Available: http://linkinghub.elsevier.com/retrieve/pii/S0898656811002919. Accessed 28 September 2011.

204. Chakrabarty a, Rexer BN, Wang SE, Cook RS, Engelman J a, et al. (2010) H1047R phosphatidylinositol 3-kinase mutant enhances HER2-mediated transformation by heregulin production and activation of HER3. Oncogene 29: 5193–5203. Available: http://www.pubmedcentral.nih.gov/articlerender.fcgi?artid=2945381&tool=pmcentrez&rendertype=abstract. Accessed 16 September 2011.

205. Wang S, Huang X, Lee C-K, Liu B (2010) Elevated expression of erbB3 confers paclitaxel resistance in erbB2-overexpressing breast cancer cells via upregulation of Survivin. Oncogene 29: 4225–4236. Available: http://www.ncbi.nlm.nih.gov/pubmed/20498641. Accessed 13 July 2011.

206. Misale S, Yaeger R, Hobor S, Scala E, Janakiraman M, et al. (2012) Emergence of KRAS mutations and acquired resistance to anti-EGFR therapy in colorectal cancer. Nature. Available: http://www.nature.com/doifinder/10.1038/nature11156. Accessed 13 June 2012.

207. Xu AM, Huang PH (2010) Receptor tyrosine kinase coactivation networks in cancer. Cancer Res 70: 3857–3860. Available: http://www.pubmedcentral.nih.gov/articlerender.fcgi?artid=2875162&tool=pmcentrez&rendertype=abstract. Accessed 14 February 2013.

208. Henjes F, Bender C, von der Heyde S, Braun L, Mannsperger H a, et al. (2012) Strong EGFR signaling in cell line models of ERBB2-amplified breast cancer attenuates response towards ERBB2-targeting drugs. Oncogenesis 1: e16. Available: http://www.pubmedcentral.nih.gov/articlerender.fcgi?artid=3412653&tool=pmcentrez&rendertype=abstract. Accessed 22 August 2013.

209. Choi B-K, Fan X, Deng H, Zhang N, An Z (2012) ERBB3 (HER3) is a key sensor in the regulation of ERBB-mediated signaling in both low and high ERBB2 (HER2) expressing cancer cells. Cancer Med 1: 28–38. Available: http://www.pubmedcentral.nih.gov/articlerender.fcgi?artid=3544427&tool=pmcentrez&rendertype=abstract. Accessed 18 March 2013.

210. Jain A, Penuel E, Mink S, Schmidt J (2010) HER kinase axis receptor dimer partner switching occurs in response to EGFR tyrosine kinase inhibition despite failure to block cellular proliferation. Cancer Res 70: 1989–1999. Available: http://cancerres.aacrjournals.org/content/70/5/1989.short. Accessed 23 April 2013.

211. Wilson TR, Lee DY, Berry L, Shames DS, Settleman J (2011) Neuregulin-1-Mediated Autocrine Signaling Underlies Sensitivity to HER2 Kinase Inhibitors in a Subset of Human Cancers. Cancer Cell 20: 158–172. Available: http://www.ncbi.nlm.nih.gov/pubmed/21840482. Accessed 16 August 2011.

212. Lakowicz JR (2006) Principles of Fluorescence Spectroscopy. Springer. Available: http://www.amazon.co.uk/Principles-of-Fluorescence-Spectroscopy-ebook/dp/B003XQF3G4. Accessed 3 September 2013.

213. Moerner WE, Fromm DP (2003) Methods of single-molecule fluorescence spectroscopy and microscopy. Rev Sci Instrum 74: 3597. Available: file:///C:/Users/nyf73524/Documents/Fluorescence microscopy bibliography/http___scitation.aip.org_getpdf_servlet_GetPDFServlet_filetype=pdf&amp. Accessed 3 August 2011.

214. Lichtman JW, Conchello J (2005) Fluorescence microscopy. Nat Methods 2. doi:10.1038/NMETH817.

215. Resch-genger U, Grabolle M, Cavaliere-jaricot S, Nitschke R, Nann T (2008) Quantum dots versus organic dyes as fluorescent labels. 5: 763–775. doi:10.1038/NMEtH.1248.

216. ATTO-TEC GmbH (2011) ATTO-TEC Fluorescent Labels and Dyes.

217. Valeur B, Berberan-Santos MN (2013) Molecular Fluorescence: Principles and Applications. Wiley-VCH. Available: http://www.amazon.com/Molecular-Fluorescence-Applications-Bernard-Valeur/dp/3527328467. Accessed 3 September 2013.

218. Petty HR (2007) Fluorescence Microscopy : Established and Emerging Methods , Experimental Strategies , and Applications in Immunology. Microsc Res Tech 709: 687–709. doi:10.1002/jemt.

219. Joo C, Balci H, Ishitsuka Y, Buranachai C, Ha T (2008) Advances in single-molecule fluorescence methods for molecular biology. Annu Rev Biochem 77: 51–76. Available: http://www.ncbi.nlm.nih.gov/pubmed/18412538. Accessed 20 July 2011.

220. Sheppard CJ, Wilson T (1978) Depth of field in the scanning microscope. Opt Lett 3: 115. Available: http://www.ncbi.nlm.nih.gov/pubmed/19684715. Accessed 3 September 2013.

221. Hell SW, Wichmann J (1994) Breaking the diffraction resolution limit by stimulated emission: stimulated-emission-depletion fluorescence microscopy. Opt Lett 19: 780–782. Available: http://www.ncbi.nlm.nih.gov/pubmed/19844443. Accessed 8 August 2013.

222. Axelrod D (1981) Cell-substrate contacts illuminated by total internal reflection fluorescence. J Cell Biol 89: 141–145. Available: http://www.pubmedcentral.nih.gov/articlerender.fcgi?artid=2111781&tool=pmcentrez&rendertype=abstract.

223. Axelrod D (2003) Total internal reflection fluorescence microscopy in cell biology. Methods Enzymol 361: 1–33. Available: http://www.ncbi.nlm.nih.gov/pubmed/12624904.

224. Mattheyses AL, Simon SM, Rappoport JZ (2010) Imaging with total internal reflection fluorescence microscopy for the cell biologist. J Cell Sci 123: 3621–3628. Available:

http://www.pubmedcentral.nih.gov/articlerender.fcgi?artid=2964103&tool=pmcentrez&rendertype=abstract. Accessed 27 June 2011.

225. Clarke DT, Botchway SW, Coles BC, Needham SR, Roberts SK, et al. (2011) Optics clustered to output unique solutions: a multi-laser facility for combined single molecule and ensemble microscopy. Rev Sci Instrum 82: 093705. Available: http://www.ncbi.nlm.nih.gov/pubmed/21974592. Accessed 10 November 2011.

226. Rolfe DJ, McLachlan CI, Hirsch M, Needham SR, Tynan CJ, et al. (2011) Automated multidimensional single molecule fluorescence microscopy feature detection and tracking. Eur Biophys J 40: 1167–1186. Available: http://www.ncbi.nlm.nih.gov/pubmed/21928120. Accessed 3 September 2013.

227. Gordon MP, Ha T, Selvin PR (2004) Single-molecule high-resolution imaging with photobleaching. Proc Natl Acad Sci U S A 101: 6462–6465. Available: http://www.pubmedcentral.nih.gov/articlerender.fcgi?artid=404067&tool=pmcentrez&rendertype=abstract. Accessed 25 September 2013.

228. Alcor D, Gouzer G, Triller A (2009) Single-particle tracking methods for the study of membrane receptors dynamics. Eur J Neurosci 30: 987–997. Available: http://www.ncbi.nlm.nih.gov/pubmed/19735284. Accessed 19 July 2011.

229. Kapanidis AN, Strick T (2009) Biology, one molecule at a time. Trends Biochem Sci 34: 234–243. Available: http://www.ncbi.nlm.nih.gov/pubmed/19362843. Accessed 13 March 2012.

230. Zlatanova J, van Holde K (2006) Single-molecule biology: what is it and how does it work? Mol Cell 24: 317–329. Available: http://www.ncbi.nlm.nih.gov/pubmed/17081984. Accessed 10 December 2012.

231. Yano Y, Matsuzaki K (2009) Tag-probe labeling methods for live-cell imaging of membrane proteins. Biochim Biophys Acta 1788: 2124–2131. Available: http://www.ncbi.nlm.nih.gov/pubmed/19646952. Accessed 18 August 2011.

232. Shaner NC, Steinbach PA, Tsien RY (2005) A guide to choosing fluorescent proteins. Nat Methods 2: 905–909. Available: http://www.nature.com/nmeth/journal/v2/n12/abs/nmeth819.html. Accessed 5 January 2012.

233. Dillingham MS, Wallace MI (2008) Protein modification for single molecule fluorescence microscopy. Org Biomol Chem 6: 3031–3037. Available: http://www.ncbi.nlm.nih.gov/pubmed/18698457. Accessed 3 June 2013.

234. Zimmer M (2002) Green fluorescent protein (GFP): applications, structure, and related photophysical behavior. Chem Rev 102: 759–781. Available: http://www.ncbi.nlm.nih.gov/pubmed/11890756.

235. Marks KM, Nolan GP (2006) Chemical labeling strategies for cell biology. 3: 591–596. doi:10.1038/NMETH906.

236. George N, Pick H, Vogel H, Johnsson N, Johnsson K (2004) Specific labeling of cell surface proteins with chemically diverse compounds. J Am Chem Soc 126: 8896–8897. Available: http://www.ncbi.nlm.nih.gov/pubmed/15264811.

237. Beckett D, Kovaleva E, Schatz PJ (1999) A minimal peptide substrate in biotin holoenzyme synthetase-catalyzed biotinylation. Protein Sci 8: 921–929. Available: http://www.pubmedcentral.nih.gov/articlerender.fcgi?artid=2144313&tool=pmcentrez&rendertype=abstract.

238. Keppler A, Kindermann M, Gendreizig S, Pick H, Vogel H, et al. (2004) Labeling of fusion proteins of O6-alkylguanine-DNA alkyltransferase with small molecules in vivo and in vitro. Methods 32: 437–444. Available: http://dx.doi.org/10.1016/j.ymeth.2003.10.007. Accessed 25 June 2013.

239. Los G V., Encell LP, McDougall MG, Hartzell DD, Karassina N, et al. (2008) HaloTag: A Novel Protein Labeling Technology for Cell Imaging and Protein Analysis. ACS Chem Biol 3: 373–382. Available: http://pubs.acs.org/doi/abs/10.1021/cb800025k. Accessed 12 June 2013.

240. Griffin B a. (1998) Specific Covalent Labeling of Recombinant Protein Molecules Inside Live Cells. Science (80-) 281: 269–272. Available: http://www.sciencemag.org/cgi/doi/10.1126/science.281.5374.269. Accessed 28 May 2013.

241. Martin BR, Giepmans BNG, Adams SR, Tsien RY (2005) Mammalian cell-based optimization of the biarsenical-binding tetracysteine motif for improved fluorescence and affinity. Nat Biotechnol 23: 1308–1314. Available: http://www.ncbi.nlm.nih.gov/pubmed/16155565. Accessed 29 May 2013.

242. Soh N (2008) Selective chemical labeling of proteins with small fluorescent molecules based on metal-chelation methodology. Sensors 8: 1004–1024. Available: http://www.mdpi.com/1424-8220/8/2/1004/pdf. Accessed 29 July 2013.

243. Scheck R, Lowder M, Appelbaum J, Schepartz A (2012) Bipartite tetracysteine display reveals allosteric control of ligand-specific EGFR activation. ACS Chem Biol. Available: http://pubs.acs.org/doi/abs/10.1021/cb300216f. Accessed 27 September 2013.

244. Kapanidis AN, Ebright YW, Ebright RH (2001) Site-specific incorporation of fluorescent probes into protein: hexahistidine-tag-mediated fluorescent labeling with (Ni(2+):nitrilotriacetic Acid (n)-fluorochrome conjugates. J Am Chem Soc 123: 12123–12125. Available: http://www.ncbi.nlm.nih.gov/pubmed/11724636. Accessed 29 July 2013.

245. Amano H, Ohuchi Y, Katayama Y, Maeda M (2001) A new fluorescent reagent for the detection of proteins having histidine-tag (his-tag). Anal Sci 17: 1469–1471. Available: http://www.jsac.or.jp/analsci/fulltext.php/17/ICAS2001/i1469/. Accessed 29 July 2013.

246. Guignet EG, Hovius R, Vogel H (2004) Reversible site-selective labeling of membrane proteins in live cells. Nat Biotechnol 22: 440–444. Available: http://dx.doi.org/10.1038/nbt954. Accessed 9 June 2013.

247. Bäumle M, Guignet E, Hovius R, Meier R, Nording P, et al. (n.d.) Nitrilotriacetate-Atto Dye Conjugates For The Fluorescence Detection Of Oligo-Histidine Tagged Proteins Characterization of the Chromophore-NTA conjugate: 5–6.

248. Hauser CTC, Tsien RY (2007) A hexahistidine-Zn2+-dye label reveals STIM1 surface exposure. Proc Natl 104: 3693–3697. Available: http://www.pnas.org/content/104/10/3693.full. Accessed 3 January 2012.

249. Cong Y, Pawlisz E, Bryant P, Balan S, Laurine E, et al. (2012) Site-specific PEGylation at histidine tags. Bioconjug Chem 23: 248–263. Available: http://www.ncbi.nlm.nih.gov/pubmed/22243664.

250. Guignet EG, Segura J-M, Hovius R, Vogel H (2007) Repetitive reversible labeling of proteins at polyhistidine sequences for single-molecule imaging in live cells. Chemphyschem 8: 1221–1227. Available: http://www.ncbi.nlm.nih.gov/pubmed/17436349. Accessed 7 July 2013.

251. Sicard R, Dhuguru J, Liu W, Patel N, Landgraf R, et al. (2012) A fluorescent reporter of ATP binding-competent receptor kinases. Bioorg Med Chem Lett 22: 5532–5535. Available: http://www.ncbi.nlm.nih.gov/pubmed/22868229. Accessed 17 September 2012.

252. Bennett V, Simmons M (2001) Analysis of fluorescently labeled substance P analogs: binding, imaging and receptor activation. BMC Chem Biol. Available: http://www.biomedcentral.com/1472-6769/1/1. Accessed 29 July 2013.

253. Stamos J, Lazarus R a, Yao X, Kirchhofer D, Wiesmann C (2004) Crystal structure of the HGF beta-chain in complex with the Sema domain of the Met receptor. EMBO J 23: 2325–2335. Available: http://www.pubmedcentral.nih.gov/articlerender.fcgi?artid=423285&tool=pmcentrez&rendertype=abstract. Accessed 29 July 2011.

254. Skerra A (2007) Alternative non-antibody scaffolds for molecular recognition. Curr Opin Biotechnol 18: 295–304. Available: http://www.ncbi.nlm.nih.gov/pubmed/17643280. Accessed 11 June 2013.

255. Skerra a (2003) Imitating the humoral immune response. Curr Opin Chem Biol 7: 683–693. Available: http://linkinghub.elsevier.com/retrieve/pii/S1367593103001479. Accessed 29 July 2013.

256. Binz HK, Amstutz P, Plückthun A (2005) Engineering novel binding proteins from nonimmunoglobulin domains. Nat Biotechnol 23: 1257–1268. Available: http://www.nature.com/nbt/journal/v23/n10/abs/nbt1127.html. Accessed 23 May 2013.

257. Tetin SY, Stroupe SD (2004) Antibodies in diagnostic applications. Curr Pharm Biotechnol 5: 9–16. Available: http://www.ncbi.nlm.nih.gov/pubmed/14965206.

258. Holliger P, Hudson PJ (2005) Engineered antibody fragments and the rise of single domains. Nat Biotechnol 23: 1126–1136. Available: http://www.ncbi.nlm.nih.gov/pubmed/16151406. Accessed 23 May 2013.

259. Lee S-C, Park K, Han J, Lee J -j., Kim HJ, et al. (2012) Design of a binding scaffold based on variable lymphocyte receptors of jawless vertebrates by module engineering. Proc Natl Acad Sci 109. Available: http://www.pnas.org/cgi/doi/10.1073/pnas.1113193109. Accessed 12 February 2012.

260. Nilsson FY, Tolmachev V (2007) Affibody molecules: new protein domains for molecular imaging and targeted tumor therapy. Curr Opin Drug Discov Devel 10: 167–175. Available: http://www.ncbi.nlm.nih.gov/pubmed/17436552. Accessed 4 September 2013.

261. De Graaf AJ, Kooijman M, Hennink WE, Mastrobattista E (2009) Nonnatural amino acids for site-specific protein conjugation. Bioconjug Chem 20: 1281–1295. Available: http://dx.doi.org/10.1021/bc800294a. Accessed 4 September 2013.

262. Young TS, Schultz PG (2010) Beyond the canonical 20 amino acids: expanding the genetic lexicon. J Biol Chem 285: 11039–11044. Available: http://www.pubmedcentral.nih.gov/articlerender.fcgi?artid=2856976&tool=pmcentrez&rendertype=abstract. Accessed 9 August 2013.

263. Green M (2004) Semiconductor quantum dots as biological imaging agents. Angew Chem Int Ed Engl 43: 4129–4131. Available: http://www.ncbi.nlm.nih.gov/pubmed/15307073. Accessed 24 May 2013.

264. Lidke DS, Arndt-Jovin DJ (2004) Imaging takes a quantum leap. Physiology (Bethesda) 19: 322–325. Available: http://www.ncbi.nlm.nih.gov/pubmed/15546848. Accessed 10 July 2013.

265. Jaiswal JK, Simon SM (2004) Potentials and pitfalls of fluorescent quantum dots for biological imaging. Trends Cell Biol 14: 497–504. Available: http://www.ncbi.nlm.nih.gov/pubmed/15350978. Accessed 22 May 2013.

266. Invitrogen (2013) Molecular Probes Handbook. Available: http://www.lifetechnologies.com/us/en/home/references/molecular-probes-the-handbook/ultrasensitive-detection-technology/qdot-nanocrystal-technology.html. Accessed 4 September 2013.

267. Lauffenburger DA, Linderman JJ (1993) Receptors: Models for Binding, Trafficking, and Signaling. New York N.Y.: Oxford University Press. Available: http://www.amazon.com/Receptors-Models-Binding-Trafficking-Signaling/dp/0195106636. Accessed 6 June 2014.

268. Kronqvist N, Malm M, Göstring L, Gunneriusson E, Nilsson M, et al. (2011) Combining phage and staphylococcal surface display for generation of ErbB3-specific Affibody molecules. Protein Eng Des Sel 24: 385–396. Available: http://www.ncbi.nlm.nih.gov/pubmed/21177282. Accessed 17 June 2011.

269. Berrow NS, Alderton D, Sainsbury S, Nettleship J, Assenberg R, et al. (2007) A versatile ligation-independent cloning method suitable for high-throughput expression screening applications. Nucleic Acids Res 35: e45. Available: http://www.pubmedcentral.nih.gov/articlerender.fcgi?artid=1874605&tool=pmcentrez&rendertype=abstract. Accessed 15 August 2013.

270. Schneider CA, Rasband WS, Eliceiri KW (2012) NIH Image to ImageJ: 25 years of image analysis. Nat Methods 9: 671–675. Available: http://dx.doi.org/10.1038/nmeth.2089. Accessed 13 July 2012.

271. Taite LJ, Yang P, Jun H-W, West JL (2008) Nitric oxide-releasing polyurethane-PEG copolymer containing the YIGSR peptide promotes endothelialization with decreased platelet adhesion. J Biomed Mater Res B Appl Biomater 84: 108–116. Available: http://www.ncbi.nlm.nih.gov/pubmed/17497680. Accessed 18 January 2012.

272. Eid K, Chen E, Griffith L, Glowacki J (2001) Effect of RGD coating on osteocompatibility of PLGA-polymer disks in a rat tibial wound. J Biomed Mater Res 57: 224–231. Available: http://www.ncbi.nlm.nih.gov/pubmed/11484185. Accessed 18 January 2012.

273. Tashiro K, Sephel GC, Weeks B, Sasaki M, Martin GR, et al. (1989) A synthetic peptide containing the IKVAV sequence from the A chain of laminin mediates cell attachment, migration, and neurite outgrowth. J Biol Chem 264: 16174–16182. Available: http://www.ncbi.nlm.nih.gov/pubmed/2777785.

274. Tessler LA, Donahoe CD, Garcia DJ, Jun Y-SS, Elbert DL, et al. (2011) Nanogel surface coatings for improved single-molecule imaging substrates. J R Soc Interface 8: 1400–1408. Available: http://www.pubmedcentral.nih.gov/articlerender.fcgi?artid=3163416&tool=pmcentrez&rendertype=abstract. Accessed 1 March 2012.

275. Rusnak DW, Lackey K, Affleck K, Wood ER, Alligood KJ, et al. (2001) The effects of the novel, reversible epidermal growth factor receptor/ErbB-2 tyrosine kinase inhibitor, GW2016, on the growth of human normal and tumor-derived cell lines in vitro and in vivo. Mol Cancer Ther 1: 85–94. Available: http://www.ncbi.nlm.nih.gov/pubmed/12467226.

276. Rusnak DW, Alligood KJ, Mullin RJ, Spehar GM, Arenas-Elliott C, et al. (2007) Assessment of epidermal growth factor receptor (EGFR, ErbB1) and HER2 (ErbB2) protein expression levels and response to lapatinib (Tykerb, GW572016) in an expanded panel of human normal and tumour cell lines. Cell Prolif 40: 580–594. Available: http://www.ncbi.nlm.nih.gov/pubmed/17635524.

277. Gilmer TM, Cable L, Alligood K, Rusnak D, Spehar G, et al. (2008) Impact of common epidermal growth factor receptor and HER2 variants on receptor activity and inhibition by lapatinib. Cancer Res 68: 571–579. Available: http://www.ncbi.nlm.nih.gov/pubmed/18199554. Accessed 15 November 2012.

278. Boggara M, Athmakuri K, Srivastava S, Cole R, Kane RS (2012) Characterization of the diffusion of epidermal growth factor receptor clusters by single particle tracking.

Biochim Biophys Acta. Available: http://www.ncbi.nlm.nih.gov/pubmed/22974816. Accessed 25 September 2012.

279. Sergé A, Bertaux N, Rigneault H, Marguet D (2008) Dynamic multiple-target tracing to probe spatiotemporal cartography of cell membranes. Nat Methods 5: 687–694. Available: http://www.ncbi.nlm.nih.gov/pubmed/18604216. Accessed 3 September 2013.

280. Ma Y, Yu Q, Cohen I (2006) Multiple Hypothesis Target Tracking Using Merge and Split of Graph's Nodes. In: Bebis G, Boyle R, Parvin B, Koracin D, Remagnino P, et al., editors. Advances in Visual Computing Pt 1 - Lecture Notes in Computer Sciences Vol 4291. Lecture Notes in Computer Science. Berlin, Heidelberg: Springer Berlin Heidelberg, Vol. 4291. pp. 783–792. Available: http://www.springerlink.com/index/10.1007/11919476. Accessed 7 October 2013.

281. Yoon JW, Bruckbauer A, Fitzgerald WJ, Klenerman D (2008) Bayesian inference for improved single molecule fluorescence tracking. Biophys J 94: 4932–4947. Available: http://www.pubmedcentral.nih.gov/articlerender.fcgi?artid=2397372&tool=pmcentrez&rendertype=abstract. Accessed 1 October 2013.

282. Geman S, Geman D (1984) Stochastic relaxation, gibbs distributions, and the bayesian restoration of images. IEEE Trans Pattern Anal Mach Intell 6: 721–741. Available: http://www.ncbi.nlm.nih.gov/pubmed/22499653. Accessed 7 October 2013.

283. Metropolis N, Rosenbluth AW, Rosenbluth MN, Teller AH, Teller E (1953) Equation of State Calculations by Fast Computing Machines. J Chem Phys 21: 1087. Available: http://link.aip.org/link/?JCPSA6/21/1087/1. Accessed 18 September 2013.

284. RAUCH HE, STRIEBEL CT, TUNG F (1965) Maximum likelihood estimates of linear dynamic systems. AIAA J 3: 1445–1450. Available: http://dx.doi.org/10.2514/3.3166.

285. Savage CR, Inagami T, Cohen S (1972) The primary structure of epidermal growth factor. J Biol Chem 247: 7612–7621. Available: http://www.ncbi.nlm.nih.gov/pubmed/4636327. Accessed 27 August 2013.

286. Jay SM, Kurtagic E, Alvarez LM, de Picciotto S, Sanchez E, et al. (2011) Engineered bivalent ligands to bias ErbB receptor-mediated signaling and phenotypes. J Biol Chem: 1–20. Available: http://www.ncbi.nlm.nih.gov/pubmed/21622572. Accessed 21 July 2011.

287. Friedman M, Nordberg E, Höidén-Guthenberg I, Brismar H, Adams GP, et al. (2007) Phage display selection of Affibody molecules with specific binding to the extracellular domain of the epidermal growth factor receptor. Protein Eng Des Sel 20: 189–199. Available: http://www.ncbi.nlm.nih.gov/pubmed/17452435. Accessed 28 July 2011.

288. Wikman M, Steffen A-C, Gunneriusson E, Tolmachev V, Adams GP, et al. (2004) Selection and characterization of HER2/neu-binding affibody ligands. Protein Eng Des Sel 17: 455–462. Available: http://www.ncbi.nlm.nih.gov/pubmed/15208403. Accessed 21 April 2012.

289. Orlova A, Magnusson M, Eriksson TLJ, Nilsson M, Larsson B, et al. (2006) Tumor imaging using a picomolar affinity HER2 binding affibody molecule. Cancer Res 66: 4339–4348. Available: http://www.ncbi.nlm.nih.gov/pubmed/16618759. Accessed 29 August 2011.

290. Wållberg H, Löfdahl P-K, Tschapalda K, Uhlén M, Tolmachev V, et al. (2011) Affinity recovery of eight HER2-binding affibody variants using an anti-idiotypic affibody molecule as capture ligand. Protein Expr Purif 76: 127–135. Available: http://www.ncbi.nlm.nih.gov/pubmed/21029777. Accessed 19 September 2011.

291. Nordberg E, Friedman M, Göstring L, Adams GP, Brismar H, et al. (2007) Cellular studies of binding, internalization and retention of a radiolabeled EGFR-binding affibody molecule. Nucl Med Biol 34: 609–618. Available: http://www.ncbi.nlm.nih.gov/pubmed/17707800. Accessed 19 July 2011.

292. Nordberg E, Ekerljung L, Sahlberg SH, Carlsson J, Lennartsson J, et al. (2010) Effects of an EGFR-binding affibody molecule on intracellular signaling pathways. Int J Oncol 36: 967–972. Available: http://www.spandidos-publications.com/ijo/36/4/967. Accessed 27 August 2013.

293. Larkin MA, Blackshields G, Brown NP, Chenna R, McGettigan PA, et al. (2007) Clustal W and Clustal X version 2.0. Bioinformatics 23: 2947–2948. Available: http://www.ncbi.nlm.nih.gov/pubmed/17846036. Accessed 7 August 2013.

294. Göstring L, Malm M, Höidén-Guthenberg I, Frejd FY, Ståhl S, et al. (2012) Cellular effects of HER3-specific affibody molecules. PLoS One 7: e40023. Available: http://dx.plos.org/10.1371/journal.pone.0040023. Accessed 27 August 2013.

295. Eigenbrot C, Ultsch M (2010) Structural basis for high-affinity HER2 receptor binding by an engineered protein. Proc … 107: 15039–15044. Available: http://www.pnas.org/content/107/34/15039.short. Accessed 27 August 2013.

296. Grabski A, Mehler M, Drott D (2005) The Overnight Express Autoinduction System: High-density cell growth and protein expression while you sleep. Nat Methods 2: 233–235. Available: http://www.nature.com/app_notes/nmeth/2005/051122/full/nmeth0305-233.html. Accessed 20 March 2014.

297. Jones JT, Ballinger MD, Pisacane PI, Lofgren J a, Fitzpatrick VD, et al. (1998) Binding interaction of the heregulinbeta egf domain with ErbB3 and ErbB4 receptors assessed by alanine scanning mutagenesis. J Biol Chem 273: 11667–11674. Available: http://www.ncbi.nlm.nih.gov/pubmed/9565587.

298. Zhang F, Crise B, Su B, Hou Y, Rose JK, et al. (1991) Lateral diffusion of membrane-spanning and glycosylphosphatidylinositol-linked proteins: toward establishing rules governing the lateral mobility of membrane proteins. J Cell Biol 115: 75–84. Available: http://www.pubmedcentral.nih.gov/articlerender.fcgi?artid=2289918&tool=pmcentrez&rendertype=abstract.

299. Umemura YM, Vrljic M, Nishimura SY, Fujiwara TK, Suzuki KGN, et al. (2008) Both MHC class II and its GPI-anchored form undergo hop diffusion as observed by single-molecule

tracking. Biophys J 95: 435–450. Available: http://www.pubmedcentral.nih.gov/articlerender.fcgi?artid=2426619&tool=pmcentrez&rendertype=abstract. Accessed 10 April 2014.

300. Selvin Ha, T. PR (2007) Single-Molecule Techniques: A Laboratory Manual.

301. Roy R, Hohng S, Ha T (2008) A practical guide to single-molecule FRET. Nat Methods 5: 507–516. Available: http://www.ncbi.nlm.nih.gov/pubmed/18511918. Accessed 27 August 2013.

302. Ruoslahti E (1996) RGD and other recognition sequences for integrins. Annu Rev Cell Dev Biol 12: 697–715. Available: http://www.ncbi.nlm.nih.gov/pubmed/8970741.

303. Groll J, Fiedler J, Engelhard E, Ameringer T, Tugulu S, et al. (2005) A novel star PEG-derived surface coating for specific cell adhesion. J Biomed Mater Res A 74: 607–617. Available: http://www.ncbi.nlm.nih.gov/pubmed/16035061. Accessed 7 October 2011.

304. Kyte J, Doolittle RF (1982) A simple method for displaying the hydropathic character of a protein. J Mol Biol 157: 105–132. Available: http://www.ncbi.nlm.nih.gov/pubmed/7108955.

305. Ikai A (1980) Extraction of the apo B cluster from human low density lipoprotein with Tween 80. J Biochem 88: 1349–1357. Available: http://www.ncbi.nlm.nih.gov/pubmed/7462184.

306. Shekaran A, Garcia AJ (2011) Nanoscale engineering of extracellular matrix-mimetic bioadhesive surfaces and implants for tissue engineering. Biochim Biophys Acta 1810: 350–360. Available: http://www.ncbi.nlm.nih.gov/pubmed/20435097. Accessed 5 August 2011.

307. Graf J, Ogle RC, Robey FA, Sasaki M, Martin GR, et al. (1987) A pentapeptide from the laminin B1 chain mediates cell adhesion and binds the 67,000 laminin receptor. Biochemistry 26: 6896–6900. Available: http://www.ncbi.nlm.nih.gov/pubmed/2962631.

308. Xiao Z, Zhang W, Yang Y, Xu L, Fang X (2008) Single-molecule diffusion study of activated EGFR implicates its endocytic pathway. Biochem Biophys Res Commun 369: 730–734. Available: http://www.ncbi.nlm.nih.gov/pubmed/18313398. Accessed 10 August 2011.

309. Lajoie P, Partridge EA, Guay G, Goetz JG, Pawling J, et al. (2007) Plasma membrane domain organization regulates EGFR signaling in tumor cells. J Cell Biol 179: 341–356. Available: http://www.pubmedcentral.nih.gov/articlerender.fcgi?artid=2064769&tool=pmcentrez&rendertype=abstract. Accessed 9 March 2012.

310. Orr G, Hu D, Ozçelik S, Opresko LK, Wiley HS, et al. (2005) Cholesterol dictates the freedom of EGF receptors and HER2 in the plane of the membrane. Biophys J 89: 1362–1373. Available:

http://www.pubmedcentral.nih.gov/articlerender.fcgi?artid=1366621&tool=pmcentrez&rendertype=abstract. Accessed 17 June 2011.

311. Balbis A, Posner BI (2010) Compartmentalization of EGFR in cellular membranes: role of membrane rafts. J Cell Biochem 109: 1103–1108. Available: http://www.ncbi.nlm.nih.gov/pubmed/20143338. Accessed 15 November 2011.

312. Pike LJ (2005) Growth factor receptors, lipid rafts and caveolae: an evolving story. Biochim Biophys Acta 1746: 260–273. Available: http://www.ncbi.nlm.nih.gov/pubmed/15951036. Accessed 13 March 2012.

313. Lajoie P, Goetz JG, Dennis JW, Nabi IR (2009) Lattices, rafts, and scaffolds: domain regulation of receptor signaling at the plasma membrane. J Cell Biol 185: 381–385. Available: http://www.pubmedcentral.nih.gov/articlerender.fcgi?artid=2700393&tool=pmcentrez&rendertype=abstract. Accessed 13 November 2012.

314. García AJ, Garcia AJ (2005) Get a grip: integrins in cell-biomaterial interactions. Biomaterials 26: 7525–7529. Available: http://www.ncbi.nlm.nih.gov/pubmed/16002137. Accessed 17 June 2011.

315. Brodbeck WG, Shive MS, Colton E, Nakayama Y, Matsuda T, et al. (2001) Influence of biomaterial surface chemistry on the apoptosis of adherent cells. J Biomed Mater Res 55: 661–668. Available: http://www.ncbi.nlm.nih.gov/pubmed/11288096.

316. Brodbeck WG, Patel J, Voskerician G, Christenson E, Shive MS, et al. (2002) Biomaterial adherent macrophage apoptosis is increased by hydrophilic and anionic substrates in vivo. Proc Natl Acad Sci U S A 99: 10287–10292. Available: http://www.ncbi.nlm.nih.gov/pubmed/12122211.

317. García AJ, Vega MD, Boettiger D (1999) Modulation of cell proliferation and differentiation through substrate-dependent changes in fibronectin conformation. Mol Biol Cell 10: 785–798. Available: http://www.ncbi.nlm.nih.gov/pubmed/10069818.

318. Shen M, Horbett TA (2001) The effects of surface chemistry and adsorbed proteins on monocyte/macrophage adhesion to chemically modified polystyrene surfaces. J Biomed Mater Res 57: 336–345. Available: http://www.ncbi.nlm.nih.gov/pubmed/11523028.

319. McClary KB, Ugarova T, Grainger DW (2000) Modulating fibroblast adhesion, spreading, and proliferation using self-assembled monolayer films of alkylthiolates on gold. J Biomed Mater Res 50: 428–439. Available: http://www.ncbi.nlm.nih.gov/pubmed/10737886.

320. Keselowsky BG, Collard DM, García AJ (2005) Integrin binding specificity regulates biomaterial surface chemistry effects on cell differentiation. Proc Natl Acad Sci U S A 102: 5953–5957. Available: http://www.pnas.org/cgi/content/abstract/102/17/5953. Accessed 6 November 2011.

321. Sofia S, Premnath V, Merrill E (1998) Poly(ethylene oxide) Grafted to Silicon Surfaces: Grafting Density and Protein Adsorption. Macromolecules 31: 5059–5070. Available: http://www.ncbi.nlm.nih.gov/pubmed/9680446. Accessed 2 November 2011.

322. Zhu J (2010) Bioactive modification of poly(ethylene glycol) hydrogels for tissue engineering. Biomaterials 31: 4639–4656. Available: http://www.pubmedcentral.nih.gov/articlerender.fcgi?artid=2907908&tool=pmcentrez&rendertype=abstract. Accessed 20 July 2012.

323. Wattendorf U, Merkle HP (2008) PEGylation as a tool for the biomedical engineering of surface modified microparticles. J Pharm Sci 97: 4655–4669. Available: http://www.ncbi.nlm.nih.gov/pubmed/18306270. Accessed 20 July 2012.

324. Harris JM, Zalipsky S, editors (1997) Poly(ethylene glycol). Washington, DC: American Chemical Society. Available: http://dx.doi.org/10.1021/bk-1997-0680. Accessed 4 September 2013.

325. Nakao A, Nagaoka S, Mori Y (1987) Hemocompatibility of hydrogel with polyethyleneoxide chains. J Biomater Appl 2: 219–234. Available: http://www.ncbi.nlm.nih.gov/pubmed/3504973.

326. Tessmar JK, Göpferich AM (2007) Customized PEG-derived copolymers for tissue-engineering applications. Macromol Biosci 7: 23–39. Available: http://www.ncbi.nlm.nih.gov/pubmed/17195277. Accessed 20 July 2012.

327. Zhou HX, Rivas G, Minton AP (2008) Macromolecular crowding and confinement: biochemical, biophysical, and potential physiological consequences. Annu Rev Biophys 37: 375–397. Available: http://www.ncbi.nlm.nih.gov/pubmed/18573087.

328. Folgiero V, Avetrani P, Bon G, Di Carlo SE, Fabi A, et al. (2008) Induction of ErbB-3 expression by alpha6beta4 integrin contributes to tamoxifen resistance in ERbeta1-negative breast carcinomas. PLoS One 3: e1592. Available: http://www.ncbi.nlm.nih.gov/pubmed/18270579.

329. Yao JZ, Uttamapinant C, Poloukhtine A, Baskin JM, Codelli JA, et al. (2012) Fluorophore targeting to cellular proteins via enzyme-mediated azide ligation and strain-promoted cycloaddition. J Am Chem Soc 134: 3720–3728. Available: http://www.ncbi.nlm.nih.gov/pubmed/22239252.

330. Atto 647N Data Sheet (n.d.). Available: https://www.atto-tec.com/attotecshop/product_info.php?language=en&info=p114_ATTO-674N.html.

331. Panchuk-Voloshina N, Haugland RP, Bishop-Stewart J, Bhalgat MK, Millard PJ, et al. (1999) Alexa dyes, a series of new fluorescent dyes that yield exceptionally bright, photostable conjugates. J Histochem Cytochem 47: 1179–1188. Available: http://www.ncbi.nlm.nih.gov/pubmed/10449539.

332. Hovius Guignet, E., Segura, J.-M., Piguet, J., Vogel, H., Bäumle, M. NV - 8 R (2006) Single Molecule Detection with Atto 647N NTA. BioFiles 1.3.

333. Biotium Inc. (2012) CF Dye Q&A: 3–5. Available: https://us.vwr.com/stibo/hi_res/CF_Dye_FAQ_Datasheet.pdf.

334. Biotium Inc. (2012) CF Dyes Selection Guide.

335. Kolmogorov A (1933) On the empirical determination of a distribution function. (Italian). G dell'Instituto Ital degli Attuari 4: 83–91.

336. Smirnov N (1939) On the estimation of the discrepancy between empirical curves of distribution for two independent samples. (Russian). Bull Moscow Univ 2: 3–16.

337. Livneh E, Benveniste M, Prywes R, Felder S, Kam Z, et al. (1986) Large deletions in the cytoplasmic kinase domain of the epidermal growth factor receptor do not affect its laternal mobility. J Cell Biol 103: 327–331. Available: http://www.ncbi.nlm.nih.gov/pubmed/3015981.

338. Benveniste M, Livneh E, Schlessinger J, Kam Z (1988) Overexpression of epidermal growth factor receptor in NIH-3T3-transfected cells slows its lateral diffusion and rate of endocytosis. J Cell Biol 106: 1903–1909. Available: http://www.ncbi.nlm.nih.gov/pubmed/3133376.

339. Danglot L, Chaineau M, Dahan M, Gendron MC, Boggetto N, et al. (2010) Role of TI-VAMP and CD82 in EGFR cell-surface dynamics and signaling. J Cell Sci 123: 723–735. Available: http://www.ncbi.nlm.nih.gov/pubmed/20144992.

340. Adkins EM, Samuvel DJ, Fog JU, Eriksen J, Jayanthi LD, et al. (2007) Membrane mobility and microdomain association of the dopamine transporter studied with fluorescence correlation spectroscopy and fluorescence recovery after photobleaching. Biochemistry 46: 10484–10497. Available: http://www.ncbi.nlm.nih.gov/pubmed/17711354.

341. Keating E, Nohe A, Petersen NO (2008) Studies of distribution, location and dynamic properties of EGFR on the cell surface measured by image correlation spectroscopy. Eur Biophys J 37: 469–481. Available: http://www.ncbi.nlm.nih.gov/pubmed/18043914. Accessed 30 August 2011.

342. Kannan B, Guo L, Sudhaharan T, Ahmed S, Maruyama I, et al. (2007) Spatially resolved total internal reflection fluorescence correlation microscopy using an electron multiplying charge-coupled device camera. Anal Chem 79: 4463–4470. Available: http://www.ncbi.nlm.nih.gov/pubmed/17489557.

343. Haugland RP (2001) Antibody conjugates for cell biology. Curr Protoc Cell Biol Chapter 16: Unit 16.5. Available: http://www.ncbi.nlm.nih.gov/pubmed/18228336.

344. Ogawa M, Kosaka N, Choyke PL, Kobayashi H (2009) In vivo molecular imaging of cancer with a quenching near-infrared fluorescent probe using conjugates of monoclonal antibodies and indocyanine green. Cancer Res 69: 1268–1272. Available: http://www.ncbi.nlm.nih.gov/pubmed/19176373.

345. Qi S, Miao Z, Liu H, Xu Y, Feng Y, et al. (2012) Evaluation of Four Affibody-Based Near-Infrared Fluorescent Probes for Optical Imaging of Epidermal Growth Factor Receptor

Positive Tumors. Bioconjug Chem. Available: http://www.ncbi.nlm.nih.gov/pubmed/22621238. Accessed 13 June 2012.

346. Cordes T, Maiser A, Steinhauer C, Schermelleh L, Tinnefeld P (2011) Mechanisms and advancement of antifading agents for fluorescence microscopy and single-molecule spectroscopy. Phys Chem Chem Phys 13: 6699–6709. Available: http://www.ncbi.nlm.nih.gov/pubmed/21311807. Accessed 24 May 2013.

347. Hughes LD, Rawle RJ, Boxer SG (2014) Choose your label wisely: water-soluble fluorophores often interact with lipid bilayers. PLoS One 9: e87649. Available: http://www.pubmedcentral.nih.gov/articlerender.fcgi?artid=3913624&tool=pmcentrez&rendertype=abstract. Accessed 21 March 2014.

348. Xiao Z, Ma X, Jiang Y, Zhao Z, Lai B, et al. (2008) Single-molecule study of lateral mobility of epidermal growth factor receptor 2/HER2 on activation. J Phys Chem B 112: 4140–4145. Available: http://www.ncbi.nlm.nih.gov/pubmed/18324805.

349. Hagen GM, Caarls W, Lidke KA, De Vries AHB, Fritsch C, et al. (2009) Fluorescence recovery after photobleaching and photoconversion in multiple arbitrary regions of interest using a programmable array microscope. Microsc Res Tech 72: 431–440. Available: http://www.pubmedcentral.nih.gov/articlerender.fcgi?artid=3131617&tool=pmcentrez&rendertype=abstract. Accessed 29 August 2013.

350. Beerli RR, Graus-Porta D, Woods-Cook K, Chen X, Yarden Y, et al. (1995) Neu differentiation factor activation of ErbB-3 and ErbB-4 is cell specific and displays a differential requirement for ErbB-2. Mol Cell Biol 15: 6496–6505. Available: http://www.pubmedcentral.nih.gov/articlerender.fcgi?artid=230902&tool=pmcentrez&rendertype=abstract.

351. Hirsch M, Wareham RJ, Martin-Fernandez ML, Hobson MP, Rolfe DJ (2013) A stochastic model for electron multiplication charge-coupled devices--from theory to practice. PLoS One 8: e53671. Available: http://www.pubmedcentral.nih.gov/articlerender.fcgi?artid=3561409&tool=pmcentrez&rendertype=abstract. Accessed 14 August 2013.

352. Weisstein EW (n.d.) Gamma Distribution on MathWorld--A Wolfram Web Resource. Available: http://mathworld.wolfram.com/GammaDistribution.html.

353. Chung SH, Kennedy RA (1991) Forward-backward non-linear filtering technique for extracting small biological signals from noise. J Neurosci Methods 40: 71–86. Available: http://www.ncbi.nlm.nih.gov/pubmed/1795554. Accessed 20 January 2014.

354. Tzahar E, Waterman H, Chen X, Levkowitz G, Karunagaran D, et al. (1996) A hierarchical network of interreceptor interactions determines signal transduction by Neu differentiation factor/neuregulin and epidermal growth factor. … Cell Biol 16: 5276. Available: http://mcb.asm.org/content/16/10/5276.short. Accessed 3 July 2013.

355. Ferguson KM, Darling PJ, Mohan MJ, Macatee TL, Lemmon MA (2000) Extracellular domains drive homo- but not hetero-dimerization of erbB receptors. EMBO J 19: 4632–

4643. Available: http://www.pubmedcentral.nih.gov/articlerender.fcgi?artid=302059&tool=pmcentrez&rendertype=abstract. Accessed 9 August 2013.

356. Vehlow A, Soong D, Vizcay-Barrena G, Bodo C, Law A-L, et al. (2013) Endophilin, Lamellipodin, and Mena cooperate to regulate F-actin-dependent EGF-receptor endocytosis. EMBO J 32: 2722–2734. Available: http://www.pubmedcentral.nih.gov/articlerender.fcgi?artid=3801443&tool=pmcentrez&rendertype=abstract. Accessed 16 December 2013.

357. Hofman EG, Ruonala MO, Bader AN, van den Heuvel D, Voortman J, et al. (2008) EGF induces coalescence of different lipid rafts. J Cell Sci 121: 2519–2528. Available: http://www.ncbi.nlm.nih.gov/pubmed/18628305. Accessed 15 August 2011.

358. Irwin ME, Mueller KL, Bohin N, Ge Y, Boerner JL (2011) Lipid raft localization of EGFR alters the response of cancer cells to the EGFR tyrosine kinase inhibitor gefitinib. J Cell Physiol 226: 2316–2328. Available: http://www.ncbi.nlm.nih.gov/pubmed/21660955. Accessed 21 July 2011.

359. Shankaran H, Wiley HS, Resat H (2006) Modeling the effects of HER/ErbB1-3 coexpression on receptor dimerization and biological response. Biophys J 90: 3993–4009. Available: http://www.pubmedcentral.nih.gov/articlerender.fcgi?artid=1459488&tool=pmcentrez&rendertype=abstract. Accessed 8 August 2011.

360. Hsieh M, Yang S, Raymond-Stinz M (2008) Stochastic simulations of ErbB homo and heterodimerisation: potential impacts of receptor conformational state and spatial segregation. IET Syst Biol 2: 256–272. Available: http://digital-library.theiet.org/content/journals/10.1049/iet-syb_20070073. Accessed 5 September 2013.

361. Huang Y, Rizzo RC (2012) A Water-based Mechanism of Specificity and Resistance for Lapatinib with ErbB Family Kinases. Available: http://www.ncbi.nlm.nih.gov/pubmed/22352796. Accessed 1 March 2012.

362. Burris H a, Hurwitz HI, Dees EC, Dowlati A, Blackwell KL, et al. (2005) Phase I safety, pharmacokinetics, and clinical activity study of lapatinib (GW572016), a reversible dual inhibitor of epidermal growth factor receptor tyrosine kinases, in heavily pretreated patients with metastatic carcinomas. J Clin Oncol 23: 5305–5313. Available: http://www.ncbi.nlm.nih.gov/pubmed/15955900. Accessed 26 May 2013.

363. Yamamoto N, Horiike A, Fujisaka Y, Murakami H, Shimoyama T, et al. (2008) Phase I dose-finding and pharmacokinetic study of the oral epidermal growth factor receptor tyrosine kinase inhibitor Ro50-8231 (erlotinib) in Japanese patients with solid tumors. Cancer Chemother Pharmacol 61: 489–496. Available: http://www.ncbi.nlm.nih.gov/pubmed/17483950. Accessed 4 July 2013.

364. Mukherjee A, Badal Y, Nguyen X-T, Miller J, Chenna A, et al. (2011) Profiling the HER3/PI3K pathway in breast tumors using proximity-directed assays identifies correlations between protein complexes and phosphoproteins. PLoS One 6: e16443.

Available: http://www.pubmedcentral.nih.gov/articlerender.fcgi?artid=3030586&tool=pmcentrez&rendertype=abstract. Accessed 24 September 2013.

365. Gazdar AF, Kurvari V, Virmani A, Gollahon L, Sakaguchi M, et al. (1998) Characterization of paired tumor and non-tumor cell lines established from patients with breast cancer. Int J Cancer 78: 766–774. Available: http://www.ncbi.nlm.nih.gov/pubmed/9833771. Accessed 6 September 2013.

366. Sahin O, Fröhlich H, Löbke C, Korf U, Burmester S, et al. (2009) Modeling ERBB receptor-regulated G1/S transition to find novel targets for de novo trastuzumab resistance. BMC Syst Biol 3: 1. Available: http://www.pubmedcentral.nih.gov/articlerender.fcgi?artid=2652436&tool=pmcentrez&rendertype=abstract. Accessed 21 August 2013.

367. Sahin Ö, Löbke C, Korf U, Appelhans H, Sultmann H, et al. (2007) Combinatorial RNAi for quantitative protein network analysis. Proc … 104: 6579–6584. Available: http://www.pnas.org/content/104/16/6579.short. Accessed 8 September 2013.

368. Song W, Welti R, Hafner-Strauss S, Rintoul D a (1993) Synthesis and characterization of N-parinaroyl analogs of ganglioside GM3 and de-N-acetyl GM3. Interactions with the EGF receptor kinase. Biochemistry 32: 8602–8607. Available: http://www.ncbi.nlm.nih.gov/pubmed/8395211.

369. Pryor MM, Low-Nam ST, Halász ÁM, Lidke DS, Wilson BS, et al. (2013) Dynamic Transition States of ErbB1 Phosphorylation Predicted by Spatial Stochastic Modeling. Biophys J 105: 1533–1543. Available: http://linkinghub.elsevier.com/retrieve/pii/S0006349513009193. Accessed 18 September 2013.

370. Shankaran H, Zhang Y, Tan Y, Resat H (2013) Model-Based Analysis of HER Activation in Cells Co-Expressing EGFR, HER2 and HER3. PLoS Comput Biol 9: e1003201. Available: http://www.ploscompbiol.org/article/info:doi/10.1371/journal.pcbi.1003201#pcbi.1003201.s001. Accessed 20 September 2013.

371. Simons K, Gerl MJ (2010) Revitalizing membrane rafts: new tools and insights. Nat Rev Mol Cell Biol 11: 688–699. Available: http://www.ncbi.nlm.nih.gov/pubmed/20861879. Accessed 2 November 2012.

372. Morone N, Fujiwara T, Murase K, Kasai RS, Ike H, et al. (2006) Three-dimensional reconstruction of the membrane skeleton at the plasma membrane interface by electron tomography. J Cell Biol 174: 851–862. Available: http://jcb.rupress.org/content/174/6/851.full. Accessed 8 August 2013.

373. Pike LJ, Han X, Gross RW (2005) Epidermal growth factor receptors are localized to lipid rafts that contain a balance of inner and outer leaflet lipids: a shotgun lipidomics study. J Biol Chem 280: 26796–26804. Available: http://www.pubmedcentral.nih.gov/articlerender.fcgi?artid=1266279&tool=pmcentrez&rendertype=abstract. Accessed 16 March 2012.

374. Mineo C, James GL, Smart EJ, Anderson RG (1996) Localization of epidermal growth factor-stimulated Ras/Raf-1 interaction to caveolae membrane. J Biol Chem 271: 11930–11935. Available: http://www.ncbi.nlm.nih.gov/pubmed/8662667.

375. Roepstorff K, Thomsen P, Sandvig K, van Deurs B (2002) Sequestration of epidermal growth factor receptors in non-caveolar lipid rafts inhibits ligand binding. J Biol Chem 277: 18954–18960. Available: http://www.ncbi.nlm.nih.gov/pubmed/11886870. Accessed 16 March 2012.

376. Hofman EG, Bader AN, Gerritsen HC, van Bergen En Henegouwen PM (2009) EGF induces rapid reorganization of plasma membrane microdomains. Commun Integr Biol 2: 213–214. Available: http://www.pubmedcentral.nih.gov/articlerender.fcgi?artid=2717522&tool=pmcentrez&rendertype=abstract. Accessed 6 September 2013.

377. Pike LJ, Miller JM (1998) Cholesterol Depletion Delocalizes Phosphatidylinositol Bisphosphate and Inhibits Hormone-stimulated Phosphatidylinositol Turnover. Biochemistry 273: 22298–22304.

378. Ariotti N, Liang H, Xu Y, Zhang Y, Yonekubo Y, et al. (2010) Epidermal growth factor receptor activation remodels the plasma membrane lipid environment to induce nanocluster formation. Mol Cell Biol 30: 3795–3804. Available: http://www.pubmedcentral.nih.gov/articlerender.fcgi?artid=2916403&tool=pmcentrez&rendertype=abstract. Accessed 18 July 2011.

379. Pike LJ, Casey L (2002) Cholesterol levels modulate EGF receptor-mediated signaling by altering receptor function and trafficking. Biochemistry 41: 10315–10322. Available: http://www.ncbi.nlm.nih.gov/pubmed/12162747.

380. Chen X, Resh MD (2002) Cholesterol depletion from the plasma membrane triggers ligand-independent activation of the epidermal growth factor receptor. J Biol Chem 277: 49631–49637. Available: http://www.ncbi.nlm.nih.gov/pubmed/12397069. Accessed 17 November 2011.

381. Ringerike T, Blystad FD, Levy FO, Madshus IH, Stang E (2002) Cholesterol is important in control of EGF receptor kinase activity but EGF receptors are not concentrated in caveolae. J Cell Sci 115: 1331–1340. Available: http://www.ncbi.nlm.nih.gov/pubmed/11884532.

382. Lambert S, Vind-Kezunovic D, Karvinen S, Gniadecki R (2006) Ligand-independent activation of the EGFR by lipid raft disruption. J Invest Dermatol 126: 954–962. Available: http://www.ncbi.nlm.nih.gov/pubmed/16456534. Accessed 13 March 2012.

383. Filosto S, Khan EM, Tognon E, Becker C, Ashfaq M, et al. (2011) EGF receptor exposed to oxidative stress acquires abnormal phosphorylation and aberrant activated conformation that impairs canonical dimerization. PLoS One 6: e23240. Available: http://www.pubmedcentral.nih.gov/articlerender.fcgi?artid=3154401&tool=pmcentrez&rendertype=abstract. Accessed 13 March 2012.

384. Westover EJ, Covey DF, Brockman HL, Brown RE, Pike LJ (2003) Cholesterol depletion results in site-specific increases in epidermal growth factor receptor phosphorylation due to membrane level effects. Studies with cholesterol enantiomers. J Biol Chem 278: 51125–51133. Available: http://www.pubmedcentral.nih.gov/articlerender.fcgi?artid=2593805&tool=pmcentrez&rendertype=abstract. Accessed 16 March 2012.

385. Dietrich C, Yang B, Fujiwara T, Kusumi A, Jacobson K (2002) Relationship of lipid rafts to transient confinement zones detected by single particle tracking. Biophys J 82: 274–284. Available: http://www.pubmedcentral.nih.gov/articlerender.fcgi?artid=1302468&tool=pmcentrez&rendertype=abstract. Accessed 17 July 2012.

386. Ahmad N, Gabius H-J, André S, Kaltner H, Sabesan S, et al. (2004) Galectin-3 precipitates as a pentamer with synthetic multivalent carbohydrates and forms heterogeneous cross-linked complexes. J Biol Chem 279: 10841–10847. Available: http://www.ncbi.nlm.nih.gov/pubmed/14672941. Accessed 12 January 2013.

387. Partridge E a, Le Roy C, Di Guglielmo GM, Pawling J, Cheung P, et al. (2004) Regulation of cytokine receptors by Golgi N-glycan processing and endocytosis. Science 306: 120–124. Available: http://www.ncbi.nlm.nih.gov/pubmed/15459394. Accessed 12 November 2012.

388. Stroop CJ, Weber W, Gerwig GJ, Nimtz M, Kamerling JP, et al. (2000) Characterization of the carbohydrate chains of the secreted form of the human epidermal growth factor receptor. Glycobiology 10: 901–917. Available: http://www.ncbi.nlm.nih.gov/pubmed/10988252. Accessed 22 January 2013.

389. Bouzigues C, Dahan M (2007) Transient directed motions of GABA(A) receptors in growth cones detected by a speed correlation index. Biophys J 92: 654–660. Available: http://www.pubmedcentral.nih.gov/articlerender.fcgi?artid=1751400&tool=pmcentrez&rendertype=abstract. Accessed 10 August 2013.

390. Lidke DS, Lidke KA, Rieger B, Jovin TM, Arndt-Jovin DJ (2005) Reaching out for signals: filopodia sense EGF and respond by directed retrograde transport of activated receptors. J Cell Biol 170: 619–626. Available: http://www.pubmedcentral.nih.gov/articlerender.fcgi?artid=2171515&tool=pmcentrez&rendertype=abstract. Accessed 21 August 2013.

391. Saxton MJ (1997) Single-particle tracking: the distribution of diffusion coefficients. Biophys J 72: 1744–1753. Available: http://www.pubmedcentral.nih.gov/articlerender.fcgi?artid=1184368&tool=pmcentrez&rendertype=abstract. Accessed 13 August 2013.

392. Das R, Cairo CW, Coombs D (2009) A hidden Markov model for single particle tracks quantifies dynamic interactions between LFA-1 and the actin cytoskeleton. PLoS Comput Biol 5: e1000556. Available: http://www.pubmedcentral.nih.gov/articlerender.fcgi?artid=2768823&tool=pmcentrez&rendertype=abstract. Accessed 10 August 2013.

393. Saxton MJ (2008) Single-particle tracking: connecting the dots. Nat Methods 5: 671–672. Available: http://www.ncbi.nlm.nih.gov/pubmed/18668034. Accessed 10 September 2013.

394. Chetverikov D, Verestói J (1999) Feature Point Tracking for Incomplete Trajectories. Computing 62: 321–338. Available: http://link.springer.com/10.1007/s006070050027. Accessed 11 September 2013.

395. Veenman CJ, Reinders MJT, Backer E (2001) Resolving motion correspondence for densely moving points. IEEE Trans Pattern Anal Mach Intell 23: 54–72. Available: http://dl.acm.org/citation.cfm?id=365695.365707. Accessed 11 September 2013.

396. Shafique K, Shah M (2005) A noniterative greedy algorithm for multiframe point correspondence. IEEE Trans Pattern Anal Mach Intell 27: 51–65. Available: http://www.ncbi.nlm.nih.gov/pubmed/15628268. Accessed 11 September 2013.

397. Sbalzarini IF, Koumoutsakos P (2005) Feature point tracking and trajectory analysis for video imaging in cell biology. J Struct Biol 151: 182–195. Available: http://www.ncbi.nlm.nih.gov/pubmed/16043363. Accessed 9 August 2013.

398. Feng L, Xu Y, Yang Y, Zheng X (2011) Multiple dense particle tracking in fluorescence microscopy images based on multidimensional assignment. J Struct Biol 173: 219–228. Available: http://www.ncbi.nlm.nih.gov/pubmed/21073957. Accessed 11 September 2013.

399. Bonneau S, Dahan M, Cohen LD (2005) Single quantum dot tracking based on perceptual grouping using minimal paths in a spatiotemporal volume. IEEE Trans Image Process 14: 1384–1395. Available: http://www.ncbi.nlm.nih.gov/pubmed/16190473. Accessed 11 September 2013.

400. Sage D, Neumann FR, Hediger F, Gasser SM, Unser M (2005) Automatic tracking of individual fluorescence particles: application to the study of chromosome dynamics. IEEE Trans Image Process 14: 1372–1383. Available: http://www.ncbi.nlm.nih.gov/pubmed/16190472. Accessed 11 September 2013.

401. Cutler PJ, Malik MD, Liu S, Byars JM, Lidke DS, et al. (2013) Multi-color quantum dot tracking using a high-speed hyperspectral line-scanning microscope. PLoS One 8: e64320. Available: http://www.pubmedcentral.nih.gov/articlerender.fcgi?artid=3661486&tool=pmcentrez&rendertype=abstract. Accessed 14 August 2013.

402. Jaqaman K, Loerke D, Mettlen M, Kuwata H, Grinstein S, et al. (2008) Robust single-particle tracking in live-cell time-lapse sequences. Nat Methods 5: 695–702. Available: http://www.pubmedcentral.nih.gov/articlerender.fcgi?artid=2747604&tool=pmcentrez&rendertype=abstract. Accessed 10 August 2013.

403. Mamot C, Drummond DC, Greiser U, Hong K, Kirpotin DB, et al. (2003) Epidermal Growth Factor Receptor (EGFR)-targeted Immunoliposomes Mediate Specific and Efficient Drug Delivery to EGFR- and EGFRvIII-overexpressing Tumor Cells. Cancer Res

63: 3154–3161. Available:
http://cancerres.aacrjournals.org/content/63/12/3154.full#F3. Accessed 8 May 2014.

404. Brock R, Hamelers IH, Jovin TM (1999) Comparison of fixation protocols for adherent cultured cells applied to a GFP fusion protein of the epidermal growth factor receptor. Cytometry 35: 353–362. Available: http://www.ncbi.nlm.nih.gov/pubmed/10213201. Accessed 8 May 2014.

405. Casella JF, Flanagan MD, Lin S (1981) Cytochalasin D inhibits actin polymerization and induces depolymerization of actin filaments formed during platelet shape change. Nature 293: 302–305. Available: http://www.ncbi.nlm.nih.gov/pubmed/7196996. Accessed 6 September 2013.

406. MacLean-Fletcher S, Pollard TD (1980) Mechanism of action of cytochalasin B on actin. Cell 20: 329–341. Available: http://www.ncbi.nlm.nih.gov/pubmed/6893016. Accessed 6 September 2013.

407. Morton WM, Ayscough KR, McLaughlin PJ (2000) Latrunculin alters the actin-monomer subunit interface to prevent polymerization. Nat Cell Biol 2: 376–378. Available: http://www.ncbi.nlm.nih.gov/pubmed/10854330. Accessed 14 August 2013.

408. Yarmola EG, Somasundaram T, Boring TA, Spector I, Bubb MR (2000) Actin-latrunculin A structure and function. Differential modulation of actin-binding protein function by latrunculin A. J Biol Chem 275: 28120–28127. Available:
http://www.ncbi.nlm.nih.gov/pubmed/10859320. Accessed 8 August 2013.

409. Kwik J, Boyle S, Fooksman D, Margolis L, Sheetz MP, et al. (2003) Membrane cholesterol, lateral mobility, and the phosphatidylinositol 4,5-bisphosphate-dependent organization of cell actin. Proc Natl Acad Sci U S A 100: 13964–13969. Available:
http://www.pubmedcentral.nih.gov/articlerender.fcgi?artid=283529&tool=pmcentrez&rendertype=abstract.

410. Zieve GW, Turnbull D, Mullins JM, McIntosh JR (1980) Production of large numbers of mitotic mammalian cells by use of the reversible microtubule inhibitor nocodazole. Nocodazole accumulated mitotic cells. Exp Cell Res 126: 397–405. Available:
http://www.ncbi.nlm.nih.gov/pubmed/6153987. Accessed 18 August 2013.

411. Mallavarapu A, Mitchison T (1999) Regulated actin cytoskeleton assembly at filopodium tips controls their extension and retraction. J Cell Biol 146: 1097–1106. Available:
http://www.pubmedcentral.nih.gov/articlerender.fcgi?artid=2169471&tool=pmcentrez&rendertype=abstract. Accessed 11 September 2013.

412. Zicha D, Dobbie IM, Holt MR, Monypenny J, Soong DYH, et al. (2003) Rapid actin transport during cell protrusion. Science 300: 142–145. Available:
http://www.ncbi.nlm.nih.gov/pubmed/12677069. Accessed 11 September 2013.

413. Wilson CA, Tsuchida MA, Allen GM, Barnhart EL, Applegate KT, et al. (2010) Myosin II contributes to cell-scale actin network treadmilling through network disassembly. Nature 465: 373–377. Available:

http://www.pubmedcentral.nih.gov/articlerender.fcgi?artid=3662466&tool=pmcentrez&rendertype=abstract. Accessed 9 August 2013.

414. Bubb MR, Senderowicz AM, Sausville EA, Duncan KL, Korn ED (1994) Jasplakinolide, a cytotoxic natural product, induces actin polymerization and competitively inhibits the binding of phalloidin to F-actin. J Biol Chem 269: 14869–14871. Available: http://www.ncbi.nlm.nih.gov/pubmed/8195116. Accessed 6 September 2013.

415. Bubb MR, Spector I, Beyer BB, Fosen KM (2000) Effects of jasplakinolide on the kinetics of actin polymerization. An explanation for certain in vivo observations. J Biol Chem 275: 5163–5170. Available: http://www.ncbi.nlm.nih.gov/pubmed/10671562. Accessed 6 September 2013.

416. Limouze J, Straight AF, Mitchison T, Sellers JR (2004) Specificity of blebbistatin, an inhibitor of myosin II. J Muscle Res Cell Motil 25: 337–341. Available: http://www.ncbi.nlm.nih.gov/pubmed/15548862. Accessed 11 September 2013.

417. Gowrishankar K, Ghosh S, Saha S, C R, Mayor S, et al. (2012) Active remodeling of cortical actin regulates spatiotemporal organization of cell surface molecules. Cell 149: 1353–1367. Available: http://www.ncbi.nlm.nih.gov/pubmed/22682254. Accessed 9 August 2013.

418. Kusumi A, Ike H, Nakada C, Murase K, Fujiwara T (2005) Single-molecule tracking of membrane molecules: plasma membrane compartmentalization and dynamic assembly of raft-philic signaling molecules. Semin Immunol 17: 3–21. Available: http://www.ncbi.nlm.nih.gov/pubmed/15582485. Accessed 10 November 2012.

419. Fritzsche M, Lewalle A, Duke T, Kruse K, Charras G (2013) Analysis of turnover dynamics of the submembranous actin cortex. Mol Biol Cell 24: 757–767. Available: http://www.ncbi.nlm.nih.gov/pubmed/23345594.

420. Collings DA, Wasteneys GO, Williamson RE (1995) Cytochalasin Rearranges Cortical Actin of the Alga Nitella into Short , Stable Rods. 36: 765–772.

421. Cole BK, Curto M, Chan AW, McClatchey AI (2008) Localization to the cortical cytoskeleton is necessary for Nf2/merlin-dependent epidermal growth factor receptor silencing. Mol Cell Biol 28: 1274–1284. Available: http://www.pubmedcentral.nih.gov/articlerender.fcgi?artid=2258752&tool=pmcentrez&rendertype=abstract. Accessed 18 December 2013.

422. Lazar C, Cresson C, Lauffenburger D, Gill GN (2004) The Na+/H+ exchanger regulatory factor stabilizes epidermal growth factor receptors at the cell surface. Mol Biol Cell 15: 5470–5480. Available: http://www.molbiolcell.org/content/15/12/5470.short. Accessed 14 October 2013.

423. Clapéron a, Guedj N, Mergey M, Vignjevic D, Desbois-Mouthon C, et al. (2012) Loss of EBP50 stimulates EGFR activity to induce EMT phenotypic features in biliary cancer cells. Oncogene 31: 1376–1388. Available: http://www.ncbi.nlm.nih.gov/pubmed/21822312. Accessed 14 October 2013.

424. Yao W, Feng D, Bian W, Yang L, Li Y, et al. (2012) EBP50 inhibits EGF-induced breast cancer cell proliferation by blocking EGFR phosphorylation. Amino Acids 43: 2027–2035. Available: http://www.pubmedcentral.nih.gov/articlerender.fcgi?artid=3472071&tool=pmcentrez&rendertype=abstract. Accessed 14 October 2013.

425. Van Bergen en Henegouwen PM, den Hartigh JC, Romeyn P, Verkleij AJ, Boonstra J (1992) The epidermal growth factor receptor is associated with actin filaments. Exp Cell Res 199: 90–97. Available: http://www.ncbi.nlm.nih.gov/pubmed/1735465. Accessed 6 September 2013.

426. Dominguez R, Holmes KC (2011) Actin structure and function. Annu Rev Biophys 40: 169–186. Available: http://www.pubmedcentral.nih.gov/articlerender.fcgi?artid=3130349&tool=pmcentrez&rendertype=abstract. Accessed 21 May 2013.

427. Bretscher A, Chambers D (2000) ERM-Merlin and EBP50 protein families in plasma membrane organization and function. Annu Rev Cell Dev Biol 16: 113–143. Available: http://www.annualreviews.org/doi/pdf/10.1146/annurev.cellbio.16.1.113. Accessed 21 January 2014.

428. Tsukita S (1999) Cortical Actin Organization: Lessons from ERM (Ezrin/Radixin/Moesin) Proteins. J Biol Chem 274: 34507–34510. Available: http://www.jbc.org/cgi/doi/10.1074/jbc.274.49.34507. Accessed 18 December 2013.

429. Antelmi E, Cardone R a., Greco MR, Rubino R, Di Sole F, et al. (2013) ß1 Integrin Binding Phosphorylates Ezrin at T567 to Activate a Lipid Raft Signalsome Driving Invadopodia Activity and Invasion. PLoS One 8: e75113. Available: http://dx.plos.org/10.1371/journal.pone.0075113. Accessed 1 October 2013.

430. Morrison H, Matzke A, Kastilan T, Pace G, Herrlich P, et al. (2007) Hepatocyte Growth Factor-induced Ras Activation Requires ERM Proteins Linked to Both CD44v6 and F-Actin. 18: 76–83. doi:10.1091/mbc.E06.

431. Hasenauer S, Malinger D, Koschut D, Pace G, Matzke A, et al. (2013) Internalization of Met requires the co-receptor CD44v6 and its link to ERM proteins. PLoS One 8: e62357. Available: http://www.pubmedcentral.nih.gov/articlerender.fcgi?artid=3633891&tool=pmcentrez&rendertype=abstract. Accessed 13 January 2014.

432. Sperka T, Geissler KJ, Merkel U, Scholl I, Rubio I, et al. (2011) Activation of Ras requires the ERM-dependent link of actin to the plasma membrane. PLoS One 6: e27511. Available: http://www.plosone.org/article/metrics/info:doi/10.1371/journal.pone.0027511;jsessionid=2BBB3B0D346257264907CAF94330F138. Accessed 18 December 2013.

433. Geißler KJ, Jung MJ, Riecken LB, Sperka T, Cui Y, et al. (2013) Regulation of Son of sevenless by the membrane-actin linker protein ezrin. Proc Natl Acad Sci U S A 110. Available: http://www.ncbi.nlm.nih.gov/pubmed/24297905. Accessed 15 December 2013.

Appendix

Supplementary Figure S1: Western Blots for HER family receptor activation in response to anti-HER2 Affibody isoforms, anti-HER3 Affibody and NRG1β-MCP

The experiments for the following figure have been performed by Dr Michela Perani from a partner laboratory in Randall's Division, King's College London, and are being reproduced with permission for clarity purposes. They are cited in the body text of the thesis as DR M Perani – personal communication.

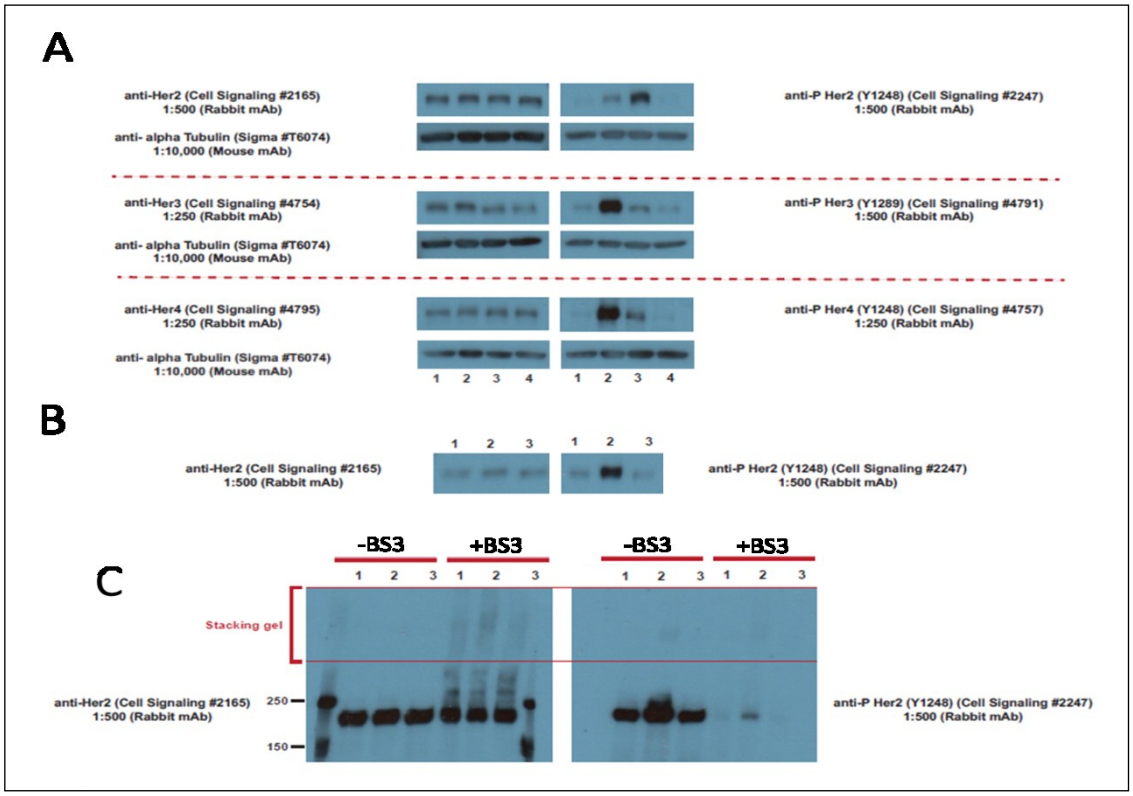

Supplementary Figure 1 - Western blots for receptor activation by anti-HER2 and anti-HER3 Affibodies and NRG1β-MCP. A) 1 = Untreated; 2 = NRG1β-MCP 100 nM; 3 = dimeric anti-HER2 Affibody 1 nM; 4 = anti-HER3 Affibody 1 nM. **B)** 1 = Unstimulated; 2 = dimeric anti-HER2 Affibody 1 nM; 3 = monomeric anti-HER2Aaffibody 1 nM. **C) Cross-linking experiment to determine dimerization potential of anti-HER2 Affibody isoforms.** 1 = Unstimulated; 2 = dimeric anti-HER2 Affibody 1 nM; 3 = monomeric anti-HER2 Affibody 1 nM